

IUPAC Series on Analytical and Physical Chemistry  
of Environmental Systems. Volume 11

---

# Biophysical Chemistry of Fractal Structures and Processes in Environmental Systems

---

*Edited by*

**PROFESSOR NICOLA SENESI**

*Department of Biology and Chemistry, University of Bari, Italy*

**PROFESSOR KEVIN J. WILKINSON**

*Department of Chemistry, University of Montreal, Canada*



A John Wiley and Sons, Ltd, Publication



---

# **Biophysical Chemistry of Fractal Structures and Processes in Environmental Systems**

---

# IUPAC SERIES ON ANALYTICAL AND PHYSICAL CHEMISTRY OF ENVIRONMENTAL SYSTEMS

## Series Editors

**Jacques Buffle**, *University of Geneva, Geneva, Switzerland*

**Herman P. van Leeuwen**, *Wageningen University, Wageningen,  
The Netherlands*

Series published within the framework of the activities of the IUPAC Commission on Fundamental Environmental Chemistry, Division of Chemistry and the Environment.

INTERNATIONAL UNION OF PURE AND APPLIED CHEMISTRY (IUPAC)

Secretariat, PO Box 13757, 104 T.W. Alexander Drive, Building 19,  
Research Triangle Park, NC 27709-3757, USA

Previously published volumes (Lewis Publishers)

**Environmental Particles** Vol. 1 (1992) ISBN 0-87371-589-6

*Edited by Jacques Buffle and Herman P. van Leeuwen*

**Environmental Particles** Vol. 2 (1993) ISBN 0-87371-895-X

*Edited by Jacques Buffle and Herman P. van Leeuwen*

Previously Published volumes (John Wiley & Sons, Ltd)

**Metal Speciation and Bioavailability in Aquatic Systems** Vol. 3 (1995)

ISBN 0-471-95830-1

*Edited by Andre Tessier and David R Turner*

**Structure and Surface Reactions of Soil Particles** Vol. 4 (1998)

ISBN 0-471-95936-7

*Edited by Pan M. Huang, Nicola Senesi and Jacques Buffle*

**Atmospheric Particles** Vol. 5 (1998)

ISBN 0-471-95935-9

*Edited by Roy M. Harrison and Rene E van Grieken*

**In Situ Monitoring of Aquatic Systems** Vol. 6 (2000)

ISBN 0-471-48979-4

*Edited by Jacques Buffle and George Horvai*

**The Biogeochemistry of Iron in Seawater** Vol. 7 (2001)

ISBN 0-471-49068-7

*Edited by David R. Turner and Keith A. Hunter*

**Interactions between Soil Particles and Microorganisms** Vol. 8 (2002)

ISBN 0-471-60790-8

*Edited by Pan M. Huang, Jean-Marc Bollag and Nicola Senesi*

**Physicochemical Kinetics and Transport at Biointerfaces** Vol. 9 (2004)

ISBN 0-471-49845-9

*Edited by Herman P. van Leeuwen and Wolfgang Koster*

**Environmental Colloids and Particles – Behaviour, Separation and Characterisation** Vol. 10 (2006)

ISBN 978-0470-024324

*Edited by Kevin J. Wilkinson and Jamie Lead*

**Biophysical Chemistry of Fractal Structures and Processes in Environmental Systems** Vol. 11 (2008)

ISBN 978-0470-014745

*Edited by Nicola Senesi and Kevin J. Wilkinson*

IUPAC Series on Analytical and Physical Chemistry  
of Environmental Systems. Volume 11

---

# Biophysical Chemistry of Fractal Structures and Processes in Environmental Systems

---

*Edited by*

**PROFESSOR NICOLA SENESI**

*Department of Biology and Chemistry, University of Bari, Italy*

**PROFESSOR KEVIN J. WILKINSON**

*Department of Chemistry, University of Montreal, Canada*



A John Wiley and Sons, Ltd, Publication

Copyright © 2008 IUPAC

Published in 2008 by

John Wiley & Sons Ltd, The Atrium, Southern Gate, Chichester,  
West Sussex PO19 8SQ, England

Telephone (+44) 1243 779777

Email (for orders and customer service enquiries): cs-books@wiley.co.uk

Visit our Home Page on [www.wiley.com](http://www.wiley.com)

All Rights Reserved. No part of this publication may be reproduced, stored in a retrieval system or transmitted in any form or by any means, electronic, mechanical, photocopying, recording, scanning or otherwise, except under the terms of the Copyright, Designs and Patents Act 1988 or under the terms of a licence issued by the Copyright Licensing Agency Ltd, 90 Tottenham Court Road, London W1T 4LP, UK, without the permission in writing of the Publisher. Requests to the Publisher should be addressed to the Permissions Department, John Wiley & Sons Ltd, The Atrium, Southern Gate, Chichester, West Sussex PO19 8SQ, England, or emailed to [permreq@wiley.co.uk](mailto:permreq@wiley.co.uk), or faxed to (+44) 1243 770620.

Designations used by companies to distinguish their products are often claimed as trademarks. All brand names and product names used in this book are trade names, service marks, trademarks or registered trademarks of their respective owners. The Publisher is not associated with any product or vendor mentioned in this book.

This publication is designed to provide accurate and authoritative information in regard to the subject matter covered. It is sold on the understanding that the Publisher is not engaged in rendering professional services. If professional advice or other expert assistance is required, the services of a competent professional should be sought.

The Publisher and the Author make no representations or warranties with respect to the accuracy or completeness of the contents of this work and specifically disclaim all warranties, including without limitation any implied warranties of fitness for a particular purpose. The advice and strategies contained herein may not be suitable for every situation. In view of ongoing research, equipment modifications, changes in governmental regulations, and the constant flow of information relating to the use of experimental reagents, equipment, and devices, the reader is urged to review and evaluate the information provided in the package insert or instructions for each chemical, piece of equipment, reagent, or device for, among other things, any changes in the instructions or indication of usage and for added warnings and precautions. The fact that an organization or Website is referred to in this work as a citation and/or a potential source of further information does not mean that the author or the publisher endorses the information the organization or Website may provide or recommendations it may make. Further, readers should be aware that Internet Websites listed in this work may have changed or disappeared between when this work was written and when it is read. No warranty may be created or extended by any promotional statements for this work. Neither the Publisher nor the Author shall be liable for any damages arising herefrom.

#### **Other Wiley Editorial Offices**

John Wiley & Sons Inc., 111 River Street, Hoboken, NJ 07030, USA

Jossey-Bass, 989 Market Street, San Francisco, CA 94103-1741, USA

Wiley-VCH Verlag GmbH, Boschstr. 12, D-69469 Weinheim, Germany

John Wiley & Sons Australia Ltd, 42 McDougall Street, Milton, Queensland 4064, Australia

John Wiley & Sons (Asia) Pte Ltd, 2 Clementi Loop #02-01, Jin Xing Distripark, Singapore 129809

John Wiley & Sons Canada Ltd, 6045 Freemont Blvd, Mississauga, Ontario L5R 4J3, Canada

Wiley also publishes its books in a variety of electronic formats. Some content that appears in print may not be available in electronic books.

#### **Library of Congress Cataloging in Publication Data**

Senesi, N. (Nicola)

Biophysical chemistry of fractal structures and processes in environmental systems / Nicola Senesi, Kevin Wilkinson.  
p. cm. — (Series on analytical and physical chemistry of environmental systems)

Includes bibliographical references and index.

ISBN 978-0-470-01474-5 (cloth : alk. paper)

1. Physical biochemistry. 2. Fractals. 3. Environmental chemistry.

I. Wilkinson, Kevin J. II. Title.

QD476.2.S36 2008

577'.14—dc22

2008011002

#### **British Library Cataloguing in Publication Data**

A catalogue record for this book is available from the British Library

ISBN 978-0-470-01474-5

Typeset in 10/12pt Times by Integra Software Services Pvt. Ltd, Pondicherry, India

Printed and bound in Great Britain by TJ International Ltd, Padstow, Cornwall

---

# Contents

---

About the Editors	vii
List of Contributors	ix
Series Preface	xi
Preface	xiii
<b>1. Introduction to the Study of Environmental Fractals</b>	<b>1</b>
<i>Nicola Senesi and Kevin J. Wilkinson</i>	
<b>2. Introduction to Fractal Geometry, Fragmentation Processes and Multifractal Measures: Theory and Operational Aspects of their Application to Natural Systems</b>	<b>11</b>
<i>Philippe Baveye, Charles W. Boast, Sarra Gaspard, Ana M. Tarquis and Humberto Millan</i>	
<b>3. Methods and Techniques for Fractal Analysis of Environmental Systems</b>	<b>69</b>
<i>Graeme Bushell</i>	
<b>4. Fractal Structures and Mechanisms in Coagulation/Flocculation Processes in Environmental Systems: Theoretical Aspects</b>	<b>111</b>
<i>Serge Stoll and Silvia Diez</i>	
<b>5. Fractal Mechanisms in Coagulation/Flocculation Processes in Environmental Systems</b>	<b>149</b>
<i>Jean Yves Bottero, Armand Masion and Jérôme Rose</i>	
<b>6. Fractal Approach to Adsorption/Desorption Processes on Environmental Surfaces</b>	<b>179</b>
<i>Zofia Sokołowska and Stefan Sokołowski</i>	
<b>7. Applications of Fractals in the Study of Humic Materials</b>	<b>221</b>
<i>James A. Rice</i>	
<b>8. Fractal Geometry and Microorganisms in the Environment</b>	<b>239</b>
<i>Lynne Boddy and Damian P. Donnelly</i>	
<b>9. Fractal Geometry of Aerosol Particles</b>	<b>273</b>
<i>Ian Colbeck</i>	
Index	317





---

## About the Editors

---



**Nicola Senesi** is Professor of Soil Chemistry and Head of the Department of Agroforestral and Environmental Biology and Chemistry of the University of Bari, Italy, where he has been actively involved in research and teaching since 1969. He has taught courses in Soil Chemistry, Soil Science, Agricultural Chemistry, Wood Chemistry and Technology, Organic Chemistry, and General and Inorganic Chemistry. He has been a visiting professor and/or scientist for various periods at universities in Canada, USA, Somalia, Indonesia, Switzerland, Argentina, Brasil, Venezuela and Colombia. Dr. Senesi is a Fellow of the American Society of Agronomy (ASA) since 1995 and the Soil Science Society of America (SSSA) since 1996, and received the Gold Medal of the

Polish Soil Science Society in 1994. He was conferred with a Doctorate Honoris Causa by the Institute National Polytechnique de Toulouse (INPT), France, in 2000. Dr. Senesi is currently President of Division VI: Chemistry and the Environment and Chair of the Subcommittee on Biophysico-Chemical Processes in Environmental Systems of IUPAC, President of MESAEP, and Vice-President of the Italian Soil Science Society (SISS), and was President of the International Humic Substances Society (IHSS) and Chairman of Division II-Soil Properties and Processes of the International Union of Soil Science (IUSS). He is currently an Associate Editor of *Geoderma*, *Soil Science*, *Pedosphere*, *Pure and Applied Chemistry* and *CLEAN-Soil, Air, Water*. Dr. Senesi's research is focused on fundamental and applied aspects of the chemistry and biochemistry of organic matter from soils and other systems and materials, and its interactions with soil-applied organic chemicals and trace metals, by the use of advanced physico-chemical techniques and biochemical tools. Specific topics of research include the abiotic interactions of herbicides and endocrine disruptors with humic substances, the complexation mechanisms between trace metals of agricultural and environmental importance and natural and artificial humic materials, the physiological and antimutagenic effects of humic substances on plants, and the implications of recycling organic wastes on soil fertility and crop production. He is also pioneering the application of fractal geometry to the study of molecular conformation and aggregation processes of natural soil organic colloids. The results of his research are documented in about 300 scientific and technical papers and about 60 book chapters and invited reviews. Dr. Senesi has also co-edited 12 books and Proceedings Volumes.



**Kevin J. Wilkinson** received a PhD in Environmental Chemistry from the National Water Research Institute of the University of Quebec (*INRS-Eau*) in 1993. Following his PhD, he joined the research group of Professor Jacques Buffle at the University of Geneva where he began to examine some of the important biophysical properties of environmental biopolymers and colloids. Following the establishment of his own research group in 1994, he focused his research onto relating the structure of environmental colloids and aggregates to their function in addition to initiating a research programme designed to develop a fundamental understanding of the chemical mechanisms of contaminant bioavailability. In 2005, he was

appointed Associate Professor of Chemistry at the University of Montreal. His teaching includes (bio)analytical and environmental chemistry. His current research interests include: (i) improving our understanding of the role(s) of microorganisms on the biophysicochemistry of trace elements and colloids; (ii) development and optimisation of novel analytical techniques for quantifying bioavailability and colloidal/aggregate structure; (iii) characterising environmental biopolymers; and (iv) determining the role of diffusion in complex environmental media (biofilms, flocs, sediments). He is currently member of the editorial board of *Environmental Chemistry* and titular member of the IUPAC Chemistry and Environment Division.

He also was editor for the previous volume in the IUPAC series on Analytical and Physical Chemistry of Environmental Systems (vol. 10): *Environmental Colloids and Particles: Behaviour, Separation and Characterisation*.

---

# List of Contributors

---

**Philippe Baveye**

*SIMBIOS Centre, University of Abertay Dundee, Kidd Building, Bell Street, Dundee DD1 1HG, UK.*

**Charles W. Boast**

*Department of Natural Resources and Environmental Sciences, University of Illinois at Urbana-Champaign, 1102 South Goodwin Avenue, Urbana, IL 61801, USA*

**Lynne Boddy**

*Cardiff School of Biosciences, Cardiff University Biomedical Building, Museum Avenue, Cardiff, CF10 3US, UK*

**Jean Yves Bottero**

*CEREGE UMR 6635 CNRS-UPCAM, Europole de l'Arbois, BP 80, 13545 Aix-en-Provence, Cedex 04, France*

**Graeme Bushell**

*School of Chemical Sciences and Engineering, The University of New South Wales, UNSW Sydney NSW 2052, Australia*

**Ian Colbeck**

*Department of Biological Sciences, University of Essex, Colchester CO4 3SQ, UK*

**Silvia Diez**

*CIEMAT, Avda. Complutense 22, 28040, Madrid, Spain*

**Damian P. Donnelly**

*Cardiff School of Biosciences, Cardiff University Biomedical Building, Museum Avenue, Cardiff, CF10 3US, UK*

**Sarra Gaspard**

*Laboratoire COVACHIMM EA3592, Département de Chimie, UFR des Sciences Exactes et Naturelles, Université des Antilles et de la Guyane, BP 250, Campus Fouillole, Pointe-à-Pitre, 97159 GUADELOUPE, FWI (French West Indies)*

**Armand Masion**

*CEREGE UMR 6635 CNRS-UPCAM, Physical Chemistry, Europole de l'Arbois, BP 80, 13545 Aix-en-Provence, Cedex 04, France*

**Humberto Millan**

*Department of Basic Science, Universidad de Granma, Apdo 21, Bayamo, Granma 85100, Cuba*

**James A. Rice**

*Department of Chemistry and Biochemistry, South Dakota State University, Box 2202, Brookings, SD 57007-0896*

**Jérôme Rose**

*CEREGE UMR 6635 CNRS-UPCAM, Europole de l'Arbois, BP 80, 13545 Aix-en-Provence, Cedex 04, France*

**Nicola Senesi**

*Dipartimento di Biologia e Chimica Agro-Forestale ed Ambientale, Università degli Studi di Bari, Via Amendola 165/A, 70126-Bari, Italy*

**Zofia Sokołowska**

*Institute of Agrophysics, Polish Academy of Sciences, Doświadczalna 4, 20290 Lublin, Poland*

**Stefan Sokołowski**

*Department for the Modelling of Physico-Chemical Processes, Marie Curie-Skłodowska University, 20031 Lublin, Poland*

**Serge Stoll**

*Department of Inorganic, Analytical and Applied Chemistry CABB, University of Geneva, Sciences II, 30 Quai Ernest Ansermet, CH-1211 Geneva 4/Switzerland*

**Ana M. Tarquis**

*Department of Applied Mathematics to Agriculture Engineering, E.T.S. de Ingenieros Agrónomos, Universidad Politécnica de Madrid, Ciudad Universitaria s.n. 28040 Madrid, Spain*

**Kevin J. Wilkinson**

*Département de Chimie, Analytique et Biophysicochimie, Université de Montréal, C.P. 6128, Montréal, QC, H3C 3J7, Canada*

---

# Series Preface

---

The main purpose of the IUPAC Series on Analytical and Physical Chemistry of Environmental Systems is to make chemists, biologists, physicists and other scientists aware of the most important biophysicochemical conditions and processes that define the behaviour of environmental systems. The various volumes of the Series thus emphasise the fundamental concepts of environmental processes, taking into account specific aspects such as physical and chemical heterogeneity, and interaction with the biota. Another major goal of the series is to discuss the analytical tools that are available, or should be developed, to study these processes. Indeed, there still seems to be a great need for methodology developed specifically for the field of analytical/physical chemistry of the environment.

The present volume of the series focuses on the use of fractal geometry to provide a quantitative description of disordered systems. By their very nature, environmental systems are disordered and are thus obvious candidates for quantitative description using fractal dimensions. In addition, the physical, chemical and biological properties and processes of natural systems can be described using a fractal approach. This includes the quantification of aggregate structures in air, water, soils and sediments; flow through porous media; distributions of organisms, adsorption phenomena and reaction kinetics. This volume was realised within the framework of the activities of the IUPAC Division of Chemistry and the Environment. We thank the IUPAC officers responsible, especially the executive director, Dr John Jost, for their support and assistance. Support from IUPAC provided the means to organize the discussion meeting of chapter authors (Bari, Italy, 2007), which formed such an essential step in the preparation and harmonisation of the various chapters of this book.

Jacques Buffle and Herman P. van Leeuwen  
Series Editors



---

# Preface

---

Fractal geometry provides a powerful approach for the quantitative description of disordered systems. In addition, it is useful for describing the processes that lead to the formation of such complex, highly irregular and random systems and their physical behaviour.<sup>1</sup> Fractals treat disorder as an intrinsic phenomenon that is described in terms of a nonintegral dimension with a degree of irregularity that is independent of scale. In weakly disordered systems, the disorder disappears as progressively smaller or larger length scales are probed, whereas there is repetition of the disorder at all length scales in strongly disordered systems. A large number of analytical techniques (light, X-ray and neutron scattering techniques; light, X-ray and electron microscopy; sedimentation and particle counting techniques; etc.) are now available to probe this repetitive disorder.

In the natural environment, there is a great need to describe complex physico-chemical systems and processes *quantitatively*. By their very nature, environmental systems are disordered and, thus, are perfect candidates for quantitative description using fractal dimensions. Indeed, many natural objects have been shown to be fractal, including star constellations, clouds, coastlines, trees, snowflakes, brain circumvolutions, proteins, cellulose, colloidal aggregates, several minerals and clays, limestones and sandstones, sediments, soils, and their organic, mineral and microbial components. In addition, the physical, chemical and biological properties and processes of natural systems may be described using a fractal approach. This includes the quantification of aggregate structures in air, water, soils and sediments; flow through porous media; distributions of organisms, adsorption phenomena and reaction kinetics.

An 'ideal' or 'regular' fractal structure exhibits 'self-similarity' over all characterization length scales, i.e. the structure can be decomposed into smaller copies of itself, so that when any portion of the structure is magnified it will appear identical to a larger part. Since natural structures tend to be self-similar over only a finite range of length scales,<sup>2</sup> they are most often referred to as 'random' fractals.

The notion of fractals can be used to describe very diverse objects according to the property of interest. In the natural sciences, a large number of physical properties and processes will depend upon the scaling behaviour of the mass, surface and pore spaces of the system (Figure 1). If the mass and the surface area scale in the same

---

<sup>1</sup> Mandelbrot, B.B. (1982). *The Fractal Geometry of Nature*. W.H. Freeman, New York.

<sup>2</sup> Pfeifer, P. and Obert, M. (1989). Fractals: basic concepts and terminology. In *The Fractal Approach to Heterogeneous Chemistry*, Avnir, D. (ed.). John Wiley and Sons, Ltd.

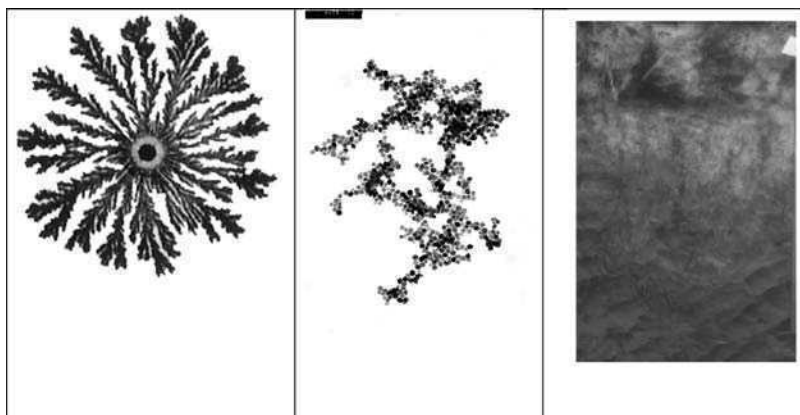


**Figure 1** Different fractals considered in environmental sciences. (a) Surface fractal: colony of *Bacillus subtilis* on agar; see Figure 8.3 for more details. (b) Mass fractal: aggregate of hematite particles formed at pH 4, ionic strength 150 mM, in the presence of natural organic matter of  $[C] = 2.8 \text{ mg dm}^{-3}$ ; see Chapters 4 and 5 for more details on aggregation processes. (c) Pore fractals: soil profile in which a (darker) preferential pathway is visible; see Figure 2.21 for more details.

manner, then the system is considered a mass fractal; if the pore space and the surface follow the same scaling law, then the system is a pore fractal; and if only the surface is fractal, then the system is considered a surface fractal. Each system can be represented by a three-dimensional network that divides the system on the basis of its distribution of mass, surface or pore sites. Although the different fractal dimensions are not always distinguished in the literature (again contributing to some of the confusion), an attempt has been made in this volume to distinguish clearly the different measurements (even when it was not made clear in the original reference!).

As a result of its practical utility for examining natural systems, fractal theory has developed in the geophysical, soil and atmospheric sciences, although little critical discussion has attempted to relate the different fields. The use of fractal concepts by scientists from very different disciplines and backgrounds has resulted in some confusion in the literature with respect to the meaning of the term fractal, nearly always resulting in unwarranted confusion, but also occasionally leading to unsound science. One of the objectives of this book is to reduce the confusion resulting from such a broad use of this important approach to the quantification of disorder. Specifically, the book was written in order: (i) to provide an introduction to the theory of environmental fractals (Chapters 1 and 2); (ii) to summarize the available techniques for quantifying fractal structures in environmental systems (Chapter 3); (iii) to describe how the fractal approach can be employed to describe environmental processes such as coagulation, flocculation, adsorption and desorption (Chapters 4–6); and (iv) to describe critically a number of important environmental applications of fractal analysis (humic substances, Chapter 7; microorganisms, Chapter 8; aerosols, Chapter 9).



In this volume, as for the other volumes in the series, the goal is to provide a critical review of the literature and a thorough explanation of the most important physico-chemical processes. This book is the result of the efforts of a number of authors, collaborators and students. The International Union of Pure and Applied Chemistry (IUPAC) provided much of the structure and funding, through the Division of Chemistry and the Environment, which allowed this project come to fruition. The role of the series editors, Professor H.P. van Leeuwen and Professor J. Buffle, is also greatly appreciated.

**N. Senesi**

*Dipartimento di Biologia e Chimica Agro-Forestale ed  
Ambientale Università degli Studi di Bari*

**K.J. Wilkinson**

*Department of Chemistry, Université de Montréal*



---

# 1 Introduction to the Study of Environmental Fractals

---

Nicola Senesi<sup>1</sup> and Kevin J. Wilkinson<sup>2</sup>

<sup>1</sup> *Dipartimento di Biologia e Chimica Agro-Forestale ed Ambientale, Università degli Studi di Bari, Via Amendola 165/A, 70126-Bari, Italy*

<sup>2</sup> *Department of Chemistry, Université de Montréal, C.P. 6128, Montréal, QC, H3C 3J7, Canada*

## 1.1 INTRODUCTION

Fractal geometry provides a powerful approach for the quantitative description of complex, highly irregular and random, i.e. disordered systems [1]. Moreover, it can be used to describe the processes leading to the formation of such systems and their physical behavior. Fractal geometry relates to structures that cannot be described by Euclidean whole number dimensions of 1 (straight lines), 2 (flat surfaces) or 3 (volumes), but instead have fractional dimensions. Surface structures can have fractal dimensions between 1 and 2 (a completely filled plane) and objects with volume can have fractal dimensions up to 3. The degree of irregularity of fractal structures is independent of scale and, thus, when they are examined under increasing magnification, more and more irregularities come into view. ‘Ideal’ or ‘regular’ fractal structures exhibit ‘self-similarity’, i.e. the structure can be broken down into smaller copies of itself. In other words, when any portion of the structure is magnified, it will appear identical to a larger part over all characterization length scales. Natural structures tend to be self-similar only over a finite range of length scales [2]. Nonetheless, since they are more closely described by fractal rather than Euclidean geometry, they are designated ‘random’ fractals. Indeed, fractal concepts have been shown to be useful to describe a large number of natural objects/systems and their physical, chemical and biological properties, including constellations, clouds, coastlines, trees, snowflakes, brain circumvolutions, proteins, colloidal aggregates, cellulose, several minerals and clays, sediments, soils and their organic, mineral and microbial components [e.g. 3–13].

## 1.2 NATURAL FRACTALS

Mathematical or nonrandom fractals are scale invariant, i.e. the pattern is the same at all scales (self-similar). Natural, real or random fractals are ‘quasi’ or ‘statistically’ self-similar over a finite length scale that is most often determined by the characterization technique that is employed. An object or process can be classified as fractal when the length scale of the property being measured covers at least one order of magnitude. Fractal structures obey a power law, allowing the fractal dimension  $D$  to be determined from experimental data:

$$p \propto v^\gamma \quad (1.1)$$

where  $p$  is the property of interest,  $v$  is the variable being measured and  $\gamma$  is an exponent that can be related to  $D$ . For example, in Figure 1.1, the dark area is a two-dimensional representation of a natural structure, e.g. a soil particle or microbial colony, with an area  $A(s)$ . The area can be estimated by counting the number of cells of size  $s^2$  that are required to cover the object. For a fractal object

$$A(s) \propto s^{2-D} \quad (1.2)$$

$D$  can be estimated by making measurements using different values of  $s$ .

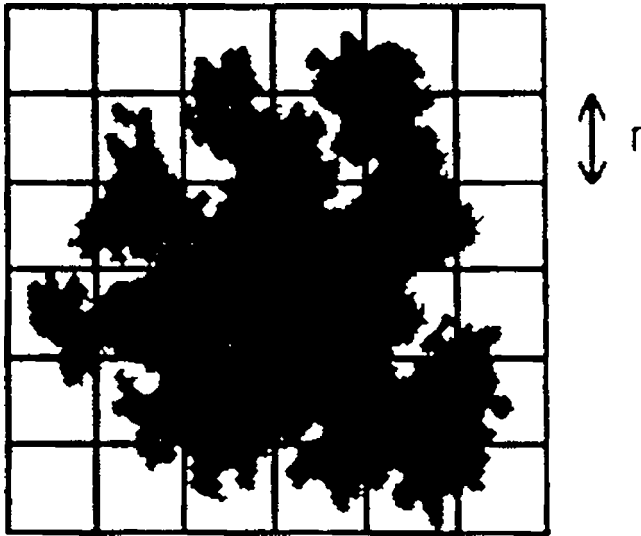


**Figure 1.1** A fractal structure overlaid by a grid of squares. In three dimensions the squares are replaced by boxes. Surface, mass and pore fractal dimensions can be estimated by counting the number of squares occupied by the object. Two-dimensional images of three-dimensional objects do not contain the full information about the object, so fractal dimensions of three-dimensional objects need to be estimated in three dimensions [11]. Reproduced with permission of John Wiley & Sons, Ltd.

### 1.3 MASS, SURFACE AND PORE FRACTALS

Environmental particles, microbial colonies, and even patterns of movement of organisms can be characterized in terms of several different fractal dimensions [14] (Table 1.1). The fractal dimension of the surface  $D_S$  (boundary/interface) of a solid structure is obviously an important characteristic, but many of the physical properties of solids also depend on the scaling behavior of the entire solid and/or of its pores. Systems where surface and mass scale similarly are termed ‘mass fractal’ systems, those where surface and the pore volumes scale similarly are described as ‘pore fractals’ and systems where only the surface is fractal are designated as ‘surface fractals’ (Table 1.1; Figure 1.2).

**Table 1.1** Classification of fractal objects based on surface ( $D_S$ ), mass ( $D_M$ ) and pore ( $D_P$ ) fractal dimensions [14]. Reproduced with permission of Academic Press, London

Classification	$D_S$	$D_M$	$D_P$	Characteristics
Surface fractal	$D^a$	$d^b$	$d$	The interface is fractal, but the actual object and the pore are not fractal
Mass fractal	$D$	$D$	$d$	Interface and the actual object are fractal
Pore fractal	$D$	$d$	$D$	Interface and pore structure are fractal

<sup>a</sup>  $D$ : general fractal dimension.

<sup>b</sup>  $d$ : Euclidean dimension of embedding space (i.e. 1, 2 or 3 respectively in one-, two- or three-dimensional systems).

As an example, consider the situation where a structure is overlaid by a grid. The underlying sites can be categorized as mass sites (occupied sites), surface sites (occupied sites with adjacent empty sites) or pore (empty) sites (Figure 1.2). In order to determine the fractal dimension, it is necessary to quantify the number of mass, surface or pore sites that fall within a distance  $R$  from a fixed site (Figure 1.3) [15].  $R$  must always be much greater than the distance between nearest neighbor sites. The quantity  $M_{\text{sites}}(R)$  refers to the ‘mass’ in a sphere of radius  $R$ . It grows with increasing  $R$  [16]:

$$M_{\text{sites}}(R) \propto R^D \quad (1.3)$$

Each type of site gives rise to a mass–radius relationship of the following form:

$$M_{\text{mass}}(R) \propto R^{D_M} \quad (1.4)$$

$$M_{\text{surface}}(R) \propto R^{D_S} \quad (1.5)$$

$$M_{\text{pore}}(R) \propto R^{D_P} \quad (1.6)$$

As  $D$  approaches Euclidean dimensions, the three types of fractal become indistinguishable.

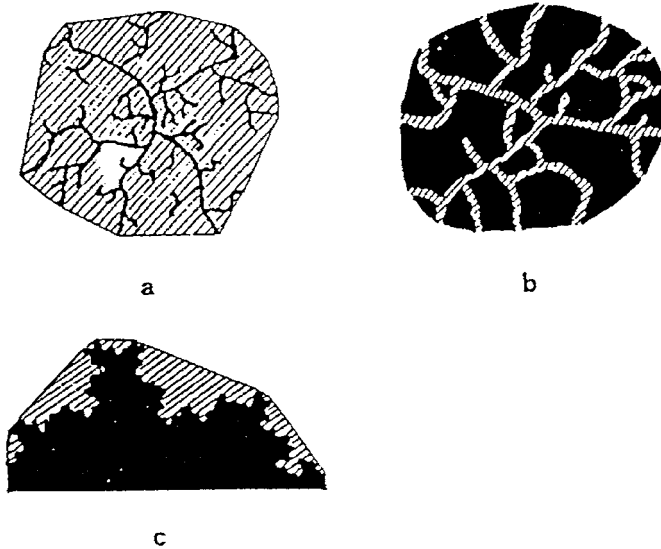


**Figure 1.2** Two-dimensional representations of mass fractal (a), surface fractal (b) and pore fractal (c) structures [14]. Reproduced with permission of John Wiley & Sons, Ltd.

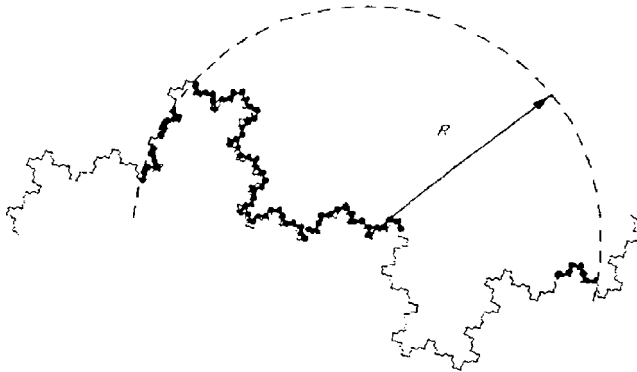


**Figure 1.3** Illustration of  $M_{\text{sites}}(R)$ . The sites are pictured as adsorbed molecules on a surface, but equally well could be monomers in a polymer chain, primary particles of a colloidal aggregate, etc. [15]. Reproduced with permission of John Wiley & Sons, Ltd.

#### 1.4 METHODS FOR ESTIMATING THE FRACTAL DIMENSION

Fractal geometry defines how objects occupy space. There are a variety of different methods that are employed for estimating  $D$ . For example, different approaches are used depending on whether biotic or abiotic components are measured or according to the size of the major components of the system. For example, an embedding,

three-dimensional space has been used to describe both the inorganic and organic components of soils. In contrast, the *in situ* distribution of soil microorganisms cannot be described using similar techniques due to the inherent difficulties involved with recording their images in an opaque substratum. One means of avoiding this problem would be to grow the microorganisms on the surfaces of the soil.

The most common experimental methods that have been proposed to estimate the fractal dimensions of environmental systems include: (a) scattering techniques; (b) turbidimetry; (c) vapor adsorption methods, (d) reaction rate methods; and (e) microscopy. Visible or laser light scattering, small-angle X-ray scattering (SAXS) and small-angle neutron scattering (SANS) (a) are based on the measurement of the fraction of incident beam intensity that is scattered by the sample as a function of the scattering angle. The fractal dimension is obtained from the experimentally measured density autocorrelation function [14, 17, 18]. Turbidimetry (b) is based on a measurement of the wavelength dependence of turbidity, i.e. determination of the scattered or nontransmitted light corresponding to a reduction in the intensity of the incident beam [19]. Static or dynamic vapor adsorption methods (c) are based on the measurement of fractal adsorption isotherms. They make use of various classical adsorption equations that have been rederived for fractal surfaces. Specifically, the number of adsorbed molecules per unit mass of sorbent, i.e. the monolayer value, is related to the size of adsorbed probe molecules [20, 21]. Measurements of reaction rates on a particle surfaces (d), i.e. catalysis, ion exchange, dissolution, etc., are performed as a function of the number of active sites available, provided that the reaction is not diffusion limited [22]. Finally, transmission (TEM) and scanning electron microscopy (SEM) and optical microscopy (e) are used to collect images that are analyzed using procedures based on the density–density autocorrelation function [23] or other image-analysis techniques [24].

The methods outlined above have been recently reviewed in relation to the fractal analysis of soil components and soil properties [6, 11]. They are also discussed in much greater detail in Chapter 3 [25]. Once data are acquired, the choice of an appropriate analysis technique is another highly critical step. For example, the box counting method is a common method for estimating the fractal dimensions of bacterial colonies and mycelial systems that is well suited to image analysis [13, 26–28]. This method has recently replaced the ‘concentric circles’ (two-point density–density correlation) method [29] that was used in several earlier studies of microbial colonies in agar and soils [e.g. 30, 31], but that was shown to exclude the extending colony margin from analysis. The technique is described in much greater detail in Chapter 3 [25], and applications are provided in Chapters 8 and 9 [32, 33].

## **1.5 APPLYING FRACTAL GEOMETRY TO QUANTIFY GROWTH, POLYMERIZATION AND AGGREGATION**

An example of how fractal geometry can be used to better understand complex environmental processes is briefly described here and more thoroughly detailed in

Chapters 4 and 5 [34, 35]. A number of computer simulations and statistical models have been proposed to explain growth, polymerization and aggregation processes that lead to the formation of fractal structures that closely resemble those found in nature. Attempts have been made to relate the fractal dimensions of aggregates to their formation mechanisms and aggregation kinetics.

Two distinct models, particle–cluster aggregation and cluster–cluster aggregation [36], have been proposed to describe aggregation processes. The particle–cluster aggregation model is based on the sequential addition of particles to a growing cluster and is not believed to be relevant for the majority of colloidal aggregation processes that occur in nature. Aggregation in natural systems is best simulated using a cluster–cluster aggregation (CLA) model [36] in which a large number of initially dispersed and randomly moving particles collide and stick to form small clusters that grow following collision with other particles and clusters.

CLA can be classified on the basis of its rate-limiting process [36]: (a) ballistic CLA, for which particles and clusters follow linear or ballistic trajectories and join at their point of first contact; (b) diffusion-limited CLA (DLCA), where particles and clusters follow random walks (Brownian motion) and the fractal dimensions of the generated clusters range between 1.75 and 1.80; (c) a reaction-limited CLA (RLCA), where a short-range repulsive barrier must be overcome before direct contact and sticking can occur between particles and/or clusters. In this final CLA class, on average, a large number of collisions are required before aggregation can take place. In RLCA, aggregates have fractal dimensions that range between  $\sim 1.9$  and  $2.1$  for  $d=3$  and  $\sim 1.5$  and  $1.6$  for  $d=2$  [36, 37].

Aggregation processes are time dependent; thus, in addition to the geometric aspects, kinetic aspects must also be considered. In real systems, two distinct regimes of colloidal aggregation are generally distinguished, i.e. fast and slow aggregation. Each regime has a different rate-limiting step, and the resulting aggregates have different fractal dimensions and size distributions. In order to make the models time dependent, a sticking coefficient  $\alpha$ , which represents the collision efficiency between two particles and/or clusters, is defined. The sticking coefficient specifies the aggregation rate and depends on the value of the energy barrier that must be overcome to obtain aggregation. Values of  $\alpha$  range between  $\alpha = 0$  and  $\alpha = 1$  for 0 % or 100 % collision efficiency respectively [38]. When  $\alpha$  is large and close to 1, aggregation is fast, limited only by the diffusion of the particles and/or clusters. Under these conditions, loose aggregates, characterized by fractal dimensions between 1.75 and 1.80, are formed (Figure 1.4) [38], in agreement with the DLCA model. In contrast, when  $\alpha$  is small (low collision efficiency), the aggregation rate is slow and the process is mainly controlled by the energy barrier that must be overcome for particle/cluster sticking to occur. In this case, dense aggregates are formed with high fractal dimensions (Figure 1.4) [38] and aggregation is best described by the RLCA model. The sticking probability and aggregation rate can be increased by a decrease of the repulsive component of the energy barrier. In practice, the repulsive barrier is decreased: (i) by decreasing the pH of the medium, with a resulting decrease in the negative



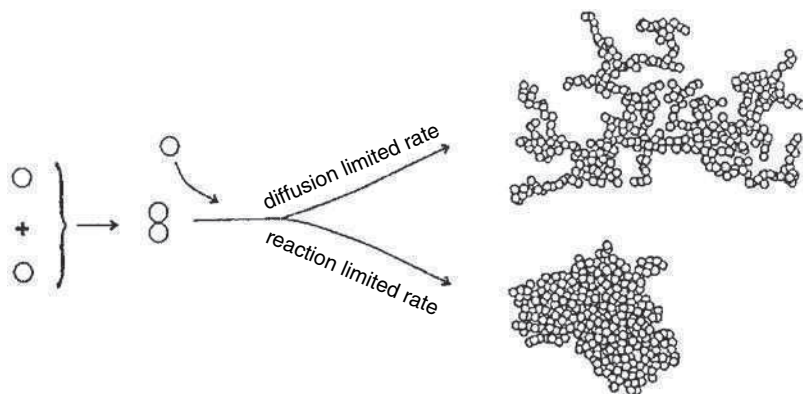


**Figure 1.4** Schematic representation of a diffusion-limited and a reaction-limited cluster-cluster aggregation process leading to aggregates of either low fractal dimension (loose aggregate) or higher fractal dimension (denser aggregate). Reproduced with permission from [19], copyright American Chemical Society.

charge on the interacting particles and clusters; (ii) by increasing the ionic strength of the medium, resulting in an increased charge screening of the particles/clusters; or (iii) by increasing temperature and/or stirring to provide greater kinetic energy to the aggregating system.

Most aggregation processes that occur in natural aquatic systems can be described adequately by the simple, limiting-case models outlined above. However, several natural aggregation processes are much more complex, in which case a variety of factors may affect the fractal dimension. For example, the fractal dimension can be significantly reduced by the effects of long-range attractive or repulsive interactions. Furthermore, in the often fragile aggregates that form in aqueous media, a number of processes, including restructuring by bending, folding and twisting and even bond breaking, can occur, resulting in a fractal dimension that is somewhat larger than that expected from simple models [36]. For fragile aggregates, deflocculation and dispersion may also result from changing environmental conditions, such as pH, concentration, salinity, etc., further complicating the interpretation of the fractal dimension that is measured for these systems. Owing to all of the above factors, it is clear that much care is required when interpreting fractal measurements of aggregation in natural systems.

## 1.6 CONCLUSIONS AND RECOMMENDATIONS

In the natural environment, there is a great need to describe complex physiochemical systems and processes quantitatively. By their very nature, environmental systems are disordered and are thus perfect candidates for their quantitative description using

fractal dimensions. Since a large number of physical properties will depend upon the scaling behavior of the mass, surface and pore spaces of the system, the notion of fractals can be used to describe very diverse objects according to the propriety of interest. Indeed, fractal geometry has been successfully employed to describe aggregate structures in water, soils and sediments, flow through porous media, organism distributions, adsorption and reaction kinetics, among other topics.

Fractal analysis cannot be applied indiscriminately. For the values that are obtained to be mechanistically valid, comparisons must be made among similar measurements of fractal dimensions (e.g. mass, surface or pore fractal dimensions) that are made using a single given analytical technique or techniques based upon similar analytical principles. Future research is required to better relate measurements that are performed in different manners and indeed to better understand the limitations of the fractal measurements. Nonetheless, the majority of future research in the field will necessarily be focused upon applying established determinations of fractal dimensions to understanding the physicochemistry of complex (i.e. natural) systems better (e.g. Chapters 4–9 [32–35, 39, 40]).

## LIST OF SYMBOLS AND ABBREVIATIONS

$D$ , $D_M$ , $D_S$ , $D_P$	fractal dimension, mass fractal dimension, surface fractal dimension, pore fractal dimension
$R$	distance from a fixed site
$M$	mass in a given distance
CLA	cluster–cluster aggregation model
DLCA	diffusion-limited CLA model
RLCA	reaction-limited CLA model
$\alpha$	sticking coefficient

## REFERENCES

- [1] Mandelbrot, B.B. (1982). *The Fractal Geometry of Nature*. W.H. Freeman & Co., New York.
- [2] Hastings, H.M. and Sugihara, G. (1993). *Fractals. A User's Guide for the Natural Sciences*. Oxford University Press, Oxford.
- [3] Richardson, L.F. (1961). The problem of contiguity: an appendix of statistics of deadly quarrels. *Gen. Syst. Yrbk.*, **6**, 139.
- [4] Morse, D.R., Lawton, J.H., Dodson, M.M. and Williamson, M.H. (1985). Fractal dimension of vegetation and the distribution of arthropod body lengths. *Nature*, **314**, 731.
- [5] Avnir, D. (1989). *The Fractal Approach to Heterogeneous Chemistry: Surfaces, Colloids, Polymers*. John Wiley & Sons, Ltd, New York.
- [6] Senesi, N. (1994). The fractal approach to the study of humic substances. In *Humic Substances in the Global Environment and Implications on Human Health*, Senesi, N. and Miano, T.M. (eds). Elsevier, Amsterdam, p. 3.

- [7] Senesi, N. (1996). Fractals in general soil science and in soil biology and biochemistry. In *Soil Biochemistry*, vol. 9, Stotzky, G. and Bollag, J.-M. (eds). Marcel Dekker, New York, p. 415.
- [8] Senesi, N. (1999). Aggregation patterns and macromolecular morphology of humic substances: a fractal approach. *Soil Sci.*, **164**, 841.
- [9] Anderson, A.N., McBratney, A.B. and Crawford, J.W. (1998). Applications of fractals to soil studies. *Adv. Agron.*, **63**, 1.
- [10] Baveye, P., Parlange, J.-Y. and Stewart, B.A. (1998). *Fractals in Soil Science*. CRC Press, Boca Raton, FL.
- [11] Okuda, I. and Senesi, N. (1998). Fractal principles and methods applied to the chemistry of sorption onto environmental particles. In *Structure and Surface Reactions of Soil Particles*, Huang, P.M., Senesi, N. and Buffle, J. (eds). IUPAC Series. John Wiley & Sons, Ltd, Chichester, UK, p. 77.
- [12] Pachepsky, Ya. A., Crawford, J.W. and Rawis, W.J. (1999). *Fractals in Soil Science*. Geoderma, Special Issue, 88, 1.
- [13] Boddy, L., Wells, J.M., Culshaw, C. and Donnelly, D.P. (1999). Fractal analysis in studies of mycelium in soil. *Geoderma*, **88**, 301.
- [14] Pfeifer, P. (1987). Characterization of surface irregularity. In *Preparative Chemistry Using Supported Reagents*, Laszlo, P. (ed.). Academic Press, London, p. 13.
- [15] Pfeifer, P. (1988). Fractals in surface science: scattering and thermodynamics of adsorbed films. In *Chemistry and Physics of Solid Surfaces*, Vanselow, R. and Howe, R. (eds). Springer, Berlin, p. 283.
- [16] Pfeifer, P. and Obert, M. (1989). Fractal basic concepts and technology. In *The Fractal Approach to Heterogeneous Chemistry: Surfaces, Colloids, Polymers*, Avnir, D. (ed.). John Wiley & Sons, Ltd, New York, p. 11.
- [17] Martin, J.E. and Hurd, J. (1987). Scattering from fractal. *J. Appl. Crystallogr.*, **20**, 61.
- [18] Schmidt, P.W. (1989). Use of scattering to determine the fractal dimension. In *The Fractal Approach to Heterogeneous Chemistry: Surfaces, Colloids, Polymers*, Avnir, D. (ed.). John Wiley & Sons, Ltd, Chichester, England, p. 67.
- [19] Horne, D.S. (1987). Determination of the fractal dimension using turbidimetric techniques. Application to aggregation protein systems. *Faraday Discuss. Chem. Soc.*, **83**, 259.
- [20] Pfeifer, P. and Avnir, D. (1983). Chemistry in noninteger dimensions between two and three: I. Fractal theory of heterogeneous surfaces. *J. Chem. Phys.*, **79**, 3558.
- [21] Avnir, D., Farin, D. and Pfeifer, P. (1984). Molecular fractal surfaces. *Nature*, **308**, 261.
- [22] Farin, D. and Avnir, D. (1989). The fractal nature of molecule-surface interactions and reactions. In *The Fractal Approach to Heterogeneous Chemistry: Surfaces, Colloids, Polymers*, Avnir, D. (ed.). John Wiley & Sons, Ltd, New York, p. 271.
- [23] Teixeira, J. (1986). Experimental methods for studying fractal aggregates. In *On Growth and Form*, Stanley, H.E. and Ostrowsky, N. (eds). Nijhoff, Dordrecht, The Netherlands, p. 145.
- [24] Kaye, B.H. (1989). Image analysis techniques for characterising fractal structure. In *The Fractal Approach to Heterogeneous Chemistry: Surfaces, Colloids, Polymers*, Avnir, D. (ed.). John Wiley & Sons, Ltd, New York, p. 55.
- [25] Bushell, G. (2008). Methods and techniques for fractal analysis of environmental systems. In *Biophysical Chemistry of Fractal Structures and Processes in Environmental Systems*, Senesi, N. and Wilkinson, K. (eds.), IUPAC Series, John Wiley & Sons Ltd, Chichester, UK, Chapter 3.
- [26] Obert, M., Pfeifer, P. and Sernetz, M. (1990). Microbial growth patterns described by fractal geometry. *J. Bacteriol.*, **172**, 1180.

- [27] Donnelly, D.P., Wilkins, M.F. and Boddy, L. (1995). An integrated image analysis approach for determining biomass, radial extent and box-count fractal dimension of macroscopic mycelial systems. *Binary*, **7**, 19.
- [28] Donnelly, D.P., Boddy, L. and Wilkins, M.F. (1999). Image analysis – a valuable tool for recording and analysing development of mycelial systems. *Mycologist*, **13**, 120.
- [29] Witten, T.A. and Sander, L.M. (1981). Diffusion-limited aggregation, a kinetic critical phenomenon. *Phys. Rev. Lett.*, **47**, 1400.
- [30] Ritz, K. and Crawford J. (1990). Quantification of the fractal nature of colonies of *Trichoderma viride*. *Mycol. Res.*, **94**, 1138.
- [31] Bolton, R.G. and Boddy, L. (1993). Characterisation of the spatial aspects of foraging mycelial cord systems using fractal geometry. *Mycol. Res.*, **97**, 762.
- [32] Boddy, L. and Donnelly, D.P. (2008). Fractal geometry and microorganisms in the environment. In *Biophysical Chemistry of Fractal Structures and Processes in Environmental Systems*, Senesi, N. and Wilkinson, K. (eds.), IUPAC Series, John Wiley & Sons Ltd, Chichester, UK, Chapter 8.
- [33] Colbeck, I. (2008). Fractal geometry of aerosol particles. In *Biophysical Chemistry of Fractal Structures and Processes in Environmental Systems*, Senesi, N. and Wilkinson, K. (eds.), IUPAC Series, John Wiley & Sons Ltd, Chichester, UK, Chapter 9.
- [34] Stoll, S. and Diez, S. (2008). Fractal structures and mechanisms in coagulation/flocculation processes in environmental systems: Theoretical aspects. In *Biophysical Chemistry of Fractal Structures and Processes in Environmental Systems*, Senesi, N. and Wilkinson, K. (eds.), IUPAC Series, John Wiley & Sons Ltd, Chichester, UK, Chapter 4.
- [35] Bottero, J.Y., Masion, A. and Rose, J. (2008). Fractal mechanisms in coagulation/flocculation processes in environmental systems. Molecular aspects. In *Biophysical Chemistry of Fractal Structures and Processes in Environmental Systems*, Senesi, N. and Wilkinson, K. (eds.), IUPAC Series, John Wiley & Sons Ltd, Chichester, UK, Chapter 5.
- [36] Meakin, P. (1991). Fractal aggregates in geophysics. *Rev. Geophys.*, **29**, 317.
- [37] Brown, W.D. and Ball, R.C. (1985). Computer simulation of chemically limited aggregation. *J. Phys. A*, **18**, L517.
- [38] Buffle, J. and Leppard, G.G. (1995). Characterization of aquatic colloids and macromolecules. 1. Structure and behavior of colloidal material. *Env. Sci. Technol.*, **29**, 2169.
- [39] Sokolowska, Z. and Sokolowski, S. (2008). Fractal approach to adsorption/desorption processes on environmental surfaces. In *Biophysical Chemistry of Fractal Structures and Processes in Environmental Systems*, Senesi, N. and Wilkinson, K. (eds.), IUPAC Series, John Wiley & Sons Ltd, Chichester, UK, Chapter 6.
- [40] Rice, J.A. (2008). Applications of fractals in the study of humic materials. In *Biophysical Chemistry of Fractal Structures and Processes in Environmental Systems*, Senesi, N. and Wilkinson, K. (eds.), IUPAC Series, John Wiley & Sons Ltd, Chichester, UK, Chapter 7.

---

## 2 Introduction to Fractal Geometry, Fragmentation Processes and Multifractal Measures: Theory and Operational Aspects of their Application to Natural Systems

---

**Philippe Baveye<sup>1</sup>, Charles W. Boast<sup>2</sup>, Sarra Gaspard<sup>3</sup>, Ana M. Tarquis<sup>4</sup> and Humberto Millan<sup>5</sup>**

<sup>1</sup> *SIMBIOS Centre, University of Abertay Dundee, Kidd Building, Bell Street, Dundee DD1 1HG, UK*

<sup>2</sup> *Department of Natural Resources and Environmental Sciences, University of Illinois at Urbana-Champaign, 1102 South Goodwin Avenue, Urbana, IL 61801, USA*

<sup>3</sup> *Laboratoire COVACHIMM EA3592, Département de Chimie, UFR des Sciences Exactes et Naturelles, Université des Antilles et de la Guyane, BP 250, Campus Fouillole, Pointe-à-Pitre, 97159 GUADELOUPE, FWI (French West Indies)*

<sup>4</sup> *Department of Applied Mathematics to Agriculture Engineering, E.T.S. de Ingenieros Agrónomos, Universidad Politécnica de Madrid, Ciudad Universitaria s.n. 28040 Madrid, Spain*

<sup>5</sup> *Department of Basic Science, Universidad de Granma, Apdo 21, Bayamo, Granma 85100, Cuba*

### 2.1 INTRODUCTION

Periodically, scientists uncover, in the treasure troves of mathematicians, a theory that allows the simple solution of a hitherto unresolved problem, or at least makes possible its formulation in a conceptual framework that eventually leads to an elegant solution. A typical example of this process is the adoption of tensor calculus by physicists in the early years of the 20th century. In the 1880s and 1890s, two Italian mathematicians, Gregorio Ricci-Curbastro (1853–1925) and Tullio Levi-Civita (1873–1941), spent years patiently elaborating a mathematical theory initially referred to as ‘absolute differential calculus’ and later known as tensor calculus. This theory attracted virtually no attention outside of mathematical circles until Albert Einstein realized that it was precisely the tool he crucially needed to develop his general theory of relativity. He

spent time familiarizing himself with tensor calculus, apparently with some difficulty on account of the abstractness of the theory, and eventually used it successfully in his work. Thereafter, the use of tensor calculus widened and became routine in a broad range of disciplines. In due time, physicists and mechanicians developed a conceptual approach to tensor calculus that differs from that of mathematicians in a number of respects (e.g. is far less abstract), yet fundamentally preserves its intrinsic rigor.

Compared with this common pattern of the adoption of a mathematical tool or theory by nonmathematicians, the case of fractal geometry is entirely atypical, and has been so from the start. Even though fractal geometry deals with mathematical objects, it was not at the onset defined or developed as a mathematical theory. Mandelbrot [1], who coined the term ‘fractal’, did not feel that it was necessary to define precisely what the term referred to. In addition, of his own admission [e.g. 2], he was more attracted by the esthetic beauty of fractals, by the ‘hypnotically intricate visual patterns and images’ [3] that one may base on fractals, than by the mathematically rigorous study of their properties. His influential book on the *Fractal geometry of nature* [4] makes numerous statements about the features of fractals, few of which have been rigorously proven. For fear, apparently, of excluding some applications that could bring fame and glory to the theory (and its progenitor), Mandelbrot’s book [4] also presents several conflicting perspectives on the nature of fractals, often leaving readers somewhat baffled as to exactly what the author had in mind.

Before mathematicians had a chance to step in and develop fractal geometry as a truly rigorous mathematical theory,<sup>1</sup> natural scientists became enthused by what they perceived as the enormous potential of fractals in their own fields, and filled gaps in the theory as needs arose. As a result of their research, fractal theory has developed in many different directions. In the resulting flurry of activity, including in fields such as geophysics and soil science, rare have been the articles or books that have attempted to analyze carefully the connections existing among the different ‘natural’ fractals identified in the real world, or between them and the mathematical beings defined and manipulated by the geometricians. Reluctance to embark on this analysis appears to have caused much confusion in the literature (e.g. see discussion in Baveye and Boast [6]); the term ‘fractal’, when applied to natural systems, often means very different things to different people, creating unnecessary difficulties in communication and occasionally leading to unsound conclusions.

A first objective of this chapter, therefore, is to attempt to fill these gaps and, in particular, to make more explicit the connection between *theoretical* and *natural* fractals. A similar approach is followed in the last section of this chapter, which deals briefly with the increasingly important multifractal measures. A second objective of this chapter is to point out that some uses of ‘fractals’ amount to little more than curve-fitting exercises, and that any attempt to relate the resulting ‘fractal’ dimensions to geometrical features of natural systems should be approached with great caution.

---

<sup>1</sup> They eventually succeeded in that endeavor, years later [e.g. 5].

This chapter (which is an outgrowth and updated version of [7]) is not meant to be a treatise on fractal geometry. Its objective is to introduce the aspects of fractal theory that have found application in environmental science and which are used in later chapters of this book. The approach adopted, which we have found useful in our courses on the subject, is to follow, at least initially, a chronological description of the genesis of fractal geometry, starting with a number of strange-looking, even monstrous-looking, curves discovered by mathematicians in the 19th century. Only after these have been described in some detail do we attempt to present to the reader the commonalities among these curves and to draw from the resulting list of shared features a relatively clear picture of the concept of fractal. Experience has taught us that this chronological approach results in far fewer misconceptions about the true nature of fractals than where fractals are defined from the onset.

As much as possible, this chapter has been written in such a way as to be self-contained and accessible to readers with little more than an elementary background in calculus. Nevertheless, numerous pointers to other sources of information are provided in case the incursion into set and measure theory found here is not sufficiently basic. In particular, Falconer [5 (pp. 3–16)] may be consulted in order to get up to speed; the mathematical concepts and the notation used throughout this chapter are introduced there.

## 2.2 A GALLERY OF MATHEMATICAL MONSTERS

### 2.2.1 The Precursors: Cantor's Set, the Devil's Staircase and the Peano–Hilbert Plane-Filling Curves

In a landmark letter, sent on 20 June 1877, to his friend Richard Dedekind, the German mathematician Georg Cantor started a revolution in the field of geometry [2]. He mentioned that he had doubts about the meaning, and even the validity, of the concept of dimension. He also proved that a surface limited by a square, which like any regular surface has a topological dimension<sup>2</sup> equal to two (in Euclidian space), does not contain more points than any one of the square's sides (of topological dimension equal to one)! Cantor's derivation showed that there is a one-to-one correspondence between points on the sides and points on the surface, so that a single number suffices to determine the position of any point in the square.

A few years later, Cantor [8] gave the concept of dimension another serious jolt and created in the process the first of what, after Henri Poincaré, came to be called the mathematical 'monsters'. Known as the Cantor set, it is also commonly termed the 'middle third', the 'ternary' or the 'triadic' Cantor set. It is constructed by a sequence

---

<sup>2</sup> The topological dimension  $D_T$  of a set is always an integer and is 0 if the set is totally disconnected (i.e. for isolated points), 1 if each point of the set has arbitrarily small neighborhoods with boundary of dimension 0 (i.e. for lines), and so on for higher dimensions [5].

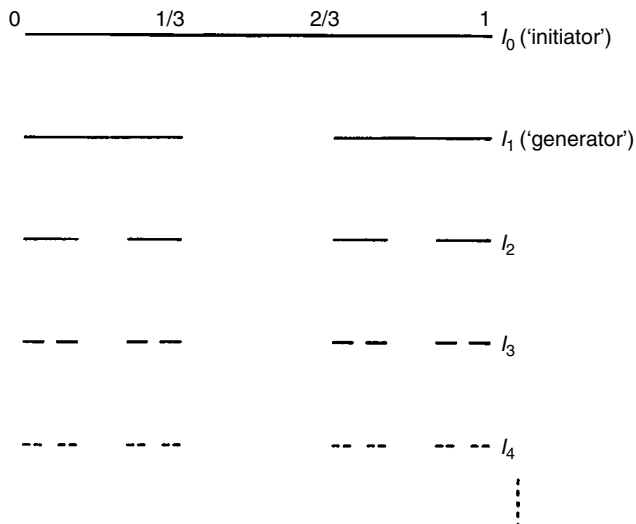


**Figure 2.1** Initial steps in the construction of the Cantor set by repeated removal of the middle third of intervals.

of removal operations from a unit-length interval, termed the initiator. This initiator is labeled  $I_0$  in Figure 2.1, where it corresponds to the interval  $[0, 1]$  (i.e. the set of numbers  $x$  such that  $0 \leq x \leq 1$ ). If one removes from this initiator the segment  $(1/3, 2/3)$  (containing the real numbers  $x$  such that  $1/3 \leq x \leq 2/3$ ), the set  $I_1$  results. This set is sometimes termed the generator and consists of the two intervals  $[0, 1/3]$  and  $[2/3, 1]$ . Removing the middle thirds of these intervals, i.e. applying the generator to each of them, yields  $I_2$ , which comprises four intervals of length  $1/9$ . At the next stage ( $I_3$ ), there are  $2^3 = 8$  intervals of length  $(1/9)/3 = 3^{-3}$ . At the  $n$ th iteration of this deletion procedure, the set  $I_n$  consists of  $2^n$  intervals, each having a length  $3^{-n}$ , and is included in all the preceding sets  $I_1, I_2, \dots, I_{n-1}$  in the sequence.

The Cantor set  $P$  can be thought of as the limit of the sequence of sets  $I_n$  when  $n$  tends to infinity. Mathematically [9], it is defined as  $\bigcap_{i=1}^{\infty} I_n$ , the intersection of all the sets  $I_n$ , with  $n$  going from one to infinity. It is obviously impossible to draw the set  $P$  itself, with its infinitesimal detail, so ‘pictures of the Cantor set  $P$ ’ are in fact only illustrations of one of the sets  $I_n$ . It is apparent from Figure 2.1 that such representations are feasible only for relatively low values of  $n$ .

At first glance, it might appear that we have removed so much of the interval  $[0, 1]$ , during the construction of the Cantor set, that nothing remains. In a sense, this is true. The (Lebesgue) measure  $m(I_n)$  of the set  $I_n$ , i.e. practically, the total length of all the  $2^n$  intervals included in  $I_n$ , is given by  $(2/3)^n$ . Since  $P = \bigcap_{n=1}^{\infty} I_n$  and  $P$  is included in  $I_n$  for every  $n$ , the measure  $m(P)$  is equal to the limit as  $n \rightarrow \infty$  of  $(2/3)^n$ , which is zero. In other words, the Cantor set has zero length and its topological dimension is zero. Yet it is an uncountable set, containing infinitely many points in any neighborhood of each of its points. Furthermore, one can show that the points



of the Cantor set can be put in one-to-one correspondence with those of the initiator  $[0, 1]$ ; mathematically,  $P$  and  $[0, 1]$  have the same ‘cardinality’. This raises some very serious questions about the use of traditional dimensions to characterize these two sets, and justifies the labels of ‘monstrous’ and ‘pathological’ that rapidly became associated with the Cantor set.

The Cantor set  $P$  has a number of striking features [5]:

1.  $P$  contains exact copies of itself at many different scales. It is clear that the part of  $P$  in the interval  $[0, 1/3]$ , or that in the interval  $[2/3, 1]$ , are geometrically similar to  $P$ , except for the fact that they are scaled down by a factor  $1/3$ . Again, the parts of  $P$  in each of the four intervals of  $I_2$  are geometrically similar to  $P$ , but scaled by a factor  $1/9$ , and so on. Some authors [e.g. 5] call this feature of  $P$  ‘self-similarity’. Strictly speaking, however, as pointed out by Feder [10 (p. 63)],  $P$  is not entirely self-similar because of the finite length of its initiator. To obtain a self-similar set, one should enlarge  $P$  by an extrapolation procedure that covers the region  $[0, 3]$  by two Cantor sets defined on the intervals  $[0, 1]$  and  $[2, 3]$ . Repetition of this procedure ad infinitum generates a self-similar set on the half-line  $[0, \infty]$ . Every time the expression ‘self-similar’ is used in the remainder of this chapter, it will have to be interpreted within the context of Feder’s comment [10].
2. The set  $P$  has a ‘fine’ structure; it contains detail at arbitrary small scales.
3. Although  $P$  has an intricate and detailed structure, the actual definition of  $P$  is straightforward.
4.  $P$  is obtained by a recursive procedure.
5. The geometry of  $P$  is not easily described in classical terms; it is not the locus of the points that satisfy some simple geometric condition, nor is it the set of solutions of any simple equation.
6. It is awkward to describe the local geometry of  $P$ . Near each of its points are a large number of other points, separated by gaps of varying lengths.
7. Although  $P$  is in some ways quite a large set (it is uncountably infinite), its size is not quantified by the usual measures such as length. By any reasonable definition,  $P$  has zero length.
8. The actual set  $P$  cannot be represented graphically.

Many of these peculiar features of the Cantor set are shared by, or at least are similar to those of, the other mathematical monsters described later in this section. The above list will also be useful when we try to define as precisely as possible what is meant by the term ‘fractal’.

Another mathematical ‘monster’, sometimes called the Cantor singular function [11], is closely related to the Cantor set. This singular function is constructed by integrating an appropriate distribution function defined on the Cantor set. One such distribution function is constructed by first considering the uniform distribution of mass on the interval  $[0, 1]$ , with total mass equal to one (in some arbitrary units). For example, one could visualize the initiator  $I_0$  of Figure 2.1, not as a line segment, but as a bar of some material with unit mass density  $\rho_0$  and length  $l_0 = 1$ . The operation

that resulted in  $I_1$  in Figure 2.1 now consists of cutting the bar into two halves of equal mass ( $= 1/2$ ) and then hammering them so that the length of each part becomes  $l_1 = 1/3$ . The total mass is conserved in the operation, while the mass density in each part becomes  $\rho_1 = 3/2$ . Repeating this process, one finds that, at the  $n$ th stage, the number of small bars is  $2^n$ , each of length  $l_n = (1/3)^n$  and of mass density  $\rho_n = (3/2)^n$ . Integrating the mass density along  $x$ , we obtain the total mass contained between  $x = 0$  and an arbitrary point  $x$  as

$$M_n(x) = \int_0^x \rho_n(x) dx \quad (2.1)$$

where  $\rho_n = (3/2)^n$  on the  $2^n$  intervals of length  $l_n = (1/3)^n$  and is identically zero everywhere else. An example of such a function  $M_n(x)$  is shown in Figure 2.2. The

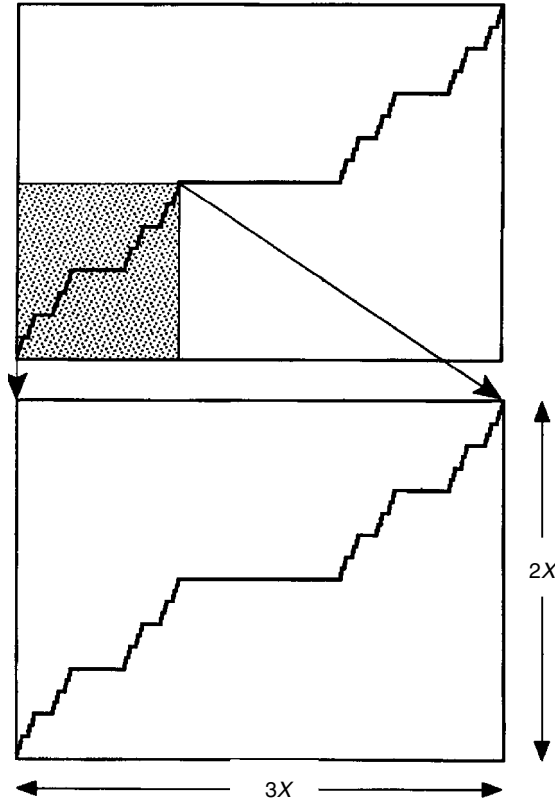


**Figure 2.2** Intermediate stage ( $n = 6$ ) in the construction of the Cantor singular function or 'Devil's staircase' (top) and schematic illustration of the self-affinity of the Cantor singular function or 'Devil's staircase' (bottom); the enlargement is identical to the original, but the enlargement (scaling) factors are different in the  $x$  and  $y$  directions.

limit of Equation (2.1) as  $n \rightarrow \infty$  is a singular function, discovered by Cantor [11], and usually referred to as the ‘Devil’s staircase’. It is a continuous, nonconstant function that is (nearly) horizontal all over except on an uncountable set (the Cantor set), of Lebesgue measure equal to zero. At each point in this uncountable set, the derivative of the Cantor singular function is given by a Dirac  $\delta$  distribution.

The Cantor singular function has many of the features of the Cantor set (listed above), except (i), i.e. it does not contain *exact* copies of itself at different scales. Inspection of Figure 2.2 (top) shows that the shape of the function  $M_n(x)$  in the interval  $[0, 1/3]$  is similar to that of the whole function (in the interval  $[0, 1]$ ), scaled down in the  $x$  direction (abscissa) by a factor of  $1/3$ . However, it is also apparent that the scaling factor in the  $y$  direction (ordinate) in Figure 2.2 (top) is not  $1/3$  but  $1/2$  (see Figure 2.2, bottom). A set or function is said to be self-affine when its scaling factors are different in different directions. Self-similarity requires these scaling factors to be identical in all directions. Therefore, the Cantor singular function or ‘Devil’s staircase’ is not self-similar, but self-affine.

Following in Cantor’s steps, another assault on the concept of dimension was made simultaneously by Peano [12] and Hilbert [13], in two short but influential articles. Both describe polygons that appear at first glance to be perfectly innocent, but nevertheless happen to fill a square more and more completely, so that, in the limit, they pass through every single point in the square.

The construction of Peano’s original curve begins with a single line segment, the initiator (stage 0 in Figure 2.3). It is substituted by the generator (stage 1), which touches (but does not cross) itself at two points labeled A and B in Figure 2.3. If each straight line segment in stage 1 is replaced by a properly scaled-down generator,

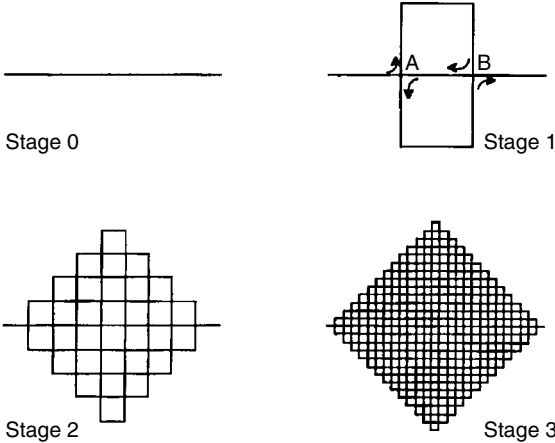


**Figure 2.3** First stages of the construction of Peano’s space-filling curve. At each step, each line segment is replaced by nine line segments scaled down by a factor of  $1/3$ .

one obtains stage 2. Independently of the direction (horizontal or vertical) of the line segments in stage 1, the scaling factor is equal to  $1/3$ . At the next stage, the scaling factor is equal to  $1/9$ , and so on. If one assumes that the length of the original line segment constituting the initiator is one, then it is easy to calculate the length of the curves at each stage. In stage 1, there are nine line segments of length  $1/3$  and the total length of the curve is three. In stage 2 there are  $9^2$  line segments of length  $1/3^2$ , amounting to a total length equal to nine. Expressed as a general rule, in each step of the construction, the resulting curve increases in length by a factor of three. In stage  $n$ , the length is thus  $3^n$ .

If one pursues the above construction procedure to the limit as  $n \rightarrow \infty$ , the number of straight-line segments and their total length tend to infinity. The result is generally termed Peano's curve and is of great interest mathematically because it is nowhere differentiable, i.e. it does not allow a tangent at any of its points (which are all 'corners'). As with the Cantor set (but for different reasons), it is impossible to visualize the structure of this curve. All one can see, at any scale, is a completely 'filled out' square, which does not look in the least similar to the early steps of the construction (see Figure 2.3). Nevertheless, the Peano curve, like  $P$ , contains exact copies of itself [e.g. 14, 15]. The same general characteristics are exhibited by Hilbert's [13] plane-filling curve, except for the fact that it is self-avoiding, i.e. it never intersects or touches itself.

### 2.2.2 The Triadic Von Koch Curve

The Swedish mathematician von Koch introduced in 1904 what is now called the (triadic) von Koch curve [e.g. 5, 14 (pp. 89–93)]. The construction of this curve, illustrated in Figure 2.4, starts with a line segment,  $I_0$ , of unit length. This initiator is replaced by the generator shown as the curve  $I_1$ , consisting of four segments of length  $1/3$ . At the next stage,  $I_2$  is constructed by replacing each line segment in  $I_1$  by a properly scaled-down version of the generator. The scaling factor is equal to  $1/3$ . The curve  $I_2$  consists of  $4^2 = 16$  segments each having a length of  $1/3^2 = 1/9$ , so that the total length of  $I_2$  is equal to  $(4/3)^2 = 16/9$ .

At the  $n$ th stage, there are  $4^n$  segments of length  $\delta_n = 3^{-n}$ , with a total length of  $L(I_n) = (4/3)^n$ . This total length  $L(I_n)$  may be expressed differently, in a way that makes explicit the dependence of  $L(I_n)$  on  $\delta_n$ . Taking the exponential of the natural logarithm of the total length  $L(I_n) = (4/3)^n$  and substituting the value of  $n$  ( $= -\ln \delta_n / \ln 3$ ) obtained by solving the equality  $\ln \delta_n = \ln 3^{-n}$  [e.g. 5 (p. 17)], one obtains

$$L(I_n) = \delta_n^{1 - \ln 4 / \ln 3} \quad (2.2)$$

Equation (2.2) corresponds to a *power-law* (or 'Paretian') relationship between  $L$  and  $\delta_n$ . Similarly, the number  $N_n$  of segments of length  $\delta_n$  is also a power-law function of  $\delta_n$ . Indeed, the equality  $L(I_n) = N_n \delta_n$  implies that  $N_n = \delta_n^{-\ln 4 / \ln 3}$ . We shall return to these important power-law dependencies in later sections of this chapter.

Even though we cannot represent it graphically, it is clear that, if we carry on the iterative procedure illustrated in Figure 2.4 to the limit where  $n \rightarrow \infty$ , the resulting

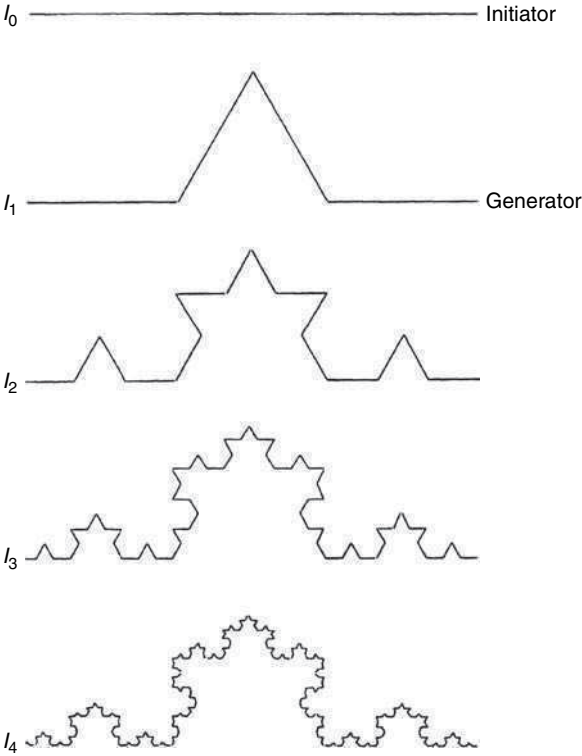


**Figure 2.4** Construction of the triadic von Koch curve. At each step, the number of line segments increases by a factor of 4.

curve (the von Koch curve) has an infinite number of vanishingly small segments and has a total length tending to infinity.

If, in Figure 2.4, one takes the part of  $I_4$  that corresponds to the interval  $[0, 1/3]$  of the initiator, and scales this part up horizontally and vertically by three, one obtains  $I_3$ . In the limit  $n \rightarrow \infty$ , however, this same scaling up of any segment of  $I_n$  would reproduce the von Koch curve itself. Furthermore, like the Peano–Hilbert space-filling curves, the von Koch curve is nowhere differentiable. All of these curves have a topological dimension equal to unity; a simple stretching operation (or ‘rectification’) transforms them into an infinite straight line.

At first sight, the von Koch curve appears less monstrous than the Cantor set or Peano’s space-filling curve. Nevertheless, it has astonishing properties, which challenge the traditional concepts of dimension. Indeed, since the von Koch curve is infinite in length and contains exact replicates of itself, any scaled-down sub-image is also of infinite length [3]. This leads to the conclusion that for any two points on the curve, no matter how close they are, the curve between them is of infinite length! In

addition, if one joins together three initiators like  $I_0$  (in Figure 2.4) to form a triangle and one performs on each initiator the iteration procedure of Figure 2.4, the resulting geometrical construct, commonly known as the von Koch ‘island’ or ‘snowflake’, has infinite length, even though it fits within a finite area!

### 2.2.3 The Sierpinski Carpet and the Menger sponge

Cantor [8] remarked that examples similar to the (Cantor) set  $P$  ‘can be easily constructed for higher dimensions’. One such example is the Sierpinski carpet. The iterative procedure leading to this carpet starts with a square initiator of side length  $l_0$  (Figure 2.5). In the next step, one divides the initiator in nine smaller squares of side length  $l_0/3$  and removes the central square. When one applies the same procedure ad infinitum to the remaining squares, a structure known as the Sierpinski carpet is obtained [e.g. 10 (p. 25)], which is Cantor-like in many respects, even though its initiator is two-dimensional. Like the Cantor set, the Sierpinski carpet is a self-similar, uncountable set with a topological dimension equal to zero. The two-dimensional Lebesgue measure of the Sierpinski carpet, i.e. practically, its area in the plane, is equal to zero, so the traditional concept of area does not provide a very useful description of the spatial coverage of the Sierpinski carpet. Some other type of dimension is needed.

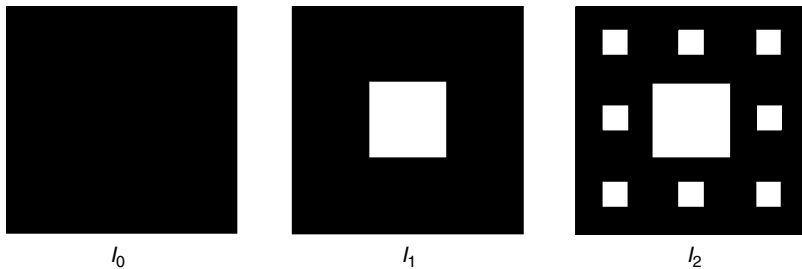


**Figure 2.5** First stages of the construction of the Sierpinski carpet.  $I_0$  is the initiator.  $I_1$  is the generator.

When the iterative process used for the construction of the Sierpinski carpet is generalized to three dimensions and when the initiator is a cube, one obtains a geometrical structure of particular interest in geophysics and soil science, the Menger sponge (Figure 2.6). The construction of the Menger sponge is very similar to that of the Sierpinski carpet. Each square face of the cube is treated in exactly the same way as the square initiator of the Sierpinski carpet. This time, extracting a square shape involves punching a hole directly through the cube at right angles to the face concerned. Thus, at the first stage  $I_1$ , three holes are punched through. This leaves 20 subcubes at one-third scale, each of which is repeatedly subdivided to create, ad infinitum, the hollowed structure of the Menger sponge. Another way to describe the recursive construction process is to consider that, at the  $n$ th stage, each cube of size

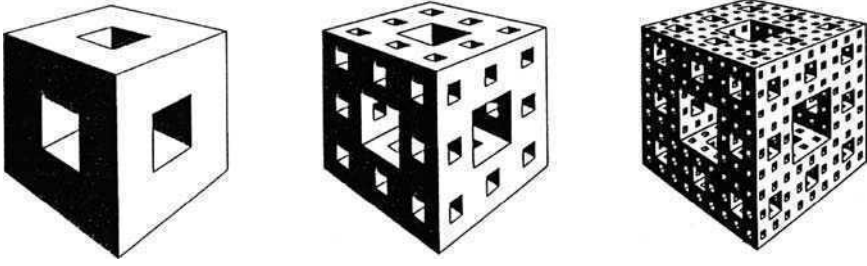


**Figure 2.6** First three stages in the construction of the Menger sponge.

$l_{n-1}$  is divided into 27 equal cubes of size  $l_n = l_{n-1}/3$ , and that the central small cube is removed along with the six cubes with which it shares faces.

This iterative construction may be envisaged from a physical standpoint. This produces mathematical relationships that will be useful later on. If the initiator is a cube of side length  $l_0$ , made of some material of uniform mass density  $\rho_0$ , the first-order structure (obtained after one iteration) would have a porosity  $\phi_1$  (void volume divided by total volume) equal to  $7/27$  and a mass density  $\rho_1$  equal to  $20\rho_0/27$ . After the second iteration, the porosity  $\phi_2$  would increase to  $329/729$  ( $\approx 0.45$ ) and the density  $\rho_2$  would decrease to  $400\rho_0/729$  ( $\approx 0.55\rho_0$ ). At the  $n$ th iteration, porosity and density would be given by

$$\phi_n = 1 - \left(\frac{20}{27}\right)^n = 1 - \left(\frac{l_n}{l_0}\right)^{3 - \ln 20 / \ln 3} \quad (2.3)$$

and

$$\frac{\rho_n}{\rho_0} = \left(\frac{20}{27}\right)^n = \left(\frac{l_n}{l_0}\right)^{3 - \ln 20 / \ln 3} \quad (2.4)$$

The second of these two equations again gives rise to a power-law relationship (as in the case of the von Koch curve).

Equations (2.3) and (2.4) will be mentioned again in a later section. For the time being, however, they can be used to illustrate some of the features of the Menger sponge, obtained when  $n \rightarrow \infty$ . Since the exponent in Equations (2.3) and (2.4) is strictly positive (indeed,  $3 - \ln 20 / \ln 3 \approx 0.273$ ),  $\phi_n$  and  $\rho_n / \rho_0$  will tend to one and zero respectively as  $n \rightarrow \infty$ . Mathematically, the three-dimensional Lebesgue measure of the Menger sponge, i.e. its volume practically, is zero. Like the Cantor set and the Sierpinski gasket, the Menger sponge is a self-similar, uncountable set of points with a topological dimension of zero. Therefore, totally against intuition, the Menger sponge is topologically equivalent to the Cantor set. Anecdotaly, there is another connection between the Menger sponge and the Cantor set. The intersections of the Menger sponge with medians or diagonals of the initial cube are triadic Cantor sets [4 (p. 144)].

### 2.2.4 Bolzano–Weierstrass-like Functions

Our rapid overview of mathematical ‘monsters’ would not be complete without a brief reference to an interesting family of continuous, nowhere differentiable functions. They are occasionally referred to as ‘Weierstrass-like’ but, for historical reasons, it seems more appropriate to call them ‘Bolzano–Weierstrass-like’.

Indeed, Bernard Bolzano [16] appears to have been the first (in a manuscript written around 1830 but published only in 1930) to provide an example of a continuous, nowhere differentiable function. A few years later, in 1872, Karl Weierstrass [17] showed that the function

$$f(x) = \sum_{n=0}^{\infty} b^n \cos(a^n x \pi) \quad (2.5)$$

has these properties, provided the product  $ab$  exceeds a certain limit. Hardy [18] showed that the conditions to be satisfied by  $a$  and  $b$  are  $0 < b < 1$ ,  $a > 1$  and  $ab \geq 1$ .

Over the years, many examples of continuous, nowhere differentiable functions have been published; see Edgar [11 (pp. 7, 341)]. One of them, the so-called Weierstrass–Mandelbrot function, assumes a particular significance in environmental science because it constitutes the theoretical basis of the first article that used fractal geometry in connection with soils data. Burrough [19] used the Weierstrass–Mandelbrot function to describe the often erratic-looking spatial variation of soil properties along transects.

The Weierstrass–Mandelbrot function  $w(t)$  is defined in complex form by [10 (p. 27), 20]

$$w(t) = \sum_{n=-\infty}^{\infty} \frac{(1 - e^{ib^n t})e^{i\varphi_n}}{b^{(2-D)n}} \quad (2.6)$$

where  $1 < D < 2$ ,  $b > 1$  and the  $\varphi_n$  are arbitrary phase constants. Each choice of the phases  $\varphi_n$  defines a specific function  $w(t)$ . For a given  $w(t)$ , one may show that the variance of increments  $V(t) = [w(t_0 + t) - w(t_0)]^2$  is a power function of time,  $t^{4-2D}$ , for  $t \rightarrow 0$  [19].

A simple function, the real part of  $w(t)$  with  $\varphi_n$  chosen as  $\varphi_n = 0$ , is the Weierstrass–Mandelbrot cosine function  $c(t)$ :

$$c(t) = \sum_{n=-\infty}^{\infty} \frac{1 - \cos b^n t}{b^{(2-D)n}} \quad (2.7)$$

The shape of this function is reasonably smooth for low values of  $D$  (see Figure 2.7). As  $D$  increases, however,  $c(t)$  begins to fluctuate widely, as if larger and larger amounts of ‘noise’ were added to an underlying trend.

Close inspection of Figure 2.7c reveals that  $c(t)$  is self-affine, like Cantor’s singular function [10 (p. 29)]. Both  $w(t)$  and  $c(t)$  are functions of a single variable.



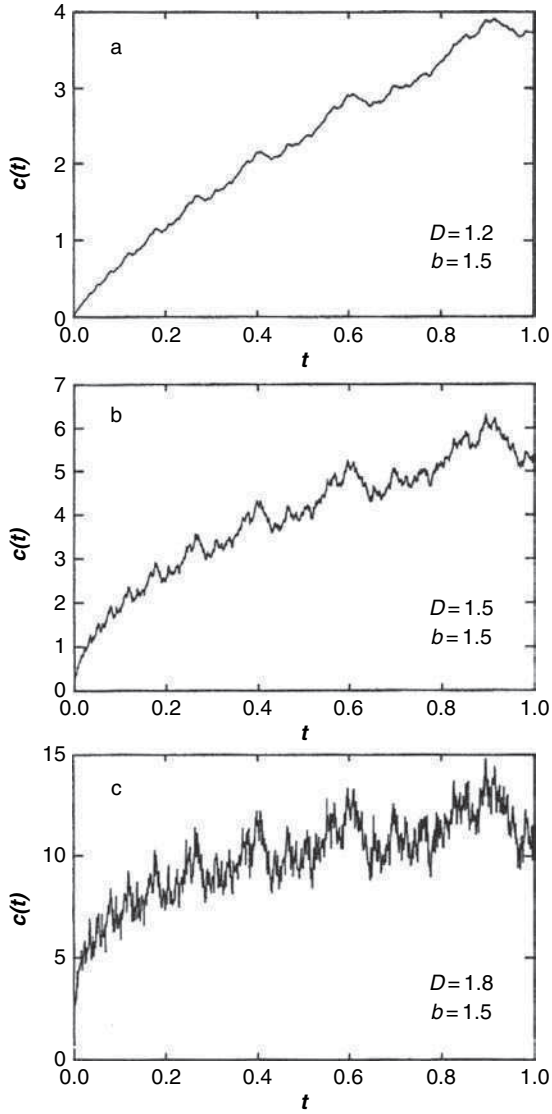


**Figure 2.7** Graphical representations of the Weierstrass–Mandelbrot cosine function  $c(t)$  with  $b = 1.5$  and (a)  $D = 1.2$ , (b)  $D = 1.5$ , and (c)  $D = 1.8$ . Modified from [10].

Multivariate Weierstrass–Mandelbrot functions have, however, been defined in the last decade [e.g. 21].

### 2.2.5 Random Monsters and Fractional Brownian Motion

The various mathematical monsters described above have been singled out for their historical significance, not because they are somehow unique. For each of them, there are an infinite number of variants. One could, for example, define the generator  $I_1$  of a Cantor-like set to be the union of two intervals  $[0, a]$  and  $[b, 1]$ , for any  $a$  and  $b$  with  $0 < a < b < 1$ . It is easy to imagine extending this definition to include three, four, or five intervals, and so on. Similarly, instead of replacing the middle-third segment in the initiator of the von Koch curve by the other two sides of an equilateral triangle, one could remove an interval of length  $a$  from the middle of the initiator, such that  $0 < a \leq 1/3$ . The interval could be replaced, for example, by the other three sides of a square or by the other two sides of a suitably short isosceles triangle.

Obviously, there are an infinite number of such sets. In addition to sharing all of the general features of the Cantor set (listed above), they are also deterministic, in the sense that their construction is based on the recursive application of an invariant and nonrandom generator.

It is straightforward to enlarge this family of monsters to include random analogues. For example, in the von Koch construction, each time the middle third of an interval is replaced by the other sides of an equilateral triangle, one might toss a coin to determine whether to position the new part above or below the removed segment. After a few steps, one gets an irregular-looking curve (see Figure 2.8), which nevertheless retains much of the ‘look’ of the von Koch curve [5, 14]. It is no longer exactly self-similar, like its nonrandom counterpart, but it is said to be ‘statistically’ self-similar. According to Feder [10 (p. 184)], a set  $S$  is statistically self-similar when  $S$  is the union of  $n$  distinct (nonoverlapping) subsets, each of which is scaled down by  $r$  from the original and is identical in all statistical respects to  $S$ . Put differently, enlargements of subsets of a statistically self-similar set have a statistical distribution identical to that of the whole set [5 (p. 225)].

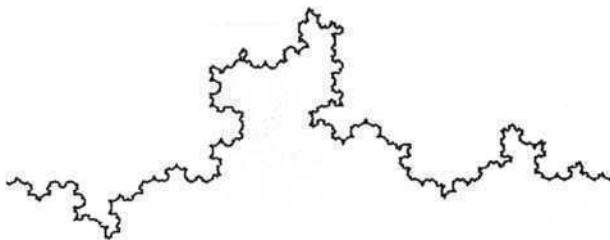


**Figure 2.8** Intermediate stage ( $I_5$ ) in the realization of a random version of the von Koch curve. Modified from [14].

As with the deterministic monsters, it is possible to relax the requirement that the scaling factor  $r$  be identical in all directions. In this case, the random set or curve is said to be ‘statistically self-affine’. Historically important examples of statistically self-affine sets are the Brownian and fractional Brownian motions.

Brownian motion, also referred to as a random walk or Wiener process, is named after the Scottish botanist Robert Brown, who in 1828 [22] described the erratic motion of pollen in aqueous suspensions observed with a light microscope. A particle undergoing Brownian motion seems to wander around without any distinct pattern (Figure 2.9). Some regions of the plane are filled densely by the particle’s trace. Increasing the resolution of the microscope and the time resolution produces a random walk that looks very much like that obtained at lower resolution.

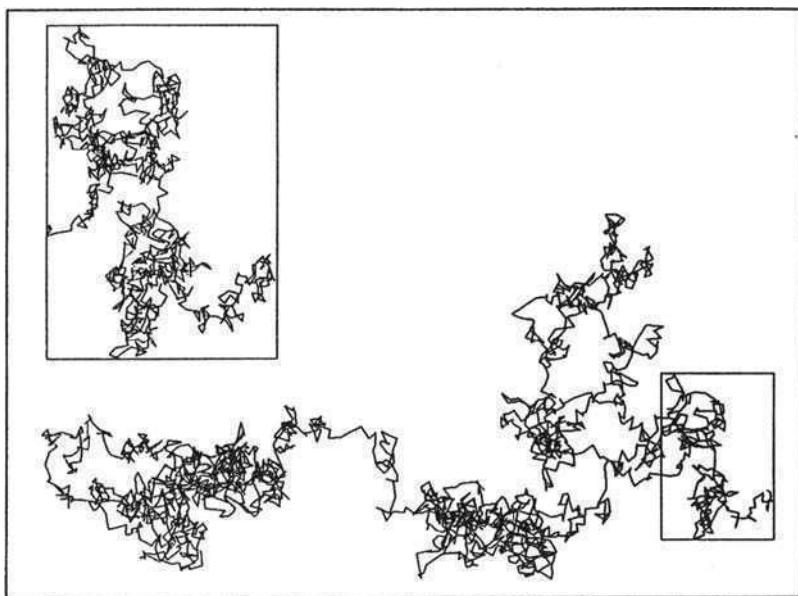


**Figure 2.9** Trace of the Brownian motion of a particle in a plane. The boxed detail of the trace (magnified in the upper left portion of the figure) suggests an invariance of scale or self-similarity: the detail looks like the whole. Modified from [14].

The Brownian motion of a microscopic particle is due to its constant bombardment by the numerous smaller molecules of the medium (e.g. water) in which it is suspended [23]. A single molecule hardly ever has enough momentum for its effect on the suspended particle to become visible under a microscope. Nevertheless, when many molecules collide with the particle from nearly the same direction at nearly the same time, they noticeably deflect it. These events are separated in time by what is commonly referred to as an ‘atomistic’ or ‘collision’ time  $\tau$ . The displacement  $\xi$  of the particle is not fixed, since it depends on the number of molecules colliding with

the microscopic particle and on their direction. Furthermore, the sizes and directions of successive displacements are uncorrelated.

In 1923, Wiener [24] proposed a rigorous mathematical model that exhibits a behavior similar to that observed in random motion. In this model, the displacement  $\xi$  is governed by a Gaussian (bell-shaped) probability distribution, with zero mean and unit variance. Therefore, if one plots the successive displacements of a particle (in one dimension for simplicity) over a certain period of time, the result (Figure 2.10a) corresponds to Gaussian, or ‘white’, noise. The sum of successive steps  $\xi_1, \xi_2, \dots, \xi_n$  of the particle during  $n$  collision times is given by

$$X(t = n\tau) = \sum_{i=1}^n \xi_i \quad (2.8)$$

where  $X$  is the position of the particle at time  $t$ , relative to its initial position at time  $t = t_0$  (Figure 2.10b). The function  $X(t)$  in Figure 2.10b is commonly referred to as the ‘graph’ or the ‘record’ of the Brownian motion and may be obtained by projection of the path of the Brownian motion onto one of the space axes.

In the limit of vanishingly small time steps ( $\tau \rightarrow 0$ ), the position  $X$  in Equation (2.8) becomes a random function, usually denoted by  $B(t)$ . This function is such that for any two times  $t_1$  and  $t_2$ , with  $t_2 \geq t_1$ :

$$|B(t_2) - B(t_1)| \propto (t_2 - t_1)^H \quad (2.9)$$

where  $\propto$  denotes proportionality and  $H$  is the Hurst exponent. The variance of the increments is given by

$$\text{var}(B(t_2) - B(t_1)) \propto (t_2 - t_1)^H \quad (2.10)$$

Early work concentrated on the ordinary ‘mathematical’ Brownian motion, with  $H = 1/2$ , and showed that this motion has a number of remarkable features. First, it cannot be represented graphically as can motion for finite  $\tau$  (Figure 2.10b). In addition, Wiener [24] showed that  $B(t)$  is continuous, as one expects, but nowhere differentiable. Thus, a particle undergoing mathematical Brownian motion does not have a well-defined velocity anywhere, and the curve  $y = B(t)$  does not have a well-defined tangent anywhere either. A related fact that illustrates the extreme irregularity of  $B(t)$  is that in every time interval, no matter how small, a particle undergoing mathematical Brownian motion travels an infinite distance! Figure 2.9 suggests that Brownian motion is statistically self-similar, and it is indeed so in  $R^n$  for  $n \geq 2$ . However, graphs of Brownian motion, such as that illustrated in Figure 2.10b, are statistically self-affine rather than self-similar.

The exponent  $H$  in Equations (2.9) and (2.10) does not have to be set equal to  $1/2$ , but may instead vary arbitrarily. When  $0 < H < 1$ , this generalization leads to the *fractional Brownian motion* (fBm), to which is associated the so-called fractional Gaussian noise (fGn), in the same manner that Gaussian noise produces the ordinary Brownian motion (see Figure 2.10).

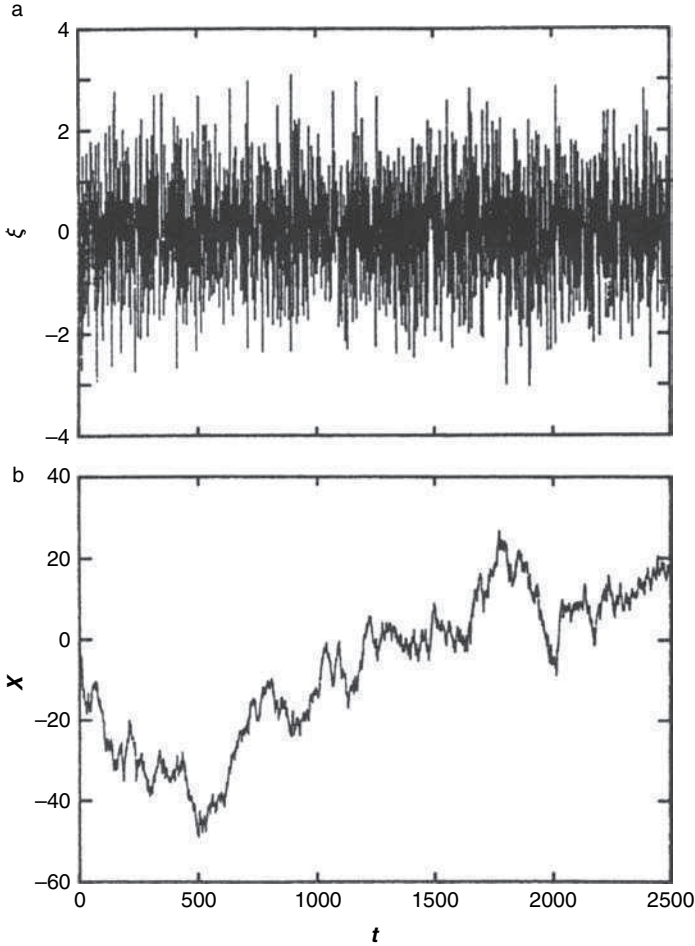


**Figure 2.10** A sequence of independent Gaussian random variables with zero mean and unit variance (Gaussian noise) ‘observed’ at every fourth time step, i.e. at intervals of length  $4\tau$ . (a) Independent random steps of the ‘particle’. (b) Position of the particle along the  $x$  axis. The time is in units of the atomistic time  $\tau$  between steps. Modified from [10].

A remarkable feature of fBm is that it generates infinitely long-run correlations (these correlations correspond, loosely, to the levels of dependence, in a probabilistic sense, of distinct spatial increments). The correlation function  $C(t)$  associated with fBm is equal to  $2^{2H-1} - 1$  [e.g. 10 (p. 170)], i.e. it depends only on the value of  $H$ . When  $H = 1/2$ , fBm reduces to ordinary Brownian motion, in which successive displacements or increments are uncorrelated ( $C(t) = 0$ ). For  $0.5 < H < 1$ , there is a positive correlation between successive increments and fBm exhibits a ‘persistent’

behavior, characterized by clear trends and relatively little noise [e.g. 10 (p. 181)]. On the other hand, for  $0 < H < 0.5$ , fBm displays ‘anti-persistence’, the correlation is negative and, as a result, graphs of the fBm appear very noisy.

As in the case of the deterministic sets and functions considered in previous sections, the topological dimension of a random monster sheds very little light on its intricate geometry. For example, both the deterministic and random triadic von Koch curves have the same topological dimension, i.e. equal to one and identical to that of a regular line segment. Fortunately, mathematicians have introduced a number of dimensions that can characterize even the most pathological sets or functions. These dimensions are defined and analyzed in detail in the following section.

## 2.3 DIMENSIONS ASSOCIATED WITH THE MATHEMATICAL MONSTERS

### 2.3.1 Hausdorff Measure and Dimension

Of all the dimensions of sets, the one introduced by Hausdorff [25] is undoubtedly the most useful for characterizing nowhere-differentiable sets. Familiarity with its definition, and with its limitations, is essential to understanding the concept of fractals.

To understand the mathematical background of the Hausdorff dimension, it is useful to first consider as an illustration the process of measuring the ‘size’ of a set of points defining a surface in three-dimensional Euclidian space  $R^3$  (Figure 2.11a). The customary measurement of this surface is its area. It can be approximated by the product  $A \equiv N(\delta)\delta^2$ , where  $N(\delta)$  is the number of squares of side length  $\delta$  needed to

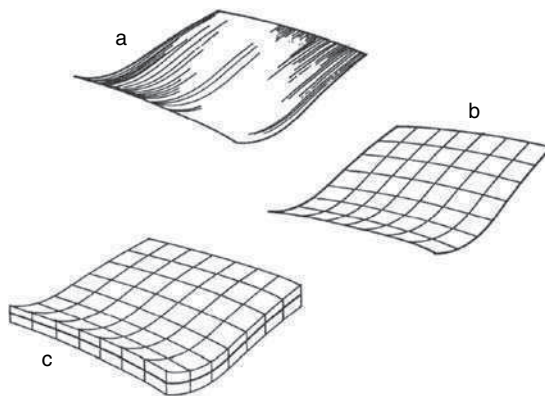


**Figure 2.11** Schematic illustration of various approaches to measuring the ‘size’ of a surface: (a) surface; (b) covering with squares; (c) covering with cubes. Modified from [10].

tile or cover the surface (Figure 2.11b). For ‘ordinary’ surfaces,  $N(\delta)$  tends to  $A_0/\delta^2$  in the limit of vanishing  $\delta$ , so that

$$A \equiv N(\delta)\delta^2 \xrightarrow[\delta \rightarrow 0]{} A_0\delta^0 = A_0 \quad (2.11)$$

where  $A_0$  is the area of the surface.

We might also try to associate a volume with the surface by calculating the sum of the volumes of the cubes of side length  $\delta$  needed to cover the surface (Figure 2.11c). Since  $N(\delta)$  tends to  $A_0/\delta^2$ , in the limit of vanishing  $\delta$ :

$$V \equiv N(\delta)\delta^3 \xrightarrow[\delta \rightarrow 0]{} A_0\delta^1 \quad (2.12)$$

which vanishes for  $\delta \rightarrow 0$ .

Formally (even though it is clearly not feasible!), we might also try to approximate the surface by the total length  $L$  of a finite number of line segments of length  $\delta$ . It is easy to see, after replacement of  $N(\delta)$  by  $A_0/\delta^2$ , that

$$L \equiv N(\delta)\delta \xrightarrow[\delta \rightarrow 0]{} A_0\delta^{-1} \quad (2.13)$$

which diverges (tends to infinity) when  $\delta \rightarrow 0$ .

The conclusion to be drawn from this (simplistic) illustration is, of course, that the only useful measure of a set of points defining an ordinary surface in  $R^3$  is the area. Interestingly, the measure of this same set of points with a ‘yardstick’ that has a lower dimension than the area (i.e. a line segment) yields an infinite (divergent) measure, while a ‘yardstick’ with a higher dimension than the area (i.e. a volume) leads to a zero measure. Therefore, the practically useful yardstick corresponds to a transition from divergent measures to zero measures. This same feature, as we shall see below, characterizes the Hausdorff dimension. The definition of the Hausdorff dimension is based on the concept of the Hausdorff measure, which itself makes use of the notion of the  $\delta$ -cover of a set.

If  $U$  denotes a nonempty subset of  $n$ -dimensional Euclidean space (i.e.  $U \subset R^n$ ), the diameter of  $U$ , i.e.  $|U|$ , is the greatest distance separating any pair of points in  $U$ . Mathematically,  $|U| = \sup \{|x - y| : x, y \in U\}$ , where  $\sup$  is the conventional abbreviation of the supremum, the smallest upper bound of a set and  $|x - y|$  is the Euclidian distance between  $x$  and  $y$ . If  $F$  (shown in Figure 2.12a) is any subset of  $R^n$ , then we can cover it with a (possibly large but countable) number of subsets  $U_i$  of  $R^n$ , such that each of the  $U_i$  has a diameter at most equal to a given  $\delta$  ( $0 < |U_i| \leq \delta$ , for each  $i$ ). This covering is done schematically in two different ways in Figure 2.12b and c. In each case,  $F$  is included in the union of all of the values of  $U_i$ . A set  $\{U_i\}$  that has this property is said to be a  $\delta$ -cover of  $F$ .

Among all the  $\delta$ -covers of  $F$ , we might be interested in determining which one is the ‘smallest’, in some sense. This  $\delta$ -cover could be defined as the one with the smallest sum of diameters. It would be equally acceptable, for example, to minimize the sums of the squares or of the third powers of the diameters. More generally, we

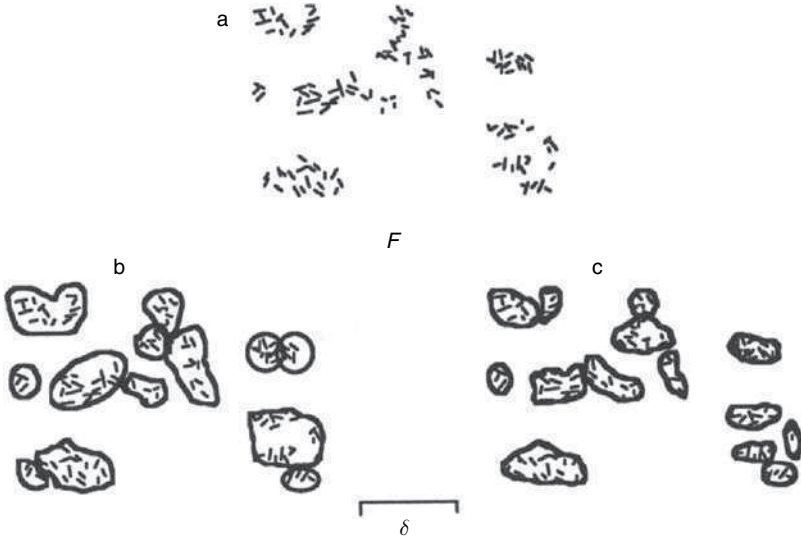


**Figure 2.12** A set  $F$  and two possible  $\delta$ -covers of  $F$ . Modified from [5].

could raise the diameters  $|U_i|$  to any nonnegative number  $s$ . For  $\delta > 0$ , we could then define [5 (p. 25)]

$$H_\delta^s(F) = \inf \left\{ \sum_{i=1}^{\infty} |U_i|^s : \{U_i\} \text{ is a } \delta\text{-cover of } F \right\} \quad (2.14)$$

where  $\inf$  represents the infimum, the largest lower bound of a set. In Equation (2.14), we look at all  $\delta$ -covers of  $F$  and we seek to minimize the sum of the  $s$ th power of the diameters.

As  $\delta$  decreases, the class of permissible covers of  $F$  in Equation (2.14) is reduced. Therefore, the infimum cannot decrease as  $\delta$  decreases. As  $\delta \rightarrow 0$ , the infimum approaches a limit which may be infinite or a real number greater than or equal to zero. This limit is defined as

$$H^s(F) = \lim_{\delta \rightarrow 0} H_\delta^s(F) \quad (2.15)$$

and is termed the  $s$ -dimensional Hausdorff measure of  $F$ . For integral values of  $s$ , the Hausdorff measure is reduced to the traditional  $n$ -dimensional Lebesgue measure (i.e. the usual  $n$ -dimensional volume), multiplied by a constant.

It is clear from Equation (2.14) that if  $\delta < 1$ , for any given set  $F$ , the terms  $|U_i|^s$  tend to decrease when  $s$  increases. Therefore,  $H_\delta^s(F)$  is nonincreasing with  $s$  for  $\delta \leq 1$



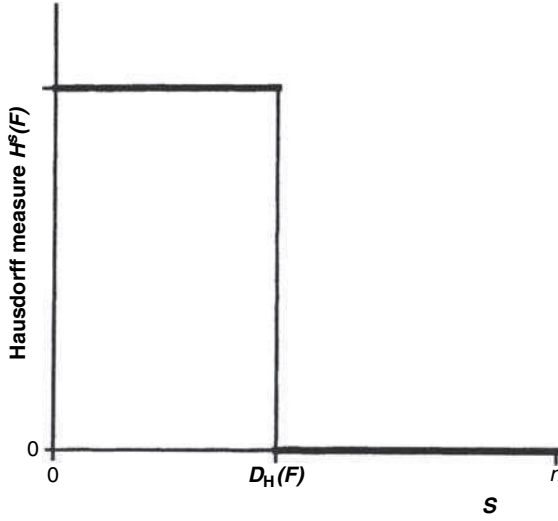


**Figure 2.13** Graph of the Hausdorff measure against  $s$  for an arbitrary set  $F$ . The Hausdorff dimension is the value of  $s$  at which the Dedekind cut, or ‘jump’, from infinity to zero occurs.

and, by Equation (2.15),  $H^s(F)$  has the same property. In fact, it is possible to show that, if  $t > s$  and  $\{U_i\}$  is a  $\delta$ -cover of  $F$ :

$$\sum_i |U_i|^t \leq \delta^{t-s} \sum_i |U_i|^s \quad (2.16)$$

Taking infima according to Equation (2.14), one finds that  $H_\delta^t(F) \leq \delta^{t-s} H_\delta^s(F)$ . Letting  $\delta \rightarrow 0$ , we see that if  $H^s(F) < \infty$ , then  $H^t(F) = 0$  for  $t > s$ . Thus, a graph of  $H^s(F)$  against  $s$  (Figure 2.13) shows that there is a critical value of  $s$  at which  $H^s(F)$  ‘jumps’ from infinity to zero. This critical value of  $s$  (at which  $H^s(F)$  may in general be undefined) is  $D_H$ , the *Hausdorff dimension* of  $F$ .

The Hausdorff dimension of the triadic Cantor set is 0.631 and that of the von Koch curve equals 1.262. This latter number is entirely consistent with the von Koch curve being somehow ‘larger than one-dimensional’ (having infinite length within a bounded domain) and ‘smaller than two-dimensional’ (having zero area). In similar fashion, it is not surprising that graphs of Brownian motions (see Section 2.2.5) have a Hausdorff dimension equal to 1.5. Not all Hausdorff dimensions of mathematical ‘monsters’ are fractional. For example, that of the Cantor singular function (Devil’s staircase) is  $D_H = 1$ , whereas the Hausdorff dimensions of the Sierpinski tetrahedron, the Peano plane-filling curve and paths of the mathematical Brownian motion in  $R^n$  ( $n \geq 2$ ) are all  $D_H = 2$ .

To say the least, the above description of the theory leading to the definition of the Hausdorff dimension does not suggest a simple and intuitive way of evaluating this dimension in practical cases. Indeed, the calculation of Hausdorff measures and dimensions is, in general, more than a little involved, even for simple sets [e.g. 26

(pp. 156–157)]. Rigorous dimension calculations often involve pages of complicated manipulations. In some cases, e.g. the Weierstrass–Mandelbrot function, there remains some uncertainty on the correct outcome of these calculations [e.g. 10 (p. 27), 20]. Nevertheless, the Hausdorff dimension has the distinct advantage of being defined for any set (cf. the handling of statistically self-similar sets in Hutchinson [27] and Graf *et al.* [28]). It can, therefore, provide a reference for comparison with values of dimensions computed via simpler, more straightforward methods (as described in the following subsections).

### 2.3.2 Similarity Dimension

A heuristic method, which often results in a number equal to the Hausdorff dimension of sets of points, leads to the definition of another dimension. Following Falconer [5 (p. 31)], let us take the Cantor set  $P$  (see Figure 2.1) as an example. It can easily be split into a left part  $P_L = P \cap [0, 1/3]$  and a right part  $P_R = P \cap [2/3, 1]$ . Both parts are geometrically similar to  $P$  but scaled down by a ratio  $1/3$ , and  $P$  is the (disjoint) union of  $P_L$  and  $P_R$ . Because the Hausdorff measure is additive and scales according to  $H^s(\lambda F) = \lambda^s H^s(F)$ , where  $F \subset \mathbb{R}^n$  and  $\lambda > 0$ , one finds that

$$H^s(P) = H^s(P_L) + H^s(P_R) = \frac{1}{3^s} H^s(P) + \frac{1}{3^s} H^s(P) \quad (2.17)$$

Assuming that at the critical value  $s = D_H(P)$ , we have  $0 < H^s(P) < \infty$  (note that this is an important assumption, but one that can be justified [5]), we may then divide Equation (2.17) by  $H^s(P)$  to get  $1 = 2(1/3)^s$  or  $s = \ln 2 / \ln 3 \approx 0.631$ .

In this estimate of the Hausdorff dimension of the Cantor set, we end up with a ratio of two natural logarithms. The denominator corresponds to the number of segments (three) into which the initiator is divided, while the numerator corresponds to the number of segments (two) that are retained in the generator. Alternatively, we could look at two as the number of copies of itself, scaled by a factor  $1/3$ , which the Cantor set contains. One could extend this reasoning to other sets and consider that, in general, a set made up of  $m$  copies of itself scaled by a factor  $1/r$  has a dimension,  $\ln m / \ln r$ . The number obtained in this way is usually referred to as the *similarity dimension*  $D_s$  of the set.

It turns out that for virtually all the deterministic monsters introduced earlier, the similarity and Hausdorff dimensions coincide. For example, it is easy to see that the triadic von Koch curve has a similarity dimension  $D_s = \ln 4 / \ln 3 \approx 1.262$ , identical to its Hausdorff dimension (see previous section). For the Sierpinski gasket,  $D_s = \ln 3 / \ln 2 \approx 1.585$ , for the Sierpinski carpet,  $D_s = \ln 8 / \ln 3 \approx 1.89$  and for the Menger sponge,  $D_s = \ln 20 / \ln 3 \approx 2.73$ ; all three  $D_s$  values are identical to the corresponding Hausdorff dimensions. In the case of ‘nonmonstrous’ sets, the similarity dimension also behaves properly. For example, if we consider a straight-line segment, divide it into four sub-segments of length scaled by a factor  $1/4$ , keep all four segments and iterate this procedure indefinitely, the similarity dimension of the

resulting set is  $D_S = \ln 4 / \ln 4 = 1$ , which is the same as the Hausdorff dimension of the set.

In Section 2.2.2, it was shown that, after  $n$  iterations in the construction of the triadic von Koch curve, the number  $N_n$  of segments of length  $\delta_n$  is a power-law function of  $\delta_n$ :  $N_n = \delta_n^{-\ln 4 / \ln 3}$ . With the introduction of the similarity dimension, and by virtue of the equality between Hausdorff and similarity dimensions for the triadic von Koch curve, this power-law relationship may also be expressed as

$$N_n = \delta_n^{-\ln 4 / \ln 3} = \delta_n^{-D_S} = \delta_n^{-D_H} \quad (2.18)$$

from which it follows that  $D_S = D_H$  may be obtained graphically from the slope of  $N_n$  versus  $\delta_n$  in a log-log graph.

Even without having recourse to this graphical method, the similarity dimension is clearly very straightforward to compute. Unfortunately, it is meaningful only for a small class of strictly self-similar sets. It cannot be used to evaluate the dimension of self-affine, statistically self-similar or statistically self-affine sets. For these, other easily measurable dimensions are necessary, like the box-counting dimension.

### 2.3.3 Box-Counting Dimension

In calculating the infimum  $H_\delta^s(F)$  in Equation (2.14), on the route to defining the Hausdorff dimension, the covering sets  $U_i$  were allowed to have various diameters, within the constraint  $|U_i| \leq \delta$ . One possible approach to a dimension that would be equally general, yet simpler to compute than the Hausdorff dimension, would be to require that the diameters of all the  $U_i$  equal  $\delta$ , or, equivalently, to replace  $|U_i|$  by  $\delta$  in Equation (2.14). Using this approach, one would obtain a number  $N_\delta(F)$ , associated with a given nonempty bounded subset  $F$  of  $R^n$ , such that

$$N_\delta(F)\delta^s = \inf \left\{ \sum_i \delta^s : \{U_i\} \text{ is a (finite) } \delta\text{-cover of } F \right\} \quad (2.19)$$

In other words,  $N_\delta(F)$  is the smallest number of sets of diameter at most  $\delta$  that can cover  $F$ .

Based on the definition of Equation (2.19), it is convenient to define a new dimension, called the *box-counting dimension*, denoted here by  $D_{BC}$ , as

$$D_{BC}(F) = \lim_{\delta \rightarrow 0} \frac{\ln N_\delta(F)}{-\ln \delta} \quad (2.20)$$

The motivation for this (apparently arbitrary) definition is that, for many sets of points, there is a nearly linear relationship between  $\ln N_\delta(F)$  and  $\ln \delta$  for small  $\delta$ , and, as  $\delta \rightarrow 0$ , the slope of this relationship approaches  $D_{BC}(F)$ . Nevertheless,  $D_{BC}(F)$  as defined by Equation (2.20) has meaning only when the limit as  $\delta \rightarrow 0$  exists (see discussion in [5]).

The dimension  $D_{BC}$  may be thought of as an indication of the efficiency with which a set may be covered by small sets of equal size, whereas the Hausdorff dimension

$D_H$  involves coverings by sets of small but perhaps widely varying size. The box-counting dimension is sometimes also referred to as the ‘Minkowski’ dimension [5], ‘Minkowski–Bouligand’ dimension [4, 29, 30], ‘Bouligand–Minkowski’ dimension [31], ‘capacity’ dimension [5, 32] or the ‘Kolmogorov entropy’ [5].

Up to this stage, the geometrical shape of  $U_i$  has not been specified in any way, which suggests that the definition of Equation (2.19) can accommodate a variety of geometries. This variety is quite large indeed. It is possible to show mathematically [5 (p. 41)] that  $N_\delta(F)$  in Equation (2.20) can be any of the following options, illustrated in Figure 2.14:

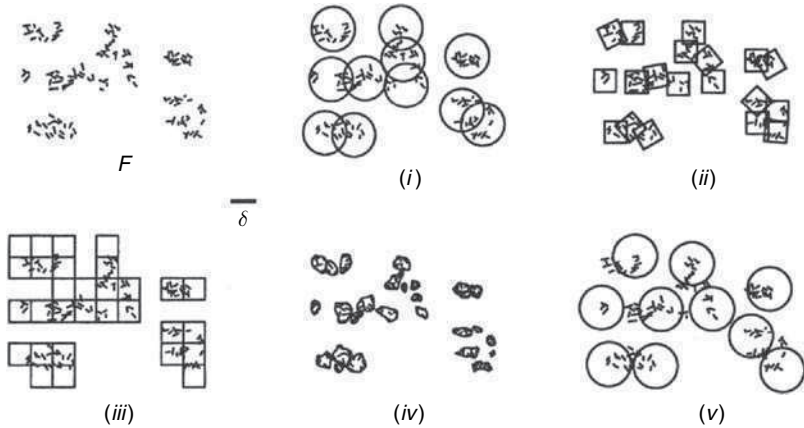


**Figure 2.14** Five ways of finding the box dimension of  $F$  (see text for details on (i)–(v)). Modified from [5].

- The smallest number of closed balls of radius  $\delta$  that cover  $F$ . (A closed ball  $B_r(x)$  is a set defined as  $B_r(x) = \{y : |y - x| \leq r\}$ , where  $x$  and  $r$  are called the center and the radius of the set.)
- The smallest number of cubes of side  $\delta$  that cover  $F$ .
- The number of ‘ $\delta$ -mesh’ cubes of side  $\delta$  that cover  $F$  (this number has been used for decades by geographers and cartographers, and justifies the ‘box-counting’ qualifier).
- The smallest number of sets of diameter at most  $\delta$  that cover  $F$ .
- The largest number of disjoint balls of radius  $\delta$  with centers in  $F$ . It is not readily obvious that this number is mathematically equivalent to the others, yet such is the case [e.g. 5 (p. 41)].

Mathematically, the definition of Equation (2.20) implies that  $N_\delta(F)\delta^s \rightarrow \infty$  if  $s < D_{BC}(F)$  and that  $N_\delta(F)\delta^s \rightarrow 0$  if  $s > D_{BC}(F)$ . In other words, the product  $N_\delta(F)\delta^s$

has a (Dedekind) cut similar to that experienced by the Hausdorff measure (cf. Figure 2.13). The analogy does not extend further, however. The limit of  $N_\delta(F)\delta^s \rightarrow 0$  as  $\delta \rightarrow 0$  does not, unfortunately, correspond to a measure on subsets of  $R^n$ . This has a number of unpleasant consequences, one of them being that countable sets of points can have nonzero box-counting dimensions. For example, the countable (compact) set  $\{0, 1, 1/2, 1/3, \dots\}$  has a Hausdorff dimension equal to zero but a box-counting dimension equal to 0.5.

A number of alternative dimensions have been proposed to overcome the difficulties associated with the traditional box-counting dimension  $D_{BC}$ . They include the lower and upper modified box-counting dimensions [5] and the packing or Tricot dimension [5, 33, 34]. Unfortunately, these dimensions reintroduce all the difficulties of calculation associated with  $D_H$ , and in some cases are even more awkward to use!

One key advantage of the box-counting dimension  $D_{BC}$  over the similarity dimension  $D_S$  is that  $D_{BC}$  can be used to evaluate the dimension of self-affine sets. In these sets, however,  $D_{BC}$  is not uniquely defined; instead, it assumes two different values: a local or small-scale value and a global or large-scale value [e.g. [10 (p. 187), 31 (p. 55), 35 (p. 8)]. In the case of the fractional Brownian motion (Section 2.2.5), the local  $D_{BC}$  value is equal to the Hausdorff dimension and is given by  $2 - H$ , where  $H$  is the Hurst exponent, whereas the global value of  $D_{BC} = 1$  [e.g. 10 (p. 189)].

### 2.3.4 Divider Dimension

In the case of curves that do not intersect themselves, it is possible to define another dimension, denoted here by  $D_D$  and generally referred to as the *divider or compass dimension*. If  $C$  is a curve in  $R^n$  and  $\delta > 0$ , we define  $N_\delta(C)$  as the maximum number of points  $x_0, x_1, \dots, x_m$  on the curve  $C$ , in that order, such that  $|x_k - x_{k-1}| = \delta$  for  $k = 1, 2, \dots, m$ . Thus,  $(N_\delta(C) - 1)\delta$  may be thought of as the length of the curve measured using a pair of dividers with points set a distance  $\delta$  apart, i.e. with ‘yardsticks’ of length  $\delta$ . Under these conditions, the divider dimension  $D_D$  is defined as [5]

$$D_D(C) = \lim_{\delta \rightarrow 0} \frac{\ln N_\delta(C)}{-\ln \delta} \quad (2.21)$$

assuming that this limit exists. It is possible to show that  $D_D \geq D_{BC}$ , when both these dimensions exist. In simple self-similar examples, such as the von Koch curve,  $D_D$  and  $D_{BC}$  are equal, but in other cases the inequality has been shown to apply. For example, fractional Brownian motion (Section 2.2.5) has a local  $D_D$  value equal to  $1/H$ , where  $H$  is again the Hurst exponent, which is always strictly larger than its local  $D_{BC}$  value, equal to  $2 - H$  [e.g. 10 (p. 189)]. Tricot [33 (p. 234)] expresses reservations about the use of the divider method to evaluate the dimension of curves that are not exactly or statistically self-similar (e.g. the west coast of Britain, which will be mentioned again in Section 2.4.1). Indeed, he argues that the divider dimension does not have a precise metric meaning in these cases.

### 2.3.5 Pointwise Dimension and Hölder Exponent

Another dimension that has interesting properties is called the ‘pointwise’ or ‘mass’ dimension [e.g. 14 (p. 736), 32 (p. 334)]. To define it, one considers a curve in  $R^n$  and samples it uniformly at a large number  $N_0$  of points, i.e. one determines the spatial coordinates of  $N_0$  points uniformly distributed along the curve. Then, one centers a ball  $B_r(x)$  of radius  $r$  at some location  $x$  on the curve, and one counts the number  $N(r, x)$  of sampled points within this ball. The probability of finding a point in this ball is given by the limit

$$\mu(B_r(x)) = \lim_{N_0 \rightarrow \infty} \frac{N(r, x)}{N_0} \quad (2.22)$$

This limit may also be viewed as the measure or ‘mass’ of the curve that is contained in the ball  $B_r(x)$ .

By analogy with previous definitions of dimensions, one may define the *pointwise dimension*  $D_p$  at the location  $x$  as follows:

$$D_p(x) = \lim_{r \rightarrow 0} \frac{\ln \mu(B_r(x))}{\ln r} \quad (2.23)$$

In some cases, the limit as  $r \rightarrow 0$  is not taken in Equation (2.23) and the ratio  $\ln \mu(B_r(x)) / \ln r$  is termed in this case the Hölder [36], coarse Hölder [37] or Lipschitz–Hölder exponent [34]. It is traditionally denoted by  $\alpha$  and it may be evaluated for any measure, defined or not by Equation (2.22). This exponent is useful to characterize ‘singular’ measures, which have no local densities (i.e. for which the limit in Equation (2.23) does not exist), and it plays an important role in the definition of multifractal measures (Section 2.6).

### 2.3.6 An Arsenal of Dimensions

The previous subsections indicate that several concepts of dimension have been proposed over the years to characterize the geometrical properties of sets of points. Many more dimensions than those presented above exist. They include, for example, the *Ljapunov dimension* [14, 26], the *spectral dimension* [34], the *information dimension*  $D_1$  [14, 26, 32, 38] and the *Fourier dimension* [5].

Another dimension, occasionally used in environmental science, is referred to as the *variogram dimension*. In Section 2.2.4, a relationship was mentioned between the variance of increments  $V(t)$  and the parameter  $D$  appearing in the formulation of the Weierstrass–Mandelbrot function  $w(t)$ . In the case of spatial functions, it is more common to compute the semi-variance (half the variance of increments), also termed the variogram. By analogy with the behavior of  $V(t)$  at the origin, for the variogram, one may postulate a power-law dependency on the spatial increment  $h$  (or ‘lag’) as  $h \rightarrow 0$  and define a variogram dimension [e.g. 19, 39].

How many dimensions are there? Their number is in principle infinite, as was illustrated elegantly by Hentschel and Proccacia [40], who defined a collection of

dimensions  $D_q$ , for  $q \geq 0$ , now often referred to as the *Rényi dimensions* [e.g. 14 (p. 736)]. The first in this collection ( $q = 0$ ) corresponds to the *box-counting dimension*  $D_{BC}$ . The second ( $q = 1$ ) is equivalent to the *information dimension*  $D_I$ , and the third ( $q = 2$ ) to the *correlation dimension*  $D_C$ . It can be proven mathematically that the Rényi dimensions  $D_q$  are decreasing with  $q$ , i.e.  $D_p \geq D_q$  if  $p < q$ . In particular, this implies that  $D_C \leq D_I \leq D_{BC}$ , where equality occurs only in special cases. In general, these dimensions are not equal.

### 2.3.7 Lacunarity

At the same time that he coined the term ‘fractal’, Mandelbrot [4] pointed out that fractal dimensions would not suffice to provide a satisfactory description of the geometry of lacunar fractals, and that at least one other parameter, which he termed ‘lacunarity’, would be necessary. The key reason for this requirement is vividly illustrated by the fact that Sierpinski carpets (Figure 2.15) with greatly different appearances can have precisely the same fractal (similarity) dimension. Therefore, the fractal dimension alone is not a very reliable diagnostic of the geometry and properties of lacunar fractals. For physical objects, such as porous media, where the geometry of interstices and pores influences a wide range of properties, this means that any attempt to find a unique relationship between the fractal dimension of these objects and, for example, their transport or dielectric properties is most probably doomed to failure, unless one also takes lacunarity explicitly into account.

Mandelbrot and co-workers [4, 41, 42] introduced the concept of lacunarity as a measure of the distribution of gap sizes in a given geometric object. In other words, lacunarity can be thought of as a measure of the ‘gappiness’ or ‘hole-iness’ of a geometric structure [43]. Objects are more lacunar if their gap sizes are distributed over a wider range. In that sense, the Sierpinski carpet of Figure 2.15a is more lacunar than that of Figure 2.15c. A more precise definition of lacunarity was introduced by Gefen *et al.* [44], who viewed lacunarity as a measure of the deviation of a geometric object from translational invariance. In a low lacunarity object, where gap

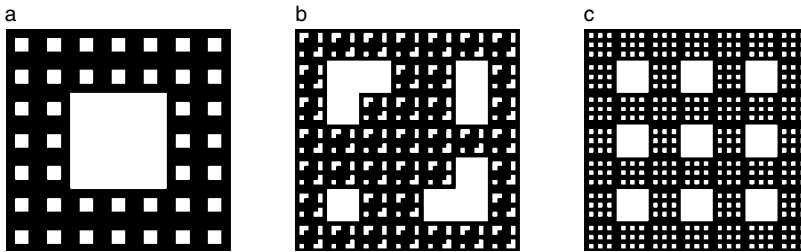


**Figure 2.15** Examples of 2nd iterate prefractals of Sierpinski carpets having different appearances, but identical fractal (similarity) dimension. In all three cases, the iterative construction process consists of dividing the initiator in  $7 \times 7 = 49$  squares, and removing  $3 \times 3 = 9$  squares. This process is associated with a similarity dimension  $D_s = \ln(49 - 9) / \ln 7 = 1.8957$ .

sizes are relatively homogeneous, different regions of the object tend to be similar to each other (as in Figure 2.15c). In contrast, in a high lacunarity object (like that in Figure 2.15a), different regions may be very dissimilar and cannot be made to coincide by simple translation. This characterization of the translational invariance of geometric objects is highly scale dependent: objects that are heterogeneous at small scales can be homogeneous when examined at larger scales or vice versa [44].

A method for calculating the lacunarity was outlined in general terms by Mandelbrot [4]. Subsequently, progress toward a usable method was made by Gefen *et al.* [44]. Allain and Cloitre [45] developed a straightforward algorithm, based on ‘gliding boxes’ (or ‘moving windows’) of increasing sizes, to evaluate the lacunarity of both deterministic and random fractals. More recently, Chappard *et al.* [46] described a different method to calculate the lacunarity, based on the mass–radius or ‘sandbox’ algorithm used routinely to estimate fractal dimensions. Both of these algorithms, and variants thereof, have been used extensively in the literature [e.g. 47–49].

In the calculation method suggested by Allain and Cloitre [45], a square structuring element or moving window of side length  $l$  is placed in the upper left-hand corner of an image of a solid geometrical structure of side length  $T$  (such that  $l \leq T$ ). The calculation algorithm records the number or ‘mass’  $m$  of pixels that are associated with the solid underneath the moving window. The window is then translated by one pixel to the right and the underlying mass is again recorded. When the moving window reaches the right side of the image, it is moved back to its starting point at the left side of the image and is translated by one pixel downward. The calculation proceeds in this fashion until eventually the moving window reaches the lower right-hand corner of the image, at which point it has explored every one of its  $(T - l + 1)^2$  possible positions above the solid.

At that juncture, one may easily compute the number  $n(m, l)$  of times a particular value of the mass  $m$  has been recorded with the moving window of side length  $l$ . Division of  $n(m, l)$  by the total number  $(T - l + 1)^2$  of possible positions of the moving window above the image yields the probability distribution function  $Q(m, l) = n(m, l) / (T - l + 1)^2$ . The statistical moments  $Z_Q^{(q)}(l)$  of this probability distribution function are defined as

$$Z_Q^{(q)}(l) = \sum_m m^q Q(m, l) \quad (2.24)$$

where  $q = 1$  and  $2$  for the first and second moments respectively, and the summation extends over all possible values of  $m$  (i.e. from  $0$  to  $l^2$  for a moving window of side length  $l$ ).

On the basis of these moments, Allain and Cloitre [45] define the lacunarity  $\Lambda_{\text{GB}}(l)$ , measured with a moving window of side length  $l$ , as

$$\Lambda_{\text{GB}}(l) = \frac{Z_Q^{(2)}(l)}{(Z_Q^{(1)}(l))^2} \quad (2.25)$$



Since the first moment  $Z_Q^{(1)}(l)$  is equal to the mean  $\mu_Q$  of the probability distribution function  $Q$ , and the second moment  $Z_Q^{(2)}(l)$  is equal to the sum of the variance  $\sigma_Q^2$  of  $Q$  and the square of the mean, i.e.  $Z_Q^{(2)}(l) = \sigma_Q^2 + \mu^2$ , one may rewrite Equation (2.25) as

$$\Lambda_{GB}(l) = \frac{\sigma^2}{\mu^2} + 1 \quad (2.26)$$

which shows, perhaps more clearly than Equation (2.25), that  $\Lambda_{GB}(l)$  is fundamentally a relative measure of the width of the distribution  $Q(m, l)$ . For a translationally invariant set, it is straightforward to show that  $Z_Q^{(2)}(l) = [Z_Q^{(1)}(l)]^2$ . Under these conditions,  $\Lambda(l)$  becomes identically equal to unity and is independent of  $l$ .

The algorithm developed by Chappard *et al.* [46] is based on the sand-box method elaborated earlier by Tél *et al.* [50]. In this algorithm, a number  $s$  of points or ‘seeds’ are selected randomly within the geometrical domain occupied by the object under study, with  $s$  taken either arbitrarily or equal to the number of seeds at which convergence is reached for a number of targeted summary statistics. Around each seed,  $k$  concentric circles are drawn and the mass  $m$  of the object that is contained in each circle is recorded as a function of the circle diameter  $l$ . Once this process has been carried out for all  $s$  seeds, one may compute a mass distribution  $n(m, l)$  that depends on the mass  $m$  and circle diameter  $l$ . This mass distribution can readily be transformed into a probability distribution function  $Q(m, l)$  via division by the number  $s$  of seeds, i.e. according to  $Q(m, l) = n(m, l)/s$ .

Using Equation (2.24) once again to define the moments of the probability distribution function  $Q(m, l)$  and remembering that the variance of  $Q(m, l)$  is equal to the difference of  $Z_Q^{(2)}(l)$  and  $(Z_Q^{(1)}(l))^2$ , one finds easily that the coefficient of variation  $cv(l)$  of  $Q(m, l)$  is given by

$$cv(l) = \frac{\sigma}{\mu} = \frac{\sqrt{Z_Q^{(2)}(l) - (Z_Q^{(1)}(l))^2}}{Z_Q^{(1)}(l)} \quad (2.27)$$

This coefficient of variation is related to  $\Lambda_{GB}(l)$  by the relation  $cv(l) = \sqrt{\Lambda_{GB}(l) - 1}$ .

Chappard *et al.* [46] use this coefficient of variation to define their lacunarity  $L_C$  as follows:

$$L_C = \frac{1}{k} \sum_l cv(l) \quad (2.28)$$

where the summation extends over all  $k$  circle diameters considered around the seeds.

Comparison of Equations (2.25) and (2.28) makes it readily apparent that  $\Lambda_{GB}(l)$  and  $L_C$  are fundamentally different concepts, even though they are both referred to as lacunarities. Indeed, whereas  $\Lambda_{GB}(l)$  depends on the side length  $l$  of the moving windows or structuring element, Chappard *et al.*’s [46] lacunarity  $L_C$  does not depend on  $l$ , as a result of the averaging of  $cv(l)$  over the number of circle radii  $k$  in

Equation (2.28). Unless one keeps in mind that there is no general agreement on the precise meaning of the term lacunarity, nor on its scale dependence, there is a high risk of confusion. Some of this confusion is evident in the literature.

2.4 FROM MATHEMATICAL MONSTERS TO ‘FRACTALS’

2.4.1 Physical Motivation

Section 2.2 introduced a large array of ‘monstrous’ mathematical beings that exhibit pathological properties defying the traditional concept of dimension. In Section 2.3, we saw that various alternatives to the traditional topological dimension have been devised by mathematicians. In spite of their multiplicity, these dimensions have tended to make the mathematical monsters somewhat less terrifying.

Observations made by scientists over the years provided additional momentum in the same direction. The physical process whose study was perhaps most influential in stimulating interest in nowhere-differentiable functions is Brownian motion, described in Section 2.2.5. Besides Brownian motion, several other physical processes contributed to foster interest in nowhere-differentiable functions. A few years after Wiener’s work, Dedebant and Wehrlé [51] studied a number of scale issues arising in meteorology and concluded that ‘many meteorological processes, observed at a very small scale, are like the continuous, nondifferentiable functions that seemed forever to belong to the realm of speculative mathematicians’ [51 (p. 83)].

More recently, Chepil [52] observed a marked and systematic decrease of the densities of soil aggregates as the size of these aggregates increased (Figure 2.16).

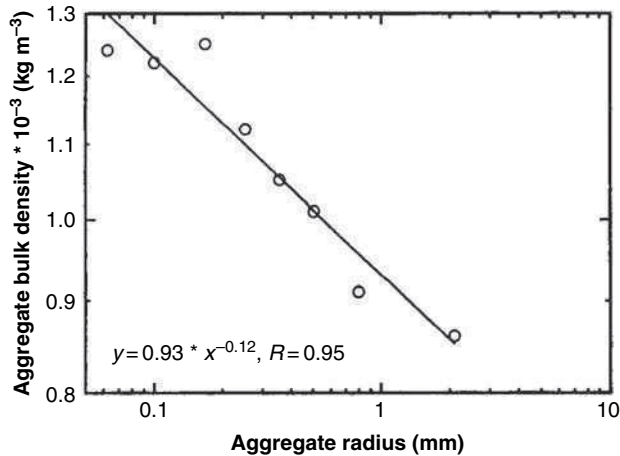


**Figure 2.16** Bulk density of soil aggregates as a function of their radius. (Data from table 4 in [52], fine sandy loam.)

This behavior, which is not intuitive from a traditional geometric standpoint, is similar to that predicted by Equation (2.4) for intermediate steps in the iterative procedure leading to the Menger sponge. Indeed, if large aggregates are viewed as containing a greater variety of pore sizes than small aggregates – corresponding to the complexity found in the later stages in the iterative construction of the Menger sponge – then in Equation (2.4) one could keep  $l_n$  and  $\rho_0$  constant and observe that, as  $l_0$  increases, the mass density  $\rho_n$  must decrease, since the exponent  $3 - \ln 20 / \ln 3$  is strictly positive ( $\approx 0.273$ ). Therefore, at least some of the features of the Menger sponge may be useful to describe the properties of soil aggregates.

Perhaps the most acute realization that the mathematical monsters of the previous section have properties very close to those routinely found in nature was made by geographers. Richardson’s [53] work is particularly significant in this respect. He measured a number of geographical curves (coastlines and country borders), using the divider or compass method, that led to the definition of  $D_D$  in Section 2.3.4. For a circle, the total length tends to a limit as the segment length goes to zero (see Figure 2.17). In all other cases, it increases as the side becomes shorter. This behavior is identical to that described above for the triadic von Koch curve (Section 2.1.2). In this latter case, the length of the  $n$ th iteration step  $l_n$  has a power-law or Paretian relationship with the ‘yardstick’ length  $\delta_n$  (see Equation (2.2)). In other words,  $L(l_n)$  and  $\delta_n$  are related via a straight line in a log–log plot. This is precisely what is observed for the various geographical curves shown in Figure 2.17.

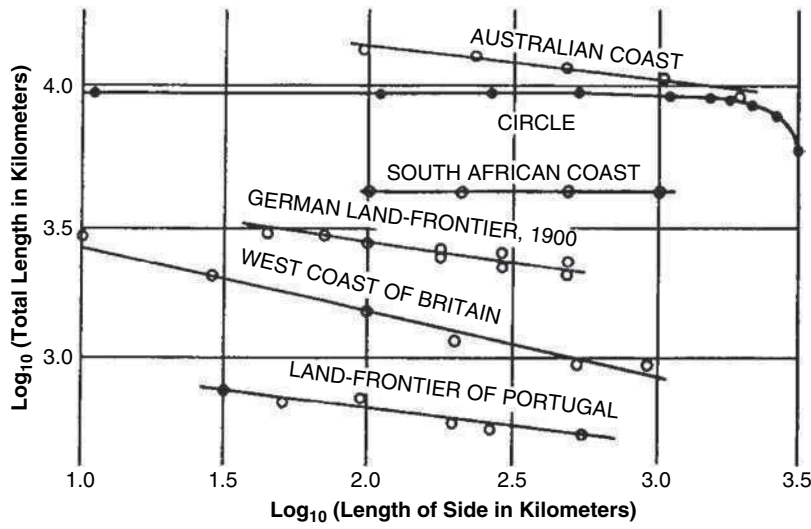


**Figure 2.17** The length of coastlines as a function of yardstick length. (Data from [53].)

### 2.4.2 ‘Definition’ of Fractals

As the examples of the previous section illustrate, many scientists observed over several decades that natural objects or processes often have features akin to those of the von Koch curve or Menger sponge. This greatly stimulated interest in these monstrous sets; in this case, as in many others, interest in geometry was driven by its applications to nature [5].

This movement led to the publication by Mandelbrot in 1975 [1] of an essay in which he highlighted the similarities among the then-known continuous, nowhere-differentiable sets. He coined for these sets the term ‘fractal’, to emphasize the fact that their Hausdorff dimensions are often fractional. In the words of Dyson [54], ‘fractal is a word invented by Mandelbrot to bring together under one heading a large class of objects that have [played] . . . an historical role . . . in the development of pure mathematics’.

Mandelbrot believed initially that one would do better without a precise definition of fractals. His original essay [1] contains none. By 1977, however, he saw the need to produce at least a tentative definition. It is the now classical statement that ‘a fractal is a set for which the Hausdorff dimension strictly exceeds the topological dimension’ [4, 5, 10]. For example, the Cantor set is a fractal, according to this viewpoint, since  $D_H = 0.631 > D_T = 0$ .

The above definition immediately proved unsatisfactory, in that it excluded a number of sets with properties very similar to those of sets that satisfied the definition and, therefore, which also ought to be regarded as fractals. Indeed, according to this definition, the Cantor singular function ( $D_H = D_T = 1$ ) and the Peano plane-filling curve ( $D_H = D_T = 2$ ) are not fractals. Various other definitions of fractals have been proposed [e.g. 4 (p. 362)], but they all seem to suffer from the same drawback.

Perhaps by modifying slightly the list of attributes of the Cantor set (Section 2.2.1), and by relaxing or deleting some of them, one could approach, as closely as possible, to a definition of the concept of fractal. This was done by Falconer [5], in what appears to be the best approximation of this concept to date. According to this author, when one refers to a set  $F$  (of points) as a fractal, one typically has one or more of the following properties in mind:

- $F$  has a fine structure, i.e. detail on arbitrarily small scales;
- $F$  is too irregular to be described in traditional geometrical language, both locally and globally;
- $F$  often has some form of self-similarity, perhaps approximate or statistical;
- usually, the ‘fractal dimension’ of  $F$  (defined in some way) is greater than its topological dimension;
- in most cases of interest,  $F$  is defined in a very simple way, *perhaps* recursively (in which case, the various stages of the iterative construction are usually referred to as prefractals).

Falconer [5] has perhaps best captured the spirit with which the above definition of fractals needs to be undertaken:

My personal feeling is that the definition of a ‘fractal’ should be regarded in the same way as the biologist regards the definition of ‘life’. There is no hard and fast definition, but just a list of properties characteristic of a living thing, such as the ability to reproduce or to move or to exist, to some extent, independently of the environment. Most living things have most of the characteristics on the list, though there are living objects that are exceptions to each of them.

While probably agreeing in principle with Falconer’s [5] perception, many authors (in the fractal geometry literature at least) tend to give preferential weight to the requirement that fractals exhibit some form of self-similarity (see above, third point in the list of attributes of fractals).<sup>3</sup> Feder [10 (p. 11)], for example, defines a fractal as a ‘shape made of parts similar to the whole in some way’. In other words, a fractal appears the same regardless of the scale of observation; its ‘look’ is scale invariant.<sup>4</sup>

Perhaps the most important aspect of the various definitions above is that they all consider fractals to be sets of points in  $R^n$ , i.e. geometric constructs. This feature will assume particular significance in Section 2.5, where we shall discuss nongeometric fractals.

As with the concept of fractals itself, a certain level of vagueness characterizes the definition of the fractal dimension. The approach advocated by Mandelbrot in 1975 [1], and reiterated in his 1982 book, is to use the expression ‘fractal dimension’ as a generic term applicable to all the variants described in Section 2.3, and to use in each specific case whichever definition is most appropriate. This suggestion is adopted by a number of authors [e.g. 56]. However, it could, potentially, lead to considerable confusion if it is followed inconsistently, particularly in cases where different dimensions assume different values (see Section 2.3 for examples). Therefore, many mathematicians consider it safer to refer to specific dimensions by name, such as the correlation dimension, instead of using the generic term ‘fractal dimension’ [e.g. 5].

### 2.4.3 ‘Natural’ versus Mathematical Fractals

Can fractals, defined as in Section 2.4.2, serve as appropriate representations of natural objects or processes? The answer to this question is (surprisingly perhaps, yet uncompromisingly) no. Strictly speaking, *there are no true (mathematical) fractals in*

<sup>3</sup> It should be kept in mind, however, that self-similarity cannot be the *sole* defining characteristic of fractals. A straight line segment is exactly self-similar, yet it hardly qualifies as a fractal!

<sup>4</sup> However, graphs like that of Figure 2.17 indicate that specific geometric features of fractals, such as perimeter length or surface area, depend strongly on observation scale. Instead of ‘scale invariance’, therefore, one might consider, with Nottale [55], that the expression ‘scale-covariance’ captures the essence of fractals better. However, exploration of this notion of ‘scale covariance’ is beyond the scope of the present chapter.

*nature* [e.g. 5, 57 (p. 319)]. Nevertheless, under specific conditions, physical objects, like soil aggregates or clouds, may have features that are very accurately described by fractals or prefractals. A similar situation pertains with other geometrical structures; there are no true straight lines or circles in nature, yet one would hardly claim that these concepts have absolutely no use in describing nature!

Two of the ways in which true fractals can fail to represent physical objects are illustrated by the attempt to use the Menger sponge as a model of soil aggregates. First, soil aggregates have a porosity strictly smaller than unity and a mass density different from zero (otherwise there would be no aggregates to speak of!), but the Menger sponge has both porosity equal to unity and zero density (Section 2.2.3). Second, even if soil aggregates exhibit self-similarity over a range of observation scales (e.g. in thin sections observed under the microscope at different magnifications), this self-similarity eventually disappears if the aggregates are viewed at sufficiently small observation scales (e.g. in the extreme, at subatomic scales) or, at the other end of the spectrum, at observation scales commensurate with the size of the aggregate itself. By contrast, the Menger sponge has a fine structure at arbitrarily small scales.

For these two reasons, the Menger sponge cannot serve as a model of soil aggregates. In discussing Chepil's [52] results, however, we have seen that the prefractals associated with the Menger sponge (i.e. the sets of points obtained at intermediate steps in the iterative procedure which leads ad infinitum to the Menger sponge) have properties that are closely related to those of real aggregates (see Figure 2.16). These prefractals have a porosity  $<1$  and a mass density  $>0$ . Analysis of other examples, such as coastlines, clouds or landscapes, can lead to the same conclusion: fractal geometry is never an exact description of nature and often the geometry of a prefractal is a closer approximation to a physical object than is its associated fractal. Although physical systems are commonly referred to as 'natural fractals' (and we shall uphold that usage in the following to conform to standard usage), the expression 'natural prefractals' would probably be far more appropriate.

When describing the geometry of a given soil aggregate with a prefractal of the Menger sponge, one has to decide on the iteration step with which this prefractal is associated. To this iteration step corresponds a dimension  $r_n$  (the individual subcube size), which represents the lower value of the range of scales at which the prefractal exhibits self-similarity. This length, when related to natural fractals, is usually referred to as the *inner cutoff length* [e.g. 57]. Physically, in the case of soil aggregates, this length is associated with the size of individual particles. On the other hand, since a soil aggregate is necessarily of finite size, there must be an upper limit to the range of scales at which it may be observed. For a given system, this upper limit, referred to as the upper or outer cutoff length, may be the actual size of the system itself. However, it may be more accurate to consider that it corresponds to the largest scale at which the system displays self-similarity.

The existence of an inner cutoff length has important consequences with respect to the evaluation of the dimensions of natural fractals. All the dimensions described in Section 2.3, except the similarity dimension, require a passage to a limit (e.g. limit

to vanishingly small ball radius, box side or divider length). For physical reasons, the use of a limit is precluded for natural fractals. In consequence, the definitions of these dimensions have to be slightly modified when one applies them to natural fractals. For example, the box-counting dimension  $D_{BC}$  can no longer be defined as in Equation (2.15). At best, one would be able to determine the number of boxes  $N_\delta(F)$  only in the range of  $\delta$  values between the inner and outer cutoff lengths. In practice, the range of  $\delta$  values accessible via measurement may be much narrower. Under these conditions, Equation (2.15) may best be replaced by defining  $D_{BC}(F)$  as the slope of the graph of  $\ln N_\delta(F)$  versus  $-\ln \delta$  over a sufficiently large range of  $\delta$  or, equivalently, by finding a best-fit value of  $D_{BC}$  in the power-law relationship  $N_\delta(F) \propto \delta^{-D_{BC}}$ .

A direct consequence of this necessary change in the definition of the various dimensions is the fact that equalities or inequalities between dimensions that have been proven mathematically in the limit of vanishingly small ball radius, grid size or divider length may no longer be valid when such limits are not taken. Furthermore, the finite length of the ‘yardsticks’ may create serious practical difficulties. One of the key ones associated with the divider method (see Section 2.3.4), for example, relates to the existence of a remainder. This remainder stems from the fact that, most often, a noninteger number of steps is required to cover a given curve. At present there is no general consensus on how to deal with this remainder [e.g. 39].

In addition to the above problems, the existence of an inner cutoff length raises the question of what is ‘fractal’ in natural fractals. To understand this point, it is useful to take once again the example of the Menger sponge. As defined in Section 2.2.3, the Menger sponge is a set of points in  $R^3$  with (Lebesgue) measure equal to zero. One may also consider that there is another set of points that is closely associated with this first one: the points that were removed during the iterative attrition process leading to the Menger sponge. In other words, to the ‘solid’ structure of the Menger sponge is associated a volume of ‘voids’. If one decides to interrupt the iterative process leading to the Menger sponge, then the ‘solid’ structure (no longer of measure equal to zero!) and the voids now have an interface. This feature is common to many natural fractals. In general, if the interface is fractal and scales like the mass of solids (i.e. follows a power law, or Paretian relationship, and has the same power-law, or Pareto-, exponent), the system is termed a *mass fractal* [e.g. 58]. If void (or pore) space and surface happen to scale alike, then the system is called a *pore fractal*, whereas if only the surface is fractal, then the system is called a *surface fractal*, or boundary fractal. In each case, one may use these fractals to characterize the dimensions introduced in Section 2.3, leading, for example, to ‘box-counting pore fractal dimensions’ or ‘correlation surface fractal dimensions’.

#### 2.4.4 Is ‘Power Law’ Equivalent to ‘Fractal’?

Repeatedly in the preceding sections, the analysis of the geometrical properties of mathematical and ‘natural’ fractals has resulted in power-law or Paretian relationships

between selected parameters. At no point in the text has this existence of a Paretian relationship been presented as a defining characteristic of fractals; it was instead obtained as a *consequence* of fractal geometry. A number of authors, however, consider that the essence of fractals is not the notion of an underlying geometry, as predicated above, but the evidence of Paretian behavior. From this viewpoint, a fractal is a set for which some statistical distribution function is a power law [e.g. 59]. Some authors [e.g. 60] label the latter fractals as *probabilistic*, to distinguish them from the geometric fractals, defined in Section 2.4.2.

To understand clearly the connections between these two types of fractals, it is worth reviewing briefly the development of the Pareto distribution and its relation to other statistical distributions in common use.

The Pareto distribution is named after the Italian-born Swiss professor of economics, Vilfredo Pareto (1848–1923). Originally, it dealt with the distribution of income over a population and may be stated as follows [61–66]:

$$N = Ax^{-a} \quad (2.29)$$

where  $N$  is the number of persons having income  $\geq x$ .  $A$  and  $a$  are positive, real parameters. The relation of Equation (2.29) is now usually referred to as the ‘Pareto distribution of the first kind’, to distinguish it from alternative forms [e.g. 67 (p. 234)]. When applied to discrete data (e.g. the length of words), it is also often referred to as the Zipf distribution [60, 64]. In the following, we shall simply call it the Pareto distribution.

When  $N$  is plotted as a function of  $x$ , for given values of  $A$  and  $a$ , the distribution of Equation (2.29) is characterized by a very long right tail. Over the years, this Paretian behavior has been observed in relation with many socio-economic and other naturally occurring quantities. Examples [e.g. 67, 68] are the distributions of city population sizes, insurance claims, occurrence of natural resources, stock price fluctuations, size of firms, and of error clusters in communication circuits, to list only a few.

Usage of the Pareto distribution to describe data exhibiting very long right tails has been criticized by many researchers on the grounds that the Pareto distribution is not the only distribution with a very long right tail and that, often, it does not convincingly outperform its competitors. Macaulay [69], in particular, argues that ‘the approximate linearity of the tail of a frequency distribution charted on a double logarithmic scale signifies relatively little, because it is such a common characteristic of frequency distributions of many and various types’. Indeed, in many cases, the exponential [38, 70], Weibull [38, 59] and lognormal [60] distributions mimic the Pareto distribution over certain ranges, or even provide a statistically better fit to data than the Pareto distribution [e.g. 65, 71].

In that context, whether or not one uses the Pareto distribution to fit experimental data often appears linked to one’s belief in the universality of the Paretian behavior, and to the deviation from Paretian behavior that one is willing to tolerate. In some well-publicized cases of the use of the Pareto distribution in the literature [e.g. 60 (figure 4.7) and discussion in 38 (p. 205)], there is enough deviation from linearity



in log–log plots, and the deviation is systematic enough over the whole range of experimental data, that skepticism in the applicability of the Pareto distribution is warranted. Yet the authors of the original articles consider a unique Pareto exponent appropriate, implying that the systems under study exhibit power-law behavior. A related issue concerns the method one uses to fit the Pareto distribution to experimental data. There are an array of methods available, including weighted or unweighted linear regression of log-transformed data, and nonlinear regression. Each of these methods may be applied to the full data set, or to a portion thereof, corresponding to points that are selected because they appear to fall on a straight line on a log–log plot. When the latter approach is adopted, one is faced with the problem of determining how big a range this linear segment should span to provide any confidence that the data indeed exhibit a power-law behavior. Brock [72] argues that data points showing linearity should span at least two or three orders of magnitude in the abscissa before one tries to fit to them with the Pareto distribution. A similar recommendation is made by other authors [e.g. 38].

Figure 2.18 illustrates some of the practical difficulties frequently encountered when trying to determine if the Pareto distribution adequately describes experimental data, and when evaluating its parameters. Originally, Cargill *et al.* [73] fitted a power law to their data via weighted linear regression, after elimination of the leftmost five data points (considered to be artifacts resulting from a less efficient extraction of copper from the ore). The weighting is proportional to the amount of ore. The Cargill *et al.* [73] regression line (dashed line in Figure 2.18) has a slope of  $-0.386$ ,

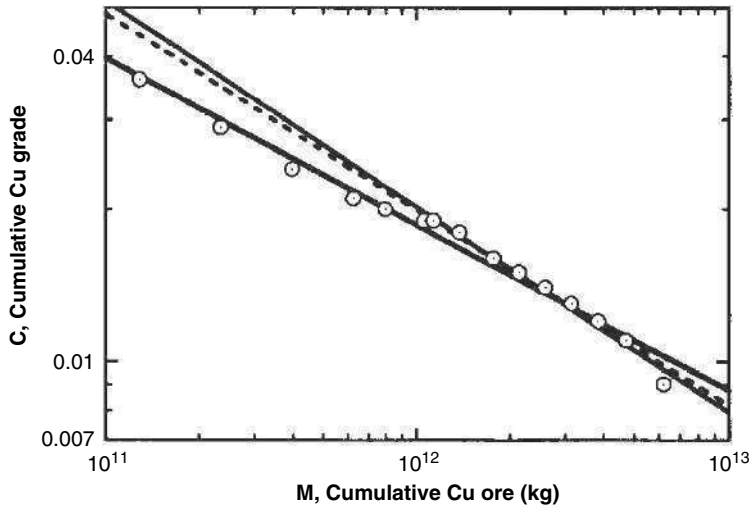


**Figure 2.18** Dependence of cumulative copper grade  $C$  on cumulative copper ore  $M$  mined in the United States (data from [73]). The meanings of the different lines are described in the text.

which, according to a formula derived by Turcotte [59], corresponds to an unspecified ‘fractal’ dimension  $D = 1.16$ . If an unweighted nonlinear regression is carried out on the same truncated data set, then the slope of the resulting regression line (thin solid line in Figure 2.18) equals  $-0.406$  (i.e.  $D = 1.22$ ), with an  $R$  value of  $0.994$ . Finally, when the Pareto distribution is fitted via an unweighted nonlinear regression to the full data set (thick solid line in Figure 2.18), the slope equals  $-0.327$  (i.e.  $D = 0.98$ ). There is some waviness in the data, but the fit is quite close ( $R = 0.995$ ), and is comparable to that found in the literature in situations where power-law behavior has been postulated. A consequence of this good fit is that the first five data points no longer appear artifactual or deviatory, as assumed by Cargill *et al.* [73] and Turcotte [59]. However, the most interesting consequence is in terms of the fractal behavior of the cumulative copper grade  $C$ . If one uses the truncated data set to estimate  $D$  and one follows Brock’s [72] recommendation, then  $C$  is not a probabilistic fractal, since its linear segment extends over less than one order of magnitude in  $M$ . On the other hand, if one considers the full data set, the linear segment spans very nearly two orders of magnitude in  $M$  and one may at least consider making the case that  $C$  is a probabilistic fractal.

A similar analysis could be performed on many data sets described in the literature [e.g. 59]. This clearly highlights the fact that the evaluation of fractal dimensions, whether of geometric or probabilistic fractals, is not straightforward. It also shows that there is often some subjectivity involved in determining whether or not a given system has a Paretian behavior. These observations affect the practical use of both the geometric and the probabilistic fractals. However, the subjectivity is particularly significant for probabilistic fractals, since evidence of Paretian behavior is their sole defining feature.

A further difference between geometric and probabilistic fractals concerns the range of values that are acceptable for the Pareto exponent  $a$  in Equation (2.29). In the various illustrations of Paretian relationships associated with mathematical monsters and fractals in preceding sections of this chapter (e.g. Equations (2.2) and (2.4)), the value of the exponent was always constrained to be (inclusively) between the topological dimension of the set and the Euclidian dimension of the embedding space  $R^n$ . No such restriction applies to the parameter  $a$  in Equation (2.29) when this equation is taken simply as the mathematical formulation of a particular statistical distribution. Clearly, when Equation (2.29) is applied to data related to the size of insurance claims or to stock price fluctuations, one cannot expect  $a$  to be restricted to a certain range (e.g.  $0 \leq a \leq 3$ ) for geometrical or physical reasons. Even when Equation (2.29) is used to describe some physical attribute of a real system, it is not guaranteed that either  $A$  or  $a$ , or even  $x$  for that matter, will have a clear physical meaning and that the values of  $a$  will be geometrically constrained. Some of the most convincing illustrations of this fact are found in applications of dimensional analysis to equations describing dynamical systems. Indeed, the so-called pi-theorem, one of the cornerstones of dimensional analysis, states that if there is a relationship among  $N + 1$  variables involving  $N$  independent dimensional units, then the relation can be expressed in

terms of a single nondimensional parameter, giving a power-law dependence [74]. This single nondimensional parameter, and consequently the coefficient and exponent of the power law, may not always have a clear physical interpretation, as is illustrated by Schmidt and Housen [74] in the case of the cratering efficiency of conventional and nuclear explosives. In all these situations, and indeed for all probabilistic fractals, the range of values that the exponent  $a$  can assume is not restricted. Cases of physical systems where this exponent (after transformation whenever necessary) leads to ‘fractal dimensions’  $>3$  are routinely reported in the literature [e.g. 59, 72, 75, 76]). Such values are entirely acceptable for probabilistic fractals [e.g. 72, 77], even though they would be meaningless for geometric fractals embedded in  $R^3$ . This distinction appears to have been frequently overlooked in the literature, as demonstrated by the lasting, yet groundless, controversy about supposedly ‘unphysical’ fractal dimensions  $>3$  for natural fractals [e.g. 78].

Because of the constraints imposed on the exponent  $a$  in the case of geometric fractals, it is clear from the above analysis that whereas a geometric fractal is automatically also a probabilistic fractal, the reverse is not true in general. In environmental science, this conclusion has particular significance with respect to the use of fragmentation models to account for the size distribution of soil particles [e.g. 76] or fragmented rocks and other geological materials [e.g. 59]. These fragmentation models are described in the following subsection.

### 2.4.5 Fragmentation Fractals

The earliest attempt to develop a fragmentation model that accounts for the Paretian distribution of the size of fractured or fragmented solids seems to have been Matsushita’s [77] fracture cascade model (see Figure 2.19). The simplest derivation of this model, in two-dimensional space, starts with a square with a unit side length. At the first stage, the square is divided into four equal subsquares of side  $1/2$ . One of these subsquares, chosen randomly, is shaded (hatched diagonally) to indicate that it will not be fractured or fragmented further. At the second stage, the remaining three subsquares are divided each into four equal sub-subsquares of side  $(1/2)^2$ , and one of them (chosen randomly) is again shaded. The same procedure is in turn applied to the remaining  $3^2$  unshaded sub-subsquares, and so on.

At the  $n$ th stage, there are  $3^{n-1}$  newly shaded squares of side  $r_n = 2^{-n}$ . For finite  $n \gg 1$ , the cumulative number  $N(r_n)$  of shaded squares of side length greater than  $r_n = 2^{-n}$  may be expressed as follows [77]:

$$N(r_n) = 1 + 3 + 3^2 + \dots + 3^{n-1} \propto 3^n = r_n^{-D_{\text{fragm}}} \quad (2.30)$$

where  $D_{\text{fragm}} \equiv \ln 3 / \ln 2 \cong 1.585$

Equation (2.30) amounts to a power-law relationship between  $N(r_n)$  and  $r_n$ , so, as  $n \rightarrow \infty$ , it defines a probabilistic fractal. Following Kaye [43], it is occasionally called a fragmentation fractal, and  $D_{\text{fragm}}$  is termed the fragmentation fractal dimension.

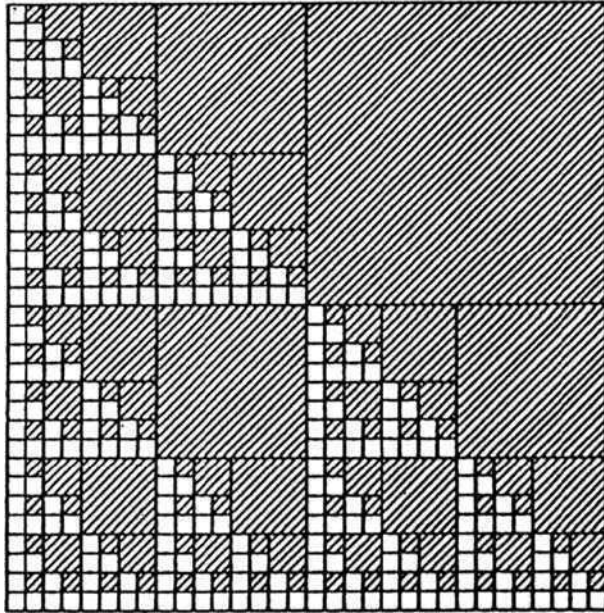


**Figure 2.19** Fifth iteration in Matsushita's fracture cascade in two dimensions. The hatched squares are arranged regularly for convenience. (Modified from [77].)

There is an interesting connection between Matsushita's [77] fracture cascade model and some of the mathematical monsters (or geometric fractals) of Section 2.2. For example, if instead of dividing the initial square in Figure 2.19 into four equal subsquares and shading one, we divide it into nine equal subsquares and shade one, it is easy to see that the collection of shaded squares that we are producing in this manner corresponds to the square holes that are punched during the attrition process leading to the Sierpinski carpet (see Section 2.2.3). The exponent  $D_{\text{fragm}}$  of Equation (2.30), under these conditions, is equal to  $\ln 8 / \ln 3 \cong 1.89$ , which is the value of the Hausdorff and similarity dimensions of the Sierpinski carpet itself (see Section 2.3.2).

The fracture cascade has been considered so far in two-dimensional space. To be applicable to the fragmentation of solid bodies, the model has to be extended to  $R^3$ . In this case (see Figure 2.20), we could start with a cube with unit side length, divide it into eight subcubes, hatch three, apply the same procedure to each of the remaining five subcubes, and so on. The resulting value of  $D_{\text{fragm}}$  would be  $\ln 5 / \ln 2 \cong 2.322$ . More generally [e.g. 38], one could consider that the initial cube is divided into  $b^3$  equal-sized subcubes of side length  $1/b$ , and that  $i$  randomly chosen subcubes are hatched, where  $b$  and  $i$  are arbitrary integers satisfying  $1 < b$  and  $1 \leq i < b^3$ . At the

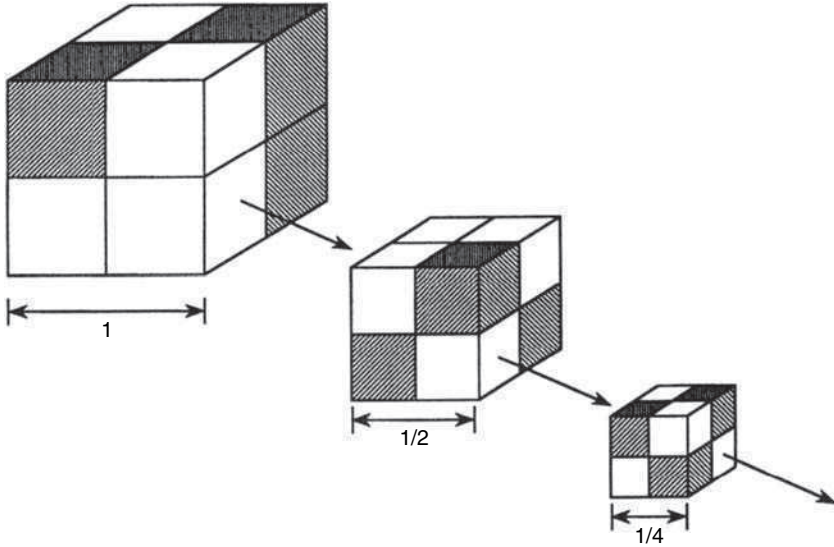


**Figure 2.20** Schematic representation of a fracture cascade in three dimensions. Three cubes are hatched (i.e. not fragmented further) at each fragmentation step.

$n$ th iteration of this procedure, the cumulative number of hatched cubes larger than  $r_n = 1/b^n$  is

$$N(r_n) = i[1 + (b^3 - i) + (b^3 - i)^2 + \dots + (b^3 - i)^{n-1}] \propto (b^3 - i)^n = r_n^{-D_{\text{fragm}}} \quad (2.31)$$

where  $D_{\text{fragm}} \equiv \ln(b^3 - i) / \ln b$ .

The power-law relationship of Equation (2.31) may be expressed differently if one introduces a ‘probability of fragmentation’  $p_c \equiv (b^3 - i)/b^3$ , representing the fraction of the  $n$ th-order cubes of size  $b^{-n}$  that are further fragmented. Under these conditions,  $D_{\text{fragm}}$  in Equation (2.31) becomes

$$D_{\text{fragm}} = \frac{\ln(b^3 p_c)}{\ln b} \quad (2.32)$$

The inequality  $1 \leq i < b^3$  (see above) implies that  $1/b^3 \leq p_c < 1$ , i.e. that  $0 \leq D_{\text{fragm}} < 3$ . This restriction on the range of values taken by  $D_{\text{fragm}}$  is a definite sign that the model described above is not satisfactory as a ‘physical’ explanation of the general Pareto distribution, since values of  $a$  in Equation (2.29) as high as 4 or 5 are routinely measured in practice [e.g. 59, 76]. On the other hand, the inequality  $D_{\text{fragm}} < 3$  has been considered by some to be an indication that geometric fractal concepts are appropriate to describe any fragmented material [59]. This viewpoint deserves further analysis, since it assumes that every fragmented material was created by a process similar to that shown in Figures 2.19 and 2.20. If fragments or particulate matter are characterized using Equation (2.29), then the exponent  $a$  characterizes only

the size of the individual fragments. It provides *no* quantitative insight concerning the geometry of the arrangement of these same fragments. By piling up or aggregating the fragments in specific ways, it may be possible to create with them various pore, mass or surface fractals. There are probably infinitely many ways to do this. However, there are also many ways to assemble the fragments to create nonfractal structures. One such structure is in fact illustrated in Figure 2.20. Indeed, it is always possible to assemble the fragments resulting from a given fracture cascade in such a way as to reconstitute the original cube, which is definitely not fractal! Arguments that the dimension found when the size distribution of a fragmented material is characterized using Equation (2.29) should obey the inequality  $a < 3$  (because  $D_{\text{fragm}} < 3$ ) are, thus, without basis.

## 2.5 OPERATIONAL ASPECTS OF THE EVALUATION OF THE FRACTAL CHARACTERISTICS OF NATURAL SYSTEMS

In the application of fractal geometry to natural systems, researchers encounter a number of daunting operational issues, some of which have been addressed in the literature in recent years [e.g. 79] (also see Chapter 3). Dubuc and Dubuc [80] summarized some of these issues in the following manner:

. . . different methods as well as different scale ranges and resolutions can lead to estimates of dimension that are drastically different. Estimates of fractal dimension will never be valuable until one fully understands the importance of the various error factors involved in the estimation process.

To illustrate one of these operational problems, associated with the resolutions of images of natural systems, we shall consider the case of the fractal analysis of a preferential pathway in an orchard soil (Figure 2.21). The image in Figure 2.21a depicts a section of a moderately well-drained soil located in the Cornell University orchard (see [81] for details). On 14 July 1995, a metal ring was pushed into the surface layer of the soil. A solution of blue food coloring was poured inside the cylinder and rapidly infiltrated into the soil. Fifteen minutes later, a 1.8 m deep trench was dug with a backhoe, followed by carefully removing soil with shovels, in order to obtain as vertical as possible a soil profile. Color slides were taken of the exposed soil facies with a hand-held camera. The slides were scanned and the software Adobe Photoshop was used to manipulate and analyze the digitized soil images. Using features of this software, images of the soil profile were coarsened at different resolutions. To ensure that all the digitized images would receive identical treatments, precisely the same field of view was cropped, i.e. delineated and cut, in each case. In addition, to maximize the contrast between stained and background soil material, the storage format of the cropped images was changed from RGB (red–green–blue) to CYMK (cyan–yellow–magenta–black), and the cyan channel was retained for further analysis. This channel corresponds very closely with the color of the dye used in the



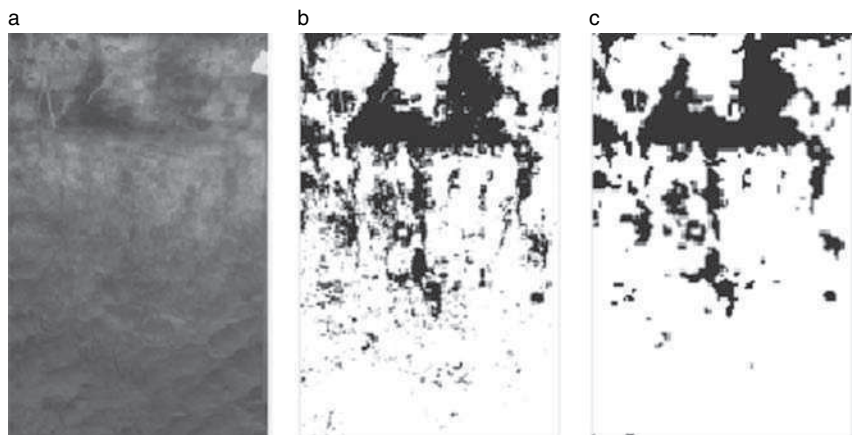


**Figure 2.21** (a) Gray-scale,  $1685 \times 2627$  pixel image of a soil profile in which a (darker) preferential pathway is visible; (b) black-and-white (binary) image obtained by thresholding (a) with the intermeans algorithm; (c) same as (b), but after the starting gray-scale image was coarsened 16 times. (The frames around (b) and (c) have been added solely to indicate the limits of the digitized images.)

field experiment, a feature that makes the stain patterns much more sharply contrasted than for any of the other channels available in Adobe Photoshop. Gray-scale versions of the cyan channels were thresholded in two different ways, using the intermeans and minimum error algorithms, to produce binary (black and white) images suitable for fractal analysis, with the preferential pathway appearing in black and the background soil in white (Figure 2.21b and c). The box-counting information and correlation mass fractal dimensions of the preferential pathway were calculated using a method proposed by Liebovitch and Toth [82].

The results of the fractal analysis of the preferential pathway (see Figure 2.22) suggest that the values found for the fractal dimension are influenced by a number of the steps involved in the analysis. The fractal dimensions determined with images thresholded with the intermeans algorithm are generally higher than those based on the minimum-error threshold (open symbols tend to be higher than full symbols in Figure 2.22). Nevertheless, quantitatively, the influence of the thresholding method on fractal dimensions remains somewhat small; the largest difference, 0.034, is found in the case of the information dimension, in the second set of points from the right in Figure 2.22. More significant, quantitatively, is the influence of the choice of a specific definition for the fractal dimension. The absolute difference among dimensions can be somewhat large, amounting to as much as 0.138 in one of the images. Nevertheless, clearly the most important source of variability of the fractal dimension is related to the resolution of the images used in the analysis. There is a marked tendency for fractal dimensions to increase with resolution, i.e. to increase when the pixel size decreases. This variation of the fractal dimension amounts to up to 0.2, which may

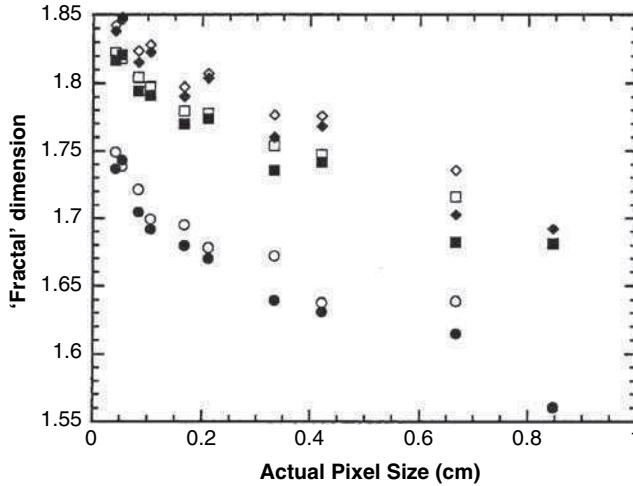


**Figure 2.22** Influence of physical pixel size (image pixel size translated into actual physical length on the soil profile) on a number of mass fractal dimensions of the preferential pathway in Figure 2.21. Open symbols correspond to images thresholded with the intermeans algorithm, whereas full symbols correspond to the minimum-error algorithm. Circles, squares, and diamonds are associated with the box-counting, information and correlation dimensions respectively. (Modified from [81].)

not appear to be large; however, one has to remember that the mass fractal dimension of the preferential pathway in Figure 2.21 can only vary between 1.0 and 2.0, by definition. In addition, calculations by Baveye *et al.* [81] on the basis of a textbook fractal, the von Koch island, suggest that the fractal dimensions of the preferential pathway might have been larger still, and might have tended toward 2.0, if images at finer resolutions had been available.

## 2.6 MULTIFRACTAL MEASURES: HOPE FOR THE FUTURE?

### 2.6.1 Definition

The introduction to fractal geometry in this chapter would not be complete without a short mention of an area that is conceptually challenging,<sup>5</sup> yet is the object of considerable interest in the literature, i.e. multifractal measures.

As with fractals, many authors try to get by without having to provide a precise definition of multifractal measures. Consequently, the term ‘multifractal measure’

<sup>5</sup> Korvin [38] humorously comments that multifractal measures are not for the squeamish!



often means different things to different people. At the same time, different terminologies are used to refer to the same concept; ‘multifractals’ is often used in lieu of, or interchangeably with, the expression ‘multifractal measures’. In the following, we shall consistently use the term ‘multifractal measures’ to underline the fact that, unlike geometric (mono)fractals, which are self-similar sets of points, multifractal measures are self-similar measures defined on specific sets of points. This definition of multifractal measures follows the treatment of Mandelbrot [36], Falconer [5] and Evertsz and Mandelbrot [37]. Other definitions will be briefly mentioned at the end of this section.

### 2.6.2 The Binomial Fractal Measure

The self-similarity of measures is best illustrated with the binomial measure [e.g. 32, 36, 37], which is generated recursively via a process known as a multiplicative cascade. This process starts (at the stage  $k = 0$ ) with a uniformly distributed unit of mass on the unit interval  $I = [0, 1]$  (see Figure 2.23a). At the next stage ( $k = 1$ ), a fraction  $m_0$  of the mass is distributed uniformly on the left half ( $I_0 = [0, 1/2]$ ) of the unit interval, and the remaining fraction  $m_1 = 1 - m_0$  is distributed uniformly on the right half ( $I_1 = [1/2, 1]$ ). At this stage, the left half thus carries the measure  $\mu(I_0) = m_0$  and the right half carries the measure  $\mu(I_1) = m_1$ . Of course, the total mass is conserved, so that  $\mu(I_0) + \mu(I_1) = \mu(I) = 1$ . For that reason,  $\mu$  appears like probabilities and could be considered as a probability measures [e.g. 37].

At the next stage ( $k = 2$ ) of the multiplicative cascade, the subintervals  $I_0$  and  $I_1$  receive the same treatment as the original unit interval. For example,  $I_0$  is split into two intervals  $I_{00} = [0, 1/4]$  and  $I_{01} = [1/4, 1/2]$  of size  $2^{-k}$ , and the mass is also fragmented as it was at stage  $k = 1$ . It is easy to see that, for example,  $\mu_{01} \equiv \mu(I_{01}) = m_0 m_1$ , with similar relations for the other measures  $\mu_{00}$ ,  $\mu_{10}$  and  $\mu_{11}$ . In other words, the measure associated with a given interval is obtained by multiplication of

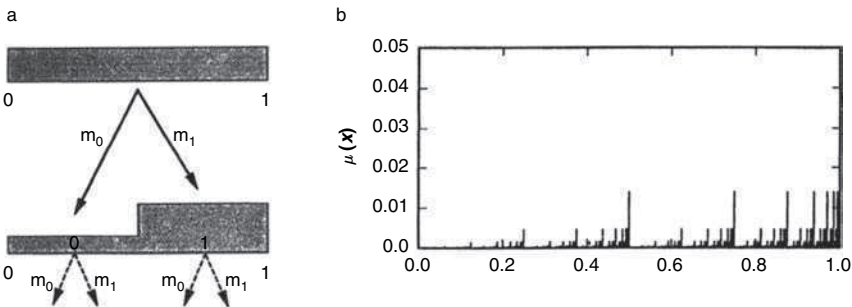


**Figure 2.23** (a) First two stages ( $k = 0$  and  $k = 1$ ) of the multiplicative cascade leading to the binomial measure, with  $m_0 = 0.25$  and  $m_1 = 0.75$ . (b) Resulting measure  $\mu(x)$  for  $k = 11$ , as a function of the segment position  $x = i \times 2^{-11}$ . (Modified from [10].)

suitable combinations of the measures  $m_0$  and  $m_1$ , hence the adjective ‘multiplicative’ that characterizes the cascade process.

At the  $k$ th stage, the measure of a given interval, say  $I_{\beta_1\beta_2\ldots\beta_k}$ , is given by

$$\mu_{\beta_1\beta_2\ldots\beta_k} = m_{\beta_1}m_{\beta_2}\ldots m_{\beta_k} = m_0^{n_0}m_1^{n_1} \quad (2.33)$$

where  $n_0$  is the number of  $\beta_i$  equal to zero and  $n_1 \equiv k - n_0$ . For example, the ‘peak’ just to the left of  $x = 0.5$  (in fact, in the interval  $[0.5 - 2^{-11}, 0.5]$ ) in Figure 2.23b corresponds to a measure  $\mu(x)$  equal to  $(0.25)(0.75)10 \approx 0.0141$ , three times smaller than that at  $x = 1$  where  $\mu(x) = (0.75)11 \approx 0.0422$  (the latter peak is hidden by the right ordinate axis). Even though it is not possible to count them all on Figure 2.23b, there are 11 peaks with a measure equal to that of the peak near  $x = 0.5$ . In general, if we write  $\xi \equiv n_0/k$ , the number of peaks with measure  $\mu = (m_0^\xi m_1^{1-\xi})^k$  is given by the number of ways one can distribute  $n_0 = \xi k$  zeros among  $k$  positions in the addresses  $\beta_1\beta_2\ldots\beta_k$  of the intervals  $I_{\beta_1\beta_2\ldots\beta_k}$ . This number of peaks is given by the binomial coefficient

$$N_k(\xi) = \binom{k}{\xi k} \equiv \frac{k!}{(\xi k)!(1 - \xi)k!} \quad (2.34)$$

which explains why the term binomial is applied to the binomial measure [e.g. 37 (p. 929)].

The limit of this process, as  $k \rightarrow \infty$ , called the binomial measure, is exactly self-similar. The mass of an arbitrary interval  $I_{\beta_1\beta_2\ldots\beta_k}$  is  $\mu_{\beta_1\beta_2\ldots\beta_k}$  times smaller than the mass, equal to unity, of the entire unit interval  $I$ . But the distribution of mass within these intervals  $I_{\beta_1\beta_2\ldots\beta_k}$  and  $I$  is distributed in exactly the same way. Indeed, by spatially rescaling the subinterval  $I_{\beta_1\beta_2\ldots\beta_k}$  by a factor  $2^k$  and renormalizing its mass by a factor  $(\mu_{\beta_1\beta_2\ldots\beta_k})^{-1}$ , one recovers the mass distribution in the interval  $I$ . It is in this sense that the multiplicatively generated binomial measure is said to be (exactly) self-similar.

Self-similar measures like the binomial measure are ‘singular’, i.e. their local density, defined as  $\lim_{\varepsilon \rightarrow 0} \mu[x, x + \varepsilon]/\varepsilon$ , is (almost) everywhere undefined. To illustrate this, let us consider the value of the binomial measure in the neighborhood of the point 0. Because of Equation (2.34),  $\mu[0, 2^{-k}] = m_0^k = (2^{-k})^{v_0}$  with  $v_0 = -\log_2 m_0$ . That is, the measure in the neighborhood of zero scales as  $\mu[0, \varepsilon] \propto \varepsilon^\alpha$ , where  $\alpha = v_0$  is the coarse Hölder exponent when  $\varepsilon$  is of finite length (see Section 2.3.5). The (nonlocal) density  $\mu/\varepsilon$ , consequently, scales like  $\varepsilon^{\alpha-1}$ , and if  $\alpha \neq 1$  (i.e. if  $m_0 \neq 1/2$ ), then the local density (the limit of the  $\mu/\varepsilon$  as  $\varepsilon \rightarrow 0$ ) is degenerate, equal to either zero (if  $m_0 < 1/2$ ) or infinity (if  $m_0 > 1/2$ ). This is true not only in the neighborhood of zero: the local density of the binomial measure is either zero or infinity almost everywhere in the interval  $[0, 1]$ .

### 2.6.3 Parameterization of Multifractal Measurements

For multifractal measures to be useful in practice, we need to find ways to characterize and parameterize their geometrical properties. This is achieved in particular by the

‘ $f(\alpha)$  curve’, whose theoretical foundation is now described. Evertsz and Mandelbrot [37] and Lavallée *et al.* [83] describe various methods for its evaluation. By simple arithmetic [e.g. 37 (p. 932)], one may show that, at stage  $k$  of the construction of the binomial measure, the coarse Hölder exponent associated with a given interval  $I_{\beta_1\beta_2\dots\beta_k}$  is

$$\alpha = \xi v_0 + (1 - \xi)v_1 \quad (2.35)$$

where  $v_1 = -\log_2 m_1$  and, as above,  $v_0 = -\log_2 m_0$ ,  $\xi \equiv n_0/k$ , and  $n_0$  is the number of  $\beta_i$  values that equal zero. If, as in Figure 2.23,  $m_0 < m_1$ , then  $v_1 < v_0$  and, by virtue of Equation (2.33),  $v_1 \leq \alpha \leq v_0$ . The extreme values of  $\alpha$  are usually denoted by  $\alpha_{\min}$  and  $\alpha_{\max}$ , so that  $\alpha_{\min} \equiv v_1 \leq \alpha \leq v_0 \equiv \alpha_{\max}$ . The limits  $\alpha_{\min}$  and  $\alpha_{\max}$  are independent of the size  $2^{-k}$  of the subintervals at stage  $k$ , i.e. are independent of the scale at which the measure is probed. The fact that the value of  $\alpha$  is bound within a fixed range makes it an ideal index to associate with the intervals within the support of the binomial measure, i.e. within the geometrical domain in which the measure assumes nonzero values. Of course, given the one-to-one relationship between  $\alpha$  and  $\xi$  in Equation (2.35) and the fact that the values of  $\xi$  are bound (within  $[0, 1]$ ) like those of  $\alpha$ , one could conceivably also use  $\xi$  as an index [e.g. 10]. However,  $\xi$  is strongly tied to the concept of multiplicative cascade, which is a given in the case of the binomial measure but does not necessarily exist for other measures [37]. By contrast,  $\alpha$  may be evaluated for any measure.

From that viewpoint, it is interesting to inquire about the values that the coarse Hölder exponent assumes over the support of the measure and about how these values are distributed. For a given  $k$ , this distribution is given by the binomial coefficient  $N_k(\xi)$  of Equation (2.34). Because of Equation (2.35), each  $\xi$  corresponds to a unique  $\alpha$ . Therefore, the number of intervals  $I_k$  of size  $2^{-k}$  with coarse Hölder exponent  $\alpha$  is given by [37]

$$N_k(\alpha) = \binom{k}{\xi(\alpha)k} \propto (2^{-k})^{-f(\alpha)} \quad (2.36)$$

where  $f(\alpha) = \log_2[\xi^{-\xi}(1 - \xi)^{-(1-\xi)}]$  with, based on Equation (2.35),  $\xi = (\alpha - \alpha_{\min})/(\alpha_{\max} - \alpha_{\min})$ .

The proportionality relationship in Equation (2.36) is an approximation based, in part, on the application of Stirling’s formula to the factorials in the binomial coefficient. Although the coarse Hölder exponent  $\alpha$  has meaning only for finite  $k$ , as  $k$  becomes very large  $N_k(\alpha) d\alpha$  is approximately ‘the number of intervals with a coarse Hölder exponent between  $\alpha$  and  $\alpha + d\alpha$ ’ [37 (p. 935)]. Thus, the function  $f(\alpha)$  provides the information needed to find the frequency distribution of  $\alpha$  for large  $k$ . The graph of the  $f(\alpha)$  curve for the binomial multifractal measure is shown in Figure 2.24a. Several of the features of this particular curve (e.g. symmetry around its maximum, local quadratic behavior near its maximum) are not generally typical of self-similar measures. Nevertheless, the  $f(\alpha)$  curve of Figure 2.24a shares

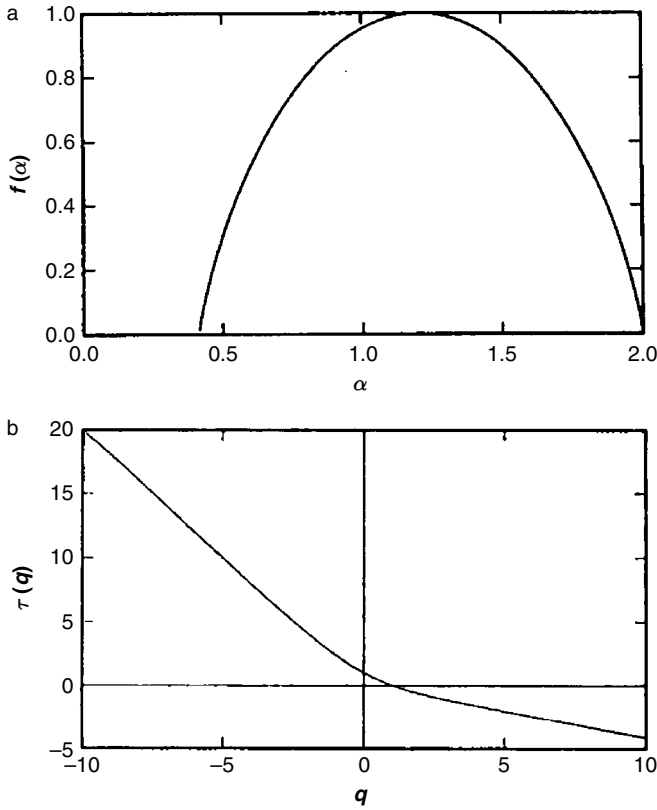


**Figure 2.24** (a)  $f(\alpha)$  curve for the binomial measure with  $m_0=0.25$  and  $m_1=0.75$ . (b) Sequence of mass exponents  $\tau(q)$  as a function of moment order  $q$ , for the binomial measure with  $m_0=0.25$  and  $m_1=0.75$ . (Modified from [10].)

two characteristics with other  $f(\alpha)$  curves: first,  $f(\alpha) \leq \alpha$  for all  $\alpha$ ; second, the maximum value of  $f(\alpha)$  corresponds to the box-counting dimension  $D_{BC}$  of the support of the measure ( $D_{BC} = 1$  for the binomial measure because its support is a line segment).

The  $f(\alpha)$  curve is not the only way to characterize the properties of multifractal measures. Another, widely used, approach to describe their features involves sequences of the *mass exponents*,  $\tau(q)$ . To define these exponents, it is convenient to consider a set  $s$  covered with  $\delta$ -mesh ‘cubes’, as in Figure 2.14(iii). Within each one of these  $\delta$ -mesh cubes, one may define a measure  $\mu$  that is similar to that of Equation (2.22) and represents the probability of finding an element (a point) of set  $s$  within the  $\delta$ -mesh cube. With this probability, one may construct, for any real number  $q$ , the measure

$$M_d(q, \delta) = \sum_{i=1}^{N(\delta)} \mu_i^q \delta^d \equiv N(q, \delta) \delta^d \xrightarrow{\delta \rightarrow 0} \begin{cases} 0, & \text{for } d > \tau(q) \\ \infty, & \text{for } d < \tau(q) \end{cases} \quad (2.37)$$

where the summation limit  $N(\delta)$  is the total number of  $\delta$ -mesh cubes that cover the set  $s$ ,  $q$  plays the role of a moment order, and  $N(q, \delta)$  is the weighted number of  $\delta$ -mesh cubes in the cover. In close analogy with the Dedekind cut in Figure 2.13, the measure  $M_d(q, \delta)$  as  $\delta \rightarrow 0$  approaches zero when  $d$  is large and approaches infinity when  $d$  is small. The value of  $d$  at the division point is called the mass exponent and is denoted  $\tau(q)$  to indicate its dependency on the moment order  $q$ .

The measure  $M_d(q, \delta)$  is characterized by a whole sequence of exponents  $\tau(q)$  that controls how the moments of the probabilities  $\{\mu_i\}$  scale with  $\delta$ . It follows from Equation (2.37) that the weighted number of  $\delta$ -mesh cubes  $N(q, \delta)$  has the form

$$N(q, \delta) = \sum_{i=1}^N \mu_i^q \propto \delta^{-\tau(q)} \quad (2.38)$$

and the mass exponent  $\tau(q)$  is given by

$$\tau(q) = -\lim_{\delta \rightarrow 0} \frac{\ln N(q, \delta)}{\ln \delta} \quad (2.39)$$

This relationship between  $\tau(q)$  and  $q$  is illustrated in Figure 2.24b for the binomial measure described previously.

If the probabilities  $\mu_i$  are normalized (i.e. the sum of the  $\mu_i$  is unity), then, by Equations (2.38) and (2.39),  $\tau(1) = 0$  (see Figure 2.24b). Another interesting special case is  $q = 0$ , where all the  $\mu_i^q = 1$  in Equation (2.38) and, therefore,  $N(q = 0, \delta) = N(\delta)$  is simply the number of  $\delta$ -mesh cubes needed to cover the set, so  $\tau(0)$  equals the box-counting dimension of the set. This suggests that the value  $q = 0$  corresponds to the value of  $\alpha$  for which  $f(\alpha)$  is maximum, and that there is a connectivity between the two ways to characterize multifractal measures. In fact, one may show that  $\tau(q)$  and  $f(\alpha)$  are intimately related via the relationships

$$\alpha(q) = -\frac{d\tau(q)}{dq} \quad (2.40)$$

and

$$f(\alpha(q)) = q\alpha(q) + \tau(q) \quad (2.41)$$

This pair of equations in effect constitutes a ‘Legendre’ transformation from the independent variables  $\tau$  and  $q$  to the independent variables  $f$  and  $\alpha$  and may be very valuable in practical situations, when one of these two sets of independent variables turns out not to be particularly easy to evaluate directly (see [84]).

Another interesting relationship exists between the sequence of exponents  $\tau(q)$  and the Rényi dimensions  $D_q$  mentioned in Section 2.3.7. One can indeed show [e.g. 10 (p. 87)] that  $\tau(q) = (1 - q)D_q$ .

### 2.6.4 Alternative Definitions of Multifractal Measurements

At this juncture, one may wonder why, for example, the binomial measure is termed multifractal. Indeed, in our coverage of the theory in the preceding two subsections, we have not provided a rationale either for the ‘multi-’ or for the ‘-fractal’ parts of this qualifier.

Following Frisch and Parisi [85], who coined the term ‘multifractals’, and a number of other authors [e.g. 86, 87], we might look at the Paretian relationship of Equation (2.36) as a manifestation of fractal behavior. If the length  $\delta \equiv 2^{-k}$  of the intervals  $I_k$  is shrunk to zero, then indeed the exponent  $f(\alpha)$  in Equation (2.36) is defined by an expression that is formally similar to Equation (2.15), defining the box-counting dimension  $D_{\text{BC}}$ . On that basis, one could consider that the geometrical support  $s$  of a multifractal measure is the union of fractal sets  $S\alpha$ , each with a particular Hölder exponent equal to  $\alpha$  and a ‘fractal’ dimension equal to  $f(\alpha)$ . In much of the literature on multifractal measures, this statement is reversed in a manner that is very similar to the one discussed in Section 2.5.1 in the case of fractals; multifractal measures, or ‘multifractals’, are defined as measures whose geometric support is the union of one or more fractal sets. Yet another definition of multifractals, occasionally found in the literature, is even farther removed from the concept introduced in Section 2.6.1. It stems from the observation that the log–log plots of specific parameters exhibit several distinct linear segments. When there are two such segments, the system is sometimes called ‘bifractal’ [e.g. 38]. When there are more than two linear segments, or when the curve in the log–log plot is nonlinear, the system has been called ‘multifractal’, but the use of the word in that context has nothing to do with the multifractal measures described here.

From a mathematical standpoint, this alternative definition of multifractal measures, due to Frisch and Parisi [85], is fraught with difficulties. Indeed, a closer look at  $f(\alpha)$  shows that it cannot be looked at as a box-counting dimension, in particular because the intervals counted by Equation (2.36) when  $\delta \equiv 2^{-k}$  is small need not be contained in those counted when  $\delta$  is much larger (since the Hölder exponent associated with an interval  $\delta_1$  is not necessarily equal to that of a larger interval which contains  $\delta_1$ !) [e.g. 5 (p. 255)]. In the case of the binomial measure, one finds [e.g. 37 (p. 935)] that the (true) box-counting dimension of each of the sets  $S\alpha$  is unity, whereas  $f(\alpha)$  varies between zero and one (see Figure 2.24a). Interestingly, it turns out that for a special class of multifractal measures, including the binomial measure, the value of  $f(\alpha)$ , for each  $\alpha$ , is equal to the Hausdorff dimension of  $S\alpha$  [37]. Therefore, some of the sets  $S\alpha$  may be geometric fractals, but this does not appear to be a general characteristic of multifractal measures.

### 2.6.5 Beyond the Binomial Measure

In the multiplicative cascade used to generate the binomial measure, the number of intervals was increased by two at each step. One could easily lift that restriction and consider instead a fixed number  $b$  of intervals, larger than two. The resulting, more

general, measures are usually termed multinomial measures [e.g. 37 (p. 935)]. Another way to expand the notion of multiplicative cascade is to use random multipliers. At each step in the cascade, the multipliers are obtained by using a random number generator, subject of course to the constraint that the total measure be conserved. This process leads to random multifractal measures, which are statistically self-similar.

The various cases considered so far have all involved multifractal measures whose geometrical supports are not fractal. It is easy to imagine measures of practical interest in environmental science that might belong to this category. Evertsz and Mandelbrot [37 (p. 922)] provide the example of the ‘quantity of groundwater’ down to some prescribed depth in a given (in general nonfractal) geographical area, such as an agricultural field, a watershed, state, country, continent or island. As one subdivides the support more and more finely, following the multiplicative pattern of Figure 2.23a, it may turn out that the distribution of the quantity of groundwater is self-similar at different stages of the cascade, i.e. at different scales of observation. In this case, the quantity of groundwater is a multifractal measure, according to the definition given above.

There are also situations where the support of a multifractal measure is itself a fractal. It is very easy to conceive a multiplicative cascade that would generate such a multifractal measure. Indeed, if in Figure 2.23a one distributes the fractions  $m_0$  and  $m_1$  of the original mass not over the two intervals  $[0, 1/2]$  and  $[1/2, 1]$  but over the intervals  $[0, 1/3]$  and  $[2/3, 1]$  respectively, then it is clear that, as  $k \rightarrow \infty$ , the support of the measure is the Cantor set. Clusters generated by a diffusion-limited aggregation (DLA) model [10, 88] can also serve as a basis for constructing multifractal measures with fractal support. In this case, one may define on the DLA cluster a measure associated with the growth probability of the cluster. It is evaluated as follows. One starts with a cluster obtained by running the DLA model a certain number of times (e.g.  $10^4$  or  $10^5$ ). The model is then run several thousand more times, but without growing the cluster further; instead, each random walker that reaches the cluster is recorded as a ‘hit’ on the element it reaches and is removed. For each site of the cluster, the sum of the number of hits may be divided by the total number of random walkers considered. In this process, a measure is defined that quantifies the probability for a given site to be contacted by a random walker. This measure assumes its highest values at the periphery of the cluster [e.g. 89], and in many cases is multifractal.

This existence of multifractal measures with a fractal support raises an interesting question that has practical consequences. One may look at a DLA cluster, for example, as a fractal or as the support of a multifractal measure. Even though these two viewpoints are not exclusive, one of them might lead to a much deeper insight into the properties of the cluster. Which one is it? In other words, is it more fruitful to concentrate on characterizing the fractality of given physical objects, or to identify multifractal measures defined on these objects and investigate their features in detail? Obviously, the answer to this question will vary from situation to situation. In the context of environmental science, it is not clear at this stage what the answer may be.

## 2.7 CONCLUSIONS AND RECOMMENDATIONS

The purpose of this introductory chapter was to present some of the key concepts of fractal geometry and multifractal measures, which will be put to use in later chapters of this book. One of the principal take-home messages of this introduction is that extreme caution needs to be exercised when applying ‘fractals’ to natural systems. Indeed, unlike with most other mathematical theories that have been used to describe natural systems, starting with Euclidian geometry, there has historically been a considerable level of vagueness and ambiguity associated with the definition of most fractal concepts. As yet, unresolved operational issues complicate the evaluation of fractal characteristics for many systems. These challenges lead to a high risk of using the same terms to mean different things, of using different terminologies to cover the same basic reality, or of having different observers end up with very different perspectives on the fractality of given systems. The literature is replete with examples of confusion that can be traced back to these inherent ambiguities in the theory. Only if one is very clear about precisely what is meant by each term, and about how given parameters are evaluated, will one be truly able to assess the usefulness of fractal geometry for the description of natural systems.

## LIST OF SYMBOLS AND ABBREVIATIONS

$A$	surface area
$a$	Paretian exponent, Lipschitz–Hölder exponent
$C$	curve
$c(t)$	Weierstrass–Mandelbrot cosine function
$C(t)$	correlation function
$D_{BC}$	box-counting dimension
$D_C$	correlation dimension
$D_D$	divider or compass dimension
$D_{\text{fragm}}$	fragmentation fractal dimension
$D_H$	Hausdorff dimension of $F$
$D_I$	information dimension
$D_p$	pointwise dimension
$D_q$	Rényi dimensions
$D_S$	similarity dimension
$D_T$	topological dimension
DLA	diffusion-limited aggregation
$F$	set of points, any subset of $R^n$
fBm	fractional Brownian motion
$\phi$	porosity
$H$	Hurst exponent



$H^s(F)$	$s$ -dimensional Hausdorff measure of $F$
$l, \delta, a, b$	length, distance
$L$	total length
$L_C$	lacunarity
$\Lambda_{GB}(l)$	lacunarity
$m$	mass
$M_n(x)$	mass density function along $x$
$\mu_i$	probability
$n, N$	number
$N_\delta(F)$	number of boxes
$P$	Cantor set
$p_c$	probability of fragmentation
$\varphi_n$	arbitrary phase constant
$Q(m, l)$	probability distribution function
$r$	scaling factor, radius
$R^3$	three-dimensional Euclidian space
$R^n$	Euclidian dimension of the embedding space
$\rho$	mass density
$t$	time
$T$	side length
$\tau$	time steps
$\tau(q)$	mass exponent
$U$	nonempty subset of $n$ -dimensional Euclidean space
$V$	volume
$V(t)$	variance of increments
$Z_Q^{(q)}(l)$	statistical moments of probability distribution function
$X$	position of the particle
$\xi$	particle displacement
$w(t)$	Weierstrass–Mandelbrot function

## REFERENCES

- [1] Mandelbrot, B.B. (1975). *Les Objets Fractals: Forme, Hasard et Dimension*. Flammarion, Paris.
- [2] Mandelbrot, B.B. (1978). Les objets fractals. *La Recherche*, **9**(85), 5–13.
- [3] Jones, H. (1991). Fractals before Mandelbrot. A selective history. In *Fractals and Chaos*, Crilly, A.J., Earnshaw, R.A. and Jones, H. (eds). Springer-Verlag, New York, pp. 7–33.
- [4] Mandelbrot, B.B. (1982). *The Fractal Geometry of Nature*. W.H. Freeman and Company, New York.
- [5] Falconer, K.J. (1990). *Fractal Geometry. Mathematical Foundations and Applications*. John Wiley & Sons, Ltd, Chichester.
- [6] Baveye, P. and Boast, C.W. (1998). Concepts of ‘fractals’ in soil science: demixing apples and oranges. *Soil Sci. Soc. Am. J.*, **62**(5), 1469–1470.

- [7] Baveye, P., and Boast, C.W. (1998). Fractal geometry, fragmentation processes and the physics of scale-invariance: an introduction. In *Fractals in Soil Science*, Baveye, P., Parlange, J.-Y. and Stewart, B.A. (eds). CRC Press, Boca Raton, FL, pp. 1–54.
- [8] Cantor, G. (1884). Über unendliche, lineare Punktmannigfaltigkeiten, *Math. Ann.*, **23**, 453–488.
- [9] Rudin, W. (1976). *Principles of Mathematical Physics* (3rd ed.). McGraw-Hill Book Company, New York.
- [10] Feder, J. (1988). *Fractals*. Plenum Press, New York.
- [11] Edgar, G.A. (ed.). (1993). *Classics on Fractals*. Addison-Wesley Publishing Company, Reading, MA.
- [12] Peano, G. (1890). Sur une courbe, qui remplit toute une aire plane. *Math. Ann.*, **36**, 157–160.
- [13] Hilbert, D. (1891). Über die reellen Züge algebraischen Curven. *Math. Ann.*, **38**, 115–138.
- [14] Peitgen, H.O., Jürgens, H. and Saupe, D. (1992). *Chaos and Fractals. New Frontiers of Science*. Springer-Verlag, New York.
- [15] Sagan, H. (1994). *Space-Filling Curves*. Springer-Verlag, New York.
- [16] Bolzano, B. (1930). *Funktionenlehre*. Prague.
- [17] Weierstrass, K. (1872). Über continuirliche Funktionen eines reellen Arguments, die für keinen Werth des letzteren einen bestimmten Differentialquotient besitzen. *Gelesen Akad. Wiss.*, 18 Juli 1872; Engl. Translation: On continuous functions of a real argument that do not have a well-defined differential quotient. In *Classics on Fractals*, Edgar, G.A. (ed.). Addison-Wesley Publishing Company, 1993, pp. 3–9.
- [18] Hardy, G.H. (1916). Weierstrass's non-differentiable function. *Trans. Am. Math. Soc.*, **17**, 301–325.
- [19] Burrough, P.A. (1981). Fractal dimensions of landscapes and other environmental data, *Nature*, **294**(5838), 240–242.
- [20] Berry, M.V. and Lewis, Z.V. (1980). On the Weierstrass–Mandelbrot fractal function. *Proc. R. Soc. A*, **370**, 459–484.
- [21] Ausloos, M. and Berman, D.H. (1985). A multivariate Weierstrass–Mandelbrot function. *Proc. R. Soc. London A*, **400**, 331–350.
- [22] Brown, R. (1828). On the existence of active molecules in organic and inorganic bodies. *Phil. Mag.*, **4**, 162–173.
- [23] Lavenda, B.H. (1985). Brownian motion, *Scientific American*, **252**(2), 70–85.
- [24] Wiener, N. (1923). Differential-space. *J. Math. Phys.*, **2**, 131–174.
- [25] Hausdorff, F. (1919). Dimension und unseres Mass. *Math. Ann.*, **79**, 157–179.
- [26] Takayasu, H. (1990). *Fractals in the Physical Sciences*. John Wiley & Sons, Ltd, Chichester.
- [27] Hutchinson, J.E. (1981). Fractals and self-similarity. *Indiana Univ. Math. J.*, **30**, 713–747.
- [28] Graf, S., Mauldin, R.D. and Williams, S. (1988). *The Exact Hausdorff Dimension in Random Recursive Constructions*. Memoirs of the American Mathematical Society 71. American Mathematical Society, Providence, RI.
- [29] Sapoval, B. (1991). Fractal electrodes, fractal membranes, and fractal catalysts. In *Fractals and Disordered Systems*, Bunde, A. and Havlin, S. (eds). Springer-Verlag, Berlin, pp. 207–226.
- [30] Schroeder, M. (1991). *Fractals, Chaos, Power Laws. Minutes from an Infinite Paradise*. W.H. Freeman and Company, New York.
- [31] Gouyet, J.-F. (1992). *Physique et Structures Fractales*. Masson, Paris.
- [32] Moon, F.C. (1992). *Chaotic and Fractal Dynamics*. John Wiley & Sons, Ltd, New York.
- [33] Tricot, C. (1995). *Curves and Fractal Dimension*. Springer-Verlag, New York.
- [34] Le Méhauté, A. (1991). *Fractal Geometries. Theory and Applications*. CRC Press Inc., Boca Raton, FL.

- [35] Family, F. and Vicsek, T. (1991). *Dynamics of Fractal Surfaces*. World Scientific, Singapore.
- [36] Mandelbrot, B.B. (1989). Multifractals measures, especially for the geophysicist. *PAGEOPH*, **131**, 5–42.
- [37] Evertsz, C.J.G. and Mandelbrot, B.B. (1992). Multifractal measures. Appendix B. In *Chaos and Fractals. New Frontiers of Science*, Peitgen, H.O., Jürgens, H. and Saupe, D. (eds). Springer-Verlag, New York, pp. 921–953.
- [38] Korvin, G. (1992). *Fractal Models in the Earth Sciences*. Elsevier, Amsterdam.
- [39] Klinkenberg, B. (1994). A review of methods used to determine the fractal dimension of linear features. *Math. Geol.*, **26**(1), 23–46.
- [40] Hentschel, H.G.E. and Procaccia, I. (1983). The infinite number of generalized dimensions of fractals and strange attractors. *Physica D*, **8**, 435–444.
- [41] Mandelbrot, B.B., and Stauffer, D. (1994). Antipodal correlations and the texture (fractal lacunarity) in critical percolation clusters. *J. Phys. A: Math. Gen.*, **27**(9), L237–L242.
- [42] Mandelbrot, B.B., Vespignani, A. and Kaufman, H. (1995). Crosscut analysis of large radial DLA – departures from self-similarity and lacunarity effects. *Europhys. Lett.*, **32**(3), 199–204.
- [43] Kaye, B.H. (1989). *A Random Walk Through Fractal Dimensions*. VCH Verlagsgesellschaft, Weinheim, Germany.
- [44] Gefen, Y., Meir, Y., Mandelbrot, B.B. and Aharony, A. (1983). Geometric implementation of hypercubic lattices with noninteger dimensionality by use of low lacunarity fractal lattices. *Phys. Rev. Lett.*, **50**(3), 145–148.
- [45] Allain, C. and Cloitre, M. (1991). Characterizing the lacunarity of random and deterministic fractal sets. *Phys. Rev. A*, **44**, 3552–3558.
- [46] Chappard, D., Legrand, E., Haettich, N., Chales, G., Auvinet, B., Eschard, J.P., Hamelin, J.P., Basle, M.F. and Audran, M. (2001). Fractal dimension of trabecular bone: comparison of three histomorphometric computed techniques for measuring the architectural two-dimensional complexity. *J. Pathol.*, **195**(4), 515–521.
- [47] Plotnick, R.E., Gardner, R.H. and O'Neill, R.V. (1993). Lacunarity indexes as measures of landscape texture. *Landscape Ecol.*, **8**(3), 201–211.
- [48] Plotnick, R.E., Gardner, R.H. Hargrove, W.W., Prestegard, K. and Perlmutter, M. (1996). Lacunarity analysis: a general technique for the analysis of spatial patterns. *Phys. Rev. E*, **53**(5), 5461–5468.
- [49] Pendleton, D., Dathe, A. and Baveye, P. (2005). Influence of image resolution and evaluation algorithm on estimates of the lacunarity of porous media. *Phys. Rev. E*, **72**(4), art. no. 0413062005.
- [50] Tél, T., Fulop, A. and Vicsek, T. (1989). Determination of fractal dimensions for geometrical multifractals, *Physica A*, **159**(2), 155–166.
- [51] Dedebeant, G. and Wehrlé, P. (1935). *Le Rôle de l'Échelle en Météorologie*. Gauthier-Villars, Paris.
- [52] Chepil, W.S. (1950). Methods of estimating apparent density of discrete soil grains and aggregates, *Soil Sci.*, **70**, 351–362.
- [53] Richardson, L.F. (1961). The problem of contiguity: an appendix of statistics of deadly quarrels. *Gen. Syst. Yrbk.*, **6**, 139–187.
- [54] Nyton, F.J. (1978). Characterizing irregularity. *Science*, **200**, 677–678.
- [55] Nottale, L. (1993). *Fractal Space-Time and Microphysics*. World Scientific, Singapore.
- [56] Edgar, G.A. (1990). *Measure, Topology and Fractal Geometry*. Springer-Verlag, New York.
- [57] Meakin, P. (1991). Fractal aggregates in geophysics, *Rev. Geophys.*, **29**(3), 317–354.
- [58] Pfeifer, P. and Obert, M. (1989). Fractals: basic concepts and terminology. In *The Fractal Approach to Heterogeneous Chemistry*, Avnir, D. (ed.). John Wiley & Sons, Ltd., New York, p. 11–43.

- [59] Turcotte, D.L. (1992). *Fractals and Chaos in Geology and Geophysics*. Cambridge University Press, Cambridge, UK.
- [60] Crovelli, R.A. and Barton, C.C. (1995). Fractals and the Pareto distribution applied to petroleum accumulation-size distributions. In *Fractals in Petroleum Geology and Earth Processes*, Barton, C.C. and La Pointe, P.R. (eds). Plenum Press, New York, p. 59–72.
- [61] Pareto, V. (1897). *Cours d'Économie Politique*, volume 2. F. Rouge, Lausanne, Switzerland.
- [62] Mandelbrot, B.B. (1960). The Pareto–Levy law and the distribution of income. *Int. Econ. Rev.*, **1**(2), 79–106.
- [63] Mandelbrot, B.B. (1963). New methods in statistical economics. *J. Polit. Econ.*, **71**(5), 421–440.
- [64] Arnold, B.C. (1983). *Pareto Distributions*. International Cooperative Publishing House, Fairland, MD.
- [65] Montroll, E.W. and Schlesinger, M.E. (1983). Maximum entropy formalism, fractals, scaling phenomena, and  $1/f$  noise: a tale of tails. *J. Stat. Phys.*, **32**(2), 209–230.
- [66] Persky, J. (1992). Pareto's law. *J. Econ. Persp.*, **6**(2), 181–192.
- [67] Johnson, N.L. and Kotz, S. (1970). *Distributions in Statistics. Continuous Univariate Distributions – I*. John Wiley & Sons, Ltd, New York.
- [68] Zipf, G. (1949). *Human Behavior and the Principle of Least Effort*. Addison-Wesley, Reading, MA.
- [69] Macaulay, F. (1922). Pareto's laws and the general problem of mathematically describing the frequency distribution of income. In *Income in the United States, its Amount and Distribution, 1909–1919*. National Bureau of Economic Research, New York, Chapter XXIII.
- [70] Brown, W.K., Karpp, R.R. and Grady, D.E. (1983). Fragmentation of the universe. *Astrophys. Space Sci.*, **94**, 401–412.
- [71] Turcotte, D.L. (1986). Fractals and fragmentation. *J. Geophys. Res.*, **91**(B2), 1921–1926.
- [72] Brock, J.R. (1971). On size distributions of atmospheric aerosols. *Atm. Environ.*, **5**, 833–841.
- [73] Cargill, S.M., Root, D.H. and Bailey, E.H. (1981). Estimating usable resources from historical industrial data. *Econ. Geol.*, **76**(5), 1081–1095.
- [74] Schmidt, R. and Housen, K. (1995). Problem solving with dimensional analysis. *Ind. Phys.*, **1**(1), 21–24.
- [75] Turcotte, D.L. and Huang, J. (1995). Fractal distributions in geology, scale invariance, and deterministic chaos. In *Fractals in the Earth Sciences*, Barton, C.C. and La Pointe, P.R. (eds). Plenum Press, New York, pp. 1–40.
- [76] Van Damme, H. (1995). Scale invariance and hydric behaviour of soils and clays, *C. R. Acad. Sci. Paris, Sér. IIA*, **320**, 665–681.
- [77] Matsushita, M. (1985). Fractal viewpoint of fracture and accretion. *J. Phys. Soc. Jpn.*, **54**(3), 857–860.
- [78] Avnir, D., Farin, D. and Pfeifer, P. (1992). A discussion of some aspects of surface fractality and of its determination. *New J. Chem.*, **16**, 439–449.
- [79] Crawford, J., Baveye, P., Grindrod, P. and Rappoldt, C. (1999). Application of fractals to soil properties, landscape patterns and solute transport in porous media. In *Assessment of Non-point Source Pollution in the Vadose Zone*, Corwin, D.L., Loague, K. and Ellsworth, T.R. (eds). Geophysical Monograph 108, American Geophysical Union, Washington, D.C., pp. 151–164.
- [80] Dubuc, B., and Dubuc, S. (1996). Error bounds on the estimation of fractal dimension, *SIAM J. Numer. Anal.*, **33**(2), 602–626.
- [81] Baveye, P., Boast, C.W., Ogawa, S., Parlange, J.-Y. and Steenhuis, T. (1998). Influence of image resolution and thresholding on the apparent mass fractal characteristics of preferential flow patterns in field soils. *Water Resour. Res.*, **34**(11), 2783–2796.

- [82] Liebovitch, L.S. and Toth, T.I. (1989). A fast algorithm to determine fractal dimensions by box counting. *Phys. Lett. A*, **141**, 386–390.
- [83] Lavallée, D., Lovejoy, S., Shertzer, D. and Ladoy, P. (1993). Nonlinear variability of landscape topography: multifractal analysis and simulation. In *Fractals in Geography*, Lam, N.S.-N. and De Cola, L. (eds). PTR Prentice Hall, Englewood Cliffs, NJ, pp. 158–192.
- [84] Folorunso, O.A., Puente, C.E., Rolston, D.E. and Pinzón, J.E. (1994). Statistical and fractal evaluation of the spatial characteristics of soil surface strength. *Soil Sci. Soc. Am. J.*, **58**(2), 284–294.
- [85] Frisch, U. and Parisi, G. (1985). Fully developed turbulence and intermittency. In *Turbulence and Predictability of Geophysical Flows and Climate Dynamics*, Ghil, M., Benzi, R. and Parisi, G. (eds). North Holland, New York, p. 84.
- [86] Halsey, T.C., Jensen, M.H., Kadanoff, L.P., Procaccia, I. and Shraiman, B.I. (1986). Fractal measures and their singularities: the characterization of strange sets. *Phys. Rev. A*, **33**, 1141.
- [87] Aharony, A. (1990). Multifractals in physics: successes, dangers and challenges, *Physica A*, **168**, 479–489.
- [88] Witten, T.A. and Sander, L.M. (1981). Diffusion-limited aggregation, a kinetic critical phenomenon, *Phys. Rev. Lett.*, **47**, 1400–1403.
- [89] Stanley, H.E. and Meakin, P. (1988). Multifractal phenomena in physics and chemistry. *Nature*, **335**, 405–409.



---

# 3 Methods and Techniques for Fractal Analysis of Environmental Systems

---

**Graeme Bushell**

*School of Chemical Sciences and Engineering, The University of New South Wales, UNSW  
Sydney NSW 2052, Australia*

## 3.1 INTRODUCTION

A wide range of techniques and methods have been used to measure fractal structure in environmental systems. Which approach is appropriate in given circumstances depends on whether an in-situ measurement is required or whether the samples may be taken for ex-situ analysis, on the size of the materials one is analysing and on their optical and mechanical properties.

We shall make a distinction between *technique*, which will refer to the process of making a measurement, and *method*, which involves processing a measurement to extract information about the fractal dimension. Both are required. Most of the techniques described here are straightforward as long as some basic steps are taken not to damage the sample. It is often the assumptions made in applying the method that introduce the most uncertainty into the results.

When measuring fractal structures in environmental systems, one is often dealing with complex assemblies of smaller subunits ('particles'). In practice, these assemblies may be naturally occurring or artificially induced and can be composed of bacterial cells, colloidal mineral particles, natural organic matter, pollutants such as surfactants and polymers, or various combinations of these. The systems may be airborne assemblies of smoke particles, dust particle assemblies in space or somewhat larger mineral and organic matter assemblies in soils or sediments. All of these structures shall be referred to by the generic term 'aggregates'.

Although there are fractal systems in the environment which are not aggregates, such as the fractal surface roughness of fractures and wear particles, the texture of clouds and the distribution of stars in the night sky, these are less often of interest in the study of environmental systems. Surface fractal dimensions are also considered important in environmental systems and, although they are subject to many of the same principles discussed later, are not treated explicitly here.

### 3.1.1 General Considerations in Measuring Systems with Fractal Structure

The measurement of fractal structure in environmental systems is accomplished by the measurement of at least two properties of the system that are related to each other through a fractal scaling law. Generally speaking, environmental systems of interest exhibit power-law scaling of mass with linear size such that

$$m_a \propto L_a^{D_m} \quad (3.1)$$

where  $m_a$  is the aggregate mass or, more generally, something that is linearly proportional to mass, such as solid volume or number of constituent particles. The number of constituent particles is usually the best defined measure in this respect.  $L_a$  is a measure of aggregate length, such as radius or diameter, and  $D_m$  is the mass fractal dimension, sometimes referred to as  $D_3$ , the fractal dimension in three-dimensional space. Choosing different measures for mass and linear size will simply result in different constants of proportionality, leaving the power law scaling unaffected. In the rest of this chapter, use will be made of a constant  $k$ , most commonly known in the literature as the power law prefactor.  $k$  will take a subscript denoting the type of aggregate radius used. For instance if we use the aggregate radius of gyration as our length, Expression (1) will become:

$$N_{0,a} = k_g \left( \frac{R_{g,a}}{R_0} \right)^{D_m} \quad (3.2)$$

where  $N_{0,a}$  is the number of primary particles in an aggregate,  $R_{g,a}$  is the aggregate radius of gyration,  $R_0$  is the primary particle radius and  $k_g$  is the prefactor pertaining to size measured as radius of gyration and most probably has a value around 1.3 for particles in point contact [1–3], increasing significantly with any sintering or short-range restructuring [1, 2, 4]. Indeed, Oh and Sorensen [1] show that the exact value of the prefactor depends on a number of factors, such as aggregation mechanism, space dimensionality, mass fractal dimension and aggregate size, and thus represents another measure that may be usefully employed to characterize aggregates.

The relationship embodied in the expression in Equation (3.1) is shown in Figure 3.1 for data obtained from a computer simulation algorithm comparable to that propounded by Thouy and Jullien [5] and has been verified countless times in the literature for widely varying systems. In this case the algorithm selected two aggregates at random, selected one particle at random from each of the two aggregates and then placed the two aggregates such that the chosen particles were next to each other. If the aggregate placement did not result in any overlapped particles *and* the centre-to-centre distance of the two aggregates was within a range determined by parameters in the simulation, then the aggregation event was accepted and the new aggregate returned to the list of all aggregates. Example structures generated using this algorithm are shown in Figure 3.2 – biasing the centre-to-centre criterion towards close placement resulted in higher mass fractal dimensions, whereas biasing towards distant placement resulted in lower mass fractal dimensions. Different mass



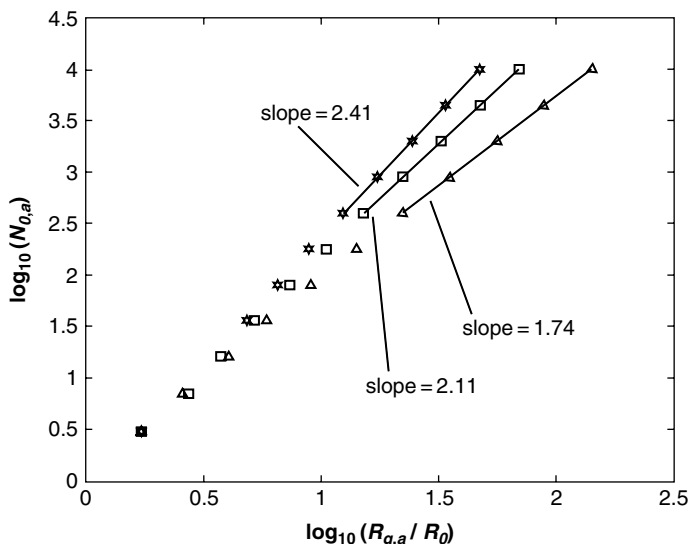


**Figure 3.1** A log–log plot of number of particles  $N_{0,a}$  in an aggregate against radius of gyration  $R_{g,a}$  of the aggregate. The data are obtained from computer simulations and show three different mass fractal dimensions, of 1.74, 2.11 and 2.41.

fractal dimensions result from different aggregate formation processes, two common cases being the so called reaction-limited cluster aggregation (RLCA) case with  $D_m = 2.1$  and the diffusion-limited cluster aggregation (DLCA) case with  $D_m = 1.8$  (see Chapter 4 for more details). Fractal scaling (in a fairly loosely defined sense) in aggregates of fine particles is so common [6] that it is the rule rather than the exception.

The problem of measuring the fractal dimension in practice is the problem of inferring values of  $m$  and  $L$  (or their equivalents). The ways in which this can be achieved are quite diverse and should be chosen with care, as techniques well suited to a particular system may perform badly with others. Gregory [7] has made an early review of some of the ways by which fractal dimension might be measured, followed later by Bushell *et al.* [8].

### 3.1.2 Fractal and Nonfractal Systems

True fractal scaling as embodied in the expression in Equation (3.1) and Equation (3.2) never occurs in nature, as natural systems always have some kind of upper and lower characteristic size beyond which the scaling breaks down. For example, many people would be comfortable with the concept that a sheet of paper is two-dimensional, but this is only really a reasonable approximation at scales much larger than the paper thickness and much smaller than the sheet's width. If we examine the sheet of paper on scales smaller than the thickness then it has characteristics of a three-dimensional

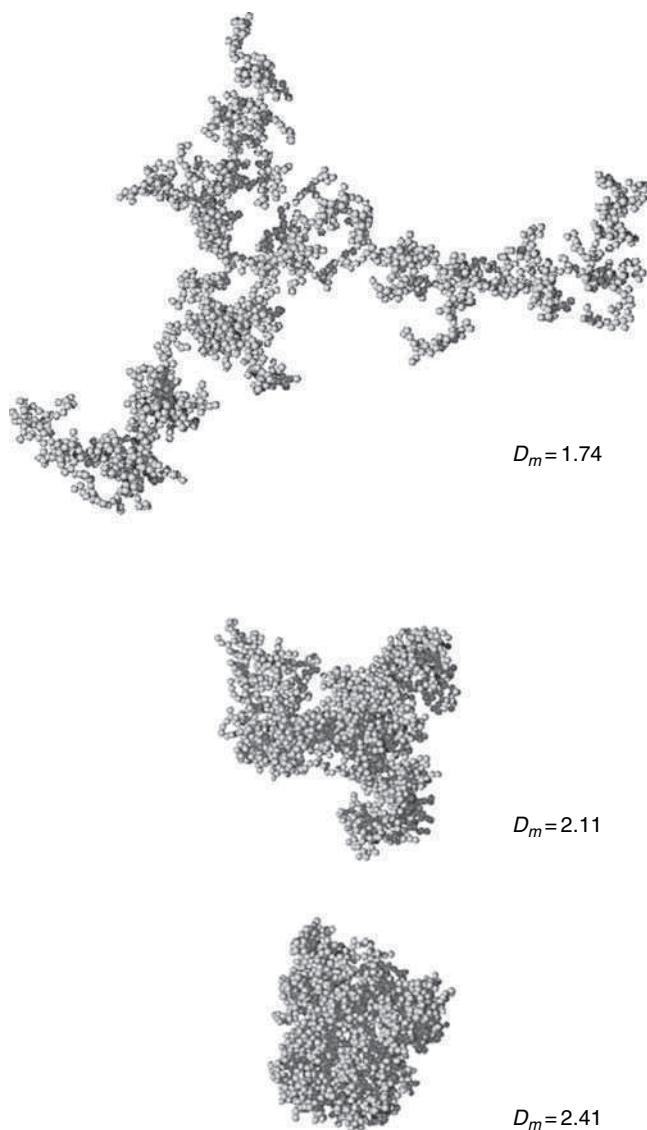


**Figure 3.2** Example aggregates drawn from classes having mass fractal dimension (from top to bottom) of 1.74, 2.11 and 2.41. Each aggregate contains 2000 primary particles. Note the increasing compactness as the mass fractal dimension increases.

body. Likewise, if we examine it on scales much larger than the length of the sheet then it begins to look like a zero-dimensional object, or a point. Fractal systems in the environment raise exactly the same questions of perspective. To the extent that

an aggregate can exhibit fractal scaling, it only occurs at scales somewhat larger than the particles comprising the aggregate and somewhat smaller than the aggregate size.

Equations (3.1) and (3.2) can also be seen in two different ways: as formulae that express the underlying physics of the system, in which the true fractal dimension is asymptotically approached as the aggregates become very large; and as purely correlative equations in which the fractal dimension is a fitting parameter to describe the scaling of the system over some limited range of aggregate size. Both meanings of fractal dimension have been used in the literature.

Taking the first of the two meanings, we are presented with the problem of knowing how large the system needs to be before ‘true’ fractal scaling emerges. This only happens when the component particle size becomes so small compared with the aggregate as not to have any significant effect on the property we are observing. Unfortunately, there is no general answer to this question, as what constitutes ‘large enough’ varies depending on which property of the system we are interested in correlating. If we are interested in the scaling of the density autocorrelation function within an aggregate (defined later), then a distance of four primary particle radii appears to be sufficient [9, 10]; if, however, we are interested in the projected area of fractal aggregates coming close to its asymptotic scaling, then Figure 3.3 (and the work of Meakin *et al.* [11]) shows that even aggregates of 10 000 particles cannot be considered ‘large enough’.

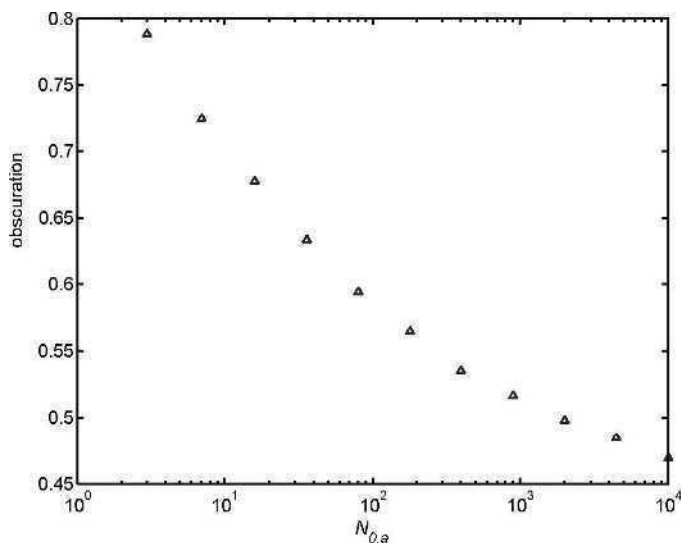


**Figure 3.3** Obscuration as a function of number of particles in an aggregate, for a simulated experiment with  $D_m = 1.74$ . Infinite aggregates with this structure are geometrically transparent, meaning that the obscuration (fractional area of particles in the aggregate projection) should be constant. The figure shows that even aggregates of 10 000 particles cannot really be considered large enough for this to be the case. This is the origin of the error for the  $D_m = 1.74$  data shown in Figure 3.6.

Fractal scaling in real systems is not only limited by upper and lower size limits imposed by the physical size of the constituent units and the whole aggregate, but there may be intermediate scales where the structure changes. This is usually a result of a change in the nature of the physical processes during growth, e.g. a change in shear intensity at different stages of a flocculation process [12] or shear-induced restructuring and breakup [13]. This kind of change in scaling can be a quite distinct transition but is commonly a smooth and continuous change. If we were to plot the mass of such aggregates versus their radius on a log-log plot we would not find the straight line characteristic of fractal systems but quite possibly a curve with regions that may be more or less straight. This means that the system cannot be considered to be self-similar and, thus, truly fractal over the full size range of the aggregate (i.e. from primary particle size to aggregate extremity), though some degree of self-similarity can be considered to hold over narrower size ranges.

This presents a rather serious problem to anyone interested in measuring the ‘fractal dimension’ of these systems. Even if the deviations from power-law scaling are not large, we may get quite different answers for fractal dimension if we use different techniques to analyse the same system. Take the example of the settling technique and the angular dependence of small-angle light scattering. Light scattering, as we shall see later, is able to resolve aggregate structure at scales much smaller than the overall size of the aggregate, probably at less than a tenth of the overall aggregate size. The settling velocity method, on the other hand, is most sensitive to the largest pores in the aggregate, i.e. the large-scale features that are larger than a tenth of the aggregate size. Even if the methods applied to these measurements were free from modelling errors (which they are not), we would still get different answers for fractal dimension if the system displays multiple levels of structure. The reason is that the two techniques are essentially probing different length scales.

### 3.1.3 Sample Handling Considerations

As far as possible, when trying to measure the fractal dimension of environmental systems we should attempt to do so *in situ*. Many of these fractal systems, particularly those with low fractal dimensions, are extremely sensitive to shear. Any attempt to move the assemblages from one place to another, such as from the environment into some sort of laboratory equipment, may result in a potentially significant level of shear-induced restructuring. This can be overcome in laboratory-based studies by performing the experiment in the very instrument that will be used to make the measurements. Examples of this are aggregation experiments performed in the sample cell of a small-angle light-scattering instrument [14], *in-situ* microscopy [15, 16] and even *in-situ* ultra-small-angle X-ray scattering (USAXS) [17]. Small-angle light-scattering experiments for flame-generated aerosols [18, 19] are always performed *in situ*.

Sampling of systems that are sheared in their natural environment is much easier. In this case, all one needs to do is make sure that in sampling the system the shear

we induce is less than that naturally experienced by the aggregates [20]. A common example of this is the kind of fundamental flocculation studies where aggregation is performed in some kind of sheared vessel. Samples of the system have been obtained by pumping through an external sampling loop [20, 21], by withdrawing sample from the vessel using tubing and a syringe [21] or by using a wide-mouthed or inverted pipette [22–24]. Structures smaller than a micrometre in overall size may be examined by X-ray and neutron scattering; for these techniques, sample handling is not normally given much consideration because structures at such scales are not generally considered sensitive to common shear environments.

## 3.2 SCATTERING

One of the more common ways of measuring the fractal dimension of aggregated matter in natural systems is through the use of small-angle scattering. X-rays, neutrons and light have all been used to probe the structure of aggregates. Although the wavelength of the radiation is different, all of these methods have a common basis, in that they rely on interference between waves scattered from individual particles within the aggregate structure. General principles will be discussed first, followed by consideration of specific applications.

### 3.2.1 Principles and Analysis

The analysis that is used to determine fractal dimension in all X-ray, neutron and most light-scattering experiments is based upon the Rayleigh–Gans–Debye (RGD) formalism. For a more detailed discussion of the development of the equations for RGD scattering, readers are referred to the book by Guinier and Fournet [25]. In addition, Sorensen [26] has written an excellent and highly readable review that gives a good qualitative description of RGD scattering and comprehensively explains the state of current knowledge on light scattering from fractal aggregates.

#### 3.2.1.1 Principle

In conducting static scattering experiments, we normally measure the scattered intensity at a number of different angles, although the quantity of physical significance is the magnitude of  $\mathbf{q}$ , the scattering wave vector:

$$q = |\mathbf{q}| = \frac{4\pi z}{\lambda} \sin\left(\frac{\theta}{2}\right) \quad (3.3)$$

where  $\lambda$  is the wavelength of the radiation in a vacuum,  $\theta$  is the scattering angle and  $z$  is the refractive index of the dispersing medium.

The idea behind the RGD theory is that the scattering body can be considered as a set of independent, noninteracting Rayleigh scattering elements. That is, that each particle in an aggregate scatters the radiation as if it were alone in space. An

interference pattern reflective of the spatial arrangement of the constituent particles of the aggregate results because the path length of the radiation from source to detector is different for light scattered from each particle in the aggregate. Thus, the scattered wave from each particle arrives at the detector with a different phase. The intensity pattern at any point in space can then be calculated as the sum of the scattered waves from each individual scatterer according to

$$I(q) = S(q)P(q) \quad (3.4)$$

where  $I(q)$  is the scattered intensity pattern as a function of scattering angle through the variable  $q$ .  $P(q)$  and  $S(q)$  are known as the form and structure factors, representing the angular scattering dependence of the individual particles and the interparticle effects respectively.

### 3.2.1.2 Form and structure factors, and the density autocorrelation function

The form and structure factors are mathematical transforms of the distribution of the scattering elements in space. If the vector  $\mathbf{r}_{ij}$  represents the displacement between scattering elements (particles)  $i$  and  $j$ , then the scalar  $\mathbf{q} \cdot \mathbf{r}_{ij}$  is the phase difference between light scattered from elements  $i$  and  $j$  at an angle  $\theta$  corresponding to vector  $\mathbf{q}$ . If  $\mathbf{q} \cdot \mathbf{r}_{ij} \lesssim 1$ , then the light scattered from  $i$  and  $j$  will be essentially in phase, leading to constructive interference. This means that the amplitudes of the scattered waves add and the scattered intensity is thus proportional to the square of the sums of the masses of the two scattering elements  $i$  and  $j$ . If  $\mathbf{q} \cdot \mathbf{r}_{ij} \gtrsim 1$ , then the phase will be more or less random and the scattering incoherent. In that case the intensities add, the resulting intensity being proportional to the sum of squares of the masses of scatterers  $i$  and  $j$ . The significance of this is that scatterers that are separated by a distance smaller than  $1/q$  will scatter in phase, essentially as a single body. Scatterers separated by distances larger than  $1/q$  will scatter incoherently. So the inverse magnitude of  $q$  acts as a probe of length scales, and the scattered intensity as a function of  $q$  provides information on how much mass exists at scales larger and smaller than  $1/q$ .

To calculate the structure factor we need information about the distances between the particles  $i$  and  $j$  comprising the aggregate. This is encapsulated in the density autocorrelation function  $g'(r)$ , which describes the distribution of separations between pairs of particles. This fundamental descriptor of aggregate structure will also make an appearance in our later discussion of aggregate hydrodynamics. It represents the average density of particles at a distance from any other particle in the aggregate:

$$g'(r) = g'(|\mathbf{r}_j - \mathbf{r}_i|) = \sum_{i=1}^N \sum_{j=1}^N \frac{1}{4\pi |\mathbf{r}_j - \mathbf{r}_i|^2} \phi(\mathbf{r}_i) \phi(\mathbf{r}_j) \quad (3.5)$$

where  $\mathbf{r}_i$  is a vector describing the position of particle  $i$  from an arbitrary fixed origin,  $\phi = 1$  if there is a particle at the position of its argument and  $\phi = 0$  otherwise, and vertical lines denote magnitude.

The structure factor is then

$$S(q) = 1 + 4\pi \int_0^\infty r^2 [g'(r) - 1] \frac{\sin(qr)}{qr} dr \quad (3.6)$$

For fractal aggregates, the structure factor is like that shown in Figure 3.4. The form factor, which is the scattered intensity pattern from monodisperse spheres, is also shown. The overall scattering is shown in Figure 3.5. The main features to note are the Guinier scattering regime at  $q < 1/R_{g,a}$  and the fractal scaling regime at  $1/R_{g,a} \ll q \ll 1/R_0$ . At  $q$  around  $1/2R_0$ , the structure factor depends predominantly on the details of the coordination behaviour of the individual particles [27]. At this scale, the structure factor is sensitive to features of the order of the diameter of the particles: when all particles have a similar size, this means particles in direct contact. A higher average coordination number means a higher number of particles in contact and a larger structure factor in that region, independent of the fractal dimension of the system.

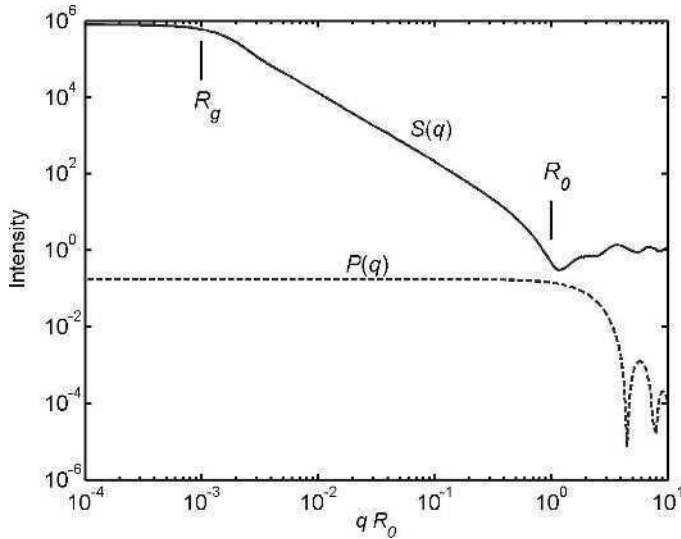


**Figure 3.4** A typical structure factor  $S(q)$  for a fractal aggregate of monodisperse spheres (solid line) and the form factor  $P(q)$  for a collection of unaggregated monodisperse spheres. In this example the spheres have unit radius, the mass fractal dimension of the aggregate is 1.8 and the radius of gyration of the aggregate is  $1000R_0$ .

At  $q \gg 1/R_0$  the structure factor approaches unity and the scattering depends almost entirely on the form factor.

The RGD scattering pattern exemplified in Figure 3.5 may be used to determine both the size and fractal dimension of an aggregate. The size may be determined from

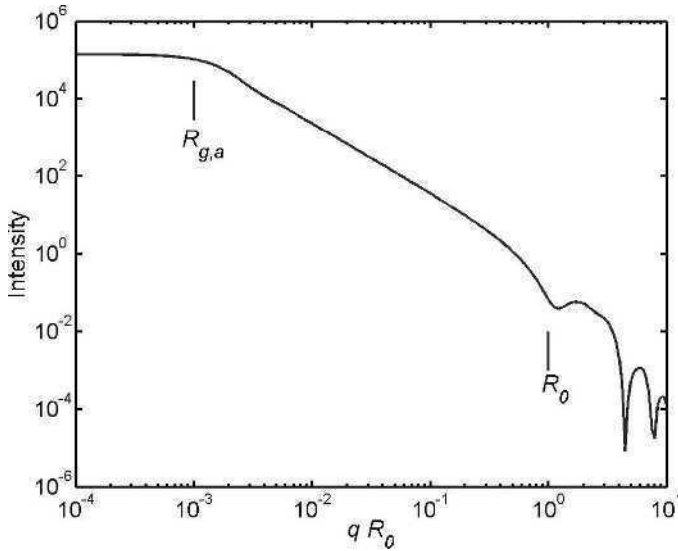


**Figure 3.5** Scattered intensity from a fractal aggregate,  $S(q)P(q)$  from Figure 3.4. The main features to note are the Guinier scattering regime at  $q < 1/R_{g,a}$  and the fractal scaling regime at  $1/R_{g,a} \ll q \ll 1/R_0$ . At  $q$  around  $1/R_0$ , the structure factor depends predominantly on the details of the coordination behaviour of the individual particles and at high  $q$  it depends on the structure of the individual particles.

the intensity data at  $q < 1/R_{g,a}$ , the Guinier regime, because in that range the scattered intensity is only a function of the radius of gyration of the aggregate, vis-à-vis

$$I(q) \propto 1 - \frac{1}{3}q R_{g,a}^2 \quad (3.7)$$

In the fractal regime, the intensity function is characterized by the power-law relationship

$$I(q) \propto q^{-D_m} \quad (3.8)$$

and the fractal dimension may be determined from the negative slope of the fractal region on a log-log plot. Clearly, the fractal region does not become fully developed until  $q$  is somewhat larger than the inverse radius of gyration. Care must be taken not to include any of the transition region in the measurement of fractal dimension. Sorensen [28] advocates that, in measuring the fractal dimension this way,  $q$  should be at least  $5/R_{g,a}$ . The author has found that another effective method is numerical differentiation of the scattered intensity data with respect to  $q$  and to take the fractal dimension as the negative of the derivative when it becomes reasonably constant.



### 3.2.1.3 Cut-off functions

The shape of the transition between the Guinier regime and the fractal regime relates to the shape of the aggregate. Physically, the density autocorrelation function does not continue fractal scaling forever, but falls to zero at lengths greater than the size of the aggregate. There have been a number of attempts to describe this decay through a so-called cut-off function, which when transformed through the RGD scattering equation (Equation (3.6)), would describe the shape of the transition region of the structure factor. These attempts have ranged from the mathematically convenient [29], to purely empirical [30, 31] and those derived from physical reasoning [3, 32, 33]. The Gaussian cut-off function is one of the simplest to use and is adequate for most purposes [26].

### 3.2.1.4 Aggregate polydispersity

Experimentally observed scattering patterns generally exhibit a much broader transition region than that depicted in Figure 3.5. This can be understood quite easily as a consequence of polydispersity in aggregate size. Each aggregate alone scatters in the manner of Figure 3.5,<sup>1</sup> smaller aggregates showing the transition from Guinier to fractal scattering at higher  $q$ , and larger aggregates at lower  $q$ .

Consider a mixture of different-sized fractal aggregates. If the aggregates are dilute enough to move independently of each other then their scattered intensities simply add. At high enough  $q$  (greater than five times the inverse radius of gyration of the smallest aggregate), we will be examining scattering from the fractal regime for all of the different-sized aggregates and, added together, these simply yield the same power law.

At very low  $q$  (less than the inverse radius of gyration of the largest aggregate) we see the sum of the Guinier scattering regimes, which yields a functionality exactly as that described in Equation (3.7). The meaning of  $R_{g,a}$  in Equation (3.7) would now be somewhat different, being an average aggregate size known as the  $z$ -average [26].

Clearly the region between the Guinier regime and the fractal regime would now be wider than is the case with monodisperse aggregates. Sorensen *et al.* [34] have shown how the width of this transition region may be exploited via a graphical method to determine the width of the cluster size distribution under the assumption of a mathematical form for the cluster size distribution and a particular cut-off function. Sorensen *et al.* have compared most of the commonly used cut-off functions and concluded that the Gaussian cut-off is adequate [35]. The author's own unpublished

---

<sup>1</sup> Actually this is not quite true. A single aggregate shows quite a lot of deviation from fractal scaling due to the inherent randomness in these structures. It would be more accurate to say that the scattering in Figure 3.5 describes the average scattering from a large number of aggregates having exactly the same radius of gyration.

work suggests that the Zeng and Meriani [33] approach<sup>2</sup> is probably the most accurate, but differences from the Gaussian are not large. In the author's opinion, the Gaussian function is accurate enough for the analysis of most real scattering experiments.

This approach to measuring cluster size distribution is analogous to (although less sophisticated than) the way that most commercial laser diffraction particle-sizing instruments extract the particle size distribution from measured scattering data – the only real difference being the model for a single scatterer that is used.<sup>3</sup>

### 3.2.2 Small-Angle Light Scattering

Light interacts primarily with the peripheral electrons in atoms and molecules and for this reason the nature of the interaction depends to a large extent on the chemical nature of the system.<sup>4</sup> The extent to which materials refract and absorb light determines which systems can be analysed using the approach described here. An excellent review of what is known about light scattering from fractal aggregates has been published [26], and the interested reader should refer there for a much more detailed discussion.

The previously presented discussion on the use of the RGD scattering approximation as a tool of use in determining aggregate size and fractal dimension has limitations when applied to light scattering. For the RGD approximation to be strictly valid, the following rather restrictive conditions must be met [36]:

$$|\zeta - 1| \ll 1 \quad (3.9)$$

$$2k'R_0|\zeta - 1| \ll 1 \quad (3.10)$$

where  $\zeta$  is the complex refractive index of the particles relative to the medium and  $k'$  is the wave number,  $2\pi/\lambda$ . Taking the example of polystyrene latex particles in water, the refractive index is 1.6. The relative refractive index is  $1.6/1.33 = 1.20$ , approximately satisfying the first condition. Taking the wavelength of incident light as  $0.6328 \mu\text{m}$ , the wavenumber is  $9.93 \mu\text{m}^{-1}$ . For the second condition to hold,  $R_0$  must be smaller than about  $0.05 \mu\text{m}$ .

Numerical exploration of the limits of validity of the RGD approximation to light scattering for fractal aggregates has been made by Farias *et al.* [37], who found that if the conditions of Equations (3.9) and (3.10) are replaced by

$$|\zeta - 1| < 1 \quad (3.11)$$

$$2k'R_0 < 0.6 \quad (3.12)$$

<sup>2</sup> This was the cut-off function used to calculate the artificial structure factor that we see in Figures 3.4 and 3.5.

<sup>3</sup> Commercial instruments work on the basis of scattering from spheres calculated using Mie theory, Sorensen *et al.*'s graphical method works on the basis of scattering from fractal aggregates calculated using RGD theory.

<sup>4</sup> This is why various types of light spectroscopy are so useful in chemical characterization.

then the size of the errors in predicting the absorption and scattering cross-sections will be less than about 10 %. Let us assume that this means that the scattered intensity at any given angle will be at most 10 % different from that expected under the RGD approximation. Let us further assume a worst-case scenario that we have 10 % departures from RGD in opposite directions at opposite ends of a decade of  $q$  range over which we are trying to measure fractal dimension. If we have a fairly typical fractal dimension around 2, then the intensity at the lower end of the  $q$  range will be 100 times that at the upper end of the  $q$  range. With maximum 10 % errors, the intensity at the lower end of the range would be 110, and at the upper end it would be 0.9. This would lead us to measure a fractal dimension of  $\log(110) - \log(0.9) = 2.09$  instead of  $\log(100) - \log(1.0) = 2.00$ .

An error of this magnitude is unlikely, as it rests on the unlikely assumption that maximal errors occur in opposite directions. In fact, the consensus in the literature suggests that fractal scaling is maintained even with significant multiple scattering within aggregates [26, 38, 39] as long as the scattering system is not close to optical resonance [39, 40]. This seems to be true for constituent particles with size of the order of the wavelength of illuminating light, but has not been tested for very large particles.

### 3.2.3 Volume Obscuration

In some ways, a more robust method of using small-angle light scattering to measure the mass fractal dimension of particle aggregates is to rely on the changing projected area of an assembly of particles as they aggregate, an idea first used by Volker Oles in 1992 [20].

#### 3.2.3.1 Principle

If we assume that the individual particles in an aggregate are large enough such that the extinction efficiency  $Q_{\text{ext}}$  for these particles is not very sensitive to particle size, then the extinction caused by an aggregate will be proportional to the projected area of that aggregate. The value of the extinction coefficient approaches two as the particle size becomes large, but for many particles does not depart very far from this value once the condition

$$2x|\zeta - 1| > 5 \quad (3.13)$$

has been achieved, where  $x$  is the size parameter of the particle ( $2\pi R_0/\lambda$ ) [36]. This is particularly the case for absorbing particles. For latex microspheres irradiated by a He-Ne laser, this is equivalent to a particle diameter larger than about five microns.

If, in addition to this condition, the particle concentration is low enough that the fraction of the total projected area obscured by other particles is small, then the obscuration observed in a scattering instrument will be proportional to the total projected area of the particles and aggregates:

$$\text{obscurtion} \propto N_a A_{p,a} \quad (3.14)$$

where  $A_{p,a}$  is the projected area of an aggregate.

If we have an aggregating fractal system, the generalized radius of aggregates  $R_a$  is related to the number of particles in an aggregate  $N_{0,a}$  by

$$N_{0,a} \propto R_a^{D_m} \quad (3.15)$$

If the total mass of the system is conserved, then the total number of aggregates in the system is related to  $N_{0,T}$ , the total number of primary particles, by

$$N_a = \frac{N_{0,T}}{N_{0,a}} \quad (3.16)$$

If the fractal dimension is higher than two, the projected area of an aggregate is related to  $R_a$  by

$$A_{p,a} \propto R_a^2 \quad (3.17)$$

Therefore, the total projected area seen by the instrument is

$$A_{p,T} = N_a A_{p,a} \propto \frac{N_{0,T}}{R_a^{D_m}} R_a^2 \quad (3.18)$$

so that

$$A_{p,T} \propto R_a^{2-D_m} \quad (3.19)$$

In other words, a plot of the log of obscuration versus log of aggregate size should show a straight line with slope of  $(2 - D_m)$ , for  $D_m > 2$ . For systems with mass fractal dimension less than two we would expect the obscuration to be constant because of the so-called ‘geometric transparency’ of these systems that ensures that essentially all particles in the structure are visible and hence contribute to the projection [11]. Oles [20] used a different formulation based on the solid volume fraction reported by a light-scattering instrument, but the principle is exactly the same.

### 3.2.3.2 Limitations

There are three major limitations of this approach: (i) it requires the constituent particles in an aggregate assembly to be large enough that the scattering efficiency is independent of size; (ii) it requires the condition of geometric opacity to be met (fractal dimension to be somewhat higher than two, aggregates to be large); (iii) it requires conservation of sample mass during a change of aggregation state. The first of these limitations is a purely practical one, in that the method cannot be applied to very small particles. The second is rather more serious, in that it has not yet been clearly established in the literature exactly what this means. The third limitation is again a practical one that limits the situations in which the method can be applied; for example, removal of particles by sedimentation will invalidate the approach.

The first limitation relates to the assumption made in derivation, that the extinction efficiency is constant as the particle size changes due to aggregation. This is probably the case for particles that comply with the condition given in Equation (3.13), since the

extinction efficiency for particles that exceed this condition commonly does not vary by more than  $\pm 50\%$ . This may sound like a lot, but remember that we are plotting extinction on a log plot to extract the fractal dimension. In practice, the extinction is likely to vary a lot less than this, since the aggregates are not solid particles composed of the same material as the primary particles but are composite structures where, to some extent, the scattering identity of the individual particles is retained. The extent to which this is the case is not known at this time.

Figure 3.6 shows a log-log plot of obscuration (normalized to the obscuration of single particles) against aggregate radius of gyration for the same data shown in Figure 3.1. The obscuration in this instance was calculated directly from the simulated aggregate geometry by dividing the total projected area of an aggregate by the total projected area of all of the particles in the aggregate, giving a fractional projected area. Thus, a collection of single particles will have an ‘obscuration’ of unity and any aggregated system will have an obscuration less than that as particles become partly obscured by other particles. Recall that the mass fractal dimensions of these systems (as characterized by the scaling of number of particles with radius of gyration in Figure 3.1) were 1.74, 2.11 and 2.41. With no knowledge of the real fractal dimension of the systems, the slope of the data in Figure 3.6 at large  $R_{g,a}$  would indicate fractal dimensions of 2.06, 2.19 and 2.35 respectively. The agreement between these and the fractal dimension obtained from  $N_{0,a}$  and  $R_{g,a}$  is only fair for the high fractal dimension cases, and says nothing about systems with low fractal

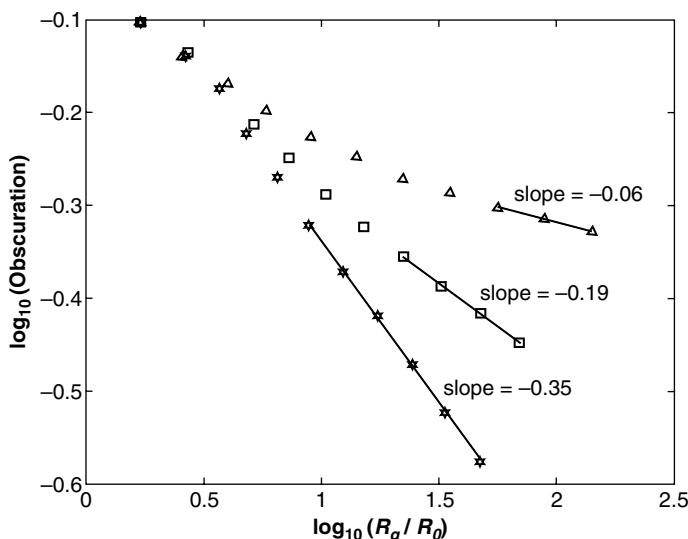


**Figure 3.6** A log-log plot of relative obscuration against aggregate radius of gyration for the three different simulated aggregate systems shown in Figure 3.1. From top to bottom, the mass fractal dimensions of the systems are 1.74 (triangles), 2.11 (squares) and 2.41 (stars).

dimensions. Given that the slope of  $\log(\text{obscuration})$  versus  $\log(R_{g,a})$  is supposed to be zero for systems with  $D_m < 2$ , the errors in slope obtained here are  $+0.06$ ,  $+0.08$  and  $-0.06$ .

These errors are probably due to the second of the two limitations listed earlier. Since the simulation data in terms of obscuration and size were determined directly from the projected area and geometry of simulated aggregates, the physics of light scattering does not yet enter into consideration. The problem arises because the derivation assumes that the aggregates are infinite in extent, so that we can use Equation (3.17) and, hence, attribute all of the loss of projected area to aggregate structure, rather than to aggregate size effects. That this is not the case is clearly illustrated in Figure 3.3, which shows the obscuration (which in this work is determined as the fractional area of single particles accounting for the whole aggregate projected area) as a function of the number of particles in the aggregate for the simulation where  $D_m = 1.74$ . Even aggregates of 10 000 particles are not large enough for the obscuration to be independent of aggregate size.

What is required here is a finite size correction to the expected cross-sectional area for aggregates of given structure. Such corrections have been derived for the problem of measuring fractal dimension from projected images of aggregates [41] but this remains to be done for projected area, relevant to the analysis presented here. Köylü *et al.* [42] cite several authors who have used an empirical relationship between fractional projected area and number of particles in an aggregate, although the relationship does not directly address the problem of partial particle obscuration as discussed here. Meakin *et al.* [11] have suggested that the projected area of finite aggregates follows the general form

$$A_{p,a} = G N_{0,a}^\gamma + B N_{0,a}^\delta \quad (3.20)$$

where  $G$ ,  $B$ ,  $\gamma$  and  $\delta$  are functions of  $D_m$ .  $\delta$  has a value between zero and one, and  $\gamma = 1$  is supposed if  $D_m < 2$  and a value of  $2/D_m$  if  $D_m > 2$ . A useful approach might be to fit Equation (3.20) to data from computer simulations so that we know  $G$ ,  $B$ ,  $\gamma$  and  $\delta$  for a range of fractal dimensions. We could then use an iterative approach whereby we analyse the experimental data to obtain an estimate for the fractal dimension, use Equation (3.20) to correct the analysis and then repeat the process with a better estimate of fractal dimension.

The third of the major limitations with this approach is the requirement that the total mass of the system in the scattering volume must be conserved so that Equation (3.16) is valid. This immediately means that most systems in natural environments cannot be analysed *in situ* using this approach, unless we have an independent way of measuring and thereby correcting for the solids concentration presented to the instrument. Most of the applications of this technique have been in the laboratory, where the solids concentration is known and constant. Even then problems may arise, as experienced by Oles [20] in his original publication. In Oles' experiment, the aggregating material eventually started to stick to the optical windows of the scattering cell, with the result that the effective solids concentration increased within the scattering

volume, leading to an increase in obscuration unrelated to aggregate structural and size effects. Oles analysed  $2.17\text{ }\mu\text{m}$  latex spheres aggregating in a Couette flow system and found that the aggregates exhibited a mass fractal dimension of 2.1 early during the aggregation process, which increased to 2.5 in later stages. The change in structure was attributed to selective breakup and reaggregation to more shear-resistant configurations.

Kusters *et al.* [22] analysed polystyrene latex particles of about  $1\text{ }\mu\text{m}$  diameter aggregated in salt solution in a stirred tank, with samples withdrawn from the tank by pipette for light-scattering measurements. They found mass fractal dimensions of around 2.5 using the volume obscuration method.

Spicer *et al.* [21] analysed  $0.87\text{ }\mu\text{m}$  particles in a stirred tank system similar to that used by Kusters *et al.* and found, using the volume obscuration method, mass fractal dimensions of 2.1 for small flocs increasing to 2.5 for larger flocs, consistent with the findings of Oles. The increase was attributed to shear-induced restructuring.

### 3.2.3.3 Small-angle multiple light scattering

A related method has been demonstrated by Lambert *et al.* [43]. This relies on the idea that multiple scattering inside an aggregate reduces the magnitude of the form factor. By measuring the scattered light at a relatively large angle ( $q$  corresponding to  $1/R_0$ ) we can measure the magnitude of the form factor and compare it with the magnitude that we would see if all the primary particles were free entities. The reduction in the magnitude of the form factor results from the reduction in effective optical contrast (refractive index of the particles divided by that of the suspending medium) caused by the presence of neighbouring particles that effectively raise the refractive index of the suspending medium. The authors present a calculation for determining the mass fractal dimension based on the known form factor for the primary particles and the measured form factor for aggregates at large angles.

The technique is only useful where the primary particles are well defined and optically identical [43]. This condition is likely to be true for bacterial aggregates, and so it should be a useful approach when examining the aggregation behaviour of individual bacterial strains.

### 3.2.3.4 Turbidity fluctuation

Another method in the volume obscuration family is the measurement of turbidity fluctuations in a flowing suspension [44]. The physical principle is the same, in that the mass fractal dimension is inferred from changes in obscuration that result from changes in aggregation state, but the implementation is rather different. In turbidity fluctuation measurement, the aggregated suspension is made to flow through a sample tube which passes between a laser diode and photodetector arrangement. Aggregate size and number are determined indirectly from the size and frequency of fluctuations in the photodetector voltage.

### 3.2.4 X-ray and Neutron Scattering

The RGD formalism introduced earlier describes X-ray scattering very well, as X-rays in general do not interact strongly with matter. This is particularly true of biological and environmental samples. This means that the interpretation of log–log scattering plots is straightforward, with the negative slope of an  $I$  versus  $q$  plot unequivocally representing the mass scaling exponent at the particular length scale corresponding to  $q$ .

X-rays have a much smaller wavelength than light which, through Equation (3.3), means that much smaller sample length scales are probed at a given angle. USAXS allows a typical range for  $q$  in experiments between  $5 \times 10^{-3}$  and  $5 \text{ nm}^{-1}$  [45], or from sub-nanometre length scales to scales of the order of 100 nm [17].

Although the relatively weak interaction of X-rays and matter makes the analysis of scattering data simpler, it makes the measurement more complex. Because the interaction occurs with all the electrons in the sample rather than just the peripheral ones, it is differences in overall electron density that provide contrast and result in scattering. The chemistry of the system is unimportant; it is the atoms and their density that matter.

For environmental samples suspended in water, the aggregates must have an electron density quite different to water. Biological materials are usually around 95% water, with the remainder being carbon and nitrogen compounds. This means that the electron density of the biological sample will be very similar to water; hence, biological samples suspended in water will be effectively invisible to X-rays, since sample concentrations are often very low. For example, Boukari *et al.* [17] reported that it took 25 min to acquire data over the whole angular range of their instrument when analysing silica particles. They used USAXS to examine the growth kinetics and structure of Stöber silica particles, showing that the early stages of that sol–gel process produced fractal structures.

Even when looking at samples with rather good contrast, such as mineral oxides in water, much longer exposure times (of the order of minutes) must be used with X-ray scattering than with light (of the order of seconds) and samples must, in general, be much more concentrated. Berthon *et al.* [45] used USAXS to measure fractal structure in resorcinol–formaldehyde gels.

The same comments made for X-ray scattering with regard to interaction with matter may be made for neutrons, only even more so. Neutrons have similar wavelengths to X-rays and so probe the same very short length scales.

The contrast for neutrons is determined by the directions of spins in atomic nuclei, which has one unique and very useful practical consequence. Hydrogen and deuterium exhibit a very, very large difference in contrast even though they are chemically identical. This has the wonderful result that we can tune the contrast in our systems by doping them with different levels of deuterium. For instance, we could suspend our sample in different mixtures of ordinary and heavy water to achieve the desired



contrast or 'refractive index'. Contrast between biological samples and water might be achieved by this means.

The same comments made for X-ray scattering with regard to analysis speed and expense apply even more so to neutron scattering. The experiments are, in general, slow and expensive compared with light scattering. For these reasons, neutron scattering is not preferred for the analysis of environmental systems except when there are very specific features of the system that indicate they would be of benefit. The ability to control contrast very selectively without changing the system chemistry is one such aspect. Schmidt has made a useful review of a range of studies in small-angle X-ray and neutron scattering [46].

### 3.3 IMAGE ANALYSIS

Images provide a great deal of information about a particulate system. Details of particle size, shape and textural features are all apparent in an image. The use of images for quantitative analysis, including the measurement of fractal dimensions, requires the use of image-processing algorithms. Balancing the great strength of image analysis in providing a wealth of structural information and the great weakness of reducing the information about a three-dimensional system to a two-dimensional representation, as well as the poor measurement statistics, when compared with the scattering techniques, represents the greatest challenge in making effective use of image analysis for structure determination.

#### 3.3.1 Principles and Analysis

The principle of geometric transparency discussed earlier is critical to how fractal structure is encoded in images of fractal objects. For large fractal structures with a mass fractal dimension  $D_m < 2$ , the area of the projected image will scale with exactly the same dimension as the mass scales in the real structure in three-dimensional space. When  $D_m > 2$  the structure is geometrically opaque, which means that the projection has no 'holes' in it and scales according to power 2 as the size of the projection increases.

What this means is that if we measure the fractal dimension describing how the area of a projected fractal scales with size, and if the dimension so obtained is less than two, then the value obtained is also the mass fractal dimension of the structure in three-dimensional space. We can express this sense of fractal scaling in images as

$$A_{p,a} \propto R^{D_A} \quad (3.21)$$

where  $A_{p,a}$  is the projected area of an aggregate image and  $D_A$  is the projected area fractal dimension, sometimes referred to as  $D_2$ . The geometric transparency argument gives us

$$D_A = D_m \quad (3.22)$$

when  $D_m < 2$ , and

$$D_A = 2 \quad (3.23)$$

when  $D_m > 2$ .

In reality this is not quite so straightforward, as the arguments around geometric transparency and opacity are only true for infinite fractals. With aggregates of finite size, the projection will display rather more ‘holes’ than would a larger fractal aggregate with the same structure. This is reflected in the form for projected area scaling suggested by Meakin *et al.* [11], reproduced as Equation (3.20). Nelson *et al.* [41] have suggested a correction to obtain the true fractal dimension  $D_m$  of the three-dimensional structure from the projected area dimension  $D_A$  and successfully applied it to images of soot aggregates.

No matter what the fractal dimension of the structure in three-dimensional space, the perimeter of the projection of the fractal will have fractal characteristics even though the projection itself may be compact. The perimeter dimension represents the scaling of the length of the perimeter  $P$  with the resolution used to measure it. This phenomenon was pointed out early on with respect to the length of coastlines, where, if the length of a coastline is measured on a map by stepping along it with a set of dividers, the measured length was found to increase as a power law as the step length was decreased. Effectively, the smaller the step length, the smaller the features of the coastline that were able to be resolved [47]. The fractal dimension describing this scaling is called the perimeter, boundary or edge dimension:

$$L_e(\varepsilon) \propto \varepsilon^{1-D_e} \quad (3.24)$$

where  $L_e$  is the measured edge length of the image,  $\varepsilon$  is the length of the ‘yardstick’ used to measure it and  $D_e$  is the edge dimension, also known as the boundary or perimeter dimension or simply  $D_1$ . For ordinary nonfractal images, such as that of a circle, the edge has unit dimension and the measured edge length will be independent of the step length  $\varepsilon$ , provided that  $\varepsilon$  is sufficiently small.

The perimeter or edge dimension, the projected area dimension and the mass dimension are all related to each other, although the relationship, at least for images of real fractal aggregates, is not trivial. Jullien *et al.* [48] made a numerical investigation of the measurement of fractal dimension from projections of computer-simulated aggregates and found that asymptotically, for large aggregates, the fractal dimension of the projection of the aggregate  $D_A$  and the perimeter dimension  $D_p$  are the same as the mass fractal dimension of the aggregate when  $D_m < 2$ . When  $D_m > 2$ ,  $D_A = 2$  and  $D_e$  decreased nontrivially with increasing mass dimension.

These conclusions, while interesting and illustrative of fundamental aspects of fractal aggregate structure, are not of any use in measuring the fractal dimensions of these structures from images because they only apply for infinitely large aggregates. When aggregates are finite in size these conclusions only hold approximately. In general, the finite size of aggregates makes it easier to ‘see through’ them, which will result in an underestimation of the fractal dimension using techniques such as box

counting [49]. A mathematical correction, such as that derived by Nelson *et al.* [41], should be applied when measuring the fractal dimension from projected images.

The behaviour of  $D_c$  for geometrically opaque aggregates raises the tantalizing possibility that some judgements about mass scaling might be made with measurements of both the projected area dimension and the perimeter dimension, but the relationship between perimeter dimension and mass dimension is, at the time of writing, not well understood. In addition, suitable finite size corrections for the perimeter dimension might be required.

Another dimension that may be measured from images is a texture dimension, which may be applied to greyscale images [50]. This has mostly found application in analysis of medical images.

### 3.3.1.1 Image preprocessing

Before the application of most algorithms that are used to deduce fractal dimensions from images, the image must be segmented, meaning that each pixel is unambiguously decided as being part of the image of the fractal or part of the background.<sup>5</sup> The simplest way of doing this is by thresholding, which takes a greyscale image that is the usual result of electronic acquisition of microscope images and assigns a particular shade of grey (threshold value) to represent the transition from black to white. Everything darker than that tone is set to black and everything lighter is set to white. More sophisticated methods for obtaining a segmented image exist, such as edge detection by gradient or Laplacian methods. Readers are referred to the book by Gonzales and Woods [51] for a detailed discussion of image processing including segmentation and edge detection.

Whichever combination of methods is chosen for segmenting the image, the extent to which the preprocessing affects the fractal analysis that follows should be tested. Where thresholding has been used for segmentation, one approach is to perform the fractal analysis with different values chosen for the threshold in preprocessing and accept the results where the returned fractal dimension does not change much with the choice of threshold value [24]. Equivalent tests should be conducted for other segmentation algorithms and parameters for the segmentation chosen that do not affect the fractal dimension results much. Another test worth doing is to take a clean image of a fractal with a known fractal dimension, such as triadic Koch island or a Sierpinski gasket, and ‘contaminate’ the image to a similar extent that experimentally derived images are contaminated by adding noise, blur or uneven lighting. If possible, the contamination should be applied with the same process that is used to measure the fractal images in the experiment. Then, the chosen image segmentation algorithm(s) and the chosen fractal analysis should be applied. The measured fractal dimension can then be compared with the analytically known fractal dimension.

---

<sup>5</sup> The algorithm explained by Cross [50] to measure the texture dimension is an exception to this, it works on a greyscale image.

Ideally, the images should be acquired in the first place in such a way as to make segmentation straightforward. One should seek the best possible image resolution and focus, and the best possible contrast between the image and the background. Failing to consider image quality in the first instance will make segmentation difficult. For example, lighting from the side should be avoided if one wants to use thresholding for image segmentation, as illustrated in Figure 3.7. In this case, some of the image is brighter than the background and some is darker, making it impossible to separate image from background on the basis of brightness. Figure 3.8 shows an image much more suited to thresholding, with white particles viewed against a black background and overhead lighting, giving excellent contrast.

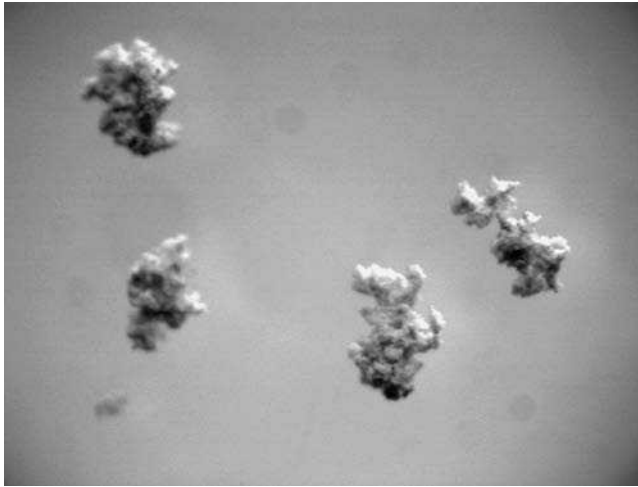


**Figure 3.7** Flocs of iron hydroxide. Not only is the image somewhat out of focus, but the sideways lighting means that part of the floc image is brighter than the background and part of it is darker. Clearly, thresholding is not going to be able to segment this image properly.

### 3.3.1.2 Image processing algorithms

Applying the various algorithms for measuring fractal dimensions for images is much easier than image preprocessing. For measurement of the perimeter dimension, the options are variations on box counting, divider or stepping methods, and aggregate population methods. For the measurement of the projected area dimension, the options are box counting, point correlation, including the sandbox method, and aggregate population methods.

The box counting method involves covering an aggregate image with square boxes of different sizes and counting the number of boxes  $N_{\text{box}}$  required to do this for each different box length  $L_{\text{box}}$ . If the boxes are made to cover the entire projection of the

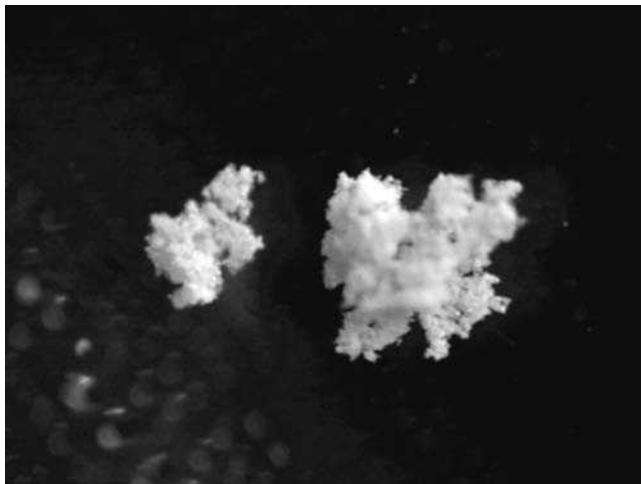


**Figure 3.8** Flocs of silica viewed against a black background with overhead lighting. Excellent contrast is achieved between the image and the background, making thresholding a good choice for image segmentation in this case.

aggregate, then the fractal dimension measured in this way will be the projected area dimension measured by box counting. If the boxes are made to cover only the outer edge of the aggregate, then the dimension will be the perimeter dimension measured by box counting. In either case:

$$D_A \text{ or } D_e = \lim_{L \rightarrow 0} \frac{-\log(N_{\text{box}})}{\log(L_{\text{box}})} \quad (3.25)$$

An easy, although tedious, way to implement this procedure is to start with a high-resolution black image of the fractal in any common image manipulation software and use an image histogram function to count the number of black pixels. This represents the number of squares of size ‘1’ required to cover the image. Next, reduce the resolution of the image by a factor of 2, ensuring that an interpolating function is used in the resize, convert any grey pixels to black and again count the image pixels. This is the number of squares of size ‘2’ required for coverage. Repeat for progressively coarser resolutions for several different images and extract the fractal dimension through Equation (3.25).

An example of this implementation of the box counting method for the measurement of the projected area dimension can be seen in Figures 3.9 and 3.10. This analysis was implemented using simple and commonly available image manipulation software,<sup>6</sup> starting with the full-resolution image and progressively halving the resolution for

<sup>6</sup> Paint Shop Pro 4.15, from Jasc Software: <http://www.jasc.com>.

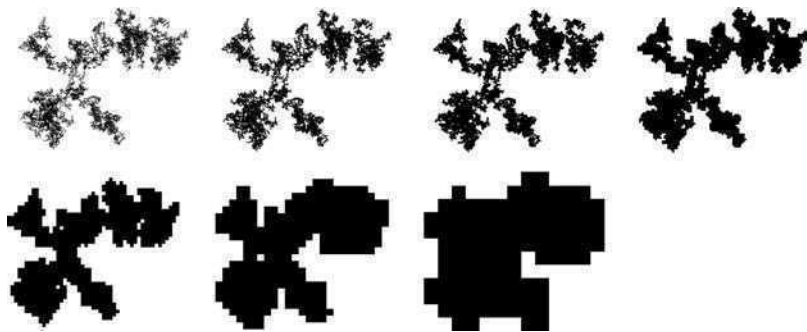


**Figure 3.9** Box-counting analysis of a projection of a computer-generated diffusion-limited cluster aggregate of 10 000 particles with mass fractal dimension of 1.88. The images have box sizes  $L$  of (top left to bottom right) 1, 2, 4, 8, 16, 32 and 64 pixels and require 205 245, 59 519, 17 062, 4895, 1436, 462 and 135 squares respectively to cover the image.

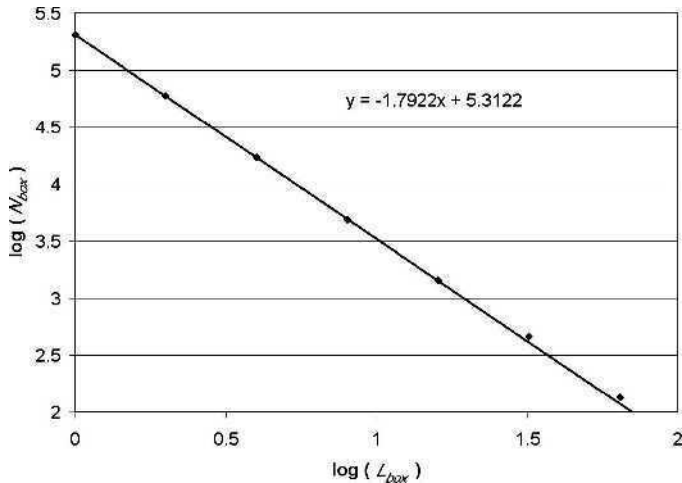


**Figure 3.10** The number of boxes versus box size from the floc shown in Figure 3.9. The slope of the curve as  $\log L$  goes to zero returns the fractal dimension.  $D_A = 1.79$  for this case, which is somewhat lower than the mass fractal dimension of 1.88 due to the finite size effects analysed by Nelson *et al.* [41].

each increase of box size. At each resolution, the image statistics displaying the total number of black pixels was recorded, representing the number of boxes required to cover the image at that resolution. The recovered fractal dimension is somewhat lower than the true value because of finite size effects.

The divider method was the original method used to measure the fractal dimension of coastlines. Manual implementation of this method may be attempted for images of

fractal aggregates, but this quickly becomes tedious. Such an implementation would involve opening a set of dividers to a distance substantially smaller than the aggregate image being measured and stepping around the perimeter, counting the number of steps required. The number of steps multiplied by the step length  $\varepsilon$  is the estimate  $L_e(\varepsilon)$  of the perimeter. The process is then repeated with ever smaller steps. Plotting  $\log(L_e)$  versus  $\log(\varepsilon)$  should (from Equation (3.24)) yield a straight line with slope  $1 - D_e$ . A much more common implementation of the divider method for computer images is the serial dilation method, which, along with box counting method, is explained by Cross [50]. Cross also reviews the use of fractal dimensions in image analysis, predominantly in the medical imaging context.

A number of computer algorithms for measuring perimeter dimension are reviewed by Allen *et al.* [52], including several computer-based implementations of the divider method. They conclude that Adler and Hancock's [53] distance transform method is a more accurate and faster analysis than the popular dilation method approach to box counting. This is generally considered the preferred method to use for measuring perimeter dimension.

For both perimeter and projected area dimensions, the aggregate population methods may be used. When an image or set of images contains projections for fractal aggregates of many different sizes but arising from the same fundamental process, the perimeter or projected area can be measured at a fixed fine resolution and then correlated to aggregate size. This assumes that all the aggregates in the population have the same fractal structure. Equation (3.21) may be used to extract  $D_A$  (or  $D_e$ ) from a log-log plot of  $A_p$  (or  $L_e$ ) versus  $L_a$ , where  $A_p$  is the projected area of an aggregate and  $L_a$  is a measure of the aggregate length.

The sandbox method is another approach to the measurement of the projected area dimension. This was the method used by Forrest and Witten to point out for the first time that aggregates of fine particles can exhibit fractal scaling [54]. The technique involves selecting a point near the centre of the image and counting the amount of projected area  $A_{p,\text{box}}$  that falls within a box of given length  $L_{\text{box}}$  centred on the chosen point. This analysis is performed for boxes of different sizes and for different chosen initial points. The projected area fractal dimension is then extracted as

$$D_A = \lim_{L \rightarrow 0} \frac{\log(A_{p,\text{box}})}{\log(L_{\text{box}})} \quad (3.26)$$

A method that lends itself much better to implementation on a computer is a direct measurement of the correlation function of the image though a two-dimensional equivalent of Equation (3.5). First, the image data are transformed such that every pixel that is part of the fractal segment (i.e. not the background) is listed as an  $x, y$  coordinate. Next, for every pixel in the segment  $i$ , we loop over all other pixels in the segment  $j$  and calculate the Euclidean distance  $r$  between them; i.e.:

$$r_{ij} = \sqrt{(x_i - x_j)^2 + (y_i - y_j)^2} \quad (3.27)$$

For an image of a fractal represented with  $N_{\text{pix}}$  pixels, these  $N_{\text{pix}}^2$  distances are distributed into bins of width  $\Delta r$  representing different distance ranges so that the total number of times  $N_r$  that a distance between  $r - \Delta r/2$  and  $r + \Delta r/2$  occurs in the image is recorded for different  $r$ . The projected area dimension may then be obtained from a plot of  $\log(N_r)$  versus  $\log(r)$ , according to

$$N_r(r) \propto r^{D_A-1} \quad (3.28)$$

These  $N_{\text{pix}}^2$  distance calculations can represent a substantial computation for high-resolution images, but this should not cause a problem for most modern computers. If computation time becomes an issue, an easy way to reduce the time while sacrificing very little in the way of accuracy is to perform the loop over  $i$  for a randomly chosen subset of pixels in the segment, rather than all pixels in the segment.

The accuracy and speed of the correlation function for measuring fractal dimension may be improved by only including pixels  $j$  which are closer to  $i$  than the aggregate edge nearest to  $i$ . This will not remove effects due to finite size and consequent increased transparency, but will eliminate gross aggregate shape effects.

### 3.3.2 Single Image Microscopy

There are many kinds of microscopy that may be used for structural analysis of fractal aggregated systems. Most microscopes give a single image of a sample and, as a result, three-dimensional information about the image is generally lost. In preparing samples exhibiting fractal properties for microscopic analysis, considerable care must be taken to ensure that the sample handling does not alter the structure one is trying to analyse.

Transmission electron microscopy has been used to measure fractal dimensions, commonly from soot or smoke particles collected directly onto the microscope grid [e.g. 55].

Bower *et al.* measured the boundary fractal dimension of lactose aggregates in 1,1,2-trichlorotrifluoroethane using serial perimeter dilation and Adler and Hancock's distance transform function [56]. They found that it decreased as shear rate and aggregate mass fractal dimension increased.

### 3.3.3 Confocal Microscopy

Confocal scanning laser microscopy (CSLM) (sometimes called confocal laser scanning microscopy and often simply abbreviated to confocal microscopy) is a relatively new technique that lends itself to fractal analysis in interesting ways (see also Chapter 5). The technique was first used to measure fractal structures by Bremer *et al.* in 1993 [57]. The most notable feature is that laser focusing allows the acquisition of an image which is a slice through the object being measured, rather than a projection of it. This allows for extremely sophisticated analysis. For example, it is possible to image slices at many different heights through a single floc and to reconstruct the exact position of every particle in three-dimensional space [58]. Having imaged and reconstructed a floc in this way, the measurement of any structural feature one



desires may be carried out. Similar measurements could be made by microtome slicing and traditional forms of microscopy, but CSLM presents fewer risks of sample modification, as the measurement can be made wet.

One of the easiest ways to measure fractal dimension with this technique is to capture images of slices through the structure and measure the fractal scaling of the image as discussed above. The dimension measured in this way is not the projected area dimension  $D_A$  discussed earlier, because the image is a slice not a projection. It turns out that the dimension measured in this way is numerically equal to the mass fractal dimension minus one, by virtue of the codimension rule [58]. The measurement of fractal dimensions by this technique is not subject to the restriction of geometric transparency, as is the case with the analysis of projected images, and so fractal dimensions well over two can be measured.

Snidaro *et al.* [59] used CSLM to measure the positions of bacteria in aggregates in three-dimensional space. Once the data were obtained they used a three-dimensional sandbox approach to measure the fractal dimension, with the sandbox centred on the centre of mass of the aggregate. They also used a two-dimensional sandbox method to obtain the two-dimensional fractal dimension, related to the usual  $D_m$  through the codimension rule. Small aggregates were shown to have a compact structure using both the two- and three-dimensional approaches.

Thill *et al.* [24] used the technique to measure the fractal dimension of Brownian and shear-aggregated latex particles, using thresholding at different levels and a two-dimensional box-counting approach. They noted that higher fractal dimensions result in an increased chance of particles obscuring other particles and thus not being included in the analysis. Dinsmore and Weitz [60] avoided this problem by refractive index matching the (transparent) particles and suspending liquid, but this is unlikely to be an available option with environmental systems.

Thill *et al.* [58] reconstructed the full three-dimensional coordinate information for latex aggregates and showed that the two-dimensional sectioning approach does indeed return the correct fractal dimension for the aggregates as determined from a three-dimensional pair correlation approach. The authors' density matched the solution and particles to avoid any sedimentation and allowed the aggregation to occur by Brownian diffusion. The aggregates were sampled using a broad (0.8 cm) pipette<sup>7</sup> and gently deposited onto the microscope slide without using a cover slip. This illustrates the level of care that needs to be taken in order to avoid the restructuring of aggregates by shearing.

Mellema *et al.* [61] used CSLM to examine the structure of casein gels and included a detailed discussion of the mechanics of the technique and how they applied it to their experiments. They used the density autocorrelation approach to measure the area dimension of the two-dimensional image slices. These authors used thresholding to

---

<sup>7</sup> Presumably the pipette was inverted, so that the sample was not drawn through the narrow opening at the tip of the pipette.

segment the image and found that the area dimension was very sensitive to the choice of threshold level used.

Schmid *et al.* [62] used CSLM to characterize activated sludge flocs. They also used the two-dimensional correlation function for images and fluorescence in-situ hybridization (FISH) to identify the organisms within the flocs during CSLM.

Dinsmore and Weitz (2002) [60] examined a model system of polymethylmethacrylate particles dyed with rhodamine in a density- and refractive-index-matched solution of decalin and cyclohexylbromide. They used CLSM to follow the (very slow) aggregation in real time and determined the particle positions in full three-dimensional detail. From this they performed a comprehensive structural analysis of the gels, including measurement of coordination numbers and backbone fractal dimension<sup>8</sup> of the structures, as well as the much more commonly measured mass fractal dimension.

Confocal microscopy has shown itself to be one of the most versatile techniques for structural analysis of biological and environmental systems, in some cases allowing computer reconstruction of the full three-dimensional detail of the scanned sample. Once this level of detail is obtained about a sample, any structural measure desired can be made upon the reconstruction using the methods described here and many others. It is well suited to large aggregates of materials whose density is not greatly different to the supporting liquid. Clearly, resolution is limited by the wavelength of light, as with any optical microscopy.

### 3.3.4 X-ray Microtomography

Although X-ray microtomography is not strictly speaking an imaging technique, two- and three-dimensional images are normally reconstructed from the raw data as a starting point for analysis. The technique works by scanning a thin X-ray beam through a sample at a number of different angles and measuring the absorbance of the X-rays by the sample. The three-dimensional structure that accounts for the observed absorbance patterns is constructed in a computer using the standard techniques of tomography.

Many of the comments made regarding confocal microscopy can also be made regarding X-ray microtomography, in that a full three-dimensional reconstruction of the scanned sample results from the analysis. Thus, fractal analysis can be made by point-to-point correlations in the three-dimensional structure or within two-dimensional slices and then applying the codimension rule.

As with X-ray scattering, the technique is not well suited to biological samples as the X-ray contrast of these systems is exceedingly poor. It does work well for mineral samples and might be applied for sediments and clays. An overview of the technique and comparison of different methods as applied to soil samples is given

---

<sup>8</sup> The backbone fractal dimension is the mass fractal dimension of the 'backbone', i.e. that chain of particles which connects two arbitrary particles in the structure.

by Gibson *et al.* [63]. At the time of writing, the practical resolution of commercial instruments is limited to the order of a couple of micrometres.

### 3.4 MISCELLANEOUS TECHNIQUES

#### 3.4.1 Settling Velocity Measurement

The settling velocity of fractal aggregates is one of their most significant features in many environmental systems. Settling velocities of fractal aggregates have been observed to be significantly higher than would be expected from impermeable spheres with the same mass and spatial extent as the aggregates [23, 64, 65]. The reason for this behaviour is that the fractal structures are often highly permeable, so that the fluid drag on the aggregates is reduced. This is clearly a function of the geometry of the aggregates and the relative velocity of the aggregates and the fluid.

The fact that the drag is geometry dependent is highly significant to many applications involving settling of aggregates because it implies that transport properties of fractally aggregated matter should depend on the fractal dimension of the system. In other words, it is important in practice to have models of settling velocity that properly account for the effects of fractal dimension. The geometry dependence of drag is also significant, in that it potentially gives us a measurement that can be used to infer structural information about aggregates.

Using settling velocity to infer fractal dimension and modelling settling velocity accurately are really two different problems with a common underlying physical basis. The first of these problems will be dealt with here; the second is beyond the scope of this chapter.

##### 3.4.1.1 Principle

When settling aggregates have reached their terminal velocity, the buoyancy force  $F_b$  and drag force  $F_d$  have reached an exact balance:

$$F_b = F_d \quad (3.29)$$

Without yet introducing any assumptions, this can be written as follows, which serves as a definition of the drag coefficient  $C_d$ :

$$m_a \left( 1 - \frac{\rho_L}{\rho_S} \right) g = \frac{1}{2} \rho_L v_t^2 A_{p,a} C_d \quad (3.30)$$

where  $m_a$  is the mass of the aggregate,  $\rho_L$  is the density of the fluid,  $\rho_S$  is the density of the solid particles comprising the aggregate,  $g$  is acceleration due to gravity,  $v_t$  is the terminal velocity of the aggregate and  $A_{p,a}$  is the projected area of the aggregate in the direction of  $v_t$ .

In the literature, the drag coefficient is often represented as the product of the drag coefficient of an impermeable sphere having the same radius of collision as the

aggregate and a correction factor given the symbol  $\Omega$  which accounts for the increase in permeability of the aggregate over the equivalent sphere.

$$C_d = \Omega C_d^* \quad (3.31)$$

where  $C_d^*$  is the coefficient of drag of an impermeable sphere having the same radius of collision as the aggregate in question. For creeping flow (which is true for most fractal aggregates in environmental systems):

$$C_d^* = \frac{24}{Re} \quad (3.32)$$

where the Reynolds number  $Re$  is given by

$$Re = \frac{2R_{c,a}\rho_L v_t}{\mu_L} \quad (3.33)$$

where  $\mu_L$  is the viscosity of the fluid and  $R_{c,a}$  is the radius of collision of the aggregate.

The use of  $A_{p,a}$  is rather difficult in practice because it is often hard to measure the actual projected area of aggregates due to (i) the geometry of typical settling experiments and (ii) limited image resolution typical in such experiments. Additionally, all of the uncertainties associated with aggregate projected area that were discussed earlier in the context of the volume obscuration method also apply here. The usual practice is to take  $A_a$  as the projected area of the sphere (or sometimes the ellipsoid) that encloses the aggregate being observed. This will overestimate the projected area because 'holes' in the projection of the aggregate will be included as part of the projected area. What this means in practice is that the correction factor  $\Omega$  is as much a correction for projected area as for the drag coefficient.

Adopting this practice, the projected area  $A_{p,a}$  of the aggregate will be

$$A_{p,a} = \pi R_{c,a}^2 \quad (3.34)$$

Making use of an equation equivalent to Equation (3.2) for the mass of the aggregate:

$$m_a = k_c \left( \frac{R_{c,a}}{R_0} \right)^{D_m} \frac{4}{3} \pi R_0^3 \rho_s \quad (3.35)$$

we can substitute into Equation (3.30) to derive an expression that will tell us about the dependence of settling velocity on size and fractal dimension:

$$k_c \left( \frac{R_{c,a}}{R_0} \right)^{D_m} \frac{4}{3} \pi R_0^3 \rho_s \left( 1 - \frac{\rho_L}{\rho_s} \right) g = \frac{1}{2} \rho_L v_t^2 \pi R_{c,a}^2 \frac{24\mu_L}{\rho_L v_t 2R_{c,a}} \quad (3.36)$$

Rewriting with  $v_t$  as the subject:

$$v_t = \frac{2k_c R_0^2 (\rho_s - \rho_L) g}{9\Omega_c \mu_L} \left( \frac{R_{c,a}}{R_0} \right)^{D_m - 1} \quad (3.37)$$

which implies that a log–log plot of settling velocity versus aggregate collision radius for a set of aggregates having a fractal dimension will yield a straight line with slope  $D_m - 1$ .

Now, let us critically examine the assumptions which underlie this analysis. If we have managed to accurately separate all of the size dependence of the system into the factor  $(R_{c,a}/R_0)^{D_m-1}$ , then Equation (3.37) will be correct. The biggest problem with this is the parameter  $\Omega_c$ . The first problem, of using settling velocity to determine an accurate value for the fractal dimension, is that of accurately knowing the  $R_{c,a}$  dependence of  $\Omega_c$ . The second problem, of modelling settling velocity accurately requires a quantitative model for  $\Omega_c$ . Clearly, the first of these two requirements is the less restrictive.

As explained above, the parameter  $\Omega_c$  is known as a permeability correction, but rightly accounts for two different effects: the extent to which the projected area of an aggregate is different to the projected area of a sphere having the same radius of collision, and the extent to which the drag coefficient of an aggregate is different to the drag coefficient of a sphere having the same projected area as the aggregate. Taking these two effects together,  $\Omega_c$  represents the extent to which the settling velocity of an aggregate is different to that of an impermeable sphere having the same drag force and radius of collision.

Looking at the meaning of  $\Omega_c$  in another way, if the hydrodynamic radius of an aggregate is the radius of a sphere that has the same settling velocity and drag force as the aggregate in question, then  $\Omega_c$  can be shown to relate the radius of collision to the hydrodynamic radius:

$$R_{h,a} = \Omega_c R_{c,a} \quad (3.38)$$

Is  $\Omega_c$  in fact constant with aggregate size as implied by Equation (3.38)? If it is, then this implies that the hydrodynamic radius is linearly related to the radius of collision, a conclusion that has considerable support in the literature [10, 66]. This would also mean that the dimensionless permeability of the aggregates is also constant with respect to aggregate size, a proposition that has had support recently [67, 68].

What are the issues relating to the shape of the aggregate, choice of size measurement and to preferential orientations in settling? Suppose that instead of the radius of collision of the aggregate we had preferred to use as a size characterization the radius of a sphere having the same projected area as the aggregate,  $R_{A,a}$ . The drag force of the system would then be expressed as

$$F_d = \frac{1}{2} \rho_L v_t^2 \pi R_{A,a}^2 \Omega_A \frac{24\mu_L}{\rho_L v_t 2 R_{A,a}} \quad (3.39)$$

The factor  $\pi R_{A,a}^2$ , which represents the projected area of the aggregate, is now strictly correct and the drag correction  $\Omega_A$  now represents a combination of drag coefficient correction and Reynolds number correction because we have used a different radius in the Reynolds number calculation. Since the different measures of aggregate radius are all linearly related to each other if the aggregates are fractal (it follows from

self-similarity), the same conclusions regarding the scaling of settling velocity with aggregate size and the constancy of the factor  $\Omega_A$  are reached. Indeed, exactly the same conclusions are reached no matter which kind of radius or diameter we choose to use as a basis for the analysis.

The equations presented so far rely on the proposition that the projected area of the aggregate is proportional to the square of the radius we are choosing to characterize the aggregate size. As discussed in the previous section on the volume obscuration method, this is only the case for very large aggregates, and is never the case for aggregates with fractal dimension less than two [23]. Johnson *et al.* [23] point out that Equation (3.37) will have a different power-law dependence between settling velocity and aggregate size depending on whether the fractal dimension is less than or greater than two and additionally make a correction to the drag coefficient for somewhat higher Reynolds numbers [ $0.1 \leq Re \leq 10$ ]. The characteristic length for the Reynolds number is taken as being the diameter of collision of the aggregate, in the absence of any better information.

As explained by Meakin *et al.* [11], the reality with respect to projected area dependence on aggregate size is rather more complex than two simple cases depending whether the fractal dimension is larger or smaller than two. Small aggregates tend to present more projected area than would be expected, because of the finite size of the primary particles. This would lead to lower settling velocities for small aggregates than might be expected from Equation (3.37), which without correction would lead to an overprediction of  $D_m$ . As with the volume obscuration analysis, the way to account for this may well be to have the projected area well characterized in terms of  $G$ ,  $B$ ,  $\gamma$  and  $\delta$  from computer simulations for aggregates with different size and structure.

### 3.4.1.2 Experimental approaches

These kinds of experiments are without exception carried out in a column of fluid, usually of the same composition as that from which the aggregates were sampled. The aggregates are introduced into the top of the column and one or more microscopes are used to measure the settling velocity. Farrow and Warren describe a floc density analyser [69] which may be used to determine the fractal dimension. Nobbs *et al.* [70] review many of the practical aspects involved in performing this type of experimental investigation.

There are a number of difficulties with the settling approach in practice. For large flocs, the settling velocity and induced drag may be large enough to restructure the aggregates under investigation because of the extremely weak mechanical strength of the aggregates [24]. Conversely, the settling velocities usually have such a small absolute value that stray convection currents can render the measurement meaningless. For this reason, control of fluid movement in the column is absolutely critical. Settling columns are usually temperature controlled by recirculated air [70] or water [71]. Particular care needs to be taken with illumination – continuous, high-intensity light

sources can easily add heat to the system and induce currents. Strobe-type illumination avoids this problem and additionally can provide very clear images, as the high but brief intensity allows a narrow aperture (good depth of field) and short exposure time (no motion blur). Introducing the flocs to the top of the settling column can also induce fluid motion in the column, both through mechanical disturbance and by introducing too much sample, which effectively creates a density gradient in the column. Using an inverted pipette to introduce aggregates one at a time without disturbing the liquid in the column is a difficult skill to master, but is the best way to avoid this kind of problem. An alternate approach to the problem of induced currents might be to introduce small ‘tracer particles’, density matched to the suspending fluid. This allows the background fluid motion to be visualized and corrected for.

### 3.4.2 Chord Length Measurement

Focused beam reflectance measurement (FBRM) is a relatively new on-line particle measurement technique that measures chord lengths using a scanning laser. The instrument is designed as a robust probe, tipped with a sapphire window through which a circularly scanning laser is focused. Particles that approach the window reflect the laser back through the instrument’s optics and the duration of the reflected signal is converted to a chord length using the known scanning speed of the laser.

Although the technique has been used to monitor flocculation [72, 73], it appears that it has not yet been used to determine the fractal dimension of these systems. This should be a relatively straightforward matter: if one assumes that the instrument samples the aggregates in an unbiased manner, then the same kind of analysis as was applied for the volume obscuration techniques can be used. If the suspension flowing past the instrument can be assumed to have a constant solids loading and the chord length distribution can be assumed to be related to the aggregate size distribution in a direct way, then the frequency of chord acquisition and the length of the chords will effectively tell us the concentration of aggregates of different sizes. This gives us the apparent solid volume fraction, which, combined with the known true solids loading, tells us the aggregate density and hence the fractal dimension.

Kovalsky and Bushell speculate that it might even be possible to measure the fractal dimension directly from the texture of the reflected laser [74].

### 3.4.3 Particle Counting Techniques

A very direct way of measuring the fractal dimension is to have direct measurement of the size of individual aggregates and of the amount of solid that comprises them, a technique sometimes referred to as the particle concentration technique

[75]. Stoll *et al.* [76] and Jackson *et al.* [77] report this kind of analysis using aperture impedance particle sizing. Aperture impedance particle sizing works by passing a suspension of particles in electrolyte through a small orifice with a voltage applied across it. Solid particles passing through the orifice reduce the amount of electrolyte available for current flow and hence change the impedance of the orifice. The change of impedance is more or less directly related to the solid volume of the particle passing through the orifice with little dependence on particle morphology. Jackson *et al.* [77] used two aperture impedance methods to determine the solid volume distribution of aggregating algal particles and additionally used image analysis to measure the size distribution of the same particles. A mass fractal dimension was then assumed that led to the best match between the two methods of size analysis, returning a value of 2.3. Sterling *et al.* [78] used a similar approach to examine the structure of crude oil and clay aggregates, except that they used forward light scattering instead of image analysis to determine the size distribution.

### 3.5 CONCLUSIONS AND FUTURE PERSPECTIVES

A wide range of techniques exist for measuring the fractal dimensions in environmental systems. Which technique should be chosen depends on the particles being measured and the environment in which they are being measured. Many of the methods outlined here, such as scattering and settling experiments, are only suitable for laboratory-based work. Others, such as image analysis and FBRM, have the potential to be used in the field.

Small particles with size of the order of the wavelength of light or less are good candidates for light scattering experiments, whereas larger particles are suitable for optical microscopy and settling experiments. Large particles of size several times the wavelength of light, but with low refractive index, could be analysed by confocal microscopy. A summary of the techniques and methods discussed here and the systems to which each is applicable is given in Table 3.1.

This chapter has illustrated how measurements from a range of different particle characterization techniques have been used to determine values for fractal dimensions. Other approaches can also be imagined. Whichever technique is chosen or devised, it is important to examine the assumptions underlying the analysis critically and to check their validity in the context of the particular system being analysed. The state of the art in measurement of fractal dimension for environmental systems at this time is probably CSLM, because the analysis requires no models or assumptions, unlike most other approaches, and is free of the two-dimensional limitation of other imaging techniques. To the extent that the sample can be handled appropriately and the measurement can be made reliably, the analysis is reliable and unambiguous.



**Table 3.1** A comparison of different techniques and methods for determining fractal dimensions in environmental systems.

Technique	Method	Particle size (order of magnitude)	Contrast	Relative density	Fractal dimension	Comments
Light scattering	Angular dependence	$< 1 \mu\text{m}$	Size dependent	Any	Any	Sensitive to short-range structure. Complications with cut-off function model form may occur at high $D_m$ . Appears to be valid even when there is multiple intra-aggregate scattering
Light scattering	Apparent volume	$> 1 \mu\text{m}$	Moderate to high	Low	High	Should be easily suspended with low shear rates. Only effective for $D_m > 2$ . Requires significant change in aggregation state over the experiment
X-ray scattering	Angular dependence	$< 100 \text{ nm}$	Nonzero	Any	Any	Size limited by scattering measurement at small angles. Complications with cut-off function model form may occur at high $D_m$
Neutron scattering	Angular dependence	$< 100 \text{ nm}$	Easily tunable	Any	Any	Size limited by scattering measurement at small angles. Complications with cut-off function model form may occur at high $D_m$ . Contrast may be easily adjusted by using media containing varying ratios of hydrogen and deuterium
Single image microscopy	Edge dimension analysis	Resolution dependent	Moderate to high	Any	Any	The relationship between edge dimension and other fractal dimensions is not straightforward. Contrast should be high enough to allow image segmentation
Single image microscopy	Projected area dimension analysis	Resolution dependent	Moderate to high	Any	$\lesssim 2$	Finite size correction should be applied. Contrast should be high enough to allow image segmentation
Confocal laser scanning microscopy	Projected area dimension analysis	$> 1 \mu\text{m}$	Low	Low	Any	Contrast should be low enough that image slices can be obtained from the interior of the structure. Higher contrasts may be used when $D_m$ is low. Density should be low enough that the aggregate structure does not deform significantly due to gravity

**Table 3.1** (Continued).

Technique	Method	Particle size (order of magnitude)	Contrast	Relative density	Fractal dimension	Comments
Settling velocity measurement	Permeability models	> 1 $\mu\text{m}$	Moderate to high	Size dependent	High	Contrast should be high enough to allow optical measurement of settling velocity. Uncertainty in permeability models is less for high fractal dimensions. Density should be in a range that corresponds to Stokes' law settling
Chord length measurement	Apparent volume	> 1 $\mu\text{m}$	Moderate to high	Any	High	Untested technique
Particle counting	Mass/size scaling	Instrument dependent	Instrument dependent	Any	Any	Particle counting measures the number of particles in each aggregate. It must be used in combination with another technique that measures size

## LIST OF SYMBOLS AND ABBREVIATIONS

### *Abbreviations*

CSLM	confocal scanning laser microscopy
FISH	fluorescence in-situ hybridization
USAXS	ultra-small-angle X-ray scattering

### *Variables*

$A$	area
$B$	an area parameter
$C$	coefficient
$D$	dimension (fractal)
$G$	another area parameter
$I$	intensity
$g$	acceleration due to gravity
$g'$	correlation function
$k$	power-law prefactor
$k'$	wave number
$L$	a generalized length
$m$	mass
$N$	number
$P$	form factor
$Q$	extinction efficiency
$q$	change in wave number on scattering
$q$	magnitude of $q$
$\mathbf{r}$	displacement vector
$r$	magnitude of $r$
$R$	radius
$Re$	Reynolds number
$S$	structure factor
$v$	velocity
$x$	size parameter of a particle
$x_i$	Cartesian coordinate of element $i$
$y_i$	Cartesian coordinate of element $i$
$z$	real refractive index
$\delta$	area exponent
$\varepsilon$	step size around a perimeter
$\phi$	function describing the presence of a particle
$\gamma$	area exponent
$\lambda$	wavelength
$\mu$	viscosity
$\pi$	pi (mathematical constant)
$\theta$	angle
$\rho$	density

$\Omega$  drag coefficient correction factor

$\zeta$  complex refractive index

### *Subscripts*

0 primary particle

1 perimeter

2 area

3 structure in three-dimensional space

a aggregate

A area

b buoyancy

box relating to a box, such as in the box-counting or sand box methods

c pertaining to the radius of collision

d drag

e pertaining to an edge or perimeter

h pertaining to the hydrodynamic radius

*i* label denoting any particular element, such as a particle or pixel different than *j*

*j* label denoting any particular element, such as a particle or pixel different than *i*

g pertaining to the radius of gyration

L fluid

m pertaining to mass

p pertaining to a projection

pix pertaining to a pixel

r pertaining to a distance

S solid

T total in the system

t terminal

## REFERENCES

- [1] Oh, C. and Sorensen, C. M. (1997). The effect of overlap between monomers on the determination of fractal cluster morphology. *J. Colloid Interface Sci.*, **193**, 17–25.
- [2] Brasil, A. M., Farias, T. L., Carvalho, M. G. and Köylü, Ü. Ö. (2001). Numerical characterization of the morphology of aggregated particles. *Aerosol Sci.*, **32**, 489–508.
- [3] Bushell, G. (1998). PhD thesis, The University of New South Wales.
- [4] Lips, A. and Duckworth, R. M. (1988). Combined study of coagulation kinetics and close-range aggregate structure. *J. Chem. Soc. Faraday Trans. I*, **84**, 1223–1242.
- [5] Thouy, R., and Jullien, R. (1996). Structure factors for fractal aggregates built off-lattice with tunable fractal dimension. *J. Phys. I France*, **6**, 1365–1376.
- [6] Meakin, P. (1988). Fractal aggregates. *Adv. Colloid Interface Sci.*, **28**, 249–331.
- [7] Gregory, J. (1997). The density of particle aggregates. *Water Sci. Technol.*, **36**, 1–13.
- [8] Bushell, G., Yan, Y.-D., Woodfield, D., Raper, J. and Amal, R. (2002). On techniques for the measurement of the mass fractal dimension of aggregates. *Adv. Colloid Interface Sci.*, **95**, 1–50.
- [9] Dimon, P. Sinha, S. K., Weitz, D. A., Safinya, C. R., Smith, G. S., Varady, W. A. and Lindsay, H. M. (1986). Structure of aggregated gold colloids. *Phys. Rev. Lett.*, **57**, 595–598.

- [10] Lattuada, M., Wu, H. and Morbidelli, M. (2003). Hydrodynamic radius of fractal clusters. *J. Colloid Interface Sci.*, **268**, 96–105.
- [11] Meakin, P., Donn, B., and Mulholland, G. W. (1989). Collisions between point masses and fractal aggregates. *Langmuir*, **5**, 510–518.
- [12] Hermawan, M., Bushell, G., Bickert, G. and Amal, R. (2004). Characterisation of short range structure of silica aggregates – implication to sediment compaction. *International Journal of Mineral Processing*, **73**, 65–81.
- [13] Lin, M. Y., Klein, R., Lindsay, H. M., Weitz, D. A., Ball, R. C., and Meakin, P. (1990). The structure of fractal colloidal aggregates of finite extent. *J. Colloid Interface Sci.*, **137**, 263–280.
- [14] Bushell, G. C., and Amal, R. (1998). Fractal aggregates of polydisperse particles. *J. Colloid Interface Sci.*, **205**, 459–469.
- [15] Bower, C., Washington, C., and Purewal, T. S. (1995). A combined rheometer and image analyser for the characterization of suspensions and aggregates in a shear field. *Measure. Sci. Technol.*, **6**, 196–201.
- [16] Chakraborti, R. K., Atkinson, J. F., and Van Benschoten, J. E. (2000). Characterization of alum floc by image analysis. *Environ. Sci. Technol.*, **34**, 3969–3976.
- [17] Boukari, H., Long, G. G. and Harris, M. T. (2000). Polydispersity during the formation and growth of the Stöber silica particles from small-angle X-ray scattering measurements. *J. Colloid Interface Sci.*, **229**, 129–139.
- [18] Köylü, Ü. Ö., Xing, Y. and Rosner, D. E. (1995). Fractal morphology of combustion-generated aggregates using angular light scattering and electron microscope images. *Langmuir*, **11**, 4848–4854.
- [19] Sorensen, C. M., Kim, W., Fry, D., Shi, D. and Chakraborti, A. (2003). Observation of soot superaggregates with a fractal dimension of 2.6 in laminar acetylene/air diffusion flames. *Langmuir*, **19**, 7560–7563.
- [20] Oles, V. (1992). Shear-induced aggregation and breakup of polystyrene latex particles. *J. Colloid Interface Sci.*, **154**, 351–358.
- [21] Spicer, P. T., Pratsinis, S. E., Raper, J., Amal, R., Bushell, G. and Meesters, G. (1998). Effect of shear schedule on particle size, density, and structure during flocculation in stirred tanks. *Powder Technol.*, **97**, 26–34.
- [22] Kusters, K. A., Wijers, J. G. and Thoenes, D. (1997). Aggregation kinetics of small particles in agitated vessels. *Chem. Eng. Sci.*, **52**, 107–121.
- [23] Johnson, C. P., Li, X. Y. and Logan, B. E. (1996). Settling velocities of fractal aggregates. *Environ. Sci. Technol.*, **30**, 1911–1918.
- [24] Thill, A., Veerapaneni, S., Simon, B., Wiesner, M., Bottero, J. Y. and Snidaro, D. (1998). Determination of structure of aggregates by confocal scanning laser microscopy. *J. Colloid Interface Sci.*, **204**, 357–362.
- [25] Guinier, A. and Fournet, G. (1955). *Small Angle Scattering of X-Rays*, John Wiley & Sons, Ltd, New York.
- [26] Sorensen, C. M. (2001). Light scattering by fractal aggregates: a review. *Aerosol Sci. Technol.*, **35**, 648–687.
- [27] Hasmy, A., Vacher, R. and Jullien, R. (1994). Small-angle scattering by fractal aggregates – a numerical investigation of the crossover between the fractal regime and the Porod regime. *Phys. Rev. B*, **50**, 1305–1308.
- [28] Cai, J., Lu, N. and Sorensen, C. M. (1995). Analysis of fractal cluster morphology parameters: structural coefficient and density autocorrelation function cutoff. *J. Colloid Interface Sci.*, **171**, 470–473.
- [29] Freltoft, T., Kjems, J. K. and Sinha, S. K. (1986). Power-law correlations and finite-size effects in silica particle aggregates studied by small-angle neutron scattering. *Phys. Rev. B*, **33**, 269–275.

- [30] Jullien, R. (1992). From Guinier to fractals. *J. Phys. I*, **2**, 759–770.
- [31] Mountain, R. D. and Mulholland, G. W. (1988). Light-scattering from simulated smoke agglomerates. *Langmuir*, **4**, 1321–1326.
- [32] Hurd, A. J. and Flower, W. L. (1988). In situ growth and structure of fractal silica aggregates in a flame. *J. Colloid Interface Sci.*, **122**, 178–192.
- [33] Zeng, Y. W. and Meriani, S. (1994). Scaling functions for the finite-size effect in fractal aggregates. *J. Appl. Crystallogr.*, **27**, 782–790.
- [34] Sorensen, C. M., Lu, N. and Cai, J. (1995). Fractal cluster size distribution measurement using static light scattering. *J. Colloid Interface Sci.*, **174**, 456–460.
- [35] Sorensen, C. M., Cai, J. and Lu, N. (1992). Test of static structure factors for describing light scattering from fractal soot aggregates. *Langmuir*, **8**, 2064–2069.
- [36] Van de Hulst, H. C. (1981). *Light Scattering by Small Particles*. Dover, New York.
- [37] Farias, T. L., Köylü, Ü. Ö. and Carvalho, M. G. (1996). Range of validity of the Rayleigh–Debye–Gans theory for optics of fractal aggregates. *Appl. Optics*, **35**, 6560–6567.
- [38] Nelson, J. (1989). Test of a mean field theory for the optics of fractal clusters. *J. Mod. Optics*, **36**, 1031–1057.
- [39] Botet, R., Rannou, P. and Cabane, M. (1997). Mean-field approximation of Mie scattering by fractal aggregates of identical spheres. *Appl. Optics*, **36**, 8791–8797.
- [40] Ortiz, G. P. and Mocán, W. L. (2003). Scaling condition for multiple scattering in fractal aggregates. *Pysica B*, **338**, 103–106.
- [41] Nelson, J. A., Crookes, R. J. and Simons, S. (1990). On obtaining the fractal dimension of a 3D cluster from its projection on a plane – application to smoke agglomerates. *J. Phys. D: Appl. Phys.*, **23**, 465–468.
- [42] Köylü, Ü. Ö., Faeth, G. M., Farias, T. L. and Carvalho, M. G. (1995). Fractal and projected structure properties of soot aggregates. *Combust. Flame*, **100**, 621–633.
- [43] Lambert, S., Moustier, S., Dussouillez, P., Barakat, M., Bottero, J. Y., Le Petit, J. and Ginestet, P. (2003). Analysis of the structure of very large bacterial aggregates by small angle multiple light scattering and confocal image analysis. *J. Colloid Interface Sci.*, **262**, 384–390.
- [44] Gregory, J. and Chung, H. (1995). Continuous monitoring of floc properties in stirred suspensions. *J. Water Supply Res. Technol. – Aqua*, **44**, 125–1313.
- [45] Berthon, S., Barbieri, O., Ehrburger-Dolle, F., Geissler, E., Achard, P., Bley, F., Hecht, A.-M., Livet, F., Pajonk, G. M., Pinto, N., Rigacci, A. and Rochas, C. (2001). DLS and SAXS investigations of organic gels and aerogels. *J. Non-Cryst. Solids*, **285**, 154–161.
- [46] Schmidt, P. W. (1991). Small-angle scattering studies of disordered, porous and fractal systems. *J. Appl. Crystallogr.*, **24**, 414–435.
- [47] Kaye, B. H. (1994). *A Random Walk Through Fractal Dimensions*. Weinheim, New York.
- [48] Jullien, R., Thouy, R. and Ehrburger-Dolle, F. (1994). Numerical investigation of two-dimensional projections of random fractal aggregates. *Phys. Rev. E*, **50**, 3878–3885.
- [49] Tence, M., Chevalier, J. P. and Jullien, R. (1986). On the measurement of the fractal dimension of aggregated particles by electron-microscopy – experimental-method, corrections and comparison with numerical-models. *J. Phys.*, **47**, 1989–1998.
- [50] Cross, S. S. (1994). The application of fractal geometric analysis to microscopic images. *Micron*, **25**, 101–113.
- [51] Gonzales, R. C. and Woods, R. E. (2002). *Digital Image Processin*, second edition. Prentice Hall, New York.
- [52] Allen, M., Brown, G. J. and Miles, N. J. (1995). Measurement of boundary fractal dimensions: review of current techniques. *Powder Technol.*, **84**, 1–14.
- [53] Adler, J. and Hancock, D. (1994). Advantages of using a discrete transform function in the measurement of fractal dimensions by the dilation method. *Powder Technol.*, **78**, 191–196.

- [54] Forrest, S. R. and Witten, T. A. (1979). Long-range correlations in smoke-particle aggregates, *J. Phys. A*, **12**, L109-L117.
- [55] Park, K., Kittelson, D. B. and McMurry, P. H. (2004). Structural properties of diesel exhaust particles measured by transmission electron microscopy (TEM): relationships to particle mass and mobility, *Aerosol Sci. Technol.*, **38**, 881-889.
- [56] Bower, C., Washington, C. and Purewal, T. S. (1997). The use of image analysis to characterize aggregates in a shear field. *Colloids Surf. A: Physicochem. Eng. Aspects*, **127**, 105-112.
- [57] Bremer, L. G. B., Bijsterbosch, B. H., Walstra, P. and van Vliet, T. (1993). Formation, properties and fractal structure of particle gels. *Adv. Colloid Interface Sci.*, **46**, 117-128.
- [58] Thill, A., Wagner, M. and Bottero, J. Y. (1999). Confocal scanning laser microscopy as a tool for the determination of 3D floc structure. *J. Colloid Interface Sci.*, **220**, 465-467.
- [59] Snidaro, D., Zartarian, F., Jorand, F., Bottero, J. Y., Block, J. C. and Manem, J. (1997). Characterization of activated sludge flocs structure. *Water Sci. Technol.*, **36**, 313-320.
- [60] Dinsmore, A. D. and Weitz, D. A. (2002). Direct imaging of three-dimensional structure and topology of colloidal gels. *J. Phys.: Condens. Matter*, **14**, 7581-7597.
- [61] Mellema, M., Heesakkers, J. W. M., van Opheusden, J. H. J. and van Vliet, T. (2000). Structure and scaling behaviour of aging rennet-induced casein gels examined by confocal microscopy and permeametry. *Langmuir*, **16**, 6847-3854.
- [62] Schmid, M., Thill, A., Purkhold, U., Walcher, M., Bottero, J. Y., Ginestet, P., Nielsen, P. J., Wertz, S. and Wagner, M. (2003). Characterisation of activated sludge flocs by confocal scanning microscopy and image analysis. *Water Res.*, **17**, 2043-2052.
- [63] Gibson, J. R., Lin, H. and Bruns, M. A. (2006). A comparison of fractal analytical methods on 2- and 3-dimensional computed tomographic scans of soil aggregates. *Geoderma*, **134**, 335-348.
- [64] Li, D. H. and Ganczarczyk, J. J. (1988). Flow through activated sludge flocs. *Water Res.*, **22**, 789-792.
- [65] Serra, T. and Logan, B. E. (1999). Collision frequencies of fractal bacterial aggregates with small particles in a sheared fluid. *Environ. Sci. Technol.*, **33**, 2247-2251.
- [66] Hess, W., Frisch, H. L. and Klein, R. (1986). On the hydrodynamic behaviour of colloidal aggregates. *Z. Phys. B - Condens. Matter*, **64**, 65-67.
- [67] Li, X. Y. and Logan, B. E. (2001). Permeability of fractal aggregates. *Water Res.*, **35**, 3373-3380.
- [68] Woodfield, D. and Bickert, G. (2001). An improved permeability model for fractal aggregates settling in creeping flow. *Water Res.*, **35**, 3807-3806.
- [69] Farrow, J. B. and Warren, L. J. (1993). Measurement of the size of aggregates in suspension. In *Coagulation and Flocculation - Theory and Applications*, Dobiás B. (ed.). Marcel Dekker, New York.
- [70] Nobbs, D., Tang, P. and Raper, J. A. (2002). The design, construction and commissioning of a low-cost optical particle size analyser specifically for measurement of settling velocities and size of flocs. *Meas. Sci. Technol.*, **13**, 297-302.
- [71] Glover, S. M., Yan, Y. -D., Jameson, G. J. and Biggs, S. (2000). Bridging flocculation studies by light scattering and settling. *Chem. Eng. J.*, **80**, 3-12.
- [72] Alfano, J. C., Carter, P. W., Dunham, A. J., Nowak, M. J. and Tubergen, K. R. (2000). Polyelectrolyte-induced aggregation of microcrystalline cellulose: reversibility and shear effects. *J. Colloid Interface Sci.*, **223**, 244-254.
- [73] Owen, A. T., Fawell, P. D., Swift, J. D. and Farrow, J. B. (2002). The impact of polyacrylamide flocculant solution age on flocculation performance. *Int. J. Miner. Process.*, **67**, 123-144.
- [74] Kovalsky, P. and Bushell, G. (2005). In situ measurement of fractal dimension using focussed beam reflectance measurement. *Chem. Eng. J.*, **111**, 181-188.

- [75] Logan, B. E. and Wilkerson, D. B. (1991). Fractal dimensions and porosities of *Zoogloea ramigera* and *Saccharomyces cerevisiae* aggregates. *Biotechnol. Bioeng.*, **23**, 389–396.
- [76] Stoll, S., Elaissari, A. and Pefferkorn, E. (1990). Fractal dimensions of latex aggregates: correlation between hydrodynamic radius and cluster size. *J. Colloid Interface Sci.*, **140**, 98–104.
- [77] Jackson, G. A., Logan, B. E., Alldredge, A. L. and Dam, H. G. (1995). Combining particle size spectra from a mesocosm experiment measured using photographic and aperture impedance (Coulter and Elzone) techniques. *Deep-Sea Res. II*, **42**, 139–157.
- [78] Sterling, M. C. Jr, Bonner, J. S., Ernest, A. N. S., Page, C. A. and Autenrieth, R.L. (2004). Characterizing aquatic sediment–oil aggregates using in situ measurements. *Mar. Pollut. Bull.*, **48**, 533–542.



---

# 4 Fractal Structures and Mechanisms in Coagulation/Flocculation Processes in Environmental Systems: Theoretical Aspects

---

**Serge Stoll<sup>1</sup> and Silvia Diez<sup>2</sup>**

<sup>1</sup> *Department of Inorganic, Analytical and Applied Chemistry CABE, University of Geneva, Sciences II, 30 Quai Ernest Ansermet, CH-1211 Geneva 4/Switzerland*

<sup>2</sup> *CIEMAT, Avda. Complutense 22, 28040, Madrid, Spain*

## 4.1 INTRODUCTION

Coagulation/flocculation, and more generally speaking aggregation, represent physical processes in which initially dispersed colloidal units (solid inorganic particles, fulvic and humic acids and biopolymers) stick together, under the influence of various attractive forces, to build characteristic structures whose size increases with time. Aggregation phenomena are not only of great importance in environmental systems, but also in many areas of colloid science, chemistry and physics and industrial processes. In natural waters and wastewater treatment plants, the transport and fate of both nutrients and toxic compounds largely depend on their interactions with colloidal particles, biopolymers and the aggregates they form. The transport and elimination of vital or detrimental compounds then depends upon the kinetics of formation, structure, and sedimentation of these aggregates (Figure 4.1). Because of the complexity and large number of biophysical and chemical factors influencing these processes, as well as the fact that natural colloids include several components, no rigorous analytical theory or models have been derived and applied to describe aggregation in environmental systems.

On the other hand, owing to the development of computers and the introduction of scaling concepts, numerical and theoretical models have recently been applied to investigate the behaviour of colloidal suspensions. These models have proven to be important and convenient tools for the systematic investigation of some of the physicochemical factors (pH, temperature, solution ionic strength, colloidal concentration and chemical surface properties) that influence the morphology of colloidal structures

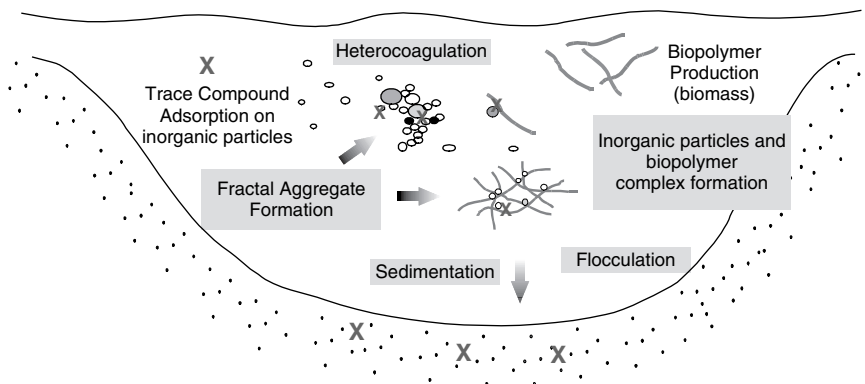


**Figure 4.1** Key mechanisms controlling the fate and transport of colloidal matter and associated trace compounds in natural waters.

induced by perikinetic aggregation (bridging flocculation by polymers, salt-induced coagulation, heteroaggregation, etc.), in addition to addressing fundamental issues such as fractal growth. Microscopic observations of natural colloids and model systems have concluded that the formation of aggregates in aquatic systems is mainly controlled by three types of colloid: compact inorganic colloids, large rigid biopolymers, and aquagenic refractory organic matter in variable proportions, sizes, and chemical properties [1].

This chapter describes some of the simulation and theoretical models used to investigate aggregation processes. The models depend upon whether the problem under consideration is defined at a microscopic or mesoscopic level and on the appropriate degree of complexity and rigour that is required to solve real practical problems of interest. Several techniques and examples will be described that are applicable to coagulation/flocculation processes in colloidal dispersions. Owing to the fact that such processes are now recognized to lead to the formation of fractal objects, fractal concepts will be discussed.

## 4.2 NATURE AND MORPHOLOGY OF AQUATIC PARTICLES/COLLOIDS: USE OF FRACTAL CONCEPTS

Aggregates formed in natural waters (rivers, lakes and oceans) and in wastewater treatment systems, as well as in controlled laboratory experiments, yield geometrical properties that can be conveniently described using fractal geometry [1–12]. The fractal concept was introduced in the 1970s by Mandelbrot [13]. His approach, essentially based on geometry, quickly became popular and is now successfully used in many areas of science for the description of complex geometrical structures that cannot be described by the classical Euclidean geometry. Full lines, surfaces and

volumes have integer linear dimensions of 1, 2 and 3, respectively, whereas open, porous, complicated structures have noninteger dimensions, i.e. fractal dimensions. The fractal dimension is thus a quantitative measure of the more or less compact nature of the structure under consideration.

Fractal structures can be divided into two groups: regular and irregular. They all exhibit a remarkable property: a self-similarity or invariance with changes in scale or size. Self-similarity means that if we enlarge a given portion of a fractal object then the new enlarged object is identical to the initial one. Regular fractal objects exhibit a regular shape with well-defined positions between branches (Figure 4.2a). They are built with deterministic and iterative rules. Irregular fractals, for which some randomness occurs during their growth, are more representative of natural aggregation processes. In that case, the self-similarity property is valid on average, i.e. the new picture obtained after enlarging a part of an irregular fractal is only statistically equivalent to the original form (Figure 4.2b).

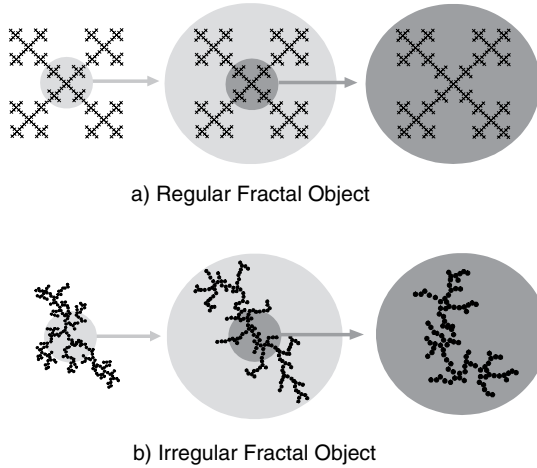


**Figure 4.2** Illustration of the self-similarity property of fractal aggregates. (a) A regular fractal aggregate: when the central (grey) part of the aggregate is enlarged (as displayed on the right), the same figure as the original one is obtained and scale invariance is verified. (b) An irregular (disordered) fractal with some randomness included in its growth where the self-similarity property now is only valid on average.

Quantitatively, the fractal character of a single large aggregate is often demonstrated by a power-law behaviour of its mass distribution in space [14, 15]. If one measures the mass  $m$  contained in a sphere of radius  $r$  centred at a given point (usually the centre of mass) of an irregular fractal aggregate, the following scaling relationship is obtained:

$$m(r) \sim r^{D_m} \quad (4.1)$$

where  $D_m$  represents the mass aggregate fractal dimension (Figure 4.3).

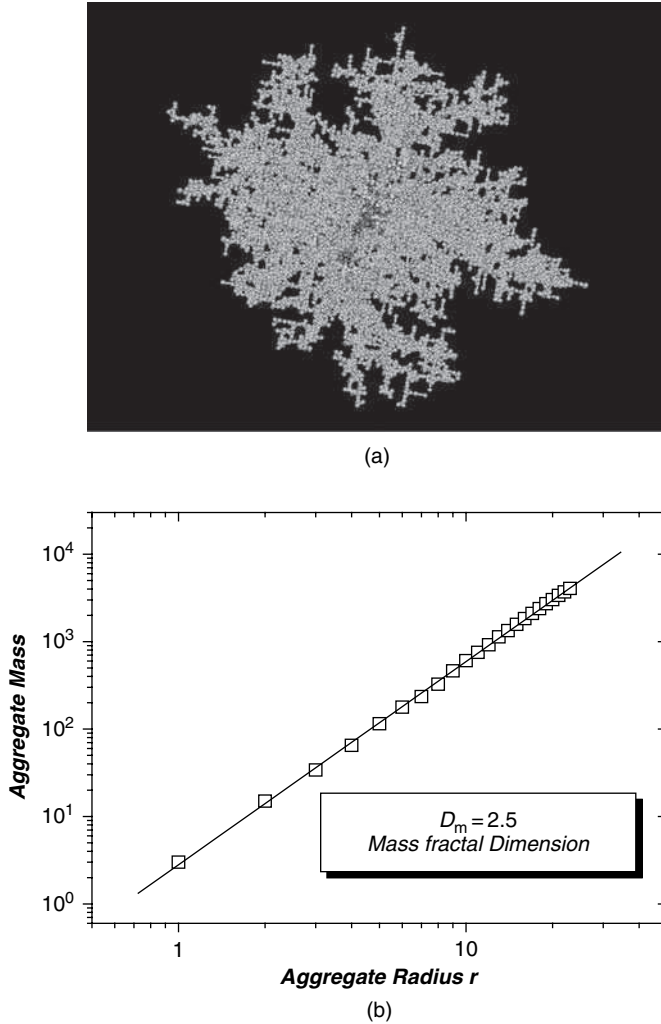


**Figure 4.3** (a) Three-dimensional computer-generated aggregate (Witten and Sanders Diffusion Limited Aggregate) consisting of 10 000 particles. In the presence of random motion of the particles, single particles are irreversibly stuck to a growing germ. (b) Log–log variation of the aggregate mass versus the aggregate size. From the slope, one can already see the fractal character of the structure. From the slope, the aggregate fractal dimension was calculated as 2.5.

The mass fractal dimension gives a quantitative description of the spatial mass repartition within an aggregate, a higher fractal dimension being representative of more compact structures. Table 4.1 presents some fractal dimensions for some computer-generated and ‘natural’ aggregates. The mass fractal dimension  $D_m$  usually

**Table 4.1** Examples of various mass fractal dimension  $D_m$  for computer-simulated, biological and inorganic aggregates in two (2D) and three dimensions (3D).

	2D	3D	Ref.
<i>Computer-generated aggregates</i>			
Witten–Sanders aggregates (DLA) <sup>a</sup>	1.71	2.49	[21]
CCA aggregates (DLCA) <sup>a</sup>	1.44	1.78	[19, 20, 30]
CCA aggregates (RLCA) <sup>a</sup>	1.55	2.09	[31, 48]
Regular fractal aggregate (Figure 4.2)	1.46	1.77	—
<i>Natural aggregates</i>			
Marine and oceanic snow	—	1.26–2.14	[6–8]
Hematite particles	—	1.8–2.1	[9–11]
Hematite particles with schizophyllan	—	1.9–2.0	[12]
<i>Inorganic aggregates</i>			
Gold colloids (DLCA)	—	1.86–2.14	[21]
Ludox silica spheres	—	1.75–2.08	[50]
Polystyrene spheres	—	1.42–2.5	[118, 144]
Latex spheres with sodium chloride	—	1.8–2.3	[98]

<sup>a</sup> See Section 4.3.

ranges between 1.4 and 2.5 for aggregates produced in natural waters, sediments, soils and in vitro.

If a system containing a number of aggregates is considered, the aggregate mass distribution is also expected to follow a power-law relationship:

$$m \sim l^{D_m} \quad (4.2)$$

where  $l$  represents a characteristic length. It is important to note that the characteristic length  $l$  for the determination of  $D_m$  is not necessarily the maximum length of the aggregate. For example, the aggregate radius of gyration  $R_g$  is defined by

$$R_g^2 = \frac{1}{N} \sum_{n=1}^N \langle (R_n - R_G)^2 \rangle \quad (4.3)$$

where  $R_G$  corresponds to the position of the centre of mass of the aggregate (Figure 4.4),  $N$  is the total number of particles within the aggregate and  $R_n$  is the position of the particle  $n$ . The minimum or maximum aggregate diameter and the aggregate equivalent sphere area diameter can also be used as characteristic lengths to derive the aggregate fractal dimensions [16–18].

Because of the inhomogeneous distribution of particles within a fractal, an important feature of fractal aggregates is the apparent decrease in the mean aggregate density  $\rho$  with the increase of the size  $R$  of aggregates:

$$\rho \sim R^{D_m-3} \quad (4.4)$$

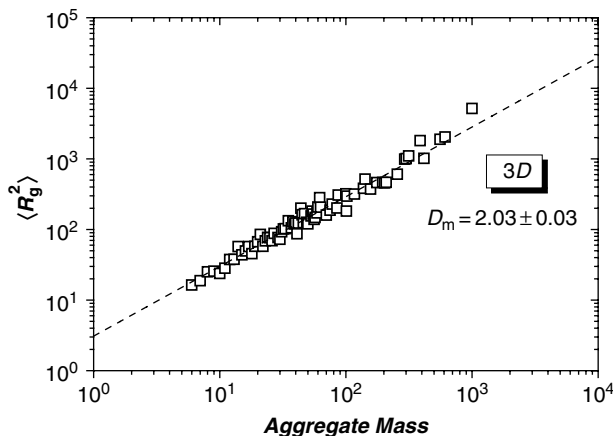


**Figure 4.4** Dependence of the mean square radius of gyration on the aggregate mass for a collection of reaction-limited cluster aggregation mechanism (RLCA) aggregates. Here, the scaling relationship  $R_g^2 \sim m^{2/D_m}$  is verified.

This property is at odds with the ordinary concept of homogeneous density expected from the properties of porous or impermeable spheres and has important consequences for the hydrodynamic properties of fractal aggregates. Indeed, many previous studies based upon Stokes' law have incorrectly calculated aggregate densities and porosities by considering aggregates as an assembly of permeable or impermeable spheres with a homogeneous distribution within the aggregate.

### 4.3 CLUSTER-CLUSTER AGGREGATION PROCESSES

The cluster-cluster aggregation (CCA) model, was introduced simultaneously, but independently, in 1983 by Jullien and co-workers [19] and Meakin [20] as a realistic model to describe aggregation, such as for gold particles [21]. The CCA model begins with a collection of elementary spherical particles which are randomly distributed in a box. Particles are moved randomly in all directions in order to mimic Brownian motion (random walk with periodic boundary conditions). When two particles come into contact, they are assumed to stick together irreversibly and form a new rigid aggregate (dimer) that diffuses according to a diffusion coefficient that is related to its size and geometry (small aggregates move faster than large aggregates). With time, larger, rigid aggregates are formed by the irreversible reactivity of the small clusters (Figure 4.5). Model iterations are stopped when only a single aggregate remains in the simulation box. Different extensions of the model have been developed to include intrinsic anisotropy, readjusting effects and polarizability [22].

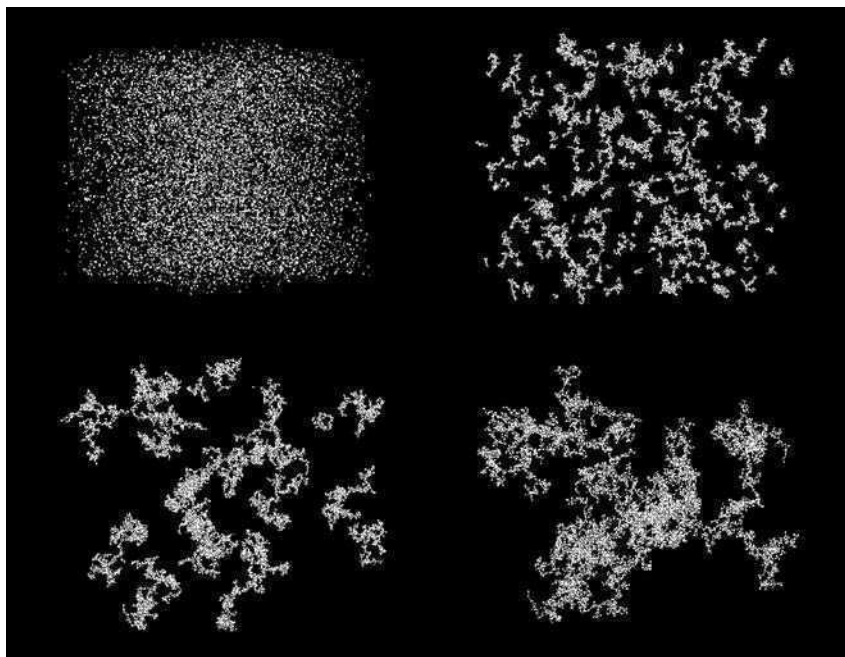


**Figure 4.5** Four stages of an off-lattice diffusion-limited CCA process using 10 000 elementary spherical particles. In this simulation, the aggregate diffusion coefficient is assumed to be controlled by the aggregate mass using  $D \sim D_0 m^{-1}$  where  $m$  represents the aggregate mass and  $D_0$  the diffusion coefficient of a single particle. The aggregates generated by this model are self-similar with a fractal dimension of 1.8.

### 4.3.1 Particle–Particle Interactions

If only the attractive van der Waals forces were operating on suspended particles in water, then one might expect the particles to stick together immediately and coagulate. Nonetheless, particles suspended in water or in solutions of high dielectric constant are usually charged due to the ionization or dissociation of surface sites or the adsorption of charged entities (multivalent ions, polyelectrolytes, humic or fulvic acids). Hence, particles generally undergo repulsive electrostatic forces originating from chemical reactions occurring at the particle–solution interface. Particle aggregation is expected to occur when the attractive van der Waals forces (which are always present) exceed the repulsive electrostatic interactions between the particles, as shown in Figure 4.6.

The Derjaguin, Landau, Verwey, Overbeck (DLVO) theory [23–25] has established the potential energy–distance relationship between two particles as a function of the characteristics of both the particles and the suspending solution. In natural systems, this approach requires compilation [26–28] of the major key physicochemical parameters that characterize the colloid material, including: (a) colloid shapes

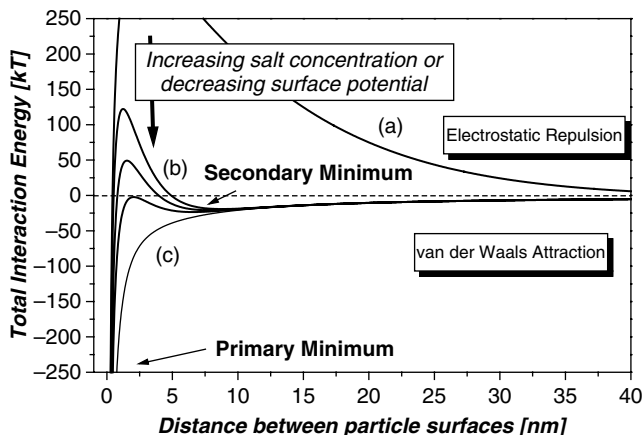


**Figure 4.6** Calculated energy profiles of DLVO interactions as a function of the distance between particle surfaces. (a) Surfaces repel strongly; colloidal particles remain stable. (b) Surfaces come into stable equilibrium if the secondary minimum is deep enough; colloids then aggregate reversibly. (c) The interaction curve approaches the pure van der Waals curve and colloids coagulate irreversibly.

and sizes; (b) colloid surface potentials and/or surface charge densities characterizing the electrical double-layer repulsion; (c) Hamaker constants, which are proportional to the electronic densities of the interacting media and control the van der Waals attraction forces; and (d) the inverse Debye length, which characterizes the diffuse double-layer thickness and the range of the repulsive double-layer forces (given by the ionic strength of the solution).

The combination of van der Waals and electrostatic forces usually results in two minima (primary and secondary minima) where aggregates are more or less stable. To achieve adhesive contact between two charged surfaces, surface potentials or charge densities must be 'lowered' into a primary minimum by screening charges by ion 'clouds' attracted close to the surface of oppositely charged particle surfaces. The attraction of two particles thus depends on the electrolyte concentration. Some energy profiles have been calculated in Figure 4.6 using the corresponding mathematical expression

$$V = \frac{\varepsilon a \psi^2}{2} \ln[1 + \exp(-\kappa h)] - \frac{Aa}{12h} \quad (4.5)$$

(where  $h$  represents the surface–surface distance between the particles) and the following conditions: particle diameter,  $2a = 1 \mu\text{m}$ ; Hamaker constant,  $A = 1.5 \times 10^{-13}$  ergs; salt (NaCl) concentration,  $0.001 \text{ mol dm}^{-3}$  (curve a),  $0.03 \text{ mol dm}^{-3}$  (curves b and c);  $\kappa^{-1} = 9.58 \times 10^{-7} \text{ cm}$ ; dielectric constant,  $\varepsilon = 78.54$ ; particle surface potential,  $\psi = 35 \text{ mV}$  (curve a),  $35/30/25 \text{ mV}$  (curves b), and  $10 \text{ mV}$  (curve c).

For highly charged surfaces in dilute electrolyte, there is a strong electrostatic long-range repulsion (Figure 4.6, curve a). The corresponding energy barrier of several



$k_B T$  units ( $1k_B T = 0.4 \times 10^{-20} \text{ J} = 0.04 \times 10^{-12} \text{ ergs}$ ) is too high to be overcome by the particles; consequently, they remain totally dispersed in the (stable) solution. As a result, when two particles move into a neighbouring position, the probability to form a physical or chemical bond (i.e. sticking probability) is practically zero. As the colloidal surface charge approaches zero (this may be achieved by adjusting the pH or by modifying the acid–base properties of the particle surface groups), or in more concentrated electrolyte solutions where charge screening is promoted, the interaction curve approaches the pure van der Waals curve. In this case, two particles now attract strongly and stick together irreversibly (Figure 4.6, curve c) in the first primary minimum.

The exact form of the DLVO potential, the influence of the DLVO forces on aggregation mechanisms and the structure of the resulting aggregates is still a major field under investigation in colloidal chemistry. It should be noted here that the DLVO validity is, in principle, limited to large particles with small curvatures and to small separation distances between the two particles.

### 4.3.2 RLCA and DLCA Concepts

Computer simulations have shown that the value of fractal dimension largely depends on whether the aggregation process is controlled by the diffusion rate of the clusters and single particles or by their chemical reactivity at the time of collision, the latter being mainly controlled by the DLVO forces. This observation, in agreement with experimental work on aerosols and colloids, has led to a new classification of aggregation processes: the reaction-limited and diffusion-limited cluster aggregation (RLCA and DLCA respectively) processes.

Key relationships exist between the kinetics of aggregate formation and the degree to which the resulting aggregates occupy the embedded space [28–34]. Several factors, such as the surface characteristics of the particles and the solution chemistry (ionic salt, pH), affect the fractal dimensions of aggregated material. If the rate of coagulation is limited by how quickly aggregates diffuse into contact, then a DLCA process is achieved. Then loose aggregates are formed with small fractal dimensions and the aggregate size-distribution is bell shaped. These structures can be explained by the fact that particles cannot penetrate the aggregate since they quickly attach to the particles with which they collide first, i.e. on the aggregate exterior. In such a case, the sticking probability  $P(i, j)$  (or adhesiveness) between two aggregates of sizes  $i$  and  $j$  to form a permanent bond is close to one.

If thermal motion is not sufficient to overcome the electrostatic repulsive barrier (which is typically of a few  $k_B T$  in the case of partial screening), then particles interact with each other many times before being able to overcome the electrostatic barrier (Figure 4.6, curve b) so as to stick together irreversibly. In that case, the sticking probability  $P(i, j)$  is somewhere between zero and one and an RLCA process is achieved. In addition, the resulting aggregates are more compact (due to the increased penetration of particles) and they have larger fractal dimensions (Figure 4.7). Owing

to the important size polydispersity of such systems, the size distribution curves are continuously decreasing functions with time.

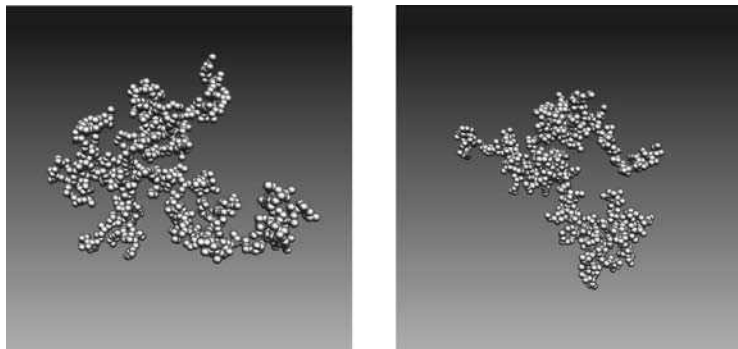


**Figure 4.7** DLCA (left) and RLCA (right) aggregates. Owing to the decrease of the sticking probability and increase of the penetration rate of the particles, the RLCA aggregate exhibits a more compact structure.

In aggregating systems, the bond formation between the colloids is described by the sticking probability factor [35, 36], which is experimentally defined as the quotient of the kinetic constant for any given conditions divided by the kinetic constant for a rapid (diffusion-limited) aggregation. In rapid coagulation,  $P(i, j) = 1$ , whereas lower values of  $P(i, j)$  are obtained under conditions of slow coagulation. For two approaching particles, Fuchs [37] derived theoretically an expression (which was later improved by Honig *et al.* [38]) for  $P(i, j)$ :

$$P(i, j) = 2a \int_0^{\infty} \frac{1}{(H + 2a)^2} \exp \left[ \frac{V(H)}{k_B T} \right] dH \quad (4.6)$$

where  $H$  is the surface to surface distance of two approaching particles of radius  $a$  and  $V(H)$  is the interaction potential,  $T$  the temperature and  $k_B$  the Boltzmann constant. The general expression for  $V(H)$  includes three contributions: electrostatic, attractive, and steric interactions. The last term is included to take into account the excluded volume of the colloids.

DLCA and RLCA processes represent *universality classes* for homoaggregation (aggregation involving similar particles), i.e. the aggregates display some characteristic features for which the kinetics of particle coagulation and the fractal structure are independent of the details of the system. One line of evidence that supports this hypothesis is the observation that the fractal dimensions of aggregates formed by RLCA are remarkably constant, as are those formed by DLCA, for many different particle types [39, 40].

### 4.3.3 Scaling Laws of Aggregate Formation

The existence of scaling laws for the aggregation *kinetics* of colloidal particles has attracted considerable interest. These concepts have become a part of the description of systems far from equilibrium, since they allow a quantitative evaluation of the role of a number of physicochemical factors on aggregation kinetics. The formation of colloidal aggregates over time due to Brownian collisions was originally established by von Smoluchowski by considering [41]

$$[g] + [n] \xrightarrow{K(g,n)} [g+n] \quad (4.7)$$

which describes the formation of aggregates composed of  $g$  and  $n$  elementary particles, where  $K(g, n)$  represents the rate constant of the reaction.

Swift and Friedlander [42] and Lushnikov [43] subsequently used von Smoluchowski's kinetic equation in its integro-differential form to derive the scaling laws of aggregate formation in the presence of an excess of electrolyte sufficient to ensure a regime of rapid aggregation:

$$\frac{\partial c(g, t)}{\partial t} = \int_0^g K(g-n, n) c(g-n, t) c(n, t) dn - 2c(g, t) \int_0^\infty c(n, t) K(g, n) dn \quad (4.8)$$

where  $c(g, t)$  gives the number of aggregates containing  $g$  associated primary particles at time  $t$ . The first term on the right-hand side represents the increase in aggregates of size  $g$  due to the collision between aggregates of sizes  $(g-n)$  and  $n$  respectively, while the second term represents the decrease of aggregates of size  $g$  due to collisions between  $g$ -fold aggregates and aggregates of any sizes. The kernel  $K$  represents the collision frequency. Scaling theory demonstrates that Equation (4.8) is invariant under the following scalar transformation:

$$c\left(\frac{g}{g_0}, t\right) = g_0^2 c(g, g_0^{1-\lambda} t) \quad (4.9)$$

provided that  $K$  is constant or a homogeneous function of degree  $\lambda$  (of the form  $g+n$  or  $gn$ ). In that case, the aggregate mass distribution  $c(g, t)$  can be represented in terms of a universal, time-invariant function  $\psi$ :

$$c(g, t) = t^{-2/(1-\lambda)} \psi[gt^{-1/(1-\lambda)}] \quad (4.10)$$

with

$$N_0(t) \sim t^{-1/(1-\lambda)} \quad (4.11)$$

where  $N_0(t)$  is the moment of order zero of the distribution, i.e.

$$N_0(t) = \int_0^\infty c(g, t) dg \quad (4.12)$$

which is equal to the total number of aggregates and elementary particle in the solution at a given time  $t$ . The function  $\psi$  does not depend explicitly on time and the first moment of the distribution scales as  $t^{-w}$ .  $w$  represents here a scaling exponent which depends on the aggregation efficiency and is equal to unity when it is maximum ( $\lambda = 0$ ).

Scaling theory can also be derived to explain the coagulation kinetics of Brownian particles in the presence of a low electrolyte concentration (RLCA conditions). With decreasing aggregation efficiency,  $w$  was found to become negative. This point can be explained by taking into account the probability of efficient collisions between  $g$ - and  $n$ -fold aggregates which is proportional to a Boltzmann factor:

$$p \sim \int_0^{\infty} \exp \left[ \frac{-\Delta G_e(x)}{k_B T} \right] dx \quad (4.13)$$

where  $\Delta G_e(x)$  is the electrostatic free-energy of two charged particles at distance  $x$ .

Equation (4.8) has also been solved numerically, and it was shown that Equation (4.10), the ‘self-preserving’ distribution, applies well after a sufficient time lag [43, 44]. Equations (4.10) and (4.11) were also derived using Monte Carlo simulations [45–47] with a collision frequency  $K(g, n)$  expressed as

$$K(g, n) = \frac{k_B T}{3\eta} (R_g(g) + R_g(n))(D_0(g) + D_0(n)) \quad (4.14)$$

where  $R_g(g)$ ,  $R_g(n)$ , and  $D_0(g)$ , and  $D_0(n)$  are respectively the radii of gyration and diffusion coefficients of aggregates composed of  $g$  and  $n$  particles, and  $\eta$  is the solvent viscosity. The long-time behaviour of  $c(g, t)$  was found to scale like

$$c(g, t) \sim t^{-w} g^{-\tau} f\left(\frac{g}{t^z}\right) \quad (4.15)$$

For diffusion coefficients of the form  $D_g \sim g^\gamma$  with  $\gamma < 0$ ,  $\tau = 0$  [48]; hence, Equations (4.10) and (4.15) are similar, with  $w = 2z$  and  $w = 2(1 - \lambda)^{-1}$  [49].

#### 4.3.4 Reversible Aggregation Process: Effects of Fragmentation and Restructuration

In the original aggregation model, aggregates remain rigid with respect to their diffusive motion and do not rearrange themselves after sticking. Although many experimental systems can be described by irreversible and rigid bonds [21], there is experimental evidence, at least on small length scales, that other phenomena are expected to play a role in nature. For example, under certain experimental conditions, aggregates obtained by a DLCA mechanism can restructure to more compact aggregates after a certain time. This behaviour has been observed in diluted colloidal systems with small gold or silica particles in which the value of the fractal dimension increases from 1.75 to 2.1 [50] or to 2.4 [51].

In practice, restructuring [52, 53] or aggregate fragmentation [54–56] is always present to some degree [57]. Compact aggregates result from the existence of combined aggregation and fragmentation processes, followed by internal reorganization. If we take into account all the detailed features of the interaction forces between particles, such mechanisms are relatively difficult to simulate in a simple way. Some critical questions then arise. How do the structures of the aggregates change with time? Do these aggregates remain fractal objects during restructuring? If so, how does the fractal dimension  $D_m$  change with time?

In order to simulate such processes, several modifications have been proposed to the fundamental aggregation models. For example, in two-dimensional modeling, some readjustments can be made to allow restructuring of the initial particle aggregates [58]. Compactification was clearly visible at small scales but surprisingly less visible when extrapolated to the infinite aggregate sizes. The fractal dimension was estimated to be 1.48, i.e. only very slightly larger than the 1.44 that was observed without restructuring.

For a three-dimensional aggregation model, Meakin and Jullien [59] introduced restructuring by taking into account rotations of the rigid clusters about their contacting particles. In that case, restructuring was more efficient, increasing the DLCA fractal dimension to about 2.2. It should be noted here that such a structural readjustment only increases the number of contacts between aggregates. As a result, the probability of reorganization is limited due to the irreversible nature of the clusters that are formed.

Fragmentation allows the particles, or aggregates, to escape after sticking. This effect is different from that obtained by simply considering a sticking probability. In this case, some reversibility is allowed, which can be chemically justified if the attractive secondary minimum of the DLVO potential is sufficiently weak. In von Smoluchowski's equation, it was assumed that aggregation was irreversible. Von Smoluchowski's equation can, however, be extended to include fragmentation processes:

$$\begin{aligned} \frac{d}{dt}(C_g) = & \frac{1}{2} \sum_{i+j=g} K(i, j)C_iC_j - \sum_{j=1} K(g, j)C_jC_g + \sum_{j=1} F(j, g)C_{j+g} \\ & - \frac{1}{2} \sum_{i+j=g} F(i, j)C_g \end{aligned} \quad (4.16)$$

where  $K(i, j)$  is the element of the reaction kernel that describes the aggregation process and  $F(i, j)$  is an element of the fragmentation kernel [54] which depends on the cluster dissociation constant  $k_d$ :

$$F(i, j) = k_d\phi[i, j] \quad (4.17)$$

where  $\phi$  is a function describing the dependence of the fragmentation rate on the aggregate sizes  $i$  and  $j$ .

In order to simulate the restructuring observed by experimentation [60], Meakin [61] and Kolb [62] considered a reversible model by modifying the original DLCA model by including random bond breaking. Although in the irreversible model [59] the effect on the fractal dimension was quite small, the fractal dimension value in the three-dimensional and two-dimensional reversible models was found to increase to 2.03 and 1.57 respectively at dynamic equilibrium. No change of  $D_m$  was observed with time.

To construct a more realistic reversible aggregation model involving the rearrangement of particles according to energetic considerations, the CCA model can be modified with a finite interparticle attraction energy  $E$  [63–66]. Shih, Aksay and Kikuchi (SAK) [63] built a lattice reversible growth model in which the nearest neighbours have a finite attraction energy. Here, the bond breaking is controlled by a Boltzmann factor rather than being random as in the previous model. From the SAK model, it was demonstrated that the aggregates can remain fractal during restructuring, with values ranging from 1.4 to 2.0 in  $d = 2$ , depending on the interparticle bonding energy and time.

The interparticle interaction can be described by a square-well potential:

$$E(r) = \begin{cases} \infty & r < d \\ -\varepsilon & d \leq r \leq \delta \\ 0 & r > \delta \end{cases} \quad (4.18)$$

where  $d$  is the diameter of the colloidal particle,  $\delta$  the attraction range and  $\varepsilon$  the depth of the interaction potential. Any attempted colloidal movements give a variation of energy  $\Delta E(r)$ , whose probability  $p$  is proportional to the exponential

$$p = \exp \left[ -\frac{\Delta E(r)}{k_B T} \right] \quad (4.19)$$

where  $\Delta E$  is the energy change due to the movement. By changing  $\varepsilon$ , the aggregation behaviour can be changed over a wide range from ramified aggregates to compact ones.

Any attempted movement consistent with the nonoverlapping restriction is accepted by considering the Metropolis rule [64]:  $\gamma < \exp(-\Delta E(r)/k_B T)$ , where  $\gamma$  is a random number uniformly distributed between zero and unity. According to this condition, the process evolves until a thermal equilibrium state is reached (see Figure 4.8).

This model shows that interparticle attractions play an important role in the aggregation process. Indeed, allowing the particles to rearrange themselves within the aggregates or even break from the aggregates encourages compaction of aggregates, and may also determine the saturated aggregate size. To illustrate the effect of restructuring, Figure 4.9 shows images obtained at the same simulation time which correspond to off-lattice reversible aggregation processes at four different values of  $\varepsilon$ . In these simulations, a ramified DLCA aggregate is considered as the initial configuration.

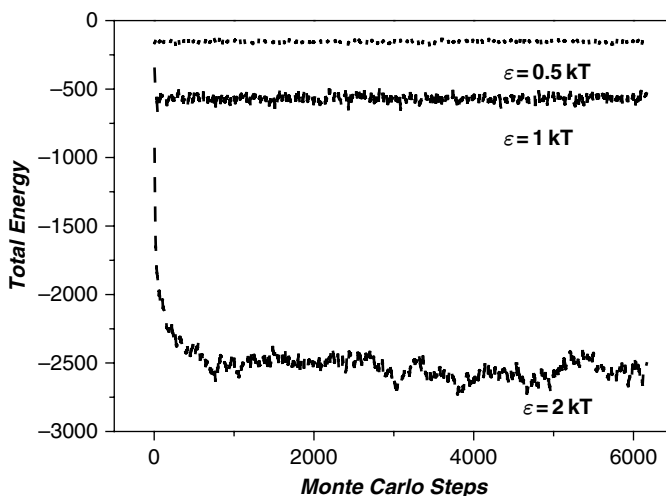


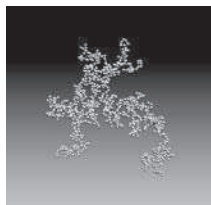
**Figure 4.8** Variation of the total energy with time (considered as Monte Carlo steps) for three different values of  $\varepsilon = 0.5, 1$  and  $2k_B T$  at  $\phi = 0.01$  (particle volume fraction). According to the metropolis condition, the system approaches an equilibrium state after a certain simulation time in all three cases. Diez-Orrite, S., Stoll, S. and Schurtenberger, P. (2005). Study of aggregate formation in colloidal systems: off-lattice Monte Carlo simulations, *Soft Matter*, **1**, 364–371. Reproduced by permission of the Royal Society of Chemistry.

When  $\varepsilon = 0.5k_B T$ , the initial DLCA aggregate is broken into very small aggregates (frequently dimers) as well as free colloidal particles. At this value of bond energy, large aggregates form rarely. These conditions correspond to experimental temperatures that are sufficiently high such that the colloidal particles have high probability to break from the aggregates due to thermal motion.

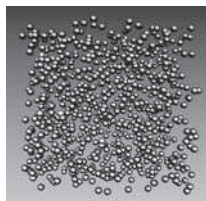
An increase of the interparticle energy promotes aggregation between colloidal particles. Simultaneously, the fragmentation process continues to produce free particles in the liquid phase. The combination of both mechanisms makes the aggregates more compact than the initial DLCA aggregate (see the largest aggregate obtained at  $\varepsilon = 2.5k_B T$  and  $3k_B T$ ), suggesting the presence of phase separation in the system [67–69].

At very high values of bond energy ( $\varepsilon = 5k_B T$ ), aggregation occurs at a faster rate than fragmentation, which makes the aggregates more ramified than aggregates obtained with less bond energy at the same simulation times. However, owing to the finite scale of the attractive interaction, reorganization within the aggregate is possible, giving an aggregate structure that is more compact at short length scales than the initial DLCA one. This suggests a  $D_m$  value slightly higher than 1.75. At a given particle concentration, the aggregate size decreases with bond energy because fragmentation is promoted. In Figure 4.10, the equilibrium aggregate size is plotted as a function of  $\varepsilon$ . The exponential decrease of the maximum aggregate size with

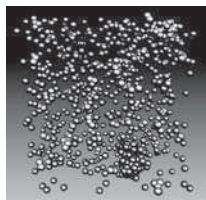
Initial DLCA aggregate  
(starting configuration)



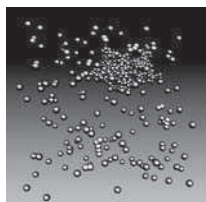
(a)



(b)



(c)



(d)



Equilibrated  
Conformations

**Figure 4.9** Influence of  $\varepsilon$ , the interaction potential value between particles, in the aggregation process: (a)  $\varepsilon = 0.5k_B T$ , (b)  $\varepsilon = 2.5k_B T$ , (c)  $\varepsilon = 3k_B T$  and (d)  $\varepsilon = 5k_B T$ . The particle volume fraction is equal to  $\phi = 0.01$ . The balance between aggregation, fragmentation and restructuring controls the particle dispersion and aggregate structure. Diez-Orrite, S., Stoll, S. and Schurtenberger, P. (2005). Study of aggregate formation in colloidal systems: off-lattice Monte Carlo simulations, *Soft Matter*, **1**, 364–371. Reproduced by permission of the Royal Society of Chemistry.



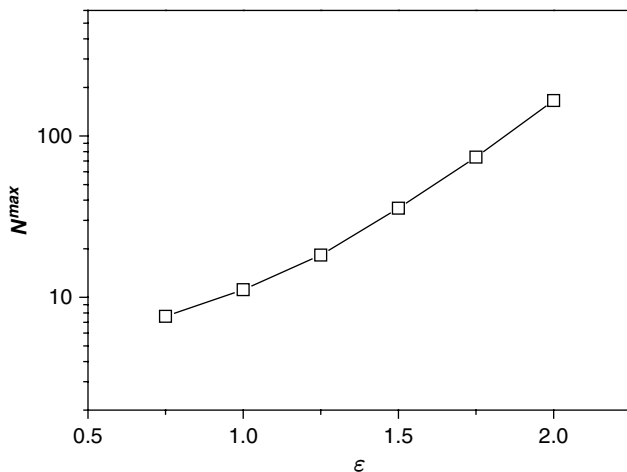


**Figure 4.10** Average maximum mass aggregate  $N^{\max}$  as a function of the interparticle interaction  $\varepsilon$  at a volume concentration  $\phi = 0.05$ .

the decrease of  $\varepsilon$  shows that aggregates cannot grow indefinitely in the aggregation process, but instead they reach a steady-state distribution of aggregate structure (see Figure 4.11). This is the main difference with the aggregates obtained by the DLCA model, for which the simulation was stopped once a single aggregate was obtained.

In order to investigate the increase of  $D_m$  with time, the aggregation process can be started with aggregates of various sizes formed by the DLCA mechanism at a

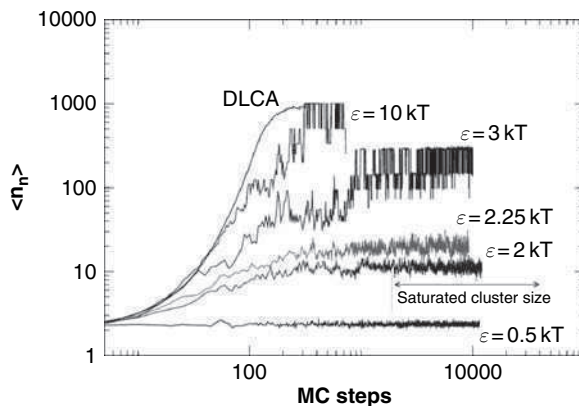


**Figure 4.11** Variation of the mean aggregate size ( $\langle n_n \rangle$ : number of elementary units) with the simulation time (Monte Carlo steps) at  $\phi = 0.05$ . The mean aggregate size is defined as  $\langle n_n \rangle = M_1/M_0$ , where  $M_i = \sum n^i N_n$  is the  $i$ th-order moment of the size distribution [69]. Diez-Orrite, S., Stoll, S. and Schurtenberger, P. (2005). Study of aggregate formation in colloidal systems: off-lattice Monte Carlo simulations, *Soft Matter*, **1**, 364–371. Reproduced by permission of the Royal Society of Chemistry.

given particle concentration. From Shih *et al.* [63], aggregates can be considered as fractal during the reversible aggregation process. Therefore, the fractal dimension corresponding to different times of the aggregation process can be calculated from a log–log plot of aggregate mass against the radius of gyration (see Figure 4.12).

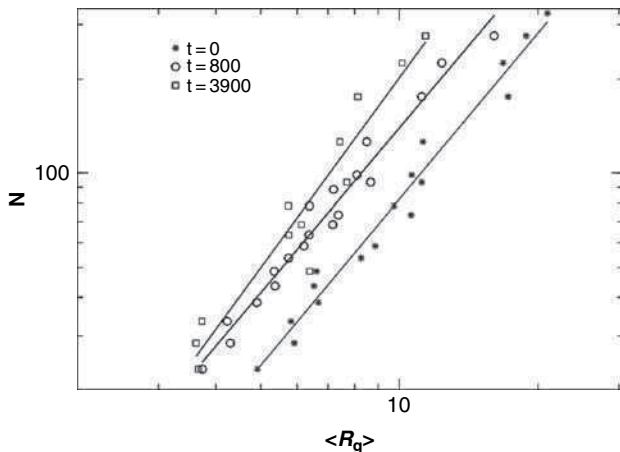


**Figure 4.12** Plot of the aggregate size  $N$  versus the mean gyration radius  $\langle R_g \rangle$  for three different moments of the aggregation process. System conditions:  $\phi = 0.01$  and  $\varepsilon = 3k_B T$ . Each point is the result of averaging over 10 samples. Diez-Orrite, S., Stoll, S. and Schurtenberger, P. (2005). Study of aggregate formation in colloidal systems: off-lattice Monte Carlo simulations, *Soft Matter*, **1**, 364–371. Reproduced by permission of the Royal Society of Chemistry.

The value of  $D_m$  increases from 1.77 at the beginning of the simulation process ( $t = 0$ , where  $t$  is measured in Monte Carlo steps) to 2.03 at  $t = 3900$  during the aggregation process, clearly showing how the aggregate structure becomes more compact as aggregation proceeds.

#### 4.3.5 Heterocoagulation Processes

Almost all simulations of nonequilibrium growth and aggregation (as reported above) are carried out under the assumption that the elementary particles are identical (homoaggregation). However, heteroaggregation involving different constituents is a much more common situation in natural systems (multicomponent systems). Both attractive and repulsive interactions can be present during heteroaggregation [70], e.g. when oppositely charged particles such as clay mineral and iron oxide or silica and alumina mixtures are considered [71, 72]. Such systems are too complicated to allow for the development of exact analytical theories, but computer simulations based on the concepts presented in Sections 4.1–4.3 can help to understand their behaviour. For example, simulations of the coagulation of a system made up of dissimilar A and B particles have been reported [73–76] and compared with experiment. The structures

and growth kinetics of clusters formed by both A and B particles having variable sticking probabilities, and the influence of their relative concentrations, have been investigated in order to determine the influence of the unsuccessful A–A and B–B collisions on the rate of A–B aggregation, and to determine optimal coagulation conditions. It has also been shown that heterocoagulation was well described by size distribution scaling laws indicating that dynamic scaling is applicable over a wide range of coagulation processes.

Aggregates produced by the heteroaggregation of A and B particles show a dependence of the fractal structures on the relative concentrations of the components. Figure 4.13 presents a series of images of heteroaggregates formed at equilibrium with identical elementary units (A and B) but at different relative concentrations. The particle number ratio of A and B had a dramatic effect on the final heteroaggregate

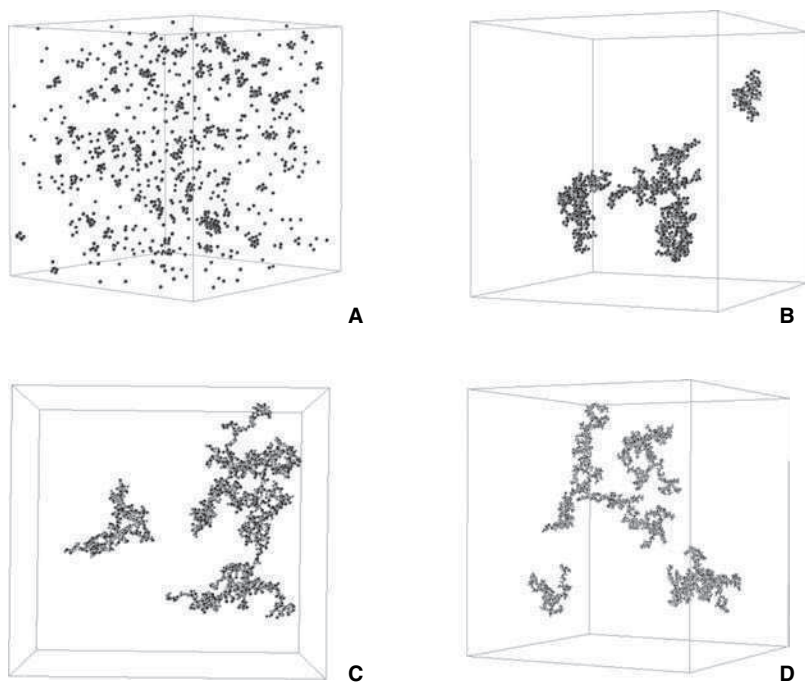


**Figure 4.13** Simulations relative to the coagulation of a three-dimensional system made up of dissimilar A (dark spheres) and B (bright spheres) particles. The influence of the unsuccessful A–A and B–B collisions on the rate of A–B aggregation and aggregate structures is illustrated here. The number of A particles was set to a constant value ( $N_a = 1000$ ) whereas the number of B particles  $N_b$  was adjusted to (a) 100, (b) 500, (c) 1000, (d) 3500. The fast coagulation regime corresponds to  $N_a = N_b$  and the formation of DLCA-type structures. Less reactive and more compact structures are obtained when  $N_a \neq N_b$ .

sizes and structures. At poor or high number ratios, aggregation is terminated at early stages. Initial aggregate sizes are small and the particles which are in excess rapidly saturate the aggregates. For optimal number ratios, heteroaggregates are large and rapidly formed. By considering all the particle positions (A and B), the fractal dimension is expected to decrease, reflecting a transition from the RLCA to the DLCA regime (Figure 4.14) and then increase again when the number ratio increases. This behaviour is mainly a geometric effect arising from the different initial particle concentrations. It should be noted that heteroaggregates, as well as the underlying structures composed only of A or only of B particles, exhibit self-similar fractal geometry.

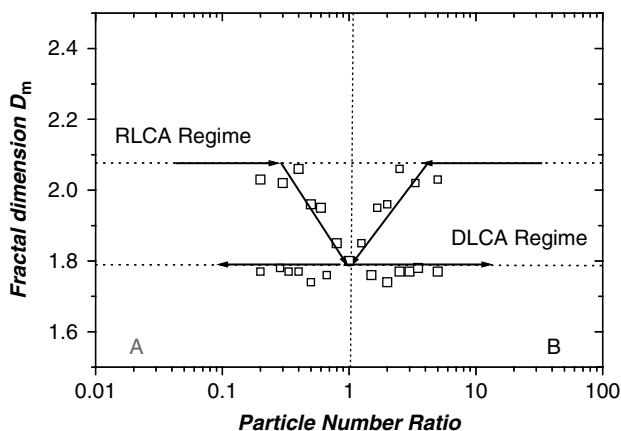


**Figure 4.14** Heteroaggregate fractal dimensions versus the particle number ratio  $N_b/N_a$ . On the one hand, the fractal dimension is calculated by considering only A particles, whereas on the other hand it is calculated by considering only B particles.

## 4.4 BRIDGING FLOCCULATION PROCESSES

It is well known that polymers may serve as bridges between colloidal particles to form flocs; nonetheless, very little quantitative information is available about their structure and formation, despite the fact that they play key roles in environmental systems [1]. Particles may not only be bridged by polymers, but may also facilitate the formation of larger aggregates due to the adsorption of several polymer segments on the same particles. This process can be seen as an example of the CCA model, where polymer conformation, reactivity and total length play important roles. Computer models once again constitute a valuable tool that allows for predictions of flocculation processes.

### 4.4.1 Model

This section describes a three-dimensional model to mimic bridging flocculation in which the size of the polymer chains is much larger than that of the interacting particles (a situation often encountered in natural waters).

Off-lattice simulations were carried out in which colloidal particles and polymer chains were confined to a cubic cell with normal periodic boundary conditions allowing them to pass freely through the periodic walls. The chains were represented at a mesoscopic scale by jointed spherical segments (pearl necklace model), and the relative sizes of chains and particles were controlled by adjusting the diameter of the colloidal particles and the length of the polymer chains through the number and size of the segments. In order to take into account a wide range of structural configurations of the chains and to adjust the polymer persistence length, from coils to rigid rods, angular constraints were imposed between the connected segments.

Particles, chains, aggregates and flocs were allowed to move in space according to their respective diffusion coefficients recomputed at each step from their masses and conformations. Brownian motion was represented by random walks. The number of random walks during a unit of (relative) time was proportional to the diffusion coefficients of the moving entities. The link between the relative and physical time was made by correlating the mean displacement of a reference particle (not participating in the aggregation process) and its diffusion coefficients.

#### 4.4.2 Kinetics and the Scaling Laws of Bridging Flocculation

Both computational [30, 31] and experimental [77–79] results indicate that the aggregation kinetics of colloids, in the absence of large biopolymer chains, can be described by power laws over long periods of time and over large aggregate size ranges. The power laws are also valid for heteroaggregation processes involving dissimilar particles [74]. Bridging flocculation involves a much more complicated system than the homoaggregation of spherical nondeformable colloids. Nonetheless, the application of similar scaling laws to bridging flocculation can be justified by the fact that, after an initial period, for which the duration is a function of the particle–biopolymer concentration ratio, the solution contains very few, if any, free particles and biopolymers (Figure 4.15). Only flocs and biopolymer–particle complexes remain in the simulation box. Following aggregation, the system behaves as if it were formed of only a single component with a sticking probability that is a function of the particle/biopolymer concentration ratio. This is an important finding, since it helps to explain why scaling laws used for single-component systems are valid for systems containing two (or more) components.

Scaling laws for the aggregation of a single component system are usually described by the analysis of the temporal variation of the number  $N(t)$  and weight  $S(t)$  average aggregate sizes, which are calculated from the size distributions. They are defined as

$$N(t) = \sum_n n C_n(t) / \sum_n C_n(t) \quad (4.20)$$

$$S(t) = \sum_n n^2 C_n(t) / \sum_n n C_n(t) \quad (4.21)$$

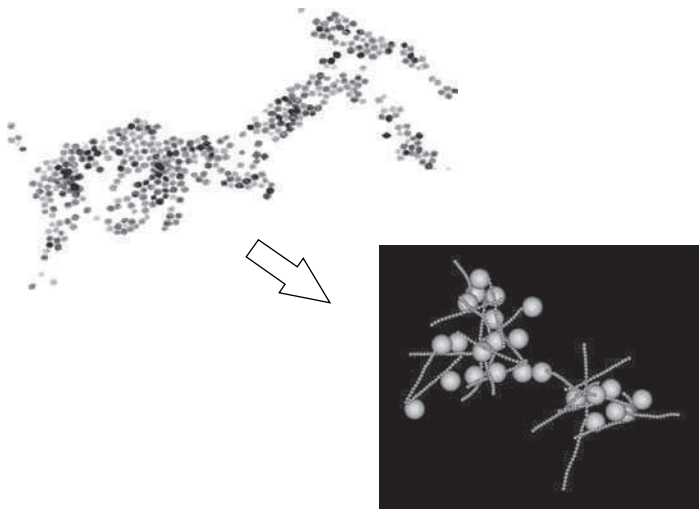


**Figure 4.15** Transmission electron micrographs of hematite in the presence of schizophyllan under conditions of rapid kinetics. Schizophyllan/hematite ratio 3.79, pH 4.5,  $I = 1 \text{ mmol dm}^{-3}$ . The three-dimensional floc obtained by computer simulation (optimum conditions) explains the presence of a local linear order observed in the hematite floc due to the presence of rigid chains.

where  $C_n(t)$  is the concentration of flocs composed of  $n$  elementary biopolymer chains at time  $t$  and  $C_1(t)$  represents the total concentration of the single biopolymer chains. From the size distribution histograms,  $S(t)$  and  $N(t)$  values can be calculated for various situations and dynamic scaling laws can be obtained by using the following relationships:

$$N(t) \sim t^w \quad (4.22)$$

$$S(t) \sim t^z \quad (4.23)$$

where  $z$  and  $w$  are scaling exponents.

The variations of  $S(t)$  and  $N(t)$  versus time are usually presented as log–log plots. The  $z$  and  $w$  values give a quantitative description of the flocculation processes under the conditions of the space dimension  $d$ , the biopolymer persistence length or rigidity  $l_p$ , biopolymer size  $l_c$  and particle/biopolymer concentration ratio  $x$ . Hence  $z(d, l_p, l_c, x)$  and  $w(d, l_p, l_c, x)$  values can be calculated for various systems [80], and comparison between experiments and computer models to isolate the key parameters controlling both structure and kinetics is possible upon parameterization of the model with experimental data.

For example, the formation kinetics and structure of hematite flocs formed in the presence of a large rigid extra-cellular polysaccharide, schizophyllan, was investigated both experimentally and theoretically. Transmission electron microscopy (TEM),

atomic force microscopy (AFM) and photon correlation spectroscopy (PCS) were used to characterize hematite particles and schizophyllan biopolymers and mixed flocs. The evolution of the floc sizes was followed and floc fractal dimensions were calculated. Interpretation of the experimental results provided information on the influence of various factors on the optimal concentration ratio of schizophyllan biopolymer/hematite for the rapid formation of flocs.

Both experiments and computer simulations demonstrated the fractal character of the mixed flocs. The optimal schizophyllan biopolymer/hematite concentration ratio obtained by simulation was smaller than that observed in laboratory experiments. The shift in the optimal dose was mainly attributed to a higher than predicted affinity of hematite for the schizophyllan aggregates present in the initial solution in addition to the presence of a large proportion of chains that did not participate in the flocculation process [12].

#### 4.4.3 Fractal Dimensions of Flocs

Physical properties, such as floc densities, settling velocities or the diffusion of compounds inside aggregates and flocs, depend on their fractal dimensions, which have to be calculated. The floc fractal dimensions can be determined directly from simulation, since each monomer and particle position is repeatedly computed during a simulation, allowing the mathematical definition of a fractal to be applied directly.

The results discussed here have been obtained using a given ‘sticking probability’ set to allow both homoaggregation among particles and the flocculation between particles and polymers. The effect of the polymer/particle concentration ratio was verified [81]. High rigid polymer chain concentrations lead to the formation of a polymeric network in which the particles were regularly distributed. In the presence of coiled polymer chains, floc structure resulted primarily from the association of particle aggregates and coiled polymers, all interacting via a classical CCA process that considers spherical units.

One important conclusion can be made: the spatial disposition of particles in flocs results from the biopolymer/particle concentration ratio in addition to the biopolymer conformations. In particular, flocculation processes with rigid biopolymers resulted in the formation of a regular network characterized by fractal dimensions that were higher than those obtained on the basis of the classical DLCA or RLCA models (Figure 4.16). Despite the highly loose structure of the aggregate that was formed, the increase in fractal dimension reflected the high order of particles in such networks.

A more refined Monte Carlo flocculation model was considered, based on energetic considerations rather than sticking probability factors, and included charged polymers (polyelectrolytes), the effect of solution pH, and the rearrangement of biopolymers at the particle surface. This model is presented in the next section, where the formation of a simple polymer–particle entity is examined, due to the required computational time.

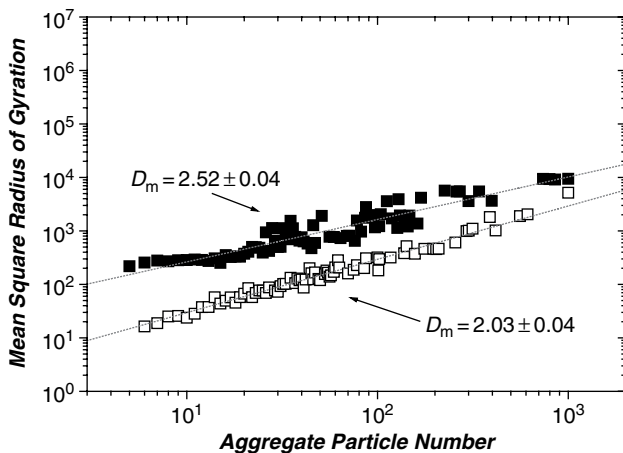


**Figure 4.16** Mean square radius of gyration versus the aggregate particle number. Open squares represent aggregates formed without the presence of rigid polymer chains. Black squares correspond to aggregates formed with the presence of rigid polymer chains (particle chain concentration ratio equal to 12.5).

#### 4.4.4 Monte Carlo Simulations: Charged Polymer Chain Adsorption on a Colloidal Particle

Owing to their important potential modifications of solution properties, mixtures of charged biopolymers (such as DNA and polysaccharides) and oppositely charged colloids (such as inorganic particles, globular proteins and micelles) have been followed with great interest in the fields of biology [82–84], wastewater treatment and industrial applications [83]. For example, the long-range attractive and/or repulsive character of the electrostatic interactions between polyelectrolytes and colloids, the role of solution chemistry, the geometry and concentration of polyelectrolytes and colloids and charge inversion are specific properties of these systems that are only partially understood. In order to better understand how polyelectrolytes (flexible, semi-flexible and rigid) interact with charged colloidal particles, a Monte Carlo approach is briefly described here [86–94]. Owing to screening effects, the role of ionic strength is discussed, since it will play a key role, in controlling both chain conformations, via the electrostatic persistence length, and the interaction energy of polyelectrolytes with the particles.

The total energy  $E_{\text{tot}}$  ( $k_B T$  units) for a given conformation is described as the sum of (i) repulsive electrostatic interactions between monomers, (ii) attractive electrostatic interactions between the chain and the particle,  $E_{\text{el}}$  and  $E_{\text{tor}}$ , and (iii) the chain stiffness or chain bending energy. Hard core interactions  $E_{\text{ev}}$  are also considered to include both monomer and particle excluded volumes.



All pairs of charged monomers within the polyelectrolyte interact via a screened Debye–Hückel long-range potential:

$$u_{\text{el}}(r_{ij}) = \frac{z_i z_j e^2}{4\pi \varepsilon_r \varepsilon_0 r_{ij}} \exp(-\kappa r_{ij}) \quad (4.24)$$

where  $z_i$  represents the amount of charge on a unit  $i$ .

Monomers interact with the particle according to the Verwey–Overbeek potential:

$$u'_{\text{el}}(r_{ij}) = \frac{z_i z_j e^2}{4\pi \varepsilon_r \varepsilon_0 r_{ij}} \frac{\exp[-\kappa(r_{ij} - \sigma_p)]}{1 + \kappa \sigma_p} \quad (4.25)$$

Free ions are usually not included explicitly in the simulations, but their overall effects on monomer–monomer and monomer–particle interactions are described via the dependence of the inverse Debye screening length  $\kappa^2$  ( $\text{m}^{-2}$ ) on the electrolyte concentration according to

$$\kappa^2 = 1000 e^2 N_A \sum_i \frac{z_i^2 C_i}{\varepsilon_0 \varepsilon_r k_B T} \quad (4.26)$$

The intrinsic chain stiffness is adjusted by a square potential with variable amplitude in order to vary its strength. This gives the bending energy:

$$E_{\text{tor}} = \sum_{i=2}^N k_{\text{ang}} (\alpha_i - \alpha_0)^2 \quad (4.27)$$

where  $\alpha_0 = 180^\circ$ ,  $\alpha_i$  represents the angle achieved by three consecutive monomers  $i - 1$ ,  $i$ , and  $i + 1$  and  $k_{\text{ang}}$  ( $k_B T / \text{deg}^2$ ) defines the strength of the angular potential or chain stiffness.

Monte Carlo simulations are usually performed according to the Metropolis algorithm in the canonical ensemble. In this method, successive ‘trial’ chain configurations are generated to obtain a reasonable sampling of low energy conformations [95]. After applying elementary movements which are randomly selected, the Metropolis selection criterion is employed either to select or reject the move. If the change in energy  $\Delta E$  resulting from the move is negative, then the move is selected. If  $\Delta E_{\text{tot}}$  is positive, the Boltzmann factor  $p$

$$p = \exp\left(\frac{-\Delta E_{\text{tot}}}{k_B T}\right) \quad (4.28)$$

is computed and a random number  $\text{rand}$  (with  $0 \leq \text{rand} \leq 1$ ) is generated. If  $\text{rand} \leq p$ , then the movement is selected. When  $\text{rand} > p$ , the trial configuration is rejected and the previous configuration is retained and considered as a ‘new’ state in calculating ensemble averages.

The monomer distribution at the particle surface is largely controlled by the value of  $k_{\text{ang}}$ . When the chain flexibility is important ( $k_{\text{ang}} \leq 0.001 k_B T / \text{deg}^2$ ), ‘tennis ball’ conformations are achieved, whereas when rigid chains are considered

( $k_{\text{ang}} > 0.001k_{\text{B}}T/\text{deg}^2$ ) the intrinsic flexibility forces the polyelectrolyte to adopt solenoid conformations, as predicted by the analytical model of Nguyen and Shklovskii [96]. Both the strong electrostatic repulsions between the consecutive turns and intrinsic chain rigidity keep the turns parallel to each other and maintain a constant distance between them. When  $C_i > 0.01 \text{ mol dm}^{-3}$ , large changes in the chain dimensions are observed with increasing the chain stiffness. As long as  $k_{\text{ang}} \leq 0.001k_{\text{B}}T/\text{deg}^2$ , loops and a tail are formed (Table 4.2;  $C_i = 0.1 \text{ mol dm}^{-3}$  and  $k_{\text{ang}} = 0k_{\text{B}}T/\text{deg}^2$ ), resulting in an increased thickness of the adsorption layer. When  $k_{\text{ang}} \geq 0.01k_{\text{B}}T/\text{deg}^2$ , and with increasing  $C_i$ , the polyelectrolyte starts to leave the surface by unwinding. Extended tails in solution are formed concomitantly with a decrease in the number of turns of the solenoid and monomers in trains (Table 4.2;  $C_i = 0.1 \text{ mol dm}^{-3}$  and  $k_{\text{ang}} = 0.02k_{\text{B}}T/\text{deg}^2$ ). By increasing further the ionic strength or the intrinsic flexibility of the chains, the polyelectrolyte becomes tangent to the particle surface with dimensions close to its free unperturbed dimensions. It must be noted that the adsorption of the charged polymers is not only controlled by the ionic

**Table 4.2** Equilibrated conformations from Monte Carlo simulations of complexes composed of a semi-flexible polyelectrolyte and a single colloidal particle as a function of the solution ionic strength  $I$  and polyelectrolyte intrinsic rigidity  $k_{\text{ang}}$ . By increasing the chain stiffness, solenoid conformations are progressively achieved at the particle surface, whereas an increase in ionic strength leads to the desorption of the polyelectrolyte.

$k_{\text{ang}} (k_{\text{B}}T/\text{deg}^2)$	$I (\text{mol dm}^{-3})$		
	0.01	0.1	1
0			
0.001			
0.02			

strength, but also by the particle diameter. Surface curvature effects will limit the amount of adsorbed monomers. Large particles allow the polyelectrolyte to be spread over the surface; small particles limit the number of adsorbed monomers.

Monte Carlo simulations provide a rewarding and invaluable approach to solving these systems, and computer simulations and theory can isolate the molecular factors that control polyelectrolyte conformations in solution. Therefore, they are extremely useful to address the optimization of colloid–polymer mixtures and guide the design of new experiments. A simple model involving one chain interacting with one particle has been described, but the same model can be extended to more concentrated systems, e.g. involving several chains (and/or colloidal particles) with explicit counter ions, co-ions and solvent molecules.

## 4.5 SETTLING VELOCITIES OF FRACTAL OBJECTS

The sedimentation of flocculated material and aggregate formation are amongst the most important processes, not only for the rational design of water treatment processes, but also for prediction of the diffusion of suspended matter and particle residence times in aquatic systems. Nonetheless, most current mathematical models used to simulate the circulation of trace compounds either do not take into account coagulation–sedimentation processes or, when they are considered, the coagulating material is described in a simplistic manner, most often as impermeable spheres that obey von Smoluchowski's theory and Stokes' law [41, 97]. In contrast, experimental data for settling rates of aggregates  $<500\text{ }\mu\text{m}$  in diameter demonstrate that natural aggregates settle 5–10 times faster than what is predicted by mathematical models, the deviations being most pronounced for poorly dense and low fractal dimension structures [98]. This implies that most of the colloidal material residence time calculations underestimate the contributions of large and open structures. While factors such as density and mass have received a great deal of attention, little importance has been given to the role of the aggregate fractal dimension. Numerical techniques based on computer simulations are expected to play an important role for solving such problems where solid–fluid hydrodynamics are important. Within this context, the main questions are: (a) how do aggregate and floc morphologies and sizes affect settling velocities? (b) is the fractal dimension a key parameter? (c) how do the hydrodynamic interactions within the aggregates and flocs, and fluid properties control settling velocities? and (d) how does the aggregate and floc cohesion and gravitational shear affect the overall structures and settling velocities?

### 4.5.1 Impermeable Aggregates

Numerous attempts have been made to develop mathematical models [99–107] to describe particle settling. Settling velocities of impermeable spheres are generally derived by balancing gravity  $F_g$ , buoyant  $F_b$ , and drag  $F_d$  forces. By introducing the

gravitational constant  $g_s$ , the suspending liquid  $\rho_l$ , the sphere density  $\rho_0$ , diameter  $d$ , and the fluid kinematics viscosity  $\eta$ , it is possible to express the settling velocity  $U$  of an impermeable sphere by the Stokes' law:

$$U = \frac{1}{18} \frac{g_s(\rho_0 - \rho_l)}{\eta} d^2 \quad (4.29)$$

Although Stokes' law is only directly applicable for slowly falling impermeable spheres (when the Reynolds number  $R_e \ll 1$ ), attempts have been made to extend its application to aggregates using modifications that include shape factors [108–113], fractal dimensions [114–117], and nonlinear drag coefficients [118–124]. However, attempts to model settling velocities using Stokes' law and empirical correction factors to account for shape modifications have had only limited success. At this time, it is neither clear whether the shape of a settling impermeable object is the primary factor affecting the deviations from Stokes' law, nor whether changes in settling velocity are linearly related to shape factors.

On the other hand, many researchers have tried to validate the use of Stokes' law for aggregates by considering the aggregate fractal dimension using a formalism based upon Stokes' law. Experimentally, the settling velocity  $U$  was not found to be proportional to the aggregate characteristic size  $l$ . For this reason, Li and Ganczarczyk [117] have defined the aggregate settling velocity as a power law function of the form

$$U \sim l^c \quad (4.30)$$

where  $c$  is a nonintegral number  $<2$  and  $l$  is a characteristic aggregate length. They then put forward the following equation [117]:

$$U \sim l^{D_m-1} \quad (4.31)$$

This relationship was used to calculate aggregate fractal dimensions from previous settling rate studies. However, this model was not found to describe the settling behaviour of fractal aggregates adequately due to the perhaps unwarranted assumption that  $D_m$  and  $l$  are the only variables affecting  $U$ , which implies that the drag coefficient will be the same for fractals as for impermeable spheres in the laminar flow region ( $R_e \ll 1$ ).

Logan and Wilkinson [116] improved the approach of Li and Ganczarczyk [117] by incorporating into the model a relationship between the aggregate projected area  $A$ ,  $l$ , and the  $2d$  aggregate fractal dimension  $d_{2f}$  to account for surface area differences between fractals and equivalent-sized spheres. Since  $A \sim l^{d_{2f}}$ , the settling velocity  $U$  resulted in

$$U \sim l^{D_m+1-d_{2f}} \quad (4.32)$$

Finally, assuming that the drag coefficient can be expressed as

$$C_d = a R_e^{-b} \quad (4.33)$$

where  $a$  and  $b$  are empirical coefficients related to the aggregate fractal dimensions, Jiang and Logan [118] proposed the following settling velocity relationship:

$$U \sim I^{(D_m - d_{2f} + b)/(2 - b)} \quad (4.34)$$

Unfortunately, this model was found to be inconsistent with experimental data [98], in particular when  $D_m < 1.7$ .

#### 4.5.2 Permeable Aggregates

Because it is likely that aggregates have significant internal flow through their structure, aggregate permeability must be considered. Fractal aggregates are expected to behave like objects that are smaller than equivalent spheres with reduced drag effects. Indeed, simulations of hydrodynamic friction using the Stokes model overestimate the friction of fractal objects.

Permeability was first considered [125–128] by applying Darcy's or Brinkman's law to a sphere with the consideration of a constant permeability in the aggregate radial direction. Owing to the fact that such an approach does not account for the nonlinear variation of pore sizes that are encountered in fractal aggregates, such models were found to be inaccurate when fractal dimension decreased from the Euclidean dimension 3 to low fractal dimension values, typically  $D_m < 2$ . In such a case, permeability is expected to increase from a minimum value at the aggregate centre to larger values in the radial direction. The smaller the fractal dimension, the more rapidly porosity increases with respect to the aggregate diameter.

To account for the increase in the internal flow in fractal aggregates with increasing diameter, equivalent spherical objects were calculated with settling velocities and drag forces equal to those of the fractal aggregates [129–132]. The relationship between the aggregate radius of gyration and the hydrodynamic radius was explored in relation to the fractal dimension and the number of primary particles in the aggregate. The conclusions drawn from this approach resulted in some important conclusions, e.g. when  $D_m > 2.0$  the power-law relationship between settling velocity and aggregate size paralleled that of impermeable settling spheres, whereas the settling velocity versus aggregate size relationship when  $D_m < 2.0$  is much more complex due to nonlinear relationships between aggregate sizes, connectivity, fractal dimensions, porosity and permeability.

Even after accounting for the aggregate size–porosity relationships, it is still not clear which is the best approach for the development of a mathematical model that considers varying permeability within an aggregate. Mathematical models [133–139] that do not integrate the many-body and long-range effects of hydrodynamic interactions within the aggregates predict only small increases in the settling velocity due to flow through the aggregates.

Extensions of Brinkman's formalism [140, 141] have facilitated the numerical solving of the Navier–Stokes equations for the flow outside the aggregate under laminar flow conditions, and the application of the Brinkman equation for flow inside

the aggregates by coupling the two models with continuity equations. Veerapaneni and Wiesner [142] calculated the hydrodynamic properties of fractal aggregates with a radially varying permeability that was calculated from the aggregate porosity. They demonstrated that, with increasing fractal dimension of the aggregate, the resistance to fluid flow through the aggregates increased, whereas the fluid collection efficiency, which is closely related to the drag coefficient of the aggregates, decreased. In addition, for realistic, three-dimensional structures, the relationship between permeability and the aggregate solid fraction has been established by adjusting the fractal dimensions and assuming a low Reynolds number [143].

To investigate flow through permeable fractal aggregates, the common numerical approach consists in solving the Navier–Stokes equations of motion [121, 144–146]. The main goal of this approach is the calculation of the friction matrix, which gives a linear relationship between the translational and rotational velocities of the aggregate elementary particles, as well as the forces and torques applied to them. Using the Kirkwood–Riseman theory [147] to calculate the translational friction coefficient on computer-generated cluster–cluster aggregates, it has been shown that large forces will be exerted on the outermost regions (i.e. most exposed particles) for an aggregate consisting of particles moving through a fluid, whereas small forces will be exerted on deeply buried particles that are screened from the hydrodynamic field. As a result, a very broad distribution of forces is achieved which has important implications on the mechanical stability of large aggregates moving in a fluid. However, owing to the computational efforts involved in such calculations, the simulated aggregate size remains, unfortunately, quite small (less than 200 particles).

## 4.6 CONCLUSIONS AND RECOMMENDATIONS

The aggregation of colloidal dispersions is still the subject of numerous studies. Fractal concepts are traditionally used to describe aggregate structures, aggregation kinetics and settling velocities. Although, in the broad sense, the qualitative analysis of the relative importance of the different factors controlling aggregation mechanism is correct, the many assumptions in aggregation models and theoretical descriptions still result in marked differences between controlled, experimental models or to results from aggregation in natural systems. Factors contributing to these differences are due, for example, to the fact that the primary particles that form the aggregates usually consist of various shapes and dimensions and exhibit chemical heterogeneities and surface roughnesses which need to be taken into account. Another limitation is that the prediction of the interparticle interactions which are needed, for example, to calculate collision efficiencies depends on the premise that particles are uniformly charged. This ignores the possible adsorption (complexation) of dissolved species such as biomacromolecules, macroions and humic substances. It should also be noted that charge regulation processes, the role of hydrodynamic interactions and magnetic interactions are rarely considered.

It is clear that more accurate calculations of collision efficiencies are still required to better understand aggregate formation, structures and fractal dimensions. This is critical, as the number of available parameters to describe colloidal dispersions is continuously increasing with the development of new characterization techniques. In summary, much improvement in our understanding of aggregation can still be acquired, especially with respect to: the kinetics of the process, the structure of the aggregated phase, and the transport of the aggregate via sedimentation processes.

## ACKNOWLEDGEMENTS

We gratefully acknowledge financial support from the Swiss National Science Foundation and the Swiss Federal Office for Education and Research. Many of the ideas that are presented here benefited from discussions with J. Buffle, E. Pefferkorn, R. Jullien, E. Balnois, A. Laguecir, S. Ulrich, H. Nguyen and M. Seijo. They are based on the results of graduate and postgraduate students over the years, in particular P. Chodanowski and R. Ferretti. We gratefully acknowledge the expert computer help of J.F. Rossignol and S. Rodak.

## LIST OF SYMBOLS AND ABBREVIATIONS

CCA	cluster–cluster aggregation
DLCA	diffusion-limited cluster aggregation
RLCA	reaction-limited cluster aggregation
DLVO	Derjarguin, Landau, Verwey, Overbeck theory
$a$	particle radius
$A$	Hamaker constant
$c(g, t)$	number of aggregates containing $g$ associated primary particles
$D_0(g)$	diffusion coefficient of an aggregate consisting of $g$ elementary particles
$D_m$	mass aggregate fractal dimension
$\Delta G_e(x)$	electrostatic free-energy of two charged particles at distance $x$
$d$	sphere diameter
$d_{2f}$	$2d$ fractal aggregate dimension (from projected area)
$D_0(n)$	diffusion coefficient of an aggregate consisting of $n$ elementary particles
$F_g$	gravity force
$F_b$	buoyant force
$F_d$	drag force
$F(i, j)$	fragmentation kernel
$g_s$	gravitational constant
$k_{arg}$	strength of the angular potential between monomers (chain stiffness)
$k_B$	Boltzmann constant
$k_d$	cluster dissociation constant

$K(g, n)$	rate constant of the reaction
$l$	aggregate characteristic length
$l_p$	biopolymer rigidity
$l_c$	biopolymer total length
$m$	aggregate mass
$N_0(t)$	moment of order zero of the aggregate size distribution
$N(t)$	number average aggregate size at time $t$
$P(i, j)$	sticking probability
$R$	aggregate size
$R_g$	aggregate radius of gyration
$R_g(g)$	radius of gyration of an aggregate consisting of $g$ elementary particles
$R_g(n)$	radius of gyration of an aggregate consisting of $n$ elementary particles
$R_G$	centre of mass of the aggregate
$S(t)$	weight average aggregate size at time $t$
$T$	temperature
$U$	settling velocity
$w$	scaling exponent for the number average aggregate size variation with time
$x$	particle/biopolymer concentration ratio
$z$	scaling exponent for the weight average aggregate size variation with time
$\eta$	fluid kinematics viscosity
$\rho$	mean aggregate density
$\rho_l$	suspending liquid density
$\rho_0$	sphere density
$\psi$	particle surface potential

## REFERENCES

- [1] Buffle, J., Wilkinson, K.J., Stoll, S., Filella, M. and Zhang, J. (1998). A generalized description of aquatic colloidal interactions: the three-colloidal component approach. *Environ. Sci. Technol.*, **32**, 2887–2897.
- [2] Senesi, N. (1996). Fractals in general soil science and in soil biology and biochemistry. In *Soil Biochemistry*, Stotzky, G. and Bollag, J.M. (eds), Vol. 9. Marcel Dekker, New York, pp. 415–472.
- [3] Elimelech, M., Gregory, J., Jia, X. and Williams, R. (1995). *Particle Deposition and Aggregation*. Butterworth-Heinemann, London.
- [4] Senesi, N. (1994). The fractal approach to the study of humic substances. In *Humic Substances in the Global Environment and Implications in Human Health*, Senesi, N. and Miano, T.M. (eds). Elsevier, Amsterdam, pp.3–41.
- [5] Stoll, S. and Buffle, J. (1995). Computer simulations of colloids and macromolecules. Aggregate formation. *Chimia*, **49**, 300–307.
- [6] Logan, B.E. and Wilkinson, D.B. (1989). Fractal geometry of marine snow and other biological aggregates. *Limnol. Oceanogr.*, **35**, 130–136.
- [7] Jackson, G.A. and Burd, A. (1998). Aggregation in the marine environment: a critical review. *Environ. Sci. Technol.*, **32**, 2805–2814.



- [8] Li, X.Y., Passow, U. and Logan, B.E. (1998). Fractal dimensions of small (15–200  $\mu\text{m}$ ) particles in Eastern Pacific coastal waters. *Deep-Sea Res.*, **45**, 115–131.
- [9] Ferretti, R., Zhang, J. and Buffle, J. (1997). Kinetics of hematite aggregation by polyacrylic acid: effect of polymer molecular weights. *Colloids Surf. A*, **121**, 203–215.
- [10] Ferretti, R., Zhang, J. and Buffle, J. (1998). Flocculation of hematite with polyacrylic acid: fractal structures in the reaction and diffusion-limited aggregation regimes. *J. Colloid Interface Sci.*, **208**, 509–517.
- [11] Zhang, J. and Buffle, J. (1996). Multi-method determination of the fractal dimension of hematite aggregates. *Colloids Surf. A*, **107**, 175–187.
- [12] Ferretti, R., Stoll, S., Zhang, J. and Buffle, J. (2003). Flocculation of hematite particles by a comparatively large rigid polysaccharide: schizophyllan. *J. Colloid Interface Sci.*, **266**, 328–338.
- [13] Mandelbrot, B.B. (1983). *The Fractal Geometry of Nature*. W.H. Freeman, New-York.
- [14] Meakin, P. (1998). *Fractals, Scaling and Growth Far from Equilibrium*. Cambridge University Press, Cambridge.
- [15] Jullien, R. and Botet, R. (1987). *Aggregation and Fractal Aggregates*. World Scientific Publishing, Singapore.
- [16] Feder, J. (1988). *Fractals*. Plenum Press, New York.
- [17] Rizzi, F., Stoll, S., Senesi, N. and Buffle, J. (2004). A transmission electron microscopy study of fractal properties and aggregation processes of humic acids. *Soil Sci.*, **169**, 765–775.
- [18] Tambo, N. and Watanabe, Y. (1979). Physical characteristics of flocs. *Water Res.*, **13**, 409–419.
- [19] Kolb, M., Botet, R. and Jullien, R. (1983). Scaling of kinetically growing clusters. *Phys. Rev. Lett.*, **51**, 1123–1126.
- [20] Meakin, P. (1983). Formation of fractal clusters and networks by irreversible diffusion limited aggregation. *Phys. Rev. Lett.*, **51**, 1119–1122.
- [21] Weitz, D. and Olivera, M. (1984). Fractal structures formed by kinetic aggregation of aqueous gold colloids. *Phys. Rev. Lett.*, **52**, 1433–1436.
- [22] Jullien, R., Botet, R. and Mors, P.M. (1987). Computer simulations of cluster–cluster aggregation. *Faraday Discuss. Chem. Soc.*, **83**, 125–127.
- [23] Derjaguin, B.V. and Landau, L. (1941). Theory of the stability of strongly charged lyophobic sols and of the adhesion of strongly charged particles in solutions of electrolytes. *Acta Physiochim.*, **14**, 633–662.
- [24] Verwey, E.J.W. and Overbeck, J.Th.G. (1948). *Theory of the Stability of Lyophobic Colloids*. Elsevier, Amsterdam.
- [25] McGown, D.N.L. and Parfitt, G.D. (1967). Improved theoretical calculation of the stability ratio for colloidal systems. *J. Phys. Chem.*, **71**, 449–450.
- [26] McBride, M.B. (1994). *Environmental Chemistry of Soils*. Oxford University Press, New York.
- [27] Greenland, D.J. and Hayes, M.H.B. (1978). *The Chemistry of Soil Constituents*. Wiley-Interscience, London.
- [28] Israelachvili, J. (1992). *Intermolecular and Surface Forces*. Academic Press, London.
- [29] Witten, T. and Sanders, L. (1981). Diffusion-limited aggregation, a kinetic critical phenomena. *Phys. Rev. Lett.*, **47**, 1400–1403.
- [30] Meakin, P. and Deutch, J.M. (1983). Monte Carlo simulation of diffusion controlled colloid growth rates in two and three dimensions. *J. Chem. Phys.*, **80**, 2115–2122.
- [31] Family, F., Meakin, P. and Vicsek, T. (1985). Cluster size distribution in chemically controlled cluster–cluster aggregation. *J. Chem. Phys.*, **83**, 4144–4150.
- [32] Broide, M.L. and Cohen, R.J. (1992). Measurements of cluster-size distributions arising in salt-induced aggregation of polystyrene microspheres. *J. Colloid Interface Sci.*, **153**, 493–508.

- [33] Pefferkorn, E., Stoll, S., Elaissari, H. and Varoqui, R. (1991). Polymer induced flocculation of latex particles aggregation process and related cluster size distributions. *Particul. Sci. Technol.*, **23**, 76–89.
- [34] Stoll, S., Lanet, V. and Pefferkorn, E. (1993). Kinetics and modes of destabilization of antibody-coated polystyrene latices in the presence of antigen: reactivity of the system IgG–IgM, *J. Colloid Interface Sci.*, **157**, 302–311.
- [35] Elimenech, M. (1992). Predicting collision efficiencies of colloidal particles in porous media. *Water Res.*, **26**, 1–8.
- [36] Romero, M.S., Martin-Rodriguez A. and de las Nieves, F.J. (2001). Electrosteric stabilization of polymer colloids with different functionality. *Langmuir*, **17**, 3505–3511.
- [37] Fuchs, N. (1934). Effect of the charge of aerosols on their stability. *Z. Phys.*, **89**, 736–742.
- [38] Honig, E.P., Roebersen, G.J. and Wiersema, P.H. (1971). Effect of hydrodynamic interaction on the coagulation rate of hydrophobic colloids. *J. Colloid Interface Sci.*, **36**, 97–109.
- [39] Sposito, G. (1997). Scaling invariance of the von Smoluchowski rate law. *Colloids Surf. A*, **120**, 101–110.
- [40] Lin, M.Y., Lindsay, H.M., Weitz, D.A. Ball, R.C., Klein, R. and Meakin, P. (1989). Universality in colloid aggregation. *Nature*, **339**, 360–362.
- [41] Von Smoluchowski, M. (1916). Drei Vorträge über Diffusion, Brownsche Molekularbewegung und Koagulation von Kolloidteilchen. *Phys. Z.*, **17**, 585–599.
- [42] Swift, D.L. and Friedlander, S.K. (1964). The coagulation of hydrosols by Brownian motion and laminar shear flow. *J. Colloid Sci.*, **19**, 621–647.
- [43] Lushnikov, A.A. (1973). Evolution of coagulating systems. *J. Colloid Interface Sci.*, **45**, 549–556.
- [44] Brock, J.R. and Hidy, G.M. (1965). Collision-rate theory and the coagulation of free-molecule aerosols. *J. Appl. Phys.*, **36**, 1857–1862.
- [45] Vicsek, T. and Family, F. (1984). Pattern formation in diffusion-limited aggregation. *Phys. Rev. Lett.*, **53**, 2281–2284.
- [46] Kolb, M. and Jullien, R. (1984). Chemically limited versus diffusion limited aggregation. *J. Phys. Lett. Paris*, **45**, 977–981.
- [47] Jullien, R., Kolb, M. and Botet, R. (1984). Scaling properties of growth by kinetic clustering of clusters. In *Kinetics, Aggregation, Gelation*, Family, F. and Landau, D.P. (eds). North Holland, Amsterdam, pp. 101–109.
- [48] Meakin, P., Vicsek, T. and Family, F. (1985). Dynamic cluster-size distribution in cluster–cluster aggregation: effects of cluster diffusivity. *Phys. Rev. B: Condens. Matter*, **31**, 564–569.
- [49] Ziff, M.R., McGrady, E.D. and Meakin, P. (1985). On the validity of Smoluchowski's equation for cluster–cluster aggregation kinetics. *J. Chem. Phys.*, **82**, 5269–5274.
- [50] Aubert, C. and Cannell, D.S. (1986). Restructuring of colloidal silica aggregates. *Phys. Rev. Lett.*, **56**, 738–741.
- [51] Liu, J., Shih, W.Y., Sarikaya, M. and Aksay, I.A. (1990). Fractal colloidal aggregates with finite interparticle interactions: Energy dependence of the fractal dimension. *Phys. Rev. A*, **41**, 3206–3213.
- [52] Dimon, P., Sinha, S.K., Weitz, D.A., Safinya, C.R. Smith, G.S., Varady, W.A. and Lindsay, H.M. (1986). Structure of aggregated gold colloids. *Phys. Rev. Lett.*, **57**, 595–598.
- [53] Ouali, L. Stoll, S. and Pefferkorn, E. (1995). The mechanisms and kinetics of the fragmentation of colloidal aggregates induced by electrostatic and electrosteric repulsion. In *Fragmentation Phenomena*, Beysens, D., Campi, X. and Pefferkorn, E. (eds). World Scientific, Singapore, pp. 64–76.
- [54] Familly, F. Meakin, P. and Deutch, J.M. (1986). Kinetics of coagulation with fragmentation: scaling behaviour and fluctuations. *Phys. Rev. Lett.*, **57**, 727–730.

- [55] Sorensen, C.M., Zhang, H.X. and Taylor, T.W. (1987). Cluster-size evolution in a coagulation–fragmentation system. *Phys. Rev. Lett.*, **59**, 363–366.
- [56] Meakin, P. and Ernst, M.H. (1988). Scaling in aggregation with breakup simulations and mean-field theory. *Phys. Rev. Lett.*, **60**, 2503–2506.
- [57] Pefferkorn, E. and Stoll, S. (1990). Aggregation/fragmentation processes in unstable latex suspensions. *J. Colloid Interface Sci.*, **138**, 261–271.
- [58] Meakin, P. and Jullien, R. (1985). Structural readjustment effects in cluster–cluster aggregation. *J. Phys. Paris*, **46**, 1543–1552.
- [59] Meakin, P. and Jullien, R. (1988). The effects of restructuring on the geometry of clusters formed by diffusion-limited, ballistic and reaction-limited cluster–cluster aggregation. *J. Chem. Phys.*, **89**, 246–250.
- [60] Bowen, M.S., Broide, M.L. and Cohen, R.J. (1985). Determination of cluster size distributions using an optical pulse particle size analyser. *J. Colloid Interface Sci.*, **105**, 605–616.
- [61] Meakin, P. (1985). The effects of random bond breaking on diffusion limited cluster–cluster aggregation. *J. Chem. Phys.*, **83**, 3645–3649.
- [62] Kolb, M. (1986). Reversible diffusion-limited cluster aggregation. *J. Phys. A: Math. Gen.*, **19**, 263–268.
- [63] Shih, W.Y., Aksay, I.A. and Kikuchi, R. (1987). Reversible-growth model: cluster–cluster aggregation with finite binding energies. *Phys. Rev. A*, **36**, 5015–5019.
- [64] Haw, M.D., Sievwright, M., Poon, W.C.K. and Pusey, P.N. (1995). Cluster–cluster gelation with finite bond energy. *Adv. Colloid Interface Sci.*, **62**, 1–16.
- [65] Jin, J.M., Parbhakar, K. and Dao, L.H. (1996). Gel formation by reversible cluster–cluster aggregation. *Phys. Rev. E*, **54**, 997–1000.
- [66] Terao, T. and Nakayama, T. (1998). Sol–gel transition of reversible cluster–cluster aggregations. *Phys. Rev. E*, **58**, 3490–3494.
- [67] Haw, M.D., Sievwright, M., Poon, W.C.K. and Pusey, P.N. (1995). Cluster-cluster gelation with finite bond energy. *Adv. Colloid Interface Sci.*, **62**, 1–16.
- [68] Diez-Orrite, S., Stoll, S. and Schurtenberger, P. (2005). Study of aggregate formation in colloidal systems: off-lattice Monte Carlo simulations. *Soft Matter*, **1**, 364–371.
- [69] Tirado-Miranda, M., Schmitt, A., Callejas-Fernández, J. and Fernández-Barbero, A. (1999). Colloidal clusters with finite binding energies: fractal structure and growth mechanism. *Langmuir*, **15**, 3437–3444.
- [70] Kim, A.Y. and Berg, J.C. (2000). Fractal heteroaggregation of oppositely charged colloids. *J. Colloid Interface Sci.*, **229**, 607–614.
- [71] Tomacz, E., Csanaky, C. and Illés, E. (2001). Polydisperse fractal aggregate formation in clay mineral and iron oxide suspensions, pH and ionic strength dependence, *Colloid Polym. Sci.*, **279**, 484–492.
- [72] Yates, P.D., Franks, G.V., Biggs, S. and Jameson, G.J. (2005). Heteroaggregation with nanoparticles: effect of particle size ratio on optimum particle dose. *Colloids Surf. A*, **255**, 85–90.
- [73] Stoll, S. and Pefferkorn, E. (1993). Kinetics of heterocoagulation, *J. Colloid Interface Sci.*, **160**, 149–157.
- [74] Meakin, P. and Djordjevic, Z.B. (1986). Cluster–cluster aggregation in two monomer systems. *J. Phys. A: Math. Gen.*, **19**, 2137–2153.
- [75] López-López, J.M., Schmitt, A., Callejas-Fernandez, J. and Hidalgo-Álvarez, R. (2004). Cluster discrimination in electrostatic heteroaggregation processes. *Phys. Rev. E*, **69**, 11 404–11 410.
- [76] López-López, J.M., Moncho-Jordá, A., Schmitt and Hidalgo-Álvarez, R. (2005). Formation and structure of stable aggregates in binary diffusion-limited cluster–cluster aggregation processes. *Phys. Rev. E*, **72**, 31 401–31 409.

- [77] Pefferkorn, E., Pichot, C. and Varoqui, R. (1988). Size distribution of latex aggregates in flocculating dispersions. *J. Phys. Paris*, **49**, 983–989.
- [78] Varoqui, R. and Pefferkorn, E. (1988). Measurements of cluster size distribution for latex particles flocculating in the presence of flexible water-soluble polymers. *Macromolecules*, **21**, 3096–3101.
- [79] Pefferkorn, E. and Stoll, S. (1990). Cluster fragmentation in electrolyte induced aggregation of latex. *J. Chem. Phys.*, **92**, 3112–3117.
- [80] Stoll, S. and Buffle, J. (1996). Computer simulation of bridging flocculation processes: the role of colloid to polymer concentration ratio on aggregation kinetics. *J. Colloid Interface Sci.*, **180**, 548–563.
- [81] Stoll, S. and Buffle, J. (1998). Computer simulation of flocculation processes: the roles of chain conformation and chain/colloid concentration ratio in the aggregate structures. *J. Colloid Interface Sci.*, **205**, 290–300.
- [82] Xia, J. and Dubin, P.L. (1994). Protein–polyelectrolyte complexes. In *Macromolecular Complexes in Chemistry and Biology*, Dubin, P. and Bock, D. (eds). Springer-Verlag, Berlin, pp. 247–271.
- [83] Darnell, J.E., Lodish, H. and Baltimore, D. (1995). *Molecular Cell Biology*, 3rd edition. Scientific American Books, New-York.
- [84] Hara, M. (1993). *Polyelectrolytes: Sciences and Technology*. Marcel Dekker, New York.
- [85] Radler, J.O., Koltover, I., Salditt, T. and Safinya, C.R. (1997). Structure of DNA–cationic liposome complexes: DNA intercalation in multilamellar membranes in distinct interhelical packing regimes. *Science*, **275**, 810–814.
- [86] Chodanowski, P. and Stoll, S. (2001). Polyelectrolyte adsorption on charged particles: a Monte Carlo approach. *Macromolecules*, **34**, 2320–2328.
- [87] Chodanowski, P. and Stoll, S. (2001). Polyelectrolyte adsorption on charged particles: size effects, *J. Chem. Phys.*, **115**, 4951–4960.
- [88] Stoll, S. and Chodanowski, P. (2002). Polyelectrolyte adsorption on an oppositely charged spherical particle. chain rigidity effects. *Macromolecules*, **35**, 9556–9562.
- [89] Brynda, M., Chodanowski, P. and Stoll, S. (2002). Polyelectrolyte–particle complex formation. Polyelectrolyte linear charge density and ionic concentration effects. *Polym. Colloid Sci.*, **280**, 789–797.
- [90] Laguecir, A., Brynda, M. and Stoll, S. (2002). Charged polymer/nanoparticle mixtures: Monte Carlo simulations, *Chimia*, **56**, 702–706.
- [91] Laguecir, A., Stoll, S., Kirton, G. and Dubin, P.L. (2003). Interactions of a polyanion with a cationic micelle: comparison of Monte Carlo simulations with experiment. *J. Phys. Chem. B*, **107**, 8056–8065.
- [92] Ulrich, S., Laguecir, A. and Stoll, S. (2004). Complex formation between a nanoparticle and a weak polyelectrolyte. Monte Carlo simulations. *J. Nanopartic. Res.*, **6**, 595–603.
- [93] Laguecir, A. and Stoll, S. (2005). Adsorption of a weakly charged polymer on an oppositely charged colloidal particle: Monte Carlo simulations investigation. *Polymer*, **46**, 1359–1372.
- [94] Ulrich, S., Laguecir, A. and Stoll, S. (2005). Titration of hydrophobic polyelectrolytes using Monte Carlo simulations. *J. Chem. Phys.*, **122**, 94 911–94 919.
- [95] Kremer, K. and Binder, K. (1988). Monte Carlo simulation of lattice models for macromolecules. *Comput. Phys. Rep.*, **7**, 259–310.
- [96] Nguyen, T.T. and Shklovskii, B.I. (2001). Overcharging of a macroion by an oppositely charged polyelectrolyte. *Physica A*, **293**, 324–338.
- [97] Chen, J.F., Luo, Y., Xu, J.H. Chen, Q.M. and Guo, J. (2006). Visualization study on sedimentation of micron iron oxide particles. *J. Colloid Interface Sci.*, **301**, 549–553.
- [98] Johnson, C.P., Xiaoyan, L. and Logan, B. (1996). Settling velocities of fractal aggregates. *Environ. Sci. Technol.*, **30**, 1911–1918.
- [99] Chellam, S. and Wiesner, M. (1993). Fluid mechanics and fractal aggregates. *Water Res.*, **27**, 1493–1496.

- [100] Logan, B.E. and Hunt, J.R. (1987). Advantages to microbes of growth in permeable aggregates in marine systems. *Limnol. Oceanogr.*, **32**, 1034–1048.
- [101] Adler, P.M. (1981). Interaction of unequal spheres: I. Hydrodynamic interaction: colloidal forces. *J. Colloid Interface Sci.*, **84**, 461–473.
- [102] Gibbs, R.J. (1985). Estuarine flocs: their size, settling velocity and density. *J. Geophys. Res.*, **90**, 3249–3251.
- [103] Kajihara, M. (1971). Settling velocity and porosity of large suspended particles. *J. Oceanogr. Soc. Jpn.*, **27**, 158–161.
- [104] Yao, K.M., Habbitan, M.T. and O'Melia, C.R. (1971). Water and waste water filtration. Concepts and applications. *Environ. Sci. Technol.*, **5**, 1105–1112.
- [105] Rajagopalan, R. and Tien, C. (1976). Trajectory analysis of deep bed filtration with the sphere-in-cell porous media model. *Am. Inst. Chem. Eng. J.*, **22**, 523–528.
- [106] Valioli, I.A. and List, E.J. (1984). Numerical simulation of a sedimentation basin. I. Model development. *Environ. Sci. Technol.*, **18**, 242–247.
- [107] Han, M. and Lawler D.F. (1992). The (relative) insignificance of  $G$  in flocculation. *J. Am. Water Works Assoc.*, **84**, 79–91.
- [108] Hutchinson, G.E. (1967). Introduction to lake biology and limnoplankton. In *A Treatise on Limnology*, vol. 2, Edmonson, Y.H. (ed.). John Wiley & Sons, Ltd, New York, pp. 27–93.
- [109] Komar, P.D., Morse, A.P. and Small, L.F. (1981). An analysis of sinking rates of natural copepod and euphausiid fecal pellets. *Limnol. Oceanogr.*, **26**, 172–180.
- [110] Namer, J. and Ganczarczyk, J.J. (1993). Settling properties of digested sludge particle aggregates. *Water Res.*, **27**, 1285–1294.
- [111] Andreadakis, A.D. (1993). Physical and chemical properties of activated sludge floc. *Water Res.*, **27**, 1707–1714.
- [112] Alldredge, A.L. and Gotschalk, C. (1988). In situ settling behavior of marine snow. *Limnol. Oceanogr.*, **33**, 339–351.
- [113] Lasso, I.A. and Weideman, P.D. (1986). Stokes drag on hollow cylinders and conglomerates, *Phys. Fluids*, **29**, 3921–3934.
- [114] Li, X. and Logan, B. (1995). Size distributions and fractal properties of particles during a simulated phytoplankton bloom in a mesocosm. *Deep Sea Res. II*, **42**, 125–138.
- [115] Hunt, J.R. (1980). Prediction of oceanic particle size distribution from coagulation and sedimentation mechanisms. *Particulates in Water: Characterization, Fate, Effects and Removal*, Kavanaugh, M.D. and Keki, J.T. (eds), Advances in Chemistry Series No. 189. American Chemical Society, New Yorkpp. 243–257.
- [116] Logan, B. and Wilkinson, D.B. (1991). Fractal dimensions and porosities of *Zoo-gloea ramigera* and *Saccharomyces cerevisiae* aggregates. *Biotechnol. Bioeng.*, **38**, 389–396.
- [117] Li D. and Ganczarczyk, J. (1987). Stroboscopic determination of settling velocity, size and porosity of activated sludge flocs. *Water Res.*, **21**, 257–262.
- [118] Jiang, Q. and Logan, B. (1991). Fractal dimensions of aggregates determined from steady-state size distributions. *Environ. Sci. Technol.*, **25**, 2031–2038.
- [119] Sutherland, D.N. and Tan, C.T. (1970). Sedimentation of a porous sphere. *Chem. Eng. Sci.*, **25**, 1948–1950.
- [120] Neale, G., Epstein, N. and Nader, W. (1973). Creeping flow relative to permeable spheres. *Chem. Eng. Sci.*, **28**, 1865–1874.
- [121] Matsumoto, K. and Sukanuma, A. (1977). Settling velocity of a permeable model floc. *Chem. Eng. Sci.*, **32**, 445–447.
- [122] Masliyah, J.H. and Polikar, M. (1980). Terminal velocity of porous spheres. *Can. J. Chem. Eng.*, **58**, 299–302.
- [123] Adler, P. (1987). Hydrodynamic properties of fractal flocs. *Faraday Discuss. Chem. Soc.*, **83**, 145–152.

- [124] Li, D.H. and Ganczarczyk, J. (1988). Flow through activated sludge flocs. *Water Res.*, **22**, 789–792.
- [125] Nguyen, H.P., Chopard, B. and Stoll, S. (2004). Hydrodynamic properties of fractal aggregates in 2D using lattice Boltzmann simulation. *Future Gener. Comput. Syst. (FGCS)*, **20**, 981–991.
- [126] Brinkman, H.C. (1947). A calculation of the viscous force exerted by a flowing fluid in a dense swarm of particles. *Appl. Sci. Res.*, **A1**, 27–34.
- [127] Masliyah, J.H., Naele, G., Malysa, K. and van de Ven, T.G.M. (1987). Creeping flow over a composite sphere: solid core with porous shell. *Chem. Eng. Sci.*, **42**, 245–253.
- [128] Gmachowski, L. (1996). Hydrodynamics of aggregated media. *J. Colloid. Interface Sci.*, **178**, 80–86.
- [129] Rogak, S.N. and Flagan, R.C. (1990). Stokes drag on self-similar clusters of spheres. *J. Colloid Interface Sci.*, **134**, 206–218.
- [130] Wiltzius, P. (1987). Hydrodynamic behavior of fractal aggregates. *Phys. Rev. Lett.*, **58**, 710–713.
- [131] Wiltzius, P. and van Saarloos, W. (1987). Reply to a Comment on ‘Hydrodynamic behavior of fractal aggregates’. *Phys. Rev. Lett.*, **59**, 2123.
- [132] Chen, Z.Y., Meakin, P. and Deutch, J.M. (1987). Comment on ‘Hydrodynamic behavior of fractal aggregates’. *Phys. Rev. Lett.*, **59**, 2121.
- [133] Durlowski, L. and Brady, J.F. (1987). Analysis of the Brinkman equation as a model for flow in porous media. *Phys. Fluids*, **30**, 3329–3341.
- [134] Chen, Z.Y., Deutch, J.M. and Meakin, P. (1984). Translational friction coefficient of diffusion limited aggregates. *J. Chem. Phys.*, **80**, 2982–2983.
- [135] Meakin, P. and Deutch, J.M. (1987). Properties of the fractal measure describing the hydrodynamic force distributions for fractal aggregates moving in a quiescent fluid. *J. Chem. Phys.*, **86**, 4648–4656.
- [136] Meakin, P., Chen, Z.Y. and Deutch, J.M. (1985). The translational friction coefficient and time dependent cluster size distribution of three dimensional cluster–cluster aggregation. *J. Chem. Phys.*, **82**, 3786–3789.
- [137] Doi, M. and Chen, D. (1989). Simulation of aggregating colloids in shear flow. *J. Chem. Phys.*, **90**, 5271–5279.
- [138] Chen, D. and Doi, M. (1989). Simulation of aggregating colloids in shear flow. *J. Chem. Phys.*, **91**, 2656–2663.
- [139] Potanin, A. (1993). On the computer simulation of the deformation and breakup of colloidal aggregates in shear flow. *J. Colloid Interface Sci.*, **157**, 399–410.
- [140] Tam, C.K. (1969). The drag on a cloud of spherical particles in low Reynolds number flow. *J. Fluid Mech.*, **38**, 537–545.
- [141] Childress, S. (1972). Viscous flow past a random array of spheres. *J. Chem. Phys.*, **56**, 2527–2539.
- [142] Veerapaneni, S. and Wiesner, M. (1996). Hydrodynamics of fractal aggregates with radially varying permeability. *J. Colloid. Int. Sci.*, **177**, 45–57.
- [143] Kim, A.S. and Stolzenbach, K.D. (2002). The permeability of synthetic fractal aggregates with realistic three-dimensional structure. *J. Colloid Interface Sci.*, **253**, 315–328.
- [144] Sonntag, R.C. and Russel, W.B. (1987). Structure and breakup of flocs subjected to fluid stresses. *J. Colloid Interface Sci.*, **115**, 378–389.
- [145] Adler, P.M. and Mills, P.M. (1975). Motion and rupture of a porous sphere in a linear flow field. *J. Rheol.*, **23**, 25–37.
- [146] Van Saarloos, W. (1987). On the hydrodynamic radius of fractal aggregates. *Physica A*, **147**, 280–296.
- [147] Kirkwood, J.G. and Riseman, J. (1948). The intrinsic viscosities and diffusion constants of flexible macromolecules in solution. *J. Chem. Phys.*, **16**, 565–573.



---

# 5 Fractal Mechanisms in Coagulation/Flocculation Processes in Environmental Systems

---

**Jean Yves Bottero, Armand Masion and Jérôme Rose**

*CEREGE UMR 6635 CNRS-UPCAM, Europole de l'Arbois, BP 80, 13545 Aix-en-Provence, Cedex 04, France*

## 5.1 INTRODUCTION

In aquatic media, coagulation–flocculation is a very general process that consists in the formation of aggregates under various constraints. The forces of aggregate formation are generally due to the modification of surface chemistry by the addition of chemical species that favor either ‘bridge’ formation among the particles or ‘chemical patches’ on the surface that decrease the repulsive energy or increase the attractive energy between particles. Most often, the term ‘coagulation’ is used to refer to surface processes occurring at the beginning of aggregate formation. Coagulants are chemicals that are able to modify the surface properties of the initial particles by adsorption/complexation. Surface properties are modified by changes in the surface charge, the diffuse-layer charge or thickness and the hydrophilic–hydrophobic balance. The consequences of such molecular-scale changes can be the formation of aggregates and flocs, which are defined here as very large aggregates.

The formation of fractal micro- or macro-aggregates starts at the molecular level. For example, the hydrolysis and growth of Al(III) or Fe(III) species far from thermodynamic equilibrium leads to the formation of aggregates when water molecules in the hydration sphere are deprotonated or displaced by hydroxyl ions. Furthermore, H<sub>2</sub>O and OH can be exchanged by other ligands whose nature has a direct influence on aggregate structure.

The aggregation of small, micrometer-sized, subunits to form large aggregates is generally determined by properties such as surface charge and coverage. In cases where charge heterogeneity is important, e.g. aggregation of clays, the aggregate structure is dominated by shape anisotropy. The basic theory describing the interaction of charged surfaces is known as the Derjaguin, Landau, Verwey, Overbeck (DLVO) theory [1–3]. It is based upon the determination of two main forces: electrostatic

repulsion between the surfaces with a maximum repulsion at a definite gap width and attraction due to van der Waals forces at small distances.

Two parameters are particularly interesting for describing flocs, i.e. size distribution and structure. Floc structure can be described on various size scales: from molecular to macroscopic. One universal concept used to describe structure is the fractal dimension. The theoretical basis and the experimental evidence for fractals evolved a great deal in the 1980s [4–7]. An important example is related to the formation of fractal aggregates in aquatic media (natural or industrial), with some consequences (not developed in this chapter) on the settling velocity [8], bacterial activity and water treatment [9–14]. In waters and wastewaters, aggregate structure influences sludge dehydration, floc settling velocities and head loss across packed beds [15, 16]. Aggregation kinetics depend on the fractal structure of aggregates, not only for geometrical reasons, but also due to the impact on hydrodynamic interactions between permeable aggregates [17]. This latter aspect is certainly the most complex and is not yet totally resolved.

The parameter used to describe the structure of fractal aggregates is the fractal dimension  $D_f$  [4–8]. This parameter is directly associated with the dimension of the object, and is different from the space dimension in which the object is contained [18]. The relationship between  $D_f$  and the aggregate geometry as described by the volume  $V$  and radius  $R$  is given by

$$V \sim R^{D_f} \quad (5.1)$$

The most common techniques that are used to measure fractal dimensions of aggregates in solution are scattering techniques (visible light, neutrons and X-rays); see Chapter 2. These techniques allow the calculation of the so-called distribution function  $P(r)$ , which scales as a power law of the distance  $r$  within a fractal object:

$$P(r) \sim r^D f^{-d} \quad (5.2)$$

where  $d$  is the space dimension containing the fractal object and  $P(r) = 0$  when  $r > 2R$ , i.e. the diameter of the aggregate.

This chapter is aimed at illustrating the mechanisms of fractal aggregate formation in environmental systems, including rivers, lakes, soils and industrial systems (e.g. water and wastewater treatment plants). In these systems, the formation of fractal aggregates is controlled by different mechanisms that must be analyzed at different length scales that range from nano- to meso- and macro-scales. In addition, when the subunits are in the submicrometer size range, structure analysis must also take into account additional aspects such as multiple scattering. Two examples have been selected to illustrate these systems. The first examines aggregate formation by hydrolysis of Fe(III) ions and the role of ‘strong’ and ‘weak’ ligands in orienting aggregate structure at micro-scales. A special investigation of the nanoscale–mesoscale relationship is also developed. The second example addresses the formation of very large aggregates that originate from micrometer-sized subunits. These aggregates are commonly formed in soils and natural water bodies, and in industrial water and wastewater facilities.



## 5.2 TECHNIQUES

### 5.2.1 Small-Angle X-Ray Scattering

Small-angle X-ray scattering (SAXS) has been shown to be the best tool to investigate aggregate size and structure parameters for suspensions of very small colloids. At the largest values of the scattering vector  $q$ , information on the shape, size and polydispersity of the subunits/nuclei can be obtained. In the case of fractal aggregates,  $D_f$  can be easily derived from the scattering intensity  $I(q)$ , according to

$$I(q) = F(q)S(q) \quad (5.3)$$

where  $F(q)$ , called the form factor, is the scattering by the subunits/nuclei, and  $S(q)$  is the interference function describing the arrangement of subunits within the aggregate. For a fractal aggregate,  $S(q)$  scales as  $q^{-D_f}$ . Thus, a rigorous determination of  $D_f$  implies that the subunits are well characterized. Another parameter of structural interest that can be derived from the SAXS curve is the pair distribution function,  $P(r)$ . It can be obtained from the correlation function  $\gamma(r)$ , which is calculated from the Fourier transform of  $I_N(q)$  of the normalized intensity:

$$\gamma(r) = \frac{\Pi^2}{2} \int q^2 I_N(q) \frac{\sin(qr)}{qr} dq \quad (5.4)$$

In this case,  $P(r) = r^2 \gamma(r)$ . The form of  $P(r)$  provides information on the size and shape of the aggregate and the coordination number of the particles in the aggregates.

### 5.2.2 Light Scattering

#### 5.2.2.1 Homogeneous particles

Dynamic light scattering allows measurement of the translational diffusion coefficient  $D_T$  of particles. For noninteracting particles, the first-order autocorrelation function  $g(r)$  is directly proportional to  $D_T$ . Polydisperse systems are analyzed using the method of cumulants, in which a distribution of exponential terms  $C(r)$  is assumed:

$$C(r) = F(\Gamma) \exp(-\Gamma r) d\Gamma \quad (5.5)$$

where  $\Gamma = D_T q^2$ ,  $q = 4\pi n \sin(\theta/2)/\lambda$ ,  $\theta$  is the scattering angle,  $n$  is the optical index and  $\lambda$  is the wavelength of the incident beam.

The function  $F(\Gamma)$  is expanded in a power series of  $r$ . The first moment (cumulant) in the expansion is the average decay constant  $\Gamma_{\text{avg}}$ , which defines an effective diffusion coefficient  $D_T$  for the particle size distribution.  $D_T$  is converted to the effective hydrodynamic radius  $r_H$  using the Stokes–Einstein relationship.

#### 5.2.2.2 Fractal aggregates

If the size of the subunits is less than  $\lambda/20$ , then the fractal dimension  $D_f$  can be calculated using the same law as for SAXS. In this case,  $D_f$  is defined in an angular

domain which varies from the size of the subunit to the size of the aggregate. However, if the size of the subunits is not very different from  $\lambda$ , then multiple scattering cannot be neglected. With respect to this point, Botet *et al.* [19] recently developed a new scattering model, called the mean-field approximation, which accounts for multiple scattering where the size of the scatterer is close to the scattering wavelength. These authors analyzed the multiple scattering results of Xu [20] by mean-field theory using Mie theory for fractal aggregates. Mean-field scattering provides solutions that are able to describe multiple scattering far from the optical resonance where the Rayleigh approximation is not consistent.

An extension of this approach takes multiple scattering into account by introducing a new parameter, the mean optical index  $\bar{n}$  [21]. This term characterizes the mean optical environment of scatterers belonging to a fractal object. In fractal aggregates, the optical contrast is defined as the optical contrast between scatterers  $n_s$  and their mean environment  $\bar{n}$ , with the scatterers' mean optical contrast denoted as  $n_s/\bar{n}$ . The form factor  $F(q)$  is thus defined by this new optical contrast. On the basis of Equation (5.3), the scattered intensity  $I(q)$  depends on the mean optical contrast of the scatterer. Therefore,  $I(q)$  contains structural information not only through  $S(q)$ , but also through the mean optical contrast that depends on the aggregate structure. In this case, the form factor  $F(q)$  can be calculated using the approximation

$$I_{\text{scatt}}(q) \propto \bar{I}_{r_s, n_s/\bar{n}}(q) S(q) \quad (5.6)$$

where  $\bar{I}_{r_s, n_s/\bar{n}}(q)$  is the Mie angular scattered intensity of a primary particle belonging to a fractal geometry characterized by a mean optical index  $\bar{n}$  which follows the mean-field approximation. The initial optical contrast  $m = n_s/n_m$  is replaced by the scatterers' mean optical contrast  $n_s/\bar{n}$ , defined with respect to the mean environment of the scatterers inside the aggregate.

The electromagnetic mean-field has been expressed by the coefficients  $\bar{d}_{1,n}^{(1)}$  and  $\bar{d}_{1,n}^{(2)}$ , used as the renormalized Mie coefficients  $a_n$  and  $b_n$  [19–21]. These new coefficients express the mean field scattered by a particle within an aggregate. They are independent of the position of the particle inside the aggregate and take into account the mean environment of the scatterers in a fractal aggregate. Far from the aggregate, each particle of a given cluster is assumed to radiate the same electromagnetic field, except for its phase. The coefficients  $\bar{d}_{1,n}^{(1)}$  and  $\bar{d}_{1,n}^{(2)}$  are expressed in terms of fractal and optical characteristics ( $a_n, b_n$ ) using the notations of Botet *et al.* [19]:

$$\bar{d}_{1,n}^{(1)} = \frac{a_n}{1 + 2L \sum_{\nu=1}^{\infty} (2\nu + 1)a_n} \quad (5.7)$$

$$\bar{d}_{1,n}^{(2)} = \frac{b_n}{1 + 2L \sum_{\nu=1}^{\infty} (2\nu + 1)b_n} \quad (5.8)$$

where

$$L = \frac{c^{2/D_f} \Gamma[1 - (2/D_f)]}{4} \frac{N}{(k R_g)^2}$$

$k$  is the wave number,  $\nu$  is a positive integer,  $R_g$  is the radius of gyration,  $N$  is the number of subunits inside the aggregate, and the fractal dimension of the aggregate is greater than two. The parameters  $D_f$ ,  $R_g$ , and  $N$  are directly related to the optical parameters.

### 5.3 NUCLEATION-PRECIPITATION OF FRESH IRON OXYHYDROXIDES

Over the years, the precipitation of iron oxides and hydroxides from acidic solutions has received considerable attention in various fields, such as catalyst synthesis, environmental sciences and industrial processes [e.g. 22–29]. Freshly formed iron hydroxide particles help to control pollution in aquatic systems, e.g. by fixation and transport of phosphates, heavy metals and other reactive inorganic and/or organic species [30–33]. The high reactivity of these iron phases is mainly due to their small size. The formation and aggregation of iron colloids, which occurs in continental and marine aquatic systems [22, 34–38], is also employed in water and wastewater treatments [35, 39, 40].

In aquatic systems, Fe(III)-aquo ions may polymerize by deprotonation to form sparingly soluble colloidal iron oxyhydroxides. Although the crystalline end-products of this reaction, such as goethite ( $\alpha$ -FeOOH) and hematite ( $\alpha$ -Fe<sub>2</sub>O<sub>3</sub>), are well characterized, the structure and shape of the intermediate phases are far from being fully elucidated. The shape and ‘porosity’ of freshly formed iron colloids and aggregates control their capacity to bind and transport a high number of elements. In some cases, e.g. where the size of the particles is not too small, a fractal approach can be useful to determine the reactivity of the iron colloids and aggregates and to explain their high specific surface and roughness. This approach, however, must be combined with a molecular-scale characterization, since these objects are very small and are not always geometrically self-similar.

General models of nucleation have been proposed [41, 42] based on the concept of similarity between the structure of polymers and the structure of the resulting crystalline phases. Nonetheless, these models have failed to predict the precipitation processes correctly. A generalized approach based on the electrostatic field theory [25, 43] was able to provide hints for understanding the formation of small clusters but could not be applied to larger ones.

#### 5.3.1 Nucleation

Several pioneering studies [41, 42, 44, 45] have developed the general concepts of polymerization, growth and precipitation of Fe(III) ions, but the intermediate

polymers and clusters have not been identified experimentally. Structural information was based on the modeling of potentiometric data, not on the observation of the objects, which became possible later by the use of X-ray absorption spectroscopy (XAS) and SAXS [39, 40, 46–51].

The structure and size of iron polymers depends on the hydrolysis ratio  $n = \text{OH}/\text{Fe}$ , time  $t$ , and nature of the anions. At low hydrolysis ratios, two Fe monomers react to form a dimer in which both octahedra share an edge. Mössbauer spectroscopy has shown that, at  $n < 0.5$ , hydrolysis of  $\text{Fe}(\text{NO}_3)_3$  at  $92^\circ\text{C}$  leads to the formation of  $\text{Fe}_2(\text{OH})_2^{4+}$  [52].

Extended edge X-ray absorption fine structure (EXAFS) spectroscopy has revealed the presence of a dimer formed from  $\text{FeCl}_3$  at  $n = 1.5$  and  $t = 10$  min [50], with the two Fe at a distance of  $3.01 \text{ \AA}$ , corresponding to Fe octahedral edge sharing [53]. The dimer could be stabilized by organic ligands such as carboxylates and proteins [45], whereas the growth of Fe species in the absence of ‘stabilizers’ continues with the formation of a trimer (Figure 5.1) [50].

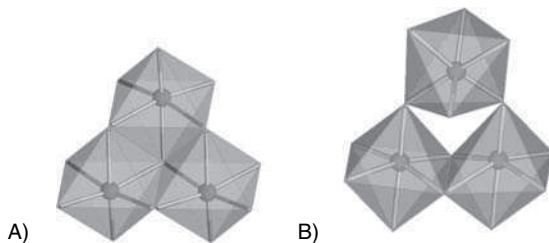


**Figure 5.1** Structure of a planar trimer (A) and a double corner trimer (B) of  $\text{Fe}_3(\text{OH})_4^{5+}$ .

In addition to the trimers, in  $\text{Fe}(\text{NO}_3)_3$  solution, for  $n = 1.5$  and  $t > 1$  h, small polymers are detected with Fe–Fe interatomic distances of  $2.85 \text{ \AA}$ ,  $3.06 \text{ \AA}$ ,  $3.52 \text{ \AA}$  and  $3.95 \text{ \AA}$ , which correspond respectively to face, edge, double corner and single corner sharing between Fe octahedra [51, 53]. The unusual Fe–Fe distance of  $2.85 \text{ \AA}$ , which is characteristic of Fe octahedra with face sharing [47, 53], has also been observed in freshly formed two-line ferrihydrite [54]. When the Fe concentration is in the decimolar range, XAS and SAXS data can be reconciled with models taking into account a limited number of Fe clusters (Figure 5.2). In more dilute solutions ( $[\text{Fe}] < 10^{-4} \text{ M}$ ), the number of edge- and corner-sharing neighbors at  $\text{pH} \sim 2.8$  suggests the formation of small Fe polymers that most likely consist of a mixture of dimers, trimers and tetramers [28]. Tetrameric species with edge and double-corner linkages were also shown to form during  $\text{Cr}^{3+}$  and  $\text{Ga}^{3+}$  hydrolysis [55].

The relevant differences measured in the very first steps of  $\text{FeCl}_3$  and  $\text{Fe}(\text{NO}_3)_3$  hydrolysis are most likely due to the nature and complexing strength of anions. In the early stages of  $\text{FeCl}_3$  hydrolysis, one or two of the six coordination sites in the Fe octahedra are occupied by chloride anions, whereas only OH and  $\text{OH}_2$  ligands

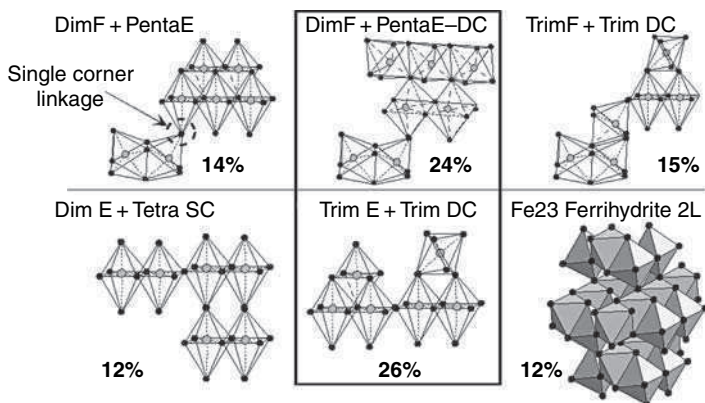


**Figure 5.2** Six possible clusters present in  $\text{Fe}(\text{NO}_3)_3$  solution at  $n = 1.5$ . Dim = dimer, trim = trimer, tetra = tetramer, penta = pentamer, F = Face, E = edge; DC = double corner; SC = single corner. All clusters correspond to substructures of larger minerals. The Fe23 ferrihydrite 2L substructure is described in [54].

are detected in  $\text{Fe}(\text{NO}_3)_3$  solutions. Consequently,  $\text{Fe}(\text{NO}_3)_3$  exhibits more binding possibilities than  $\text{FeCl}_3$ , which likely includes single-corner bonds whose free energy of formation of  $105 \text{ kJ mol}^{-1}$  is lower than that of a double-corner bond [43].

Marked differences between the polymerization mechanisms of  $\text{Fe}(\text{NO}_3)_3$  and  $\text{FeCl}_3$  have also been shown to occur at higher hydrolysis ratios (or times). In the case of  $\text{Fe}(\text{NO}_3)_3$ , the cluster radii increase with hydrolysis ratio [48]. In particular, some authors have suggested that the dodecamer  $\text{Fe}_{12}(\text{OH})_{34}^{2+}$  may form in solutions of  $\text{Fe}(\text{NO}_3)_3$  at  $n > 2.3$  [56], whereas others have postulated the formation of the polycation  $[\text{FeO}_4\text{Fe}_{12}(\text{OH})_{24}(\text{H}_2\text{O})_{12}]^{7+}$  with a structure similar to that of the  $\text{Al}_{13}$  polymer [57]. In contrast, the size of aggregate subunits formed from  $\text{FeCl}_3$  does not appear to vary with the hydrolysis ratio [58]. On the basis of SAXS, EXAFS and Ar adsorption data, it has been suggested that the polymer  $\text{Fe}_{24}\text{O}_{12}(\text{OH})_{32}^{16+}$ , which shows a local structure similar to akaganeite ( $\beta\text{-FeOOH}$ ), can form [50] (Figure 5.3).

### 5.3.2 Diffusion, Aggregation, Fractal and Nonfractal Growth

In contrast to  $\text{FeCl}_3$  hydrolysis, the hydrolysis of  $\text{Fe}(\text{NO}_3)_3$  leads to a more chaotic evolution of Fe polymers and Fe nuclei. Two possible mechanisms have been suggested to explain this observation. The first consists of crystal growth or precipitation based on ion diffusion and includes the following steps [59]: (i) diffusion of  $\text{Fe}(\text{III})$  ions to the surface of the nucleus; (ii) dehydration of Fe at the surface; (iii) adsorption of dehydrated Fe; (iv) diffusion of Fe on the surface to a more energetically favorable position. In contrast to the ion diffusion mechanism, the growth of Fe species appears to be explained better by the aggregation of primary polymers. This second

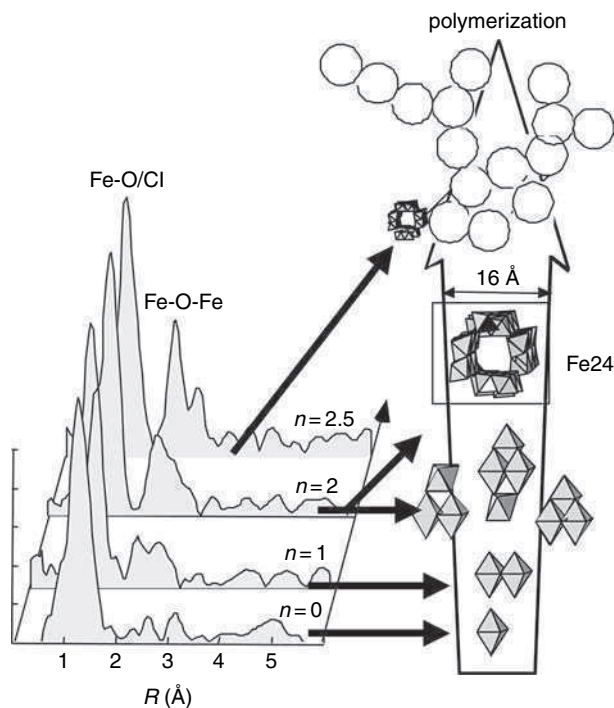


**Figure 5.3** XAS Fe K-edge radial distribution function  $R$  and structural evolution of Fe polycations during hydrolysis in  $\text{FeCl}_3$  solution.

mechanism, i.e. the formation of larger polymers or precipitates, which are generally amorphous at ambient temperatures, has been studied using a fractal approach [48, 58].

In the case of  $\text{FeCl}_3$ , particle sizes measured by photon correlation spectroscopy (PCS) and SAXS [58] decrease with time and increase with  $n$  at a constant time. For example, at  $t = 24$  h, the hydrodynamic radius  $r_H$  of the particles is 12 nm at  $n = 1.5$  and 200 nm at  $n = 2.7$ . Owing to the small size of Fe aggregates, SAXS curves do not show any fractal behavior at  $n = 1$ , whereas suspensions of  $\text{Fe}_{24}$  subunits appear arranged in fractal aggregates at  $n = 2.0$  and  $2.5$  [58]. With increasing  $n$ , the sticking of polycations follows the usual rules of clustering as controlled by van der Waals interactions. An increase to  $n = 3$  causes the formation of precipitates that exhibit a characteristic scattering curve with an apparent fractal dimension of  $D_f = 2$ . In solutions at  $n = 1$ , the polycations feature a highly positive charge and the aggregation mechanism depends on long-range dipolar magnetic interactions with each subunit acting as a dipole that can realign in prevalently linear aggregates. More subunits are formed when  $n$  increases, but the positive charge at the subunit surface decreases, especially at  $n > 2.5$ , i.e. just before the flocculation threshold of the sols. For this

condition, electrostatic repulsion decreases and electrostatic attractive interactions become responsible for the fractal arrangement of colloids. The various steps of  $\text{FeCl}_3$  polymerization are summarized in Figure 5.3.

In the case of  $\text{Fe}(\text{NO}_3)_3$ , aggregates are thought to take up a linear or semi-linear shape at the local range-order that consists of 4–5, 3–4, 7 and 9 subunits for  $n = 1.5$ , 2.0, 2.2 and 2.5 respectively [49]. At  $t < 10$  min, greater branching and polydispersity is observed for  $n = 2.2$  and 2.5, whereas aggregates have a fractal geometry with an apparent fractal dimension of  $D_f = 1.75$  for  $n = 2.8$ , typical of a cluster–cluster aggregation mechanism. Although this value is lower than that measured for  $\text{FeCl}_3$  solutions at  $n = 2.7$  ( $D_f = 2$ ), some authors have suggested that less aggregated and less dense, small particles can form in  $\text{Fe}(\text{NO}_3)_3$  solutions compared with  $\text{FeCl}_3$  solutions [59].

### 5.3.3 The Effect of Strong Competing Ligands: The Case of Phosphate

When in competition with O and OH ligands, the presence of species such as phosphate, silicate, and organic matter is thought to affect the composition, structure, morphology and reactivity of Fe hydrolysis products [60–67].  $\text{PO}_4^{3-}$  ions hinder the hydrolysis of  $\text{Fe}^{3+}$  cations by affecting the size and crystallinity of the particles even at low  $[\text{PO}_4]/[\text{Fe}]$  molar ratios [61]. For example, EXAFS spectra at the Fe K-edge have indicated that, for  $n = 1$  and  $[\text{P}]/[\text{Fe}] \approx 0.2$ , Fe nucleation is extensively blocked at the dimerization step (Figure 5.4) [68] and that Fe–O–P linkages are formed [69]. For  $n = 1.5$ , dimers are the major Fe species (Figure 5.4) with P in the second coordination sphere of Fe at a distance of 3.2–3.3 Å [65, 67]. Binding of phosphate to the Fe dimers inhibits the binding of a third Fe octahedron to the dimer, unlike what occurs in  $\text{FeCl}_3$  solutions. For  $n = 2.0$ , each phosphate is able to bind three Fe dimers [69] in order to form small aggregates with a size of approximately 100–120 Å [58].

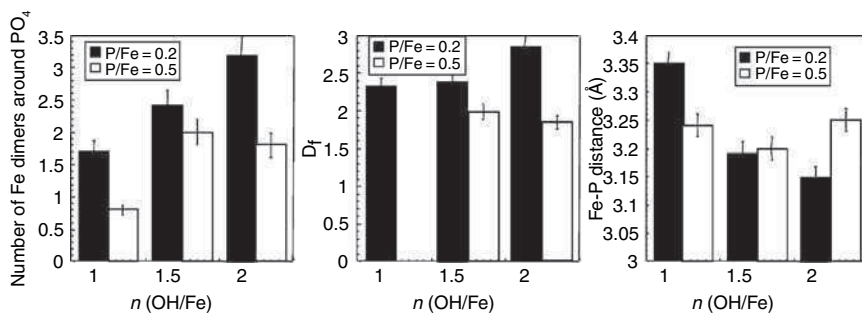


**Figure 5.4** Number of Fe dimers surrounding each phosphate at various  $n$  and  $\text{P/Fe}$  ratios.

The fractal dimensions measured for  $n = 1.0$ , 1.5 and 2.0 are respectively 2.3, 2.4 and 2.85, and do not correspond to any classical aggregation mechanism. Nonetheless, structures tend to become denser and denser as  $n$  increases. At the semi-local



scale, the evolution of  $D_f$  with increasing  $n$  is very well correlated to the structural evolution at the local scale (Figure 5.5). EXAFS analysis indicates that the P–Fe distances decreased progressively from 3.35 to 3.15 Å as  $n$  increased from 1.0 to 2.0. Furthermore, the number of Fe atoms bound to a phosphate tetrahedron also increased with  $n$  without modifying the overall size of the aggregates, thus causing an additional density increase.

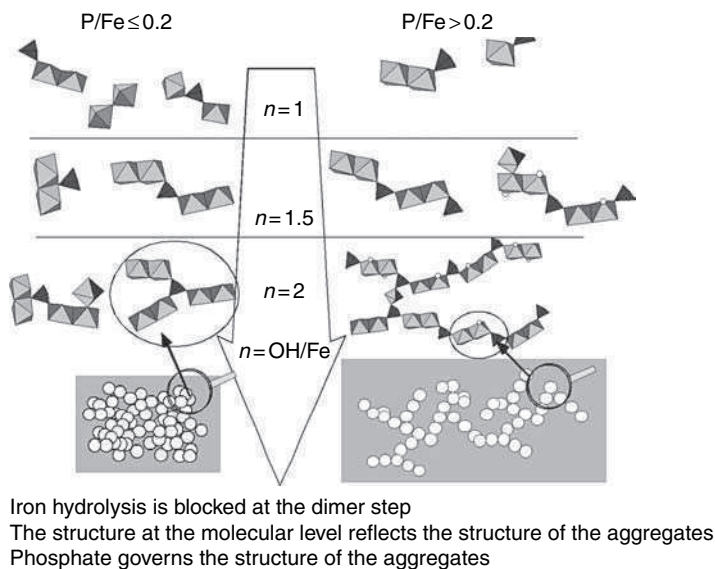


**Figure 5.5** Evolution of the Fe–PO<sub>4</sub> polymers during the hydrolysis of Fe–PO<sub>4</sub> solutions at various P/Fe ratios.

The structure of the system is modified drastically by an increase in the P/Fe ratio to 0.5 (Figures 5.4 and 5.5) [70]. For  $n = 1.5$ , the size of the aggregates is too high ( $>350$  Å) to be measured by SAXS and the fractal dimension is much lower than in the case of  $P/Fe = 0.2$ . The  $D_f$  value corresponds to a cluster–cluster-type aggregation mechanism with a sticking probability lower than unity, which suggests that the aggregates have a branched structure formed by connected subunits of small Fe dimer–PO<sub>4</sub> complexes. For  $n = 2.0$ , as to the opposed to the rapidly settling precipitate that is formed at lower  $P/Fe$ , a gel is generated with more than 80% of the Fe as dimers and the rest as isolated monomers. Similar to the  $n = 1.5$  case, the structure of the  $n = 2.0$  sample is not uniform over the whole  $q$  range. The value of  $D_f = 1.85$  that is measured at high  $q$  is slightly lower than that for  $n = 1.5$  and characteristic of a gel formed by a cluster–cluster aggregation. For  $n = 2.0$ , Fe monomers are thought to form bridges that bind two aggregates together, thus inducing the gelation process and preventing the aggregates from moving freely or approaching each other, leading to a less dense structure. The observation that the structures formed at  $P/Fe = 0.5$



are much more open than those obtained at the same hydrolysis ratio at  $P/Fe = 0.2$  (Figure 5.5) may be due to the difference in stoichiometry of the two sample series. The first reactions that occur, i.e. the condensation of a first and a second Fe dimer onto a phosphate tetrahedron, are the most energetically favorable. Owing to the lower partial charge on the phosphate and to the steric hindrance created by the presence of two dimers, which reduces considerably the accessibility of the unoccupied sites on phosphate tetrahedra, a higher energy barrier must be overcome at  $P/Fe = 0.2$ . At this  $P/Fe$  ratio, the condensation of a third Fe dimer would result in dense structures. At  $P/Fe = 0.5$ , i.e. at a 2.5 times higher amount of phosphate, the probability of forming three dimer–phosphate units becomes even lower, since they are energetically disadvantaged with respect to two dimer–phosphate clusters. Thus, more linear and less dense structures that are characterized by a lower fractal dimension are formed (Figure 5.5).

### 5.3.4 Aggregation/Precipitation in Fe–SiO<sub>4</sub> Systems

#### 5.3.4.1 Effect of Si on Fe crystallization

As Si and Fe are two of the most abundant elements in the Earth's crust, there is a long history of studies describing the interactions between these elements. For example, the first quantitative report of the formation of an  $FeSiO(OH)_3^{2+}$  complex in dilute solution dates to the 1960s [71]. Structural studies of the Fe–Si systems have received much attention and focused mainly on the role of Si on the crystallization of the Fe oxides and oxyhydroxides. In this context, many authors have found that even low levels of Si are likely to affect the size and shape of the Fe–Si precipitates significantly. For example, the presence of Si is shown to hinder the formation of goethite, and lead to the preferential formation of metastable ferrihydrite [61, 72]. Under acidic conditions, SiO<sub>4</sub> is assumed to participate in the aggregation of nanosized (10–20 nm) goethite crystals [73]. Si contents as low as 0.1 mol% are found to delay considerably the dissolution–reprecipitation processes that transform ferrihydrite into goethite [24]. The zero point charge (ZPC) of the surface is displaced towards higher pH in the presence of Si. This effect is consistent with the formation of an Fe–O–SiO<sub>3</sub> complex at the ferrihydrite surface, thus impeding its dissolution and transformation into goethite [74–77]. More recent data obtained over extended pH and Fe/Si ranges suggest that polymeric Si species can form at the surface of ferrihydrite [78]. These Fe–O–Si complexes are also shown to prevent the formation of hematite from ferrihydrite, which typically is favored by heating [79].

Although the above investigations are fundamental in determining to what extent the presence of Si modifies the chemistry of Fe, they generally do not attempt to describe the structure of 'X-ray diffraction (XRD)-invisible' or amorphous Fe species. In addition, the samples generally undergo heating and/or aging processes that favor the formation of crystalline structures. As a consequence, the speciation and structure of fresh Fe–Si phases, for which no organized structure is expected, have long been neglected. Although synchrotron-based SAXS and especially XAS techniques have

gained popularity since the mid 1980s, the structure of freshly prepared Fe–Si systems has been studied only recently [28, 80–82]. These studies cover Fe hydrolysis over a large range of pH, Fe concentrations and Si/Fe molar ratios.

#### 5.3.4.2 Nucleation and growth of Fe–Si species in the first step of hydrolysis

Analyses by Fe K-edge EXAFS show that, at low pH and in large excess of Si (Si/Fe = 5), Fe essentially forms edge-sharing Fe dimers for which each Fe binds one  $\text{SiO}_4$  tetrahedron [28]. In these studies, samples are filtered to eliminate solids that may have formed, and no visible aggregation occurs within the first few hours of aging. The formation of solid phases is observed in more concentrated Fe solutions (e.g.  $[\text{Fe}] = 0.2 \text{ mol l}^{-1}$ ) and at lower Si/Fe ratios. For Si/Fe = 1 and Si/Fe = 2, the analysis of the  $n = 0.5$  sample reveals the presence of monomeric Fe [83]. The formation of edge-sharing dimers is detected at  $n = 1.0$ , but significant amounts of monomeric Fe are still present within the precipitate. These results indicate that Fe speciation in the aggregates is very similar to that observed in solution [28]. However, contrary to the dissolved species, and similar to other systems [84], Si was not found in the local environment of Fe in the precipitates. A significant Fe polymerization is observed by increasing the hydrolysis ratio from  $n = 1$  to  $n = 1.5$ . The total number of neighbors  $N_{\text{tot}}$  detected by EXAFS is higher at Si/Fe = 1 ( $N_{\text{tot}} = 3.11$ ) than at Si/Fe = 2 ( $N_{\text{tot}} = 2.47$ ). This result is mainly due to the higher number of double corner linkages at Si/Fe = 1 ( $N_{\text{DC}} = 1.63$ ) compared with Si/Fe = 2 ( $N_{\text{DC}} = 1.18$ ).

Similar scattering curves are obtained for samples at  $n = 0.5$  and  $n = 1.5$  (Figure 5.6) [83]. Linear domains are present at high  $q$ . For Si/Fe = 1, the slopes of the curves measured between  $q = 0.04 \text{ \AA}^{-1}$  and  $q = 0.20 \text{ \AA}^{-1}$  are  $-1.6$  at  $n = 0.5$  and  $-2.3$  at  $n = 1.5$ , whereas the slopes are  $-1.2$  at  $n = 0.5$  and  $-1.9$  at  $n = 1.5$  for Si/Fe = 2. Although fractal dimensions cannot be derived from these slopes due to the limited  $q$  range and varying  $I_0$ , the slopes can be used to define general trends in the structure of Fe–Si aggregates. Indeed, with an increasing hydrolysis ratio, denser structures are formed, while increasing the concentration of Si lead to more open aggregates.

For  $q$  values lower than  $\sim 0.04 \text{ \AA}^{-1}$ , the scattering curves showed a marked increase in intensity, especially for the systems at  $n = 0.5$ . This effect was also observed for other Fe systems (e.g. chloride, nitrate, phosphate) at  $n = 1.0$  and  $n = 1.5$  [48, 58, 70], which suggests that this feature is not specific to a particular Fe system but can be generally related to a low hydrolysis ratio ( $n < 1.5$ ) [83]. Nonetheless, neither the exact cause(s) nor the influence of the actual structural features on the increased intensity has been elucidated. For this reason, the low  $q$  portion of the scattering curves is generally not considered in the computation of the pair distribution functions  $P(r)$  (Figure 5.7). At  $n = 0.5$ , the first peak of the  $P(r)$  function, which corresponds to the radius of the subunit, is located at almost the same value, i.e.  $r = 6 \text{ \AA}$  for both Si/Fe ratios. The presence of  $6 \text{ \AA}$  clusters can only be explained by formation of Fe monomer– $\text{SiO}_4$  complexes, whose occurrence as dissolved species can be predicted

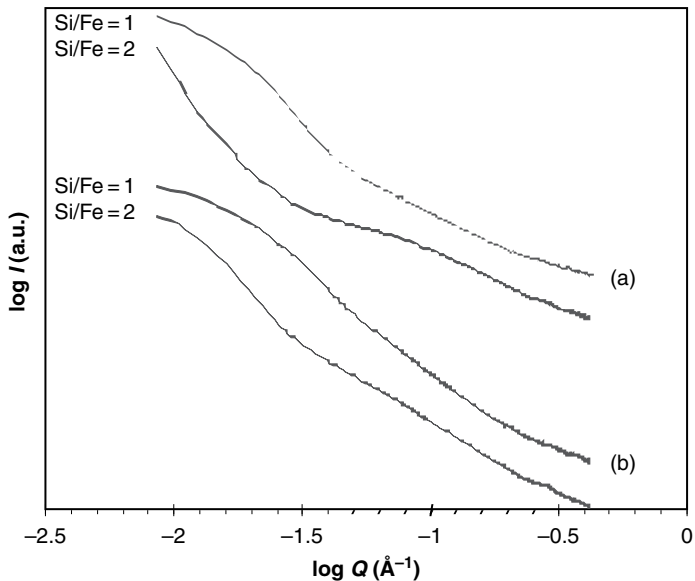


**Figure 5.6** SAXS curves of Fe-SiO<sub>4</sub> colloids obtained at  $n = 0.5$  (a) and  $n = 1.5$  (b). Curves are shifted in intensity for better clarity.

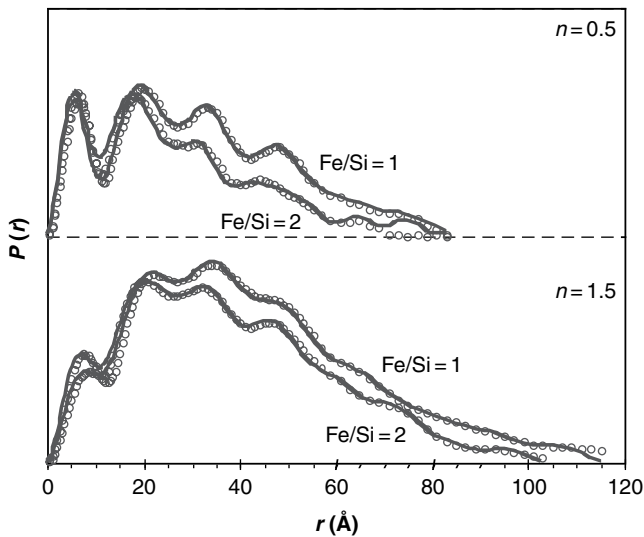


**Figure 5.7** Experimental (full lines) and simulated (circles)  $P(r)$  functions for Fe-SiO<sub>4</sub> colloids obtained at  $n = 0.5$  and  $n = 1.5$

by equilibrium calculations at acidic pH [28]. The presence of Fe–O–Si bonds at such a low  $n$  value (i.e. even before Fe nucleation) is indicative of a high affinity between Fe and SiO<sub>4</sub> ligands. At  $n = 1.5$ , the shift of the first peak of  $P(r)$  towards larger  $r$  values, i.e.  $r = 7.2$  Å (Si/Fe = 1) and  $r = 6.5$  Å (Si/Fe = 2), is consistent with the increased Fe polymerization. The higher  $N_{\text{tot}}$  value for Si/Fe = 1 is correlated with the larger subunit size.

The  $P(r)$  functions are fitted with linear combinations of theoretical curves using roughly spherical subunits [83], the number of which per unit volume increases with increasing  $n$ . This result can be attributed to the presence of denser structures, as suggested from the slopes of the scattering curves. Furthermore, at a fixed  $n$  value, the number of spherical subunits decreases with increasing Si concentration, also as suggested from the slopes. Nonetheless, extreme care should be taken in interpreting these results in terms of structure, because the models do not provide any indication of the nature of bonds between the subunits. Considering the pH conditions, the presence of polymerized Si species that are able to connect Fe subunits is very likely. However, unfortunately, the nature and structure of Si species cannot be determined from SAXS due to the low electron contrast of Si compared with the heavier Fe, making Si ‘invisible’ on the scattering curves.

The influence of SiO<sub>4</sub> and PO<sub>4</sub> on the first steps of hydrolysis ( $n \leq 2$ ) differs greatly, although both ligands have a strong affinity for Fe. PO<sub>4</sub> is shown to block Fe polymerization from the lowest P/Fe ratios and predominantly form Fe dimers in all Fe–P systems at  $n \geq 1.5$  [85, 86]. In contrast, in the presence of SiO<sub>4</sub>, Fe speciation and probably Si speciation varies with  $n$  and with the Si/Fe ratio. Furthermore, larger Fe clusters are formed. Therefore, the similarities in the evolution of aggregate structure that are observed, i.e. a denser structure obtained with increasing  $n$  or a decreasing ratio of ligand/Fe) appear to be purely coincidental.

#### 5.3.4.3 Nature and structure of Fe–Si species at pH $\geq 3$

The speciation and structure of Fe–Si systems have also been examined between pH 3 and 10 at  $n > 3$  and Si/Fe = 0 to 4 [80–82]. Based upon XRD results, the phases that are formed are generally amorphous with only small amounts of poorly crystallized akaganeite detected at pH 3.

The level of Fe polymerization within the aggregates is indicated by  $N_{\text{tot}}$ , i.e. the total number of Fe neighbors around the central Fe atom (Figure 5.8). The  $N_{\text{tot}}$  values are higher in samples without SiO<sub>4</sub>. At all pH values, the presence of SiO<sub>4</sub> results in less polymerized Fe species, i.e.  $N_{\text{tot}}$  decreases markedly from Si/Fe = 0 to Si/Fe = 1, whereas a further excess of Si (up to Si/Fe = 4) leads to an increase of  $N_{\text{tot}}$ . The formation of single and double corner linkages (SC and DC respectively) between Fe ions decreases sharply with the increasing Si/Fe ratio, whereas the evolution of edge (Ed) linkages follows that of  $N_{\text{tot}}$  (Figure 5.8). These results suggest that the growth regime of the Fe species is dependent on the Si/Fe ratio. At low Si concentrations (Si/Fe  $\leq 0.5$ ), the presence of both edge and corner linkages is consistent with

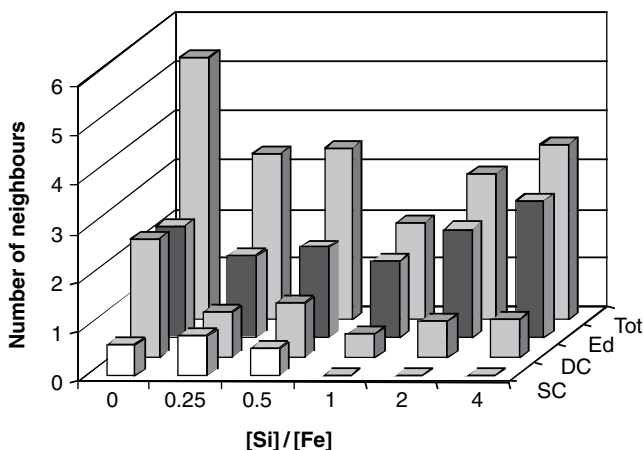


**Figure 5.8** Number of Fe neighbors around the central Fe ion as a function of the Si/Fe ratio at pH 3. SC: single corner; DC: double corner; Ed: edge; Tot: total.

the formation of three-dimensional structures, whereas the predominance of edge linkages at  $\text{Si}/\text{Fe} > 1$  suggests a two-dimensional growth.

Some information on Si speciation can be provided by Fourier transform infrared (FTIR) analysis in the spectral region between  $800$  and  $1300\text{ cm}^{-1}$ . A simultaneous increase of the absorption bands at  $930\text{ cm}^{-1}$  (Si–O–Fe) and at  $800\text{ cm}^{-1}$  and  $1300\text{ cm}^{-1}$  (symmetric and asymmetric Si–O–Si stretching respectively) is observed. Si polymerization increases with increasing Si and decreases with increasing pH, due to the higher solubility of Si at  $\text{pH} \geq 7$  [81]. Despite the presence of Fe, for samples with the highest Si polymerization level, i.e.  $\text{Si}/\text{Fe} = 4$  at pH 3 and pH 5 and  $\text{Si}/\text{Fe} = 2$  at pH 3, detection of  $^{29}\text{Si}$  by NMR at about  $-100\text{ ppm}$  indicated the presence of Fe-free domains within the samples [81].

Information on the spatial arrangement of Si within these silica pockets can be obtained by measuring the magnetization  $S$  as a function of time. Indeed,  $S(t)$  scales as  $(Ct)^{\beta/6}$  or  $t^\alpha$ , where  $C$  is a constant and  $\beta$  is the dimensionality of the spin system. The slopes of the  $\log S(t)$  versus  $\log t$  plots yielded an average value of  $\beta = 2.2$ . Si K-edge EXAFS data can provide additional details on Si speciation in these systems, but they are often difficult to interpret.

In agreement with XRD results, the absence of correlation peaks in SAXS curves (Figure 5.9) indicates the presence of amorphous and disordered Fe–SiO<sub>4</sub> aggregates. All curves display a linear portion for  $q < 0.075\text{ Å}^{-1}$  (Figure 5.9), but since  $I_0$  is not determined, only apparent fractal dimensions can be derived from the slopes measured in this  $q$  range (Table 5.1). Nonetheless, given that the subunits are small, the influence of  $I_0$  on the low  $q$  part of the SAXS curves is expected to be minimal; therefore, the apparent fractal dimensions derived from the  $\log I(q)$  versus  $\log q$  plots are considered to be good estimates of the rigorous values of  $D_f$ . Hereafter,

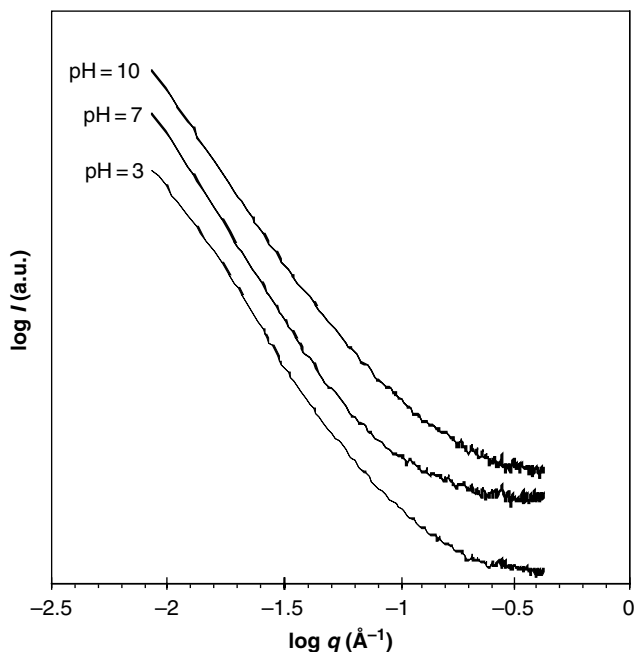


**Figure 5.9** SAXS curves of Fe-SiO<sub>4</sub> aggregates at pH  $\geq 3$ .

**Table 5.1** Fractal dimension of Fe-SiO<sub>4</sub> aggregates at pH  $\geq 3$ .

	pH 3	pH 7	pH 10	pH 7 (aged)
Si/Fe = 0.5	1.98	2.36	2.44	2.19
Si/Fe = 1.0	2.70	2.56	2.35	2.39
Si/Fe = 2.0	2.36	2.53	2.62	2.36

fractal dimensions determined in this manner are referred to as *apparent* fractal dimensions.

The high  $D_f$  values of all Fe-Si samples (Table 5.1) suggests the presence of dense structures consistent with a ligand-driven aggregation mechanism, as is the case for similar Fe- or Al-ligand systems [14, 70, 86, 87]. Since the scattering of Fe-Si systems is dominated by the heavier Fe species, data for both the ‘Fe structure’ ( $D_f = 2.36$ ) and the ‘Si structure’ ( $D_f = 2.2$ ) are only available for the sample with Si/Fe = 2 at pH 3. No correlation was found between the growth regime of Fe species and their semi-local-scale arrangement. Actually, the two-dimensional Fe species at Si/Fe = 2.0 form denser structures than the three-dimensional Fe clusters at Si/Fe = 0.5. For these two Si/Fe ratios, the increase of fractal dimension with pH was attributed to the denser

packing of Fe species favored by the decrease of size measured for Si polymers. On the contrary, at Si/Fe = 1, the observed depolymerization of Si at high pH resulted in lower  $D_f$  values.

The evolution of  $D_f$  is not only dependent on  $\text{SiO}_4$  speciation [82], but also on Fe speciation, i.e.  $D_f$  decreases linearly with increasing Fe polymerization ( $N_{\text{tot}}$ ; Figure 5.10). The semi-local structure of the Fe–Si aggregates is controlled by Fe complexation (presumably on the corner sites) by  $\text{SiO}_4$ , which causes dense aggregation and results in almost all  $D_f$  values being above 2.2.

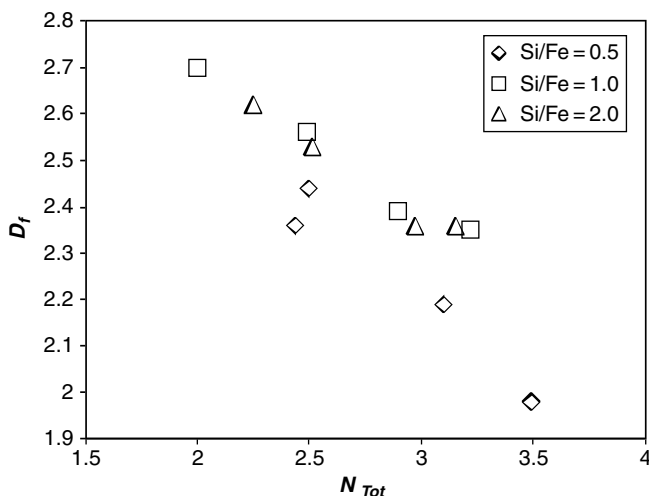


**Figure 5.10** Evolution of  $D_f$  with Fe polymerization  $N_{\text{tot}}$  for Fe– $\text{SiO}_4$  aggregates at  $\text{pH} \geq 3$ .

### 5.3.5 General Remarks

The examples of the Fe– $\text{PO}_4$  and Fe– $\text{SiO}_4$  systems illustrate well some general findings about the local and semi-local structure of metal–ligand aggregates. While the hydrolysis of metal cations yields phases of well-defined structure at equilibrium, the same process in the presence of ligands only rarely results in the formation of organized solids, even after appropriate heating/aging. The presence of the ligands delayed or inhibited the crystallization process. On a local scale, the polymerization of the metal cation was hindered by ligand complexation at its growth sites. In addition, ligand-induced depolymerization of already-formed metal species could be observed [88]. The structure of aggregates at the semi-local scale was also very sensitive to the presence of ligands. While classical diffusion-limited cluster aggregation was observed in their absence, a dense aggregation of metal monomers and polymers by ligand-driven bridging and/or charge screening was observed in their presence.

Although the measurement of the fractal dimension of an aggregate can be performed with various imaging, scattering and settling techniques [89], the options available for the characterization of the semi-local-scale order (i.e. up to approximately 1000 Å) are limited to a few microscopic and scattering methods. Although imaging techniques such as transmission electron microscopy (TEM), scanning electron microscopy (SEM), and atomic force microscopy (AFM) are very versatile, they suffer from poor statistics, sample opacity, and poor transfer of information obtained in two dimensions to three-dimensional aggregates. Thus, X-ray scattering represents the main analytical tool for determining  $D_f$  in this size range. Although scattering in heterogeneous systems is dominated by the heavier elements and no direct information about the arrangement of the lighter elements can be derived from SAXS data, the structural information provided by SAXS in the case of metal–ligand aggregates remains very valuable.

Aggregate fractal dimensions measured by SAXS are often significantly larger than two. When interpreting the evolution of  $D_f$  with pH and/or ligand concentration, two typical situations must be considered: (a) metal speciation remains relatively unaffected by modifications of pH and/or ligand concentrations (and typically consists of monomers and oligomers, e.g. Fe–PO<sub>4</sub>); (b) metal speciation evolves with experimental conditions (e.g. Fe–SiO<sub>4</sub>). In the first case, the scattering centers remain constant and variations of the fractal dimension reflect changes in ligand chemistry and/or structure. In the second case, although the ligand chemistry and structure still affect the overall density of the aggregate and the corresponding fractal dimension, structural changes in the size and shape of metal species, to which scattering is very sensitive, will dominate the signal and control, to a large extent, the evolution of  $D_f$ . These trends are obvious only where an adequate difference in atomic number exists between the metal cation and the ligand (e.g. Fe–P, Fe–Si, Al/Fe–C). Where the metal and ligand produce similar electron contrast (e.g. Al–Si) [13, 90], additional data from independent techniques may be required to interpret structural data correctly.

## 5.4 FRACTAL DIMENSIONS OF VERY LARGE FLOCS BUILT WITH MICROSIZED UNITS

A rapid and accurate determination of aggregate structure is desirable for understanding particle aggregation processes that occur in freshwater and marine environments, in water and wastewater treatment plants and for modeling various environmental phenomena [9, 91–94]. Among the techniques used for the optical determination of structural parameters [95–99], light scattering is certainly one of the most powerful for studying the evolution of the structure of large aggregates that are formed of units in the submicrometre size range. The relatively few studies that use light scattering in this context have used both numerical simulation and an experimental validation of the optical properties of well-known colloids.



### 5.4.1 Numerical Simulations

Some authors [19, 100–102] have tentatively calculated the mean optical contrast of scatterers within different computer-generated aggregates. More recently [101], using the approach described in Section 5.2 [19], and the same definition for the mean optical contrast generated by the presence of neighboring particles around a central particle within a fractal aggregate, the influence of the physical parameters  $R_g$  and  $D_f$  has been tested on computer-generated fractal aggregates with  $D_f > 2.0$ .

#### 5.4.1.1 The influence of $D_f$ on the $m/\overline{m}$ ratio

For fractal dimensions close to two, an observed decrease of the scatterers' high mean optical contrast  $m/\overline{m}$  with increasing fractal dimension (Figure 5.11) can be explained by the increasing number of neighbors around the scatterer. For  $D_f > 2$ , the scatterers' mean optical contrast is constant and tends towards the value of 1.05, which suggests that the scatterers are embedded in a compact structure. For  $D_f > 2.3$ , scattering is small and the mean optical contrast is constant and close to unity. In this range of  $D_f$  values, the average number of close neighbors around the scatterers is nearly constant and the neighbors exert a dominant influence on the scattering behavior of a particle within an aggregate.

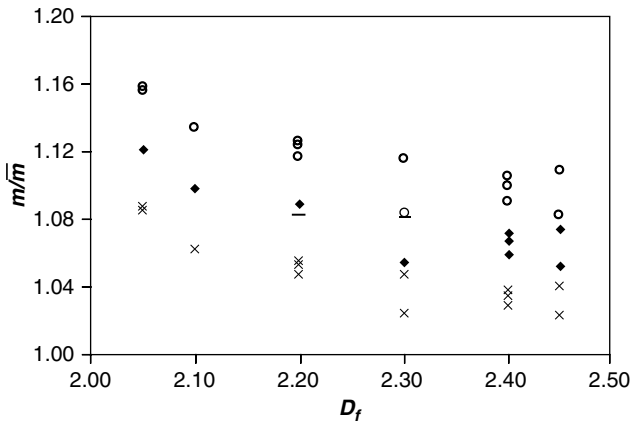


**Figure 5.11** Scatterers' mean optical contrast  $m/\overline{m}$  as a function of the fractal dimension  $D_f$  of aggregates made of 250 primary particles: ( $\circ$ ) extinction values; ( $\times$ ) scattering values; ( $\blacklozenge$ ) mean scattering and extinction values; ( $-$ ) mean values for aggregates that do not fit accurately the fractal model. Reproduced by permission of Elsevier.

The slope of the plot of the scatterers' mean optical contrast as a function of  $D_f$  can be explained by the evolution of the neighbors' local concentration around the scatterers. In an infinite fractal aggregate, the number of neighbors  $n_{\text{inf}}$  surrounding a particle at a distance  $r_{\text{inf}}$  (below which multiple scattering is important) is proportional

to  $(r_{\text{inf}}/r_s)D_f$ . One can assume that  $m/\bar{m}$  evolves with the possible multiple scattering paths  $p_{\text{ms}}$ :

$$p_{\text{ms}} = 1 + n_{\text{inf}} + n_{\text{inf}}^2 + n_{\text{inf}}^3 + \cdots + n_{\text{inf}}^x \quad (5.9)$$

where  $x$  is the multiple scattering order. When  $p_{\text{ms}}$  increases,  $m/\bar{m}$  decreases. According to Equation (5.9),  $1/p_{\text{ms}}$  decreases less quickly at high fractal dimensions than it does at low fractal dimensions. Thus, even if it is impossible to explain the decrease of  $m/\bar{m}$  with  $D_f$  precisely, the trends are consistent with the theoretical expectations.

#### 5.4.1.2 The influence of $R_g$ on the $m/\bar{m}$ ratio

The evolution of the  $m/\bar{m}$  ratio as a function of  $R_g$  for five sets of aggregates with 50, 100, 150, 200 and 250 subunits is shown in Figure 5.12. Circles have diameters that are proportional to the fractal dimension. For each set of aggregates,  $m/\bar{m}$  increases with  $R_g$ , which in turn decreases with increasing fractal dimension. The  $R_g$  value can thus be used to characterize the aggregate structure. It would appear that whatever the number of monomers in an aggregate, variations of the scatterers' mean optical contrast depend on the mean environment of the scatterers.

Although determination of the form factor  $\bar{I}_{r_s, n_s/\bar{n}}(q)$  depends on  $R_g$  and  $D_f$ , an increase in the number of subunits  $N$  appears to cause variations in the mean optical

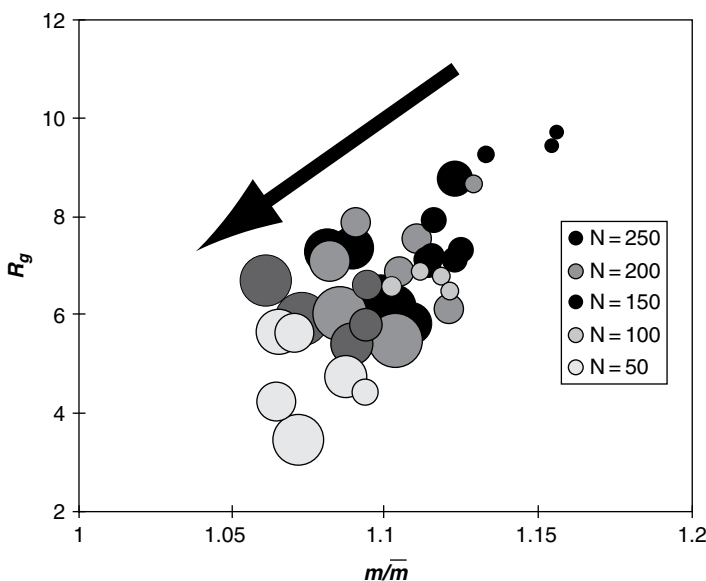


**Figure 5.12**  $R_g$  versus  $m/\bar{m}$  for aggregates of  $N$  primary particles. The circle diameters are directly proportional to the aggregate fractal dimensions  $D_f$ . Reproduced by permission of Elsevier.

contrast when the fractal geometry is not strictly consistent, in contrast to theoretical predictions. The scatterers' mean optical contrast increases slowly with  $N$ , independent of the fractal dimension [12, 103]. Structural changes and an evolution of the aggregate size do not influence the mean optical contrast in the same way, i.e. an increase in size slightly increases the mean optical contrast, whereas an increase in fractal dimension causes the optical contrast to decrease. The difference in the two behaviors is more pronounced when the fractal dimension is low. In the case of aggregation kinetics, both size and structure of the aggregates change during the reaction. In summary, the scatterers' mean optical contrast can provide useful information on aggregate size and structure.

#### 5.4.2 Experimental Validation

The concepts developed above have been tested experimentally with suspensions of latex beads [103]. From light-scattering experiments, the experimental scattered intensity  $I_{\text{exp}}(\theta)$  has been normalized for the number of scatterers:

$$I_{\text{norm}}(\theta) = I_{\text{exp}}(\theta) \frac{V_s}{\phi V_{\text{cell}}} = \frac{I_{\text{exp}}(\theta)}{N_s} \quad (5.10)$$

where  $V_s$  is the volume of the primary scatterer,  $\phi$  is the volume fraction of scatterers in the suspension,  $V_{\text{cell}}$  is the scattering volume and  $N_s = \phi V_{\text{cell}}/V_s$  is the number of scatterers in the scattering volume. The magnitude of scattering vector  $q$ , is related to the maximum interference distance  $d$  by

$$qd = \pi \quad (5.11)$$

At large  $q$  values,  $S(q)$  tends towards unity ( $1/q \ll r_s$ ) and variations of the scattering intensity  $I_{\text{norm}}(q)$  are essentially due to form factor changes. In order to follow these changes, the largest available  $q$  that is associated with an interference distance  $d$  that is smaller than the monomer diameter has been selected. The intensity at this particular angle is given by

$$I_{\text{norm}}(\theta_s) = \frac{I_{\text{exp}}(\theta)}{N_s} \quad (5.12)$$

A numerical model is used to compute the scattered intensity  $I_{\text{num}}(\theta)$  according to Mie theory. At the lowest volume fraction,  $I_{\text{num}}(\theta_s)$  fits  $I_{\text{norm}}(\theta_s)$  and no multiple scattering arises, such that the evaluation of parameters for the numerical model is straightforward. The mean optical contrast is adjusted to compute the normalized theoretical values  $I_{\text{num}}(\theta_s)$  so as to fit the variation of  $I_{\text{norm}}(\theta_s)$  as a function of  $\phi$ . It is then possible to calculate the value of the mean optical contrast by fitting the form factor.

From a kinetic point of view, the value of the mean optical contrast can be obtained at each step of the aggregation process. In addition, from the correlation between the mean optical contrast and the aggregate structure that is established by numerical simulation, it is possible to determine aggregate structure at each aggregation stage.

Figure 5.13 shows the evolution of the  $m/\bar{m}$  ratio as a function of the volume fraction  $\phi$  for  $4 \times 10^{-6} \leq \phi \leq 1.4 \times 10^{-5}$  and for an optical contrast  $n_s/n_m = 1.2$ . In this case, the theoretical result is in very good agreement with the normalized experimental scattered intensities. At  $\phi \leq 10^{-6}$ , Mie theory is in good agreement with the experimental data and it is thus reasonable to conclude that multiple scattering is insignificant. At  $\phi > 1.4 \times 10^{-5}$ ,  $m/\bar{m}$  decreases as  $\phi$  increases.

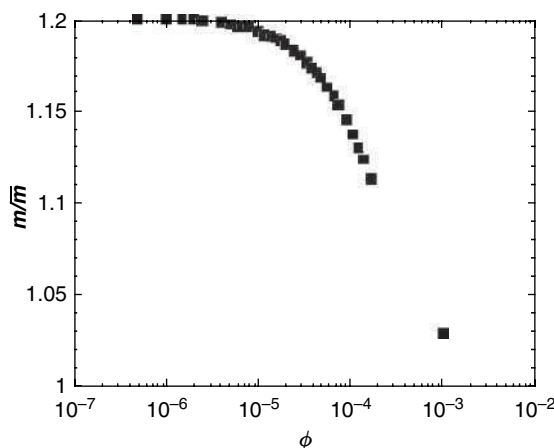


**Figure 5.13** Evolution of  $m/\bar{m}$  with the volume fraction  $\phi$ . Reproduced by permission of Elsevier.

For aggregates of latex beads, the normalized intensity  $I_{\text{norm}}(\theta)$  decreases as a function of the scattering angle in the high  $q$  range. Figure 5.14 shows the normalized scattering intensities for a velocity gradient  $G$  of  $63 \text{ s}^{-1}$  [98]. During aggregation, the local average number of neighbors around the scatterer increases. As previously observed (Figure 5.13), the increased concentration of local scatterers is associated with a decrease of normalized scattered intensity  $I_{\text{norm}}(\theta)$  at large angles. Using the mean field approximation [19], it is possible to associate a mean optical contrast [101] with each aggregation step. Using the same data treatment procedure as was applied to latex beads in suspension, the normalized scattering intensity at the angle  $\theta_s$  (or  $q_s$ ) can be used to extract the value of the mean optical contrast  $m/\bar{m}$  which best fits  $I_{\text{norm}}(\theta_s)$  values.

When the mean optical contrast  $m/\bar{m}$  is known, it is possible to compute the form factor  $\bar{I}_{rs, n_s/\bar{n}}(q)$  by taking into account the mean environment of scatterers in the aggregate. In such a case, fractal dimensions can be calculated from the established correlation [101] and an experimental structure factor  $S_{\text{exp}}(q)$  can be extracted. As aggregation proceeds, the variation of  $D_f$  can be plotted as a function of the  $m/\bar{m}$  ratio. This procedure allows the calculation of fractal dimension for a scattering-angle range at which the scattering intensity is not ‘polluted’ by the aggregate size distribution.

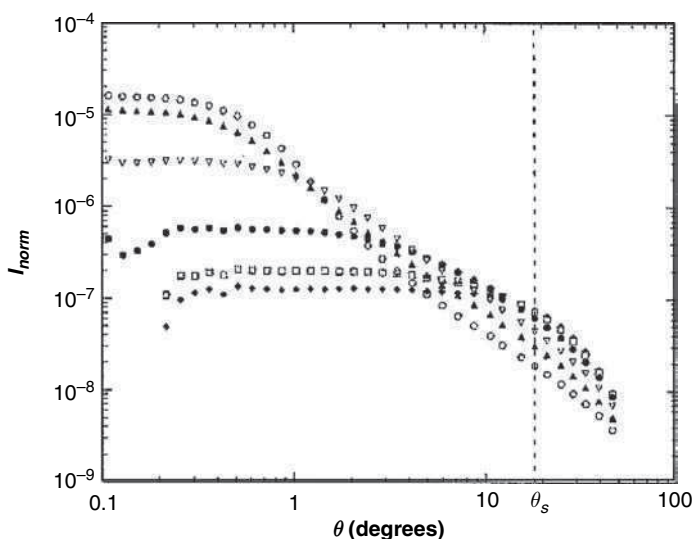


**Figure 5.14**  $I_{\text{norm}}(\theta)$  at different aggregation times: ( $\blacklozenge$ )  $t = 60$  s, ( $\square$ )  $t = 300$  s, ( $\bullet$ )  $t = 840$  s, ( $\nabla$ )  $t = 1440$  s, ( $\blacktriangle$ )  $t = 2040$  s, ( $\circ$ )  $t = 3600$  s. Reproduced by permission of Elsevier.

In the intermediate  $q$  range, the  $S_{\text{exp}}(q)$  slope changes during aggregation as a result of the scatterers' arrangement inside the aggregates and as a function of the scatterers' mean optical contrast and aggregate size distribution. The detailed evolution of the slope is due to a combination of the size polydispersity and structure of the aggregates [103, 104].

## 5.5 CONCLUSIONS AND RECOMMENDATIONS

The processes at the origin of aggregation in environmental media are complex. Hydrolysis, surface complexation and adsorption occur, sometimes in opposition. Complexation can limit hydrolysis and growth, producing subunits in the nano-size range, which often results in the formation of fractal aggregates. The mesoscale structure is largely dependent on molecular-scale arrangements, as was discussed for the Fe- $\text{PO}_4$  or Fe- $\text{SiO}_4$  systems. The structural characterization of such systems requires the use of different experimental approaches in the nanoscale and mesoscale size ranges. In particular, EXAFS and SAXS techniques have demonstrated a close relationship between the structure of complexes formed between  $\text{PO}_4$  and Fe atoms and the fractal dimension. In particular, when the number of  $\text{PO}_4$  units increases around the central Fe, the fractal dimension also increases.

The structure of nano- and meso-scale systems is now well understood. The characterization of large (much greater than micrometer) aggregates formed of

micrometer-sized subunits using spectroscopy (e.g. light scattering) is not trivial. The necessity to have fast and reliable measurements of the structure and/or size distribution is of high interest. Recent work has shown that data should be revised in the light of this new approach. The good agreement between the structural values calculated from surface quasi-elastic light scattering and classical light scattering demonstrates that the fractal dimension can be determined from large angle static light scattering measurements. Both techniques allow the non-destructive, rapid (less than 30 minutes per sample), *in situ* structural determination of fractal aggregates. Nevertheless, structural information can only be extracted in cases where the nature and shape of the subunits are well known.

### LIST OF ABBREVIATIONS AND SYMBOLS

EXAFS	extended X-ray absorption fine structure
NMR	nuclear magnetic resonance
PCS	photon correlation spectroscopy
SAXS	small-angle X-ray scattering
XAS	X-ray absorption spectroscopy
XRD	X-ray diffraction
ZPC	zero point of charge
$d$	interference distance
$D_f$	fractal dimension
$D_T$	translational diffusion coefficient
$F(q)$	form factor
$g(r)$	first order of the auto-correlation function
$I(q)$	Scattering intensity versus the moment of the wave vector $q$
$I_N(q)$	normalized by $N$ (number of dispersed particles) of $I(q)$
$I_{\text{num}}(\theta)$	numerical intensity
$I_{\text{exp}}(\theta)$	experimental intensity $I$
$m = n_s/n_m$	initial optical contrast
$\bar{n}$	mean optical index
$n_m$	optical index of the medium
$n_s/\bar{n}$	scatterers' mean optical contrast
$N_{\text{tot}}$	total number of Fe neighbors
$V_s$	primary scatterer volume
$V_{\text{cell}}$	scattering volume
$P(r)$	autocorrelation function
$q$	moment of the wave vector $\mathbf{q} = 4\pi \sin \theta/\lambda$
$r$	distance
$r_H$	hydrodynamic radius
$r_s$	radius of the subunit
$R$	radius

$S(q)$	structure factor or interference function
$V$	volume
$\phi$	volume fraction of scatterers
$\gamma(r)$	pair-correlation function
$\lambda$	wavelength of the incident beam
$2\theta$	scattering angle

## REFERENCES

- [1] Mandelbrot, B. (1982). *The Fractal Geometry of Nature*. W.H. Freeman, New York.
- [2] Meakin, P. (1984). Computer simulation of cluster-cluster aggregation using linear trajectories: results from three-dimensional simulations and a comparison with aggregates formed using Brownian trajectories. *J. Colloid Interface Sci.*, **102**, 505–512.
- [3] Meakin, P. and Jullien, R. (1988). The effects of restructuring on the geometry of clusters formed by diffusion-limited, ballistic, and reaction-limited cluster cluster aggregation. *J. Chem. Phys.*, **89**, 246–250.
- [4] Vicsek, T. (1989). *Fractal Growth Phenomena*. World Scientific, London.
- [5] Meakin, P. (1990). The effects of attractive and repulsive interactions on 3-dimensional reaction-limited aggregation, *J. Colloid Interface Sci.*, **134**, 235–244.
- [6] Li, D. and Ganczarczyk, J.J. (1990). Structure of activated sludge flocs. *Biotechnol. Bioeng.*, **35**, 57–65.
- [7] Li, D. and Ganczarczyk, J.J. (1991). Size distribution of activated sludge flocs. *Res. J. Water Pollut. Cont. Fed.*, **63**, 806–814.
- [8] Zartarian, F., Mustin, C., Villemin, G., Ait-Ettager, T., Thill, A., Bottero, J.Y., Mallet, J.L. and Snidaro, D. (1997). Three-dimensional modeling of an activated sludge floc. *Langmuir*, **13**, 35–40.
- [9] Lambert, S., Moustier, S., Dussouillez, P., Barakat, M., Bottero, J.Y., Petit, J.L. and Ginestet, P. (2003). Analysis of the structure of very large bacterial aggregates by small-angle multiple light scattering and confocal image analysis, *J. Colloid Interface Sci.*, **262**, 384–390.
- [10] Bottero, J.Y., Tchoubar, D., Axelos, M.A.V., Quienne, P. and Fiessinger, F. (1990). Flocculation of silica colloids with hydroxy aluminum polycations. Relation between floc structure and aggregation mechanisms. *Langmuir*, **6**, 596–602.
- [11] Masion, A., Vilgé-Ritter, A., Rose, J., Stone, W.E.E., Teppen, B.J., Rybacki, D. and Bottero, J.Y. (2000). Coagulation-flocculation of natural organic matter with Al salts: speciation and structure of the aggregates. *Environ. Sci. Technol.*, **34**, 3242–3246.
- [12] Johnson, C.P., Li, X. and Logan, B.E. (1996). Settling velocities of fractal aggregates. *Environ. Sci. Technol.*, **30**, 1911–1918.
- [13] Adachi, Y. and Tanaka, Y. (1997). Settling velocity of an aluminium-kaolinite floc. *Water Res.*, **31**, 449–454.
- [14] Veerapaneni, S. and Wiesner, M.R. (1994). Particle deposition on an infinitely permeable surface dependence of deposit morphology on particle size. *J. Colloid Interface Sci.*, **162**, 110–122.
- [15] Derjaguin, B.V. (1934). Friction and adhesion. IV. The theory of adhesion of small particles. *Kolloid Z.*, **69**, 155–164.
- [16] Derjaguin, B.V. and Landau, L. (1941). Theory of the stability of strongly charged lyophobic sols and the adhesion of strongly charged particles in solution of electrolytes. *Acta Physicochim. URSS*, **14**, 1386–1399.

- [17] Verwey, E.J.W. and Overbeek, J.T.G. (1948). *Theory of the Stability of Lyophobic Colloids*. Elsevier, Amsterdam.
- [18] Vicsek, T. (1983). Fractal models for diffusion controlled aggregation. *J. Phys. A: Math. Gen.*, **16**, L647–L652.
- [19] Botet, R., Rannou, P. and Cabane, M. (1997). Mean-field approximation of Mie scattering by fractal aggregates of identical spheres. *Appl. Opt.*, **36**, 8791–8797.
- [20] Xu, Y.L. (1995). Electromagnetic scattering by an aggregate of spheres. *Appl. Opt.*, **34**, 4573–4588.
- [21] Botet, R., Rannou, P. and Cabane, M. (1995). Sensitivity of some optical-properties of fractals to the cutoff functions. *J. Phys. A: Math. Gen.*, **28**, 297–316.
- [22] Buffle, J. (1993). Sampling and characterization of environmental particles. In *Environmental Particles*, Vol. 2, Buffle, J. and VanLeeuwen, H. P. (eds). Lewis, Chelsea, pp. 5–74.
- [23] Brinker, C.J. and Sherer, G.W. (1990). *Sol–Gel Science. The Physics and Chemistry of Sol–Gel Processing*. Academic Press, San Diego, CA.
- [24] Cornell, R.M. and Schwertmann, U. (1996). *The Iron Oxides Structure, Properties, Reactions, Occurrence and Uses*. VCH, New-York.
- [25] Jolivet, J.P., Livage, J. and Henry, M. (2000). *Metal Oxide Chemistry and Synthesis: From Solution to Oxide*. John Wiley & Sons, Ltd, Paris.
- [26] VonGunten, U. and Schneider, W. (1991). Primary products of the oxygenation of iron(II) at an oxic–anoxic boundary: nucleation, aggregation and aging. *J. Colloid Interface Sci.*, **145**, 127–139.
- [27] Schwertmann, U., Friedl, J. and Stanjek, H. (1999). From Fe(III) ions to ferrihydrite and then to hematite. *J. Colloid Interface Sci.*, **209**, 215–223.
- [28] Pokrovski, G.S., Schott, J., Farges, F. and Hazemann, J.L. (2003). Iron(III)–silica interactions in aqueous solution: insights from X-ray absorption fine structure spectroscopy. *Geochim. Cosmochim. Acta*, **67**, 3559–3573.
- [29] Sherman, D.M. and Randall, S.R. (2003). Surface complexation of arsenic(V) to iron(III) (hydr)oxides: structural mechanism from ab initio molecular geometries and EXAFS spectroscopy. *Geochim. Cosmochim. Acta*, **67**, 4223–4230.
- [30] Sigg, L. (1985). Metal transfer mechanisms in lakes; the role of settling particles. In *Chemical Processes in Lakes*, Stumm, W. (ed.). John Wiley & Sons, Ltd, New York, pp. 283–310.
- [31] Manceau, A. (1995). The mechanism of anion adsorption on iron oxides: evidence for the bonding of arsenate tetrahedra on free Fe(O, OH)<sub>6</sub> edges. *Geochim. Cosmochim. Acta*, **59**, 3647–3653.
- [32] Manceau, A., Schlegel, M.L., Musso, M., Sole, V.A., Gauthier, C., Petit, P.E. and Trolard, F. (2000). Crystal chemistry of trace elements in natural and synthetic goethite. *Geochim. Cosmochim. Acta*, **64**, 3643–3662.
- [33] Rose, J., Vilgé, A., Olivie-Lauquet, G., Masion, A., Frechou, C. and Bottero, J.Y. (1998). Iron speciation in natural organic matter colloids. *Colloids Surf. A: Physicochem. Eng. Aspects*, **136**, 11–19.
- [34] Buffle, J., Vitre, R.R.D., Perret, D. and Leppard, G.G. (1989). Physico-chemical characteristics of a colloidal iron phosphate species formed at the oxic–anoxic interface of a eutrophic lake. *Geochim. Cosmochim. Acta*, **53**, 399–408.
- [35] Waite, T.D. (2002). Challenges and opportunities in the use of iron in water and wastewater treatment. *Rev. Environ. Sci. Biotechnol.*, **1**, 9–15.
- [36] Emmenegger, L., Schonenberger, R.R., Sigg, L. and Sulzberger, B. (2001). Light-induced redox cycling of iron in circumneutral lakes. *Limnol. Oceanogr.*, **46**, 49–61.
- [37] Price, N.M. and Morel, F.M.M. (1998). Biological cycling of iron in the ocean. In *Metal Ions in Biological Systems*, Vol. 35, Sigel, A. and Sigel, H. (eds). Marcel Dekker, New York, pp. 1–36.



- [38] Barbeau, K., Rue, E.L., Bruland, K.W. and Butler, A. (1991). Photochemical cycling of iron in the surface ocean mediated by microbial iron(III)-binding ligands. *Nature*, **413**, 409–413.
- [39] Leprince, A., Fiessinger, F. and Bottero, J.Y. (1984). Polymerized iron chloride: an improved inorganic coagulant. *J. Am. Water Wks Assoc.*, **76**, 93–97.
- [40] Tchoubar, D. and Bottero, J.Y. (1996). Nucleation–growth in non-equilibrium conditions of Al and Fe(III) oxide–hydroxide nanophases. *C.R. Acad. Sci. Paris*, **322**, 523–534.
- [41] Dousma, J. and DeBruyn, P.L. (1976). Hydrolysis–precipitation studies of iron solutions. I. Model for hydrolysis and precipitation from Fe(III) nitrate solutions. *J. Colloid Interface Sci.*, **56**, 527–539.
- [42] Flynn, C.M. (1984). Hydrolysis of inorganic iron(III) salts. *Chem. Rev.*, **84**, 31–41.
- [43] Henry, M., Jolivet, J.P. and Livage, J. (1992). Aqueous chemistry of metal cations: hydrolysis, condensation and complexation. In *Structure and Bonding*, Vol. 77, Reisfeld, R. and Jorgensen, C.K. (eds). Springer Verlag, Berlin, pp. 154–206.
- [44] Schneider, W. (1984). Hydrolysis of iron(III) – chaotic olation versus nucleation. *Comments Inorg. Chem.*, **3**, 205–223.
- [45] Schneider, W. (1988). Iron hydrolysis and the biochemistry of iron – the interplay of hydroxide and biogenic ligand. *Chimia*, **42**, 9–20.
- [46] Combes, J.M., Manceau, A., Calas, G. and Bottero, J.Y. (1989). Formation of ferric oxides from aqueous solutions: a polyhedral approach by X-ray absorption spectroscopy. I. Hydrolysis and formation of ferric gels. *Geochim. Cosmochim. Acta*, **53**, 583–594.
- [47] Combes, J.M., Manceau, A. and Calas, G. (1990). Formation of ferric oxides from aqueous solutions: a polyhedral approach by X-ray absorption spectroscopy: II. Hematite formation from ferric gels. *Geochim. Cosmochim. Acta*, **54**, 1083–1091.
- [48] Bottero, J.Y., Tchoubar, D., Arnaud, M. and Quienne, P. (1991). Partial hydrolysis of ferric nitrate salt. Structural investigation by dynamic light scattering and small angle X-ray scattering. *Langmuir*, **7**, 1365–1369.
- [49] Bottero, J.Y., Arnaud, M., Villieras, F., Michot, L.J., DeDonato, P. and François, M. (1993). Surface and textural heterogeneity of fresh hydrous ferric oxides in water and in the dry state. *J. Colloid Interface Sci.*, **159**, 45–52.
- [50] Bottero, J.Y., Manceau, A., Villieras, F. and Tchoubar, D. (1994). Structure and mechanisms of formation of FeOOH(Cl) polymers. *Langmuir*, **10**, 316–319.
- [51] Rose, J., Manceau, A., Masion, A. and Bottero, J.Y. (1997). Structure and mechanisms of formation of FeOOH(NO<sub>3</sub>) oligomers at the early stages of hydrolysis. *Langmuir*, **13**, 3240–3246.
- [52] Johnston, J.H. and Lewis, D.G. (1986). A study of the initially formed hydrolysis species and intermediate polymers and their role in determining the product iron oxides formed in the weathering of iron. In *Industrial Applications of the Mössbauer Effect*, Long, G.J. and Stevens, J.G. (eds). Plenum Press, New York, pp. 565–593.
- [53] Manceau, A. and Combes, J.M. (1988). Structure of Mn and Fe oxides and oxyhydroxides – a topological approach by EXAFS. *Phys. Chem. Miner.*, **15**, 283–295.
- [54] Janney, D.E., Cowley, J.M. and Buseck, P.R. (2001). Structure of synthetic 6-line ferrihydrite by electron nanodiffraction. *Am. Mineral.*, **86**, 327–335.
- [55] Michot, L.J., Montarges-Pelletier, E., Lartiges, B.S., D'Espinose, J.B. and Briois, V. (2000). Formation mechanism of the Ga13 Keggin ion: a combined EXAFS and NMR study. *J. Am. Chem. Soc.*, **122**, 6048–6056.
- [56] Ciavatta, L. and Grimaldi, M. (1975). On the hydrolysis of the iron(III) ion, Fe<sup>3+</sup>, in perchlorate media. *J. Inorg. Nucl. Chem.*, **37**, 163–169.
- [57] Bradley, S.M. and Kydd, R.A. (1993). Comparison of the species formed upon base hydrolyses of gallium(III) and iron(III) aqueous solutions: the possibility of existence of an [FeO<sub>4</sub>Fe<sub>12</sub>(OH)<sub>24</sub>(H<sub>2</sub>O)<sub>12</sub>]<sup>7+</sup> polyoxocation, *J. Chem. Soc. Dalton Trans.*, 2407–2413.

- [58] Tchoubar, D., Bottero, J.Y., Quienne, P. and Arnaud, M. (1991). Partial hydrolysis of ferric chloride salt. Structural investigation by photon correlation spectroscopy and small angle X-ray scattering. *Langmuir*, **7**, 398–402.
- [59] Kandori, K., Aoki, Y., Yasukawa, A. and Ishikawa, T. (1998). Effects of metal ions on the morphology and structure of haematite particles produced from forced hydrolysis reaction. *J. Mater. Chem.*, **8**, 2287–2292.
- [60] Schneider, W. and Schwyn, B. (1987). The hydrolysis of iron in synthetic, biological, and aquatic media. In *Aquatic Surface Chemistry*, Stumm, W. (ed.). Wiley-Interscience, New York, pp. 167–196.
- [61] Kandori, K., Uchida, S., Kataoka, S. and Ishikawa, T. (1992). Effects of silicate and phosphate ions on the formation of ferric oxide hydroxide particles. *J. Mater. Sci.*, **27**, 719–728.
- [62] He, Q.H., Leppard, G.G., Paige, C.R. and Snodgrass, W.J. (1996). Transmission electron microscopy of a phosphate effect on the colloid structure of iron hydroxide. *Water Res.*, **30**, 1345–1352.
- [63] Deng, Y. (1997). Formation of iron(III) hydroxides from homogeneous solutions. *Water Res.*, **31**, 1347–1354.
- [64] Masion, A., Rose, J., Bottero, J.Y., Tchoubar, D. and Garcia, F. (1997). Nucleation and growth mechanisms of Fe oxyhydroxides in the presence of  $\text{PO}_4$  ions. 4. Structure of the aggregates. *Langmuir*, **13**, 3886–3889.
- [65] Vilgé-Ritter, A., Rose, J., Masion, A., Bottero, J.Y. and Lainé, J.M. (1999). Chemistry and structure of aggregates formed with Fe salts and natural organic matter. *Colloids Surf. A: Physicochem. Eng. Aspects*, **147**, 297–308.
- [66] Mayer, T.D. and Jarrell, W.M. (2000). Phosphorus sorption during iron(II) oxidation in the presence of dissolved silica. *Water Res.*, **34**, 3949–3956.
- [67] Pullin, M.J. and Cabaniss, S.E. (2003). The effects of pH, ionic strength, and iron–fulvic acid interactions on the kinetics of non-photochemical iron transformations. I. Iron(II) oxidation and iron(III) colloid formation. *Geochim. Cosmochim. Acta*, **67**, 4067–4077.
- [68] Rose, J., Manceau, A., Bottero, J.Y., Masion, A. and Garcia, F. (1996). Nucleation and growth mechanisms of Fe oxyhydroxide in the presence of  $\text{PO}_4$  ions. 1. Fe K-edge EXAFS study. *Langmuir*, **12**, 6701–6707.
- [69] Rose, J., Flanck, A.M., Masion, A., Bottero, J.Y. and Elmerich, P. (1997). Nucleation and growth mechanisms of Fe oxyhydroxides in the presence of  $\text{PO}_4$  ions. 2. P K-edge EXAFS study. *Langmuir*, **13**, 1827–1834.
- [70] Masion, A., Rose, J., Bottero, J.Y., Tchoubar, D. and Elmerich, P. (1997). Nucleation and growth mechanisms of Fe oxyhydroxides in the presence of  $\text{PO}_4$  ions. 3. Speciation of Fe by small angle X-ray scattering. *Langmuir*, **13**, 3882–3885.
- [71] Weber, W.J. and Stumm, W. (1965). Formation of a silicato-iron(III) complex in dilute aqueous solution. *J. Inorg. Nucl. Chem.*, **27**, 237–239.
- [72] Cornell, R.M. and Giovanoli, R. (1987). The influence of silicate species on the morphology of goethite ( $\alpha\text{-FeOOH}$ ) grown from ferrihydrite ( $5\text{Fe}_2\text{O}_3 \cdot 9\text{H}_2\text{O}$ ). *J. Chem. Soc Chem. Commun.*, 413–414.
- [73] Glasauer, S., Friedl, J. and Schwertmann, U. (1999). Properties of goethites prepared under acidic and basic conditions in the presence of silicate. *J. Colloid Interface Sci.*, **216**, 106–115.
- [74] Anderson, P.R. and Benjamin, M.M. (1985). Effects of silicon on the crystallization and adsorption properties of ferric oxides. *Environ. Sci. Technol.*, **19**, 1048–1053.
- [75] Vempati, R.K. and Loepfert, R.H. (1989). Influence of structural and adsorbed Si on the transformation of synthetic ferrihydrite. *Clays Clay Miner.*, **37**, 273–279.
- [76] Hansen, H.C.B., Raben-Lange, B., Raulund-Rasmussen, K. and Borggaard, O.K. (1994). Monosilicate adsorption by ferrihydrite and goethite at pH 3–6. *Soil Sci.*, **158**, 40–46.

- [77] Hansen, H.C.B., Wechte, T.P., Raulund-Rasmussen, K. and Borggaard, O.K. (1994). Stability constants for silicate adsorbed to ferrihydrite. *Clay Miner.*, **29**, 341–350.
- [78] Swedlund, P.J. and Webster, J.G. (1999). Adsorption and polymerisation of silicic acid on ferrihydrite, and its effect on arsenic adsorption, *Wat. Res.*, **33**, 3413–3422.
- [79] Glasauer, S., Hug, P., Weidler, P.G. and Gehring, A.U. (2000). Inhibition of sintering by Si during the conversion of Si-rich ferrihydrite to hematite. *Clays Clay Miner.*, **48**, 51–56.
- [80] Doelsch, E., Rose, J., Masion, A., Bottero, J.Y., Nahon, D. and Bertsch, P.M. (2000). Speciation and crystal chemistry of iron(III) chloride hydrolyzed in the presence of SiO<sub>4</sub> ligands. 1. An Fe K-edge EXAFS study. *Langmuir*, **16**, 4726–4731.
- [81] Doelsch, E., Stone, W.E.E., Petit, S., Masion, A., Rose, J., Bottero, J.Y. and Nahon, D. (2001). Speciation and crystal chemistry of Fe(III) chloride hydrolyzed in the presence of SiO<sub>4</sub> ligands. 2. Characterization of Si–Fe aggregates by FTIR and <sup>29</sup>Si solid state NMR. *Langmuir*, **17**, 1399–1405.
- [82] Masion, A., Doelsch, E., Rose, J., Moustier, S., Bottero, J.Y. and Bertsch, P.M. (2001). Speciation and crystal chemistry of iron(III) chloride hydrolyzed in the presence of SiO<sub>4</sub> ligands. 3. Semi-local scale structure of the aggregates. *Langmuir*, **17**, 4753–4757.
- [83] Doelsch, E. (2000) *Le système Fe(II)–Fe(III)/Si en milieu aqueux. Caractérisation multi-échelles*. Thesis, Aix-Marseille 3, Aix en Provence.
- [84] Manceau, A., Ildefonse, P., Hazemann, J.L., Flank, A.M. and Gallup, D. (1995). Crystal-chemistry of hydrous iron silicate scale deposits at the Salton-Sea geothermal-field. *Clays Clay Miner.*, **43**, 304–317.
- [85] Masion, A., Tchoubar, D., Bottero, J.Y., Thomas, F. and Villières, F. (1994). Chemistry and structure of Al(OH)/organic precipitates. A small angle X-ray scattering study. 1. Numerical procedure for speciation from scattering curves. *Langmuir*, **10**, 4344–4348.
- [86] Masion, A., Bottero, J.Y., Thomas, F. and Tchoubar, D. (1994). Chemistry and structure of Al(OH)/organic precipitates. A small angle X-ray scattering study. 2. Speciation and structure of the aggregates. *Langmuir*, **10**, 4349–4352.
- [87] Masion, A., Thomas, F., Tchoubar, D., Bottero, J.Y. and Tekely, P. (1994). Chemistry and structure of Al(OH)/organic precipitates. A small angle X-ray scattering study. 3. Depolymerization of the Al<sub>13</sub> polycation by organic ligands. *Langmuir*, **10**, 4353–4356.
- [88] Amirbahman, A., Gfeller, M. and Furrer, G. (2000). Kinetics and mechanisms of ligand-promoted decomposition of the Keggin Al<sub>13</sub> polymer. *Geochim. Cosmochim. Acta*, **64**, 911–919.
- [89] Bushell, G.C., Yan, Y.D., Woodfield, D., Raper, J. and Amal, R. (2002). On techniques for the measurement of the mass fractal dimension of aggregates. *Adv. Colloid Interface Sci.*, **95**, 1–50.
- [90] Axelos, M.A.V., Tchoubar, D. and Bottero, J.Y. (1989). Small angle X-ray scattering investigation of the silica/water interface: evolution of the structure with pH. *Langmuir*, **5**, 1186–1190.
- [91] Zhang, J., Huguenard, C., Scarnecchia, C., Menghetti, R. and Buffle, J. (1999). Stabilization and destabilization of hematite suspensions by neutral and anionic polyacrylamide. *Colloids Surf. A: Physicochem. Eng. Aspects*, **151**, 49–63.
- [92] Zartarian, F., Mustin, C., Bottero, J.Y., Villemain, G., Thomas, F., Allières, L., Champenois, M., Grulois, P. and Manem, J. (1994). Spatial arrangement of the components of activated sludge flocs. *Water Sci. Technol.*, **30**, 243–250.
- [93] Zhang, J. and Buffle, J. (1996). Multi-method determination of the fractal dimension of hematite aggregates. *Colloids Surf. A: Physicochem. Eng. Aspects*, **107**, 175–187.
- [94] Sorensen, C.M., Cai, J. and Lu, N. (1992). Light-scattering measurements of monomer size, monomers per aggregate, and fractal dimension for soot aggregates in flames. *Appl. Opt.*, **31**, 6547–6557.

- [95] Teixeira, J. (1986). Experimental methods for studying fractal aggregates. In *On Growth and Form*, Stanley, H.E. and Ostrowsky, N. (eds). Martinus Nijhoff, Boston, MA, pp. 145–162.
- [96] Rarity, J.G. and Pusey, P.N. (1986). Light scattering from aggregating systems: static, dynamic (QELS) and number fluctuations. In *On Growth and Form*, Stanley, H.E. and Ostrowsky, N. (eds). Martinus Nijhoff, Boston, MA, pp. 218–222.
- [97] Waite, T.D. (1999). Measurement and implications of floc structure in water and wastewater treatment. *Colloids Surf. A: Physicochem. Eng. Aspects*, **151**, 27–41.
- [98] Thill, A., Veerapaneni, S., Simon, B., Wiesner, M., Bottero, J.Y. and Snidaro, D. (1998). Determination of structure of aggregates by confocal scanning laser microscopy. *J. Colloid Interface Sci.*, **204**, 357–362.
- [99] Oles, V. (1992). Shear-induced aggregation and breakup of polystyrene latex particles. *J. Colloid Interface Sci.*, **154**, 351–358.
- [100] Xu, Y.L. and Gustafson, B.A.S. (1997). Experimental and theoretical results of light scattering by aggregates of spheres. *Appl. Opt.*, **36**, 8026–8030.
- [101] Lambert, S., Thill, A., Ginestet, P., Audic, J.M. and Bottero, J.Y. (2000). Structural interpretations of static light scattering patterns of fractal aggregates: I. Introduction of a mean optical index: numerical simulations. *J. Colloid Interface Sci.*, **228**, 379–385.
- [102] Bohren, C.F. and Huffman, D.R. (1983). *Absorption and Scattering of Light by Small Particles*. John Wiley & Sons, Ltd, New York.
- [103] Thill, A., Lambert, S., Moustier, S., Ginestet, P., Audic, J.M. and Bottero, J.Y. (2000). Structural interpretations of static light scattering patterns of fractal aggregates: II. Experimental study. *J. Colloid Interface Sci.*, **228**, 386–392.
- [104] Teixeira, J. (1988). Small-angle scattering by fractal systems. *J. Appl. Crystallogr.*, **21**, 781–785.

---

# 6 Fractal Approach to Adsorption/Desorption Processes on Environmental Surfaces

---

**Zofia Sokołowska<sup>1</sup> and Stefan Sokołowski<sup>2</sup>**

<sup>1</sup> *Institute of Agrophysics, Polish Academy of Sciences, Doświadczalna 4, 20290 Lublin, Poland*

<sup>2</sup> *Department for the Modelling of Physico-Chemical Processes, Marie Curie–Sktodowska University, 20031 Lublin, Poland*

## 6.1 INTRODUCTION

The term ‘fractal’ and the concept of fractal dimension were introduced by Mandelbrot [1]. Since Mandelbrot’s work, many scientists have used fractal geometry as a means of quantifying natural structures and as an aid in understanding physical processes occurring within these structures. Fractals are objects that appear to be scale invariant. Mandelbrot defines them as ‘shapes whose roughness and fragmentation neither tend to vanish, nor fluctuate up and down, but remain essentially unchanged as one zooms in continually and examination is refined’. The above property is called ‘scale invariance’. If the transformations are independent of direction, then the fractal is self-similar; if they are different in different directions, then the fractal is self-affine (see Chapter 2).

Natural objects are not fractals in the mathematical sense because they do not exhibit scaling over an infinite range of scales, but their fractal character is demonstrated over a finite scale range from a lower limit  $r_{\min}$  to an upper limit  $r_{\max}$ . Nonetheless, fractals may provide a useful characterization of natural structures between the two limits  $[r_{\min}, r_{\max}]$ . Fractal dimensions can be defined in several different ways, depending on the object under study and the measurements being made (see Chapter 2). The fact that there are different fractal dimensions may, in some cases, lead to confusion with respect to which fractal dimension is being employed. In the case of adsorption studies, two types of fractal, i.e. the surface fractal and mass fractal, are important.

Surface fractals have a fractal boundary but a compact, nonfractal bulk. Common to all methods of fractal analysis is that ‘yardsticks’ of different size probe the surface. Depending on the method, the probes may be molecules of different size,

electromagnetic waves diffracted at different angles, liquid menisci with different radii of curvature, etc. In general, in the case of surface fractals in a three-dimensional space, the number of yardsticks  $N(r)$  of linear size  $r$  necessary to cover the surface scales as

$$N(r) \propto r^{D_s} \quad (6.1)$$

and the exponent  $D_s$  by definition is the surface fractal dimension. The mathematical definition of the surface fractal dimension is

$$D_s = \lim_{r \rightarrow 0} [\ln N(r) / \ln r] \quad (6.2)$$

Equation (6.1) can be generalized to the case of objects in a  $d$ -dimensional space. If  $D_s$  coincides with  $D_{\text{top}}$ , the topological dimension of the system, then the system is Euclidean. In general, for any system  $D_{\text{top}} \leq D_s \leq d$ . Obviously, in the case of real surfaces, the mathematical definition cannot be applied because the size of the smallest yardstick is always greater than zero. Therefore, in the real world, Equation (6.1) is satisfied only within some finite range,  $r \in [r_{\text{min}}, r_{\text{max}}]$ , called the fractality range. Typically, irregularities fill the entire fractal surface, but in some cases only a part of the surface is fractal [1]. For example, the set of irregularities may correspond to the active sites of a catalyst surface, to the sites of preferential adsorption, etc. [2].

In a mass fractal, the entire bulk of mass solid is not compact but porous. For mass fractal, the mass  $m$  inside a characteristic length scale  $r$  scales according to

$$m \propto r^{D_M} \quad (6.3)$$

where  $D_M$  is the mass fractal dimension that is smaller or equal to the dimension of Euclidean space.

Pfeifer *et al.* [3] introduced the term ‘pore fractal’ for which not the solid phase, but ‘an empty space’ scales according to Equation (6.3). If the ‘mass’ of pores scales according to Equation (6.3), then their volume (in three-dimensional space) scales as

$$V_p \propto r^{3-D_p} \quad (6.4)$$

where  $D_F$  is the pore fractal dimension whose value in a three-dimensional space is in the range  $0 \leq D_p \leq 3$ . For  $D_p = 2$ , the distribution of pore sizes is uniform. For increasing values of  $D_F$ , the relative number of pores whose size is close to the minimum pore size increases. An adsorbent with a pore fractal dimension  $D_p = 3$  should have pores of one size only.

The question can be posed whether the exponent  $\alpha$  in the power law  $y \propto t^\alpha$  relating the quantities  $t$  and  $y$  can always be interpreted in terms of a fractal dimension. Clearly, if this power law is applied to any arbitrary data, then one cannot expect  $\alpha$  to be restricted to a certain range (e.g.  $0 \leq \alpha \leq 3$ ). Even if the power law is used to describe some physical attribute of a real system, it cannot be guaranteed that the exponent will have a clear physical meaning nor that its values will be geometrically constrained. For example, cases of physical systems where this exponent leads to ‘fractal dimensions’ that were greater than three have been reported in the literature

[4, 5]. In some cases, such values can be considered to be ‘probabilistic’ fractals. For a discussion of this problem, see the review of Baveye and Boast [6] and the references quoted therein, in addition to Chapter 2 in this book.

A vast majority of theories describing the physical adsorption of fluids on solids employ models which are based on Euclidean geometry. Usually, the adsorbing surfaces have been modeled as planar surfaces, straight-line step edges, slit-like or cylindrical pores, etc. In contrast, many systems of practical importance, e.g. soils and soil components, have structures that cannot be described in such terms. In this respect, the network formed by the pores in soils apparently forms ‘an iterative structure’, i.e. smaller pores are sub-pores of larger pores, etc. Owing to this effect, models in which structural features span a wide range of length scales, i.e. treating surface irregularities as recurrent and nested rather than as isolated entities, are required.

A fractal adsorbing surface has the same structural features at length scales that are comprised between the inner cut-off limit  $r_{\min}$  and the upper cut-off limit  $r_{\max}$ . Its irregularity is described by the surface fractal dimension  $D_s$ . The fact that the complexity of the adsorbing surface is captured by a single number is extremely convenient and appealing, and allows for a great simplification of the theoretical description of adsorption phenomena.

The purpose of this chapter is to describe the developments and various aspects of adsorption phenomena on fractal surfaces. The review is arranged as follows. After this introductory section, Section 6.2 describes the methods of evaluating fractal dimensions using the so-called thermodynamic approach developed by Neimark [7, 8]. Section 6.3 provides an overview of adsorption equations of gases on geometrically nonuniform, but energetically homogeneous, solid surfaces. The description of adsorption on both geometrically and energetically nonuniform surfaces is discussed in Section 6.4. Examples of applications of the approaches described in Sections 6.2–6.4 to the studies of soil materials are presented in Section 6.5.

## 6.2 EVALUATION OF FRACTAL DIMENSION

### 6.2.1 Monolayer Capacities of Molecules of Different Sizes

The monolayer capacity  $N_m$ , i.e. the number of adsorbed particles that cover the adsorbing surface and form a monomolecular layer, can be determined from standard adsorption measurements. The monolayer capacity is then used to calculate the surface area  $S = N_m \omega$ , where  $\omega$  is the cross-sectional area of adsorbed molecules [9], which is proportional to the square of the molecular diameter  $\sigma$ . For fractal surfaces:

$$N_m \propto \omega^{-D_s/2} \quad (6.5)$$

where  $N_m$  is evaluated from adsorption data and  $D_s$  is the surface fractal dimension [10]. Numerous literature data [11–19] reveal that, in most cases, the fractal model is applicable, with  $D_s$  values falling in the theoretical range of  $2 \leq D_s \leq 3$ .



Nonetheless, an initial difficulty may arise with respect to the correct assessment of the cross-sectional surface area of the adsorbate molecule, which also depends on the adsorbate–adsorbent interaction since this can change the orientation of the adsorbed molecules. Often, the adsorbed molecule occupies not only the site on the surface, but also some neighboring volume, thus creating steric difficulties for the adsorption of other molecules and leading to a possible underestimation of the monolayer capacity [20]. Moreover, in the case of some specific interactions, e.g. associative interactions, the structure of the adsorbed layer may change as an effect of adsorbate–adsorbate interactions. Under these circumstances, it may be useful to refer to appropriate literature data for  $\omega$  [9].

Although in some cases, the values of  $D_s$  obtained from Equation (6.5) are not bounded within the limits of 2 and 3, values of  $D_s \leq 2$  are still interpretable in terms of the fractal dimension, namely as a subset of all surface points. On the other hand, values of  $D_s > 3$  cannot be interpreted in terms of geometrical dimension. Apart from inaccurate models that are applied to evaluate  $\omega$ , there are several effects that can lead to apparent values of  $D_s > 3$ . These include superposition of the fractals, some sieving effects, chemisorption and the nonfractal distribution of adsorbing sites [10].

On some substrates, such as expanding clay minerals, the adsorption of different molecules may occur according to different mechanisms. For example, the adsorption of nonpolar molecules can occur only on external surfaces, whereas polar molecules can also enter interlayer spaces. Consequently, application of Equation (6.5) to polar and nonpolar molecules may lead to different results [16, 21].

The range of the power law applicability is limited to a given set of  $\sigma$  (or  $\omega$ ) values. In most cases, the smallest value of  $\sigma$  is for argon, water vapor or nitrogen; thus, these molecules are the most frequently used in adsorption experiments. Unless polymer molecules are used, the range of available molecular sizes is rather small. Furthermore, molecules in the gas phase may not be able to reach all the vacant adsorption sites. For example, if the path involves a linear extension smaller than the dimension of the molecule (bottle neck), then the measured  $N_m$  will be smaller than the value that would have been obtained if molecules were able to cross the bottle neck. In conclusion, the value of  $D_s$  reflects ‘an effective geometry’ as seen by the specific set of adsorbed molecules.

The value of  $D_s$  is not related to sample porosity. For example, adsorption on either a nearly nonporous or a porous carbon adsorbent, e.g. carbon black or Vulcan 3D [11], gave similar  $D_s$  values, i.e.  $D_s = 2.07$  and  $2.04$  respectively.

Application of Equation (6.5), therefore, should always take into account the question about which surface’s fractal dimension is actually measured in adsorption experiments. According to the mathematical derivation of this equation, the centers of the ‘yardstick molecules’ are theoretically located at the geometrical surface of the underlying solid. However, each molecule that is adsorbed within the first layer adjacent to the solid is located at a certain distance from the surface, which is determined not only by the geometry of the underlying solid, but also by the form



of the gas–solid interaction potential. The relationship between the fractal dimension of the underlying solid and the fractal dimension of the surface at which adsorption actually occurs has been discussed in the literature [22–25]. However, in contrast to previous work [22–25], in simulations of the adsorption of spherical particles on deterministic fractal curves, each vertex of the generated fractal curve is treated as the center of the adsorbing potential [26]. The energy of interaction of a gas molecule of diameter  $\sigma$  with the whole curve was assumed to be equal to the sum of interactions of the molecule with all vertices, and the energy of interaction of the vertex  $i$  with the molecule can be described by a Lennard–Jones (12, 6) function [27]:

$$u_i(r) = 4\varepsilon \left[ \left( \frac{\sigma_s}{r} \right)^{12} - \left( \frac{\sigma_s}{r} \right)^6 \right] \quad (6.6)$$

where the energy  $\varepsilon$  and size parameter  $\sigma_s$  depend on the kind of adsorbed molecules, and  $r$  is the distance between the vertex and the molecule. According to the Lorentz–Berthelott mixing rules,  $\sigma_s = (\sigma_a + \sigma)/2$ , where  $\sigma_a$  is the distance between the nearest vertices. The first layer of adsorbed molecules is located at the curve  $\Sigma_M$  that passes through the minima of the adsorbing potential, and the geometry of this curve depends on the size of adsorbed molecules  $\sigma$ . Examples of the curves  $\Sigma_M$  evaluated for a set of adsorbate molecules of different diameters  $\sigma$  are shown in Figure 6.1a. The fractal dimension can be computed by evaluating the number of spheres of diameter  $\sigma$  that are necessary to cover the curve  $\Sigma_M$ . Obviously, a new curve  $\Sigma_M$  is generated for each value of  $\sigma$ . Figure 6.1b compares the fractal dimension determined according to the

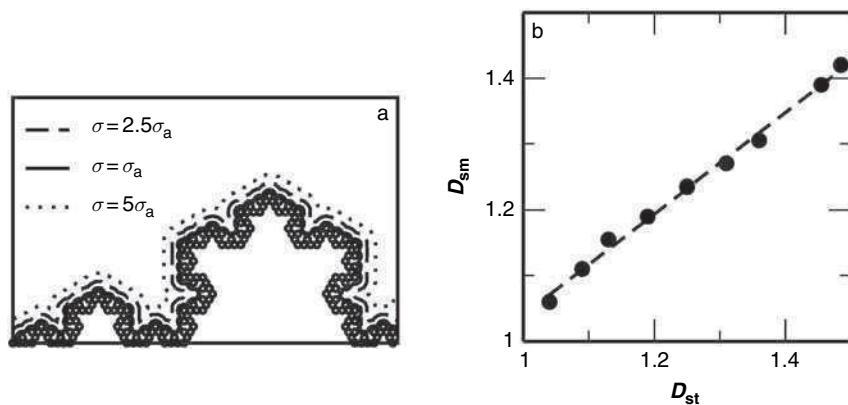


**Figure 6.1** (a) Examples of three curves  $\Sigma_M$  passing through minima of adsorption potential. Curves have been generated for molecules of three different sizes  $\sigma$ . (b) Correlation between the theoretical fractal dimension  $D_{st}$  and a fractal dimension that has been evaluated for the curves passing through the minima of the adsorption potential  $D_{sm}$ . Results shown refer to diadic and triadic Koch curves. Reproduced by permission of the American Chemical Society [26].

above procedure  $D_{sm}$  with the theoretical surface fractal dimension of the underlying substrate  $D_{st}$ . In the case of diadic and triadic Koch curves [26], the fractal dimension calculated by accounting for energetic adsorption conditions was always lower than the mathematical fractal dimension of the underlying substrate.

The number of particles (or granules)  $N_g$ , of an adsorbent substrate in a constant volume  $V$  scales with the size of the particles  $r_g$  according to  $N_g \propto r_g^{-3}$ . It follows that the number of molecules necessary to cover these particles with a monomolecular layer  $N_{mg}$  scales as

$$N_{mg} \propto r_g^{D_s-3} \quad (6.7)$$

Equation (6.7) offers an alternative method to Equation (6.5) for the evaluation of the surface fractal dimension, which relies on the evaluation of the monolayer capacity for a series of adsorbent samples that have a constant volume and contain adsorbent particles in the size interval  $r_{g,min}, r_{g,max}$  [12, 15, 28–30].

A method that can be considered as a combination of the two described above has been proposed by Van Damme and Fripiat [21], who have applied the concept of the surface fractal dimension to adsorption on the so-called pillared clays [31, 32]. If, prior to the adsorption of small molecules having a cross-section  $\omega$ ,  $n_p$  large molecules (the pillars) of cross-section  $\omega_p$  are deposited on the surface, then the number of small molecules necessary to reach monolayer coverage on the remaining ‘free’ surface is given by

$$N'_m = N_m - n_p \left( \frac{\omega_p}{\omega} \right)^{D_s/2} \quad (6.8)$$

where  $N_m$  is the monolayer capacity of the initial bare surface. By varying the number of deposited pillars and measuring the monolayer capacities of  $N_2$ , it is possible to obtain the value of  $D_s$ . This method, however, is rather hard to implement as a general method.

### 6.2.2 The Thermodynamic Method of Neimark

The method of Neimark [7, 8, 33, 34] for the determination of the surface fractal dimension of a microporous solid is based on the adsorption isotherm equation that was developed by Kiselev [35]. This equation relates the surface area of pores filled by the adsorbate  $S(x)$  to the amount of adsorbed molecules  $N(x)$  at a given relative pressure  $x = p/p_0$ :

$$S(x)\phi = \frac{kT}{V_m} \int_{N(x)}^{N_p} -\ln(x) dN \quad (6.9)$$

where  $p$  is the pressure,  $p_0$  is the saturated vapor pressure,  $\phi$  is the surface tension,  $V_m$  is the molar volume of the adsorbate and  $N_p$  is the maximum adsorbed amount in the pores, i.e. the value of the adsorption when  $p \rightarrow p_0$ . The product  $S(x)\phi$  in Equation (6.9) represents the work connected with the formation of a phase boundary

between the liquid-like adsorbed film and the gas phase, which equals the work corresponding to the growth of the adsorbed film as represented by the right-hand side of Equation (6.9). Physically, this situation corresponds to the representation of an adsorbate surface as an ensemble of surfaces, each with a constant curvature. The radius of curvature of the liquid meniscus  $\sigma_c$  plays the role of a yardstick. According to the Kelvin equation,  $\sigma_c \propto \phi / \ln(x)$  [27, 35], because  $S \propto \sigma_c^{2-D_s}$ , Equation (6.9) yields

$$D_s = 2 + \frac{d}{d[\ln(-\ln(x))]} \left[ \ln \int_{N(x)}^{N_p} -\ln(x) dN \right] \quad (6.10)$$

Equation (6.10) was derived based upon thermodynamics alone without invoking any structure mode [7, 8]. The range of validity of the Kelvin equation corresponds to the range of mesopores [27].

A similar method was suggested for the calculation of the surface fractal dimension based on measurements of mercury porosimetry. The surface area measured by covering the surface with gauges of size  $\sigma_g$  scales as  $S \propto \sigma_g^{2-D_s}$ . In the case of mercury porosimetry, the gauge corresponds to the average radius of curvature  $r$  of the meniscus at the mercury–solid sample interface. Assuming that the pore space is represented by a bundle of nonintersecting pores of the same geometry (e.g. cylindrical, slit-like, etc.), the radius  $r$  is related to the mercury pressure  $p$  by the Washburn relationship:

$$p = \frac{C_1}{r} \quad (6.11)$$

where  $C_1$  is a constant. The Washburn relationship plays a similar role to the Kelvin equation in the case of adsorption experiments.

Rootare and Prenzlöw [36] derived the following relationship between the surface of pores  $S_1$  and the volume of the intruded mercury  $V$ , i.e. the volume of pores of radius  $r$ :

$$S_1 = C_2 \int_0^V p dV' \quad (6.12)$$

In Equation (6.12),  $C_2 = -1/(\phi \cos \alpha)$  is a constant that is related to the surface tension  $\phi$  and the cosine of the contact angle of mercury at the mercury–solid interface  $\alpha$ . This area is interpreted as the one that would be measured by spheres of radius  $r$ . The total surface area of an adsorbent  $S$  is the sum of the surface area of the sample–mercury interphase at the beginning of the intrusion process  $S_0$  and the inner pore surface  $S_1$ . If  $S_0$  is neglected, then [7, 8]

$$D_s = 2 + \frac{d}{d(\ln p)} \left[ \ln \int_0^V p dV' \right] \quad (6.13)$$

Equation (6.13) requires only the measurement of the dependence of the volume of the intruded mercury on the applied pressure, and can be used to investigate irregularities of the solids within the range of scales provided by mercury intrusion data. Application of the mercury porosimetry technique has been reported in several papers studying soils [14, 17, 33, 37–45].

Both Equations (6.10) and (6.13) require some comments. If Equation (6.10) is used to analyze experimental data, then a problem often encountered is related to adsorption hysteresis in the mesopores. The results of calculations may depend on which branch of the isotherm (adsorption or desorption) is used as the basis of calculations. In such cases, one should preferentially employ the desorption branch in order to conform to the Kelvin theory of pore filling [8, 27, 46]. Nonetheless, values of the fractal dimension that are calculated from the adsorption and desorption isotherms should be comparable for those samples showing fractal properties over a sufficiently wide range of pore sizes [7, 8].

Another problem is related to the fact that  $N_p$  is ill defined and it can be difficult to evaluate from experimental data. In particular, if the liquid adsorbate wets the adsorbent, then adsorption diverges as the pressure approaches the saturated vapor pressure. This divergence is due to the growth of a film at the solid surface. In the case of mesoporous adsorbents, the value of  $N_p$  is usually assumed to be equal to the amount of adsorbate at the end of the capillary condensation loop [7, 8].

A similar problem is encountered for the analysis of mercury porosimetry data. The approach based on Equation (6.13) neglects the surface area of the sample–mercury interphase at the beginning of the intrusion process  $S_0$ . If Equation (6.10) is applied to data over a range of mercury pressures, then the effect of neglecting  $S_0$  may be significant. Therefore, Equation (6.10) should be corrected by incorporating  $S_0$ , thus obtaining

$$D_s = 2 + \frac{d}{d(\ln p)} \left[ \ln \left( S_0 + C_2 \int_0^p p \, dV' \right) \right] \quad (6.14)$$

However, the porosimetric method does not directly measure the initial area  $S_0$ . To evaluate  $S_0$ , Kozak *et al.* [40] modified Neimark's approach based on the application of Equation (6.14). In addition to Neimark's approach, other alternative approaches have been developed that are aimed at evaluating the fractal dimension from mercury intrusion data [47].

## 6.3 ISOTHERMS DESCRIBING ADSORPTION ON FRACTAL SURFACES

### 6.3.1 Brunauer–Emmet–Teller Theory Applied to Fractal Surfaces

The Brunauer–Emmet–Teller (BET) model of adsorption is one of the most common tools for surface analysis, and is also recommended by IUPAC [48] as a standard tool for surface area determination. According to the BET model, adsorption occurs

on an ideally flat ( $D_s = 2$ ) and energetically homogeneous surface. The energy of an adsorbate with  $N_1$  molecules in the first layer and  $N_2$  molecules in higher layers is  $N_1\varepsilon_1 + N_2\varepsilon_2$ , where  $\varepsilon_1$  and  $\varepsilon_2$  are the energies of adsorption in the first and in the higher layers respectively. The adsorption energy of molecules in the higher layers is assumed to be equal to the heat of condensation of the bulk adsorbate,  $\varepsilon_2 = \varepsilon_c$ . This theory neglects the long-range interactions between the adsorbent and the adsorbate, and the filling of all higher layers is governed by adsorbate–adsorbate interactions. If there is no restriction imposed on the maximum number of adsorbed layers, then the number of adsorbed molecules  $N$  grows with increasing the gas pressure  $p$ :

$$\frac{N}{N_m} = \frac{1}{1-x} \frac{g(x)}{1+g(x)C} \quad (6.15)$$

where  $g(x) = x/(1-x)$ ,  $x = p/p_0$  and  $C = \exp[-(\varepsilon_1 - \varepsilon_2)/kT]$ ,  $x$  corresponds to the relative pressure,  $p_0$  is the saturated vapor pressure,  $k$  is the Boltzmann constant and  $T$  is the absolute temperature. The ratio  $N/N_m$  gives the relative coverage of the surface, which is also a measure (in units of the adsorbate diameter  $\sigma$ ) of the mean film thickness.

The success of Equation (6.15) in describing experimental isotherms for a variety of systems has likely made it the most widely used isotherm equation in surface sciences. Therefore, it is quite obvious to extend BET theory to the case of adsorption on a fractal surface. In this respect, two approaches have been reported. The first [3, 22] is based on the idea that as the film thickness grows it fills all the surface irregularities, and consequently the number of adsorption sites in consecutive layers  $N^{(n)}$  decreases. This decrease is described by a power law:

$$N^{(n)} = n^{2-D_s} N^{(0)} \quad (6.16)$$

where  $n$  is the layer number and  $N^{(0)}$  is the number of bare surface sites,  $N^{(0)} = N_m$ .

For a finite system, this scaling holds only up to  $n_{\max} \approx R_{\max}/\sigma$ , where  $\sigma$  is the diameter of the adsorbate molecule and  $R_{\max}$  is the outer cut-off of the fractal regime. The isotherm equation has the form

$$\vartheta(x) = \frac{N}{N_m} = \frac{f(x, D_s)}{1 + C\tilde{g}(x)} \quad (6.17)$$

where

$$f(x, D) = \sum_{n=1}^{n_{\max}} n^{2-D_s} \sum_{j=n}^{n_{\max}} j^{D_s-2} x^j, \quad (6.18)$$

$$\tilde{g}(x) = \sum_{n=1}^{n_{\max}} x^n \quad (6.19)$$

and  $\vartheta(x)$  is the surface coverage. For  $n_{\max} \rightarrow \infty$ , the function  $\tilde{g}(x)$  reduces to the term  $x/(1-x)$  in Equation (6.15). For a planar surface with  $D_s = 2$ , Equation (6.17)

reduces to the usual BET equation, Equation (6.15). For  $D_s = 3$ , Equation (6.17) assumes the form [49]

$$\vartheta(x) = \frac{N}{N_m} = \frac{Cx}{[Cx + (1-x)^2]\{1 + \ln[1/(1-x)]\}} \quad (6.20)$$

The low-pressure behavior ( $x \rightarrow 0$ ) of Equation (6.17) is given by

$$\frac{N}{N_m} = C[x + (2^{D-2} + 1 - C)x^2 + O(x^3)] \quad (6.21)$$

where  $O(x^3)$  denotes the rest of the order of  $x^3$ . Equation (6.21) indicates that, at relative pressures where the contributions of order  $x^2$  become important, the isotherms on fractal and on planar surfaces begin to differ. This regime is important for the determination of the monolayer capacity  $N_m$ .

For any value of the relative pressure  $x$ , the amount of adsorbed molecules per surface site,  $\theta = N/N_m$ , decreases with increasing  $D_s$ . This occurs because, for a given number of surface sites, increasing  $D_s$  imposes increasing spatial restrictions on the growth of the film thickness. When the pressure approaches the saturated vapor pressure, i.e. for  $p \rightarrow p_0$  or for  $x \rightarrow 1$ , the asymptotic behavior of the adsorption isotherms is described by the power law [3]

$$\frac{N}{N_m} \approx \frac{\Gamma(3 - D_s)}{(1-x)^{3-D_s}} \quad \text{for } 2 \leq D_s < 3 \quad \text{and} \quad \frac{N}{N_m} = \ln[1/(1-x)] \quad \text{for } D_s = 3 \quad (6.22)$$

where  $\Gamma$  is the gamma function. The divergence of the isotherm for  $p \rightarrow p_0$  means that the fractal surface, similarly to a geometrically flat surface adsorbs infinitely thick layers. For  $D_s = 3$ , the divergence is logarithmic.

Equation (6.17) suffers from the deficiency that during its derivation, ‘multiple-surface’ effects were neglected. Nonetheless, for the filling of a slit-like pore, the film grows from two opposite adsorbing surfaces and stops growing when the two films meet. A BET-like theory that takes into account multiple-surface effects has been developed by Cole *et al.* [50]. Such an approach replaces the  $D_s$ -dimensional surface by an equivalent system of pores, each of which can be treated as independent. In each pore, coverage can be evaluated from standard BET theory for adsorption between two plates by assuming that the maximum number of adsorbed layers  $n_{\max}$  and the pore width  $H$  are related via  $2\sigma n_{\max} = H$ . In other words, adsorption in a single pore is given by

$$\theta(x; n_{\max}) = \frac{Cx}{1-x} \frac{1 + (n_{\max} + 1)x^{n_{\max}} + n_{\max}x^{n_{\max}+1}}{1 + (C-1)x - Cx^{n_{\max}+1}} \quad (6.23)$$

The total number of adsorbed molecules is calculated by summing up the contributions from individual pores:

$$\vartheta(x) = \frac{N}{N_m} = (D_s - 2) \int_1^\infty n^{1-D_s} \theta(x; n) \, dn \quad (6.24)$$

The surface fractal dimension enters Equation (6.24) through the pore size distribution [50]. Equation (6.24) holds for any surface with  $2 \leq D_s \leq 3$ . Despite the quite different form of the isotherms in Equations (6.17) and (6.24), the numerical values of adsorption that are calculated from these equations agree well, up to  $x \approx 0.7$ .

The asymptotic behavior of Equation (6.24) can be described as follows: for a geometrically flat surface,  $D_s = 2$  and Equation (6.24) yields the classical BET isotherm [3]. For  $x \rightarrow 1$ , the growth of the adsorbed film scales as

$$\frac{N}{N_m} \propto \frac{\Psi(D)}{(1-x)^{3-D_s}} \quad \text{for } 2 \leq D_s < 3 \quad \text{and} \quad \frac{N}{N_m} \propto \frac{\ln[1/(1-x)]}{2} \quad \text{for } D_s = 3 \quad (6.25)$$

where

$$\Psi(D_s) = \int_0^\infty t^{2-D_s} \frac{d}{dt} \left( \frac{t}{1 - \exp(t)} \right) dt \quad \text{for } 2 < D_s \leq 3$$

$$\text{and } \Psi(D_s) = 1 \quad \text{for } D_s = 2 \quad (6.26)$$

The function  $\Psi(D_s)$  is remarkably close to unity except when  $D_s$  values approach 3. From Equations (6.22) and (6.26), it follows that, for  $D_s = 3$  and for relative pressures approaching unity, Equation (6.24) predicts a film thickness that is two times lower than that predicted by Equation (6.17). This is due to the fact that Equation (6.17) tends to overestimate the surface coverage. The overestimation may be as large as a factor of two because, in Equation (6.24), up to one half of all adsorbing surfaces act as a ‘ceiling’ rather than as a ‘base’ for the film growth.

For very low pressures, Equation (6.24) reduces to

$$\frac{N}{N_m} = C \left[ x + (2 - C)x^2 + O \left( \frac{x^2}{-\ln(x)} \right) \right] \quad (6.27)$$

For  $x \rightarrow 0$ , Equations (6.17) and (6.24) coincide and are independent of the surface fractal dimension. However, in contrast to Equation (6.17), the term  $x^2$  resulting from Equation (6.24) is independent of the fractal dimension. The region  $x < 0.15$  is of interest for the determination of the monolayer capacity. Thus, for any value of  $D_s$ , monolayer capacities  $N_m$  can be determined from the standard BET method as long as the experimental measurements are restricted to the range of low relative pressures.

Both Equations (6.22) and (6.25) predict that, for  $x \rightarrow 1$ , the growth of the film is described by the power law

$$\ln \left( \frac{N}{N_m} \right) \propto (D_s - 3) \ln(1 - x) \quad (6.28)$$

Film growth is independent of the substrate–film interaction, i.e. the parameter  $C$ . There is a simple heuristic justification of the exponent  $D_s - 3$  in the power law given above [3]. On a planar surface, the mean film thickness for  $x \rightarrow 1$  can be estimated as  $\sigma/(1-x)$ . This suggests that, for an arbitrary surface, the film volume is  $V[\sigma/(1-x)]$ ,

where  $V(z)$  is the volume of all points located within the film at distances lower than or equal to  $z$ . Since the derivative  $dV(z)/dz$  can be interpreted as the surface area measured by molecules of diameter  $z$ ,  $dV(z)/dz|_{z=\sigma}$  should be equal to the specific surface area  $N_m\sigma^2$ . Therefore, from Equation (6.17), it is possible to deduce that for a fractal surface and for  $z \sigma$ :

$$V(z) = B\sigma^3 \left(\frac{z}{\sigma}\right)^{3-D_s} \quad (6.29)$$

where  $B$  is a constant. After substitution of  $z = \sigma/(1-x)$ , the power law is recovered in Equation (6.25) from Equation (6.29). For  $z$  values down to  $\sigma$ , Equation (6.29) can be corrected by including an additional term that ensures correct behavior at  $z = \sigma$ :

$$V(z) = B\sigma^3 \left(\frac{z}{\sigma}\right)^{3-D} + B'\sigma^3 \quad (6.30)$$

The constants  $B$  and  $B'$  can be evaluated when the value of the derivative of the function  $V(z)$  at  $z = \sigma$  is  $V'(\sigma) = N_m\sigma^2$  and when  $V(\sigma) = N_m\sigma^3$  is the volume of the monolayer. These two conditions uniquely fix the values of  $B$  and  $B'$ . Consequently:

$$V(z) = \frac{N_m\sigma^3}{(3-D_s)[(z/\sigma)^{3-D} - (D_s-2)]} \quad (6.31)$$

The dependence of the Equations (6.17) and (6.24) and Equations (6.22) and (6.25) on the surface fractal dimension  $D_s$  offers a method for measuring  $D_s$  from a single experimental isotherm. This may be done by fitting Equations (6.22) or (6.25) to the data obtained at relative pressures close to unity. In such a case, it is necessary to determine how large  $x$  should be in order for the asymptotic Equations (6.17) and (6.25) to be valid. A simple estimate proposed by Pfeifer *et al.* [3] follows from the requirements that  $N/N_m > 2$ , since the adsorption energy of molecules adsorbed in the second and higher layers is independent of the energy of interaction with the solid substrate. This estimate yields  $x > 1 - 2^{-1/(3-D_s)}$  as a minimal condition for the relative pressure  $x$  to be in the asymptotic regime. For  $D_s = 2.5$ , this condition gives  $x > 0.75$ , whereas the asymptotic regime is shifted towards higher relative pressures for larger values of  $D_s$ .

To make a definitive statement about the fractal dimension and the length range, it would be useful to carry out analyses of adsorption data evaluated using different adsorbates. Unfortunately, such analyses are not always possible. Furthermore, since different adsorbate molecules can only be specifically adsorbed by a given type of site, some parts of the adsorbent are left almost completely uncovered and the values of  $D_s$  obtained for different adsorbates may be different.

Equations (6.13) and (6.16) were developed to describe adsorption on a surface of topological dimension  $D_{\text{top}} = 2$ , in three-dimensional space  $d = 3$ . Equation (6.17) can also be generalized to the case of an arbitrary topological and space dimension [3]. This generalization may be important because, in the case of the adsorption on fractal soil materials including clusters of aggregated colloids, polymeric substances (e.g. humic substances), etc.,  $D_{\text{top}} = 1$  rather than  $D_{\text{top}} = 2$ . Finally, it should be noted



that fractal analogues of the BET isotherm have been developed by some authors [49, 51–54].

### 6.3.2 Frenke–Halsey–Hill Theory

The Frenkel–Halsey–Hill (FHH) isotherm was originally developed to describe the growth of thick films and wetting phenomena on a flat surface and was later extended to studying adsorption on fractal surfaces [3, 55]. In contrast to BET theory, FHH theory applies to long-range adsorbate–absorbent interactions and its approach is closely related to the so-called potential theory of adsorption of Eucken and Polanyi (see Ref. [35]).

A common method for deriving the FHH adsorption isotherm is to determine the chemical potential of an adsorbate at a distance  $z$  from the substrate with respect to that in the bulk state. If the adsorbing surface is flat and if the adsorbed film is structurally similar to the bulk liquid adsorbate at a given temperature, then the difference between the chemical potentials,  $\Delta$  is

$$\Delta\mu = \mu_{\text{film}} - \mu_{\text{bulk}} = -\frac{A}{z^3} \quad (6.32)$$

where  $A$  is a (positive) constant. Equation (6.32) is based on the fact that, for a planar adsorbing surface, the molecule–substrate potential can be modeled by the Lennard–Jones (9, 3) function:

$$v(z) = \varepsilon \left[ \left( \frac{z_0}{z} \right)^9 - \left( \frac{z_0}{z} \right)^3 \right] \quad (6.33)$$

where  $\varepsilon$  and  $z_0$  are constant [27]. A final important assumption is that the vapor coexisting with the adsorbed film is ideal, i.e.

$$\Delta\mu = kT \ln \left( \frac{p}{p_0} \right) = kT \ln(x) \quad (6.34)$$

Since at distances larger than the monolayer distance ( $z > \sigma$ ) the repulsive energy  $(z_0/z)^9$  can be neglected, from Equations (6.32) and (6.33) it is possible to derive

$$-\frac{A}{z^3} = kT \ln(x) \quad (6.35)$$

Equation (6.35) is the FHH isotherm that describes the continuous growth of film thickness with increasing relative pressure. For a flat surface, the film thickness is related to the adsorbed amount  $N$  through  $z = N\sigma/N_m$ . Consequently, for a flat surface, the multilayer film growth is governed by

$$\ln \left( \frac{N}{N_m} \right) \propto -\frac{1}{3} \ln[-\ln(x)] \quad (6.36)$$

Since Equation (6.35) also provides a characteristic distance scale for a fractal surface, it is possible to construct the surface at the distance  $z$  from the fractal

solid, which is in turn an ‘equidistance surface’. According to the potential theory of adsorption, the adsorption energy on this surface can be approximated by  $-kT \ln(x)$ . The corresponding surface coverage can be found by calculating the volume within the bounds of the equidistance surface  $V(z)$ . If one neglects the  $B'\sigma^3$  term in Equation (6.30) and normalizes the volume  $V(z)$  so that  $V(\sigma) = N_m \sigma^3$ , then

$$\frac{N}{N_m} = \left[ \frac{A}{kT\sigma^3} - \ln x \right]^{(3-D_s)/3} \quad (6.37)$$

Note that the behavior predicted by FHH theory in the regime  $N/N_m \rightarrow 1$  is physically meaningless because, at small values of  $z$ , the repulsive energy term in Equation (6.33) cannot be neglected. The log–log plot of Equation (6.37):

$$\ln \left( \frac{N}{N_m} \right) \propto \left( \frac{D_s - 3}{3} \right) \ln[-\ln(x)] \quad (6.38)$$

allows direct evaluation of the value of  $D_s$  as the slope of a straight line that approximates the experimental data.

The basic assumption underlying the FHH approach is that the potential energy over a fractal surface should depend only on  $z$  and it is given by the ‘flat surface expression’, i.e. by the relation  $-A/z^3$ . This assumption neglects effects due to the energetic heterogeneity of adsorbing surfaces.

Since the FHH method is relatively simple, it was widely used for determining the surface fractal dimension of several solids, including active carbons [35, 56], aerogels [57], metal films, oxides and related compounds [55]. In particular, Pfeifer and Lui [55] have provided an almost comprehensive review on this topic. Section 6.5 will briefly review applications to soils.

The potential energy in Equation (6.33) assumes that the contributions from several nearby adsorbing surfaces are rare, i.e. that multiple-surface effects are unimportant. This adsorption regime is usually called the ‘van der Waals regime’. In the case of adsorption inside a porous network, the surface–molecule attraction is stronger than that predicted by the  $z^{-3}$  power law, due to the ‘overlapping surface’ effect. In such cases, adsorption is governed by the so-called capillary condensation mechanism. A discussion of an FHH isotherm that obeys this mechanism was presented in [35, 55], whereas an outline of the derivation of this isotherm based on [58] is provided below. In the case of adsorption in porous networks, the FHH isotherm was shown to be a generalization of the well-known Dubinin–Radushkevich (DR) equation [59, 60]:

$$\theta_{DR}(x; R) = \exp\{-M_{DR} R^2 [kT \ln(x)]^2\} \quad (6.39)$$

which describes the filling process of a pore whose diameter is  $R$  and where  $M_{DR}$  is a positive constant. In order to derive the FHH equation, Avnir and Jaroniec [58] considered a network of structurally heterogeneous pores of sizes in the range  $[R_{\min}, R_{\max}]$ .

If the pores are independently filled and the filling of each pore is described by the DR equation, then the overall adsorption isotherm is

$$\frac{N}{N_m} = \vartheta(x) = \int_{R_{\min}}^{R_{\max}} \theta_{\text{DR}}(x; R) J(R) dR \quad (6.40)$$

where  $J(R)$  is the pore size distribution. For fractal pores, the size distribution has the form [48, 61]

$$J(R) = J_0 R^{2-D_s} \quad (6.41)$$

where

$$J_0 = \frac{3 - D_s}{R_{\max}^{3-D_s} - R_{\min}^{3-D_s}} \quad (6.42)$$

is the normalization constant. The values  $R_{\min}$  and  $R_{\max}$  are the experimental bounds, i.e.  $R_{\min}$  is the finest resolution at which fractality prevails ( $R_{\min}$  greater than or equal to the size of the adsorbate molecules) and  $R_{\max}$  is either the upper limit of fractality of the object or the upper size limit of the pores for which Equation (6.39) is valid. Equation (6.40) can be rewritten as

$$\vartheta(x) = \int_0^\infty \theta_{\text{DR}}(x; R) J(R) dR - \int_0^{R_{\min}} \theta_{\text{DR}}(x; R) J(R) dR - \int_{R_{\max}}^\infty \theta_{\text{DR}}(x; R) J(R) dR \quad (6.43)$$

where the last two terms can be neglected at relative pressures of  $x > 0.05$  [58]. The first integral can be evaluated analytically, giving

$$\vartheta(x) = \frac{N}{N_m} = K [-kT \ln(x)]^{-(3-D_s)} \quad (6.44)$$

where the constant  $K = 0.5 J_0 \Gamma[(3 - D_s)/2] M_{\text{DR}}^{(D_s-3)/2}$  depends on the adsorbent–adsorbate interaction.

In summary, the FHH approach yields a straight line:

$$\ln N \propto -\frac{1}{m} \ln[-\ln(x)] \quad (6.45)$$

which allows determination of the fractal dimension from the slope ( $-1/m$ ). If adsorption occurs according to the van der Waals mechanism, then the fractal dimension is

$$D_s = 3 \left( 1 - \frac{1}{m} \right) \quad (6.46)$$

whereas if adsorption is governed by the capillary condensation mechanism, it is

$$D_s = 3 - \frac{1}{m} \quad (6.47)$$

It has been shown [55] that it is possible to distinguish between the two adsorption regimes based upon the magnitude of the exponent ( $1/m$ ). In particular, adsorption occurs according to the van der Waals mechanism if  $1/m < 1/3$ , whereas it occurs by the capillary condensation (or capillary wetting) mechanism if  $1/m > 1/3$ .

### 6.3.3 Fractal Analogue of the Dubinin–Astakhov Adsorption Isotherm

The DR isotherm describing adsorption in a single pore is a special case of a more general isotherm known in the literature as the Dubinin–Astakhov (DA) isotherm [35, 62]:

$$\theta_{\text{DA}}(x; R) = \exp\{-M_{\text{DR}} R^n [kT \ln(x)]^n\} \quad (6.48)$$

where  $n$  can assume values from 1 to 6 [59, 62]. In the case of microporous carbons with cylindrical pores, the values of  $n$  are usually in the range from 1 to 2. For molecular sieves and clay minerals (slit-like pores), they are close to 2, whereas for zeolites possessing pores in quite complex networks the value of  $n$  can be as high as 6.

The isotherm described by Equation (6.48) can be extended to the case of porous adsorbents whose pore-size distribution is governed by Equation (6.41). In Equation (6.40), it is possible to replace the integrand  $\theta_{\text{DR}}(x; R)$  of Equation (6.39) with  $\theta_{\text{DA}}(x; R)$  of Equation (6.48) to obtain [35]

$$\frac{N}{N_m} = J_0(R_{\min}, R_{\max}) \{M_{\text{DR}} [-kT \ln(x)]^n\}^{(3-D_s)/n} \left\{ \gamma \left[ \frac{3-D_s}{n}, R_{\max}^n M_{\text{DR}} (kT \ln x)^n \right] - \gamma \left[ \frac{3-D_s}{n}, R_{\min}^n M_{\text{DR}} (kT \ln x)^n \right] \right\} \quad (6.49)$$

where

$$\gamma(a, b) = \int_0^b t^{a-1} \exp(-t) dt \quad (6.50)$$

is the incomplete gamma function.

The main properties of the isotherm described by Equation (6.49) and its application to experimental adsorption data and related thermodynamic formulae (e.g. adsorption enthalpies, adsorption entropies) are discussed in papers [35, 63], which are devoted mainly to porous carbon adsorbents.

### 6.3.4 A Generalized Form of the Pore Size Distribution

The adsorption isotherm described by Equation (6.49) was derived by assuming that the distribution of the pore sizes is governed by Equation (6.41). However, for real adsorbents, several types of pore-size distribution have been observed, leading to the application of a gamma-type function [62–65]:

$$J(R) = J_0(R_{\min}, R_{\max}) R^{n-1} (R^n - R_0^n)^v \exp[-Q(R^n - R_0^n)] \quad (6.51)$$

where  $Q$ ,  $R_0$ ,  $\nu$  and  $n$  are constants. The normalization constant  $J_0$  depends on the pore range  $[R_{\min}, R_{\max}]$ . For  $Q = 0$  and  $R_0 = 0$ , Equation (6.51) reduces to the distribution function described in Equation (6.41) with  $D_s$  related to the parameters  $\nu$  and  $n$  through  $D_s = 3 - n(\nu + 1)$ . If the pore-size distribution in Equation (6.51) is substituted into Equation (6.40) and the integration is carried out within the limits ( $R_{\min} = 0$ ,  $R_{\max} = \infty$ ), then the isotherm

$$\frac{N}{N_m} = \vartheta(x) = \{M_{\text{DR}}[-kT \ln(x)]^n / Q + 1\}^{-(\nu+1)} \quad (6.52)$$

is obtained, which can reduce to the FHH isotherm under certain assumptions [65].

Recently, Terzyk *et al.* [35] have proposed a ‘hybrid’ model that describes adsorption on porous solids and which takes into account the possibility of adsorption in pores and on external surfaces that are characterized by different fractal dimensions. The resulting adsorption isotherm is the sum of two terms, each involving the relevant fractal exponent. The first term describes the pore filling and the second term accounts for the adsorption on external surfaces. Nonetheless, to the best of our knowledge, the hybrid isotherm of Terzyk *et al.* [35] has not yet been applied to describe experimental data.

### 6.3.5 Fractal Analysis Applied to Adsorption Data

Numerous publications are available on the determination of fractal dimensions from adsorption data and on the application of fractal analysis to studies of adsorption properties and changes occurring during the modification of adsorbants. Section 6.5 provides a comprehensive review of studies devoted to soils, whereas this section outlines very briefly studies not involving soils. Nevertheless, the methods, techniques and theoretical approaches that are described in this section are likely also useful for the investigation of soils. In most studies, the main objective was to calculate and compare the fractal dimensions that were obtained using different approaches.

For example, Fadeev *et al.* [13] investigated different fractal regimes in silicas by comparing  $D_s$  values obtained from mercury intrusion,  $N_2$  and benzene adsorption and the chemisorption of chlorosilanes. Porosity, pore fractal dimensions and surface fractal dimensions were interrelated. The silicas that were investigated behaved as surface fractals in the range of  $r_{\min} = 0.4$  nm to  $r_{\max} = 0.9$  nm.  $D_s$  values obtained from adsorption and chemisorption measurements varied from 2.05 to 2.90. The surface fractal dimension of the silicas obtained from mercury intrusion data were higher and ranged from 2.6 to 3. Various techniques used for the determination of surface fractal dimensions were discussed by Park [42]. Mahnke and Mögel [49] applied a modified fractal BET isotherm to the analysis of  $N_2$  adsorption on a  $\text{TiO}_2$ -ceramic ultrafiltration membrane. A value of  $D_s \approx 2.4$  was obtained by fitting their experimental data to the theoretical isotherm of Equation (6.17), whereas a value of  $D_s = 2.49$  was obtained when Neimark’s method was employed (Equation (6.13)). According to these authors, the observed difference in  $D_s$  was due to the different

assumptions used by two methods. In particular, it was stressed that the fractal BET equation ignores totally the lateral attractive interactions occurring in the adsorbed phase.

$D_s$  values that were obtained by fitting  $N_2$  adsorption data for three shales to the FHH isotherm equation were lower (2.39, 2.24 and 2.20) than those obtained by small-angle neutron scattering (SANS; 2.83, 2.75 and 2.59) [66]. The differences were explained by showing that the theoretical adsorption isotherms that were obtained using a power-law distribution of uncoupled spherical pores exhibited the same general features as the experimental isotherms [66]. The authors thus concluded that the origin of the discrepancies could be attributed to the fact that, at low relative pressure, adsorption is governed by capillary condensation, whereas the van der Waals mechanism prevails at high relative pressure. Since the two possible regimes are partially superimposed, the relationship between the surface fractal dimension and the coefficient ( $1/m$ ) of the FHH isotherm is not unique (cf. Equations (6.46) and (6.47)); thus, the reliability of the surface fractal dimensions evaluated from adsorption data may be questioned.

The relatively large differences observed between  $D_s$  values of clay minerals that are calculated from monolayer capacities for various adsorbates and those obtained from SAXS and NMR experiments led Malekani *et al.* [67] to conclude that the three methods measured a  $D_s$  value that was 'seeing' the material from a different perspective. In particular, SAXS probed chemical heterogeneity through the contrast in electron density while the adsorption method probed physical surface irregularity and the NMR technique measured the mass distribution of structural sites [35].

Other researchers [68, 69] have reached similar conclusions. In particular, studies on freeze-dried organic gels led to  $D_s \approx 2.55$  when the FHH isotherm equation was applied to  $N_2$  adsorption data and  $D_s > 2.6$  when SAXS was used [68]. For three shale samples, Ma *et al.* [69] found that the  $D_s$  values obtained from  $N_2$  adsorption data were significantly lower than those obtained from SANS experiments. The authors [69] suggested that the discrepancies were due to the different properties of the dense liquid phase in the small and large pores and to the different volumes that were occupied by the adsorbed film with respect to that probed by SANS. In conclusion, while SANS (and SAXS) 'sees' the total porosity of a system (including inaccessible pores), adsorbate molecules can only penetrate pores that are both larger than their molecular diameter and accessible.

On the other hand, Weidler *et al.* [70] observed reasonable agreement between  $D_s$  values ( $2.55 \pm 0.05$ ) obtained from SAXS and  $N_2$  adsorption data for two synthetic goethites whose surface morphology was modified by HCl treatment in order to obtain different porosities. Micropores were formed by short acid treatments and longer treatments caused the removal of pore walls, leading to the release of Fe. The best agreement between  $D_s$  values from  $N_2$  adsorption and those from SAXS experiments was observed for treatments ranging from 2 to 5 h. Similar agreement was obtained by Diduszko *et al.* [71] for  $D_s$  values determined on activated carbons when comparing benzene adsorption data and SAXS experiments.

Jaroniec *et al.* [72] extensively evaluated fractal dimensions of a model porous solid by simulating adsorption isotherms, then using a density functional approach, and then finally analyzing data obtained by different methods. The surface fractal dimension depended on the range of pore sizes analyzed, thus confirming the validity of the FHH method.

Fractal analysis was also applied to investigate the structural changes of a number of modified adsorbents. In particular, Weidler and Stanjek [73] studied N<sub>2</sub> adsorption on synthetic ferrihydrite samples that were heated at different temperatures for different times. They showed that the fractal dimensions were helpful when interpreting the structural transformations that occurred during thermal treatment. Sonwane *et al.* [17] used  $D_s$  values determined from N<sub>2</sub> adsorption measurements, mercury porosimetry, SAXS and SANS to investigate the structure of mesoporous crystalline MCM-4 molecular sieves of different pore sizes.

Tatler and Erdem-Senatarlar [74] showed that the values of fractal dimensions measured at zeolite A borders over a wide range of reagent concentrations, temperatures and equilibration times depended on the synthesis process used. Furthermore, values were useful to predict the type of zeolite that was formed. In a subsequent study, Erdem-Senatarlar *et al.* [75] observed that the H-form of an NaY zeolite that was obtained by calcination of the NH<sub>4</sub>-exchanged form featured a higher adsorption capacity and a higher surface fractal dimension ( $D_s = 2.43$ ) than those of the original sample.

The measurement of the fractal dimensions of the pore spaces in building materials has allowed the development of a mathematical model that relates the water content of the porous material to the relative humidity of the surrounding environment at a given temperature, enabling predictions of water suction and adsorption [76]. The fractal approach has also been suggested for use in predictions of other technologically important properties of building materials, including resistance to frost, thermal conductivity and specific heat.

The  $D_s$  values of chars that were produced from three Chinese coals at different burn-off ratios were obtained by N<sub>2</sub> adsorption/desorption using the fractal BET equation and by scanning electron microscopy analysis [77].  $D_s$  values reached a maximum in the 35–45 wt% char burn-off interval and then decreased with increasing the carbon burn-off ratio.

The fractal approach was also used to investigate adsorption and desorption mechanisms of water vapor on active carbons that were derived from coconut shell, coal, coke and pitch fiber featuring a wide range of BET specific surface areas [78].  $D_s$  values were measured for the water clusters adsorbed on primary carbon centers. Values ranging from 1.64 to 1.67 implied a diffusion-limited aggregation model on a pore wall plane, whereas higher  $D_s$  values (up to 1.86), measured at a relative pressure  $x = 0.95$ , implied the formation of water clusters that were partly merged vertically to the walls.

Rizkalla *et al.* [79] studied the influence of surface fractality on the solid–liquid interface reactivity of magnesium oxides, hydroxides and silicates by determining

their fractal dimensions from mercury intrusion and  $N_2$  adsorption data by application of the FHH isotherm equation and the method of Neimark. For magnesium silicate samples, good agreement was found between  $D_s$  values obtained by the Neimark method ( $D_s = 2.85$ ) and by the FHH isotherm equation ( $D_s = 2.87$ ), whereas a less satisfactory agreement was obtained for magnesium oxides and hydroxides. The mercury porosimetry method usually yielded  $D_s$  values that were lower than those obtained by adsorption methods. Furthermore, a correlation between the acid neutralization activity and the fractal properties was shown to exist for these adsorbent surfaces [79].

Podkościelny *et al.* [80] and Kano *et al.* [81] extended the theories used for gas adsorption to adsorption from binary liquid mixtures. In particular, the former authors [80] investigated the adsorption of aliphatic alcohols, benzene and aliphatic ketones on silica gels having  $D_s = 2.61$  and  $2.69$ , whereas the latter authors [81] studied the adsorption of several organic compounds from water on activated carbons having high  $D_s$  values ( $D_s \approx 3$ ).

Laszlo *et al.* [82] compared the fractal dimensions of carbonaceous composite materials evaluated by: (a)  $N_2$  adsorption data using the FHH equation; (b) adsorption data of gaseous  $N_2$  and iodine and aqueous solutions of methylene blue, 2,3,4-trichlorophenol and naphthalene using Equation (6.5); and (c) SAXS experiments.  $D_s$  values obtained using (a) and (b) were very different. For example, fractal dimensions determined for a carbonaceous adsorbent derived from auto tires gave  $D_s = 2.56$  when applying the FHH equation, as opposed to  $D_s = 2.96$  when using Equation (6.5). The authors suggested that observed discrepancies were potentially due to inaccurate values of the cross-sectional area estimated for the adsorbed molecules and employed in Equation (6.5). For example, for the adsorption of polar molecules with different binding possibilities from aqueous solutions, their orientation at the surface and, consequently, the value of their cross-sectional area might be influenced by solute composition. Furthermore, carbonaceous samples with a high ash content have a large number of active mineral sites where the configuration of adsorbed polar molecules is uncertain.

Numerical modeling studies have also been employed to investigate the behavior of adsorbates by fractal surfaces and fractal pores. For example, Park *et al.* [83] developed a computer method for which five fractal surfaces with  $D_s$  values ranging from 2.262 to 2.771 were generated. The reaction of CO with  $O_2$  on the surfaces was simulated by a Monte Carlo method. The results showed that catalytic CO oxidation proceeded more efficiently on surfaces with higher fractal dimensions. In addition, as the surface fractal dimension became higher, the first-order kinetic transition (i.e. transition from a highly reactive phase to a practically nonreactive phase) was shifted to a higher partial pressure of CO. This implied that the poisoning of the catalyst surface occurred for more complex surfaces at a higher CO partial pressure.

Applications of a molecular dynamics simulations to investigations of the microstructure and dynamic properties of nanoporous silica gels yielded densities down to  $0.7 \text{ g ml}^{-1}$  and mass fractal dimensions of 2.6 or higher [84]. The specific surfaces that



were calculated for the porous silicas were in good agreement with those obtained from adsorption experiments; thus, the authors suggested that the algorithm that was used could be applied to other computer simulations of adsorption.

By measuring surface fractal dimensions using adsorption isotherms, Fuji *et al.* [85] studied the surface structure of nonporous silica powders that were modified with *n*- and *t*-butyl alcohol and the effects of surface structure on wettability. The monotonous increase of the fractal dimension with increasing density of *t*-butoxy groups suggested that this functional group was rigid and did not change its conformation. On the other hand,  $D_s$  variations for the surface that was modified with *n*-butyl alcohol (*n*-surface) indicated that the structure of *n*-butoxy groups was flexible and that its conformation changed with the group density. At low densities, the *n*-butoxy groups tended to lie parallel to the surface, whereas at higher densities their orientation was perpendicular to the surface. By comparing molecular dynamics simulations with experimental results, it was shown that variations of the mobility of the methyl group in the *n*-butoxy group were closely related to changes of the  $D_s$  value of the *n*-surface. Furthermore, variations in the conformations of the *n*-butoxy groups as obtained from molecular dynamics simulations were in good agreement with the change in wettability of the *n*-modified surface.

## 6.4 ADSORPTION ON ENERGETICALLY AND GEOMETRICALLY NONUNIFORM SURFACES

The description of adsorption on geometrically uniform but energetically heterogeneous surfaces has been frequently discussed in the literature [60, 86]. For planar and energetically homogeneous surfaces, adsorption equilibria have been often described in terms of Equation (6.15), the BET equation, with the constant  $C$  being a function of the adsorption energy. The assumption of energetic homogeneity can be removed by considering the total measured adsorption as the sum of ‘local’ processes, each occurring on sites of the same adsorption energy. If these processes are independent, then the total adsorption isotherm  $\vartheta_t(x)$  for any assigned surface heterogeneity is

$$\vartheta_t(x) = \int_{\Delta} \chi(\varepsilon) \theta_1(x, \varepsilon) \quad (6.53)$$

where  $\theta_1(x, \varepsilon)$  is the local isotherm that governs adsorption on sites of adsorption energy  $\varepsilon$ ,  $\chi(\varepsilon)$  is the energy distribution function and  $\Delta$  is the range of possible energies of adsorption. This range is usually assumed to be  $\Delta = [\varepsilon_m, \infty)$ , where  $\varepsilon_m$  is the lowest value of the energy of adsorption, which is assumed to be equal to the energy of condensation of the adsorbate  $\varepsilon_c$ . A number of isotherm equations can be derived assuming different analytical forms of  $\theta_1(x, \varepsilon)$  and  $\chi(\varepsilon)$ . On the other hand, if the function  $\theta_1(x, \varepsilon)$  is known and  $\vartheta_t(x)$  is experimentally determined, then

Equation (6.53) is an integral equation for  $\chi(\varepsilon)$ . Numerous methods of solution of Equation (6.53) with respect to  $\chi(\varepsilon)$  are available in the literature [60, 64, 86].

Although several aspects of adsorption on energetically heterogeneous surfaces have been studied, including that of phase transitions [60, 86], most emphasis was placed on the effect(s) of energetic heterogeneity. Energetically and geometrically, heterogeneities might also be related. The energetic heterogeneity is associated with the presence of adsorbing sites of different chemical properties and with pores of different geometries. Since the adsorbing potential depends on the geometric characteristics of the pores, energetic heterogeneity may also result from geometric nonuniformity. However, the considerations above do not imply that the fractal dimensions must be a function of  $\varepsilon$ , nor that the energy distribution must be a function of  $D_s$ .

The simulations discussed in Section 6.2.1 were aimed at checking how the fractal dimension of the geometric adsorbent surface was related to the fractal dimension of a surface passing through the minima of the adsorbent–adsorbate molecular potential. A similar numerical experiment can also be used to search for the dependence of the fractal dimension on the energy of adsorption  $\varepsilon$ . The simulations in Section 6.2.2 can be repeated [16, 23] by assuming that the molecular energy can vary from site to site with sites distributed differently along the investigated fractal curve. Two topographic models of the surface have been used: (a) the patch model, where sites of equal energy are grouped into patches and (b) the random topographic model, where different sites are distributed randomly over the whole surface. After distributing the adsorbing sites of different energies on the fractal curve, the curve passing through the minima of the fluid–solid potential could be evaluated. The curve was then used to evaluate the fractal dimension according to the method described in Section 6.2.1. The main result was that the fractal dimension  $D_s$  was, in general, only slightly dependent upon the energetic heterogeneity of adsorbing centers on the surface. Nonetheless, the numerical experiments that were performed should not be considered as being exhaustive of all of the possibilities of a distribution of energetic centers along the fractal curve. Because these experiments have a statistical character, it is impossible to ascertain whether the results could be applied to any fractal surface. Very probably, surfaces exist for which the influence of energetic heterogeneity on the fractal dimension is different from that described above. In particular, the simulation described above was performed for adsorption on external surfaces, i.e. where multiple surface effects were neglected.

#### 6.4.1 Models Based on No Correlations between Energetic and Geometric Heterogeneities

The function  $\chi(\varepsilon)$  refers to the total energetic heterogeneity of an adsorbent, and provides no information about the topography of energetic centers on a surface. Similarly,  $D_s$  is a global characteristic of the adsorbent, i.e. it does not refer to any specific site on the surface. However, in the case of a patchwise topography, it is

possible to imagine a model in which each patch is characterized by its own fractal dimension. On the contrary, no possibility exists to define the fractal dimension for a given kind of energetic center for the case of a random topography. Consequently, Equation (6.53) can be generalized as [15, 23, 30, 44]

$$\vartheta_t(x, D_s) = \int_{\Delta} \chi(\varepsilon) \theta_t(x, \varepsilon; D_s) \quad (6.54)$$

where  $\theta_t(x, \varepsilon; D_s)$  is the local adsorption isotherm on the surface as characterized by the  $D_s$  value of the entire surface. By integrating Equation (6.54) with different functions  $\chi(\varepsilon)$ , the corresponding isotherm equations can be developed. In particular, by assuming that the local adsorption isotherm can be described by Equation (6.17), the fractal BET equation, one obtains

$$\vartheta_t(x, D_s) = \frac{N}{N_m} = \frac{f(x, D_s)}{g(x)} \int_{\Delta} \chi(\varepsilon) \frac{g(x) \exp[(\varepsilon - \varepsilon_c)/kT]}{1 + g(x) \exp[(\varepsilon - \varepsilon_c)/kT]} d\varepsilon \quad (6.55)$$

where the functions  $f(x, D_s)$  and  $g(x)$  are defined in Section 6.3. The form of Equation (6.55) is identical to that developed for geometrically uniform surfaces, such that the mathematical methods described in [47, 60, 64] can be applied. In particular, using the so-called condensation approximation, where  $B_{DR}$  is a positive constant and  $g_m = \exp[(\varepsilon_c - \varepsilon_m)/kT]$ , it can be shown that

$$\vartheta_t(x, D_s) = \frac{f(x, D_s)}{g(x)} \exp \left( -B_{DR} \left\{ \ln \left[ \frac{g(x)}{g_m} \right] \right\} \right) \quad (6.56)$$

is related to a quasi-Gaussian distribution of the form

$$\chi(\varepsilon) = 2B_{DR} \left( \frac{\varepsilon - \varepsilon_m}{kT} \right) \exp \left[ -B_{DR} \left( \frac{\varepsilon - \varepsilon_m}{kT} \right)^2 \right] \quad (6.57)$$

In the case of flat surfaces, Equation (6.56) reduces to the DR isotherm in Equation (6.39).

The function  $\chi(\varepsilon)$  possesses a single maximum, but in many cases the extremely complex nature of the adsorbent requires a more general approach that can allow for several maxima in the distribution functions, each corresponding to adsorption centers. Jaroniec and Madey [60] proposed the use of the following function:

$$\chi(\varepsilon) = \frac{\partial}{\partial \varepsilon} \exp \left\{ \sum_{i=1,L} b_i [(\varepsilon - \varepsilon_m)/kT]^2 \right\} \quad (6.58)$$

where  $\{b_1, b_2, \dots, b_L\}$  are the distribution parameters, which must be selected in such a way that  $\chi(\varepsilon) \geq 0$ . The distribution in Equation (6.58) is normalized:

$$\int_{\Delta} \chi(\varepsilon) d\varepsilon = 1 \quad (6.59)$$

From Equations (6.55) and (6.58) one obtains

$$\vartheta_t(x; D_s) = \frac{N}{N_m} = \frac{f(x, D_s)}{g(x)} \exp \left\{ \sum_{j=1, L} b_j \ln^i [g(x)/g_m] \right\} \quad (6.60)$$

Any application of Equation (6.60) to experimental data requires knowledge of the surface fractal dimension of the adsorbent investigated so that the evaluation of the energy distribution function is reduced to an approximation of the experimental data using Equation (6.60). This calculation is most conveniently performed using a method quite similar to that described by Jaroniec and Madey [60] for geometrically uniform surfaces.

The approach described above was applied to the analysis of  $N_2$  and  $H_2O$  adsorption data on different horizons of an Orthic Luvisol [15, 30].  $D_s$  values of the soil samples were determined from adsorption and monolayer capacities of both adsorbates on grain samples of different sizes (see Section 6.2.1).  $D_s$  values calculated from water adsorption data ranged from 2.25 to 2.35, whereas those evaluated from  $N_2$  adsorption data were slightly higher, ranging from 2.38 to 2.40. Because of the different chemical character of  $N_2$  and water vapor, the adsorption centers for these substances are different. In particular, only external adsorbing surfaces are available to  $N_2$  molecules, whereas water molecules may also explore the internal spaces of soil particles. As a result, monolayer capacities of water vapor are higher than those resulting from  $N_2$  experimental data. Experimental isotherms were used to determine the coefficients  $\{b_i\}$  and compute the distribution functions  $\chi(\varepsilon)$  for soil samples. Finally, adsorption on energetically and geometrically nonuniform surfaces has also been studied by Lefebvre *et al.* [87], Giona *et al.* [46] and Tsunoda *et al.* [88].

#### 6.4.2 Generalized Fractal BET Equation for Adsorption on Geometrically and Energetically Nonuniform Porous Solids

It has been stressed in this chapter that the statistical independence of the fractal dimension and the energy distribution function can be assumed only for adsorption on external surfaces or in mesopores. Adsorption by a fractal porous network that takes into account the possible correlations between  $D_s$  and adsorption energies has been described by Rudziński *et al.* [89, 90].

In the simple case of a porous network with ‘chemically uniform’ surfaces, the dependence of the adsorption energy on the pore size can be easily determined. In particular, if the network is composed of slit-like pores and the interaction of a molecule with a single pore surface is described by Equation (6.34), then the potential energy of a molecule inside the pore can be calculated by summing the potentials from the two surfaces. The minima on the potential curves are identified as the adsorption energies. If the distribution of pore sizes  $J(R)$  is fractal, then  $\chi(\varepsilon)$  depends on the type of distribution, and in turn on the  $D_s$  value. Rudziński *et al.* [89, 90] postulated

the following functional form for the dependence between the energy of adsorption and the pore-size parameter  $R$ :

$$R = \exp[-F(\varepsilon)] \quad (6.61)$$

where  $F(\varepsilon)$  is a function describing the individual features of the adsorption system. By assuming that  $R_{\min} = 0$ , the following isotherm equation could be derived:

$$\vartheta_t(x, D_s) = \left( \frac{r_0}{R_{\max}} \right)^{3-D_s} \exp \left\{ - \left[ \frac{3-D_s}{2} \right] \left( \frac{\partial^2 F(\varepsilon)}{\partial \varepsilon^2} \right)_{\varepsilon=\varepsilon_0} \left[ kT \ln \left( \frac{x}{x_0} \right) \right]^2 \right\} \quad (6.62)$$

where  $x_0 = \exp[(\varepsilon_0 - \varepsilon_c)/kT]$ ,  $r_0 = \exp[-F(\varepsilon_0)]$  and  $\varepsilon_0$  is a constant. Equation (6.62) is equivalent to Equation (6.56), except that the coefficient  $[kT \ln(x/x_0)]^2$  depends linearly on the fractal dimension  $D_s$ .

One of the assumptions underlying the theory described above was that the lower fractality range was zero. The problem of the limits  $[R_{\min}, R_{\max}]$  has already been discussed in Section 6.3. While accepting the ‘classical’ pore size distribution, Equation (6.41), along with its limited range of applicability,  $[R_{\min}, R_{\max}]$ , one can describe only a part of the experimental isotherm corresponding to pressures in the relevant range  $[p_{\min}, p_{\max}]$ . To derive an isotherm equation that could be valid over the entire range of pressures, Rudziński *et al.* [89, 90] considered a new model of geometrical heterogeneity, according to which real adsorbents are never totally irregular (fractal) and never perfectly regular, but instead they have a structure that is intermediate between the two extremes. The isotherm for such adsorbents, which were named ‘partially correlated’, has the form

$$\ln \left\{ \frac{N/[M_m f(x, D_s)]}{1 + N/[M_m f(x, D_s)]} \right\} = A_0 + A_1 kT \ln g(x) + A_2 [kT \ln g(x)]^2 \quad (6.63)$$

where  $\{A_i\}$  are the constants.

Unfortunately, the evaluation of the parameters that are described by Equations (6.62) and (6.63) requires the use of rather sophisticated numerical procedures because the isotherms are in a nonlinear form relating the amount of adsorbed molecules to the relative pressure. To evaluate these parameters, Terzyk *et al.* [35] constructed a special algorithm that was able to fit the theoretical isotherm described by Equation (6.63) to the experimental data. This algorithm was a hybrid of a random search method and an evolutionary searching procedure. Numerical calculations of the parameters in Equations (6.62) and (6.63) require special care, and large differences in values might be obtained using different strategies for the calculations.

## 6.5 FRACTAL ANALYSIS OF ADSORPTION DATA OBTAINED ON SOILS AND SOIL MINERALS

### 6.5.1 Soil Minerals

Soil solid phases consist of a very complex mixture of inorganic and organic components that determine the physical and physicochemical properties of the soils. Organic components, which are usually present in much smaller quantities than inorganic components, include plant and animal residues at various stages of decomposition, living cells and tissues of soil organisms, and substances synthesized in soil, the so-called humic substances. Inorganic components include primary and secondary minerals ranging in size from very fine colloids to large rocks. In soils, the sand and silt fractions consist exclusively of primary minerals, whereas minerals in the clay fraction are predominantly secondary and include layered silicates, and various oxides, carbonates and sulfur minerals. The term 'clay mineral' refers to soil inorganic materials less than  $2\text{ }\mu\text{m}$  in effective diameter and comprises minerals with the sheet silicate structure of phyllosilicates. The secondary minerals that are dominant in the soil clay fraction are kaolinites, smectites, vermiculites, mica and especially montmorillonites.

Soil clay minerals often differ in their properties from those of pure minerals. In particular, they are generally much less ordered and smaller in size than pure minerals. Often, neighboring particles or sheets overlap. Furthermore, they exhibit surface irregularities at the molecular scale and a nonuniform microporous structure. Determinations of the fractal dimensions of clay minerals have been reported in several papers [11, 21]. For montmorillonite, a value of  $D_s \approx 2$  has been measured [11, 21, 91, 92], whereas other authors [87, 93, 94] have obtained a higher value of  $D_s = 2.7$ , e.g. by measuring  $\text{N}_2$  isotherms. Sokołowska and co-workers [15, 16] analyzed the monolayer capacities of montmorillonite with nonpolar and polar adsorbates and found values of  $D_s = 2.1$  and  $2.3$  respectively. Similar differences in  $D_s$  values were also observed for kaolinite [16, 21, 91, 93]. The origin of these differences is probably related to the fact that experiments were carried out on mineral samples of different origins. Small, but variable, amounts of strongly bound water could change surface geometries.

One of the questions that can be answered with the help of adsorption measurements concerns the microtexture of natural clay minerals. Several idealized models for the texture of soil clays (see [5]) have been considered, but rather than assuming one model a priori, one should try to gain useful information from experimental relationships between the size of clay particles and apparent density or surface area and internal porosity, as described in Sections 6.1 and 6.2.1. Experiments aiming at the evaluation of the microtextures of clay minerals were carried out by Ben Ohoud and van Damme [95], who studied kaolinite, sepiolite, palygorskite and 20 monoionic montmorillonite samples. The accessible surface area  $S$  of consecutive fractions of size  $r$  was measured by  $\text{N}_2$  adsorption using the classical BET method, whereas the open porosity  $P$  was measured from the amounts of adsorbed  $\text{N}_2$  at a relative vapor

pressure of  $x = 0.99$ . These authors [95] also determined mass (fragmentation) fractal dimensions by measuring the volume occupied by a mass of powdered particles of a given size. They found, within experimental error, a value of  $D_M = 3$  for all clays studied, i.e. the samples were not mass fractals. In contrast, the behavior of the accessible surface area and open porosity of samples was much more interesting [95]. For the fibrous clays, kaolinite and La-saturated montmorillonite, the values of  $S$  and  $P$  were independent of the grain size, i.e. the surface fractal dimension  $D_s = 3$ , which suggested that the ideally porous model was applicable in these cases. All of the other montmorillonite samples were characterized by a linear dependence of  $\ln(S)$  versus  $\ln(r)$  over a quite wide range of  $r$  values. The slopes of these curves led to nontrivial values of  $D_s$  ( $2 < D_s < 3$ ). Furthermore, the same power laws were obtained for porosity with scaling exponents that were in very good agreement with  $D_s$  values. In addition, pronounced correlations between  $D_s$  values and the coherence length, i.e. the thickness of the ordered stacks of elementary clay sheets determined from X-ray diffraction, were observed [95].

A question has arisen with regard to the possible existence of a relationship between the properties of exchangeable cations and  $D_s$  values, which implies the possible capacity of different cations to generate stacks of smectite lamellae. In this respect, highly charged and/or small cations with a large polarizing power would be expected to have a strong local ordering tendency and, thus, be able to form these stacks. The left panel of Figure 6.2 displays the values of  $D_s$  obtained from  $N_2$  adsorption data [30, 95], whereas the right panel shows the average adsorption energies of water vapor on different monoionic forms of montmorillonite [96]. The trends shown here

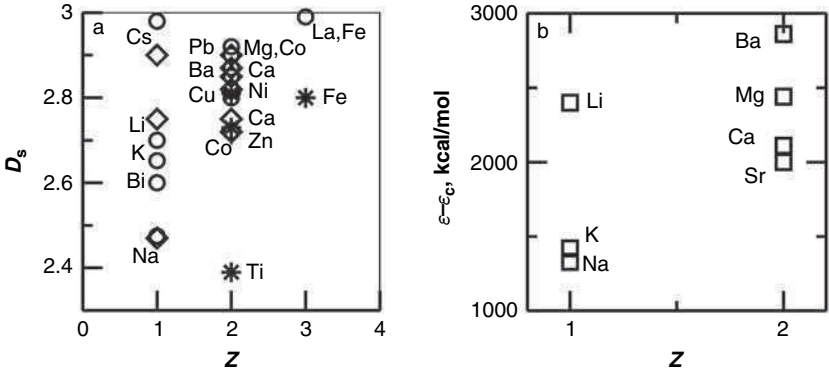


**Figure 6.2** (a) Values of surface fractal dimensions  $D_s$  obtained from  $N_2$  adsorption data from the authors (diamonds), from [30] (circles), and from [95] (stars). (b) Average adsorption energies of water vapor (data from [96]) on various monoionic forms of montmorillonite as a function of the cation charge  $Z$ . Reproduced by permission of the Polish Academy of Sciences.

are consistent, i.e. highly charged trivalent ions yield very high  $D_s$  values, bivalents yield intermediate values and monovalent ions yield generally lower  $D_s$  values. The same trend is valid for the average adsorption energies, although a closer look shows that the correlation between the polarizing power and  $D_s$  is not simple. For example, in the presence of the large and monovalent ion  $\text{Cs}^+$ , a very high  $D_s$  value is obtained. Thus, the fine structure of the hydration shells in the interlayer space and type of the cation interacting with montmorillonite sheets should be taken into account.

Recently, Huang *et al.* [97] provided a good illustration of the contribution of fractal analysis to the determination of the adsorption mechanism and the effects of cation exchange on the pore and surface structure of montmorillonite. Results of fractal analysis of  $\text{N}_2$  adsorption data were compared with X-ray diffraction and differential scanning calorimetry patterns. Subsequently, isotherms were measured for benzene, hexane and cyclohexane adsorption onto cation-exchanged montmorillonite. An important finding was that Ti cations produced structural modifications that caused the opening of pores, with an increase of pore size, pore volume and pore connectivity with the result of an instantaneous smoothing of the surface.

Wang *et al.* [98] studied the effects of the adsorption of basic dyes such as basic green and basic violet on a Ti-exchanged calcium montmorillonite. The changes in surface and pore structure and the adsorption behavior of the titanium montmorillonites were evaluated using fractal analysis and the FHH equation applied to the experimental  $\text{N}_2$  adsorption isotherms. The decrease in the BET surface area of the montmorillonites that followed the adsorption of the dyes was interpreted in terms of a partial reduction in surface roughness (surface screening effect) and a partial inhibition of  $\text{N}_2$  displacements within the pores (pore blocking effect). Changes in the  $D_s$  value before and after dye adsorption were used to evaluate these two effects with respect to the changes in mean pore size.

Bentonite, which usually contains more than 50 % montmorillonite, is often used as a back-filling buffer material to prevent groundwater contamination because of its low hydraulic conductivity and ability to expand and fill up openings. In this context, Xu and co-workers [92, 94] proposed a method to determine the surface fractal dimensions of swelling materials. They derived a relationship between the normalized water volume and the vertical overburden pressure of the form

$$\frac{V_w}{V_m} \propto p^{D_s-3} \quad (6.64)$$

where  $V_w$  is the water volume confined by the montmorillonite in bentonite,  $V_m$  is the volume of montmorillonite in the bentonite, and  $p$  is the overburden pressure. The fractal dimension of Wyoming bentonite obtained from the swelling test,  $D_s = 2.64$ , was nearly equal to that evaluated from  $\text{N}_2$  adsorption using the FHH equation,  $D_s = 2.65$ , and larger than that measured by mercury porosimetry,  $D_s = 2.44$ . The authors [94] interpreted this discrepancy as resulting from an ‘oversimplified



assumption' in the interpretation of mercury porosimetry data, which considers the pore space as bundles of nonintersecting tubes.

The so-called pillared montmorillonities are prepared by intercalating oligomeric metal hydroxide ions into interlayers [31]. Pillared clays have high surface areas and the structural parameters of their micropores vary as function of the pillaring material and preparation conditions. These materials show promise for use as high-performance adsorbents and active catalysts. Yamazaki *et al.* [99] performed N<sub>2</sub> adsorption experiments to investigate the structure of pores and sizes of pillars of montmorillonites pillared with Al and Cr.

Szücz *et al.* [32] prepared a series of substrates with different Pd contents (Pd-nanophase reactors) by depositing Pd nanoparticles on the surface and in the micropores of a montmorillonite pillared with aluminum oxide. The N<sub>2</sub> adsorption and SAXS data showed that the deposition of Pd nanoparticles inside the micropores decreased the specific surface area and the porosity of the substrate.  $D_s$  values determined from SAXS experiments increased with increasing amounts of deposited Pd. In particular, the value of  $D_s$  increased from 2.76 for nonmodified pillared montmorillonite to 2.83 for montmorillonite containing 2.09 % Pd and 2.9 for the substrate containing 2.53 % Pd.

In general, the surfaces of soil clay minerals are covered by amorphous oxyhydroxides and organic matter [100]. Fine grains of soils are often composed of random aggregates of clays, oxides and organic matter, including organo-mineral complexes, which are very common in soils. The structure and reactivity of both the organic and the mineral components are modified drastically when combined.

Tombácz *et al.* [101] carried out a systematic investigation on samples of montmorillonite and kaolinite covered with natural organic matter and synthetic humic acids in order to determine the role of organic coatings on clay interfacial properties. A rough polyionic layer was shown to form on the surface of clay particles, causing a decrease of in the pore volume and the specific surface area and a simultaneous increase of the surface fractal dimension from  $D_s = 2.25$  (uncoated kaolinite) to  $D_s = 2.34$  (coated kaolinite) and from  $D_s = 2.47$  (uncoated montmorillonite) to  $D_s = 2.61$  (coated montmorillonite). Similar studies were conducted by Sokołowska and Sokołowski [102] for evaluating changes to the surface properties of kaolin following interactions with a natural humic acid.

Józefaciuk *et al.* [38] used water vapor adsorption/desorption and mercury porosimetry to investigate modifications occurring in bentonite, illite and kaolin samples that were treated with randomly methylated  $\beta$ -cyclodextrin (RAMEB). With increasing amounts of RAMEB, the surface areas and micropore volumes of the minerals decreased, whereas their surface fractal dimensions increased. The observed changes suggested the occurrence of strong interactions between the RAMEB and the clay minerals, in contrast to previous findings [103] that implied that RAMEB and minerals could coexist as separate, nonreactive phases.

### 6.5.2 Whole Soils

Various processes and phenomena that occur in soils, e.g. the movement of gases, the movement of water due to hydraulic gradients and the distribution of organic and inorganic constituents, are markedly influenced by the irregularities of both the external surfaces of soil particles and the inner surfaces of soil pores. The fractal approach offers the possibility of being able to quantify the intrinsic heterogeneity of soil and related soil properties at different scales. Surprisingly, except in the case of some soil components like carbonaceous adsorbents and clay minerals, adsorption methods have rarely been employed to investigate the geometric heterogeneity of soils.

Adsorption studies of soil geometric heterogeneity which have used a fractal approach include: (i) the comparison of the fractal dimensions evaluated from adsorption data with values obtained by other methods [24, 33, 43, 102, 104–110]; (ii) the use of the fractal dimension, in some cases together with the energy distribution function  $\chi(\varepsilon)$  to characterize soils [24, 43, 44, 107–114]; and (iii) the monitoring of changes to soils caused by degradation, organic matter removal, alkalization, acidification, cultivation, etc. [14, 33, 38, 39, 41, 43, 44, 102, 104, 105, 109, 114, 115].

Surface fractal dimensions of a number of Cambisols and Luvisols were determined using the FHH equation from data obtained from  $N_2$  and water vapor adsorption isotherms. Values were compared with those obtained from the mercury intrusion method and with mass fractal dimensions that were evaluated from particle-size distributions using a modified number-based method [108] (Figure 6.3). This method was proposed by Kozak *et al.* [116] in order to correct some inconsistencies of previous approaches

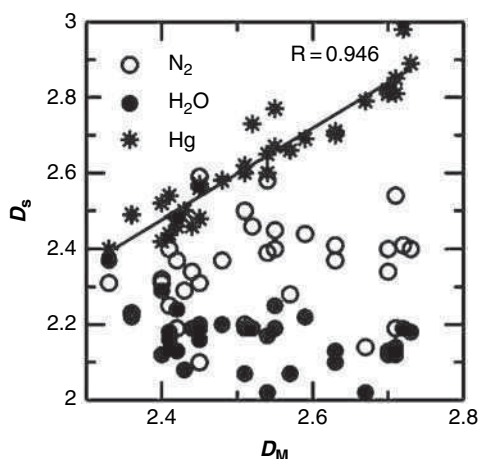


**Figure 6.3** Correlations between the mass fractal dimension  $D_M$  and the surface fractal dimensions  $D_s$  obtained from  $N_2$  and  $H_2O$  adsorption data and from mercury porosimetry data for a number of Cambisol and Luvisol samples [108]. The correlation coefficient  $R$  refers to the latter data. Reproduced by permission of Wiley-VCH.

in estimating the mass fractal dimensions of soils [e.g. 117, 118].  $D_s$  values evaluated from  $H_2O$  adsorption data ranged from 2.02 to 2.25 for Luvisols and from 2.02 to 2.37 for Cambisols.  $D_s$  values obtained from  $N_2$  isotherms were generally higher, ranging from 2.14 to 2.41 for Luvisols and from 2.10 to 2.59 for Cambisols. These results suggested that different surface sites with different fractality were responsible for adsorption of  $H_2O$  and  $N_2$  molecules and that the gas–solid interface was smoother for  $H_2O$  adsorption. The capacity of  $H_2O$  molecules to form hydrogen bonds may be an important factor for smoothing the adsorbed layer. However, not only water adsorption, but also water absorption may occur in soils, potentially distorting evaluations of the fractal dimension. In contrast,  $N_2$  molecules are mainly adsorbed via van der Waals forces; thus, the geometry of the interface might be expected to resemble that of the underlying solid more closely. No significant correlation related  $D_s$  values evaluated from  $N_2$  adsorption isotherms and mercury porosimetry data for the soils investigated, possibly because these two methods provide information on different geometrical scales. On the other hand,  $D_M$  values of these soils were positively correlated with  $D_s$  values obtained from mercury porosimetry [108].

Ślawiński *et al.* [106] applied the so-called ‘pore–solid–fractal’ (PSF) model to describe water retention curves that were measured for six peat soils in order to obtain their  $D_M$  values. Furthermore,  $D_s$  values were determined by applying the FHH equation to water vapor adsorption and desorption and  $N_2$  adsorption isotherms. The PSF model gave  $D_M$  values ranging from 2.88 to 2.94. In contrast to the results described above for Cambisols and Luvisols [108],  $D_s$  values obtained from  $N_2$  adsorption isotherms ( $2.25 \leq D_s \leq 2.575$ ) were lower than those evaluated from water adsorption ( $2.58 \leq D_s \leq 2.70$ ) and desorption ( $2.63 \leq D_s \leq 2.75$ ) isotherms.

Removal of carbohydrates from soil samples that were collected from a long-term (12 years) managed grassland increased  $D_s$  values from 2.75 to 2.85 [33]. Furthermore, these values were close to those obtained from mercury intrusion experiments on the same soils (cultivated with barley) [14]. Based upon these experiments, Pachepsky *et al.* [14] concluded that long-term management affected the specific soil surface area, but not the  $D_s$  values. Although no differences in  $D_s$  values were measured in the specific pore dimension range from a few nanometers to about 100 nm, differences in surface roughness could exist in other ranges [42, 105, 119].  $D_s$  values obtained by applying the FHH isotherm equation to water vapor adsorption data were used to characterize various Bulgarian soils, including leached chernozem, smolnitza, mountainous light-gray podzol and meadow zinnamonic soils [110] and to describe the changes in physicochemical properties with the profile depth of solonetz soils [45].

Water vapor and  $N_2$  adsorption data were collected for several Polish alluvial soils [24, 109] with the aim of determining their surface and energetic heterogeneity using the theory outlined in Section 6.4. All samples investigated contained only small amounts of micropores and mesopores; therefore, the fractal dimensions were evaluated using the FHH equation and by assuming a van der Waals adsorption regime. The  $D_s$  values that were obtained were always smaller than 2.5, and those obtained

from the water adsorption isotherm were generally smaller than those estimated from  $N_2$  adsorption data. Weak correlations were found between the  $D_s$  values and the clay fraction percentages (Figure 6.4) and the cation exchange capacity. Even weaker correlations were observed between the average adsorption energies and these parameters. Furthermore, no correlation was observed between  $D_s$  values obtained from  $H_2O$  and  $N_2$  adsorption isotherms or between  $D_s$  and average adsorption energy.

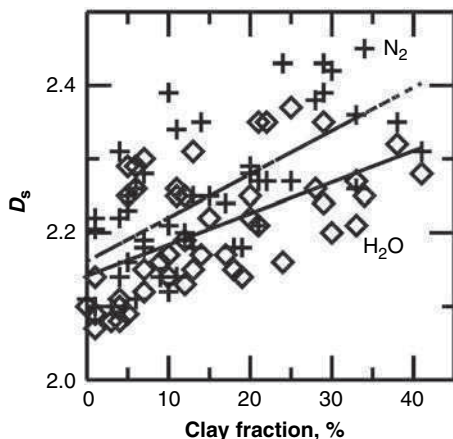


**Figure 6.4** Correlations between the fractional clay content and the surface fractal dimension  $D_s$  obtained from  $H_2O$  and  $N_2$  adsorption data of several alluvial soils [109]. Reproduced by permission of Elsevier.

The fractal approach provides a convenient means for monitoring structural changes that may occur during various types of soil alteration. For example, soil acidification generally leads to a loosening of soil structure and an increase in the water permeability, whereas alkalization leads to soil slacking and a loss of water permeability. These effects imply contrasting change of the pore system for acid and alkaline soils. In contrast, Józefaciuk *et al.* [39] observed that pore volumes and radii generally decreased both with increasing soil acidification or alkalization, whereas the fractal dimension of mesopores decreased after acidification but increased slightly after alkalization. The decreased fractal dimension with acidification corresponds to a smoother porous soil surface.

Model investigations performed on clays [101, 102, 120, 121] and whole soils [43, 111, 122] showed the important role of organic matter in determining the surface heterogeneity of these adsorbents. In particular, Sokołowska *et al.* [43] investigated in the laboratory how the leaching of dissolved organic carbon (DOC) by solutions of NaOH at various pH values could alter surface properties of an Anthropogenic Regosol. The experiment was conducted on two soil portions: one was unchanged (A), whereas the other (B) was subjected to an acid pretreatment of 0.01 M HCl for 2 days, wash with 0.01 M NaCl and distilled water and a final drying. The soil portion B lost

about 5% of its total organic carbon, while the remaining organic material was peptized and deflocculated and the inorganic soil components experienced surface changes. The pore size distributions of both soil samples were obtained with the FHH equation on data measured by mercury intrusion and water vapor adsorption. Measured soil pore radii did not change from pH 3 to about pH 7, whereas they increased linearly above pH 8 (Figure 6.5). On the other hand,  $D_s$  values decreased almost linearly from about 2.8 (pH 3) to about 2.65 (pH 12), corresponding to an increased leaching of organic matter over the pH range investigated. Similar investigations were carried out on other soils [114, 122].

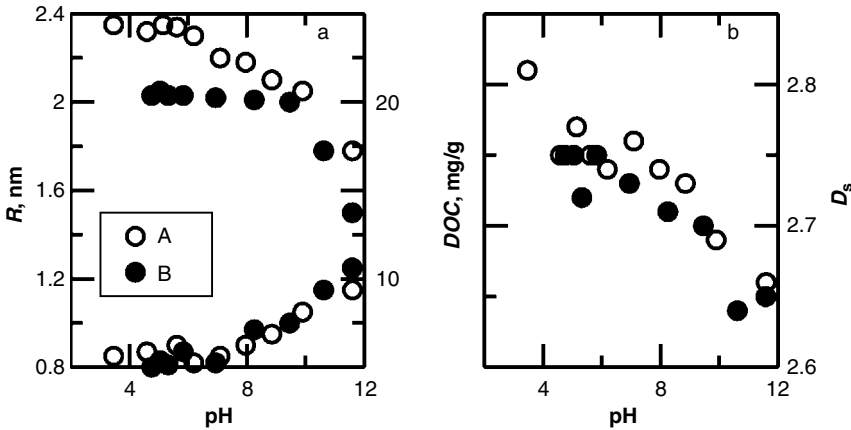


**Figure 6.5** (a) Amount of DOC (top circles) and average pore radius  $R$  (bottom circles) and (b) surface fractal dimension  $D_s$  as a function of pH for two soils (A and B) [43]. Reproduced by permission of World Scientific.

Peat soils are typically rich in organic matter and subject to drainage; thus, secondary transformations depend greatly on drainage intensity. As a result, peat soils may exhibit different physicochemical properties, including different amounts of bound water, different kinds and contents of humic substances, and different sorption and exchangeable properties. Transformations in peat soils are accompanied by (i) changes in the geometrical and energetic characteristics of the soil particle surface, which can be revealed by evaluating soil porosity from mercury porosimetry data, and (ii) energetic and geometric heterogeneity, which can be evaluated from water vapor and  $N_2$  adsorption isotherms [44, 106–108, 123]. Weakly transformed peats exhibited significantly smaller  $D_s$  values (about 2.4) than extensively transformed ones ( $D_s > 2.6$ ). The  $D_s$  values obtained from mercury porosimetry data were usually smaller than those derived from  $N_2$  adsorption data fitted in the FHH isotherm. These results indicated that secondary transformation of peat soils caused an increased surface roughness. Further studies carried out on peat samples that were thermally treated at 50, 100 and 150°C, showed that the surface roughness of most transformed

samples diminished with an increase in temperature [44, 107]. For some samples, however, the temperature effect was opposite. In general, it was difficult to relate these changes to other physicochemical characteristics of the peat soils investigated.

## 6.6 CONCLUSIONS AND RECOMMENDATIONS

This review has illustrated various applications of fractal concepts to the description of adsorption/desorption processes on environmental materials. The surface fractal dimension  $D_s$  can be determined by several independent methods, among which those based on adsorption measurements are shown to be the most convenient and straightforward. However, a comparison of fractal dimensions calculated from different approaches was shown to be problematic; therefore, the need for further studies in this field is evident.

Particular attention has been paid to the discussion of the fractal approach to the adsorption of gases by clay minerals and soils. Further promising developments are expected when applying fractal concepts in new environmental fields. For example, promising research has been conducted very recently on the fractal description of ion adsorption and on the influence of surface roughness on the electric properties of the double layer [124, 125]. Processes and models leading to the preparation of adsorbents with fractal surfaces have also been investigated [126].

Adsorption processes are controlled by the energetic properties of the adsorbent and adsorbate, to the distribution of sites where adsorption occurs and to the geometric heterogeneity of the adsorbent. Discriminating the contribution of each of these factors to the adsorption process as a whole is particularly challenging and requires an appropriate combination of experiment and computer modeling. Despite the substantial progress in the latter field, only rather simple models of selected soil components (e.g. clay minerals) have been used in computer simulations so far [127, 128]. Large-scale off-lattice simulations of gas adsorption onto soils remain extremely difficult. Therefore, the further development of methods for performing computer simulations to investigate the formation of natural adsorbents and the structure of adsorbed layers will be extremely helpful.

In the past few years, the concept of ‘quenched–annealed’ mixtures has been widely applied to the study of the structure and thermodynamic properties of fluids adsorbed in disordered porous matrices [129]. According to this approach, computer simulations and integral-equation theories [129] describing gas adsorption have been proposed that are based on the equilibration of adsorbate molecules in a matrix of particles frozen in a disordered configuration and sampled from a given probability distribution. The novelty of this approach is that the structure of the porous network can be implicitly incorporated into the description by using a static structure factor of the adsorbent. In particular, the porous adsorbent can be considered as being formed by processes leading to the formation of mass fractals, e.g. particle–cluster or cluster–cluster diffusion-limited aggregation processes [130]. Although the concept

of ‘quenched–annealed’ mixtures appears to be very promising for modeling gas adsorption onto soils, to the best of our knowledge, only a single paper that describes preliminary attempts to apply such models to adsorption processes in soils [131] has been published on this topic. Developments in this direction are encouraged and expected.

## LIST OF SYMBOLS AND ABBREVIATIONS

BET	Brunauer, Emmet and Teller theory of adsorption and isotherm equation
DA	Dubinin–Astakhov isotherm equation
DOC	dissolved organic carbon
DR	Dubinin–Raduskhevich isotherm equation
FHH	Frenkel, Halsey and Hill theory of adsorption and isotherm equation
NMR	nuclear magnetic resonance
RAMEB	randomly methylated $\beta$ -cyclodextrin
SANS	small-angle neutron scattering
SAXS	small-angle X-ray scattering
$B_{\text{DR}}$	constant of the Dubinin–Raduskhevich isotherm equation
$C$	constant of the Brunauer, Emmet and Teller isotherm equation
$d$	space dimensionality
$D_{\text{M}}$	mass fractal dimension
$D_{\text{p}}$	pore fractal dimension
$D_{\text{s}}$	surface fractal dimension
$D_{\text{top}}$	topological dimension
$J(R)$	pore-size distribution function
$m$	constant of the Frenkel, Halsey and Hill isotherm equation
$N$	amount of adsorbed molecules
$N_{\text{m}}$	monolayer capacity
$N_{\text{p}}$	maximum adsorbed amount in the pores
$p$	pressure
$p_0$	saturated vapor pressure
$r_{\text{min}}$	lower range of fractality
$r_{\text{max}}$	upper range of fractality
$R$	pore size (diameter)
$R_{\text{min}}$	minimum pore size
$R_{\text{max}}$	maximum pore size
$S$	surface area
$u(r)$	Lennard–Jones (12, 6) interaction potential
$v(z)$	molecule–surface potential energy
$V$	volume
$V_{\text{m}}$	molar volume

$V_p$	pore volume
$x$	relative pressure
$\chi$	adsorption energy distribution function
$\Delta$	range of adsorption energies
$\varepsilon$	adsorption energy
$\varepsilon_i$	adsorption energy in the $i$ th adsorbed layer
$\varepsilon_m$	the lowest value of the adsorption energy
$\phi$	surface tension
$\mu$	chemical potential
$\Delta\mu$	difference of chemical potentials
$\sigma$	molecular diameter
$\vartheta$	adsorption isotherm, surface coverage
$\vartheta_i$	local adsorption isotherm
$\vartheta_t$	total adsorption isotherm

## REFERENCES

- [1] Mandelbrot, B.B. (1982). *The Fractal Geometry of Nature*. W.H. Freeman, New York, pp. 118–119.
- [2] Pfeifer, P. and Obert, M. (1989). Fractals: basic concepts and terminology. In *The Fractal Approach to Heterogeneous Chemistry*, Avnir, D. (ed.). John Wiley & Sons, Ltd, Chichester, pp. 11–43.
- [3] Pfeifer, P., Obert, M. and Cole, M.W. (1989). Fractal BET and FHH theories of adsorption: a comparative study. *Proc. R. Soc. London Ser. A* **423**, 169–188.
- [4] Mark, D.M. and Aronson, P.B. (1984). Scale-dependent fractal dimensions of topographic surfaces: and empirical investigation with application in geomorphology and computer mapping. *Math. Geol.*, **16**, 671–683.
- [5] Van Damme, H. (1998). Structural hierarchy and molecular accessibility in clayey aggregates. In *Fractals in Soil Science*, Baveye, P., Parlange, J.-Y. and Stewart, B.A. (eds). CNC Press, Boca Raton, FL, pp. 55–74.
- [6] Baveye, P. and Boast, C.W. (1997). Fractal geometry, fragmentation process and the physics of scale-invariance: an introduction. In *Fractals in Soil Science*, Baveye, P., Parlange, J.-Y. and Stewart, B.A. (eds). CNC Press, Boca Raton, FL, pp. 1–54.
- [7] Neimark, A.V. (1992). A new approach to the determination of the surface fractal dimension of porous material. *Physica A*, **191**, 258–262.
- [8] Neimark, A.V. (1990). Determination of the surface fractal dimensionality from the results of an adsorption experiment. *Russ. J. Phys. Chem.*, **64**, 1397–1403.
- [9] McClellan, A.L. and Harnsberg, H. (1967). Cross sectional areas of molecules adsorbed on solid surfaces. *J. Colloid Interface Sci.*, **23**, 577–599.
- [10] Farin, D. and Avnir, D. (1990). The fractal nature of molecule–surface interactions and reactions. In *The Fractal Approach to Heterogeneous Chemistry*, Avnir, D. (ed.). John Wiley & Sons, Ltd, Chichester, pp. 271–293.
- [11] Avnir, D., Farin, D. and Pfeifer, P. (1983). Chemistry in noninteger dimension between two and three. II. Fractal surfaces of adsorbents. *J. Chem. Phys.*, **79**, 3566–3571.
- [12] Avnir, D., Farin, D. and Pfeifer, P. (1984). Molecular fractal surfaces. *Nature*, **308**, 261–263.
- [13] Fadeev, Yu.A., Borisova, O.R. and Lisichkin, G. (1996). Fractality of porous silica: a comparison of adsorption and porosimetry data. *J. Colloid Interface Sci.*, **183**, 1–5.



- [14] Pachepsky, Y.A., Korsunskaja, L.P. and Hajnos, M. (1996). Fractal parameters of soil pore surface area under a developing crop. *Fractals*, **4**, 97–104.
- [15] Sokołowska, Z. (1989). On the role of surface heterogeneity in the adsorption processes on soils. *Probl. Agrofiz.*, **58**, 3–165.
- [16] Sokołowska, Z., Stawiński, J., Patrykiewicz, A. and Sokołowski, S. (1989). A note on fractal analysis of adsorption process by soils and soil minerals. *Int. Agrophys.*, **5**, 3–12.
- [17] Sonwane, C.G., Bhatia, S.K. and Calos, N.J. (1999). Characterization of surface roughness of MCM-41 using methods of fractal analysis. *Langmuir*, **15**, 4603–4612.
- [18] Tatler, M. (2002). Inorganic adsorbates classified by fractal analysis. *Sep. Purif. Technol.*, **29**, 265–270.
- [19] Xu, W., Zerda, T.W., Yang, H. and Gerspacher, M. (1996). Surface fractal dimension of graphitized carbon black particles. *Carbon*, **34**, 165–171.
- [20] Gavrilov, K.B., Okunev, A.G. and Aristov, Yu.I. (1996). Monolayer physical adsorption in narrow pores. Apparent surface dimension. *React. Catal. Lett.*, **58**, 39–49.
- [21] Van Damme, H. and Fripiat, J.J. (1985). A fractal analysis of adsorption on pillared swelling clays. *J. Chem. Phys.*, **82**, 2785–2789.
- [22] Fripiat, J.J., Gatinéau, L. and van Damme, H. (1986). Multilayer physical adsorption on fractal surfaces. *Langmuir*, **2**, 562–567.
- [23] Sokołowska, Z. (1989). On the physical adsorption on geometrically and energetically heterogeneous solid surface. *Z. Phys. Chem., (Leipzig)*, **270**, 1113–1120.
- [24] Sokołowska, Z. (2001). Surface area and surface fractal dimensions of the selected alluvial soils. *Pol. J. Soil Sci.*, **34**, 39–47.
- [25] Van Damme, H., Levitz, P., Bergaya, F., Altcover, J.F., Gatinéau, L. and Fripiat, J. (1986). Monolayer adsorption on fractal surfaces: a simple two-dimensional simulations. *J. Chem. Phys.*, **85**, 615–624.
- [26] Sokołowska, Z., Patrykiewicz, A. and Sokołowski, S. (1989). The fractal dimension of geometrically irregular solid surfaces: the role of attractive molecule-surface interactions. *Langmuir*, **5**, 938–941.
- [27] Nicholson, D. and Parsonage, N.G. (1982). *Computer Simulation and the Statistical Mechanics of Adsorption*. Academic Press, London.
- [28] Pfeifer, P., Avnir, D. and Farin, D. (1984). Scaling behaviour of surface irregularity in the molecular domain from adsorption to fractal catalysts. *J. Stat. Phys.*, **36**, 399–714.
- [29] Rahman, M.S. (1997). Physical meaning and interpretation of fractal dimensions of fine particles measured by different methods. *J. Food Eng.*, **32**, 447–456.
- [30] Sokołowska, Z. (1989). On the role of energetic and geometric heterogeneity in sorption of water vapour by soils: application of a fractal approach. *Geoderma*, **45**, 251–265.
- [31] Gil, A., Vicenteand, M.A. and Korili, S.A. (2005). Effect of the Si/Al ratio on the structure and surface properties of silica-alumina-pillared. *J. Catal.*, **229**, 119–126.
- [32] Szűcs, A., Király, Z., Berger, F. and Dékány, I. (1998). Preparation of hydrogen sorption of Pd nanoparticles on Al<sub>2</sub>O<sub>3</sub> pillared clays. *Colloids Surf. A*, **139**, 109–118.
- [33] Hajnos, M., Korsunskaja, L. and Pachepsky, Ya. (2000). Soil pore properties in managed grasslands. *Soil Till. Res.*, **55**, 63–70.
- [34] Kutarov, V.V. and Kats, B.M. (1993). Determination of the fractal dimension of ion-exchange fibres from adsorption data. *Russ. J. Phys. Chem.*, **67**, 1854–1856.
- [35] Terzyk, A.P., Gauden, P.A. and Kowalczyk, P. (2003). Fractal geometry concept in physical adsorption on solids. *Arab. J. Sci. Eng.*, **28**, 1–35.
- [36] Rootare, H.M. and Prenzlow, C.F. (1967). Surface areas from mercury porosimeter measurements. *J. Chem. Phys.*, **71**, 2733–2736.
- [37] Bartoli, F., Bird, N., Gomendy, V. and Vivier, H. (1999). The relationship between silty soil structures and their mercury porosimetry curve counterparts: fractals and percolation. *Eur. J. Soil Sci.*, **50**, 9–22.

- [38] Józefaciuk, G., Muranyi, A. and Fevvyensi, E. (2001). Effect of cyclodextrins on surface and pore properties of soil clay minerals. *Environ. Sci. Technol.*, **35**, 4947–4952.
- [39] Józefaciuk, G., Hoffmann, C. and Marschner, B. (2002). Effect of extreme acid and alkali treatment on pore properties of soil samples. *J. Plant Nutr. Soil Sci.*, **165**, 59–66.
- [40] Kozak, E., Sokołowska, Z., Sokołowski, S. and Wierzchoś, J. (1995). Surface fractal dimension of soil materials from pore size distribution data. I. A comparison of two methods of determination. *Pol. J. Soil Sci.*, **27**, 77–85.
- [41] Pachepsky, Y.A., Polubesova, T.A., Hajnos, M., Sokołowska, Z. and Józefaciuk, G. (1995). Fractal parameters of pore surface area as influenced by simulated soil degradation. *Soil Sci. Soc. Am. J.*, **59**, 68–75.
- [42] Park, Y. (2000). Fractal geometry of porous materials. *Fractals*, **8**, 301–306.
- [43] Sokołowska, Z., Hajnos, M. and Sokołowski, S. (1998). Effect of leaching of dissolved organic carbon on fractal dimension of soils. In *Fractals and Beyond. Complexities in the Science*. Novak, M.M. (ed.). World Scientific, Singapore, pp. 231–239.
- [44] Sokołowska, Z., Hajnos, M., Borówko, M. and Sokołowski, S. (1999). Adsorption of nitrogen on thermally treated peat soils: the role of energetic and geometric heterogeneity. *J. Colloid Interface Sci.*, **219**, 1–10.
- [45] Toth, T. and Józefaciuk, G. (2002). Physicochemical properties of a solonchic topsequence. *Geoderma*, **106**, 137–159.
- [46] Giona, M., Giustiniani, M. and Ludlow, D. (1995). Influence of geometric and energetic heterogeneity on adsorption isotherms. *Fractals*, **3**, 235–250.
- [47] Bernal, J.L. P. and Bello, M.A. (2001). Fractal geometry and mercury porosimetry. Comparison and application of proposed models on building stones. *Appl. Surf. Sci.*, **185**, 99–107.
- [48] Rouquerol, J., Avnir, D., Fairbridge, C.W., Everett, D.H., Haynes, J. H., Pernicone, N., Ramsay, J.D.F., Sing, K.S. W. and Unger, K.K. (1994). Recommendations for the characterization of porous solids. *Pure Appl. Chem.*, **66**, 1739–1765.
- [49] Mahnke, M. and Mögel, H.J. (2003). Fractal analysis of physical adsorption on material surfaces. *Colloids Surf. A*, **216**, 215–228.
- [50] Cole, M.W., Holter, N.S. and Pfeifer, P. (1986). Henry's law of adsorption on fractal surfaces. *Phys. Rev. B*, **33**, 8806–8809.
- [51] Khali, N.R., Pan, M. and Sandi, G. (2000). Determination of fractal dimensions of solid carbons from gas and liquid phase adsorption isotherms. *Carbon*, **38**, 573–588.
- [52] Segars, R. and Piscitelle, L. (1996). Verification and application of a new adsorption model for fractal surfaces, In *Disordered Materials and Interfaces*, Cummins, HZ, Durian, DJ, Johnson, DL. and Stanley, HE (eds). Materials Research Society Symposium Proceedings, Vol. 407. MRS, Warrendale, PA, pp. 349–354.
- [53] Aguerre, R.J., Viollaz, P.E. and Suárez, C. (1996). A fractal isotherm for multilayer adsorption in foods. *J. Food Eng.*, **30**, 227–238.
- [54] Kats, B.M. and Kutarov, V.V. (1996). Fractal dimension of polymer sorbents. *Langmuir*, **12**, 2762–2764.
- [55] Pfeifer, P. and Lui, K.-Y. (1997). Multilayer adsorption as a tool to investigate the fractal nature of porous adsorbents. In *Equilibria and Dynamics of Gas Adsorption on Heterogeneous Solid Surfaces*, Rudziński, W., Steele, W.A. and Zgrablich, G. (eds). Studies in Surface Science and Catalysis, Vol. 104. Elsevier, New York, pp. 625–677.
- [56] Lee, S.-B., Pyun, S.-I. and Rhree, C.-K. (2003). Determination of the fractal dimensions of green MCMB and MCMB heat-treated at 800–1200°C by using gas adsorption method. *Carbon*, **41**, 2427–2451.
- [57] Jarzębski, A.B., Lorenc, J. and Pająk, L. (1997). Surface fractal characteristics of silica aerogels. *Langmuir*, **13**, 1280–1285.
- [58] Avnir, D. and Jaroniec, M. (1989). An isotherm equation for adsorption on fractal surfaces of heterogeneous porous materials. *Langmuir*, **5**, 1431–1433.

- [59] Dubinin, M.M. (1975). *Adsorption and Porosity*. WAT, Warsaw.
- [60] Jaroniec, M. and Madey, R. (1988). *Physical Adsorption on Heterogeneous Solid Surfaces*. Elsevier, Amsterdam.
- [61] Pfeifer, P. and Avnir, D. (1983). Chemistry in noninteger dimensions between two and three. *J. Chem. Phys.*, **79**, 3558–3565.
- [62] Do, D.D. (1998). *Adsorption Analysis: Equilibria and Kinetics*. ICP, London.
- [63] Erdem-Senatarlar, A. and Tatler, M. (2000). Effects of fractality on the accessible surface area values of zeolite adsorbents. *Chaos Soliton. Fract.*, **11**, 953–960.
- [64] Cerofolini, G.F. and Rudziński, W. (1997). Theoretical principles of single- and mixed-gas adsorption equilibria on heterogeneous solid surfaces. In *Equilibria and Dynamics of Gas Adsorption on Heterogeneous Solid Surfaces*, Rudziński, W., Steele, W.A. and Zgrablich, G. (eds). Studies in Surface Science and Catalysis, Vol. 104. Elsevier, Amsterdam.
- [65] Gauden, P.A. and Terzyk, A.P. (2000). The normalisation of the micropore-size distribution function in the Polanyi–Dubinin type of adsorption equations. *J. Colloid Interface Sci.*, **227**, 482–494.
- [66] Qi, H., Ma, J. and Wong, P. (2002). Adsorption isotherms of fractal surfaces. *Colloids Surf. A*, **206**, 401–407.
- [67] Malekani, K., Rice, J.A. and Lin, J.S. (1996). Comparison of techniques for determining the fractal dimensions of clay minerals. *Clays Clay Miner.*, **44**, 677–685.
- [68] Mathieu, A., Blacher, S., Pirard, R., Pirard, J.P., Sahouli, B. and Brouers, F. (1997). Freeze-dried resorcinol–formaldehyde gels. *J. Non-Cryst. Solids*, **212**, 250–261.
- [69] Ma, J., Qi, H. and Wong, P.Z. (1999). Experimental study of multilayer adsorption on fractal surfaces in porous media. *Phys. Rev. E*, **59**, 2049–2059.
- [70] Weidler, P.G., Degovics, G. and Laggner, P. (1998). Surface roughness created by acidic dissolution of synthetic goethite monitored with SAXS and N<sub>2</sub>-adsorption isotherm. *J. Colloid Interface Sci.*, **197**, 1–8.
- [71] Diduszko, R., Świątkowski, A. and Trznadel, B.J. (2000). On surface micropores and fractal dimension of activated carbon determined on the basis of adsorption and SAXS investigations. *Carbon*, **38**, 1153–1162.
- [72] Jaroniec, M., Kruk, M. and Olivier, J.P. (1997). Fractal analysis of composite adsorption isotherms obtained by using density functional theory data for argon in slit-like pores. *Langmuir*, **13**, 1031–1035.
- [73] Weidler, P.G. and Stanjek, H. (1998). The effect of dry heating of synthetic 2-line and 6-line ferrihydrite: II. Surface area, porosity and fractal dimension. *Clay Miner.*, **33**, 277–284.
- [74] Tatler, M. and Erdem-Senatarlar, A. (1998). Fractal dimension as a tool to guide zeolite synthesis. *Chaos Soliton. Fract.*, **9**, 1803–1812.
- [75] Erdem-Senatarlar, A., Tatler, M. and Sirkecioglu, A. (2000). The relationship of the geometric factor in the Dubinin–Astakhov isotherm equation with the fractal dimension. *Colloids Sur. A*, **173**, 51–59.
- [76] Stazi, A., D’Orazio, M. and Quagliarini, E. (2002). In-life prediction of hydrometric behaviour of buildings materials: an application of fractal geometry to the determination of adsorption and suction properties, *Build. Environ.*, **37**, 733–739.
- [77] Song, H., Min, L., Jun, X., Lushi, S., Peisheng, L., Heng, S. and Xuexin, S. (2004). Fractal characteristic of three Chinese coals. *Fuel*, **83**, 1307–1313.
- [78] Tsunoda, R. (1999). Fractal approach to adsorption isotherms of water vapor on active carbons. *J. Colloid Interface Sci.*, **218**, 269–274.
- [79] Rizkalla, N., Hildgen, P. and Thibert, R. (1999). Influence of the fractal character of model substances on their reactivity at solid–liquid interface. *J. Colloid Interface Sci.*, **215**, 43–53.

- [80] Podkościelny, P., Dąbrowski, A. and Leboda, R. (2001). Fractal approach of adsorption from liquid mixtures on silica gel. *Colloids Surf.*, **182**, 219–229.
- [81] Kano, F., Abe, I., Kamaya, H. and Ueda, I. (2000). Fractal model for adsorption on activated carbon surfaces: Langmuir and Freundlich adsorption. *Surf. Sci.*, **467**, 131–138.
- [82] Laszlo, K., Bota, A., Nafy, L.G., Subklew, G. and Schwunger, M.J. (1998). Fractal approach of activated carbons from solid waste materials. *Colloids Surf. A*, **138**, 29–37.
- [83] Park, H., Kim, H. and Lee, S. (1997). Monte Carlo simulations of catalytic CO oxidation on fractal surface of dimension between two and three. *Surf. Sci.*, **380**, 514–521.
- [84] Beckers, J.V. L. and de Leeuw, A.W. (2000). Molecular dynamics simulation of nanoporous silica. *J. Non-Cryst. Solids*, **261**, 87–100.
- [85] Fuji, M., Ueno, S., Takei, T., Watanabe, T. and Chikazawa, M. (2000). Surface structural analysis of fine silica powder modified with butyl alcohol. *Colloid Polym. Sci.*, **278**, 30–36.
- [86] Borówko, M. (2002). Adsorption on heterogeneous surfaces. In *Adsorption, Theory, Modeling and Analysis*, Tóth, J. (ed.). Marcel Dekker, New York, pp. 105–174.
- [87] Lefebvre, Y., Lacelle, S. and Jolicoeur, C. (1992). Surface fractal dimension of some industrial minerals from gas-phase adsorption isotherms. *J. Mater. Res.*, **7**, 1888–1891.
- [88] Tsunoda, R., Ozawa, T. and Ando, J.-I. (1998). Ozone treatment of coal and coffee grounds-based active carbons: water adsorption and surface fractal micropores. *J. Colloid Interface Sci.*, **205**, 265–270.
- [89] Rudziński, W., Lee, S.-L., Yan, C.-C.S. and Pańczyk, T. (2001). A fractal approach to adsorption on heterogeneous solid surfaces. I. The relationship between geometric and energetic surface heterogeneities. *J. Phys. Chem.*, **105**, 10 847–10 856.
- [90] Rudziński, W., Lee, S.-L., Yan, C.-C.S. and Pańczyk, T. (2001). A fractal approach to adsorption on heterogeneous solid surfaces. II. Thermodynamic analysis of experimental data. *J. Phys. Chem.*, **105**, 10 857–10 866.
- [91] Xu, Y.F. (2004). Surface irregularities of soils in molecular domain. *Chaos Soliton. Fract.*, **21**, 435–444.
- [92] Xu, Y.F., Matsuoka, H. and Sun, D.A. (2003). Swelling characteristics of fractal-textured bentonite and its mixtures. *Appl. Clay Sci.*, **22**, 197–209.
- [93] Celis, R., Cornejo, J. and Hermosin, M.C. (1996). Surface fractal dimension of synthetic clay-hydrous iron oxides associations from nitrogen adsorption and mercury porosimetry. *Clay Miner.*, **31**, 355–356.
- [94] Xu, Y.F., Sun, D.A. and Yao, Y. (2004). Surface fractal dimension of bentonite and its application to determination of swelling properties. *Chaos Soliton. Fract.*, **19**, 347–356.
- [95] Ben Ohoud, M. and van Damme, H. (1990). The fractal texture of swelling clays. *C. R. Acad. Sci., Paris, Ser. II*, **311**, 665–670.
- [96] Stawiński, J. and Sokołowska, Z. (1982). An energetic effect of water vapour desorption from the surface of clay minerals. *Z. Prob. Post. Nauk Roln.*, **281**, 219–226.
- [97] Huang, F.-C., Lee, J.-F., Lee, C.-K. and Chao, H.-P. (2004). Effects of cation exchange on the pore and surface structure and adsorption characteristics of montmorillonite. *Colloids Surf. A*, **239**, 41–47.
- [98] Wang, C.-C., Juang, L.-C., Hsu, T.-C., Lee, C.-K., Lee, J.-F. and Huang, F.-C. (2004). Adsorption of basic dyes onto montmorillonite. *J. Colloid Interface Sci.*, **273**, 80–86.
- [99] Yamazaki, T., Nakamura, Y. and Ozawa, S. (2001). Investigation on pore structure formed in a pillared montmorillonite interlayer using adsorption methods and a carbonization technique. *J. Colloid Interface Sci.*, **239**, 440–446.
- [100] Pfefferkorn, E. (1997). Structure and stability of natural organic matter/soil complexes and related synthetic and mixed analogues. *Adv. Colloid Interface Sci.*, **73**, 127–200.
- [101] Tombácz, E., Szkers, M., Baranyi, L. and Michéli, E. (1998). Surface modification of clay minerals by organic polyions. *Colloids Surf. A*, **141**, 379–384.

- [102] Sokołowska, Z. and Sokołowski, S. (1999). Influence of humic acid on surface fractal dimension of kaolin: analysis of mercury porosimetry and water vapour adsorption data. *Geoderma*, **88**, 233–249.
- [103] McCray, J.E., Boving, T.B. and Brusseau, M.L. (2000). Cyclodextrin-enhanced solubilization of organic contaminants with implications for aquifer remediation. *Ground Water Monit. Remed.*, **20**, 94–103.
- [104] Hajnos, M., Józefaciuk, G., Sokołowska, Z., Greiffenhagen, A. and Wessolek, G. (2003). Water storage, surface and structural properties of sandy forest humus horizons. *J. Plant Nutr. Soil Sci.*, **166**, 625–634.
- [105] Pachepsky, Y.A., Yakovchenko, V., Rabenhorst, M.C., Pooley, C. and Sikora, L.J. (1996). Fractal parameters of pore surfaces as derived from micromorphological data: effect of long-term management practices. *Geoderma*, **74**, 305–325.
- [106] Sławiński, C., Sokołowska, Z., Walczak, R., Borówko, M. and Sokołowski, S. (2002). Fractal dimension of peat soils from adsorption and from water retention experiments. *Colloids Surf. A*, **208**, 289–301.
- [107] Sokołowska, Z., Hajnos, M., Hoffmann, Ch., Renger, M. and Sokołowski, S. (2000). Surface fractal dimension of thermally treated peat soils from adsorption isotherms of nitrogen. *J. Plant Nutr. Soil Sci.*, **163**, 441–446.
- [108] Sokołowska, Z., Hajnos, M., Hoffmann, Ch., Renger, M. and Sokołowski, S. (2001). Comparison of fractal dimensions of soils estimated from adsorption isotherms, mercury intrusion and particle size distribution. *J. Plant Nutr. Soil Sci.*, **164**, 591–599.
- [109] Sokołowska, Z., Borówko, M., Reszko-Zygmunt, J. and Sokołowski, S. (2002). Adsorption of nitrogen and water vapor by alluvial soils. *Geoderma*, **107**, 330–354.
- [110] Sokołowska, Z., Raychev, T. and Arsova, A. (2002). Surface area and surface fractal dimension of selected Bulgarian soils. *Soil Sci. Agrochem. Ecol.*, **37**, 147–149.
- [111] De Las Cuevas, C. (1997). Pore structure characterization in rock salt. *Eng. Geol.*, **47**, 17–30.
- [112] Filgueira, R.R., Sarli, G.O., Piro, A.I. and Fournier, L.L. (1998). Surface-fractal dimension of soil aggregates and rock particles. In *Fractals and Beyond. Complexities in the Science*, Novak, M.M. (ed.). World Scientific, Singapore, pp. 223–229.
- [113] Okuda, I. and Senesi, N. (1998). Fractal principles and methods applied to chemistry of sorption onto environmental particles. In *Structure and Surface Reactions of Soil Particles*, ed. Huang, P.M., Senesi, N. and Buffle, J. (eds). John Wiley & Sons, Ltd, Chichester, pp. 77–105.
- [114] Józefaciuk, G. and Sokołowska, Z. (2003). The effect of removal of organic matter, iron oxides and aluminium oxides on the micropore characteristics of the soil clay fraction. *Pol. J. Soil Sci.* **36**, 111–118.
- [115] Józefaciuk, G. and Sokołowska, Z. (1999). Effect of extreme acid and alkaline treatment on energetic and geometric heterogeneity of surface of muscovite. *Acta Agrophys.*, **23**, 47–57.
- [116] Kozak, E., Pachepsky, Y.A., Sokołowski, S., Sokołowska, Z. and Stępniewski, W. (1996). A modified number-based method for estimating fragmentation fractal dimensions of soils. *Soil Sci. Soc. Am. J.*, **60**, 1291–1297.
- [117] Rasiyah, V., Kay, B.D. and Perfect, E. (1993). New mass-based model for estimating fractal dimensions of soil aggregates. *Soil Sci. Soc. Am. J.*, **57**, 891–895.
- [118] Perfect, E. and Kay, B.D. (1991). Fractal theory applied to soil aggregation. *Soil Sci. Soc. Am. J.*, **55**, 1552–1558.
- [119] Giménez, D., Allmaras, R.R., Nater, E.A. and Huggins, D.R. (1997). Fractal dimension for volume and surface interaggregate pores: scale effects. *Geoderma*, **77**, 19–38.
- [120] Sokołowska, Z., Hajnos, M., Józefaciuk, G., Hoffmann, Ch. and Renger, M. (1997). Influence of humic acid on water adsorption characteristics of kaolin and quartz. *Z. Pflanz. Bodenk.*, **160**, 327–331.

- [121] Józefaciuk, G., Hajnos, M., Sokołowska, Z. and Renger, M. (1995). Influence of surface coverage by humic acids on surface free energy and wettability of quartz and kaolin. *Pol. J. Soil Sci.*, **37**, 29–35.
- [122] Raychev, T., Józefaciuk, G. and Sokołowska, Z. (2003). Effect of organic matter removal on fractal dimension of soil clay fraction. *Bulg. J. Ecol. Sci.*, **11**, 73–74.
- [123] Sokołowska, Z. (2002). Fractal dimension of the peat–muck soils at different state of their secondary transformation. *Acta Agrophys.*, **68**, 193–204.
- [124] Kulkarni, P., Sureshkumar, R. and Biswas, P. (2003). Multiscale simulation of irreversible deposition in presence of double layer interactions. *J. Colloid Interface Sci.*, **260**, 36–48.
- [125] Ruiz, G.A., Felice, C.J. and Valentinuzzi, M.E. (2005). Non-linear response of electrode–electrolyte interface at high current density. *Chaos Soliton. Fract.* **25**, 649–654.
- [126] Eikerling, M., Kornyshev, A.A. and Lustd, E. (2005). Optimized structure of nanoporous carbon-based double-layer capacitors. *J. Electrochem. Soc.* **152**, E24–E33.
- [127] Meleshyn, A. and Bunnenberg, C. (2005). Swelling of Na/Mg-montmorillonites and hydration of interlayer cations: a Monte Carlo study. *J. Chem. Phys.* **123**, art. no. 074706.
- [128] Schmidt, S.R., Katti, D.R., Ghosh, P. and Katti, K.S. (2005). Evolution of mechanical response of sodium montmorillonite interlayer with increasing hydration by molecular dynamics. *Langmuir*, **21**, 8069–8076.
- [129] Pizio, O. (2000). Adsorption in random porous media. In *Computational Methods in Surface and Colloid Science*, Borówko, M. (ed.). Marcel Dekker, New York. pp. 292–346.
- [130] Krakowiack, V., Kierlik, E., Rosinberg, L.-L. and Trajus, G. (2001). Adsorption of a fluid in an aerogel: integral equation approach. *J. Chem. Phys.*, **115**, 11 289–11 298.
- [131] Sokołowska, Z., Sokołowski, S. and Pizio, O. (2002). Modelling of adsorption of gases in disordered porous materials. *Acta Agrophys.*, **84**, 111–122.



---

# 7 Applications of Fractals in the Study of Humic Materials

---

**James A. Rice**

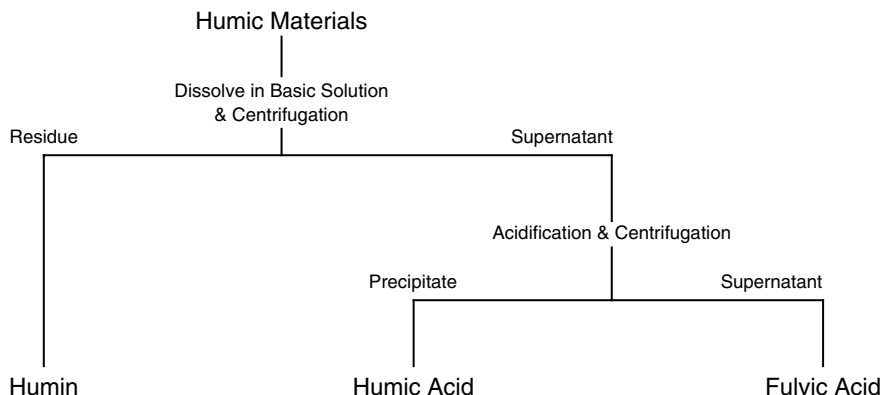
*South Dakota State University, Department of Chemistry & Biochemistry, Box 2202,  
Brookings, SD 57007-0896*

## 7.1 INTRODUCTION

Natural organic matter (NOM) in the environment can be classified into two broad categories, humic and nonhumic substances [1–5]. Nonhumic substances are generally described as those NOM components that belong to recognized molecular compound classes, such as sugars, peptides, lipids, fatty acids, etc. Humic materials are NOM components that cannot be so conveniently compartmentalized. They are generally described as refractory, heterogeneous, polyelectrolytic organic substances that color waters, sediments, or soils brown or black. Humic substances are divided into three fractions based on an operational definition that traces its origin back into the soils literature. They are operationally defined by their solubility in an aqueous solution as a function of the solution pH (Figure 7.1): *humic*, which is insoluble in an aqueous solution at any pH value; *humic acid*, which is soluble in an alkaline aqueous solution but precipitates in acidic conditions; and *fulvic acid*, which is soluble in an aqueous solution at any pH value.<sup>1</sup> A variety of texts describe the chemical nature of each fraction in detail [1–5]. Typical chemical characteristics of each fraction are shown in Figure 7.2.

---

<sup>1</sup> Humic's insolubility obviates its presence in a dissolved organic matter aquatic sample. In aquatic systems, the operational definitions of humic and fulvic acids are stated somewhat differently [4]. Humic acid and fulvic acid are defined by the aqueous solution pH necessary to desorb them from XAD-8 resin: fulvic acid can be desorbed with water; humic acid is desorbed with an alkaline aqueous solution. However, the defining operational characteristic, solubility in an aqueous solution as a function of pH, is consistent in both operations. Thus, the use of the term fulvic acid in this paper refers to the humic substance fraction soluble in aqueous solution at any pH value, and the term humic acid refers to the humic substance fraction soluble in alkaline aqueous solution but insoluble under acidic conditions.

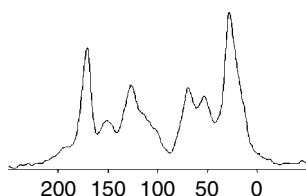


**Figure 7.1** Operational nature of the definitions of each of the three fractions of humic substances.

The characteristic that remains associated with each humic fraction after its separation from an NOM sample is an extreme degree of heterogeneity. The general consensus is that each humic fraction is a very complex mixture [8, 9] whose components represent a continuum of chemical and molecular properties. The literature is replete with references to the inability to subdivide humic and fulvic acid into components that represent a quantitatively significant fraction of the whole sample [8]. It has even been suggested that ‘...no two molecules of a humic substance are exactly alike...’ [10]. There has been some success in further fractionating the components of humin [11]. But even this fractionation ends with a material that conforms to the operational definition of humic acid, though its chemical characteristics allow it to be distinguished from humic acid. MacCarthy and Rice [12] have proposed that not only is this heterogeneity the defining characteristic of humic materials, but in fact it also represents an environmental feedback that has emerged to ensure that humic materials persist to perform their ecological functions.

In any case, the heterogeneity of each humic fraction limits the application of conventional structural determination approaches. If the defining chemical characteristic of humic materials is, in fact, the lack of a single, characteristic chemical structure, then a primary structure of humic or fulvic acid does not exist (though certainly the individual components that comprise a humic material have primary structures)! Even the determination of secondary structures becomes quite problematic from this perspective. What is left to explore are the tertiary and quaternary structures which result from molecule–molecule, aggregate–molecule, and aggregate–aggregate interactions. Conceptual models of humic materials acknowledging this realization have begun to appear [13–15]. These types of interaction, and these types of structure, are ideally suited to study by a fractal approach.



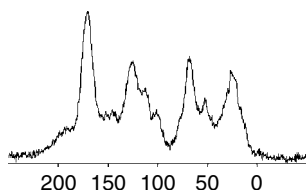
**Humic Acid***Elemental Composition*

55.1%C, 5.0%H, 3.5%N, 1.8%S, 35.6%O

*Acidic Functional Group Content*

Total Acidity: 5.0 meq/g

Carboxyl Acidity: 2.5 meq/g

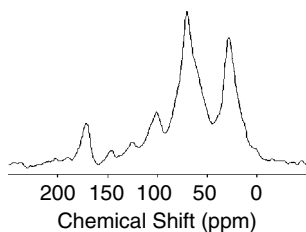
**Fulvic Acid***Elemental Composition*

46.2%C, 4.9%H, 2.5%N, 1.2%S, 45.6%O

*Acidic Functional Group Content*

Total Acidity: 8.7 meq/g

Carboxyl Acidity: 5.2 meq/g

**Humin***Elemental Composition*

56.1%C, 5.5%H, 3.7%N, 0.4%S, 34.7%O

*Acidic Functional Group Content*

Total Acidity: 6.4 meq/g

Carboxyl Acidity: 1.3 meq/g

**Figure 7.2**  $^{13}\text{C}$  DPMAS NMR spectra of the three humic fractions isolated from a peat soil using the procedure outlined in Figure 7.1. Carbon-type distributions generally used to describe samples are aliphatic (0–50 ppm), carbohydrate (50–110 ppm), aromatic (110–190 ppm) and carboxyl (190–220 ppm). Elemental data [6] are average elemental compositions for each humic fraction. Functional group analyses are for these specific samples [7]. There is considerable variation in these chemical characteristics among samples, and between environments, for each fraction. For descriptions of compositional variations in humic materials from different environments the reader is referred to the references [1–5].

## 7.2 METHODS FOR DETERMINING FRACTAL PROPERTIES AND BEHAVIOURS OF HUMIC MATERIALS

The majority of the studies utilizing a fractal approach to study humic materials have employed some form of scattering: light scattering [16–19], small-angle x-ray scattering (SAXS) [18–25], small-angle neutron scattering (SANS) [26–32], or turbidimetry [33–38]. The SAXS and SANS techniques have the advantage of being able to be applied to solid- or solution-phase samples. Static light-scattering data and SAXS

or SANS data can be combined to cover a larger characterization length-scale that allows particles of a broad size-distribution to be studied. The application of scattering methods to the study of the fractal properties of materials have been described in detail by Schmidt [39], Homer [32], Martin and Hurd [40], and Bushell in Chapter 3 of this book. Raper and Amal [17] give a concise description of the theory of light scattering from fractal objects. The reader is directed to these references for detailed discussion of the theory of these methods. A brief introduction follows.

Most of the information in a scattering experiment will be found at scattering angles that satisfy the criterion

$$0.1 \leq ql \quad (7.1)$$

where  $l$  is the diameter of the scattering particle. The scattering vector,  $q$ , is defined as

$$q = \frac{4\pi}{\lambda} \sin \frac{\theta}{2} \quad (7.2)$$

where  $\lambda$  is the wavelength of the incident radiation and  $\theta$  is the scattering angle. The fractal properties of a scatterer are obtained in the Porod scattering regime when Equation (7.1) is satisfied [39, 40]. It can be shown that the intensity of the radiation scattered by a particle consisting of mass fractal scatterers as function of  $q$  is approximated by

$$I(q) \approx N_s I_0(qa) D_m \Gamma(D_m - 1) \frac{\sin \left[ (D_m - 1) \frac{\pi}{2} \right]}{(qa)^{D_m}} \quad (7.3)$$

where  $N_s$  is the number of scatterers,  $I_0(qa)$  is the scattered intensity from a single scatterer and  $\Gamma(D_m - 1)$  is a gamma function [39, 40]. This is a power law where  $I(q)$  is proportional to the power law exponent  $D_m$ . The power-law exponent is the slope of the linear portion of a log-log plot of  $I(q)$  versus  $q$ . If the material is a mass fractal, then  $D_m$  will satisfy the condition  $D_m \leq 3$  and the fractal dimension is the absolute value of  $D_m$ . For a surface fractal it can be shown that

$$I_0(qa) \approx \pi N_0 \delta^2 I_e \Gamma(5 - D_s) x \sin \left[ \frac{\pi(D_s - 1)}{2} \right] q^{-(6-D_s)} \quad (7.4)$$

where  $N_0$  is a constant,  $I_e$  is the scattered intensity from a single electron, and  $\Gamma(5 - D_s)$  is a gamma function [39, 40]. Equation (7.4) also describes a power law where  $I(q)$  is proportional to a power law exponent represented by  $-(6 - D_s)$ . The exponent can again be obtained from the slope of a log-log plot of  $I(q)$  versus  $q$ . If the material is a surface fractal, then the power-law exponent satisfies the condition  $3 \leq (6 - D_s) \leq 4$ . The surface fractal dimension  $D_s$  is readily obtained by subtraction.

Several other methods, notably turbidimetry [33–38], have also been used to characterize humic materials. Turbidimetry is a variation on scattering where the transmitted

light is observed as opposed to the scattered light. The turbidity  $\tau$  of a particle suspension can be described by

$$\tau = \left[ \frac{32\pi^2 n^2 \left( \frac{d\eta}{dc} \right)^2}{3N\lambda^4} \right] c M_w Q \quad (7.5)$$

where  $d\eta/dc$  is the refractive index increment,  $N$  is Avogadro's number,  $c$  is the concentration of particles with molar mass  $M_w$  in a monodisperse assemblage, and  $Q$  is the turbidity dissipation function. The value of  $Q$  is a consequence of the internal interference of light scattered at all angles. For a fractal object:

$$Q = \frac{3}{8} \int_0^\pi P(\theta) S(q) \sin \theta (1 + \cos^2 \theta) d\theta \quad (7.6)$$

where  $P(\theta)$  is the particle form factor and  $S(q)$  is the structure factor that describes the distribution of scatterers within the particle and is given by Equation (7.7) for intermediate values of  $q$ :

$$\lim_{q \rightarrow \infty} S(q) = 1 + \frac{1}{(q\alpha)^D} D\Gamma(D-1) \sin \left[ (D-1) \frac{\pi}{2} \right] = 1 + \frac{\text{const}}{(q\alpha)^D} \approx (q\alpha)^{-D} \quad (7.7)$$

This expression is a power law that can be used to evaluate scattering by a mass fractal object [30]. If Equation (7.7) is substituted into Equation (7.6), which is then substituted into Equation (7.5),  $\tau$  can be directly related to  $D$  for large scatters. Senesi *et al.* [33] describe the derivation of this relationship in detail.

The use of scattering to measure fractal properties of humic materials is limited by what is often referred to as the 'characteristic length scale', which is a function of the wavelength used (Equation (7.2)). If a scattering particle is larger than this length, then the entire particle cannot be observed (see Chapter 3 for a detailed description of the application of scattering techniques for determining fractal dimensions). Thus, this length forms the upper limit for the fractal regime that can be observed under a particular set of conditions. It is possible to extend the particle or cluster size that is being observed using two different wavelengths, e.g. by combining SAXS and static light scattering, or using SAXS and ultra-small-angle X-ray scattering. However, the extension of the characteristic length scale is usually not more than one order of magnitude in  $q$ . Because aggregation phenomena in humic materials span particle-size ranges from the nanoscale to the macroscopic scale, the characteristic length scale does limit the applicability of scattering techniques in large-particle humic systems.

Microscopy is a technique that can be used to study the fractal nature of larger particles, even to the point of flocculation. Transmission electron micrographs reveal what appears to be a fractal structure [41] whose fractal dimension would be amenable to measurement by counting methods. In these methods, object images are digitized and superimposed on a grid. Pixels representing a cluster within each grid unit are counted using commercial software to generate the greatest distance between pixels attributed to a particular cluster. Equation (7.8) describes a power-law relationship

between the particle mass  $M$  and length  $l$  where the power-law exponent is the mass fractal dimension:

$$M \propto l^{D_m} \quad (7.8)$$

The mass fractal dimension is obtained from a log–log plot of  $M$  versus  $l$ . This technique is described in detail in Chapter 3.

Other, nonhumic components of NOM have also been studied using a fractal approach. These studies and the methods they employ are reviewed in Chapter 4.

### 7.3 WHAT FRACTALS HAVE SHOWN US ABOUT HUMIC MATERIALS

There have been approximately two dozen papers published in the peer-reviewed literature since 1992 that have used the concept of fractals to characterize humic materials [16–38, 42]. Most of the studies were done in a burst of interest during a 7-year period in the 1990s; there have been five papers published in the peer-reviewed literature on the application of fractals to the study of humic materials other than reviews [15, 32, 43, 44] since 1999. Two common applications of fractal geometry have been to study the mass distribution of colloidal humic materials and the aggregation processes that produced them.

There have been a number of studies reported that have examined the effect of the presence or absence of humic materials and NOM on the fractal properties of other colloidal materials such as hematite, clays, colloidal hydrous oxides and similar materials [e.g. 45–48]. However, since the focus of this chapter is on the use of a fractal approach to explore the unique nature of humic materials, these studies are not discussed in this chapter.

#### 7.3.1 Particle Structure

Studies of humic materials employing fractal geometry have generally focused on solution-state samples, and most of these studies have been directed towards humic acid (Table 7.1). Exceptions to this generalization are studies using turbidimetry that characterize aqueous suspensions of humic acid particles [33–38] and the application of fractals to describe the surface morphology of humin [23–25].

Humic and fulvic acid particles in solution that have been characterized to date have demonstrated mass fractal behavior (Table 7.1). The fractal dimensions reported for humic acid samples in alkaline solutions using scattering methods in the range  $2 \leq D_m \leq 3$ . Particles with mass fractal dimensions in this range can be viewed as open, three-dimensional aggregates with structures that become more space filling as  $D_m$  approaches 3. Humic materials behave like anionic polyelectrolytes in solution (particles are smaller and more subject to phase separation at low pH and high ionic strengths [10, 49], and they aggregate as a function of concentration [13, 50]. Thus, it is difficult to make direct comparisons between samples or sample source-environments

**Table 7.1** Fractal dimensions reported for humic materials from various environments. Samples that had been modified are not included in this table. Roman numerals are used for reference to discussion in text. Table adapted from Homer [32].

Sample source			Technique	Notes		Fractal dimension	Ref.
<b>Solution state</b>							
<i>Humic acid</i>							
I	Stream sediment		SAXS	Basic solution, [HA] = 6.7 g m <sup>-3</sup>		$D_m = 2.5$	[20]
	Peat		SAXS	Basic solution, [HA] = 2.0 g m <sup>-3</sup>		$D_m = 2.1$	[16]
	Soil		SANS	pH 5, 3.6 g m <sup>-3</sup>		$D_m = 2.3$	[26]
	Unspecified IHSS HA		SANS	pH 5, 2.9 g m <sup>-3</sup>		$D_m = 2.3$	[26]
II	Soil		SANS	pH 5, scattering from five dilutions normalized with respect to concentration collapse to master curve		$D_m = 2.35$	[30]
III	Soil		SANS	pH 5	[C] = 10 g m <sup>-3</sup> [C] = 15 g m <sup>-3</sup> [C] = 20 g m <sup>-3</sup>	$D_m = 2.10$ $D_m = 2.14$ $D_m = 2.02$	[32]
IV	Aldrich		SANS	[C] = 0.4 g m <sup>-3</sup>	pH 5 pH 2 pH 10 pH 11 pH 11, Ca <sup>2+</sup> added	$D_m = 2.41$ $D_m = 2.45$ $D_m = 2.56$ $D_m = 2.66$ $D_m = 2.66$	[32]
V	IHSS (1S103H)	peat	TEM	1 g m <sup>-3</sup>	pH 3, 10 h equilibration pH 6, 10 h equilibration	$D_m = 1.75$ $D_m = 1.52$	[42]
V	IHSS (1S102H)	soil	TEM	1 g m <sup>-3</sup>	pH 3, 10 h equilibration pH 6, 28 h equilibration	$D_m = 1.72$ $D_m = 1.80$	[42]
V	IHSS (1S106H)	soil	TEM	1 g m <sup>-3</sup>	pH 3, 10 h equilibration pH 6, 10 h equilibration	$D_m = 1.86$ $D_m = 1.54$	[42]
V	soil		TEM	1 g m <sup>-3</sup>	pH 3, 4 h equilibration pH 6, 28 h equilibration	$D_m = 1.73$ $D_m = 1.52$	[42]
<i>Fulvic acid</i>							
	Groundwater		SAXS	Aquatic NOM sample, [NOM] = 45 mg m <sup>-3</sup>		$D_m = 1.6$	[20]

**Table 7.1** (Continued).

Sample source			Technique	Notes			Fractal dimension	Ref.
<b>Solid state</b>								
<i>Humic acid</i>								
	Stream sediment		SAXS				$D_s = 2.2$	[20]
	Lignite		SAXS				$D_s = 2.3$	[20]
<i>Fulvic acid</i>								
	Stream sediment		SAXS				$D_s = 2.3$	[20]
	Lignite		SAXS				$D_s = 2.8$	[20]
	Soil		SAXS				$D_s = 2.5$	[20]
	Groundwater		SAXS	Aquatic NOM sample			$D_m = 2.5$	[20]
<i>Humic</i>								
	Soil		SAXS				$D_s = 2.7$	[24]
	Soil		SAXS				$D_s = 2.4$	[24]
	Soil		SAXS				$D_s = 2.9$	[24]
							$D_m = 2.9$	
	Peat		SAXS				$D_s = 2.2$	[24]
							$D_m = 2.2$	
<b>In suspension</b>								
<i>Humic acid</i>								
VI	IHSS (1S106H)	soil	Turbidity	pH 3 pH 4 pH 5 pH 6 pH 7 pH 3 pH 4 pH 5 pH 6	[HA] = 30 mg m <sup>-3</sup>     [HA] = 40 mg m <sup>-3</sup>    		$D_m = 2.77$ $D_m = 2.46$ $D_m = 2.20$ $D_m = 2.11$ $D_m = 1.86$ $D_m = 2.57$ $D_m = 2.55$ $D_m = 2.31$ $D_m = 1.78$	[35]
VI	IHSS (1S102H)	soil	Turbidity	pH 3 pH 4 pH 5 pH 6 pH 7 pH 3 pH 4 pH 5 pH 6	[HA] = 30 mg m <sup>-3</sup>     [HA] = 40 mg m <sup>-3</sup>    		Nonfractal Nonfractal $D_m = 2.55$ $D_m = 2.13$ $D_m = 1.71$ Nonfractal Nonfractal Nonfractal $D_m = 1.95$	[35]
VI	IHSS (1S103H)	peat	Turbidity	pH 3 pH 4 pH 5	[HA] = 30 mg m <sup>-3</sup>		$D_s = 2.79$ $D_s = 2.87$ $D_s = 2.87$	[35]

$D_s$ : surface fractal dimension;  $D_m$ : mass fractal dimension; HA: humic acid; NOM: unfractionated natural organic matter sample. IHSS: International Humic Substances Society.

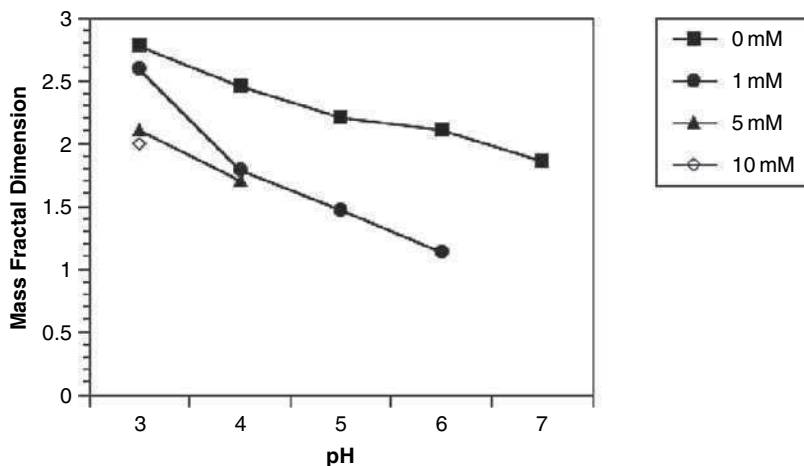
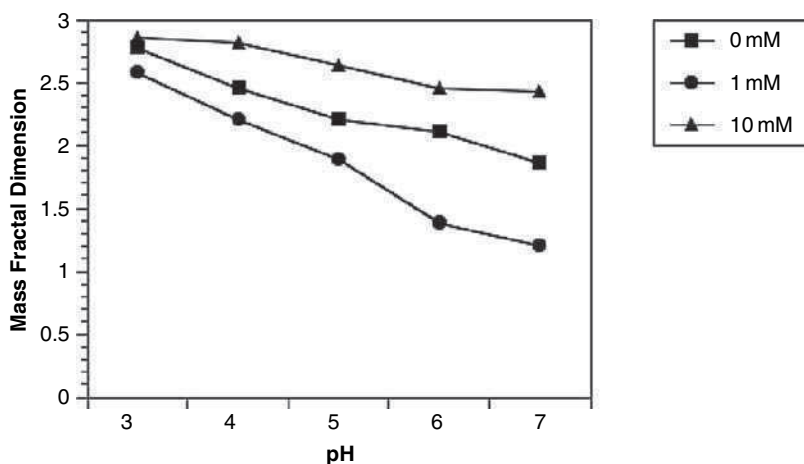
because of variations in the pH, ionic strength, and humic material concentration used to prepare samples.

Humic acids characterized by transmission electron microscopy (TEM) in acidic solutions (Table 7.1; V) display mass fractal dimensions  $D_m < 2$ , even after aging for 28 h. These values are considerably smaller than those reported for SAXS or SANS measurements of humic acids in solution, regardless of whether the solution was basic or acidic at the time of the measurements (Table 7.1). They are also smaller than the dimensions reported for the same samples obtained by turbidimetry (Table 7.1; VI). There are insufficient data and dissimilar experimental conditions (pH, ionic strength, sample source, etc.) to allow a definitive explanation of the differences between the  $D_m$  values of humic acids characterized by SAXS, SANS and TEM. These observations, however, suggest at least two possibilities: that there are methodological differences that 'see' different components of the sample (here, it would be useful to know what fraction of the original sample's organic carbon was actually present on the TEM grids imaged) or that humic acid particles go through a range of fractal structures as the concentration increases and/or the solution pH decreases.

The fractal properties reported for suspensions of humic particles can be characteristic of either mass fractals or surface fractals (Table 7.1; VI), apparently depending on the nature of the sample and the medium. At around pH 5, an increase in humic acid concentration, either in solution (Table 7.1; IV) or in suspension (Table 7.1; VI), results in an increase in  $D_m$ ; this suggests that the aggregates are becoming more space filling (i.e. more tightly packed), consistent with the general view that humic acid aggregation increases with increasing concentration. But data also exist from solutions of varying humic acid concentrations at pH 5 (Table 7.1; III) which suggest that the fractal dimension of a humic acid at this pH is independent of concentration. This contradiction does not appear to have been resolved; but, based on its operational definition, pH 5 probably represents a lower limit for humic acid solubility, and aggregation may have already begun to occur in the samples, especially given the relatively high concentrations used (Table 7.1; III). This final point could explain why  $D_m$  was reported to be independent of concentration.

Studies where pH and/or ionic strength have been varied (Figure 7.3) are generally consistent with a polyelectrolyte nature for humic acids: fractal dimensions increase with decreasing pH and increasing ( $\text{CaCl}_2$ ) ionic strength, indicating the development of a more dense, space-filling aggregate structure. The increase in  $D_m$  is presumably the result of charge screening (increase of ionic strength) or proton binding and hydrogen bonding (decrease of pH) engendering intermolecular interactions leading to changes such as coiling, compaction, etc. within the aggregate structure. This is consistent with Ghosh and Schnitzer's [49] original qualitative depiction of the variations in the structure of humic and fulvic acids with respect to pH and ionic strength changes.

The fractal dimension of the one aquatic (groundwater) NOM sample in solution reported to date has a  $D_m = 1.6$  (Table 7.1). This sample was characterized at a realistic environmental concentration of  $[\text{NOM}] = 45 \text{ mg dm}^{-3}$ . A  $D_m = 1.6$  is indicative of

**A. NaCl****B. CaCl<sub>2</sub>**

**Figure 7.3** Effect of ionic strength (as NaCl or CaCl<sub>2</sub> concentration) and pH on the mass fractal dimension of a soil humic acid. Fractal dimensions are taken from Senesi *et al.* [35], and were determined by turbidimetry (see text for details).

a more linear aggregate structure than that discussed above for humic acid in solution. A more linear structure is similar to the results obtained from TEM images of very dilute solutions of humic acids (Table 7.1; V). It is also consistent with the depiction of colloid/macromolecular interactions for NOM based on electron microscopy and computational studies [51].



In contrast to their solution characteristics, humic and fulvic acids in the solid state are surface fractals. Values of  $D_s$  are in the range  $2 \leq D_s \leq 3$  (Table 7.1). To date, these values are observed even with the varying pH or ionic strength conditions that existed when the samples were isolated.

Humin is an organo-mineral composite [11] that is the least studied of the humic materials [52], and this is reflected in the small number of studies examining its fractal characteristics. Humin isolated from three mineral soils and a peat soil (Table 7.1) displays  $D_s$  values ranging from 2.5 to 2.9 over length scales of 1 to 15 nm. Two of these samples also have components that exhibit mass fractal behavior (Table 7.1), an observation that, while repeated, has not been satisfactorily explained. Selective, sequential removal of the organic matter from the surface of humin particles results in a decrease in  $D_s$  and concomitant decrease in surface-pore size and increase in surface area [25]. These results suggest that the mineral components of humin have smoother surfaces over these length scales than the original humin organo-mineral composite, and that it is the organic matter coatings that are responsible for the particle surface roughness. It was also noted in these studies that the humic acid-like component of humin exhibited a fractal nature being a mass fractal in solution and a surface fractal in the solid state.

### 7.3.2 Aggregation Mechanisms

In Chapter 4, the various aggregation mechanisms operant in fractal systems are reviewed, e.g. reaction-limited aggregation (RLA) and diffusion-limited aggregation (DLA). For a detailed discussion of these mechanisms the reader is referred to that chapter and the references it contains. In the late 1990s, Homer [32] and Senesi [44] reviewed studies of humic material aggregation using a fractal approach. Since then, little in the way of new insights into either the mechanism or the applications of fractal aggregation has been presented.

The early fractal studies of humic materials alluded to the application of sample fractal dimensions for the description of aggregation mechanisms operant in these systems. In the first paper reporting a fractal nature for humic materials in solution, Österberg noted that the observed fractal dimensions were indicative of an RLA process [26].

It is difficult to make generalizations from such a limited body of work that has used different samples, pHs, concentrations, ionic strengths, etc. With that as a caveat, subsequent investigations have discussed their results in terms of either RLA or DLA mechanisms [16, 18, 27, 28, 32, 34, 35, 42, 44], depending on pH. An RLA mechanism is suggested as dominant at higher pH conditions presumably because ionized functional groups generate electrostatic repulsions that hinder aggregation [16, 26, 28, 34, 35]. At low pH values, a DLA mechanism seems to be dominant, probably because charge neutralization has minimized or eliminated electrostatic repulsions. It has been reported that as a humic aggregate ages it undergoes a restructuring that tends to produce a more space-filling particle [28, 29, 42] with

a concomitant increase in the fractal dimension (Figure 7.4). This behavior is consistent with the polyelectrolytic characteristics of these materials. The restructuring phenomenon is characteristic of RLA, where components of a fractal aggregate can reorganize with time to form denser particles [53].

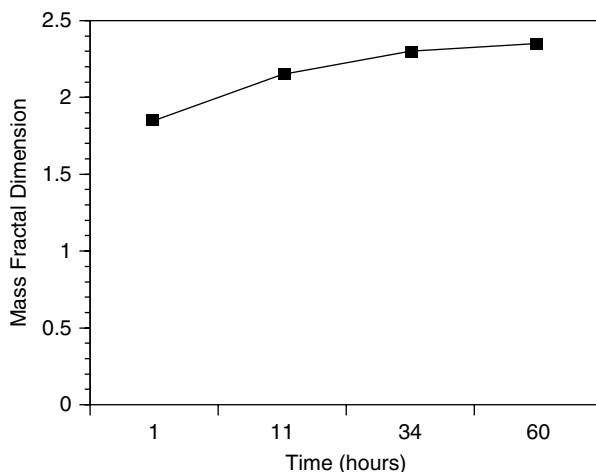


**Figure 7.4** Effect of time on the mass fractal dimension of a soil humic acid. Fractal dimensions are taken from Österberg *et al.* [28], and were determined by SANS (see text for details).

## 7.4 WHAT FRACTALS COULD TELL US ABOUT HUMIC MATERIALS

A fractal approach to the study of the chemistry and geochemistry of humic materials has a number of possible applications that the limited number of papers published on this property have only begun to consider. In the paragraphs below, a few possible examples are given. To fully realize the insights that a fractal approach could provide will require systematic study of a suite of carefully isolated and well-characterized humic substances. The International Humic Substances Society (IHSS) has such a collection of standard and reference humic materials that would be an ideal sample suite for this purpose [54, 55].

### 7.4.1 Controls on the Fractal Dimension

In 1999, Homer [32] noted that ‘sparse’ data existed to correlate the chemical characteristics of a humic material with its fractal dimension or aggregation mechanism. For example, a preliminary study is described that may be the only attempt to correlate the carbon types present in a humic sample to its fractal properties. Humic acids with a greater proportion of aromatic carbon than carbohydrate carbon (determined from a  $^{13}\text{C}$  NMR spectrum) had larger fractal dimensions than those with smaller

proportions of aromatic carbon. In the same report, Homer [32] suggested that functional group concentrations might also play a role. Though they represent a very limited data set, the fractal dimensions presented in Rice and Lin [12] seem to suggest that humic particle morphologies may vary with source environment. While the correlations from these comparisons may only weakly infer a cause-and-effect relationship, a systematic study of the chemical properties of a suite of carefully-characterized humic and fulvic acids could, at the very least, point the way towards more specific studies of the chemical interactions resulting in the fractal aggregate structures observed for humic materials.

#### **7.4.2 Effect of Environmental Variables on Aggregate Structure**

While the solution parameters discussed certainly fall within the realm of environmental variables, their limits in most natural environments are relatively constrained; for example, pH usually varies only between  $\sim 5$  and 8 [56]. Humic materials are strong ligands for multivalent cations and these same cations readily flocculate humic materials, for some cations at very low concentrations. The resulting aggregates and the aggregation process(es) that form them could be studied with a fractal approach. For example,  $\text{Ca}^{2+}$  [35] and  $\text{Fe}^{3+}$  [32] have been cursorily examined. Calcium ions produced a particle with surface fractal properties (as opposed to mass fractal behavior) at all pH values. Contrary to the expected increase in fractal dimension,  $\text{Fe}^{3+}$  did not change the observed value of  $D_m$  for the humic acid studied, but it did increase the intensity of scattered neutrons as a result of what was believed to be an increase in aggregate size. Homer [32] proposes that this could be the result of either an increase in humic aggregate cluster size or the formation of new clusters from previously unaggregated components in a humic sample.

#### **7.4.3 Environmental Applications of the Fractal Nature for Humic Materials**

Studies carried out on humic materials that have utilized fractals have focused on characterizing their structural organization and/or their aggregation behavior. The real power of a fractal approach lies not in simply characterizing humic materials, but in applying it to modeling and predicting the chemical and geochemical behavior of these materials in the environment.

For example, Dachs and coworkers [57, 58] have developed a fractal approach that takes the 'geometric heterogeneity' of humic materials into account when modeling their interaction with organic contaminants. This approach [57] utilizes the different interaction probabilities of the active contaminant binding sites on fractal surfaces to accommodate linear and nonlinear sorption isotherms (i.e. 'dual-mode' sorption) using coverage extent, physical and chemical properties of the adsorbate and the existence of equilibrium conditions. An extension of this approach [58] treats partitioning as sorption to the inner sites of a fractal sorbent, in much the same manner that a hydrophobic organic chemical is viewed as partitioning into a humic

material. In this approach, molecules are adsorbed at the outer sites on a fractal aggregate in a relatively fast process. With time, molecules slowly diffuse into the fractal aggregate and bind to the inner sites. In this process, partitioning is a significant contribution to the overall sorption process at long equilibration times. Interestingly, this sequence of events is what Kohl *et al.* [59] have observed when solid-state  $^{19}\text{F}$  NMR is used to follow the interaction of hexafluorobenzene with natural organic matter sorbents.

## 7.5 CONCLUSIONS AND RECOMMENDATIONS

A fractal approach seems ideally suited to the study of higher order structural organization and interactions in humic materials. But in the 15 years since it has been first applied to them, there has been surprisingly little interest in applying this tool to advancing the understanding of the unique nature of these ubiquitous materials by any other than those who initially adopted it. There have been surprisingly few papers exploring the fractal nature of humic materials published during this time. However, there have been some basic insights into the fractal nature of humic materials that have come from this early work.

Humic materials have been shown to be mass fractal aggregates in solution or in suspension, and surface fractals in the solid state. The fractal dimensions of both fractal types are generally between 2 and 3. But there has been no systematic study of how the fractal dimension varies with environmental variables (pH, ionic strength, humic concentration, sample source, identity and concentration of multivalent cations, aggregate size, etc.).

A basic recognition has emerged that the aggregation of humic material can be described using a fractal approach. DLA is generally operant under acidic conditions and RLA becomes more important as the pH increases.

The real value of a fractal approach in the study of humic materials will not be realized until it can be applied in a manner that describes properties, reactions or geochemical behavior for which we previously had no vocabulary.

## LIST OF SYMBOLS AND ABBREVIATIONS

DLA	diffusion-limited aggregation
HA	humic acid
IHSS	International Humic Substances Society
NOM	natural organic matter
NMR	nuclear magnetic resonance
RLA	reaction-limited aggregation
SAXS	small-angle X-ray scattering
SANS	small-angle neutron scattering
TEM	transmission electron microscopy

$c$	concentration of particles with a particular molar mass
$D$	fractal dimension
$D_m$	mass fractal dimension
$D_s$	surface fractal dimension
$I_e$	scattered intensity from a single electron
$I_0$	incident intensity
$I_0(qa)$	scattered intensity from a single scatterer
$I(q)$	intensity of scattered radiation as a function of the scattering vector $q$
$l$	diameter of a scattering particle
$M$	particle mass
$M_w$	molar mass
$N$	Avogadro's number
$N_s$	number of scattering particles
$P(\theta)$	particle form factor
$q$	scattering vector
$Q$	turbidity dissipation function
$S(q)$	structure factor
$d\eta/dc$	refractive index increment
$\lambda$	wavelength of the incident radiation
$\theta$	scattering angle
$\Gamma$	gamma function
$\tau$	turbidity

## REFERENCES

- [1] Stevenson, F.J. (1982). *Humus Chemistry*. John Wiley & Sons, Ltd, New York.
- [2] Kononova, M.M. (1966). *Soil Organic Matter*, Nowakowski, T.A. and Newman, A.C.D. (transl.). Pergamon Press, Oxford.
- [3] Orlov, D.S. (1985). *Humus Acids of Soils*. Kothekar, V. (transl.), A.A. Balkema, Rotterdam.
- [4] Thurman, E.M. (1985). *Organic Geochemistry of Natural Waters*. Martinus Nijhoff/Dr Junk, Dordrecht.
- [5] Aiken, G.R., McKnight, D.M., Wershaw, R.L. and MacCarthy, P. (eds). (1985). *Humic Substances in Soil, Sediment, and Water*. John Wiley & Sons, Ltd, New York.
- [6] Rice, J.A. and MacCarthy, P. (1991). Statistical evaluation of the elemental composition of humic substances. *Org. Geochem.*, **17**, 635–648.
- [7] Rice, J.A. (1988). *Studies on humus. I. Statistical studies on the elemental composition of humus; II. The humin fraction*. PhD dissertation, Colorado School of Mines, Golden, CO.
- [8] MacCarthy, P. and Rice, J.A. (1985). Spectroscopic methods (other than NMR) for determining functionality in humic substances. In *Humic Substances in Soil, Sediment, and Water: Geochemistry, Isolation, and Characterization*, Aiken, G.R., McKnight, D.M., Wershaw, R.L. and MacCarthy, P. (eds). John Wiley & Sons, Ltd, New York, pp. 527–559.
- [9] Hayes, M.H.B., MacCarthy, P., Malcolm, R.L. and Swift, R.S. (1989). Structures of humic substances: the emergence of 'forms'. In *Humic Substances II. In Search of Structure*, Hayes, M.H.B., MacCarthy, P., Malcolm, R.L. and Swift, R.S. (eds). Wiley-Interscience, Chichester, pp. 689–733.

- [10] Swift, R.S. (1985). Fractionation of soil humic substances In *Humic Substances in Soil, Sediment, and Water: Geochemistry, Isolation, and Characterization*, Aiken, G.R., McKnight, D.M., Wershaw, R.L. and MacCarthy, P. (eds). John Wiley & Sons, Ltd, New York, pp. 387–408.
- [11] Rice, J.A. and MacCarthy, P. (1990). A model of humin. *Environ. Sci. Technol.*, **24**, 1875–1877.
- [12] MacCarthy, P. and Rice, J.A. (1991). An ecological rationale for the heterogeneous nature of humic substances. In *Scientists on Gaia*, Schneider S. and Boston, P.J. (eds). MIT Press, Cambridge, MA, pp. 339–345.
- [13] Wershaw, R.L. (1993). Model for humus in soils and sediments. *Environ. Sci. Technol.*, **27**, 814–816.
- [14] Piccolo, A. (2001). The supramolecular structure of humic substances. *Soil Sci.*, **166**, 810–832.
- [15] Tombácz, E. (2002). Interfacial and colloidal properties of humic substances. *Magy. Kem. Foly. Kem. Kozl.*, **108**, 435–443.
- [16] Ren, S.-Z., Tombácz, E. and Rice, J.A. (1996). Dynamic light scattering from fractals in solution: Application of dynamic scaling theory to humic acid. *Phys. Rev. E*, **53**, 2980–2983.
- [17] Raper J.A. and Amal, R. (1993). Measurement of aggregate fractal dimension using static light scattering. *Part. Part. Syst. Charact.*, **10**, 239–245.
- [18] Tombácz, E., Rice, J.A. and Ren, S.-Z. (1997). Fractal structure of polydisperse humic acid particles in solution studied by scattering methods. *ACH Models Chem.*, **134**, 877–888.
- [19] Rice, J.A., Tombácz, E. and Malekani, K. (2000). Applications of light and X-ray scattering to characterize the fractal properties of soil organic matter. In *Fractals in Soil Science, Developments in Soil Science* 27, Pachepsky, Ya.A., Crawford, J.W. and Rawls, W.J. (eds). Elsevier, Amsterdam, pp. 161–174.
- [20] Rice, J.A. and Lin, J.S. (1993). Fractal nature of humic materials. *Environ. Sci. Technol.*, **27**, 413–414.
- [21] Rice, J.A. and Lin, J.S. (1994). Fractal dimensions of humic materials. In *Humic Substances in the Global Environment and Implications on Human Health*, Senesi, N. and Miano, T.M. (eds). Elsevier, Amsterdam, pp. 115–120.
- [22] Dékány, I., Szekeres, M., Marosi, Balázs, T.J. and Tombácz, E. (1994). Interaction between ionic surfactants and soil colloids: adsorption, wetting and structural properties. *Prog. Colloid Polym. Sci.*, **95**, 73–90.
- [23] Malekani, K., Lin, J.S. and Rice, J.A. (1997). Fractal characterization of the surface of the humin fraction of soil organic matter. In *Fractal Frontiers*, Novak, M.M. and Dewey, T.G. (eds). World Scientific, Singapore, pp. 367–381.
- [24] Malekani, K., and Rice, J.A. (1997). Fractal character of humin and its components. *Fractals*, **5**, 83–100.
- [25] Malekani, K., Lin, J.S. and Rice, J.A. (1997). The effect of sequential organic matter removal on the surface morphology of humin. *Soil Sci.*, **162**, 333–342.
- [26] Österberg, R. (1992). Fractal dimensions of humic acids: a small angle neutron scattering study. *Eur. Biophys. J.*, **21**, 163–167.
- [27] Österberg, R. and Mortensen, K. (1994). The growth of fractal humic acids: cluster correlation and gel formation. *Radiat. Environ. Biophys.*, **33**, 269–276.
- [28] Österberg, R., Szajdak, L. and Mortensen, K. (1994). Temperature-dependent restructuring of fractal humic acids: a proton-dependent process. *Environ. Int.*, **20**, 77–80.
- [29] Österberg, R. and Mortensen, K. (1994). Fractal geometry of humic acids. Temperature-dependent restructuring studied by small-angle neutron scattering. In *Humic Substances in the Global Environment and Implications on Human Health*, Senesi, N. and Miano, T.M. (eds). Elsevier, Amsterdam, 127–132.

- [30] Österberg, R. and Mortensen, K. and Ikai, A. (1995). Direct observation of humic acid clusters, a nonequilibrium system with a fractal structure. *Naturwissenschaften*, **82**, 137–139.
- [31] Österberg, R. (2002). Fractal structure and reactions of the two-phase humic acid system. *Trends Geochem.*, **2**, 95–99.
- [32] Homer, V.J. (1998). Fractal probes of humic aggregation: scattering techniques for fractal dimension determinations. In *Fractals in Soil Science*, Baveye, P., Parlange, J.-Y. and Stewart, B.A. (eds). CRC Press, Boca Raton, FL, pp. 75–112.
- [33] Senesi, N., Lorusso, G.F., Miano, T.M., Maggipinto, G., Rizzi, F.R. and Capozzi, V. (1994). The fractal dimension of humic substances as a function of pH by turbidity measurements. In *Humic Substances in the Global Environment and Implications on Human Health*, Senesi, N. and Miano, T.M. (eds). Elsevier, Amsterdam, pp. 121–126.
- [34] Senesi, N., Rizzi, F.R., Dellino, P. and Acquafredda, P. (1996). Fractal dimension of humic acids in aqueous suspension as a function of pH and time. *Soil Sci. Soc. Am. J.*, **60**, 1773–1780.
- [35] Senesi, N., Rizzi, F.R., Dellino, P. and Acquafredda, P. (1997) Fractal humic acids in aqueous suspensions at various concentrations, ionic strengths, and pH values. *Colloids Surf. A*, **127**, 57–68.
- [36] Costa da Silva, A., Sa Mendonca, E. and Reis, C. (2003). Fractal dimension of humic acids in different experimental conditions. *Quim. Nova*, **26**, 344–346.
- [37] Costa da Silva, A., Sa Mendonca, E. and Reis, C. (2000). Fractal dimension of humic acids. *Rev. Brasil. Cienc. Solo*, **24**, 759–766.
- [38] Costa da Silva, A. (2000). Fractal dimension of humic acids by turbidimetry. *Rev. Ceres*, **47**, 103–112.
- [39] Schmidt, P. (1989). Use of scattering to determine the fractal dimension. In *The Fractal Approach to Heterogeneous Chemistry*, Avnir, D. (ed.). John Wiley & Sons, Ltd, Chichester, pp. 67–79.
- [40] Martin, J.E. and Hurd, A.J. (1987). Scattering from fractals. *J. Appl. Crystallogr.*, **20**, 61–78.
- [41] Chen, Y. and Schnitzer, M. (1989). Sizes and shapes of humic substances by electron microscopy. In *Humic Substances II. In Search of Structure*, Hayes, M.H.B., MacCarthy, P., Malcolm, R.L. and Swift, R.S. (eds). Wiley–Interscience, Chichester, pp. 621–638.
- [42] Rizzi, F.R., Stoll, S., Senesi, N. and Buffle, J. (2004). A transmission electron microscopy study of the fractal properties and aggregation processes of humic acids. *Soil Sci.*, **169**, 765–775.
- [43] Senesi, N. (1994). The fractal approach to the study of humic substances. In *Humic Substances in the Global Environment and Implications on Human Health*, Senesi, N. and Miano, T.M. (eds). Elsevier, Amsterdam, pp. 3–41.
- [44] Senesi, N. (1999). Aggregations patterns and macromolecular morphology of humic substances: a fractal approach. *Soil Sci.*, **164**, 841–856.
- [45] Amal, R., Raper, J.A. and Waite, T.D. (1992). Effect of fulvic acid adsorption on the aggregation kinetics and structure of hematite particles. *J. Colloid Interface Sci.*, **151**, 244–257.
- [46] Schmidt, C., Thieme, J., Neuhausler, U., Schulte-Ebbert, U., Abbt-Braun, G., Specht, G. and Jacobsen, C. (2000). Association of particles and structures in the presence of organic matter. In *AIP Conference Proceedings, 507 (X-Ray Microscopy)*. American Institute of Physics, pp. 313–318.
- [47] Waite, T.D., Amal, R., Ngo, H. and Vigneswaran, S. (1993). Effects of adsorbed organic matter on size, structure and filterability of iron oxyhydroxide flocs. *Water Sci. Technol.*, **27**, 133–142.

- [48] Sokolowska, Z. and Sokolowski, S. (1999). Influence of humic acid on surface fractal dimension of kaolin: analysis of mercury porosimetry and water vapour adsorption data. *Geoderma*, **88**, 233–249.
- [49] Ghosh, K. and Schnitzer, M. (1980). Macromolecular structures of humic substances. *Soil Sci.*, **129**, 266–276.
- [50] Guetzloff, T.F. and Rice, J.A. (1994). Does humic acid form a micelle? *Sci. Total Environ.*, **152**, 31–35.
- [51] Rizzi, F.R., Stoll, S., Senesi, N. and Buffle, J. (2004). A transmission electron microscopy study of the fractal properties and aggregation processes of humic acids. *Soil Sci.*, **169**, 765–775.
- [52] Rice, J.A. and MacCarthy, P. (1988). Comments on the literature of the humin fraction of humus. *Geoderma*, **43**, 65–73.
- [53] Meakin, P. (1988). Fractal aggregates. *Adv. Colloid Interface Sci.*, **28**, 249–331.
- [54] Campbell, W.L. and Malcolm, R.J. (1985). Preparation, homogenization, and storage of earth standards used and distributed by the International Humic Substances Society. *Org. Geochem.*, **8**, 109.
- [55] Swift, R.S. (1996). Organic matter characterization. In *Methods of Soil Analysis. Part 3. Chemical Methods*. SSSA Book Series No. 5. Soil Science Society of America, Madison, WI, pp. 1011–1069.
- [56] Baas Beeking, L.G.M., Kaplan, I.R. and Moore, D. (1960). Limits of the natural environment in terms of pH and oxidation–reduction potentials. *J. Geol.*, **68**, 243–284.
- [57] Dachs, J. and Bayona, J.M. (1997). Langmuir-derived model for diffusion- and reaction-limited adsorption of organic compounds on fractal aggregates. *Environ. Sci. Technol.*, **31**, 2754–2760.
- [58] Dachs, J. and Eisenreich, S.J. (2001). Adsorption and partitioning of organic compounds onto/into fractal sorbents. *Langmuir*, **17**, 2553–2537.
- [59] Kohl, S.D., Toscano, P.J., Hou, W. and Rice, J.A. (2000). Solid-state  $^{19}\text{F}$  NMR investigation of hexafluorobenzene sorption to soil organic matter. *Environ. Sci. Technol.*, **34**, 204–210.



---

# 8 Fractal Geometry and Microorganisms in the Environment

---

**Lynne Boddy<sup>1</sup>** and **Damian P. Donnelly<sup>2</sup>**

*Cardiff School of Biosciences, Cardiff University, Biomedical Building, Museum Avenue, Cardiff, CF10 3US, UK*

## 8.1 INTRODUCTION

During the last two or three decades, microbial ecologists have concentrated on quantifying numbers (individual cells or colony forming units) and/or biomass in natural environments, as a measure of ‘how much is there’. However, such measures provided little indication of what the microorganisms are doing [1], nor of how the biomass is spatially distributed. Microorganisms are able to deploy the same amount of biomass in different ways, depending on species, resources available and other external environmental factors (see Sections 8.3–8.5).

Many microorganisms (including bacteria and fungi) have modular body forms. When new modules are formed, e.g. by fission or budding, the modules commonly remain attached to the body from which they were formed, but sometimes they become detached and are able to function as separate physiological units [2]. Effectively, they have iterative, indeterminate growth patterns, tend to branch, and are sessile except when in dispersal phases. Such modular organisms contrast with unitary organisms, such as higher animals that generally exhibit noniterative, determinate growth patterns, are nonbranched and are motile. Since modular organisms have simple organisation, tend to lack motility at some stages of their life, and often have external digestion, they are vulnerable to environmental changes. However, they commonly have considerable phenotypic plasticity, i.e. genotype can be expressed differently under different environmental conditions. Thus, microorganisms often exhibit different physiologies and/or morphologies under different environmental regimes. Fungi exhibit considerable morphological and physiological plasticity (Section 8.3.2 and 8.5). Bacteria, on the other hand, are physiologically very plastic, but less so morphologically, though colony characteristics can sometimes change

(Sections 8.3.1 and 8.4). Arguments have been put forward that bacterial colonies are not self-similar [3], but, like many naturally irregular structures, many modular organisms, including fungi and some bacteria under some conditions, are often approximately fractal. Colonies are, however, self-similar only over a finite range of length scales.

Fractal geometry has been used to describe quantitatively inter- and intra-specific differences, within-colony differences, and environmentally induced differences in the morphology of bacteria and fungi (Sections 8.3–8.5). Since microbial morphology is most easily seen on artificial media, many studies have been performed in solid agar culture (Section 8.3), but this reflects the real world poorly, and studies are increasingly being undertaken in more realistic microcosms and even field situations (Sections 8.4 and 8.5). The vast majority of these studies have concerned fungi; hence, these are emphasised, though the work on bacteria is also summarised. Some natural environments are themselves fractal, e.g. soil, and this affects the diversity, density and distribution of the inhabitant microorganisms (Section 8.6). Further, a range of mathematical models have been developed to explain fractal growth of microbial colonies [e.g. 4–8], but consideration of this topic is beyond the scope of this chapter.

## 8.2 DETERMINING FRACTAL DIMENSION OF MICROORGANISMS

The two fractal dimensions of surface and mass provide different measurements of the morphology of microbial colonies. The surface fractal dimension (a subset of the mass fractal dimension) only describes the morphology of the edges of the colony, i.e. where, in images (see below), white pixels from the colony occur adjacent to black pixels of the background, including exterior edges at the colony margins and interior edges, e.g. where internal gaps persist between cords<sup>1</sup> and hyphae of fungi. In terms of more regular geometric shapes, this would equate to describing the morphology of the perimeter. For nonfractal shapes, perimeters are linear with a Euclidean dimension of one, fractal shapes have perimeter values greater than one but less than the Euclidean area dimension (length and breadth) of two. The mass fractal dimension, on the other hand, includes all colony pixels, including those at perimeters and those interior to the perimeter. Thus, mass fractal dimension describes the morphology of the entire colony area, which will have values between the nonfractal values of two for completely filled areas and one for mycelia in which all colony pixels are at a linear perimeter (in 2 dimensions).

---

<sup>1</sup> Mycelial cords: linear organs formed from hyphae aggregating together, behind a mycelial growing front. They often have a thickened outer rind and are differentiated internally for rapid transport of water and nutrients.

The colonies of many bacteria and some fungi, or at least some fungi during early stages of outgrowth from a resource, are entirely space-filled at the centre, being only fractal at their boundaries, i.e. they are surface fractal (Chapter 1). In contrast, many fungi growing in terrestrial environments have gaps within their colonies, the structures being mass fractal. Fractal dimension is an appropriate means of quantifying the way in which these microorganisms deploy their biomass, but it is obviously necessary to use both mass fractal  $D_M$  and surface fractal  $D_S$  dimensions.

Fractal dimensions have most commonly been determined from images of microorganisms in sterile agar culture and nonsterile soil microcosms. The latter have been used to great effect to visualise and quantify the changes in morphology of macroscopic mycelial systems of saprotrophic, pathogenic and ectomycorrhizal fungi. Microcosms, ranging in size from 20 cm × 20 cm to 57 cm × 57 cm, and consisting of soil compacted to ensure mycelial growth at the soil surface, are inoculated with resources, e.g. wood, leaf litter or plant roots precolonised with fungi (e.g. Figures 8.1 and 8.2). As microbial systems develop, be they on agar, soil or other substrata, images are captured over time for morphological quantification.

Image analysis involves a series of predefined steps to extract the image of the microbe from the rest of the microcosm. Mycelia (a radially extending, interconnecting series of tubes, e.g. Figure 8.1a) growing in soil are the most complex systems used so far, thus the steps in image analysis and determination of fractal dimension are outlined below for these systems. Mycelial areas are marked out by user defined pixel lines (Figure 8.1b), and unwanted areas such as resources are masked by being set to pixel values of 0 (black) (Figure 8.1c). Image quality may also be improved by applying software filters to remove image ‘noise’. Finally, the image is ‘thresholded’, whereby the user defines a greyscale boundary above which all pixels are set to white (pixel value = 1) and below which all values are set to black (pixel value = 0) (Figure 8.1c). This produces a binary image typically with the mycelium as a white image on a black background. There will obviously be some user bias during manual thresholding. However, provided that illumination has been constant throughout an experiment, the same threshold value can be used on each image for consistency, and is unlikely to result in a change in fractal dimension of more than about  $\pm 0.01$ .

A number of methods (Chapter 2) have been used for estimating  $D$ , including concentric rings, length-projected area, length number scaling and box counting, but the latter has been by far the most common [9].

### 8.2.1 Determining Fractal Dimensions by the Concentric Ring Technique

The mass fractal dimension can be estimated by overlaying an image with a series of concentric rings of different radius:

$$M(r) = Cr^{D_M} \quad (8.1)$$

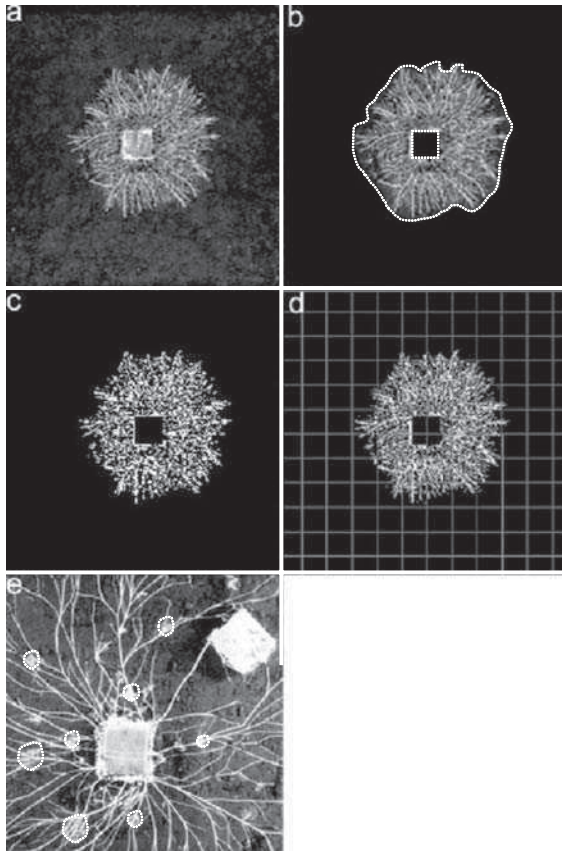


**Figure 8.1** Image preprocessing of mycelial systems in soil microcosms: (a) unprocessed image; (b) masking of central inoculum and uncolonised soil area; (c) thresholded binary image; (d) overlaid grid for box-count determination of fractal dimension; (e) close-up of mycelial colonisation of wood resources and localised mycelial patch production (encircled dotted lines).

where  $M(r)$  is the mass contained within a circle of radius  $r$ ,  $C$  is a constant and  $D_M$  is the mass fractal dimension [10]. It is advisable to use at least five different radii. Analysis should not be taken to the edge of colonies due to boundary effects [10]. Constructing double logarithmic (Robertson) plots of  $M$  against  $r$  allows determination of the slope, which is equivalent to  $2D_M - 1$  [11].

### 8.2.2 Determining Fractal Dimensions by the Box-Counting Technique

Box counting involves overlaying a series of grids of square boxes (with sizes of 3–63 pixels being appropriate for fungal mycelia in small microcosms) onto an image of the colony (Figure 8.1d). The number of boxes intersecting pixels representing the

organism (rather than the matrix upon which it is growing) is recorded. Fractal images obey the power law over a range of length scales [12]:

$$N(s) \approx cs^{-D_{\text{BM}}} \quad (8.2)$$

where  $N(s)$  is the total number of boxes of side length  $s$ , which intersects the image;  $c$  is a constant; and  $D_{\text{BM}}$  is the box-count fractal dimension. The total number of boxes  $N$  intersected by the set comprises both interior boxes (i.e. boxes that contain white pixels only) and border boxes (i.e. boxes that contain at least one white pixel and which contain or adjoin at least one black pixel):

$$N(s) = N_{\text{border}}(s) + N_{\text{interior}}(s) \quad (8.3)$$

Surface fractal dimensions  $D_{\text{BS}}$  are estimated from the linear portion of a plot of  $\log N_{\text{border}}(s)$  against  $\log s$ :

$$\log N_{\text{border}}(s) = \log c + (-D_{\text{BS}}) \log s \quad (8.4)$$

Similarly, mass fractal dimension  $D_{\text{BM}}$  is estimated by regression of the linear part of a plot of  $N_{\text{interior}}(s)$  against  $\log s$ . However, since natural structures are only self-similar over a finite range of length scales, departures from the power law occur at very large and very small box sizes [11, 13–15]. Upper limits of length scale range are determined by the largest gap within the image (in practice usually 25 % of the maximum width of the image set) and lower limits by the pixel size of the image, and in mycelia this will be limited by individual hyphae [11, 14]. Since border boxes are not entirely filled, the area is progressively overestimated by the use of increasingly larger box sizes. To avoid this overestimation a correction is needed [16]. Thus,  $D_{\text{BM}}$  is estimated by regression analysis on the linear portion of a plot of  $\log[N(s) - 1/2 N_{\text{border}}(s)]$  against  $s$  [16].

Imaging software techniques enable analysis of both entire images and analysis of distinct local areas of interest (AOIs). AOIs are typically demarked from the rest of the image by user defined pixel lines (Figure 8.1e), and either copied or removed from the main image for subsequent separate analysis. This approach is particularly useful in quantifying fungal mycelia, as these systems often display a range of morphologies during colonisation of heterogeneous substrates. Thus, a single mycelium may be composed of a number of regions of differing fractal dimension, e.g. mycelial patches colonising discrete resources within soil (Figure 8.1e), and production of overgrowth fans during interaction with other fungi (Figure 8.2).

### 8.2.3 Potential Sources of Error

One potential source of error in determining the fractal dimension from images is the resolution of the image constraining the size of the boxes that may be used. Ideally, the image resolution should be such that the smallest picture element is the same size as the smallest hyphal width. In reality, the image may not be fractal at all length scales and the power-law behaviour not obeyed for all box sizes, departures occurring

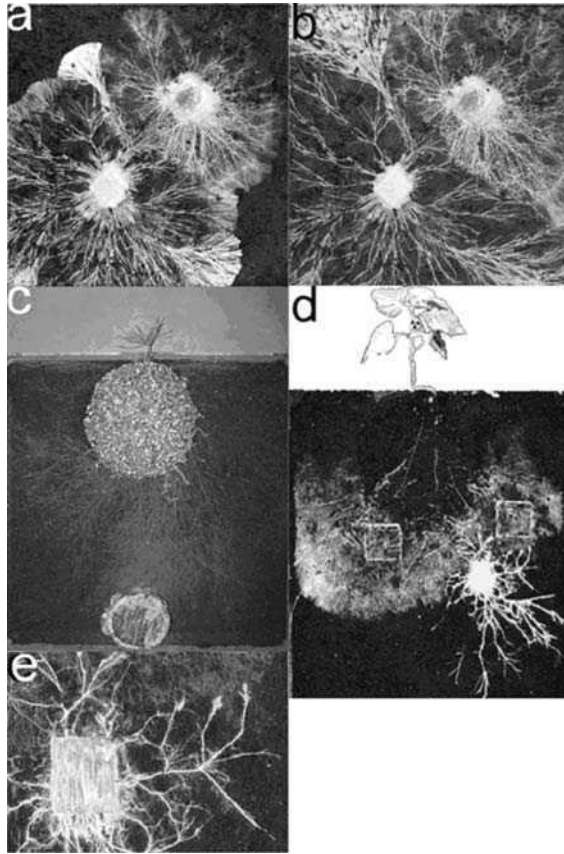


**Figure 8.2** Digital images of mycelial systems interacting on nonsterile soil (a, b) and peat (c–e). (a, b) Interactions between *Stropharia caerulea* (top right) and *Hypholoma fasciculare* (bottom left) after (a) 35 days and (b) 63 days. Note dense fan production by *Hypholoma fasciculare*. (c) Interaction between *Paxillus involutus* mycorrhizal with *Pinus sylvestris* seedlings and the root pathogen *Rhizina undulata* on peat. (d) Interaction between *Paxillus involutus* mycorrhizal with *Betula pendula* seedlings and the decomposer *Phanerochaete velutina* in microcosms (30 cm  $\times$  25 cm) comprising a thin layer (0.2 cm deep) of nonsterile peat (c–e). (e) Detail of the microcosm shown in (d) showing truncation of *Phanerochaete velutina* cords by interaction with *Paxillus involutus*.

at very small and very large box sizes. In practice, the box size upper limit has been approximated as 25 % of the maximum width of the image (feret diameter) [15]. The lower box size limit using a finite resolution imaging system is determined by the pixel size of the image, as detail below this resolution cannot be resolved. In practice, this has been determined experimentally (D.P. Donnelly, unpublished) and the lower limit to which the power law was maintained was at boxes sizes of 3 pixel side length for images of 512 $\times$ 512 pixels.

One of the crucial steps in image processing is the production of a binary image that distinguishes regions of interest from other background regions, achieved through user-defined threshold selection of pixel values at and above which all pixels are white and below which pixels are black. During the thresholding, a false-colour image of the thresholded pixel level is displayed on the image, enabling the user to determine the best possible level that distinguishes the mycelium. If the threshold is set too high, then background will be included as mycelium and an overestimate of mycelial  $D_{\text{BM}}$  produced, and a possible underestimate of  $D_{\text{BS}}$  through loss of perimeter pixels. The converse will be true if the threshold level is set too low: parts of the mycelium will be included as background and a low  $D_{\text{BM}}$  will be artificially produced. This may also increase  $D_{\text{BS}}$ , as artificial erosion of mycelium image could increase the irregularity of the perimeter and add perimeters to mycelial interiors where no gaps really exist.

### 8.2.4 Methods Used in Three Dimensions

The fractal nature of bacterial aggregates (flocs) has implications for transport processes, including movement of dissolved respiratory gases to and from the outside of the aggregate, and for movement of dissolved nutrient sources and metabolic products. Several methods have been employed to estimate fractal dimensions of flocs in three dimensions. One approach is to measure light scattering of suspended flocs [17, 18]. The two-slopes method calculates fractal dimensions  $D_3$  from the slope of the cumulative size distribution for maximum length  $l$  and the slope of the cumulative solid volume  $V$  [17]:

$$D_3 = \frac{S(l)}{S(V)} \quad (8.5)$$

where  $S(l)$  and  $S(V)$  are the exponents of the cumulative size distributions.  $D_3$  can also be determined from the small-angle light scattering of laser light by flocs [17]:

$$I(Q) \propto Q^{-D_3} \quad (8.6)$$

where  $I(Q)$  is the intensity of the scattered light.  $Q = (4\pi n/\lambda) \sin(\theta/2)$ , where  $n$  is the refractive index of the medium,  $\lambda$  is the wavelength of laser light, and  $\theta$  is the scattering angle. The slope of the plot of  $\log(I(Q))$  against  $\log(Q)$  gives the fractal dimension  $D_3$  within certain limits (i.e. this is only valid for size ranges much greater than the monomer size and up to a limited upper size) [17]. Other methods are also being developed to determine fractal dimension from light scatter data [18].

Confocal optical microscopy can be used to take a sequence of randomly chosen images through a bacterial floc. Methodologies for calculation of three-dimensional fractal dimensions have been described for this approach [18–20]. One method determines the fractal dimension of each section  $D_f$  using a two-point correlation function  $C(r)$  [20]:

$$C(r) = \int p(r') p(r+r') dr' \sim r^{D_f-d} \quad (8.7)$$



where  $d$  is the Euclidean space dimension, i.e. 2 in two-dimensional sections, and  $p(r)$  is the density at point  $r$ .  $D_f$  is obtained from the slope of a plot of  $\log(C(r))$  versus  $\log(r)$ . Since flocs are of limited size, corrections for border effects are needed: for each cell centre, only correlations with other cells closer than the nearest edge are included [20]. Provided that cells are visible in at least two consecutive sections, it is possible to deduce the position of cells in three-dimensional space. The two-point correlation function (Equation (8.7)) can then be computed for  $d = 3$  [20].

Another approach to determining the fractal dimension of three-dimensional flocs has been to view them individually by light microscopy to measure the largest floc length [21]. Fractal dimension can be determined from the scaling relationship [21]:

$$N \sim l^{D_3} \quad (8.8)$$

where  $N$  is the number of cells in an aggregate,  $D_3$  is the fractal dimension of the cluster, and  $l$  is the longest length of the cluster. This has been termed a length-projected scaling method. Equation (8.8) is nondimensionalised by dividing by the average cell size  $l_c$ :

$$N = a_1 \left( \frac{l}{l_c} \right)^{D_3} \quad (8.9)$$

where  $a_1$  is a constant.

Fractal dimensions in two dimensions  $D_2$  can be determined from the flocs' projected surface area, since aggregate projected surface area  $A$  is related to aggregate length  $l$  [21]:

$$A = a_2 l^{D_2} \quad (8.10)$$

where  $a_2$  is a proportionality constant.

## 8.3 FRACTAL DIMENSION OF MICROORGANISMS IN ARTIFICIAL MEDIA

### 8.3.1 Bacteria and Unicellular Fungi

The majority of studies of fractal geometry of bacteria and unicellular fungi (yeasts) have been performed in agar culture, in which the solidity of the medium, nutrient concentration, inhibitory chemicals and incubation conditions (temperature) have been varied. With regard to bacterial pathogens,<sup>2</sup> *Escherichia coli*, *Citrobacter freundii*, *Klebsiella pneumoniae*, *Proteus mirabilis*, *Salmonella anatum*, *Salmonella typhimurium* and *Serratia marcescens* produced colonies with  $D_{BM}$  values between 1.7 and 1.8 [22, 23], whereas *Klebsiella ozaenae* had more open colonies,  $D_{BM} = 1.6$  [24]. Colony morphology is dramatically affected by nutrient supply [19, 20] and nonlethal concentrations of antibiotics [5]. For example, the fractal dimension of

<sup>2</sup> Organisms which kill other organisms, tissues or cells.



*Paenibacillus dendritiformis* decreased from 2 to about 1.8 on agar in the presence of  $3 \mu\text{g ml}^{-1}$  co-trimoxazole (Septrin) [25]. Changes in these systems were attributed to changes in chemotactic signalling between bacteria, resulting in a shift in colonial morphology.

Studies of bacteria from the natural environment, e.g. on *Bacillus subtilis*, also revealed effects of growth medium on colony pattern formation: circular colonies, colonies with dense branching, spreading colonies without openings, colonies with concentric rings and fractal colonies were produced depending upon the agar and nutrient concentration [26]. Fractal colonies developed on medium with a low peptone concentration (Figure 8.3); indeed, low nutrient concentration seems to be a general requirement for production of fractal bacterial colonies [26, 27]. Various species of fungi which form yeast also appear to produce different growth patterns, including compact, dense-branching and fractal growth, depending on the nutrient concentration of agar [28].

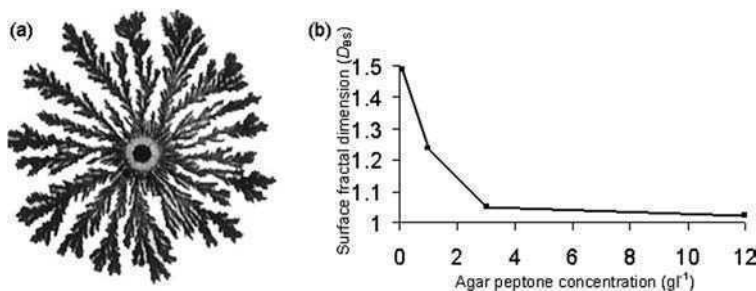


**Figure 8.3** (a) *Bacillus subtilis* colony on agar containing  $1 \text{ g l}^{-1}$  peptone (after [4]). (b) Effect of agar peptone concentration on the fractal dimension of *Bacillus subtilis* (data derived from [4]).

The ability of many bacteria to swarm and of cells to move within colonies [29] is crucial to pattern production in bacterial colonies. Intricate communication and cooperative behaviour between individual bacterial cells within colonies are undoubtedly essential for self-organization of colonies, though aspects of colony morphology can be at least partially accounted for by ideas of pattern formation from nonbiological systems [2, 5, 30].

Not surprisingly, actinomycetes, whose cells remain in chains forming mycelia, produce fractal structures. Indeed, the first fractal analysis of microbial colonies was on *Streptomyces griseus* [14]. Fractal dimension increased with time with a  $D_{\text{BM}}$  of up to  $1.49 \pm 0.01$ .

Fractal dimensions of both bacteria and yeast flocs have also been determined in liquid culture in the laboratory, providing a useful quantification of fluid dynamic environment effects upon microbial aggregates. The bacterium *Zoogloea ramigera* had a  $D_s = 1.69 \pm 0.11$  (determined from projected area, Section 8.2.4)

and a  $D_M = 1.79 \pm 0.28$  (determined by length-number scaling, Section 8.2.4) when grown in rotating test tubes [21]. However, when grown in a bench-top fermentor, aggregates lost their mass fractal characteristics ( $D_M$  almost 3), but had a  $D_S = 1.78 \pm 0.11$ . The yeast *Saccharomyces cerevisiae* had higher fractal dimensions ( $D_S = 1.92 \pm 0.08$ ,  $D_M = 2.66 \pm 0.34$ ) than the bacterium when growing in rotating test tubes [21].

The structure of large bacterial flocs, produced by adding cationic polymers to liquid culture medium, has also received attention. Interest arises from applications such as liquid–solid separation in bioprocessing industries and in drinking water and wastewater treatment. Fractal dimensions of *Escherichia coli* flocs at different times determined by two methods, small-angle light scattering and confocal image analysis, were between 1.9 and 2.19 (Section 8.2.4 [18]). *Escherichia coli* flocs, flocculated with chitosan, had fractal dimensions of  $1.99 \pm 0.08$  and  $2.14 \pm 0.04$  (determined by the small-angle light scattering and two-slopes methods, Section 8.2.4) [17].

### 8.3.2 Mycelial Fungi

Growth of a range of mycelial fungi, including saprotrophs, plant pathogens and mycorrhizal formers, has been examined on solid agar, and to a lesser extent in liquid medium. The whole range of fractal dimensions has been found in two dimensions (Figures 8.4 and 8.5), from close to unity for species producing linear rhizomorphs<sup>3</sup> (Figure 8.4d) to complete space filling (Table 8.1). Fractal dimensions vary between and among species, depending on abiotic conditions and on time. With regard to the time, the lowest fractal dimensions, which then rise, are often found immediately after the germination of spores. For example,  $D_{BM} = 1.05$ – $1.2$ , 72 h after germination and  $D_{BM} = 1.43$ – $1.57$  by 116 h with *Armillaria luteus* [33]. Likewise,  $D_{BM}$  increased from 1.4 to about 2 over 5 h with *Trichoderma viride*, implying denser packing of hyphae with time [10]. On the other hand, fractal dimensions may decrease later on, e.g.  $D_{BM}$  dropped from 1.73 at 20 days to 1.65 at 40 days with *Aspergillus oryzae* [36]. The  $D_{BM}$  of *Armillaria* rhizomorphs was not, however, correlated with time [32].

Increase in fractal dimension implies that the colony is filling space more, whereas a decrease implies that the mycelium is thinning out. However, global measures of  $D_{BM}$  may mask changes occurring in different regions. Because of the dynamic and modular nature of mycelial systems, mycelia may undergo morphological changes in one area concomitant with changes elsewhere in the same mycelium. Image analysis allows discrete morphological regions to be extracted and analysed separately (e.g. Figure 8.1e), e.g. localised fractal dimensions of mycelial fans produced as a result of interspecific mycelial interactions (Figure 8.2). This highlights the requirement for appropriate use and interpretation of fractal dimension alongside visual examination of mycelial images.

---

<sup>3</sup> Linear organs of mycelial fungi, which often have a thick rind, are differentiated internally and extend by apical growth of the whole organ.

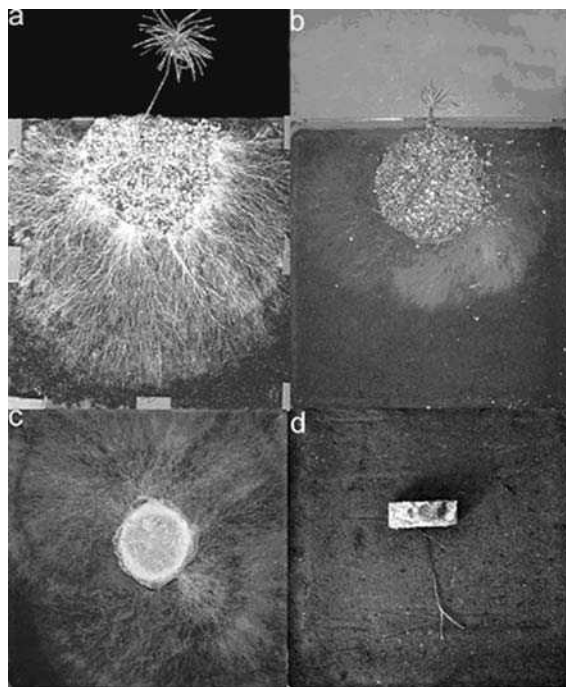


**Figure 8.4** Digital images of ectomycorrhizal mycelial systems of: (a) *Suillus bovinus* and (b) *Paxillus involutus* in peat microcosms (in association with *Pinus sylvestris*); (c) the pine root pathogen *Rhizina undulata* extending from a 50 cm<sup>3</sup> section of pine stem; (d) *Armillaria ostoyae* extending from a 8 cm<sup>3</sup> pine wood resource across nonsterile soil compacted in 24 cm × 24 cm trays.

Carbon and nutrient content of the agar medium can have large effects on fractal dimension. For example, four ectomycorrhizal species had a fractal dimension of almost 2 on a basal medium designed to give good growth of these species, but between 1.2 and 1.79 when glucose content was reduced by a half or three-quarters [37].

The presence of heavy metals, added as chloride salt in concentrations of 0.005–3 mmol l<sup>-1</sup>, had differential effects on *Achlya bisexualis*: there was an increase in  $D_{BS}$  with Cu, Co and Hg, but no effect with Zn and Cd [31]. With 0.5 mmol l<sup>-1</sup> Cu,  $D_{BS}$  increased from 1.3 to nearly 1.5, and  $D_{BS}$  increased to 1.6 with 3 mmol l<sup>-1</sup> Hg. It was suggested that the increase in fractal dimension may have arisen from disrupted tip growth and branching at the edge of the mycelium. In terms of mycelial pattern formation as a whole, it has been suggested that the wide range of morphologies that develop arise by mycelia operating as nonlinear (i.e. regulated by feedback), hydrodynamic systems with indeterminate (i.e. indefinitely expandable) boundaries [39].

Fractal dimension has also been occasionally determined for fungi growing in liquid culture. When cultures are agitated, mycelia tend to form pellets. In one study,

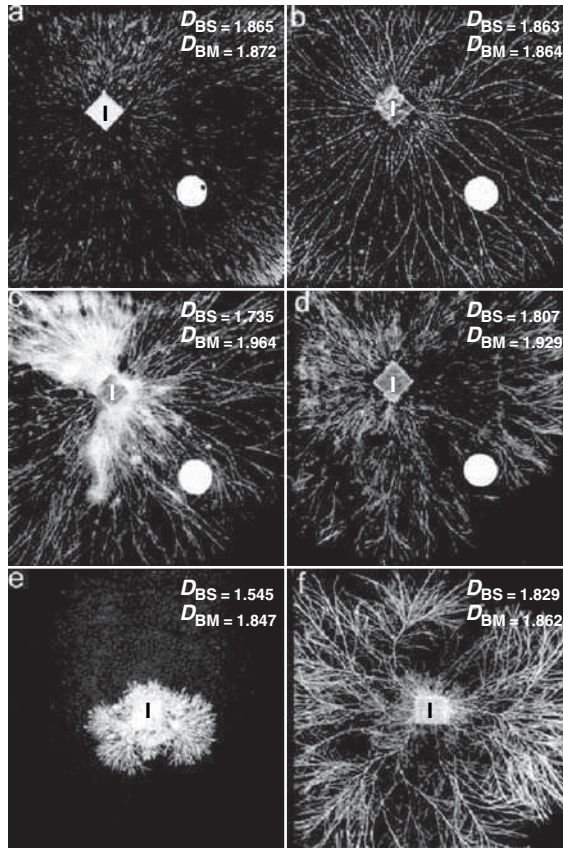


**Figure 8.5** Digital images of mycelial systems of (a) *Agrocybe gibberosa*, (b) *Phallus impudicus*, (c) *Stropharia caerulea*, (d) *Stropharia aeruginosa* after 28 days, (e) *Coprinus picaceus* after 180 days (image courtesy of Alaa Alawi) and (f) *Resinicium bicolor* after 30 days (image courtesy of G.M. Tordoff), extending from 4 cm<sup>3</sup> beech wood resources onto non-sterile soil which has been compacted in 24 cm × 24 cm trays. White circles (a–d) are inert plastic caps; I are inocula. Note the differences between the mass ( $D_{BM}$ ) and surface ( $D_{BS}$ ) fractal dimensions of the species.

*Aspergillus niger* had values of  $D_{BM} = 1.3$ – $1.47$  [34]. Fractal dimension has also been used in analysis of fragment size distribution, when mycelia have been fragmented in a homogeniser to form inoculum [40]. With the wood decay basidiomycete *Phanerochaete chrysosporium*,  $D_{BM}$  decreased with increasing shear force [40].

A major problem with all of these studies on agar and in liquid media is that nutrients are, at least initially, distributed homogeneously, which is far from the situation in the natural environment, where there is considerable spatial heterogeneity over a range of scales. To get slightly closer to the field situation, sheets of cellophane

**Table 8.1** Examples of fractal dimensions of mycelial fungi, from different ecological groups, growing on artificial media.

Species	Ecological group	Taxonomic group	Growth conditions	Measurement technique	Fractal dimension <sup>a</sup>	Ref.
<i>Achlya bisexualis</i>	Saprotroph	Oomycota	Agar media with added heavy metals	Box counting	$D_{BS} = 1.26\text{--}1.6$	[31]
<i>Armillaria calvescens</i>	Saprotroph, rhizomorph former	Basidiomycota	Agar, at different times during rhizomorph development over many days	Box counting	$D_{BM} = 1.46 \pm 0.01$ ; $1.40 \pm 0.07$	[32]
<i>Armillaria luteus</i> (= <i>A. gallica</i> )	Saprotroph, rhizomorph former	Basidiomycota	Agar, at different times during colony development to 74 h	Box counting	$D_{BM} = 1.05\text{--}1.20$	[33]
<i>Armillaria luteus</i> (= <i>A. gallica</i> )	Saprotroph, rhizomorph former	Basidiomycota	Agar, at different times during rhizomorph development over many days	Box counting	$D_{BM} = 1.47 \pm 0.03$ ; $1.45 \pm 0.03$	[32]
<i>Armillaria ostoyae</i>	Tree root pathogen, rhizomorph former	Basidiomycota	Agar, at different times during colony development to 116 h	Box counting	$D_{BM} = 1.43\text{--}1.57$	[33]

**Table 8.1** (Continued).

Species	Ecological group	Taxonomic group	Growth conditions	Measurement technique	Fractal dimension <sup>a</sup>	Ref.
<i>Armillaria sinapina</i>	Saprotroph, rhizomorph former	Basidiomycota	Agar, at different times during rhizomorph development over many days	Box counting	$D_{BM} = 1.54 \pm 0.03$ ; $1.40 \pm 0.04$	[32]
<i>Ashbya gossypii</i>	Saprotroph	Ascomycota	Agar	Box counting	$D_{BM} = 1.94$ $D_{BS} = 1.45$	[14]
<i>Aspergillus niger</i>	Saprotroph	Deuteromycota/Ascomycota	Pellets formed in liquid culture	Box counting	$D_{BM} = 1.3$ – $1.47$	[34]
<i>Aspergillus oryzae</i>	Saprotroph	Deuteromycota/Ascomycota	Agar, at different times during colony development	Box counting	$D_{BM} = 1.55$ – $1.8$	[35]
<i>Aspergillus oryzae</i>	Saprotroph	Deuteromycota/Ascomycota	Liquid-like medium (0.15 %)	Box counting	$D_{BM} = 1.63$ – $1.73$	[36]
<i>Coltricia perennis</i>	Ectomycorrhiza former	Basidiomycota	Agar with different concentrations of inorganic nitrogen and glucose	Concentric rings	$D_M = 1.47$ – $2.12$	[37]
<i>Trichoderma viride</i>	Saprotroph	Deuteromycota/Ascomycota	Agar, at different times during colony development	Concentric rings	$D_M = 1.4$ – $2.0$	[10]

<i>Laccaria bicolor</i>	Ectomycorrhiza former	Basidiomycota	Agar with different concentrations of inorganic nitrogen and glucose	Concentric rings	$D_M = 1.64\text{--}2.6$	[37]
<i>Lactarius hepaticus</i>	Ectomycorrhiza former	Basidiomycota	Agar with different concentrations of inorganic nitrogen and glucose	Concentric rings	$D_M = 1.20\text{--}1.79$	[37]
<i>Macrophomina phaseolina</i>	Pathogen of beans	Ascomycota	Agar at different times during colony development	Box counting	$D_{BM} = 1.21\text{--}1.84$	[38]
<i>Paxillus involutus</i>	Ectomycorrhiza former	Basidiomycota	Agar with different concentrations of inorganic nitrogen and glucose	Concentric rings	$D_M = 1.70\text{--}2.18$	[37]

---

<sup>a</sup> All fractal values were estimated in two dimensions: fractal dimensions greater than 2 presumably reflect inaccuracies in the estimation procedure.

were inoculated with single germinated spores of *T. viride*, that were placed in Petri dishes, to which a discrete nutrient source (cylinder of agar  $<2\text{ mm}^3$ , containing 2 % glucose, 0.2 %  $\text{NaNO}_3$  and 0.2 %  $\text{KH}_2\text{PO}_4$ ) was added 2 cm away from the germling [41]. Almost all of the mycelial biomass grew in the half of the dish which contained the nutrient source, and there was greater plane filling between the inoculum and the new resource as opposed to the mycelium extending at  $90^\circ$  from this line. This type of phenomenon has now been explored in much more detail in more realistic soil microcosms (Section 8.5).

In addition to the characterization of fungal colonies, fractal dimension has been correlated with acid phosphatase and exoenzyme secretion [42, 43]. The white rot fungus *Pycnoporus cinnabarinus* was grown on agar containing different concentrations of the dye Remazol Brilliant Blue R, and fractal dimension and enzyme activity were measured over time [43]. There was a positive correlation between fractal dimension (i.e. branching complexity) and enzyme activity. Fractal analysis, therefore, has been suggested as a means of evaluating hyphal morphology linked to potential to secrete exoenzymes, which is important for optimization of bioreactor substrate concentration [43, 44]. Jones and Lonergan [43] also suggested that fractal analysis may be useful in developing processes to optimise exoenzyme yield in solid and liquid culture.

#### **8.4 FRACTAL DIMENSION OF BACTERIA IN THE NATURAL ENVIRONMENT (PARTICULARLY ACTIVATED SLUDGE)**

There appears to be little information on the fractal dimension of bacteria in the natural environment or in microcosms. What is available largely concerns bacterial flocs in activated sludge. Natural activated sludge flocs are complex, multi-level structures that may thus require several fractal dimensions to characterize them [45]. Their formation probably includes the following stages: (1) bacteria form compact flocculi; (2) the latter group together to form microflocs; (3) microflocs aggregate to form flocs [46]. The flocculi were more compact (i.e. have a larger fractal dimension) than the microflocs. When microflocs formed they incorporated filamentous bacteria and extracellular polymeric bridging material, leading to a more open structure. Stage of floc formation, and fractal dimension at that stage, is an important determinant of what limits chemical reactions in flocs. Thus, flocculi are reaction limited, whereas microflocs are subject to diffusion limitation.

Floc structure changes under different conditions, for example freezing and thawing produced more rounded pores [47]. Floc structure affects settleability and filterability. Some flocs settle rapidly and others more slowly. For flocs from two different sewage treatment plants, flocs with fractal dimensions (determined using a two-point correlation function; Section 8.2.4) of 1.9 and 1.8 settled more slowly than flocs with fractal dimensions of 2.2 and 2.1 [47]. Differences in fractal dimension reflected different species compositions. Though the fractal dimension values reflect heterogeneity



within activated plants, differences were not evident between plants. However, differences between the plants in other floc descriptors emphasised the need for more than one indicator of heterogeneity. The fractal dimensions have also been assessed in activated sludge under different operating conditions, but not found to be significantly different [48].

Additionally, fractal dimension has been used in analysis of images of activated sludge to distinguish between flocs and filaments [49]. It is now also used to quantify biofilms on surfaces [50, 51].

### 8.5 FRACTAL DIMENSIONS OF FUNGI IN THE NATURAL ENVIRONMENT (PARTICULARLY SOIL)

There is now a large body of data on the fractal dimension of fungi in soil microcosms. Most of the studies have involved saprotrophic wood and litter-decaying basidiomycetes, though ectomycorrhizal fungi and root pathogens have been considered recently. These studies have almost all centred around growth in two dimensions, in trays of soil (or peat), incubated horizontally or vertically. The soil is usually compressed to encourage mycelial growth on the surface. Usually, trays of soil containing saprotrophic cord-forming fungi or root pathogenic fungi have been incubated horizontally (e.g. Figures 8.4c and d, 8.5, 8.6, 8.7), and trays of fungi ectomycorrhizal in association with plants have been incubated vertically (e.g. Figures 8.4a and b), when the fractal dimension of a single species has been assessed. When interactions among and between these three ecological groups (i.e. saprotrophs, pathogens and mycorrhizas) have been examined, systems containing mycorrhizas have always been incubated vertically, irrespective of the ecological role of the opponent. Horizontal two-dimensional systems mimic the location of growth of saprotrophic cord-forming fungi well (they are often found at the soil–litter interface in woodlands), though they do also ramify in three dimensions. Two-dimensional systems, however, are much less realistic for the other ecological groups. Further, it has been shown, experimentally, that extension can be much more rapid over surfaces than through soil

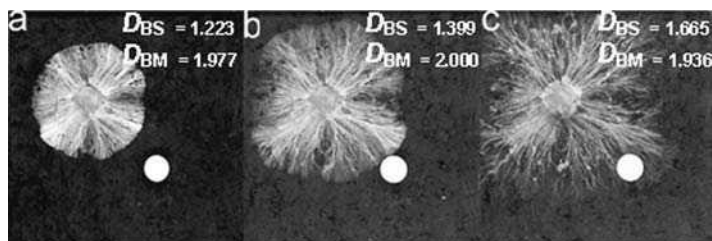


**Figure 8.6** Digital images showing development of a mycelial system of *Hypholoma fasciculare* after (a) 14 days, (b) 21 days and (c) 35 days, extending from 4 cm<sup>3</sup> beech wood resource onto nonsterile soil compacted into 24 cm × 24 cm trays.

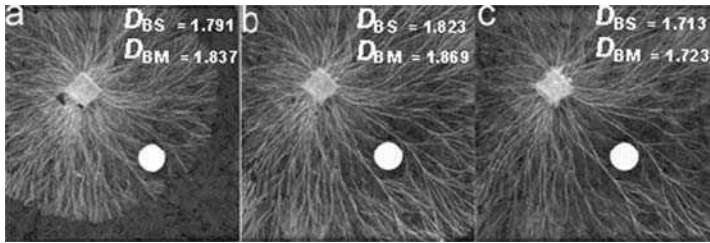


**Figure 8.7** Digital images showing development of a mycelial system of *Phanerochaete velutina* after (a) 14 days, (b) 21 days and (c) 35 days, extending from a 4 cm<sup>3</sup> beech wood resource onto nonsterile soil compacted into 24 cm × 24 cm trays.

[52], and that mycelial distribution within soil is affected by soil structure [53, 54]. Also, mathematical models have indicated that mycelial pattern development will differ in three dimensions from that in two dimensions [55]. Therefore, it must be borne in mind that mycelial growth in three dimensions may be different from that represented in two dimensions. Nonetheless, these studies in two-dimensional soil microcosms form a good starting point for understanding space filling in the natural environment.

There is considerable variation in the  $D_{BM}$ ,  $D_{BS}$  and  $D_{BM}:D_{BS}$  ratio of different species, and this can be related to their ecological strategies (Section 8.5.1). These values are not constant for a species, but vary with: time (Section 8.5.2); amount and nutritional quality of the resource from which they are growing (Section 8.5.3); nutrient availability in the soil through which they are extending (Section 8.5.4); microclimate, including temperature and water regime (Section 8.5.5); encounter by other organisms, including fungi (Section 8.5.6) and invertebrates (Section 8.5.7).

### 8.5.1 Interspecific Variation and Ecological Strategies

Different species have inherently different patterns of deployment of biomass in space as evidenced by fractal geometry (Figures 8.4–8.7) [33, 56–60]. At early stages of outgrowth from resources, some fungi produce surface fractal structures, characterised by dense, relatively slowly extending fronts (Figure 8.6a and Figure 8.8a and c). Such a growth form would likely be successful in discovering resources that are relatively homogeneously distributed and/or in plentiful supply, and could be considered to be short-range foraging. Examples can be found amongst fungi exhibiting all three of the main nutritional strategies: (i) saprotrophs, e.g. *Hypholoma fasciculare*, *Stropharia caerulea* and *Stropharia aeruginosa* (Figures 8.6, 8.5c and 8.5d respectively); (ii) necrotrophs, e.g. *Rhizina undulata* as it grows saprotrophically through soil (Figure 8.4c); (iii) ectomycorrhizal formers, e.g. *Paxillus involutus* and *Suillus bovinus*, as they sequester mineral nutrients during outgrowth from root tips into soil (Figure 8.4a and b).

Other fungi produce mass fractal structures when growing in soil, characterised by well-defined, rapidly extending cords that would be successful in discovery of large, sparsely distributed organic resources. Examples include saprotrophs, e.g. *Agrocybe gibberosa*, *Coprinus picaceus*, *Phallus impudicus*, *Phanerochaete velutina* and *Resinicium bicolor* (Figures 8.5a, 8.5e, 8.5b, 8.7 and 8.5f respectively). At the furthest extreme, the ‘honey fungi’ or ‘bootlace fungi’ (*Armillaria* species) produce relatively unbranched systems of rhizomorphs, fed from large food bases, and have fractal dimensions much closer to unity than most other fungi (Figure 8.4d [32]).

### 8.5.2 Temporal Changes in Fractal Dimension

Fractal dimensions of colonies change with time. Often there is an initial increase followed by a gradual decrease over time (Figures 8.6–8.8 [15, 56, 57, 60]). Systems that are initially surface fractal, e.g. that of *Hypholoma fasciculare*, become increasingly

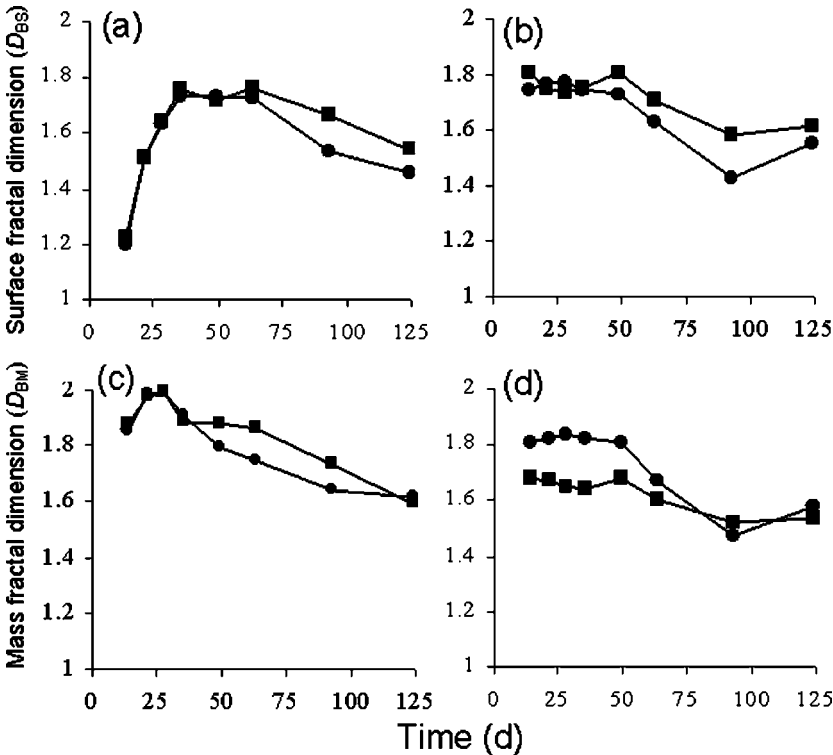


**Figure 8.8** Change with time of surface (a, b) and mass (c, d) fractal dimensions of mycelial systems of (a, c) *Hypholoma fasciculare* and (b, d) *Phanerochaete velutina* extending from a 4 cm<sup>3</sup> beech wood resources across nonsterile soil, compacted in 24 cm × 24 cm trays, either to inert control baits (squares) or 4 cm<sup>3</sup> uncolonised wood resources (circles) (modified from [61]).

more open structures with time, i.e. become mass fractal (Figure 8.8a and c, [15, 56]). Nonaggregated hyphae and minor cords die back in nonperipheral regions, leaving a more open, persistent mycelial network behind the actively growing, foraging margin (Figure 8.6). As hyphal tips digress, with increasing radial extent, different regions of the mycelial front become increasingly independent from each other and from the original food source, though tangential interconnections decrease this independence [56]. The largest microcosm systems examined to date have been  $0.33 \text{ m}^2$ , whereas individual systems in the field can cover several to many square metres or even hectares, and become even more open [56, 62]. Although natural mycelial networks in the field have been excavated to provide estimates of extent and presence/absence over time [63], they have not yet been mapped in sufficient detail to allow fractal analysis.

### 8.5.3 Effect of Inoculum Quantity and Quality

Carbon and mineral nutrient status of the inoculum can have a major influence on extra-resource biomass production and deployment [57, 59, 64] (Table 8.2). With *Resinicium bicolor*,  $D_{\text{BM}}$  and  $D_{\text{BS}}$  significantly increased with increasing inoculum size ( $0.5\text{--}16 \text{ cm}^3$ ) [59] (Table 8.2). Likewise, with *Phanerochaete velutina* and *Hypholoma fasciculare*, the fractal dimension of mycelium was significantly greater when it extended from  $8 \text{ cm}^3$  wood inocula than from  $0.2$  and  $0.5 \text{ cm}^3$  wood inocula [66]. In contrast, there was little difference in either  $D_{\text{BM}}$  or  $D_{\text{BS}}$  when *Stropharia caerulea* extended from  $0.5$  and  $4 \text{ cm}^3$  wood inocula [64]. Greater fractal dimensions of mycelium from larger inocula presumably reflect the greater availability of carbon and nutrients for generating extra-resource mycelial biomass.

The age of the inoculum (i.e. state of decay) also significantly affects fractal dimension: *Stropharia caerulea* systems developing from 84-day-old beech wood inocula ( $0.5 \text{ cm}^3$ ) took 10 days longer to achieve the  $D_{\text{BM}}$  and  $D_{\text{BS}}$  values of systems growing from 22-day-old inocula [64]. This may be interpreted as insufficient nutrients being available for extra-resource mycelial growth in the well-decayed wood. The role of nutrients in determining the fractal dimension of extra-resource mycelia was further emphasised in studies where wood inocula were initially colonised on nutrient-rich and nutrient-poor agar, more nutrients being taken into the wood resource from the former than from the latter [57, 59] (Table 8.2).  $D_{\text{BM}}$  and  $D_{\text{BS}}$  of *Resinicium bicolor* mycelium were significantly larger when inocula had been colonized on malt agar than on water agar to which no additional nutrients had been added [59]. Likewise, fractal dimensions were significantly larger for wood precolonized on agar for 12 months rather than 3 months. In all of these examples, higher fractal dimensions were correlated with higher or similar extension rates and hyphal coverage. This is important for interpretation, indicating that space filling is not at the expense of extension. In contrast to the above results,  $D_{\text{BM}}$  and  $D_{\text{BS}}$  values for *Phanerochaete velutina* extending from inocula colonised

**Table 8.2** Effect of nutrient status on fractal dimension of fungal mycelia growing out of wood inocula across soil.

Species	Variables investigated	Size of wood inoculum (cm <sup>3</sup> )	Effect on fractal dimension (approximate values)	Ref.
<i>Hypholoma fasciculare</i>	Soil N	4	$D_{BM}$ was significantly higher (1.65–1.82) with N (up 0.27 mg g <sup>-1</sup> N) addition to soil than control (1.59–1.8) (wood inocula colonized on nutrient-free agar). $D_{BM}$ (1.62–1.74) was also significantly higher than controls (1.54–1.63). There were similar effects when wood inocula were colonized on nutrient-enriched agar	[57]
<i>Phallus impudicus</i>	Soil N	4	$D_{BM}$ (1.55–1.75) and $D_{BS}$ (1.4–1.75) were not significantly affected by N (0.27 mg g <sup>-1</sup> N) or P addition to soil	[57]
<i>Phanerochaete velutina</i>	Soil N, P	0.5	$D_{BM}$ (1.2–1.55) and $D_{BS}$ (1.25–1.6) were not significantly affected by N or P (up 0.27 mg g <sup>-1</sup> ) addition to soil	[65]
<i>Phanerochaete velutina</i>	Soil N	4	$D_{BM}$ was significantly higher (1.56–1.73) with N (up 0.27 mg g <sup>-1</sup> N) addition to soil than control (1.53–1.63) (wood inocula colonized on nutrient free agar). $D_{BM}$ (1.56–1.68) was also significantly higher. There were similar effects when wood inocula were colonized on nutrient-enriched agar	[57]
<i>Stropharia caerulea</i>	Soil N	0.5	Significantly greater $D_{BM}$ (1.75–1.85) on soil with 0.13 mg g <sup>-1</sup> N added than control or 0.27 mg g <sup>-1</sup> N added	[65]
<i>Stropharia caerulea</i>	Soil P	0.5	Significantly greater $D_{BM}$ (1.8–1.9) on soil with 0.13 mg g <sup>-1</sup> P added than control	[65]

**Table 8.2** (Continued).

Species	Variables investigated	Size of wood inoculum (cm <sup>3</sup> )	Effect on fractal dimension (approximate values)	Ref.
<i>Phanerochaete velutina</i>	Inoculum nutrient status	4	$D_{BM}$ and $D_{BS}$ were often significantly greater from wood inocula colonized on agar lacking nutrients than agar to which nutrients had been added	[57]
<i>Resinicium bicolor</i>	Inoculum nutrient status/age	0.5–16	$D_{BM}$ varied significantly depending on the nutrient status of the agar on which the wood inoculum was colonized, and the age or the length of time the inoculum had been colonized: agar with no added nutrients for 3 months (1.5), or 12 months (1.58), malt agar for 3 months (1.6) or 12 months (1.64)	[59]
<i>Resinicium bicolor</i>	Inoculum size	0.5–16	$D_{BM}$ of mycelia extending from 16 cm <sup>3</sup> inocula (1.25–1.53) were significantly higher than from 0.05 cm <sup>3</sup> inocula (1.2–1.3)	[59]
<i>Stropharia caerulea</i>	New resource size	0.05	Neither $D_{BM}$ (1.45–1.65) nor $D_{BS}$ (1.28–1.64) were significantly affected by encountering new wood resources of 0.06 to 4.0 cm <sup>3</sup> compared with controls (inert Perspex) over 70 days	[64]
<i>Stropharia caerulea</i>	New resource size	0.15 <i>Urtica dioica</i> rhizomes	$D_{BS}$ (1.25–1.7) was not significantly affected by encountering new <i>Urtica dioica</i> resources of 0.06 to 4.0 cm <sup>3</sup> compared with controls (inert Perspex) over 70 days. However, $D_{BM}$ of controls (1.69) was significantly higher than that of mycelia encountering <i>Urtica dioica</i> resources at 48 days	[64]

on enriched agar were slightly lower (though not necessarily significantly) than from those colonized on Noble agar [57] (Table 8.2). The reasons for this are not clear.

#### 8.5.4 Effect of Resource Status of the Environment and Encounter of New Resources

Soil nutrient status and encountering new resources dramatically affects mycelial pattern formation. This is illustrated by a study in which soil nutrient status was: (i) lowered, by 'diluting' with sand (1:1); (ii) lowered as in (i) but its initial phosphate concentration maintained by adding  $\text{NH}_4\text{K}_2\text{PO}_4$ ; (iii) increased by adding  $\text{NH}_4\text{K}_2\text{PO}_4$  to 10 times the original concentration [57]. With *Phanerochaete velutina* and *Hypholoma fasciculare*  $D_{\text{BM}}$  and  $D_{\text{BS}}$  values were significantly higher on the soils to which phosphate was added (Table 8.2). With *Phallus impudicus*, however, there was no significant difference. Likewise, in a similar study, *Stropharia caerulea* systems had significantly higher  $D_{\text{BM}}$  and  $D_{\text{BS}}$  values when soil was enriched with nitrogen and phosphorus but *Phanerochaete velutina* was unresponsive [65] (Table 8.2). Clearly, *Phanerochaete velutina*, *Hypholoma fasciculare* and *Stropharia caerulea* all responded to the plethora of nutrients by increased branching to allow increased uptake of nutrients. *Hypholoma fasciculare* and *Stropharia caerulea*, with their surface fractal structures (Section 8.5.1), are responsive to changes in the environment, whereas *Phallus impudicus*, with its mass fractal structure and long-range foraging strategy, is less responsive (see below). *Phanerochaete velutina* is also mass fractal with a long-range foraging strategy, and usually less responsive to environmental change than short-rangers, e.g. *Hypholoma fasciculare* and *Stropharia caerulea* (see below), but is evidently sensitive to some environmental variables.

An increase in fractal dimension (i.e. space filling) is one means of taking up more nutrients from soil, due to greater surface area available for absorption. This was clearly demonstrated in a study in which new, uncolonized resources were added to mature systems of *Phanerochaete velutina* on a nutrient-poor soil [67]. Arrival of the new resource caused an immediate demand for nutrients, for production of mycelium and enzymes, to enable colonization and decay of the new resource. Numerous small patches of mycelium with high fractal dimension developed in these systems, and  $^{32}\text{P}$  tracer studies showed these patches to be sites of nutrient uptake. The fractal dimension of mycelia also increased significantly in response to new resources in studies with other fungi.  $D_{\text{BM}}$  increased when *Stropharia caerulea* growing across soil from *Urtica dioica* rhizomes ( $0.15\text{ cm}^3$ ) encountered additional dead rhizomes ( $0.1\text{--}1.2\text{ cm}^3$ ), though there was no such change when mycelium growing from wood ( $0.5\text{ cm}^3$ ) resources encountered additional wood resources ( $0.06\text{--}4\text{ cm}^3$ ) [64] (Table 8.2). Soil carbon also affects fractal dimension. In the only study to date on this variable, *Resinicium bicolor* had significantly higher  $D_{\text{BM}}$  and  $D_{\text{BS}}$  on ashed soil (i.e. soil void of carbon) [59].

8.5.5 Effect of Non-Nutrient Microenvironment

Water potential<sup>4</sup> (which determines ease or difficulty of obtaining water), temperature and pH all affect fractal structure of mycelial systems. Moreover, they exert interactive effects with each other and with other abiotic variables, e.g. sand content of soil [66, 68]. Temperature effects on fractal dimensions of *Stropharia caerulea* were variable (Table 8.3) [69]. At 5 °C, it took 9 days longer to achieve the  $D_{BS}$  values obtained at 10–20 °C, and 12 days longer to achieve the  $D_{BM}$  values for *Stropharia caerulea*. At 25 °C, both fractal dimensions of *Stropharia caerulea* were significantly lower than values of mycelial systems at 10–20 °C, until 26–29 days. There were also slight intraspecific differences between strains of *Stropharia caerulea* [69]. For *Phanerochaete velutina*, both fractal dimensions at 5 °C were significantly less than at 10–25 °C for the first 20 days and 14 days respectively. It is unclear what is mediating these temperature effects.

**Table 8.3** Effect of temperature on the fractal geometry of mycelial systems of *Stropharia caerulea* and *Phanerochaete velutina*, extending from beech (*Fagus sylvatica*) wood block inocula across soil after 30 days. Data from [69].

Species		5 °C	10 °C	15 °C	20 °C	25 °C
<i>Phanerochaete velutina</i>	$D_{BS}$	1.72	1.65	1.72	1.65	1.72
	$D_{BM}$	1.73	1.67	1.73	1.67	1.73
<i>Stropharia caerulea</i>	$D_{BS}$	1.6	1.75	1.7	1.7	1.48
	$D_{BM}$	1.6	1.8	1.74	1.78	1.53

There were clear trends in the effect of water potential on fractal dimensions of *Stropharia caerulea*:  $D_{BS}$  decreased (1.7–1.35 approximately) with increasing water potential (i.e. getting wetter) from –0.02 MPa to –0.002 MPa (Figure 8.9) [69]. For *Phanerochaete velutina*, there was no significant effect of soil water potential on  $D_{BS}$ , although  $D_{BM}$  was sometimes higher on soils drier than –0.006 MPa. These experiments were performed under constant conditions; however, soil water potential is rarely constant in the natural environment. Rather, it increases following rain and then gradually decreases. Such occurrences were mimicked in an experiment in which cord systems established in 24 cm × 24 cm trays were subject to wetting and drying events immediately after addition of a wood resource behind the mycelial margin, or 20 days after addition of the new resource [68]. Wet shifts were achieved by gradually adding deionised water over several days to raise the water potential from –0.019 MPa to –0.009 MPa, equivalent to field capacity; dry shifts were achieved

<sup>4</sup> Defined as the free energy of water in a system relative to that of a reference pool of pure water (megaPascals). Effectively, it indicates the ease/difficulty that a microorganism would have in extracting water from an environment. The lower the water potential (i.e. the more negative), the harder it is to obtain water.



by removing lids for 11 days, allowing soil to dry to  $-0.056$  MPa. Wet shifts resulted in a significant increase in  $D_{BM}$  in the part of the system containing the new resource, whereas there was no such change following dry shifts.

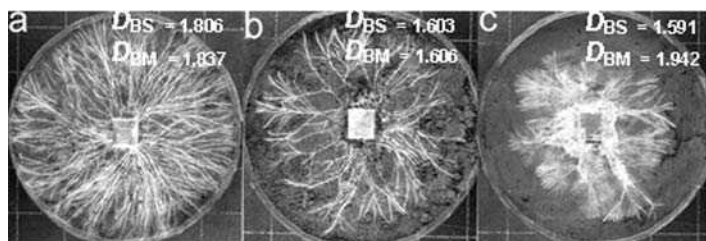


**Figure 8.9** Effect of soil water potential on morphology of *Stropharia caerulea* extending from  $4\text{ cm}^3$  beech wood resources, across nonsterile soil compacted in 13 cm diameter trays at (a)  $-0.02$  MPa (b)  $-0.06$  MPa and (c)  $-0.006$  MPa.

Soil pH considerably affects some species: *Phanerochaete velutina* had a much lower fractal dimension at pH 7 than at pH 5–6 (1.3 and 1.55–1.67 respectively) [60], though the reason for this is not known. In contrast, *Coprinus picaceus* often failed to grow out of wood resources at pH 4.4, but when it did it grew significantly slower than at higher pH. However, similar amounts of extra-resource biomass were produced at all pHs, and this was achieved at lower pHs by much greater space filling.

### 8.5.6 Changes in Fractal Dimension during Interspecific Microbial Interactions

As mycelia grow through soil they inevitably encounter other mycelia, resulting in antagonistic interactions [70]. The outcomes can be: (a) deadlock, where neither fungus gains any territorial advantage; (b) replacement, where one fungus replaces the other and gains the replaced fungus's territory; (c) partial replacement, where some but not all of the opponents territory is gained; and (d) mutual replacement, where fungus A gains some of the territory held by fungus B, but the mycelium of fungus B simultaneously makes inroads into the territory held by fungus A.  $D_{BM}$  and  $D_{BS}$  have only been quantified in two papers on interactions between mycelia in soil [33, 61]. *Stropharia caerulea* mycelia were allowed to interact with mycelia of four other saprotrophic basidiomycetes, individually, in trays of compressed soil [61].  $D_{BM}$  or  $D_{BS}$  varied depending on interaction combination (Table 8.4). Importantly, there were often localized changes in mycelial morphology (Figure 8.2) and fractal dimension that reflected defensive responses and sometimes resulted in penetration into the opponent's territory. In another study *Armillaria luteus* rhizomorph systems encountered those of other *Armillaria* species and of conspecifics in sand microcosms [33]. Only occasionally did this result in differences in  $D_{BM}$  compared with systems

growing alone. Changes in foraging pattern also occur during interactions between saprotrophic and ectomycorrhizal mycelium [71] (Figure 8.2).

**Table 8.4** Changes in fractal geometry of mycelial systems during interactions between *Stropharia caerulea* and other cord-forming, saprotrophic basidiomycetes in trays of compressed soil. Data from [61].

Other species	Outcome of interaction	Change in $D_{BM}$ and $D_{BS}$	
		<i>Stropharia caerulea</i>	Other species
<i>Agrocybe gibberosa</i>	Initially deadlock, but <i>Agrocybe gibberosa</i> completely encircling <i>Stropharia caerulea</i> . Subsequently, fans of <i>Stropharia caerulea</i> mycelium extended over <i>Agrocybe gibberosa</i>	Production of dense localised fans ( $D_{BM} = 1.89 \pm 0.04$ )	No change in $D_{BM}$ or $D_{BS}$
<i>Hypholoma fasciculare</i>	Deadlock, but mutual replacement in one system	Differences not usually significant	High $D_{BM}$ ( $1.83 \pm 0.03$ ), non-invasive, lateral fans were produced elsewhere (Figure 8.2) No change in $D_{BM}$ consistently lowered
<i>Phanerochaete velutina</i>	<i>Stropharia caerulea</i> was rapidly replaced	$D_{BM}$ and $D_{BS}$ were significantly reduced	$D_{BM}$ was significantly reduced
<i>Phallus impudicus</i>	Temporary defensive ridges produced by <i>Stropharia caerulea</i> , but these were breached in a few places and the fungus was replaced when <i>Phallus impudicus</i> reached the wood blocks	Differences not usually significant	No change in $D_{BM}$ or $D_{BS}$

8.5.7 Effects of Invertebrate Grazing and Destructive Disturbance

Fungal mycelia concentrate mineral nutrients as they decompose organic resources; therefore, they form a highly nutritious food for soil invertebrates [72]. Much research has focused on the grazing of soil invertebrates on fungal mycelia, but the spatial implications due to fungal growth responses have received little attention. Microarthropod grazing results in dramatic changes in mycelial morphology (Figure 8.10), including changes in fractal structure [73]. When the collembolan

*Folsomia candida* grazed on *Hypholoma fasciculare*, at different grazing intensities (20, 40 or 60 collembola added to mycelia with a radius of 1.5 cm), there was no significant difference in  $D_{BM}$ , but  $D_{BS}$  differed significantly: from 30 days  $D_{BS}$  was significantly higher in controls and decreased monotonously with increased grazing intensity. Not only do effects vary depending on grazing intensity, but also on collembolan species and fungal species [74].

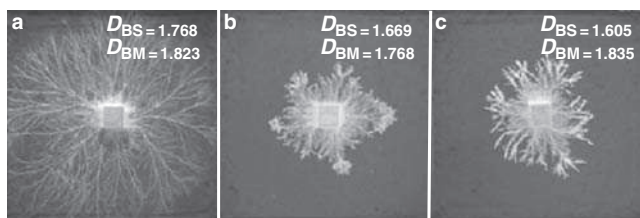


**Figure 8.10** Mycelium of *Phanerochaete velutina* extending from 4 cm<sup>3</sup> beech wood resource, across nonsterile soil compacted into 24 cm × 24 cm trays: (a) ungrazed; and grazed by (b) *Folsomia candida* or (c) *Proistoma minuta* (collembola) (images courtesy of George M. Tordoff). Collembola were added when the mycelial systems had extended 4 cm from the wood resource.

Grazing is one form of destructive disturbance. More extensive disturbance could result from the activity of large animals. In an experiment to simulate major destructive disturbance, cord systems of *Phanerochaete velutina*, developing from wood blocks on soil, were completely severed and removed from zero, three or four faces of the wood cubes [75]. Where mycelia were completely severed, regrowth had the same  $D_{BM}$  (1.6) as undisturbed systems. However, when mycelium were severed from three sides, regrowth initially had the same  $D_{BM}$  (1.6) as unsevered parts, but following subsequent removal there was only limited regrowth from the severed sides, and a much lower  $D_{BM}$  (1.4). The systems had developed a distinct polarity (i.e. growth predominantly in one direction).

## 8.6 SOIL AS A FRACTAL HABITAT AND ITS RELEVANCE TO MICROBIAL ECOLOGY

From the foregoing (Section 8.5), it is evident that soil properties can influence large-scale mycelial behaviour, even in a largely two-dimensional setting. In three dimensions, soil structure will have a large effect on the spatial and temporal dynamics of microbial populations and the processes which they bring about. The fractal properties of soil have effects on habitable space, movement of predators and prey, movement of water, nutrients and gases, and also physiological and biochemical effects. Equally, sediments are fractal, and indeed other microbial environments, such as biofilms, have been shown to have some fractal properties [76]; thus, some of the following will also apply to them.

The surface area available in soil to micro- and macro-organisms depends on scale of measurement. For organisms of different size, this can be estimated using a scale of measurement equivalent to the size of the organism in question. Clearly, the smaller the organism, the greater is the potential habitable space. This idea has been used to relate body size to population densities and species diversity of microarthropods and protozoa in soil [77–81]. Understanding where predators can reside is important to understanding their effects on microbial prey. Obviously, small soil pores will provide refuges for microorganisms to which larger predatory organisms are unable to gain access. Information on the fractal geometry of soils can indicate the extent of refuges for particular microbes from predators of particular sizes. For example, in a soil with a fractal dimension of 2.36, predatory protozoa will be unable to gain access to half of the potential habitat space for bacteria [39].

Fractal structure also differentially affects the movement of organisms in soil. Thus, even if larger microorganisms are less mobile than smaller ones they can often move through soil more rapidly because lack of access to smaller pores reduces effective tortuosity [39]. Though we are not aware of the use of fractal geometry to assess movement of microorganisms in soil or other fractal environments, it has been used to describe and analyse animal movement [82]. Caution must be urged, and such an approach should be avoided unless self-similarity can be demonstrated over appropriate ranges of scales for the organisms under consideration [82]. Movement patterns of microorganisms and micro-fauna can be fractal for some of the time, though more directed movement can occur in the presence of attractants [e.g. 83, 84]. In a study in which nematodes (*Caenorhabditis elegans*) were allowed to move on a homogeneous layer of agar with or without localised bacterial (*Escherichia coli*) food sources, or in a more heterogeneous environment (created by adding a monolayer of sand grains to the two treatments), the fractal dimension of trails were significantly higher for the treatment without structure or bacteria than for the other treatments [83]. Results were interpreted as the foraging strategy allowing the nematode to escape structural traps, e.g. pores which are ‘dead ends’, and then to react to gradients of attractants (bacteria patches).

With regard to movement of nutrients, gases, metabolites, etc., it has been convincingly demonstrated mathematically [39] that both the fractal dimension and the fracton dimension<sup>5</sup> [85, 86] influence diffusion rate. This is because ‘lacunarity’

---

<sup>5</sup> The fracton (or spectral) dimension describes structure within a fractal network [39, 85]. For example it is useful for describing physical processes, e.g. flow, through a fractally porous network, e.g. soil. The fracton dimension  $\bar{d}$  can be calculated using a random-walk technique on a digital image. Effectively, starting at a random point within a fractally porous network, a random step can be taken to any of the eight surrounding pixels. If the pixel has not been visited previously then 1 is added to the number of sites visited  $S_N$  and 1 to the total number of sites  $N$ . If the pixel has already been visited, then 0 is added to  $S_N$  and 1 to  $N$ . The process continues until a boundary is hit or until some predefined limit of  $N$  is reached. The fracton dimension can be determined from the relationship  $S_N \propto N^{\bar{d}/2}$ .

(i.e. the arrangement and magnitude of holes [87]) may significantly influence the processes that occur in soil [39]. Lacunarity affects the variability of fractal dimension at a particular resolution. Consequently, it is not appropriate to use classical diffusion equations for soil [39]. Equation (8.12) is appropriate [85]:

$$\frac{\partial c}{\partial t} = \nabla \cdot (D(r) \nabla c) \quad (8.11)$$

where  $D(r)$  is the diffusion coefficient given by

$$D(r) \sim r^{-\theta}; \quad \theta = 2(DN - \bar{d})/\bar{d} \quad (8.12)$$

where  $c$  is the concentration,  $r$  is the distance (at time  $t$ ) of the particle under consideration from its starting point,  $\bar{d}$  is the fracton dimension, and  $D_N$  is the fractal dimension.

## 8.7 CONCLUSIONS AND RECOMMENDATIONS

Using fractal geometry to describe the way in which microbial biomass is distributed in space is clearly extremely valuable. It has allowed comparison of mycelial organisms under different conditions in agar, soil and water, and has revealed small differences that were not evident from visual observation or from other morphological descriptors [e.g. 65]. It is far superior to the use of density, which is another measurement commonly used to estimate space filling, but which is entirely inappropriate as the number of units of length, area or volume that are identified varies according to the scale of observation.

Fractal dimensions alone do not reveal the whole picture of growth and distribution of biomass of microorganisms. Linear extension rate is useful to use together with fractal dimension, though it must be interpreted with caution: rapid extension is often interpreted as being indicative of a vigorous organism growing under ‘good’ conditions, but it could indicate the opposite, being an ‘escape’ response. Surface coverage, measured by pixel counts in two dimensions can also be useful. Qualitative descriptions should not be abandoned, but used jointly with these other descriptors, as microorganisms can sometimes have very different branching patterns despite having similar values for fractal dimension, surface coverage and extension rate [57] (Figures 8.4–8.7). Further, other mathematical tools, such as graphing theory/network analysis, may be valuable adjuncts to fractal dimension, since they can quantify connectedness within different parts of systems, and can be used to examine effects of breaking connections, i.e. robustness/resilience [88, 89].

To date, most work on the fractal geometry of microorganisms in the natural environment has centred on fungi growing in two dimensions across the surface of soil and, to a lesser extent, microbial flocs in water. Clearly, there is considerable scope for extending studies of unicellular microorganisms into the natural environment. With regard to studies of fungi on soil, immediate priorities must be to try

to visualise the distribution of mycelia in three dimensions and to relate the fractal nature of soil to mycelial distribution.

## ACKNOWLEDGEMENTS

Some of the information in this review was obtained during tenure of a Natural Environment Research Council award (A/S/2000/00411). Thanks also to Colin W. Morris for mathematical advice.

## LIST OF SYMBOLS AND ABBREVIATIONS

$D_B$	surface fractal dimension
$D_{BM}$	mass fractal dimension determined by the box-counting method
$D_{BS}$	surface fractal dimension determined by the box-counting method
$D_3$	fractal dimension of a three-dimensional object determined by the two slopes method
$D_f$	fractal dimension of each section in a three-dimensional object
$D_M$	mass fractal dimension
$D(r)$	diffusion coefficient

## REFERENCES

- [1] Ritz, K., Dighton, J. and Giller, K.E. (eds). (1994). *Beyond the Biomass*. John Wiley and Sons, Ltd, Chichester.
- [2] Andrews, J.H. (1991). *Comparative Ecology of Microorganisms and Macroorganisms*. Springer, New York.
- [3] Ruzicka, M.C., Fridich, M. and Burkhard, M. (1995). A bacterial colony is not self similar. *Physica A*, **216**, 382–385.
- [4] Golding, I., Koslovsky, Y., Cohen, I. and Ben-Jacob, E. (1998). Studies of bacterial branching growth using reaction-diffusion models for colony development. *Physica A*, **260**, 510–554.
- [5] Ben-Jacob, E., Cohen, I., Golding, I., Gutnick, D.L., Tcherpakov, M., Helbing, D. and Ron, I.G. (2000). Bacterial cooperative organization under antibiotic stress. *Physica A*, **282**, 247–282.
- [6] López, J.M. and Jensen, H.J. (2002). Generic model of morphological changes in growing colonies of fungi. *Phys. Rev. E*, **65**, art. no. 021903.
- [7] Ginovart, M., López, J.M., Valls, J. and Silbert, M. (2002). Individual based simulations of bacterial growth on agar plates. *Physica A*, **305**, 604–618.
- [8] Boswell, G.P., Jacobs, H., Ritz, K., Gadd, G.M. and Davidson, F.A. (2005). The development of fungal networks in complex environments. *Bull. Math. Biol.* **69**, 605–634.
- [9] Senesi, N. and Boddy, L. (2002). A fractal approach for interactions between soil particles and microorganisms. In *Interactions between Soil Particles and Microorganisms. Impact on the Terrestrial Ecosystem*, Huang, P.M., Bollag, J.-M. and Senesi, N. (eds). John Wiley and Sons, Ltd, Chichester, pp. 41–84.

- [10] Ritz, K. and Crawford, J. (1990). Quantification of the fractal nature of colonies of *Trichoderma viride*. *Mycol. Res.*, **94**, 1138–1141.
- [11] Marx, G.H. and Davey, C.L. (1990). Applications of fractal geometry. *Binary*, **2**, 169–175.
- [12] Hastings, H.M. and Sugihara, G. (1993). *Fractals. A User's Guide for the Natural Sciences*. Oxford University Press, Oxford.
- [13] Pfeifer, P. and Obert, M. (1989). Fractal basic concepts and technology. In *The Fractal Approach to Heterogenous Chemistry – Surfaces, Colloids, Polymers*, Avnir, D. (ed.). John Wiley and Sons, Ltd, New York, pp. 11–43.
- [14] Obert, M., Pfeifer, P. and Sernetz, M. (1990). Microbial growth patterns described by fractal geometry. *J. Bacteriol.*, **172**, 1180–1185.
- [15] Donnelly, D.P., Wilkins, M.F. and Boddy, L. (1995). An integrated image analysis approach for determining biomass, radial extent and box-count fractal dimension of macroscopic mycelial systems. *Binary*, **7**, 19–28.
- [16] Kaye, B.H. (1989). Image analysis techniques for characterising fractal structure. In *The Fractal Approach to Heterogenous Chemistry – Surfaces, Colloids, Polymers*, Avnir, D. (ed.). John Wiley and Sons, Ltd, Chichester, pp. 55–66.
- [17] Tang, S., Mar, Y. and Sebastine, I.M. (2001). The fractal nature of *Escherichia coli* biological flocs. *Colloids Surf. B: Biointerfaces*, **20**, 211–218.
- [18] Lambert, S., Moustier, S., Dussouillez, P., Baracat, M., Bottero, J.Y., Le Petit, J. and Ginestet, P. (2003). Analysis of the structure of very large bacterial aggregates by small-angle multiple light scattering and confocal image analysis. *J. Colloid Interface Sci.*, **262**, 384–390.
- [19] Texeira, J. (1988). Small-angle scattering by fractal systems. *J. Appl. Crystallogr.*, **21**, 781–785.
- [20] Thill, A., Wagner, M. and Bottero, J.Y. (1999). Confocal scanning laser microscopy as a tool for the determination of 3D floc structure. *J. Colloid Interface Sci.*, **220**, 465–467.
- [21] Logan, B.E. and Wilkinson, D.B. (1991). Fractal dimensions and porosities of *Zoogloea ramigera* and *Saccharomyces cerevisiae* aggregates. *Biotechnol. Bioeng.*, **38**, 389–396.
- [22] Matsuyama, T. and Matsushita, M. (1992). Self-similar colony morphogenesis by Gram-negative rods as the experimental model of fractal growth by a cell population. *Appl. Environ. Microbiol.*, **58**, 1227–1232.
- [23] Nakahara, A., Shimada, Y., Wakita, J., Matsushita, M. and Matsuyama, T. (1996). Morphological diversity of the colony produced by bacteria *Proteus mirabilis*. *J. Phys. Soc. Jpn.*, **65**, 2700–2706.
- [24] Das, I., Kumar, A. and Singh, U.K. (1997). Non-equilibrium growth of *Klebsiella ozaenae* on agar plates. *Indian J. Chem., Sect. A*, **36**, 197–200.
- [25] Ben-Jacob, E. (2002). Self-organization in biological systems. *Nature* **415**(6870), 370–370.
- [26] Fujikawa, H. (1994). Diversity of the growth-patterns of *Bacillus subtilis* colonies on agar. *FEMS Microbiol. Ecol.*, **13**, 159–168.
- [27] Matsuyama, T. and Matsushita, M. (1993). Fractal morphogenesis by a bacterial-cell population. *Crit. Rev. Microbiol.*, **19**, 117.
- [28] Boschke, E. and Bley, T. (1998). Growth patterns of yeast colonies depending on nutrient supply. *Acta Biotechnol.*, **18**, 17–27.
- [29] Kawasaki, K., Mochizuki, A., Matsushita, M., Umeda, T. and Shigesada, N. (1997). Modelling spatio-temporal patterns generated by *Bacillus subtilis*. *J. Theor. Biol.*, **188**, 177–185.
- [30] Ben-Jacob, E., Shochet, O., Cohen, I., Tenenbaum, A., Czirók, A. and Vicsek, T. (1995). Cooperative strategies in formation of complex bacterial patterns. *Fractals – Interdiscipl. J. Complex Geom. Nature*, **3**, 849–868.



- [31] Lundy, S.D., Payne, R.J., Giles, K.R. and Garrill, A. (2001). Heavy metals have different effects on mycelial morphology of *Achlya bisexualis* as determined by fractal geometry. *FEMS Microbiol. Lett.*, **201**, 259–263.
- [32] Mihail, J.D. and Bruhn, N. (2005). Foraging behaviour of *Armillaria* rhizomorph systems. *Mycol. Res.*, **109**, 1195–1207.
- [33] Mihail J.D., Obert, M., Bruhn, J.N. and Taylor, S.J. (1995). Fractal geometry of diffuse mycelia and rhizomorphs of *Armillaria* species. *Mycol. Res.*, **99**, 81–88.
- [34] Ryoo, D. (1999). Fungal fractal morphology of pellet formation in *Aspergillus niger*. *Biotechnol. Technol.*, **13**, 33.
- [35] Matsuura, S. and Miyazima, S. (1993). Colony morphology of the fungus *Aspergillus oryzae*. In *Fractals in Biology and Medicine*, Nonnenmacher, T.F., Losa, G.A. and Weibel, E.R., (eds). Birkhauser, Basel, pp. 276–282.
- [36] Matsuura, S. and Miyazima, S. (1993). Formation of ramified colony of fungus *Aspergillus oryzae* on agar media. *Fractals*, **1**, 336–345.
- [37] Baar, J., Comini, B., Elferink, M.O. and Kuyper, T.W. (1997). Performance of four ectomycorrhizal fungi on organic and inorganic nitrogen sources. *Mycol. Res.*, **101**, 523–529.
- [38] Mihail J.D., Obert, M., Taylor, S.J. and Bruhn, J.N. (1994). The fractal dimension of young colonies of *Macrophomina phaseolina* produced from microsclerotia. *Mycologia*, **86**, 350–356.
- [39] Rayner, A.D.M., Ramsdale, M. and Watkins, Z.R. (1995). Origins and significance of genetic and epigenetic instability in mycelial systems. *Can. J. Bot.*, **73**, S1241.
- [40] Jones, C.L., Lonergan, G.T. and Mainwaring, D.E. (1993). Mycelial fragment size distribution – an analysis based on fractal geometry. *Appl. Microbiol. Biotechnol.*, **39**, 242–249.
- [41] Crawford, J.W., Ritz, K. and Young, I.M. (1993). Quantification of fungal morphology, gaseous transport and microbial dynamics in soil: an integrated framework utilising fractal geometry. *Geoderma*, **56**, 157–172.
- [42] Jones, C.L., Lonergan, G.T. and Mainwaring, D.E. (1995). Acid-phosphatase positional correlations in solid-surface fungal cultivation: a fractal interpretation of biochemical differentiation. *Biochem. Biophys. Res. Commun.*, **208**, 1159–1165.
- [43] Jones, C.L. and Lonergan, G.T. (1997). Prediction of phenol-oxidase expression in a fungus using the fractal dimension. *Biotechnol. Lett.*, **19**, 65–69.
- [44] Jones, C.L. (1996). 2-D wavelet packet analysis of structural self-organization and morphogenic regulation in filamentous fungal colonies. In *Complex Systems Conference – From Local Interactions to Global Phenomena*, Charles Sturt University, Wodonga, Australia. <http://www.swin.edu.au/chem/bio/cs96/camjones.htm> [accessed 15 Nov 2004].
- [45] Chu, C.P. and Lee, D.J. (2004). Multiscale structures of biological flocs. *Chem. Eng. Sci.*, **59**, 1875–1883.
- [46] Gorczyca, B. and Ganczarczyk, J. (2001). Fractal analysis of pore distributions in alum coagulation and activated sludge flocs. *Water Pollut. Res. J. Can.*, **36**, 687–700.
- [47] Schmid, M., Thill, A., Purkhold, U., Walcher, M., Bottero, J.Y., Ginestet, P., Nielsen, P.H., Wuertz, S. and Wagner, M. (2002). Characterization of activated sludge flocs by confocal laser scanning microscopy and image analysis. *Water Res.*, **37**, 2043–2052.
- [48] Da Motta, M., Pons, M.-N., Roche, N. and Vivier, H. (2001). Characterisation of activated sludge by automated image analysis. *Biochem. Eng. J.*, **9**, 165–173.
- [49] Cenens, C., Jenné, R. and van Impe, J.S. (2002). Evaluation of different shaped parameters to distinguish between flocs and filaments in activated sludge images. *Water Sci. Technol.*, **45**, 85–91.
- [50] Arnold, J.W. and Bailey, G.W. (2000). Surface finishes on stainless steel reduce bacterial attachment and early biofilm formation: scanning electron and atomic force microscopy study. *Poult. Sci.*, **79**, 1839–1845.



- [51] Yang, X., Beyenal, H., Harkin, G. and Lewandowski, Z. (2000). Quantifying biofilm structure using image analysis. *J. Microbiol. Methods*, **39**, 109–119.
- [52] Otten, W. and Gilligan, C.A. (1998). Effect of physical conditions on the spatial and temporal dynamics of the soil-borne fungal pathogen *Rhizoctonia solani*. *New Phytol.*, **138**, 629–637.
- [53] Harris, K., Young, I.M., Gilligan, C.A., Otten, W. and Ritz, K. (2003). Effect of bulk density on the spatial organization of the fungus *Rhizoctonia solani* in soil. *FEMS Microbiol. Ecol.* **44**, 45–56.
- [54] Otten, W., Harris, K., Young, I.M., Ritz, K. and Gilligan, C.A. (2004). Preferential spread of the pathogenic fungus *Rhizoctonia solani* through structured soil. *Soil Biol. Biochem.*, **36**, 203–210.
- [55] Regalado, C.M., Crawford, J.W., Ritz, K. and Sleeman, B.D. (1996). The origins of spatial heterogeneity in vegetative fungal mycelia: a reaction-diffusion model. *Mycol. Res.*, **100**, 1473–1480.
- [56] Boddy, L. (1999) Saprotrophic cord-forming fungi: meeting the challenge of heterogeneous environments. *Mycologia*, **91**, 13–32.
- [57] Boddy, L., Wells, J.M., Culshaw, C. and Donnelly, D.P. (1999). Fractal analysis in studies of mycelium in soil. *Geoderma*, **88**, 301–328.
- [58] Donnelly, D.P., Boddy, L. and Leake, J.R. (2004). Development, persistence and regeneration of foraging ectomycorrhizal mycelial systems in soil microcosms. *Mycorrhiza*, **14**, 37–45.
- [59] Zakaria, A.J. and Boddy, L. (2002). Mycelial foraging by *Resinicium bicolor*: interactive effects of resource quantity, quality and soil composition. *FEMS Microbiol. Ecol.*, **40**, 135–142.
- [60] Owen, S.L. (1997). Comparative development of the mycelial cord-forming fungi *Coprinus picaceus* and *Phanerochaete velutina*, with particular emphasis on pH and nutrient reallocation. PhD thesis, University of Wales, Cardiff.
- [61] Donnelly, D.P. and Boddy, L. (2001). Mycelial dynamics during interactions between *Stropharia caerulea* and other cord-forming, saprotrophic basidiomycetes. *New Phytol.*, **151**, 691–704.
- [62] Smith, M.L., Bruhn, J.N. and Anderson, J.B. (1992). The fungus *Armillaria bulbosa* is among the largest and oldest living organisms. *Nature*, **356**, 428–431.
- [63] Thompson W. and Rayner A.D.M. (1982). Structure and development of mycelial cord systems of *Phanerochaete laevis* in soil. *Trans. Br. Mycol. Soc.*, **78**, 193–200.
- [64] Donnelly, D.P. and Boddy, L. (1997). Resource acquisition by the mycelial-cord-former *Stropharia caerulea*: effect of resource quantity and quality. *FEMS Microbiol. Ecol.*, **23**, 195–205.
- [65] Donnelly, D.P. and Boddy, L. (1998). Developmental and morphological responses of mycelial systems of *Stropharia caerulea* and *Phanerochaete velutina* to soil nutrient enrichment. *New Phytol.*, **138**, 519–531.
- [66] Bolton, R.G. and Boddy, L. (1993). Characterization of the spatial aspects of foraging mycelial cord systems using fractal geometry. *Mycol. Res.*, **97**, 762–768.
- [67] Wells, J.M. Donnelly, D.P. and Boddy, L. (1997). Patch formation and developmental polarity in mycelial cord systems of *Phanerochaete velutina* on a nutrient-depleted soil. *New Phytol.*, **136**, 653–665.
- [68] Wells, J.M., Thomas, J. and Boddy, L. (2001). Soil water potential shifts: developmental responses and dependence on phosphorus translocation by the cord-forming basidiomycete *Phanerochaete velutina*. *Mycol. Res.*, **105**, 859–867.
- [69] Donnelly, D.P. and Boddy, L. (1997). Development of mycelial systems of *Stropharia caerulea* and *Phanerochaete velutina* on soil: effect of temperature and water potential. *Mycol. Res.*, **101**, 705–713.

- [70] Boddy, L. (2000). Interspecific combative interactions between wood-decaying basidiomycetes – a review. *FEMS Microbiol. Ecol.*, **31**, 185–194.
- [71] Leake, J.R., Donnelly, D.P. and Boddy, L. (2002). Interactions between ectomycorrhizal and saprotrophic fungi. In *Mycorrhizal Ecology. Ecological Studies*, Vol. 157, Van der Heijden, M.G.A. and Sanders, I. (eds). Springer-Verlag, Berlin, pp. 346–372.
- [72] Booth, R.G. and Anderson, J.M. (1979). The influence of fungal food quality on the growth and fecundity of *Folsomia candida* (Collembola: isotomidae). *Oecologia*, **38**, 317–323.
- [73] Kampichler, C. Rolschewski, J., Donnelly, D.P. and Boddy, L. (2004). The impact of collembolan grazing on the growth strategy of the cord-forming fungus *Hypholoma fasciculare*. *Soil Biol. Biochem.*, **36**, 591–599.
- [74] Tordoff, G.M., Jones, T.H. and Boddy, L. (2006). Grazing by *Folsomia candida* (Collembola) affects the mycelial morphology of the cord-forming basidiomycetes *Hypholoma fasciculare*, *Phanerochaete velutina* and *Resinicium bicolor* differently during early outgrowth onto soil. *Mycol. Res.*, **110**, 335–345.
- [75] Donnelly, D.P. and Boddy, L. (1998). Repeated damage results in polarised development of foraging mycelial systems of *Phanerochaete velutina*. *FEMS Microbiol. Ecol.*, **26**, 101–108.
- [76] Zahid, W.M. and Ganczarczyk, J.J. (1994). Structure of RBC biofilms. *Water Environ. Res.*, **66**, 100–106.
- [77] Morse, D.R., Lawton, J.H., Dodson, M.M. and Williamson, M.H. (1985). Fractal dimension of vegetation and the distribution of arthropod body lengths. *Nature*, **314**, 731–733.
- [78] Kampichler, C. and Hauser, M. (1993). Roughness of soil pore surface and its effects on available habitat space of microarthropods. *Geoderma*, **56**, 223.
- [79] Brown, S. (2002). Aspects of soil protozoa on a grassland farm. *Protistology*, **37**, 359–360.
- [80] Finlay, B.J. and Fenchel, T. (2001). Protozoan community structure in a fractal soil environment. *Protist*, **152**, 203–218.
- [81] Finlay, B.J., Black, H.I.J., Brown, S., Clarke, K.J., Estaban, G.S., Hindle, R.M., Olmo, J.L., Rollett, A. and Vickerman, K. (2000). Estimating the growth potential of the soil protozoan community. *Protist*, **151**, 69–80.
- [82] Turchin, P. (1996). Fractal analyses of animal movement: a critique. *Ecology*, **77**, 2086–2090.
- [83] Anderson, A.R.A., Young, I.M., Sleeman, B.D., Griffiths, B.S. and Robertson, W.M. (1997). Nematode movement along a chemical gradient in a structurally heterogeneous environment. I. Experiment. *Fundam. Appl. Nematol.*, **20**, 157–163.
- [84] Jonsson, P.R. and Johansson, M. (1997). Swimming behaviour, patch exploitation and dispersal capacity of a marine benthic ciliate in flume flow. *J. Exp. Mar. Biol. Ecol.*, **215**, 135–153.
- [85] Orbach, R. (1986). Dynamics of fractal networks. *Science*, **231**, 814–819.
- [86] Havlin, S. and Ben-Avraham, D. (1987). Diffusion in disordered media. *Adv. Phys.*, **36**, 695–798.
- [87] Mandelbrot, B.B. (1982). *The Fractal Geometry of Nature*. W.H. Freeman, New York.
- [88] Bebbler, D., Tlalka, M., Hynes, J., Darrah, P., Ashford, A., Watkinson, S.C., Boddy, L. and Fricker, M. (2006). Imaging complex nitrogen dynamics in mycelial networks. In *Fungi in the Environment*, Gadd, G.M., Watkinson, S.C. and Dyer, P. (eds). Cambridge University Press, Cambridge, UK, pp. 3–21.
- [89] Bebbler, D.P., Hynes, J., Darrah, P.R., Boddy, L. and Fricker, M.D. (2007). Biological solutions to transport network design. *Proc. Royal Soc. B*, **274**, 2307–2315.

---

# 9 Fractal Geometry of Aerosol Particles

---

**Ian Colbeck**

*Department of Biological Sciences, University of Essex, Colchester CO4 3SQ, UK*

## 9.1 INTRODUCTION

Aerosol particles are ubiquitous in the troposphere and have important effects on human health, climate and the environment. They also have significant pharmaceutical and industrial applications. Combustion-generated particles, often called carbonaceous, smoke or soot, are an important component of most atmospheric aerosols, with fossil fuel and biomass burning being the major anthropogenic sources. Diesel engines in particular emit large amounts of soot particles. Soot or 'black carbon' particles commonly aggregate into clusters having highly irregular, complex morphologies and varied sizes, surface areas and degrees of aggregation. These clusters are generally called 'chain aggregates'. The change in morphology due to aggregation has profound implications on a wide range of particle properties, including density, transport, and potential health effects. Hence, soot morphology is of great importance from an environmental point of view. Soot particles warrant special attention because of their long-range transport [1], complex role in climate [2], and large surface area that may facilitate heterogeneous reactions [3]. They are generally very hydrophobic, but they may become hydrophilic through physical and/or chemical changes that occur during atmospheric aging. Chain aggregates are also important in technical applications, as in the commercial manufacture of engineered nanoparticles such as carbon black for rubber fillers, titania for pigments, platinum catalysts for diesel soot traps and in tin oxide for gas sensors. Calculating the health hazard from the aerodynamic diameter can lead to serious underestimation of the actual hazard and, furthermore, the aerodynamic diameter can give a false impression of the physical magnitude of the aerosol when considering the design of respirators and filters. Nonspherical particles have a surface area orders of magnitude bigger than anticipated from their aerodynamic diameters and, hence, can carry large quantities of adsorbed chemicals into the lung. Since aerodynamic diameters underestimate the actual size of fractal clusters, it is often found that, for instance, diesel exhaust may be trapped

by a relatively inefficient coarse filter compared with that predicted to be necessary based on aerodynamic size.

The advance of aerosol science has often necessitated the simplified treatment of aerosols as comprising spherical particles. Even rather simple nonspherical shapes, such as ellipsoids, chains or fibres, have not been easy to work with, either in theoretical treatments or in the laboratory. It has been shown in experiments [4] and simulations [5] that some aerosol particles, particularly those derived from combustion processes (i.e. grown by diffusion-limited aggregation (DLA)), are fractal-like (Figure 9.1). The most striking feature of a fractal is its scale invariance or self-similarity. This means that they have dilation symmetry, i.e. they look the same on all scales. Mathematical fractals are scale invariant over all scales, yet nature provides numerous examples of objects that are fractals over a finite range of scales, e.g. coast lines [6]. If any part of a fractal is magnified, then it appears similar to the object as a whole. The aggregated particles mentioned above do not have strict geometrical similarity, but do satisfy the criteria for fractals. An important characteristic of these structures is a power-law relationship between the mass, or number of primary particles  $N$  of monomer radius  $a$ , and the radius of gyration  $R_g$  of the cluster of the form

$$N = \varepsilon \left( \frac{R_g}{a} \right)^{D_f} \quad (9.1)$$

where  $D_f$  is the fractal dimension and an indicator of morphology, providing additional information on the number density of the structure, with a larger value indicative of tighter particle packing;  $\varepsilon$  is the fractal prefactor, also known as the structural

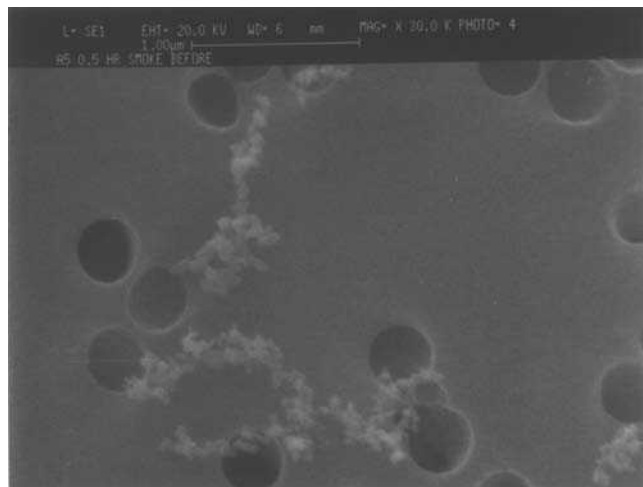


**Figure 9.1** Electron micrograph of a fractal cluster of carbonaceous smoke on a  $0.4\text{ }\mu\text{m}$  Nuclepore filter. The black circles are pores in the filter.

coefficient, which is taken by many workers as unity [7], although literature values vary between 1.23 [8] and 3.47 [9]. In general, the values based on numerically simulated aggregates are systematically inferior to those inferred from experiments. Brasil *et al.* [10] attempted to identify a possible universal value for the fractal prefactor. They estimated the fractal properties of simulated aggregates using morphological concepts and light-scattering theories. From three different populations of aggregates studied, they concluded that the most appropriate value for the prefactor, independent of aggregate size and composition, was 1.27. These results were in very good agreement with numerical predictions reported by previous authors [9, 11, 12]. It is possible that the large discrepancy in the literature values may result from partial sintering between neighbouring particles of aggregates combined with the fact that real aggregate populations are polydisperse.

The fractal dimension provides a quantitative measure of the degree to which a structure fills the physical space beyond its topological dimension. Whereas a smooth line is confined to one dimension and a smooth surface to two, a fractal, with wrinkles on wrinkles, begins to infringe on other dimensions (Figure 9.2) [13]. From a topological viewpoint, the dimension of all the lines in this Figure 9.2 is one. However, the theory of fractals suggests that such curves can be described by allocating a fractional number between one and two which will describe their space-filling ability. Using this similar concept, a rugged surface can be given a number between two and three which indicates how the structure fills the space it occupies. For example, if the primary particles are aligned in a straight line, then  $D_f = 1$ , and for particles on a regular two-dimensional array,  $D_f = 2$ . For  $D_f = 3$ , a uniform compact aggregate is implied. For a typical fractal cluster,  $D_f$  is lower than the space dimension and is

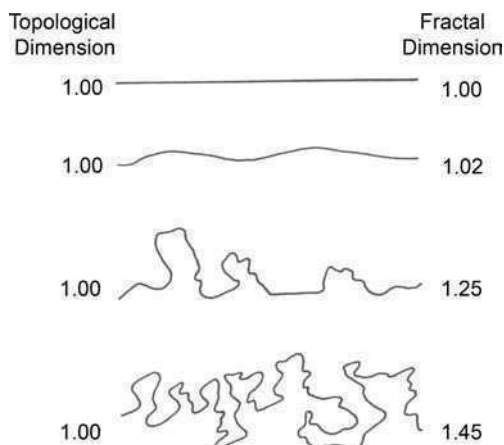


**Figure 9.2** The basic concept that the dimension of a physical quantity can be extended by adding fractional quantities related to the ruggedness of a system to the topological dimension [13]. Reproduced with permission of Wiley-VCH.

usually noninteger, implying a structure intermediate between these idealised forms. The higher the fractal dimension, the more compact the structure it describes. Whereas all the various shape diameters vary as the particle size changes, the fractal dimension is constant over a range of particle sizes, provided that the clusters form under similar conditions.

Fractal aggregates occur in aerosols as a result of random aggregation and the formation process has been the subject of extensive simulation work [14, 15]. Many models have been postulated, e.g. DLA for particle–cluster, cluster–cluster, ballistic cluster–cluster and reaction-limited cluster–cluster. Particle–cluster aggregation, or DLA, occurs when single monomers diffuse to and stick to a stationary, growing cluster. The resulting three-dimensional clusters yield a fractal dimension of  $\sim 2.5$ , although it has been shown that those aggregates are not fractal over the entire range of their length scales [16]. The introduction of the cluster–cluster model allowed the simulation of realistic aggregate morphologies in which  $D_f$  values were comparable to those obtained by experiment. Cluster–cluster aggregation, or diffusion-limited cluster aggregation (DLCA), occurs when all clusters diffuse and then stick when they randomly touch. In three-dimensional models, aggregate growth by DLCA results in a typical mean value  $D_f \approx 1.8$ , while growth by ballistic limited cluster–cluster aggregation gives  $D_f \approx 1.95$  [17]. The ballistic particle–cluster model produces aggregates with a higher fractal dimensions ( $D_f \approx 2.97$ ). This type of aggregation is, for instance, encountered when nanoparticles attach to larger aggregates in free molecular conditions (gas mean free path much greater than nanoparticle diameter). If the sticking probability is significantly less than one, then the reaction-limited cluster aggregation (RLCA) regime is entered and  $D_f \approx 2.09$ . Only cluster–cluster aggregates occur in aerosols, with the DLA morphology finding applications in other areas [18]. Flame-derived inorganic particulates are not truly fractal because the ready identification of morphologically distinct primary particles places a lower bound on self-similarity; as a result, they are more appropriately characterised as fractal-like. Table 9.1 [19] summarises the fractal dimension predicted by various aggregation models in two- and three-dimensional space. Cluster–cluster aggregation is now one of the most firmly established and extensively researched processes leading to the formation of fractals.

**Table 9.1** Fractal dimension for various aggregation models as a function of spatial dimension. Data from Meakin [19].

	Spatial dimension	
	2	3
Particle–cluster	1.71	2.50
Cluster–cluster	1.45	1.80
Cluster–cluster (ballistic)	1.55	1.95
Particle–cluster (ballistic)	2.00	2.97
Cluster–cluster (chemical)	1.61	2.09

## 9.2 METHODS AND TECHNIQUES

### 9.2.1 Introduction

Many workers have found it convenient to work with what is defined as the boundary fractal of the aggregate, obtained from the two-dimensional projection of the structure. Others have studied the internal structure of aggregates and obtained the mass or density fractal dimension. With both the boundary and density fractal dimensions some information is lost. However, each measurement method yields different details and there is diagnostic information on formation dynamics of the aerosol embedded in the fractal structure [13]. For instance, the boundary fractal yields information on the internal structure and state of subdivision of the aggregate [20], whilst the density fractal provides greater information on the optical properties. The fractal structure of smoke from diesel engines contains information on the burning conditions within the engine. The fractal dimension of the emergent soot is frozen information on the combustion dynamics in the engine, and it has been shown that large, elongated aggregates are produced by diesel engines at low air/fuel ratios [21]. The mass fractal dimension of soot and other aerosols produced by combustion processes is becoming an important element in any models for use in predicting future climate changes. Climate modellers will need to know both the mass fractal dimension, to understand the scattering behaviour of the aerosols, and the boundary fractal dimensions, which govern the rate at which particles settle out of the atmosphere.

First of all, if one looks at the ruggedness of the projected boundary of the aggregate one can describe the structure of the boundary in terms of a boundary fractal dimension. This parameter is a measure of the ruggedness of the boundary. Such boundary fractal dimensions have been studied by various image analysis techniques, with the most familiar technique being described as the structured walk or yardstick method. The perimeter of the particle (Figure 9.3a) is bounded by straight incremental segments each of length  $\Lambda$  (Figure 9.3b). As the magnitude of the increment decreases, the perimeter increases as more fine structure is included. It is common practice to plot the logarithm of the perimeter as a function of the logarithm of the length scale. A graph of this kind is known for historic reasons as a Richardson plot (Figure 9.3c). It can be seen in this figure that there are two linear relationships and it can be shown that it is useful to describe the data line at coarse resolution as defining the structural fractal dimension of the profile. The structural fractal dimension  $D_s$  is useful in describing the aerodynamic behaviour of an aggregated aerosol and can also describe the way in which the profile physically interacts with its surroundings. The fractal dimension deduced from the data generated at high resolution is the textural fractal dimension  $D_T$ . Both of these fractal dimensions are boundary fractals [6].

However, for aggregates formed from solid primary particles with a narrow size distribution, such as a typical combustion-generated aerosol, one is more concerned with the internal structure of the cluster. There are various techniques based on electron or optical microscopy, which use digitised images to determine the fractal dimension



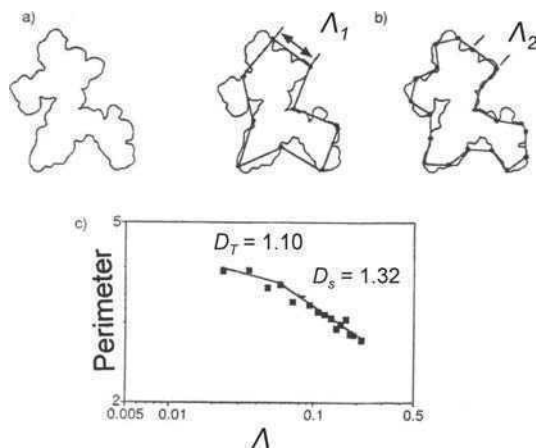


**Figure 9.3** Concepts of fractal geometry: (a) profile of aggregate; (b) structured walk explorations; (c) Richardson plot of a series of explorations of the aggregate

in two-dimensional space [22]. However, care should be taken, as, for example, the deposition of the aggregates on a filter can lead to erroneous results if restructuring has occurred. Additionally, this approach suffers from finite size effects, primary particle overlap and screening effects and cluster anisotropy [23, 24]. By testing image analysis methods with model aggregates it has been shown that the value of the fractal dimension depends on the chosen evaluation method and that the true fractal dimension can be severely underestimated [9, 25, 26]. Brasil *et al.* [27] devised a semi-empirical scheme which should overcome many of these problems. By correlating the structural properties of computer-simulated three-dimensional aggregates of well-defined geometries with those of their two-dimensional projections, they were able to derive simple rules for extracting the fractal dimension from electron micrographs. This semi-empirical scheme has been applied in practice by Wentzel *et al.* [28] when determining the fractal dimension of various soot aerosols. Even so, it is recommended that collection densities on a microscope substrate should be not great and that the aggregates should occupy 10 % of the area or less.

There is a method due to Voss [29] for determining the fractal dimension whereby a series of snapshots covering a specified size range are analysed. This allows one to evaluate the fractal dimension of a large aggregate with samples covering only 100 or so primary particles. However, image analysis methods are generally time consuming and unable to monitor small and fast structural changes of the aggregates. Hence, in-situ three-dimensional methods are generally favoured.

For example, one alternate technique for studying the morphology of aerosols is to probe the system using visible or UV radiation [30–33]. When the aggregate structure is explored by such a technique one is not measuring the configuration of the profile in space but, rather, exploring the way that the subunits of the aggregate



are packed to occupy three-dimensional space. Thus, fractal dimensions measured by light-scattering studies should properly be called mass fractal dimensions. Various other in-situ methods have been reported, again measuring the density fractal. These methods include techniques based on the aerodynamic and mobility properties [34, 35], kinematic coagulation [36], a modified Millikan cell [37, 38] and a combination of differential mobility analysis with inductively coupled plasma optical emission spectrometry [39]. Where not explicitly stated, the fractal dimensions quoted in the quoted publications refer to the mass (density) fractal dimension.

### 9.2.2 Scattering Methods

In-situ optical techniques are highly desirable because of their ability to provide remote sensing in hostile environments (see Chapter 2). Both theoretical [40] and experimental [24, 32, 41–45] research has shown how it is possible to use light scattering to measure the mean size and fractal dimension.

Scattering intensity versus angle is one of most fundamental measurements for particle sizing. In a scattering experiment, a beam of light of wavelength  $\lambda$  is directed onto a sample and the scattered intensity is measured as a function of scattering angle  $\theta$  to the incident direction. If the scattering object is a fractal of fractal dimension  $D_f$ , then the intensity as a function of angle is given by  $I(q) \propto q^{-D_f}$ , where  $I(q)$  is the scattered intensity (often called the structure factor) and  $q$  is the scattered wave vector,  $q = 4\pi\lambda^{-1} \sin \theta/2$ . From a plot of  $\log(I)$  versus  $\log(q)$  one can, in principle, determine the radius of gyration, fractal dimension, polydispersity of the aggregate size distribution and monomer size (Figure 9.4). Such information can be obtained without knowledge of the refractive index of the particle [43]. A plot of  $I$  versus  $q$  exhibits changes of slope whenever  $q^{-1}$  passes through a length scale of the system. From Figure 9.4, it can be seen that at small  $q$  the scattering is approximately constant: this area is the Rayleigh regime. As  $q$  increases, the slope eventually changes, and this indicates an aggregate length scale related to the radius of gyration. The power-law regime is a region of constant slope where  $I$  is proportional to  $q^{-D_f}$ . Hence, the gradient in this region is equal to the negative fractal dimension. As  $q$  increases further, another change in gradient occurs, indicating the monomer radius. Larger values of  $q$  fall into the monomer regime. If data beyond  $q R_g > 5$  are not available, then the fractal dimension measurement should only be considered as qualitative.

Di Stasio *et al.* [46] used this technique to study the agglomeration kinetics of growing soot generated in a diffusion atmospheric flame. The number of primary particles per aggregate and the number concentration of clusters were evaluated on the basis of the measured angular patterns of the scattered-light intensity. They found that the kinetics of the coagulation process that yields to the formation of chain-like aggregates by soot primary particles can be described with a constant coagulation kernel in accord with the Smoluchowski coagulation equation in the free molecular regime. Earlier, this group [44] investigated particle morphology in an ethylene–air diffusion flame for different flow rates of the fuel gas. It is reported that soot

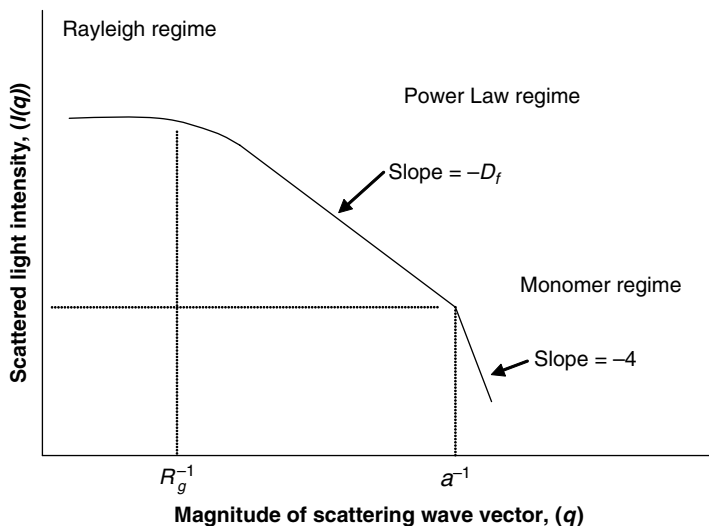


**Figure 9.4** Schematic representation of the scattered light intensity  $I(q)$  versus  $q = 4\pi\lambda^{-1} \sin \theta/2$ , where  $\theta$  is the scattering angle, from an ensemble of fractal aggregates of dimension  $D_f$  on a log-log plot [43]. Reprinted with permission from *Aerosol Science & Technology*, 'Light scattering by fractal aggregates', **35**, 648–687, Copyright 2001. Mount Laurel, NJ.

aggregates, at the early stages of the agglomeration process, first grow as elongated chain-like structures and then, at later stages, assume more compact morphologies with significantly smaller sizes. Thus, branched elongated aggregates grow up at low heights-above-burner with a fractal dimension that is practically constant ( $\sim 1.3$ ). At larger heights-above-burner they self-reorganise into much shorter clusters with a fractal dimension increasing up to 1.9. It is proposed that this rearrangement of soot fractal aggregates can be explained in terms of local heat transfer balance at the cluster surface, which could cause, in the case of chain-like aggregates, a supplementary oxidation inside the pores of soot with possible breaking of the graphitic layers that act as bridges between primary particles within an aggregate. By constraining soot to a cylindrical annular flame front with a radial thickness that appears thin relative to the increasing dimensions of the soot aggregates, thus confining them to a two-dimensional space during aggregation, Sorensen and Hageman [47] were able to show that such aggregates have a fractal dimension of 1.40. This is consistent with simulations of two-dimensional DLCA. Wang and Sorensen [48] considered large values of  $qR_g$  to differentiate between single-cluster and polydispersity effects and showed that the effects are significant, enough even to allow a measurement of the polydispersity of the aerosol.

Recently, Kim and Choi [49] have developed an in situ light-scattering method for online measurement of aggregate size and morphology. Planar multi-angular light-scattering measurements were interpreted by Rayleigh–Debye–Gans scattering theory

for fractal aggregates in order to obtain the mean radius of gyration and the fractal dimension along the flame axis simultaneously, which are the parameters characterizing size and morphology of aggregates. The system developed was applied to study the evolution of silica aggregates produced in a methane–air premixed flat flame. To confirm the suitability of the method as an online measurement of the growth of aggregates, they compared the results with those obtained by conventional point measurements and found that the two results agreed well with each other. They found that the fractal dimension increased with height above the flame but that its variation became very small above 15 cm, where the fractal dimension was approximately constant at 1.7.

### 9.2.3 Aerodynamic/Mobility Methods

Schmidt-Ott [34, 50] reported on a method which involves comparing the mobility radii of the aggregated particle before and after tempering. He showed that temperature increase induced reconstruction of silver aggregates, as observed by a decrease in mobility diameter, until a close-packed form was produced, i.e. tempering causes the aggregate to collapse until  $D_f \approx 3$ . Kutz and Schmidt-Ott [35] have described a method which was based on a comparison of the mobility equivalent radius, determined by differential mobility analysis, with the ratio of mass and drag, measured by a low-pressure impactor. For silver aggregates produced by heating silver up to 1000°C, they found a fractal dimension of 2.06. Weber and Friedlander [51] introduced a model to describe this rearrangement process based on the change in free energy per primary particle during restructuring. The excess free energy compared with the final state drives the aggregate to become more compact, which results in an increase in the coordination number, as estimated from the changing fractal dimension of the aerosol aggregates. This restructuring behaviour of aggregated nanoparticles has recently been reviewed [52]. They identified three steps in the restructuring process: compaction, internal rearrangement, and evaporation. A clear connection was observed between the particle size and the compacting temperature: the smaller the particle, the lower the temperature.

The fractal dimension can be estimated via the mass mobility relationship [53, 54] based on the scaling laws developed by Schmidt-Ott *et al.* [55]. In this relationship, it is assumed that the number of the primary particles  $N$  is proportional to the particle mass  $M_p$ , which requires the primary particle size distribution to be constant for all values of number of primary particles per aggregate as well as the assumption that the primary particle density is constant (which may not be strictly true if the aggregate is coated by a second species). The mass mobility relationship is given by

$$M_p = C \left( \frac{d_m}{d_p} \right)^{D_f} \quad (9.2)$$

where  $C$  is a constant,  $d_p$  is the diameter of the individual spherules comprising the aggregate and  $d_m$  is the mobility diameter (a diameter relating to a particle's mobility

in an electric field [56]). It follows that the particle volume (the volume of the particle is comprised of all material and all void spaces enclosed within the particle envelope) is directly proportional to  $N$ . Equation (9.2) can then be rewritten thus:

$$d_v^3 = C \left( \frac{d_m}{d_p} \right)^{D_f} \quad (9.3)$$

Here,  $C$  is a constant and  $d_v$  the volume equivalent diameter. Since  $d_m$  can be measured with instruments such as a differential mobility analyser (DMA) or scanning mobility particle sizer (SMPS) and  $d_v$  can be estimated as a function of  $N$  (for a given  $d_p$ ) as described above, then Equation (9.3) can be used to estimate a fractal dimension based on the mass–mobility relationship with known values of  $d_p$  and  $N$ . The fractal dimension may be obtained from Equation (9.2) as the slope of  $\log(M_p)$  versus  $\log(d_m)$ .

An alternative method for estimating  $D_f$  (for values of 2 or larger) can be derived using the results of Rogak *et al.* [57] and Schmidt-Ott [50]. For  $D_f \geq 2.0$ :

$$d_{va}^3 = \frac{C}{d_p^{D_f}} d_m^{D_f-2} \quad (9.4)$$

where  $C$  is a constant and  $d_{va}$  is the particle diameter in the free molecular regime (i.e. the mean free path of the gas is greater than the particle diameter). Then:

$$d_{va}^3 = C d_m^{D_f-2} \quad (9.5)$$

Hence, if the fractal dimension  $D_f = 2$ , then  $d_{va}$  is a constant. By plotting  $\log(d_{va})$  versus  $\log(d_m)$ , values of  $D_f > 2$  can be determined. This relationship has been shown to hold for all particles in the continuum regime, and for particles with  $D_f \geq 2$  in any flow regime [54, 55, 58]. For fractal dimensions  $D_f \lesssim 2$ , the interior spherules are no longer shielded by spherules on the exterior and, consequently, drag and mass are simply functions of the number of primary particles and scale together. In this case  $d_{va}$  and  $d_m$  measurements would not contain the information needed to determine  $D_f$  (i.e. when  $D_f < 2$ ). It is uncertain how far into the transition regime this relationship holds for particles with  $D_f \leq 2$  [54]. Based on the above, DeCarlo *et al.* [54] estimated aerodynamic and mobility diameters as a function of number of primary particles. These calculations predicted two distinct values of the fractal dimension based on the mass–mobility relationship and depending on the size of the aggregate. For an aggregate with  $N \leq 60$ ,  $D_f = 2.46$ , whereas for  $N \geq 60$ ,  $D_f = 1.79$ . These values of the fractal dimension are consistent with those observed for some types of combustion-generated soot [54, 59]. The decrease in  $D_f$  occurring with the transition to the large  $N$  regime can be interpreted as being due to fractal aggregates with fewer primary particles filling a larger fraction of the volume around their centre of mass than aggregates with much larger  $N$ .

Slowik *et al.* [59] used the mass–mobility relationship to investigate the impact of fuel equivalence ratio  $\Phi$  on soot morphology produced by a propane–oxygen flame. Two types of soot particle were observed, depending on the fuel equivalence ratio. For  $\Phi < 4$ , the fractal dimension of the particles was approximately  $1.7 \pm 0.15$ . These

particles were composed mostly of black carbon, with the organic carbon content increasing as  $\Phi$  increased. For  $\Phi > 4$ , the particles were nearly spherical, with a fractal dimension of  $2.95 \pm 0.10$ . These particles were composed of about 50 % polyaromatic hydrocarbons, 45 % black carbon and 5 % aliphatic hydrocarbons.

By combining inductively coupled plasma optical emission spectrometry with an epifluorimeter and a differential mobility analyser (DMA), it is possible to determine, simultaneously, the mass, surface area and diameter of aggregated aerosols [39]. From these measurements, the fractal dimension and the monomer size may be determined. The results indicate that silver aggregates, produced by spark discharge in argon, possess various fractal dimensions. A substantial increase in the density of the aggregates occurred by heating, even in the temperature range where the primary particle size remained unchanged. This increase was due to internal rearrangement leading to a more compact packing. In the domain of fractal-like structures, heating resulted in a gradual increase in mass fractal dimension from  $\sim 1.8$  to  $\sim 3$ . The restructuring rate was governed by the temperature and the heating time. The results show that the applied methods have the potential to tailor aggregate shape in order to match special requirements in the production of aggregated structures. The papers by Burtscher and co-workers [60, 61] compare the mobility diameter and the mass of the particle to give the fractal dimension of aggregates from various combustion systems. Since some volatile species are emitted in the gas phase and condense on the particles when the exhaust gas cools down, the output from the exhaust pipe was passed through a thermodesorber. A fractal dimension of 3 was found with the thermodesorber at ambient temperature, whilst if the volatile fraction was removed by setting the desorber temperature to  $350^\circ\text{C}$ , the particles became smaller and the fractal dimension decreased to 2.2. It was suggested that particles consist of an aggregated, nonvolatile core, covered by a volatile liquid material which forms a droplet. As soon as the liquid is removed, the aggregated structure of the core is exposed.

It is also possible to use a combination of two steady-flow instruments in series: one classifying the particles according to mobility diameter and the other according to aerodynamic diameter. In these studies, the density of DMA-classified particles is measured by an impactor. Schleicher *et al.* [62] and Skillas *et al.* [63] used a single-stage low-pressure impactor. McMurtry *et al.* [64] studied the particle density dimension of atmospheric aerosols by classifying particles with a DMA and then measured the particle mass with an aerosol particle mass analyser [65]. They hypothesized that the less 'massive' particles consisted of chain-aggregated soot. Maricq *et al.* [66] studied the density and the fractal dimension of diesel particles by using a DMA and an electrical low-pressure impactor (ELPI). They classified particles by DMA and then measured the aerodynamic size of the classified particles with the ELPI. Although a large number of individual particles are measured rapidly, these methods are time-consuming because one particle size has to be measured at a time. This method can give an average fractal dimension, because an ensemble of fractal-like aggregate particles is present in the aerosol, although no actual values were reported.

All of the methods based on mass and mobility measurements introduced above require mobility size classification. Often the aerosols need to be size fractionated for further analysis and a separate size distribution measurement is needed. Virtanen *et al.* [67] have used an on-line method to estimate the effective density, fractal dimension, and size distribution of particles based on parallel measurements made by an SMPS and ELPI. A fitting procedure is used to find the particle density as a function of particle size and the fractal dimension. The method has been tested by simulation and by experimental measurements of particles with varying morphology. For fractal dimension values between 2.2 and 3.0, fractal dimension was measured with an accuracy of 0.1, and effective density was measured with 15 % relative accuracy. Recall that this method is only valid for fractal dimension values  $> 2$ . Van Gulijk *et al.* [58] also used a combination of SMPS and ELPI. For diesel soot, they found a fractal dimension of  $2.42 \pm 0.12$ , close to the value of  $2.15 \pm 0.10$  for flame-generated soot and  $2.3 \pm 0.1$  for vehicle exhaust particles reported by Maricq and Xu [68]. These values may be also compared with those reported by Skillas *et al.* [63], who found values between 2 and 2.5 (except for idle engines, where they found a value of about 3), and Bartscher [61], who found 2.2 for carbon core soot particles of spark engines. One of the main conclusions of the Van Gulijk *et al.* [58] work is that the performance of both instruments is affected by the fractal-like structure of diesel soot. The ELPI, if it is set to measure the aerodynamic diameter, gives an underestimation of the apparent size of particles due to their fractal-like structure. As a result, the number of particles is overestimated. Electrical mobility analysers are normally calibrated for spherical particles. As a consequence, data obtained from the instrument cannot directly provide the surface area and volume distributions for nanoparticle aggregates, although a new theory enabling this has recently been published (see Section 9.3.4). The SMPS is affected by multiple charging of soot aggregates, larger than 1000 nm, which are abundantly present in diesel exhaust gas and are not removed by the impaction stage at the inlet due to their small effective density. Multiple charging leads to an underestimation of the size of the aggregates and hampers size classification in the instrument. The SMPS capability to measure particles down to 3 nm is an advantage when compared with the ELPI. Ideally, both instruments should be used.

It is evident that the above direct measurements of the fractal dimension can be performed in various ways, e.g. light scattering [41–45], combining a DMA and an impactor [69], and exposed surface and mobility of the aggregates using a DMA, an ephiphanometer and a condensation particle counter [39]. Other authors have developed methods and theories that describe the fractal structure as a function of the effective density of the aggregate [66–68]. The different approaches are not in contradiction, as Smallwood *et al.* [70] have shown that the effective density is linked to the fractal scaling laws.

The coupling between the radius of gyration and the mobility diameter is nontrivial; the radius of gyration is a function of the geometric structure of the aggregate, whereas the mobility diameter is a function of the interaction between the aggregate and the carrier gas. The mechanical mobility of an aerosol particle is proportional to its radius

of gyration [34, 50, 55]. It has been argued that the scaling law holds approximately for particles down to a single monomer [50], whereas others [48, 71] say that it does not hold for very small aggregates (consisting of a few primary particles) in the free molecule regime. Papers describing light-scattering methods have the advantage that the technique measures the radius of gyration rather than the mobility diameter and thereby circumvents the nontrivial coupling between them. A disadvantage of light scattering is that scattering models are complex and may introduce uncertainties, e.g. unknown refractive indexes for the particles, skewed particle size distributions, and aggregate restructuring can influence the outcome of the measurement. In contrast, the alternative derivation [34] is based on models that describe the friction force that gases exert on moving particles. These models are straightforward when compared with models for light scattering by aerosols. Unfortunately, a quantitative comparison between the two approaches is not straightforward, since the experimental methods are based on very different measuring principles.

Comparison of the various values of the fractal dimension quoted in the literature is difficult, as aggregates that were generated with different sources or measured with different techniques tend to have different values for the fractal dimension. Generally, soot formed by internal combustion has a fractal dimension different from that produced by burners. In the absence of scanning electron microscopy (SEM) and transmission electron microscopy (TEM) micrographs, comparison is difficult. The different histories of the soot particles in internal combustion engines and burners may be responsible for the different fractal dimensions. It has already been mentioned that volatile compounds may condense and restructure the aggregates. Methane, propane and acetylene flames produce drier soots, as no heavy hydrocarbons are present. Other factors which could be responsible include soot oxidation, sintering and adsorption of gases, liquids and solids. These differences in the history of the soot particle and combustion conditions, together with the various measurement techniques, could well explain the differences in the reported fractal dimensions.

A fundamental point of concern is that the fractal dimension is a rather coarse characteristic for the fractal-like structure of soot particles. Modelling studies have shown that the fractal dimension is weakly dependent on the number of primary particles in the aggregate [19]. This, together with the different history of each individual soot aggregate in the combustion chamber, results in a distribution of fractal dimensions. The fractal dimension determined by all the direct techniques represents an average over the ensemble of aggregates. Nevertheless, studies have indicated that the fractal dimension is precise enough to distinguish between different engine loads: the lower the engine load, the higher the fractal dimension [63]. Hence, the fractal dimension is a useful tool to study the characteristics of diesel soot.

Computer simulations have shed light on the aggregation processes [17, 19, 72]. Assumptions are required concerning the nature of the aggregate motion between collisions, as well as the nature of the collision process. Such assumptions may approximate the physics of actual collisions or may be a highly idealised version of the real process. Additionally, these models will give a too optimistic prediction



for the fractal dimension of real-life soot aggregates, as they do not incorporate the history of the soot particles.

### 9.2.4 Other Techniques

For one cluster falling with velocity  $v_1$  and colliding with another moving with velocity  $v_2$ , the velocity of the resultant particle  $v_3$  is given by  $v_1' + v_2' = v_3'$ , where  $\gamma = D_f / (D_f - 1)$  [36]. Hence, if measurements of  $v_1$ ,  $v_2$  and  $v_3$  are made, the fractal dimension may be obtained. To observe the process of kinematic coagulation and to measure the settling velocities, a camera with output to a video-recorder can be used. The process of kinematic coagulation could then be traced and photographed from the recorded images. The fractal dimension for carbonaceous (butane) particles ranged from 1.61 to 2.38 with an average value of 1.97. For magnesium oxide, the fractal dimension ranged from 1.10 to 1.41 with an average value of 1.19.

Colbeck and Wu [73] have developed a relationship between aerodynamic diameter  $d_a$  and volume equivalent diameter  $d_v$  which enables the fractal dimension to be determined:

$$d_a = C d_v^{[1.5(D_f - 1)]/D_f} \quad (9.6)$$

The calculation of average, volume-equivalent, diameters was based upon total suspended particulate mass and the total number of particles, the latter determined by a condensation particle counter. Aerodynamic size distributions were determined via sedimentation. The operational assumption in this technique is that an insignificant number of the total number of aerosol particles are in the range below  $0.1 \mu\text{m}$ . The above method was utilised to determine the fractal dimension of smoke produced from a butane flame and from burning magnesium. For the former, a fractal dimension of  $1.96 \pm 0.10$  was reported and for the latter a value of  $1.08 \pm 0.03$  was obtained. The low value for the magnesium oxide aggregates can be explained by a tip-to-tip variation of the particle-cluster model. In the tip-to-tip model, two clusters with opposite charges on their tips collide. Electrostatic attraction affects their relative motion prior to collision, resulting in a more linear cluster and, thus, a lower fractal dimension. In this method, the deduced fractal dimension is an average value for the ensemble of aerosol particles.

The fractal dimension has also been determined from measurements of the terminal velocity  $V_{TS}$  of a cluster and the electric field strength  $E$  required to balance the gravitational force [74]. This technique utilises the classical Millikan cell. A plot of  $\log(V_{TS})$  against  $\log(E)$  enables the fractal dimension to be computed from the gradient:

$$\log(V_{TS}) = C + \left(1 - \frac{1}{D_f}\right) \log(E) \quad (9.7)$$

where  $C$  is a constant. This method assumes that the clusters are spherically symmetrical and they possess the same number of charges. These problems have been overcome by using a similar technique in conjunction with a photoemission method



which enables the fractal dimension for single aggregates in three dimensions to be determined [37]. In this method, a modified Millikan cell is used to obtain in-situ measurements of mass fractal dimension for single butane aggregates in the transition/continuum regime [75]. The method relies on the measurement of the aerodynamic diameter and the absolute mass of the aggregate using a photoemission method. Hence, the volume-equivalent diameter and the measured aerodynamic diameter allow the dynamic shape factor and the mobility equivalent diameter to be calculated. The latter diameter is equivalent to the hydrodynamic diameter  $d_h$ . The relationship between  $d_h$  and the radius of gyration  $R_g$  has been investigated both theoretically and experimentally and may then be used to derive the fractal dimension [76]:

$$R_g = d_h \left( \frac{D_f}{D_f + 2} \right)^{1/2} \quad (9.8)$$

The only parameters required for these determinations are an accurate estimation of the sedimentation velocity and various balance voltages in the cell. As a verification of the technique and equations, polyvinyltoluene particles were used as calibration standards. Mass fractal dimensions vary from 2.96 to 2.99 and show excellent agreement to the theoretical value of 3, hence verifying the method.

A further development of the modified Millikan cell has enabled the in-situ determination of the fractal dimension after which the aggregate may be 'plucked' from the cell by inserting a 3 mm diameter SEM aluminium stub [77]. Despite all reasonable measures to minimise the handling of the sample, it was concluded that most of the captured aggregates were lost from the stub during the SEM gold-coating evacuation cycles. However, successful fractal analysis was performed on the SEM images obtained for two aggregates. For one, the mass fractal dimension was 2.08 and the structural fractal dimension was 1.32, whilst for the other the respective values were 2.29 and 1.06. No firm conclusions could be drawn from these figures, although internal features may be lost to a greater extent for a larger mass fractal dimension and these could be omitted when calculating the structural fractal dimension.

Several studies suggested the following relationship between the projected area and number of primary particles [9, 27, 78–80]:

$$N = \varepsilon \left( \frac{A_a}{A_p} \right)^\alpha \quad (9.9)$$

where  $A_a$  is the projected area of the aggregate,  $A_p$  is the mean projected area of primary particles,  $\varepsilon$  is an empirical constant, and  $\alpha$  is an empirical projected area exponent. Koylu *et al.* [80] suggested  $\alpha = 1.09$  and  $\varepsilon = 1.15$ , whilst Oh and Sorensen [11] reported that  $\alpha = 1.19$  and  $\varepsilon = 1.81$ . The radius of gyration can also be extracted from projected properties. Studies [9, 27, 80] have suggested that the maximum projected length  $L$  can be used as a substitute of  $R_g$  (i.e.  $L/2R_g = \text{constant}$ ). Based on numerical and experimental work, Koylu *et al.* [80] suggested  $L/2R_g = 1.49$  for  $N > 100$ , whilst Oh and Sorensen [11] and Brasil *et al.* [27] found that  $L/2R_g = 1.45$

and 1.50 respectively using numerical simulations. Hence, the fractal dimension based on maximum length can be determined as follows:

$$N = k_L \left( \frac{L}{2a} \right)^{D_{fL}} \quad (9.10)$$

where  $k_L$  is the prefactor and  $D_{fL}$  is the fractal dimension when the maximum projected length is treated as the characteristic size instead of the radius of gyration. For small aggregates ( $N < 100$ ), the ratio  $(L/2R_g)$  is not constant [80], and its value is influenced by the degree of overlapping [11]. For aggregates with  $D_f < 2$ , projected properties found using TEM can be used to determine the fractal dimension with good accuracy whilst for  $D_f > 2$  the projected properties fail to predict the actual properties accurately, most likely due to primary particle screening effects [80].

Using this method, Park *et al.* [81] analysed TEM images of diesel particles and showed that the projected area equivalent diameter nearly equals the mobility diameter in the mobility size range from 50 to 220 nm. Doubly charged particles and possible ‘fragments’ were observed for the DMA-classified particles. The fractal dimension calculated from the TEM images of mobility-classified aggregates  $D_{fL}$  was 1.75. The fractal dimension was also determined using particle mass and mobility size [50, 53] and a value of 2.35 was reported. These authors showed that the relationship between the projected area diameter and the maximum projected length can be used to find the relationship between  $D_{fL}$  and fractal dimension determined from mobility–mass measurements. In this case:

$$D_{fL} = \frac{D_f}{1.26} \quad (9.11)$$

By using Equation (9.11) with the measured value of the fractal dimension determined from mobility–mass measurements one obtains  $D_{fL} = 1.87$ . The difference between the two values can be accounted for by experimental error and the assumption that the projected area diameter nearly equals the mobility diameter.

Wentzel *et al.* [28] also used the projected maximum length method in order to determine the morphology of various soots. The fractal properties of 37 diesel soot aggregates were determined from TEM images. The average fractal dimension  $D_{fL}$  of diesel soot derived from TEM was  $1.70 \pm 0.13$ . A second independent approach to determine the fractal properties of soot, based on computer simulations of the aerosol dynamics, was also used [82]. A good reproduction of the time evolution of mass and number concentrations and of the mobility size distribution was achieved. The primary particle diameters obtained from the computer simulations ( $25 \pm 3$  nm for diesel soot) were in excellent agreement with the TEM results. The fractal dimension of diesel soot calculated by computer simulation was  $1.9 \pm 0.2$ , consistent with the value obtained from TEM image analysis.

Fractional Brownian motion (FBM) theory can, because of its self-similarity and long correlation properties, provide both a description and a mathematical model for many highly complex natural shapes and textures. FBM analysis can derive the fractal parameter, the Hurst coefficient  $H$ , to represent the characteristics of a nonstationary

zero-mean Gaussian random function such as the fluctuation of soot aggregate textures. The value of  $H$  ranges from zero to one and is related to the fractal dimension by  $D_f = D_e + 1 - H$ . The parameter  $D_e$  represents the Euclidean dimension, which equals one for linear data. Luo *et al.* [83] first extracted the multiscale  $H$  values to represent the fractal texture of airborne particles by applying FBM combined with the Fourier-domain maximum likelihood estimator. They then explored the application of FBM analysis to SEM micrographs of soot aggregates emitted by a dynamometer [84]. By directly quantifying the surface texture of fractal-like aggregates to extract their Hurst coefficients, the fractal dimension of such particles was found to be in the range 1.6 to 1.7. The impact of image properties on  $D_f$  measurements due to digital image processing and data recording was also investigated. A twofold change in SEM magnification size gave rise to a 7 % deviation in the fractal dimension, and scaling up from the original image increased the discrepancy compared with miniaturisation. Brightness was not a serious interference factor, as its variance did not exceed the grey level value of 80. These results give more confidence to earlier measurements based on image analysis.

Gwaze *et al.* [85] have recently shown that the fractal dimension of aggregates from biomass combustion is, on average, 1.83 and so consistent with aggregate formation by DLCA. Importantly, the fractal dimension was determined by three different techniques:  $D_f = 1.84 \pm 0.05$  from projected surfaces in the SEM images;  $D_f = 1.80 \pm 0.13$  from the relationship between mobility and number of primary particles; and  $D_f = 1.83 \pm 0.05$  from the mass and radius of gyration relationship. Although each technique has its limitations, this paper does give confidence in the different approaches to the determination of the fractal dimension of aggregates.

## 9.3 APPLICATIONS

### 9.3.1 Combustion Aerosols

Diesel particulate emissions are a major source of fine and ultrafine atmospheric particles. These particles are of current interest due to their suspected adverse health effects and their impacts on the Earth's radiation balance, visibility impairment, and atmospheric chemistry. Diesel particles are typically aggregates of fine primary particles coated with condensed organic films. The most common technique to characterise the structure of the aggregates is TEM, which provides projected two-dimensional properties of aggregates. Thus, the actual structural properties of aggregates are inferred from the projected properties. However, few studies of the structural properties of aggregates produced from diesel engines have been reported.

Comparison of fractal dimensions reported in the literature is difficult, because soot that was generated with different sources or measured with different techniques tends to have different values for the fractal dimension. Cai and Sorensen [71] found

a fractal dimension of 1.8 for soot that was generated with a methane burner and measured by light scattering, whilst Kütz [86] found 2.13 for spark-generated soot. Luo *et al.* [83] found values in the range 1.6–1.7. The difference with diesel soot suggests that soot particles formed by internal combustion have a different fractal dimension than soot generated from burners. Kütz and Schmidt-Ott [69] report that condensation of vapour on aggregates induces restructuring, leading to denser, higher  $D_f$ , structures. Burtscher [61] and Lepperhof *et al.* [87] found evidence that adsorption of hydrocarbons on soot particles increases the fractal dimension. Methane- and acetylene-flame-generated soots tend to be much drier because no heavy hydrocarbons are present in these flames. Nevertheless, the studies by Skillas *et al.* [63] showed that the fractal dimension is precise enough to distinguish between different engine loads: the lower the engine load, the higher the fractal dimension. They suggested that as the load increases the air/fuel ratio decreases and more primary soot particles are produced. At low loads, the fractal dimension is close to 3 and this reduces to 2.1 at higher loads. For low engine loads, the agglomeration process is mainly governed by monomer–cluster aggregation, whereas cluster–cluster agglomeration significantly competes with monomer–cluster aggregation at high loads, lowering the fractal dimension. In contrast to this, work by Park *et al.* [53] and Maricq and Xu [68] found a small systematic increase in fractal dimension with decreasing engine power. A closer examination of the Skillas *et al.* [63] data reveals that, except for a few points at low load, the majority of their data lie within  $D_f = 2.4 \pm 0.15$ . This general consistency in fractal dimension also extends to spark-generated soot, where Schleicher *et al.* [62] found  $2.05 < D_f < 2.35$  from DMA/low-pressure impactor measurements.

Colbeck *et al.* [88] analysed various smokes and found textural fractal dimensions in the range 1.12–1.27 for petrol, diesel, fuel, oil, paraffin, butane and wood (Table 9.2), whilst the mass fractal dimensions were 2.04, 1.88, 1.97 and 2.35 for diesel, fuel oil, butane and wood respectively. This wide range represents a

**Table 9.2** Fractal dimensions of different smokes [88]. Reprinted from *J. Aerosol Sci.*, Vol. 28, Colbeck, I., Atkinson, B. and Johar, Y., The morphology and optical properties of soot produced by different fuels, 715–723. Copyright (1997), with permission from Elsevier.

Fuel	Fractal dimension	
	Textural	Mass
Petrol	1.27	—
Diesel	1.25	2.04
Fuel oil	1.15	1.99
Paraffin	1.19	—
Butane	1.25	1.97
Wood	1.12	2.35

correspondingly broad variation in structure and suggests that chemical composition might affect the final structure. Chakrabarty *et al.* [89] also found a range of fractal dimensions for different wildland fuels (sagebrush, poplar wood, ponderosa pine wood, dambo grass, ponderosa pine needles and white pine needles). From SEM images, the fractal dimension was determined from the relationship between the number of primary particles per aggregate and the radius of gyration (Equation (9.10)), yielding values between 1.67 and 1.83. The textural fractal dimension was also obtained and reported to be in the range 1.10–1.19. It should be noted that the presence of collapsed semi-liquid aggregate chains in some of the samples suggests the presence of organic coatings on some of the black carbon cores. Liu *et al.* [90] studied the morphology of flame-generated submicrometre aerosols by characterizing both fly ash generated in a pilot-scale coal combustor and controlled-composition inorganic aerosols. They found that the fly ash was fractal-like with mass fractal dimensions of 1.9–2 and prefactors (see Equation (9.1)) of 1.1–1.5. The morphology of submicrometre, flame-generated inorganic aerosols is known to be fractal-like. Flame-generated silica, magnesia, sodium-doped silica, and magnesium-doped silica produced under identical conditions were also fractal-like with mass fractal dimensions 1.7–1.8 and prefactors of 1.6–1.8. No dependence of these structural parameters on chemical composition, flame residence time, or particle number density was observed over the ranges considered. Changing chemical composition did, however, lead to order of magnitude changes in primary particle diameter without any corresponding change in aggregate structure. These findings are consistent with a growth process governed in the late stages by cluster–cluster aggregation. Further, they indicate that for flame-synthesised materials produced in the overall decreasing temperature gradient characteristic of coal combustors and industrial flame reactors, the aerosol aggregate structure will not be affected by changes in chemical composition under conditions of coalescence-limited growth. The various values of the fractal dimension for compounds associated with ash derived from coal combustion are given in Table 9.3. Most measurements are consistent with a value of approximately 1.8 reported in computer simulations of the coagulation of aggregates in three dimensions in both the free molecular and continuum regimes [17, 95]. However, fractal dimensions of approximately 2.5 are expected when growth is dominated by the diffusion of primary particles to an existing aggregate [62]. The values for MgO show considerable variation, and this is a consequence of the particle generation method. The combustion conditions were closely controlled in the work of Liu *et al.* [90], resulting in well-defined, uncharged, primary particles with an average diameter of 5 nm. On the other hand, the combustion of magnesium ribbon produced polydisperse charged primary particles [36, 73].

The ability to characterise aggregate morphology quantitatively, through the fractal dimension, has motivated research on aggregate structure and led to the discovery of ‘superaggregates’, i.e. structures with fractal dimensions that differ from the substructures [96–98]. Using small-angle light scattering, in laminar diffusion flames for a wide range of heavily sooting fuels, a fractal dimension of approximately

**Table 9.3** Fractal dimensions for compounds found in fly ash [90]. Reproduced with permission of American Association of Aerosol Research 'The effect of chemical composition on the fractal-like structure of combustion-generated inorganic aerosols, *Aerosol Sci. Technol.*, **33**, 459–469'. Copyright 2000. Mount Laurel, NJ.

Material	Fractal dimension	Synthesis method	Measurement method	Reference
MgO	$1.08 \pm 0.03$	Mg ribbon combustion	Settling, SEM	[73]
MgO	$1.19 \pm 0.02$	Mg ribbon combustion	Settling	[36]
TiO <sub>2</sub>	$1.66 \pm 0.67$	Alkoxide thermal decomposition	TEM	[57]
SiO <sub>2</sub>	1.7–1.9	Commercial fumed silica	TEM	[4]
SiO <sub>2</sub>	$1.49 \pm 0.15$	Seeded premixed flame	Light scattering	[91]
SiO <sub>2</sub>	$1.84 \pm 0.08$	Commercial fumed silica	Light scattering	[92]
SiO <sub>2</sub>	$2.52 \pm 0.05$		Light scattering	[93]
Al <sub>2</sub> O <sub>3</sub>	1.54	Seeded counter diffusion flame	TEM	[94]
Bituminous coal	$2.05 \pm 0.06$	Pilot-scale combustion facility	TEM	[90]
SiO <sub>2</sub>	$1.67 \pm 0.07$	Nebulising precursor-containing liquid solutions in flame	TEM	[90]
SiO <sub>2</sub>	$1.71 \pm 0.15$	As above	TEM	[90]
SiO <sub>2</sub>	$1.70 \pm 0.03$	As above	TEM	[90]
MgO	$1.81 \pm 0.12$	As above	TEM	[90]

1.8 was obtained, which is a result of a three-dimensional DLCA process. With increasing height above the burner, which corresponds to increasing time for the soot to grow, a very intense, second phase appears. This scattering behaviour may be interpreted to indicate a phase of around 12  $\mu\text{m}$  soot with a fractal dimension of  $\sim 2.6$  for length scales of 1.2–12  $\mu\text{m}$  and  $\sim 1.8$  for scales smaller than 0.3  $\mu\text{m}$  down to the primary particle size (25 nm as determined by TEM). These results support a scenario in which supramicrometre aggregates are created by a percolation of the submicrometre aggregates with mass fractal dimensions similar or equal to 1.8. For less sooty flames, only the submicrometre soot is seen. These measurements have been corroborated by computer simulation [99]. As agglomeration evolves, the largest cluster develops a hybrid structure with mass fractal dimension similar or equal to 2.6 over large length scales, whereas the early time dilute-limit fractal structure is frozen at smaller length scales. The largest cluster is thus an aggregate of smaller aggregates with a different fractal dimension (see Figure 9.5). Current theories for aggregation kinetics involving the Smoluchowski equation are not adequate to describe these dense systems. Hence, both experimental and theoretical research are needed for this cluster dense regime. While there has been some success in modelling the growth dynamics of the aggregates, quantitative results are lacking.

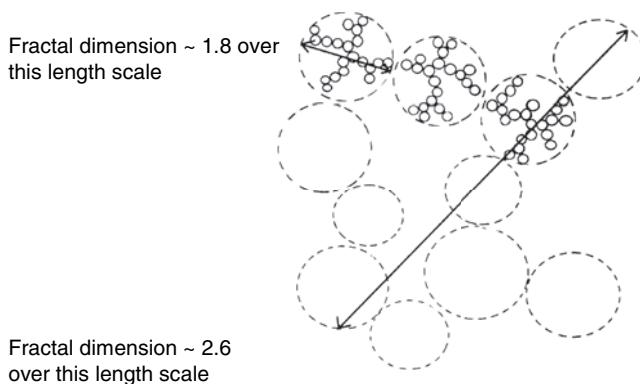


**Figure 9.5** Superaggregate: an aggregate of one morphology composed of smaller aggregates of different morphology [96]. Reproduced with permission of Elsevier.

### 9.3.2 Atmospheric Aerosols

Ambient air contains varying fractions of carbonaceous particulates and aggregates, mixtures of carbonaceous particulates and inorganic crystalline particulates often composed of thousands of nanocrystals [100]. The morphology of atmospheric aggregates influences their effects on public health, water vapour nucleation, and absorption and scattering of light. For example, aggregate transport rates determine their atmospheric residence time and patterns of deposition in the lung, but mathematical models of aggregate transport and light scattering are usually based on the assumption that the primary particles that compose the aggregates are monodisperse [56].

Despite numerous algorithms and experimental techniques for determining the fractal dimension of aerosols, a quantitative description of atmospheric aerosols is rare. Those which have been reported have involved image analysis of ambient aerosols collected on a filter or TEM grid [23, 101–103]. Kindratenko *et al.* [102] concluded that fractal analysis allows the unequivocal identification of particles source. For samples from Siberia they quote a textural fractal dimension of  $1.09 \pm 0.015$  for fly ash and  $1.04 \pm 0.015$  for soil. However, the majority of the fly ash particles examined were spherical and did not exhibit any fractality. This suggests that, in this case, fly ash was formed by different mechanisms.

Fractal analysis can also provide information on the formation processes of aerosols [23]. A range of mass fractal dimensions were reported for carbonaceous aerosols in Phoenix, Arizona, indicating variations of DLA. Aggregates were divided into groups: those with  $D_f < 2$  and those with  $D_f > 2$ . For the former, a mean fractal dimension of  $1.65 \pm 0.15$  was reported. For the other aggregates there was evidence that restructuring may have occurred [23]. The range of fractal dimensions found forms a continuum from 1.35 to 1.89. Cluster–cluster aggregation is the dominant



formation process for  $1.7 < D_f < 1.9$ , whereas formation can be explained by the tip-to-tip model of cluster-cluster aggregation for aggregates with  $D_f = 1.35$  to  $1.6$ . Fractal dimensions for the Phoenix aerosol appear to be independent of aggregate size, but morphology is affected by factors such as fuel composition and air-to-fuel ratios. Hence, it may be possible to use fractal analysis for source apportionment of aerosols. It should be noted that the aggregates in this study were relatively large in size (of the order of  $1\text{ }\mu\text{m}$ ), whereas more recent studies revealed smaller aggregates (of the order  $100\text{ nm}$ ). These ultrafine aggregates, which make up the greatest proportion of the aerosol by number, have much less possibility for variation in space-filling structure than large aggregates.

Dye *et al.* [104] determined the fractal dimension of aggregates at a roadside and background site in Plymouth, UK. The aerosol was classified into aggregate and non-aggregate groups. At the roadside and background site, aggregate particles accounted for 94 % and 89 % respectively of the particles analysed. Mass fractal dimensions of  $1.56 \pm 0.09$  and  $1.57 \pm 0.09$  and boundary fractal dimensions of  $1.15 \pm 0.09$  and  $1.13 \pm 0.08$  were measured for the roadside and background sites respectively. This morphology change may be due to the inclusion of particles from other nonaggregate sources that have a low fractal dimension or, more probably, it is indicative of a smoother, aged roadside aerosol at the background site. The results indicate an increase in boundary fractal dimension with aggregate size at both sites. The greatest difference between the sites occurs in the 120–220 nm size range, which suggests that the change from fresh roadside aggregates to aged, compacted and smoothed background aggregates is important in the size range above 120 nm.

These conclusions were supported by Xiong and Friedlander [105], who analysed 102 particles collected in the Los Angeles area. This work showed that mass fractal dimension increased from near one to more than two as the number of primary particles making up the aggregates increased from 10 to 180. In one set of measurements, the fraction of the particles present as aggregates was about 60 % for particles with aerodynamic diameters between 50 and 75 nm and 34 % for the range 75 to 120 nm. The primary particles that make up atmospheric aggregates are more polydisperse than soot aggregates generated from a single laboratory source, an ethane-oxygen flame. Most measurements were made in the Los Angeles area, where the aggregates may represent a signature for diesel emissions. Rural aggregate concentrations in the size range 50 to 120 nm were less than 1 % of the concentrations at urban sites. The increase in mass fractal dimension with  $N$  can be explained by the aggregation of short chains with low mass fractal dimension values to form larger aggregates with higher mass fractal dimension. Such an increase has been observed in computer simulations of the aggregation of an aerosol cloud of unitary particles in a fixed volume of gas [106]. At rural sites, values of the mass fractal dimension showed no trend with  $N$ , and were in the range 1.5–2 as expected for cluster-cluster aggregation. This result may be due to the absence of fresh sources of aggregates containing short chains. Mullholland *et al.* [106] concluded that inferences can be drawn concerning atmospheric aggregation dynamics from measurements of aggregate fractal properties, but simulations



of aggregate dynamics should take into account the distribution of the mass fractal dimension as well as aggregate size.

TEM images were used to calculate the average surface area of the aggregates, which was estimated by summing the surface area of the primary particles composing the aggregates and dividing by the number of aggregates. Each stage on an impactor fractionates aerosols into a different size range based on aerodynamic diameter. For aggregates on stage 8 of the impactor (size range 50–75 nm) the average surface area was  $0.188 \mu\text{m}^2$ . A sphere of unit density depositing on the same stage would have a surface area of  $0.031 \mu\text{m}^2$ . Thus, the area of a spherical particle of equivalent aerodynamic diameter would underestimate the aggregate surface area by approximately a factor of six. For the largest aggregate investigated, the value of the surface area was 26 times that of the value corresponding to the aerodynamic diameter. These results have implications for human health, as the high surface area of the aggregates provides adsorption sites for toxic substances, such as polycyclic aromatic hydrocarbons.

Various uncertainties are associated with these measurements. A low-pressure impactor was used to determine the aggregate concentration. This method assumes that the 50 % aerodynamic cut-off diameter of the impactor is a step function, above which the collection efficiency is 100 %. It was further assumed that the aerodynamic cut-off diameter is equivalent to the electrical mobility diameter, which, on theoretical grounds, is not expected to be true for aggregates. There is also a small uncertainty in the concentration measured with the DMA, associated with the adjustments for charging inefficiencies and sampling losses. It is also possible that aggregates break up in the impactor, giving a high count compared with the atmospheric concentration.

The above studies used collection methods that may have changed the morphology of the aerosol during collection. McDonald and Biswas [107] captured particles via size-independent electrostatic precipitation at two sites in St Louis. For the aggregates examined, the mass fractal dimension ranged from 1.39 to 1.89 with a mean value of 1.69. The temporal variation in mass fractal dimension was also determined and found to be 1.65 in the morning, 1.49 around midday and 1.87 in the evening. It is suggested that variation in vehicle type may be responsible, with cars dominating traffic flow in the early morning and evening and trucks more abundant during the day. McDonald *et al.* [108] determined the fractal dimension of atmospheric aerosol from four sites in Greater Cincinnati. At sites in the vicinity of major highways the mass fractal dimension was of the order  $1.60 \pm 0.09$ , whilst at a site not influenced by traffic-type combustion emissions the mass fractal dimension was  $1.41 \pm 0.09$ . At this latter site the aggregate particles mostly result from aggregation of freshly nucleated particles. It appears likely that fractal analysis will continue to be developed and will provide an invaluable tool for the identification and apportionment of particles.

Johnson *et al.* [109] sampled atmospheric particles of diameter 0.2–2  $\mu\text{m}$  in the Mexico City Metropolitan Area. Although they didn't determine the fractal dimension, they noted that the aerosols collected in city traffic were almost entirely carbonaceous, consisting of soot aggregates with liquid coatings suggestive of unburned lubricating

oil and water. Processing of the soot by ammonium sulphate occurs rapidly, resulting in more compact, internally mixed particles. This has important implications, as the internally mixed nature of processed soot particles is expected to affect the heterogeneous chemistry of the soot surface, including the interaction with water during wet removal. Additionally, the observation of an oil coating on fresh soot particles should be examined more closely, both in terms of reactivity and consequences for human health.

The studies to date provide only snapshots for a few sites. Much more data will be needed to characterise atmospheric aggregates sufficiently to permit reliable estimates of their large-scale effects. However, the suggestion that the fractal dimension varies from urban to rural locations has public health implications. Urban aggregates have a large surface area and a small aerodynamic diameter [13]. Particles with the same size in background air have a lower fractal dimension and, hence, a smaller surface area and larger aerodynamic diameter. Penetration of particles into the respiratory system is governed by the aerodynamic diameter, and so urban aerosols will penetrate more deeply, with a larger surface area, than more aged aerosols at background sites.

### 9.3.3 Restructuring

Despite an immediate need to quantify the lifetime of soot in the atmosphere better, relatively little is currently understood regarding the processing of soot in the atmosphere, particularly in urban environments. Aggregate restructuring has been attributed to a number of mechanisms, including humidity, tempering, electrostatic processes, condensation, evaporation, compaction, internal rearrangement, coagulation, pressure and wind shear.

#### 9.3.3.1 Humidity-Induced Restructuring

Freshly emitted soot is hydrophobic. However, aging processes such as coagulation, condensation, and chemical reactions can occur. Once sufficient water-soluble material has coated the soot's surface, the particles become globally hydrophilic. The atmospheric lifetime of hydrophilic aerosols is considerably shorter than that of hydrophobic aerosols. Hence, the aging process of soot is one of the key uncertainties governing its lifetime, burden, and radiative forcing. Laboratory studies demonstrate that aged soot attracts and retains water, and can be efficiently removed from the troposphere by entrapment in existing liquid cloud droplets or by activation as cloud condensation nuclei [110].

Some measurements have indicated that there may be modification of fractal morphology by atmospheric processes [111, 112]. As a consequence of humidity cycling, the morphology of the tenuous aggregates becomes more compact and 'spheroidal', resulting in an increase of  $D_f$ . Jullien and Meakin [113] concluded that such a phenomenon would be important in the consideration of subsequent aggregate atmospheric lifetimes and optical properties. Various laboratory experiments have demonstrated the existence of a number of different mechanisms by which aerosols

can be restructured. Some mechanisms investigated are: (1) temperature gradient and mechanical shear in colloids [114]; (2) the tempering of silver aerosols ( $D_f \approx 2.18$ ) at 80 to 270 °C into coalesced spheres for which  $D_f \approx 3$  [50]; (3) electrostatic-induced restructuring of single in situ butane smoke aggregates in discrete steps to values as high as  $D_f \approx 2.2$  [38]; and (4) compaction/internal rearrangement [52]. Another mechanism that may be of importance for larger aggregates in the supermicrometre range is the effect of wind shear. However, such investigations under atmospheric conditions are currently unknown to the author.

Humidity-induced restructuring under high humidities or low supersaturations, however, remains more thoroughly investigated than other mechanisms to date. An investigation by Hallett *et al.* [112] noted a moderate restructuring effect on acetylene smoke, while a type of aviation fuel exhibited virtually no effect. Compaction was attributed to capillary forces acting upon branched chains, facilitated by the condensation of humidity on hydrophilic components of the aggregate. Later studies used fractal analysis to quantify the degree of restructuring as a function of relative humidity. Under humid conditions, Colbeck *et al.* [115] observed an increase in the fractal dimension from  $D_f \approx 1.8$  to 2.0–2.5 with time for butane smoke aggregates. A curve-fit analysis of their data (Figure 9.6) suggests an exponential increase of  $D_f$  with relative humidity. For typical cloud supersaturations of 1 %, a value  $D_f \approx 2.0$  is

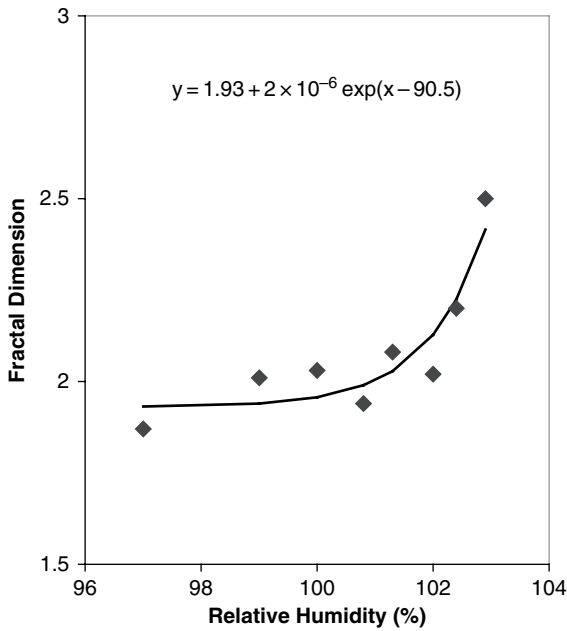


**Figure 9.6** Mean values of the fractal dimension for butane smoke aged for 4 h and then subject to various relative humidities and supersaturations (data from [115]).

implied for up to five humidity cycles. A further humidity cycling study by Huang *et al.* [21] investigated the restructuring of diesel aggregates in an environmental SEM. Increases in the boundary fractal dimension for three different sulphur-content fuels were observed, where the high-sulphur case (0.084 wt % S) surprisingly exhibited no significant increase and was attributed to possible pre-sampling restructuring. Ramachandran and Reist [116] found that, when an aerosol composed of irregularly shaped aggregates is subject to condensation followed by evaporation, the aggregates change from a branched, chainlike structure to a more regular, near-spherical or clumplike structure reflected by a decrease in the structural fractal dimension. The textural fractal dimension remains constant because the primary particles, of which the aggregates are composed, do not change in shape. The degree of supersaturation and the number of condensation–evaporation cycles that the aerosol undergoes are major factors that influence morphological change. Even at low supersaturations, increasing the number of condensation–evaporation cycles makes the aggregates more regular and thus decreases the structural fractal dimension.

To investigate the influence of the hygroscopicity, comparative measurements between pure soot aerosol and soot particles pretreated with *n*-butanol vapour were carried out [117]. Electron microscope analysis showed that the size distribution of initially pure soot aerosol did not shift significantly after the interaction with water droplets, whereas the size distribution of *n*-butanol-processed soot aerosol shifted to smaller sizes with the mean size reduced by a factor of three. This size redistribution could be explained by the assumption that wettable particles penetrate inside a water droplet during the coagulation, and, by being uniformly squeezed by capillary forces and subsequent water evaporation, become more compact and, consequently, smaller. The structure analysis data have shown that the fractal dimension of soot aggregates increased from  $1.72 \pm 0.15$  to  $1.87 \pm 0.15$  as a result of such densification of the microstructure [117]. The transformation will be more pronounced in clouds and fogs, as the characteristic size of atmospheric water droplets is substantially larger than the droplets used in this study.

These studies illustrate the ease with which aggregates can be restructured by humidity cycling. The tenuous nature of supermicrometre aggregates has been further demonstrated in the restructuring of individual particles suspended in a modified Millikan cell. Various degrees of compaction could be induced with limiting values of  $D_f$  as high as 2.2. As each aggregate exhibited different limiting values, it may be suggested that restructuring mechanisms are not only dependent on external influences (i.e. humidity cycling, etc.), but also on individual aggregate morphology. To what extent humidity-induced restructuring is relevant to atmospheric processes would require further investigation to measure  $D_f$  under realistic conditions.

Direct in-situ atmospheric observations of humidity-induced restructuring are difficult to obtain and remain sparse. Most evidence for humidity processing has come from laboratory and ground-based measurements. Trials on the humidity processing of atmospheric samples attributed a decrease in size to the restructuring of freshly emitted smoke [69]. In the same trials, laboratory experiments indicated that aggregate

size may be important in the degree of final restructuring obtained. While size was not directly measured, the degree of restructuring increased for larger smoke aggregates, a result supported in later experiments [38]. A humidity processing study by Weingartner *et al.* [118] on petrol- and diesel-derived smoke demonstrated a small degree of restructuring for aggregates with a mobility diameter of  $\sim 100$  nm at humidities as low as 50–60 %. This may give an indication of the initial restructuring possible under typical humidity conditions encountered in the boundary layer. Restructuring at  $< 95$  % relative humidity is also implied for the results of Colbeck *et al.* [115] in Figure 9.5, where it is suggested that  $D_f$  increases from an initial value of 1.8–1.9 to  $\sim 1.9$ –1.95. Such conclusions, however, need more verification due to the overall sparseness of data and diverse experimental conditions.

The possible degree of cloud-processing-induced restructuring has been hinted at by the absence of tenuous combustion aggregates in atmospheric samples [119, 120]. Katrinak *et al.* [23] reported many restructured aggregates. Various restructuring mechanisms were postulated, including humidity processing, aging, and combustion conditions. Some aggregates exhibited coatings, determined by electron energy-loss spectroscopy to contain sulphate and nitrate compounds, which may have been present during formation or formed subsequently through coagulation/photochemical activity.

The most intermediate effect of restructuring would be to alter the aggregate radiative properties. Whether this is significant on a global basis remains to be assessed. Traditionally, Mie theory, which is directly applicable to spherical particles and may be extended to other regular shapes (e.g. cylinders, ellipsoids), has been used to predict aerosol optical properties. However, it is not directly applicable to fractal clusters or other complicated particle shapes. The erroneous application of Mie theory has led to predictions of optical properties that are strongly dependent on the extent of particle aggregation. However, because the coagulating carbonaceous particles are not spherical, they maintain a larger effective surface area than spheres would and, thus, the optical properties remain largely unaffected by the increasing particle size. There are several techniques available for calculating the optical properties of aggregates. A rigorous discussion of the techniques is beyond the scope of this chapter, and the reader is referred to either Chapter 2 or Sorensen [43] for further details.

As shown by Zuberi *et al.* [110], chemically aged soot particles can become significantly hydrophilic and have a strong attraction for water. Increased hydrophilicity has strong implications on its lifetime in the atmosphere. Hydrophilic soot particles can be entrained inside existing liquid cloud droplets, leading to efficient removal by wet scavenging. At high supersaturations, these particles may also act as cloud condensation nuclei and, consequently, be removed by rainout. If cloud condensation nuclei concentrations rise, then competition for the total available liquid water may result in smaller cloud particles and, hence, increased scattering of radiation and overall cooling effects. The entrainment of highly absorbing black soot cores within liquid droplets may lead to a local warming and evaporation of the clouds, known as the cloud-burning effect [2].

In summary, the typical final restructured value  $D_f \approx 2.0$ – $2.2$  for laboratory results may be compared with a value  $D_f \approx 2.2$  for simulations [72, 113]. In this model, diffusion-limited cluster–cluster aggregates restructured in discrete steps to  $D_f \approx 2.2$ , after which further increase was not possible. The situation in the atmosphere is more complex, and there probably exists a spectrum of  $D_f$  values in the range 1.8 to 2.0–2.2, dependent mainly on aggregate age and meteorological conditions encountered.

### 9.3.3.2 Thermal Restructuring

As was mentioned briefly in Section 9.2.3, aggregates can adopt more compact conformations when heated, a phenomenon known as thermal restructuring. Weber and Friedlander [51] have shown that, for silver aggregates, the mobility diameter begins to decrease at about 100°C and levels off around 350°C when the aggregates have reached a close-packed state with a fractal dimension of approximately 3. A similar behaviour, although at different temperatures, has been observed for other materials [52]. Experiments have shown that the smaller the particle, the lower the compacting temperature. This is a consequence of the well-known phenomenon of melting-point depression, which states that the melting point is lowered as the diameter of the particle is decreased.

Restructuring is driven by the deviation of the free energy of the low fractal dimension aggregate from the value for the compact state. The rate of restructuring is an activated process, and the restructuring energy can be found from an Arrhenius plot [51]. The activation energy for silver was similar to the bond energy calculated from the bulk Hamaker constants. This indicates that restructuring most likely occurs when aggregate branches rotate around the weakest bonds, and not from single primary particles detaching and relocating.

### 9.3.3.3 Elastic Properties

Another aspect of chain aggregate behaviour is their elastic properties. This phenomenon was first reported by Friedlander *et al.* [121], who observed that titania chain aggregates stretch under tension and contract when the tension is relaxed. They generated titania chain aggregates by thermal decomposition and deposited them on a transmission electron microscope grid. A typical aggregate selected for study with a fractal dimension of approximately 2.3, was about 250 nm in length and composed of a few hundred individual primary particles about 7 nm in diameter. After 10 to 20 min in the electron beam, a hole developed in the film near the aggregate. As the hole grew, the aggregate which bridged the gap began to stretch but remained connected to both sides of the receding film. After stretching up to 90 % the aggregate broke loose from one side and contracted to a folded chain on the other side of the hole. Chain aggregates made of other transition metal oxides showed similar behaviour [122, 123]. However, aggregates composed of relatively large primary particles, about 36 nm in diameter, did not exhibit the phenomenon, suggesting that it may be limited to chains composed of primary particles probably less than 10–20 nm. Suh and Friedlander [123]

examined aggregated composed of carbon. Initially, the stretching of the chains took place by the unravelling of kinks along the aggregate. Reversing the system led to folding of the extended chain without showing elastic behaviour. When stretching was resumed, the chain eventually became taut and then broke at the site of the smallest primary particle. The elastic behaviour is probably associated with local folding of chain segments due to van der Waals forces. Under tension, folded chains straighten; but when the tension is relaxed the folds tend to reform, but not reversibly. Rotation and sliding probably occur at the boundaries between particles during stretching.

These phenomena may have significant potential for the development of ductile or elastic ceramics and could play a role in the action of nanoparticle additives such as fumed silica and carbon black, used to improve the properties of rubber.

### 9.3.4 Heterogeneous Reactions

Heterogeneous reactions on combustion-generated fractals may well be of importance for the transformation of atmospheric pollutants. According to their surface properties, such particles are suspected, and in a number of cases have been shown, to interact with gaseous environmental chemicals, radicals, and other reactive intermediates. Of particular interest are the exhaust emissions from aircraft, where measurements have shown that not only carbonaceous particles contribute to contrail formation, but also that the aerosol surface areas are of central importance for ozone changes caused by heterogeneous chemical reactions [124, 125]. Aircraft impact studies have motivated laboratory investigations of heterogeneous soot reactions. In particular, heterogeneous reactions of nitrogen oxides on soot surfaces have attracted considerable attention during recent years since they may have an influence on the  $\text{NO}_x/\text{HNO}_3$  ratio and on the  $\text{HO}_x$  balance of the atmosphere [126–128]. Reactive uptake of nitrogen species and ozone on soot has been proposed to explain discrepancies between observations and model calculations [126, 127, 129]. Recent work by Kleffmann and Wiesen [130] suggests that the reactions of  $\text{HNO}_3$  and  $\text{HNO}_3 + \text{NO}$  on soot surfaces are unimportant for a ‘renoxification’ of the atmosphere and do not represent an atmospheric  $\text{HO}/\text{NO}$  source, as earlier laboratory data had been determined under experimental conditions not prevailing in the atmosphere, i.e. very high reactant concentrations, thus leading to unrealistic conclusions.

For in-depth studies, knowledge of the transport properties and information on the surface area of fractal particles is required. Often, the surface area of soot aggregates is based on the sum of the surfaces of the monomers comprising the aggregate, or aggregates are assumed to be spherical. This issue has been addressed by Coelho *et al.* [131], who developed a detailed framework for calculating uptake rates of gases on fractal particles. They validated their model against laboratory data and found that model-calculated surface/mass ratios of soot aggregates were consistent with laboratory measurements. By not taking the fractal nature into account, derivations of the aggregate mass and the surface area enhancement factor were in error by at least an order of magnitude.



For a single aggregate, the mass flux  $J_f$  of a diffusing species may be given by

$$J_f = 5.65 DC_\infty D_f R_g \left(1 + \frac{1}{\text{PeDa}}\right)^{-1} \quad (9.12)$$

where

$$\text{PeDa} = \frac{K_s R_g}{D} \frac{2.55}{D_f} \left(\frac{R_g}{a}\right)^{D_f-2} \quad (9.13)$$

and  $D$  is the gas diffusion coefficient of the species,  $K_s$  is the surface reaction rate constant,  $\text{PeDa}$  is the Peclet–Dahmköhler number and  $C_\infty$  is the concentration away from the aggregate. By incorporating a factor for the geometric standard deviations, these equations may be extended to a lognormal distribution of aggregates [131].

This flux may be compared with that for a sphere of radius  $R_g$ . In the diffusion-limited regime ( $\text{PeDa} \gg 1$ ):

$$\frac{J_f}{J_{\text{sphere}}} = 0.45 D_f \quad (9.14)$$

and the aggregate effectively acts as a sphere of radius equal to the radius of gyration multiplied by roughly half of the fractal dimension. In the reaction-limited regime ( $\text{PeDa} \ll 1$ ) the ratio is

$$\frac{J_f}{J_{\text{sphere}}} = 1.15 \left(\frac{R_g}{a}\right)^{D_f-2} \quad (9.15)$$

For a fractal dimension of two, aggregates act approximately as spheres with a radius equal to the radius of gyration. However, for values that are different from two,  $J_f$  and  $J_{\text{sphere}}$  differ significantly, as shown in Figure 9.7.

Bekki *et al.* [132] used the above theory to investigate the uptake of chemical species on atmospheric soot in the lower stratosphere and the boundary layer. The uptake was found to be mostly reaction limited, justifying the assumption of proportionality between the soot surface area and the uptake rate. However, the uptake occurs in the transition regime for the relatively compact aggregates.

The mass of a fractal  $m_f$  may be approximated by

$$\frac{m_f}{m} \approx \left(\frac{R_g}{a}\right)^{D_f-3} \quad (9.16)$$

where  $m$  is the mass of a sphere of radius  $R_g$ . For soot aggregates found in the upper troposphere/lower stratosphere, the average radius is about 100 nm, whilst the monomers are of the order of 20 nm [133]. For studies which have ignored the fractal morphology and assumed spherical particles, the masses of individual aggregates could have been overestimated by a factor of 5–10 (Figure 9.8).

The surface area enhancement  $E_s$  is a measure of the enhanced area of an aerosol when its geometry deviates from a sphere. It can be approximated by

$$E_s \approx 1.2 \left(\frac{R_g}{a}\right)^{D_f/3} \quad (9.17)$$



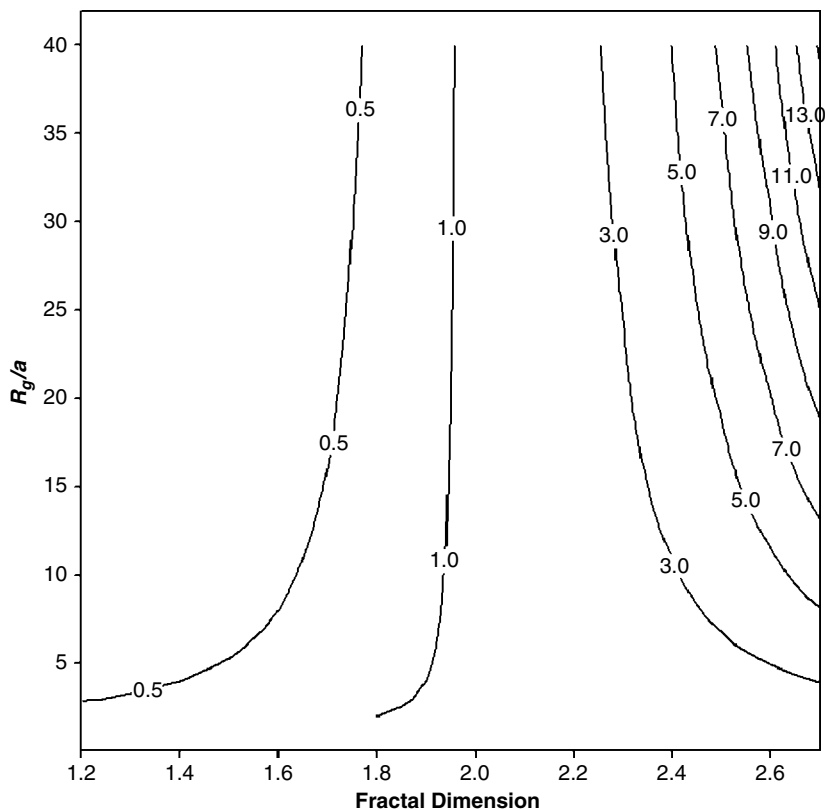


**Figure 9.7** Ratio of the uptake fluxes to a fractal and a spherical particle as a function of the fractal dimension and  $R_g/a$ .

For typical soot aggregates in the upper troposphere/lower stratosphere the enhancement factor is in the range 2.7 to 3.5 (Figure 9.9). This is an order of magnitude lower than that used in modelling studies [126].

It should be borne in mind that there are limitations in the theory developed by Coelho *et al.* [131] and Bekki *et al.* [132]. The uptake on the soot surface is assumed to be a pseudo-first-order process in the framework, but uptake can be a complex multistep process [134, 135], depending on the environmental conditions. Also, carbonaceous particles can contain a very large organic fraction that is mixed with an insoluble fraction composed predominantly of elemental carbon. The organic fraction is also strongly reactive [136].

Surface area distributions are also of great interest in applications to possible adverse health effects of ultrafine atmospheric aerosols and to the monitoring of the products of nanoparticle aerosol reactors. In the past, such calculations have been

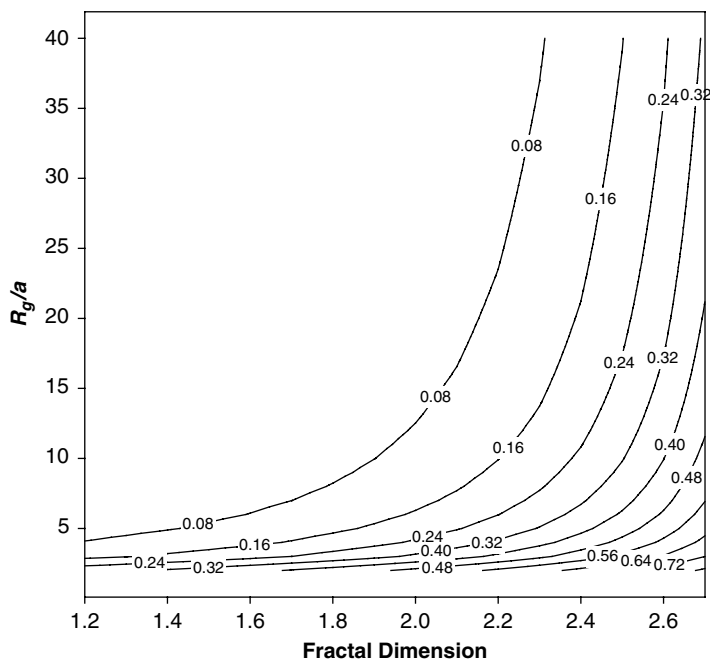


**Figure 9.8** Ratio of the mass of a fractal to that of a spherical particle as a function of the fractal dimension and  $R_g/a$ .

based on time-consuming image analysis of electron micrographs of individual chain aggregates. However, recently, a method has been described which makes it possible to relate aggregate surface area and volume distributions to the electrical mobility diameter [137, 138]. This method is only applicable for aggregates composed of uniform primary particles, with all surfaces directly exposed to collisions with molecules from the surrounding gas, i.e. a mass fractal dimension less than two. The analysis takes into account the friction coefficient and charging efficiency of chain aggregates, under the assumption that the primary particles composing the aggregates are at least one order of magnitude smaller than the mean free path of the surrounding gas.

Lall and Friedlander [138] compared the surface area and the volume of aggregates with those of a sphere with an equivalent mobility diameter. Their results indicate that the surface area distributions are somewhat underpredicted if the calculations are based on the assumption of spherical particles. However, the volume distributions are greatly overpredicted, by an order of magnitude in some cases. Figure 9.10 shows the difference in the surface area distribution for spherical particles and idealised aggregates. For a primary particle of 18.5 nm diameter the difference in peak heights of the distributions was 17 % and the total aggregate surface area based on mobility diameter is underpredicted by about 15 %. For smaller primary particles, the ratio of

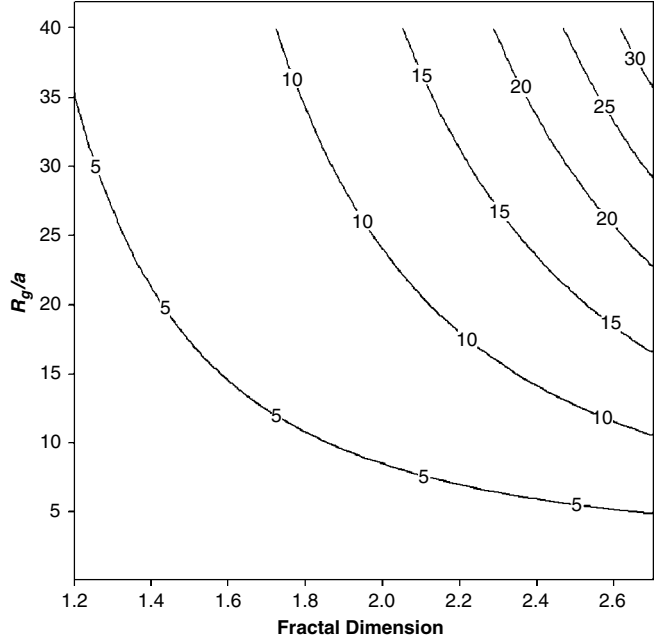


**Figure 9.9** Fractal surface area enhancement as a function of the fractal dimension and  $R_g/a$ .

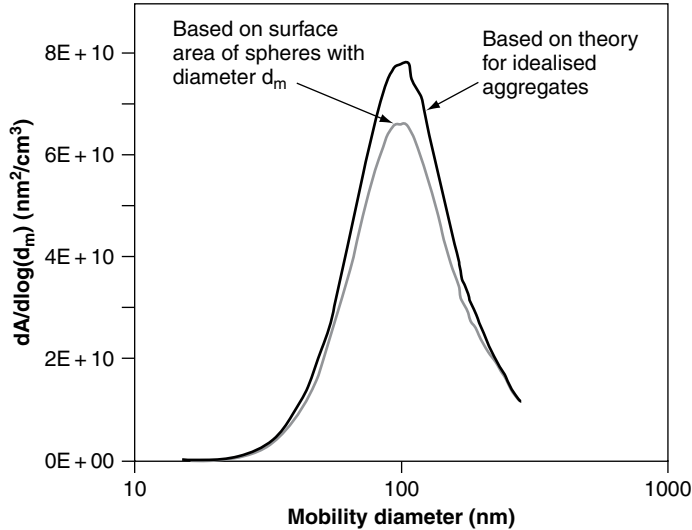


**Figure 9.10** Surface area distribution based on spherical particles compared with the surface area distribution for silver aggregates using the theory of Lall *et al.* [138] for idealized aggregates. Primary particle size:  $18.5 \pm 3.5$  nm. Reproduced with permission of Elsevier.

the surface area of the aggregates to that of spheres with the same mobility diameter is expected to be much higher.

Aggregate volumes calculated from the theory agreed well with those measured by electron microscopy. The precision of the technique is limited by the accuracy of estimation of charge distribution on aggregates, which is about 10 %. Hence, this method appears to give realistic information on aggregate volumes and surface areas without the use of electron microscopy. Therefore, it should be possible to determine aggregate surface area and volumes in real time without time-consuming image analysis.

Section 9.3.3 reported that the fractal morphology may be altered in the atmosphere. This restructuring modifies the surface area available for heterogeneous reactions. Adsorption and exchange of molecules at the surface also lead to partial or complete saturation of the chemically active sites. However, the results demonstrate that accounting for the fractal morphology of carbonaceous aggregates can substantially improve calculations of their properties or dynamics. Errors in deriving soot surface areas or uptake rates may prevent quantitative analysis of the impact of soot on atmospheric chemistry.

## 9.4 CONCLUSIONS AND RECOMMENDATIONS

Many physical characteristics of aerosols are determined by combinations of their size and morphology. However, morphology is often ignored, despite its influence on the drag force and, hence, transport properties. Transport properties determine how particles deposit, and how they are size-classified by aerosol instrumentation. There is evidence that aggregate morphology influences injury to lung cells [139]. Aggregate surface areas depend on their morphology and may be much larger than that of compact particles. Larger surface areas may result in the adsorption of increased amounts of biochemically active chemical components within the lungs. Morphology is also central to light scattering by aerosols and so is crucial to the climate change debate. Atmospheric processing may also lead to changes in the fractal dimensions of aggregate particles, as they undergo cloud processing and/or grow by condensation. Recent measurements have shown that optical absorption by black carbon plays an important role in direct radiative effects of aerosols. In polluted atmospheres, the forcing effects of aerosol absorption can be equal in magnitude to scattering. Therefore, the optical properties of coated and uncoated aggregate soot particles need to be well understood. Also, hygroscopicity influences the tendency of particles to form cloud droplets, and may influence deposition in the lung or elsewhere. It is very likely that the fractal properties of coated hygroscopic particles would change during cloud processing, and such changes would lead to changes in optical and transport properties. Morphology also plays an important role in source apportionment, where it can be used to differentiate between chemically similar particles created by different processes. Collision

rates among fractal structures are higher than those for spherical particles and this probably reduces atmospheric residence times.

The characterisation of particle shape has been an active research area and source of contention for over 50 years. The application of fractal geometry to aerosol science lies in the necessity to parameterise complex aerosol shapes, such as those produced by combustion processes. Both computer simulation and experiments have been important in establishing our knowledge of fractal aggregates. Various in-situ techniques have been presented allowing the fractal dimension of both a single aggregate and an ensemble to be calculated.

In many industrial applications, aerosol particles with a well-defined structure are needed. Therefore, methods are required to determine the geometrical structure of aggregated aerosol particles. Moreover, these methods should be able to monitor small and fast structural changes of the aggregates. Then, one would be able to investigate the influences of the production conditions upon the resulting aggregate structure. The determination of structure after deposition of the aggregates on, for example, a filter can lead to wrong results and needs much preparation and evaluation time. In contrast to the sampling methods, in-situ methods are fast and do not suffer from large influences on the particle structure. With both the boundary and mass fractal dimension, some information is lost. However, each measurement method yields different details and there is diagnostic information on formation dynamics of the aerosol embedded in the fractal structure.

The fractal characterization of aerosols has received increasing attention in recent years. Progress has been made in the study of such aspects as the hydrodynamic, diffusional, optical and elastic properties of fractal objects. However, little is known of the electrical properties of fractal aerosols. It is important both from basic and technological points of view to extend theories and experiments to fractals. The charging of fractal materials can give rise to interesting new phenomena which are not usually encountered in compact materials. The charging of low-density structures (e.g. smokes) could lead to their break-up; the possibility of restructuring them into more compact clusters could lead to a dramatic enhancement in their electrical mobilities. This result may have industrial applications in electrostatic precipitators for the removal of fractal clusters.

There are indications that the fractal dimension of atmospheric aggregates are dependent on the time of day, suggesting that this may be used as an indicator of aerosol sources, or the history of aggregates prior to sampling. On-line methods for measuring particle morphology in the ultrafine region would contribute to an understanding of the nature and significance of shape in engineered nanoparticles. These methods would further advance the ability to characterise aerosol exposure and flux measurements in terms of particle number, surface area and mass, and would contribute to reconciling disparate measures of aerosol properties that are dependent on particle morphology. From the engineering view point, such measurements could provide rapid feedback on particle morphology and structure to monitor and control generation processes.

**LIST OF SYMBOLS AND ABBREVIATIONS**

DLA	diffusion-limited aggregation
DLCA	diffusion-limited cluster aggregation
DMA	differential mobility analyser
ELPI	electrical low-pressure impactor
FBM	fractional Brownian motion
RLCA	reaction-limited cluster aggregation
SEM	scanning electron microscopy
SMPS	scanning mobility particle sizer
TEM	transmission electron microscopy
$a$	monomer radius
$A_a$	projected area of the aggregate
$A_p$	mean projected area of primary particles
$C$	arbitrary constant
$C_\infty$	concentration away from the aggregate
$d_a$	aerodynamic diameter
$D$	gas diffusion coefficient
$D_e$	Euclidean dimension
$D_f$	fractal dimension
$D_{fL}$	fractal dimension when the maximum projected length is treated as the characteristic size
$d_h$	hydrodynamic diameter
$d_m$	mobility diameter
$d_p$	diameter of the individual spherules
$d_v$	volume equivalent diameter
$d_{va}$	particle diameter in the free molecular regime
$D_S$	structural fractal dimension
$D_T$	textural fractal dimension
$E$	electric field strength
$E_s$	surface area enhancement
$H$	Hurst coefficient
$I(q)$	scattered intensity
$J_f$	mass flux to fractal
$J_{\text{sphere}}$	mass flux to sphere
$K_s$	surface reaction rate constant
$L$	maximum projected length
$m$	mass of a sphere
$m_f$	mass of a fractal
$M_p$	particle mass
$N$	number of primary particles
PeDa	Peclet–Dahmköhler number
$q$	scattered wave vector

$R_g$	radius of gyration
$v_i$	velocity of cluster $i$
$V_{TS}$	terminal velocity
$\alpha$	empirical projected area exponent
$\varepsilon$	fractal prefactor
$\theta$	scattering angle
$\Lambda$	incremental length
$\lambda$	wavelength
$\Phi$	fuel equivalence ratio

## REFERENCES

- [1] Ramanathan, V., Crutzen, P.J., Lelieveld, J., Mitra, A.P., Althausen, D., Anderson, J., Andreae, M.O., Cantrell, W., Cass, G.R., Chung, C.E., Clarke, A.D., Coakley, J.A., Collins, W.D., Conant, W.C., Dulac, F., Heintzenberg, J., Heymsfield, A.J., Holben, B., Howell, S., Hudson, J., Jayaraman, A., Kiehl, J.T., Krishnamurti, T.N., Lubin, D., McFarquhar, G., Novakov, T., Ogren, J.A., Podgorny, I.A., Prather, K., Priestley, K., Prospero, J.M., Quinn, P.K., Rajeev, K., Rasch, P., Rupert, S., Sadourny, R., Satheesh, S.K., Shaw, G.E., Sheridan, P. and Valero, F.P.J. (2001). Indian Ocean experiment: an integrated analysis of the climate forcing and effects of the great Indo-Asian haze. *J. Geophys. Res. Atmos.*, **106**, 28 371–28 398.
- [2] Ackerman, A.S., Toon, O.B., Stevens, D.E., Heymsfield, A.J., Ramanathan, V. and Welton, E.J. (2000). Reduction of tropical cloudiness by soot. *Science*, **288**, 1042–1047.
- [3] Chughtai, A.R., Kim, J.M. and Smith, D.M. (2003). The effect of temperature and humidity on the reaction of ozone with combustion soot: implications for reactivity near the tropopause. *J. Atmos. Chem.*, **45**, 231–243.
- [4] Forest, S.R. and Witten, T.A. (1979). Long-range correlations in smoke particle aggregates. *J. Appl. Phys. A*, **12**, L109–L117.
- [5] Witten, T.A. and Sander, L.M. (1981). Diffusion-limited aggregation, a kinetic critical phenomenon. *Phys. Rev. Lett.*, **47**, 1400–1403.
- [6] Kaye, B. (1993). *Chaos and Complexity*. VCH, Weinheim.
- [7] Wu, M.K. and Friedlander, S.K. (1993). Note on the power-law equation for fractal-like aerosol aggregates. *J. Colloid Interface Sci.*, **159**, 246–248.
- [8] Cai, J., Lu, N.L. and Sorensen, C.M. (1995). Analysis of fractal cluster morphology parameters – structural coefficient and density autocorrelation function cutoff. *J. Colloid Interface Sci.*, **171**, 470–473.
- [9] Samson R.J., Mulholland, G.W. and Gentry, J.W. (1987). Structural analysis of soot aggregates. *Langmuir*, **3**, 272–281.
- [10] Brasil, A.M., Farias, T.L. and Carvalho, M.G. (2000). Evaluation of the fractal properties of cluster–cluster aggregates. *Aerosol Sci. Technol.*, **33**, 440–454.
- [11] Oh, C. and Sorensen, C.M. (1997). The effect of overlap between monomers on the determination of fractal cluster morphology. *J. Colloid Interface Sci.*, **193**, 17–25.
- [12] Sorensen, C.M. and Roberts, G.C. (1997). The prefactor of fractal aggregates. *J. Colloid Interface Sci.*, **186**, 447–452.
- [13] Kaye, B. (1989). *A Random Walk Through Fractal Dimensions*. VCH, Weinheim.
- [14] Smirnov, B.M. (1990). The properties of fractal clusters. *Phys. Rep. Rev. Sect. Phys. Lett.*, **188**, 1–78.
- [15] Viscek, T. (1992). *Fractal Growth Phenomena*. World Scientific, San Francisco, CA.

- [16] Oh, C. and Sorensen, C.M. (1998). Structure factor of diffusion-limited aggregation clusters: local structure and non-self-similarity. *Phys. Rev. E*, **57**, 784–790.
- [17] Meakin, P. (1984). Effects of cluster trajectories on cluster-cluster aggregation – a comparison of linear and Brownian trajectories in two-dimensional and three-dimensional simulations. *Phys. Rev. A*, **29**, 997–999.
- [18] Baron, P.A., Sorensen, C.M. and Brockmann, J.E. (2001). Nonspherical particle measurements: shape factors, fractals and fibers. In *Aerosol Measurement*, 2nd edition, Baron, P.A. and Willeke, K. (eds). Wiley Interscience, New York, pp. 705–749.
- [19] Meakin, P. (1999). A historical introduction to computer models for fractal aggregates. *J. Sol–Gel Sci. Technol.*, **15**, 97–117.
- [20] Schaeffer, D.W. (1988). Fractal models and the structure of materials. *MRS Bull.*, **13**, 1023–1027.
- [21] Huang, P.F., Turpin, B.J., Pihl, M.J., Kittelson, D.B. and McMurry, P.H. (1994). Effects of water condensation and evaporation on diesel chain aggregate morphology. *J. Aerosol Sci.*, **25**, 447–459.
- [22] Cleary, T., Samson, R. and Gentry, J.W. (1990). Methodology for fractal analysis of combustion aerosols and particle clusters. *Aerosol Sci. Technol.*, **12**, 518–525.
- [23] Katrinak, K.A., Rez, P., Perkes, P.R. and Buseck, P.R. (1993). Fractal geometry of carbonaceous aggregates from an urban aerosol. *Environ. Sci. Technol.*, **27**, 539–547.
- [24] Oh, C. and Sorensen, C.M. (1999). Scaling approach for the structure factor of a generalized system of scatterings. *J. Nanopart. Res.*, **1**, 369–377.
- [25] Tence, M., Chevalier, J.P. and Jullien, R. (1986). On the Measurement of the fractal dimension of aggregated particles by electron-microscopy – experimental method, corrections and comparison with numerical models. *J. Phys. (Paris)*, **47**, 1989–1998.
- [26] Rogak, S.N. and Flagan, R.C. (1992). Characterization of the structure of aggregate particles. *Part. Part. Syst. Char.*, **9**, 19–27.
- [27] Brasil, A.M., Farias, T.L. and Carvalho, M.G. (1999). A recipe for image characterization of fractal-like aggregates. *J. Aerosol Sci.*, **30**, 1379–1389.
- [28] Wentzel, M., Gorzawski, H., Naumann, K.H., Saathoff, H. and Weinbruch, S. (2003). Transmission electron microscopical and aerosol dynamical characterization of soot aerosols. *J. Aerosol Sci.*, **34**, 1347–1370.
- [29] Voss, R.F. (1984). Multiparticle fractal aggregation. *J. Stat. Phys.*, **36**, 861–872.
- [30] Colbeck, I. (1995). Fractal analysis of aerosol particles. *Anal. Proc.*, **32**, 383–386.
- [31] Colbeck, I. and Nyeki, S. (1992). Optical and dynamical investigations of fractal clusters. *Sci. Prog.*, **76**, 149–166.
- [32] Bonczyk, P.A. and Hall, R.J. (1992). Measurement of the fractal dimension of soot using uv laser radiation. *Langmuir*, **8**, 1666–1670.
- [33] Sorensen, C.M., Cai, J. and Lu, N. (1992). Light scattering measurements of monomer size, monomers per aggregate, and fractal dimension for soot aggregates in flames. *Appl. Opt.*, **31**, 6547–6557.
- [34] Schmidt-Ott, A. (1988). In-situ measurement of the fractal dimensionality of ultrafine aerosol particles. *Appl. Phys. Lett.*, **52**, 954–956.
- [35] Kutz, S. and Schmidt-Ott, A. (1990). Use of a low-pressure impactor for fractal analysis of submicron particles. *J. Aerosol Sci.*, **21**, S47–S50.
- [36] Wu Z.F., Colbeck, I. and Simons, S. (1994). Determination of the fractal dimension of aerosols from kinetic coagulation. *J. Phys. D Appl. Phys.*, **27**, 2291–2296.
- [37] Nyeki, S. and Colbeck, I. (1994). The measurement of the fractal dimension of individual in-situ soot aggregates using a modified Millikan cell technique. *J. Aerosol Sci.*, **25**, 75–90.
- [38] Nyeki, S. and Colbeck, I. (1995). Fractal dimension analysis of single, in-situ, restructured carbonaceous aggregates. *Aerosol Sci. Technol.*, **23**, 109–120.



- [39] Weber, A.P., Baltensperger, U., Gaggeler, H.W. and Schmidt-Ott, A. (1996). In situ characterization and structure modification of aggregated aerosol particles. *J. Aerosol Sci.*, **27**, 915–929.
- [40] Mountain, R.D. and Mulholland, G.W. (1988). Light scattering from simulated smoke aggregates. *Langmuir*, **4**, 1321–1326.
- [41] Zhang, H.X., Sorensen, C.M., Ramer, E.R., Olivier, B.J. and Merklin, J.F. (1988). In-situ optical structure factor measurements of an aggregating soot aerosol. *Langmuir*, **4**, 867–871.
- [42] Gangopadhyay, S., Elminyawi, I. and Sorensen, C.M. (1991). Optical structure factor measurements of soot particles in a premixed flame. *Appl. Opt.*, **30**, 4859–4864.
- [43] Sorensen, C.M. (2001). Light scattering by fractal aggregates: a review. *Aerosol Sci. Technol.*, **35**, 648–687.
- [44] Di Stasio, S. (2001). Observation of restructuring of nanoparticle soot aggregates in a diffusion flame by static light scattering. *J. Aerosol Sci.*, **32**, 509–524.
- [45] Riefler, N., di Stasio, S. and Wriedt, T. (2004). Structural analysis of clusters using configurational and orientational averaging in light scattering analysis. *J. Quant. Spectrosc. Radiat. Transfer*, **89**, 323–342.
- [46] Di Stasio, S., Konstandopoulos, A.G. and Kostoglou, M. (2002). Cluster–cluster aggregation kinetics and primary particle growth of soot nanoparticles in flame by light scattering and numerical simulations. *J. Colloid Interface Sci.*, **247**, 33–46.
- [47] Sorensen, C.M. and Hageman, W.B. (2001). Two-dimensional soot. *Langmuir*, **17**, 5431–5434.
- [48] Wang, G.M. and Sorensen, C.M. (1999). Diffusive mobility of fractal aggregates over the entire Knudsen number range. *Phys. Rev. E*, **60**, 3036–3044.
- [49] Kim, H.W. and Choi, M. (2003). In situ line measurement of mean aggregate size and fractal dimension along the flame axis by planar laser light scattering. *J. Aerosol Sci.*, **34**, 1633–1645.
- [50] Schmidt-Ott, A. (1988). New approaches to in-situ characterization of ultrafine aggregates. *J. Aerosol Sci.*, **19**, 553–563.
- [51] Weber, A.P. and Friedlander, S.K. (1997). In situ determination of the activation energy for restructuring of nanometer aerosol agglomerates. *J. Aerosol Sci.*, **28**, 179–192.
- [52] Karlsson, M.N.A., Deppert, K., Karlsson, L.S., Magnusson, M.H., Malm, J.O. and Srinivasan, N.S. (2005). Compaction of agglomerates of aerosol nanoparticles: a compilation of experimental data. *J. Nanopart. Res.*, **7**, 43–49.
- [53] Park, K., Cao, F., Kittelson, D.B. and McMurry, P.H. (2003). Relationship between particle mass and mobility for diesel exhaust particles. *Environ. Sci. Technol.*, **37**, 577–583.
- [54] DeCarlo, P.F., Slowik, J.G., Worsnop, D.R., Davidovits, P. and Jimenez, J.L. (2004). Particle morphology and density characterization by combined mobility and aerodynamic diameter measurements. Part 1: theory. *Aerosol Sci. Technol.*, **38**, 1185–1205.
- [55] Schmidt-Ott, A., Baltensperger, U., Gaggeler, H.W. and Jost, D.T. (1990). Scaling behaviour of physical parameters describing aggregates. *J. Aerosol Sci.*, **21**, 711–717.
- [56] Colbeck, I. (1998). *Physical and Chemical Properties of Aerosols*. Blackie Academic and Professional, London
- [57] Rogak, S.N., Flagan, R.C. and Nguyen, H.V. (1993). The mobility and structure of aerosol aggregates. *Aerosol Sci. Technol.*, **18**, 25–47.
- [58] Van Gulijk, C., Marijnissen, J.C.M., Makkee, M., Moulijn, J.A. and Schmidt-Ott, A. (2004). Measuring diesel soot with a scanning mobility particle sizer and an electrical low-pressure impactor: performance assessment with a model for fractal-like agglomerates. *J. Aerosol Sci.*, **35**, 633–655.
- [59] Slowik, J.G., Stainken, K., Davidovits, P., Williams, L.R., Jayne, J.T., Kolb, C.E., Worsnop, D.R., Rudich, Y., DeCarlo, P.F. and Jimenez, J.L. (2004). Particle morphology

- and density characterization by combined mobility and aerodynamic diameter measurements. Part 2: application to combustion-generated soot aerosols as a function of fuel equivalence ratio. *Aerosol Sci. Technol.*, **38**, 1206–1222.
- [60] Burtcher, H., Kunzel, S. and Hüglin, C. (1998). Characterization of particles in combustion engine exhaust. *J. Aerosol Sci.*, **29**, 389–396.
- [61] Burtcher, H. (2000). Characterization of ultra fine particle emissions from combustion systems. *Soc. Automot. Eng.: Tech. Pap. Ser.*, SAE 2000-01-1997.
- [62] Schleicher, B., Kunzel, S. and Burtcher, H. (1995). In-situ measurement of size and density of submicron aerosol particles. *J. Appl. Phys.*, **78**, 4416–4422.
- [63] Skillas, G., Kunzel, S., Burtcher, H., Baltensperger, U. and Siegmann, K. (1998). High fractal-like dimension of diesel soot aggregates. *J. Aerosol Sci.*, **29**, 411–419.
- [64] McMurry, P.H., Wang, X., Park, K. and Ehara, K. (2002). The relationship between mass and mobility for atmospheric particles: a new technique for measuring particle density. *Aerosol Sci. Technol.*, **36**, 227–238.
- [65] Ehara, K., Hagwood, C. and Coakley, K.J. (1996). Novel method to classify aerosol particles according to their mass-to-charge ratio – aerosol particle mass analyser. *J. Aerosol Sci.*, **27**, 217–234.
- [66] Maricq, M.M., Podsiadlik, D.H. and Chase, R.E. (2000). Size distributions of motor vehicle exhaust PM: a comparison between ELPI and SMPS measurements. *Aerosol Sci. Technol.*, **33**, 239–260.
- [67] Virtanen, A., Ristimäki, J. and Keskinen, J. (2004). Method for measuring effective density and fractal dimension of aerosol aggregates. *Aerosol Sci. Technol.*, **38**, 437–446.
- [68] Maricq, M.M. and Xu, M. (2004). The effective density and fractal dimension of soot particles from premixed flames and motor vehicle exhaust. *J. Aerosol Sci.*, **35**, 1251–1274.
- [69] Kutz, S. and Schmidt-Ott, A. (1992). Characterization of aggregates by condensation induced restructuring. *J. Aerosol Sci.*, **23**, S357–S360.
- [70] Smallwood, G.J., Clavel, D., Gareau, D., Sawchuk, R.A., Witze, P.O., Axelsson, B., Bachalo, W.D. and Gulder, O.L. (2002). Concurrent quantitative laser-induced incandescence and SMPS measurements of EGR effects on particulate emissions from a TDI diesel engine. *Soc. Automot. Eng.: Tech. Pap. Ser.*, SAE 2002-01-2715.
- [71] Cai, J., and Sorensen, C.M. (1994). Diffusion of fractal aggregates in the free molecular regime. *Phys. Rev. E*, **50**, 3397–3400.
- [72] Meakin, P. and Jullien, R. (1988). The effects of restructuring on the geometry of clusters formed by diffusion-limited, ballistic, and reaction-limited cluster cluster aggregation, *J. Chem. Phys.*, **89**, 246–250.
- [73] Colbeck, I. and Wu, Z. (1994). Measurement of the fractal dimensions of smoke aggregates. *J. Phys. D: Appl. Phys.*, **27**, 670–675.
- [74] Colbeck, I., Eleftheriadis, K. and Simons, S. (1989). The dynamics and structure of smoke aerosols. *J. Aerosol Sci.*, **20**, 875–878.
- [75] Colbeck, I., Nyeki, S. and Wu, Z. (1992). In situ measurement of the fractal dimension of aerosols. *J. Aerosol Sci.*, **23**, S365–S368.
- [76] Rogak, S.N. and Flagan, R.C. (1990). Stokes drag on self-similar clusters of spheres. *J. Colloid Interface Sci.*, **134**, 206–218.
- [77] Nyeki, S., Colbeck, I. and Kaye, B.H. (1994). Measurement of the fractal dimension of individual soot aggregates in two and three dimensions. In *Proceedings of Fourth International Aerosol Conference*, 29 August–2 September, Los Angeles, pp. 32–33.
- [78] Meakin, P., Donn, B. and Mulholland, G.W. (1989). Collisions between point masses and fractal aggregates. *Langmuir*, **5**, 510–518.
- [79] Megaridis, C.M. and Dobbins, R.A. (1990). Morphological description of flame-generated materials. *Combust. Sci. Technol.*, **71**, 95–109.

- [80] Koylu, U.O., Xing, Y.C. and Rosner, D.E. (1995). Fractal morphology analysis of combustion-generated aggregates using angular light scattering and electron microscope images. *Langmuir*, **11**, 4848–4854.
- [81] Park, K., Kittelson, D.B. and McMurry, P.H. (2004). Structural properties of diesel exhaust particles measured by transmission electron microscopy (TEM): relationships to particle mass and mobility. *Aerosol Sci. Technol.*, **38**, 881–889.
- [82] Naumann, K.H. (2003). COSIMA – a computer program simulating the dynamics of fractal aerosols. *J. Aerosol Sci.*, **34**, 1371–1397.
- [83] Luo, C.H., Wen, C.Y., Liaw, J.J., Chiu, S.H. and Lee, W.M.G. (2004). Texture characterization of atmospheric fine particles by fractional Brownian motion analysis. *Atmos. Environ.*, **38**, 935–940.
- [84] Luo, C.H., Lee, W.M.G., Lai, Y.C., Wen, C.Y. and Liaw, J.J. (2005). Measuring the fractal dimension of diesel soot agglomerates by fractional Brownian motion processor. *Atmos. Environ.*, **39**, 3565–3572.
- [85] Gwaze, P., Schmid, O., Annegarn, H.J., Andreae, M.O., Huth, J. and Helas, G. (2006). Comparison of three methods of fractal analysis applied to soot aggregates from wood combustion. *J. Aerosol Sci.*, **37**, 820–838.
- [86] Kutz, S. (1994). In-situ Methoden zur Bestimmung von Struktureigenschaften gasgetragener Aggregate. PhD thesis, University of Duisburg.
- [87] Lepperhof, G., Stommel, P., Luers, B. and Searles, R.A. (2000). Vehicle study on the impact of diesel fuel sulfur content on the performance of DeNox catalysts and the influence of DeNox catalysts on particle size and number. *Soc. Automot. Eng.: Tech. Pap. Ser.*, SAE 2000-01-1877.
- [88] Colbeck, I., Atkinson, B. and Johar, Y. (1997). The morphology and optical properties of soot produced by different fuels. *J. Aerosol Sci.*, **28**, 715–723.
- [89] Chakrabarty, R.K., Moosmuller, H., Garro, M.A., Arnott, W.P., Walker, J., Susott, R.A., Babbitt, R.E., Wold, C.E., Lincoln, E.N. and Ha, W.M. (2006). Emissions from the laboratory combustion of wildland fuels: particle morphology and size. *J. Geophys. Res.*, **111**, D07204. DOI: 10.1029/2005JD006659
- [90] Liu, B.Y.B., Srinivasachar, S. and Helble, J.J. (2000). The effect of chemical composition on the fractal-like structure of combustion-generated inorganic aerosols. *Aerosol Sci. Technol.*, **33**, 459–469.
- [91] Hurd, A.J. and Flower, W.L. (1988). In situ Growth and Structure of Fractal Silica Aggregates in a Flame, *J. Colloid Interface Sci.*, **122**, 178–192.
- [92] Martin, J.E., Schaefer, D.W. and Hurd, A.J. (1986). Fractal geometry of vapor-phase aggregates. *Phys. Rev. A*, **33**, 3540–3543.
- [93] Sinha, S.K., Fretøft, T. and Kjems, J.K. (1984). Observations of power law correlations in silica particle aggregates by small-angle neutron scattering. In *Kinetics of Aggregation and Gelation*, Family, F. and Landau, D.P. (eds). North-Holland, New York, pp. 87–90.
- [94] Xing, Y., Rosner, D.E., Koylu, U.O. and Tandon, P. (1997). Morphological evolution of nanoparticles in diffusion flames: measurements and modelling. *AIChE J.*, **43**, 2641–2649.
- [95] Jullien, R., Kolb, M. and Botet, R. (1984). Aggregation by kinetic clustering of clusters in dimensions  $D$  greater than 2, *J. Phys. Lett. (Paris)*, **45**, L211–L216.
- [96] Kim, W.Y., Sorensen, C.M., Fry, D. and Chakrabarti, A. (2006). Soot aggregates, superaggregates and gel-like networks in laminar diffusion flames. *J. Aerosol Sci.*, **37**, 386–401.
- [97] Kim, W., Sorensen, C.M. and Chakrabarti, A. (2004). Universal occurrence of soot super-aggregates with a fractal dimension of 2.6 in heavily sooting laminar diffusion flames. *Langmuir*, **20**, 3969–3973.
- [98] Sorensen, C.M., Kim, W., Fry, D., Shi, D. and Chakrabarti, A. (2003). Observation of soot superaggregates with a fractal dimension of 2.6 in laminar acetylene/air diffusion flames. *Langmuir*, **19**, 7560–7563.

- [99] Fry, D., Chakrabarti, A., Kim, W. and Sorsensen, C.M. (2004). Structural crossover in dense irreversibly aggregating particulate systems. *Phys. Rev. E*, **69**, art. no. 061401.
- [100] Murr, L.E. and Bang, J.J. (2003). Electron microscope comparisons of fine and ultra-fine carbonaceous and non-carbonaceous, airborne particulates. *Atmos. Environ.*, **37**, 4795–4806.
- [101] Xie, Y., Hopke, P.K., Casuccio, G. and Henderson, B. (1994). Use of multiple fractal dimensions to quantify airborne particle shape. *Aerosol Sci. Technol.*, **20**, 161–168.
- [102] Kindratenko, V.V., Vanespen, P.J.M., Treiger, B.A. and Vangrieken, R.E. (1994). Fractal dimensional classification of aerosol particles by computer-controlled scanning electron microscopy. *Environ. Sci. Technol.*, **28**, 2197–2202.
- [103] Lee, C.T. and Chou, C.C.K. (1994). Application of fractal geometry in quantitative characterization of aerosol morphology. *Part. Part. Syst. Char.*, **11**, 436–441.
- [104] Dye, A.L., Rhead, M.M. and Trier, C.J. (2000). The quantitative morphology of roadside and background urban aerosol in Plymouth, UK. *Atmos. Environ.*, **34**, 3139–3148.
- [105] Xiong, C. and Friedlander, S.K. (2001). Morphological properties of atmospheric aerosol aggregates. *Proc. Nat. Acad. Sci. U.S.A.*, **98**, 11 851–11 856.
- [106] Mulholland, G.W., Samson, R.J., Mountain, R.D. and Ernst, M.H. (1988). Cluster size distribution for free molecular agglomeration. *Energ. Fuels*, **2**, 481–486.
- [107] McDonald, R. and Biswas, P. (2004). A methodology to establish the morphology of ambient aerosols. *J. Air Waste Manage. Assoc.*, **54**, 1069–1078.
- [108] McDonald, R., Hu, S.H., Martuzevicius, D., Grinshpun, S A., LeMasters, G. and Biswas, P. (2004). Intensive short term measurements of the ambient aerosol in the Greater Cincinnati airshed. *Aerosol Sci. Technol.*, **38**, 70–79.
- [109] Johnson, K.S., Zuberi, B., Molina, L.T., Molina, M.J., Iedema, M.J., Cowin, J.P., Gaspar, D.J., Wang, C. and Laskin, A. (2005). Processing of soot in an urban environment: case study from the Mexico City Metropolitan Area. *Atmos. Chem. Phys.*, **5**, 3033–3043.
- [110] Zuberi, B., Johnson, K.S., Aleks, G.K., Molina, L.T. and Laskin, A. (2005). Hydrophilic properties of aged soot. *Geophys. Res. Lett.*, **32**, art. no. L01807.
- [111] Li, J., Anderson, J.R. and Buseck, P.R. (2003). TEM study of aerosol particles from clean and polluted marine boundary layers over the North Atlantic. *J. Geophys. Res. Atmos.*, **108**, art. no. 4189.
- [112] Hallett, J., Hudson, J.G. and Rogers, C.F. (1989). Characterization of combustion aerosols for haze and cloud formation. *Aerosol Sci. Technol.*, **10**, 70–83.
- [113] Jullien, R. and Meakin, P. (1989). Simple models for the restructuring of 3-dimensional ballistic aggregates. *J. Colloid Interface Sci.*, **127**, 265–272.
- [114] Kantor, Y. and Witten, T.A. (1984). Mechanical stability of tenuous objects. *J. Phys. Lett. (Paris)*, **45**, L675–L679.
- [115] Colbeck, I., Appleby, L., Hardman, E.J. and Harrison, R.M. (1990). The optical properties and morphology of cloud-processed carbonaceous smoke. *J. Aerosol Sci.*, **21**, 527–538.
- [116] Ramachandran, G. and Reist, P.C. (1995). Characterization of morphological changes in aggregates subject to condensation and evaporation using multiple fractal dimensions. *Aerosol Sci. Technol.*, **23**, 431–442.
- [117] Mikhailov, E.F., Vlasenko, S.S., Kramer, L. and Niessner, R. (2001). Interaction of soot aerosol particles with water droplets: influence of surface hydrophilicity. *J. Aerosol Sci.*, **32**, 697–711.
- [118] Weingartner, E., Baltensperger, U. and Burtscher, H. (1995). Growth and structural change of combustion aerosols at high relative humidity. *Environ. Sci. Technol.*, **29**, 2982–2986.
- [119] Lioussse, C., Cachier, H. and Jennings, S.G. (1993). Optical and thermal measurements of black carbon aerosol content in different environments – variation of the specific attenuation cross-section, sigma. *Atmos. Environ. Part A: Gen. Top.*, **27**, 1203–1211.

- [120] Zhang, X.Q., Turpin, B.J., McMurry, P.H., Hering, S.V. and Stolzenburg, M.R. (1994). Mie theory evaluation of species contributions to 1990 wintertime visibility reduction in the Grand Canyon. *J. Air Waste Manage. Assoc.*, **44**, 153–162.
- [121] Friedlander, S.K., Jang, H.D. and Ryu, K.H. (1998). Elastic behaviour of nanoparticle chain aggregates. *Appl. Phys. Lett.*, **72**, 173–175.
- [122] Ogawa, K., Vogt, T., Ullmann, M., Johnson, S. and Friedlander, S.K. (2000). Elastic properties of nanoparticle chain aggregates of  $\text{TiO}_2$ ,  $\text{Al}_2\text{O}_3$ , and  $\text{Fe}_2\text{O}_3$  generated by laser ablation. *J. Appl. Phys.*, **87**, 63–73.
- [123] Suh, Y.J. and Friedlander, S.K. (2003). Origins of the elastic behaviour of nanoparticle chain aggregates: measurements using nanostructure manipulation device, *J. Appl. Phys.*, **93**, 3515–3523.
- [124] Karcher, B. (1999). Aviation-produced aerosols and contrails, *Surv. Geophys.*, **20**, 113–167.
- [125] Fichter, C., Marquart, S., Sausen, R. and Lee, D.S. (2005). The impact of cruise altitude on contrails and related radiative forcing, *Meteorol. Z.*, **14**, 563–572.
- [126] Bekki, S. (1997). The possible role of aircraft-generated soot in the middle latitude ozone depletion. *J. Geophys. Res. Atmos.*, **102**, 10 751–10 758.
- [127] Hauglustaine, D.A., Ridley, B.A., Solomon, S., Hess, P.G. and Madronich, S. (1996).  $\text{HNO}_3/\text{NO}_x$  ratio in the remote troposphere during MLOPEX 2: evidence for nitric acid reduction on carbonaceous aerosols? *Geophys. Res. Lett.*, **23**, 2609–2612.
- [128] Lary, D.J., Shallcross, D.E., and Toumi, R. (1999). Carbonaceous aerosols and their potential role in atmospheric chemistry. *J. Geophys. Res. Atmos.*, **104**, 15 929–15 940.
- [129] Lary, D.J., Lee, A.M., Toumi, R., Newchurch, M.J., Pirre, M. and Renard, J.B. (1997). Carbon aerosols and atmospheric photochemistry. *J. Geophys. Res. Atmos.*, **102**, 3671–3682.
- [130] Kleffmann, J. and Wiesen, P. (2005). Heterogeneous conversion of  $\text{NO}_2$  and NO on  $\text{HNO}_3$  treated soot surfaces: atmospheric implications. *Atmos Chem. Phys.*, **5**, 77–83.
- [131] Coelho, D., Bekki, S., Thovet, J.F. and Adler, P.M. (2000). Uptake on fractal particles 1. Theoretical framework. *J. Geophys. Res. Atmos.*, **105**, 3905–3916.
- [132] Bekki, S., David, C., Law, K., Smith, D.M., Coelho, D., Thovet, J.F. and Adler, P.M. (2000). Uptake on fractal particles 2. Applications. *J. Geophys. Res. Atmos.*, **105**, 3917–3928.
- [133] Blake, D.F. and Kato, K. (1995). Latitudinal distribution of black carbon soot in the upper troposphere and lower stratosphere, *J. Geophys. Res. Atmos.*, **100**, 7195–7202.
- [134] Chughtai, A.R., Brooks, M.E. and Smith, D.M. (1996). Hydration of black carbon. *J. Geophys. Res. Atmos.*, **101**, 19 505–19 514.
- [135] Smith, D.M. and Chughtai, A.R. (1996). Reaction kinetics of ozone at low concentrations with *n*-hexane soot. *J. Geophys. Res. Atmos.*, **101**, 19 607–19 620.
- [136] De Gouw, J.A. and Lovejoy, E.R. (1998). Reactive uptake of ozone by liquid organic compounds. *Geophys. Res. Lett.*, **25**, 931–934.
- [137] Lall, A.A. and Friedlander, S.K. (2006). On-line measurement of ultrafine aggregate surface area and volume distributions by electrical mobility analysis: I. Theoretical analysis. *J. Aerosol Sci.*, **37**, 260–271.
- [138] Lall, A.A., Seipenbusch, M., Rong, W. and Friedlander, S.K. (2006). On-line measurement of ultrafine aggregate surface area and volume distributions by electrical mobility analysis: II. Comparison of measurements and theory. *J. Aerosol Sci.*, **37**, 272–282.
- [139] Carero, A.D.P., Hoet, P.H.M., Verschaeve, L., Schoeters, G. and Nemery, B. (2001). Genotoxic effects of carbon black particles, diesel exhaust particles, and urban air particulates and their extracts on a human alveolar epithelial cell line (A549) and a human monocytic cell line (THP-1). *Environ. Mol. Mutagen.*, **37**, 155–163.



---

# Index

---

Page references in bold type refer to tables; those in italics to figures.

- Achlya bisexualis* **251**  
Acidification 210  
Actinomycetes 247  
Activated sludge 254–5  
Adsorption  
    Brunauer–Emmet–Teller (BET)  
        modelling 186–91  
    dyes 206  
    inside porous networks 192–4  
    kinetics 183–4  
    from liquid mixtures 198  
    modelling 181–2  
    monolayer capacity 181–4  
    on nonuniform surfaces 199–200  
        no-correlation models 200–2  
    of polymers onto colloid surfaces  
        134–7  
    soils 208–12  
Aerosols  
    atmospheric 293–6  
    restructuring 296–301  
Agar 249  
Aggregates  
    aerosol 276, 279–80  
    chain 273, 296–301  
    definition 69  
    mass fractal dimension 72  
    mass scaling 70  
Aggregation 6–7  
    aerosols 285–6  
        superaggregates 292  
    cluster–cluster, *see* Cluster–cluster  
        aggregation  
    determining factor and fractal dimension  
        119–20  
    diffusion-limited 61, 122–3, 233, 276  
    humic materials 231–2  
    iron compounds 155–7  
        with phosphate 157–9  
    iron oxyhydroxides 153–66  
    iron–silica complexes 164–5  
    kinetics 121–2  
    overview 111–12  
    reaction-limited 6, 119–20, 231  
    *see also* Coagulation  
Algorithms, image analysis 90–4  
Alkalinization 210  
Analytic techniques 5, **103–4**, 150,  
    151–3  
    aerosols 277–89  
        mobility methods 281–6  
        other 286–7  
    flocculation 132–3  
    humic materials 223–6  
    scattering, *see* Scattering techniques  
    settling velocity measurement  
        97–101  
    X-ray microtomography 96–7  
Aperture impedance particle sizing  
    101–2  
Applications  
    aerosol analysis  
        atmospheric aerosols 293–6  
        soots 290–3  
    humic materials 233–4  
Aquatic particles 112–16  
Aquatic samples, humic compounds  
    229–30  
*Armillaria luteus* 248, **251**  
*Aspergillus niger* 250, **251**  
Atmospheric samples, heterogeneous  
    reactions 302–4



- Bacillus subtilis* 247
- Bacteria 85, 95  
   in artificial media 246–8  
   in environment 254–5  
   phenotypic plasticity 239–40
- Bentonite 206
- Binomial fractal measure 55–6, 57–9
- Biological samples 86
- Biomass soot 289, 291
- Bolzano–Weierstrass functions 22–4
- Boundary fractal dimension, *see* surface  
   fractal, dimension, aerosols
- Box-counting 33–5, 34, 90–2  
   microorganisms 242–4
- Bridging flocculation 130–7
- Brinkman's law 139–40
- Brownian motion 26–8, 288–9
- Brunauer–Emmett–Teller (BET) adsorption  
   modelling 186–91, 197  
   on heterogeneous surfaces 202–3
- Cambisols 309–10
- Cantor set 13–15, 21, 31
- Cantor singular function 15–17, 16, 42
- Capillary condensation 192–3
- Carbohydrates 209
- Carbonaceous materials 198, 273
- Casein gels 95–6
- Cation exchange, and fractal dimension  
   205–6
- Chain aggregates 273  
   restructuring 296–301
- Characteristic length scale 225
- Charcoal 197
- Chord length measurement 101, **105**
- Citrobacter freundii* 246
- Clays 204–5  
   adsorption behaviour 196  
   adsorption characteristics 182
- Cloud-burning effect 299
- Cluster–cluster aggregation (CCA) 6  
   fragmentation 122–8  
   heterogeneous particles 128–30  
   particle interactions 117–19  
   reaction- and diffusion-limited  
     mechanisms 119–20  
   scaling laws 121
- Coagulants 149
- Coagulation 111–12  
   in environment 149–50  
   *see also* Aggregation
- Coal ash 291, **292**
- Coastlines 35, 41
- Coltricia perennis* **252**
- Confocal microscopy 94–6, **104**
- Contrast  
   and aggregate radius 168–9  
   and fractal dimension 167–8  
   neutrons 86–7  
   optical  
     and form factor 170–1  
     and lighting 90, 91  
   X-rays 86
- Cutoff functions 79
- Cutoff length 44–5
- Debye–Hückel potential 135
- Density autocorrelation function 76–8
- Density fractal dimension, *see* Mass fractal,  
   dimension
- Derjaguin, Landau, Verwey, Overbeek  
   (DLVO) theory 117–19, 149–50
- Devil's staircase 13–18
- Diesel particulates 289–90
- Differential mobility analyser (DMA) 283
- Diffusion  
   inorganic compounds 155–6  
   nutrients 266–7
- Diffusion-limited aggregation (DLA) 61,  
   122–3, 233  
   aerosols 276  
   and multifractal measures 61
- Diffusion-limited cluster aggregation  
   (DLCA) 6, 119–20, 276  
   humic materials 231  
   restructuring 122–3
- Dissolved organic carbon (DOC) 210–211
- Divider 92–3
- DLA, *see* Diffusion-limited aggregation
- Drag 97–8
- Dubinin–Astakhov (DA) isotherm 194
- Dubinin–Radushkevich (DR) isotherm  
   192–3
- Dyes 206  
   adsorption 206
- Ectomycorrhizal fungi 255, 256
- Elastic properties, chain aggregates 300–1
- Electrical low-pressure impactor (ELPI)  
   283–4
- Electron microscopy 5  
   humic acid 229



- Elemental composition, humic fractions 223
- Engine load, and fractal dimension (of particle) 290–1
- Escherichia coli* 246, 248, 266
- Exponential distributions 46–7
- Extended edge X-ray absorption fine structure (EXAFS) spectroscopy 154
- Flocs 133, 150  
   bacterial 245, 248  
   in sludge 254–5  
   large 166–71  
   structural parameters 150
- Fly ash **292**
- Focused beam reflectance measurement (FBRM) 101
- Form factor 76–8  
   and contrast 169–71
- Fractal dimension 1, 2, 4–5, 42, 275  
   and adsorption energy 202–3  
   aerosols, limitations of characterization 285  
   and aggregate radius 114  
   bacterial colonies 246–7  
   in environment 254–5  
   and cation exchange 205–6  
   definition 43  
   determination 4–5, 52–4  
     from adsorption data  
       experiments 195–9  
       monolayer capacity 181–4  
       thermodynamic method 184–6  
     adsorption methods  
       monolayer capacity 181–4  
       thermodynamic 184–6  
   aerodynamic methods 281–6  
   aerosols 277  
   algorithms 90–4  
   box-counting 33–5, 91–2, 242–4  
   by optical scattering 77–87  
   divider 35, 93  
   Hausdorff 28–32  
   microorganisms, box-counting method 242–5  
   other methods 36–7  
   similarity 32–3
- flocs 133, 150  
   large 166–71
- fungi  
   change with time 257–8  
   in environment 255–6  
   environmental factors 262–3  
   mycelial, in culture **251–3**  
   and nutrient status **259–60**  
   humic substances **227–8**, 232–3  
   impermeable aggregates, and settling velocity 138–9  
   and inner cutoff length 44–5  
   microorganisms  
     concentric ring technique 241–2  
     *see also* Fractal dimension, fungi  
   and optical contrast 167–8  
   and permeability 139  
   pore 3, 180  
     soils 210  
   superaggregates 293  
   surface  
     and adsorption 180–1  
     measurement 183–4  
     thermodynamic method 184–6  
   peat soils 209  
   and topological dimension 275  
   and uptake flux 303  
   variation with scale 73–4
- Fractals  
   classification **3**  
   definition 2, 42–3  
   natural vs. theoretical 43–4
- Fractal scaling, in natural systems 71–4
- Fractal structure, measurement 70–1
- Fractional Brownian motion 26–8, 288–9
- Fracture cascade 49–52, 51, 52
- Fragmentation fractals 49–52
- Fragmentation processes 122–8
- Frenke–Halsey–Hill (FHH) isotherm 191–4, 196
- Fuels 290–1
- Fulvic acid 21, 222, 223, **227–8**
- Fungi  
   incubation 255–6  
   mycelial 242, 248–54  
     growth patterns, invertebrate grazing 264–5  
   phenotypic plasticity 239  
   unicellular 246–8
- Gaussian noise 26, 27
- Geometric fractals 48
- Geometric transparency 87–8
- Gliding box algorithm 38–9
- Goethites 196–7
- Grazing 264–5

- Haematite, flocculation 132–3  
 Hausdorff dimension 28–32, 42  
 Health hazard assessment 273, 303–4  
 Heavy metals, and fungal growth 249  
 Heteroaggregation 128–30  
 Heterogeneous reactions, aerosols 301–6  
 Hilbert's curve 18  
 Hölder exponent 36, 57  
 Honey fungi 257  
 Humic acid 221, 222, 223, **227**, **228**  
 Humic materials  
   analytic techniques 223–5  
   definition 221  
   particle structure 226–31  
 Humidity 296–301  
 Humin 221, 222, 223, **228**  
 Hydrolysis ratio  
   and iron polymer size 154  
   and scattering intensity, iron  
     complexes 160  
*Hypholoma fasciculare* **259**, 261  
  
 Image analysis  
   algorithms 90–4  
   microscopy 94–6  
   preprocessing 89–90  
     and fractal dimension estimation 52–4  
   fungi 242  
   principles 87–9  
   resolution (of image) 243–5  
 Inductively coupled plasma optical emission  
   spectrometry 283  
 Inner cutoff length 4, 45  
 Inoculum 258–61  
 International Humic Substances Society  
   (IHSS) 232  
 Invertebrate grazing 264–5  
 Iron oxides and hydroxides 153–66  
 Iron–silica complexes 159–66  
 Iron trichloride 154–5, 156  
 Iron trinitrate 154  
 Irregular fractal aggregates 113  
 Isotherms  
   adsorption, heterogeneous surfaces 199  
   Brunauer–Emmet–Teller (BET)  
     186–91  
   Dubinin–Radushkevich (DR) 192–3  
   Frenk–Halsey–Hill (FHH) 191–4,  
     196  
   Kiselev 184–5  
   Kaolinite 204, 205, 207  
   Kinematic coagulation, aerosols 286  
   Kinetics  
     adsorption 183–4  
     aggregation 6, 119–20, 121–2  
     bridging flocculation 131–3  
   Kirkwood–Riseman theory 140  
   Kiselev isotherm 184–5  
   *Klebsiella* bacteria 246  
  
*Laccaria bicolor* **253**  
*Lactarius hepaticus* **253**  
 Lacunarity 37–40  
   and nutrient diffusion 266–7  
 Latex 95, 169–71  
 Lennard–Jones function 191  
 Ligands, competition 157–9  
 Light microscopy  
   lighting and contrast 90, 91  
   and microbial flocs 246  
 Light scattering techniques, aerosols  
   279–81  
 Luvisols 208–9  
  
*Macrophomina phaseolina* **253**  
 Magnesium compounds 197–8  
 Mass exponent 58–9, 58  
 Mass fractal 3, 4, 180  
   definition 45  
   dimension 3, 4, **115**  
     humic materials 226  
 Mass-mobility relationship 281–3  
 Mass, scaling with size 70, 114–16  
 Matushita fracture cascade 49–50  
 Mean-field approximation 152  
 Menger sponge 20–1  
   and soil aggregates 44, 45  
 Mercury porosimetry 185–6  
 Metropolis algorithm 124–5, 135  
 Microbes  
   fractal dimension 240–6  
   interspecific interactions 263–4, **264**  
   *see also* Bacteria; Fungi  
 Microscopy 94–6, **104**  
   humic materials 225–6  
 Mie theory 299  
 Millikan cell 286, 287  
 Minkowski dimension, *see* Box-counting  
 Mobility diameter  
   and radius of gyration 284–5  
   and surface area 304–6, 305

- Modelling, heterogeneous surfaces 200
- Molecules, diameter, and monolayer capacity 181–3
- Monolayer capacity 181–4
- Monte Carlo simulations
- adsorption 198
  - polymers 134–7
- Montmorillonite 204, 205
- pillared 207
- Multifractal measures 54–61
- definition 60
  - parameters 56–9
- Multiplicative cascade 55–6, 60–1
- Mycelial structures 242, 244, 248–54, 255
- Navier–Stokes equations 140
- Necrotrophic fungi 256
- Nematodes 266
- Neutron scattering 86–7
- Nitrogen oxides, and soot 301
- Nucleation
- iron oxides and hydroxides 153–5
  - iron–silica complexes 160–2
- Nutrients
- availability, and fungal growth 258, **259–60**, 261
  - diffusion in soils 266–7
- Optical microscopy 94–6
- confocal 94–6, 104
- Optical scattering 80–1, 151–3, 166, 245–6
- aerosols 279
- Organic matter, and soil surface heterogeneity 210–211
- Paenibacillus dendritiformis* 246–7
- Palladium 207
- Pareto distribution 45–9
- Particle counting 101–2, **105**
- Particle number, and projected area 287
- Particle–particle forces, and aggregate rearrangement 124–5
- Particle size, and analytic technique choice 102
- Paxillus involutus* **253**
- Peano's curve 17–18, 42
- Peat soils 209, 211–12
- Perikinet aggregation 112
- Perimeter dimension, projected images 88
- Permeability, and settling velocity 139–40
- pH, humic acids 229
- Phallus impudicus* **259**, 261, 264
- Phanerochaete velutina* **259**, 261, 264
- Phosphates 157–9
- Pointwise dimension, *see* Mass fractal, dimension
- Polydispersity 79–80
- Polymers
- adsorption onto particle 134–7
  - 'bridging' in flocculation 130
  - iron, nucleation 154
- Pore fractal 3, 180, 210
- definition 45
- Pores
- adsorption 188, 194–5
  - networks, adsorption energies 202–3
- Power-law parametric relationships, *see* Scaling laws
- Predators 266
- Prefractals 44–5
- Preprocessing, images 89–90
- Pressure, and adsorption 186–91
- Probabilistic fractals 48
- Projected area dimension
- algorithms 93–4
  - and mass fractal dimension 87–8
  - and particle number 287
- Proteus mirabilis* bacteria 246
- Pycnoporus cinnabarinus* 254
- Quenched–annealed mixtures 212–13
- Radius of gyration, and mobility diameter 284–5
- Random fractals 1, 24
- Randomly methylated  $\beta$ -cyclodextrin (RAMEB) 207
- Rayleigh–Gans–Debye (RGD) formalism 75–6
- Reaction-limited aggregation (RLA), humic materials 231
- Reaction-limited cluster aggregation (RLCA) 6, 119–20
- Rearrangement (of aggregate particles) 123–8, 296–301, 306
- Regular fractal aggregates 113
- Rényi dimension 36–7, 59
- Resinicium bicolor* 258
- Restructuring 95, 123–8, 296–301, 306
- Reynolds number 98
- Ricci-Curbastro, Gregorio 11
- Richardson plot 277, 278

- Salmonella* bacteria 246
- Sample handling 95
- Samples
  - handling 74–5
  - lighting 90
  - in water, and X-ray scattering 86
- Sandbox algorithm 39, 93
  - and confocal microscopy 95
- SANS (small-angle neutron scattering) 5, 86–7
- Saprotrophic fungi 255, 256
- SAXS (small-angle X-ray scattering) 5, 151, 166
- Scale invariance, aerosols 274
- Scaling laws 45–9
  - aggregation 121–2
  - bridging flocculation 131–3
  - mass 70, 114–16
  - radius of gyration 115–16
- Scanning electron microscopy (SEM) 5
- Scattering techniques 75–87, **104**
  - and aerosols 279–81
  - compared with adsorption analysis 196–7
  - form and structure factors 76–8
  - humic materials 223–4, 223–6
  - neutron 5, 86–7
  - optical 80–5, 151–3, 166, 245–6
    - intensity 169–71
    - mean-field approximation 152
  - turbidimetry 5, 85, 224–5
  - principles 75–6
  - X-ray 151, 166, 223–4
- Segmentation (of images) 89
- Self-affinity 16
- Self-similarity 1, 42, 43, 113
  - multifractal measures 55–6
  - statistical 24
- Serratia marcescens* 246
- Settling velocity
  - aggregates
    - divergence from models 137
    - impermeable 137–9
    - permeable 139–40
  - measurement 97–101, **105**
- Shales 196
- Shearing, and fractal dimension 74–5
- Sierpinski carpet 20, 32, 37, 50
- Silicas 157, 159–65
  - adsorption behaviour 195–6
  - powders 199
- Silver aggregates 281, 283, 300
- Similarity dimension 32–3
- Simulations, optical scattering 167–9
- Single image microscopy 94
- Sludge 254–5
- Small-angle light scattering (SALS) 80–1
  - volume obscuration 81–5
- Small-angle multiple light scattering 85
- Small-angle neutron scattering (SANS) 5, 86–7
- Small-angle X-ray scattering (SAXS) 5, 151, 166
  - humic materials 223–4
- Smectite lamellae 205
- Smokes, fractal dimension **290**
- Smoluchowski equation 121, 123
- Soil 40–1, 44, 208–12
  - as habitat 265–7
  - soil minerals 204–7
- Solids, humic particles **228**
- Soot 273, 279–80, 282–3
  - fractal dimension, comparison 289–90
  - humidity-induced restructuring 296–300
- Stokes law, and settling velocity 138
- Stropharia caerulea* 258–61, **259**, 261, 263, **264**
- Structure factor 76–8, 77
- Superaggregates 291–2, 293
- Surface area, and uptake, aerosols 303–4
- Surface forces 117–19
  - and restructuring 124–8
- Surface fractal 3, 4
  - definition 45
  - dimension, aerosols 277
- Surfaces, mathematical, characterization 28–30
- Suspensions, humic particles **228**, 229
- Temperature, and fungal growth 262
- Tensor calculus 11–12
- Terminal velocity, aerosol clusters 286–7
- Thermal restructuring 300
- Thresholding 89–90
- Tomography 245–6
- Transmission electron microscopy (TEM) 5
  - humic acid 229
- Trichoderma viride* 248, **252**, 254
- Turbidimetry 5, 85, 224–5

Universality classes 120  
Uptake, onto aerosol particles  
301–3

van der Waals forces 117–19  
Vapor adsorption 5  
Variogram dimension 36–7  
Verwey–Overbeek potential 135  
Volume obscuration 81–5  
von Koch curve 18–20, 19, 24,  
183

Washburn relationship 185  
Weierstrass–Mandelbrot function 22–4, 23

X-ray microtomography 96–7  
X-ray scattering 86, 151, 166, 223–4

Yeasts 246, 248

Zeolites 197  
Zipf distribution 46  
*Zoogloea ramigera* 247–8